4th INTERNATIONAL CONFERENCE ON SIMULATION AND MODELLING IN THE FOOD AND BIO INDUSTRY

2006

FOODSIM'2006

EDITED BY

Paolo Masi

and

Gerardo Toraldo

JUNE 15-17, 2006

NAPLES, ITALY

A Publication of EUROSIS-ETI

4th International FOODSIM Conference

NAPLES, ITALY
JUNE 15-17, 2006

Organised by:
ETI- The European Technology Institute

Sponsored by
EUROSIS, The European Simulation Society

Co-Sponsored by

ENITIAA
Ghent University
NIZO Food Research
SISTAL

Hosted by

University of Naples Federico II
Naples, Italy

EXECUTIVE EDITOR

PHILIPPE GERIL
(BELGIUM)

EDITORS

General Conference Chairs

Paolo Masi, Universita' di Napoli, Federico II, Agricultural School, Portici, Italy
Gerardo Toraldo, Universita' di Napoli, Federico II, Agricultural School, Portici, Italy
Annalisa Romano, Universita' di Napoli, Federico II, Agricultural School, Portici, Italy

INTERNATIONAL PROGRAMME COMMITTEE

Simulation in Food Engineering and Processing
Thomas Becker, University of Hohenheim, Stuttgart, Germany
Martin Mitzscherling, University of Hohenheim, Stuttgart, Germany
Jean-Yves Monteau, ENITIAA, Nantes cedex 3, France
Rallou Thomopoulos, INRA - UMR IATE, Montpellier Cedex 1, France
Jan L. Top, Agrotechnology and Food Innovations B.V., Wageningen, The Netherlands
Maykel Verschueren, NIZO food research B.V, Ede, The Netherlands
Olivier Vitrac, INRA-UMR FARE, Reims Cedex 2, France

Simulation in Food Sciences and Biotechnology
Abdeltif Amrane, LARCIP-ENSCR Renner, France
Cédric Brandam, ENSIACET – INPT, Toulouse, France
Imogen Foubert, Ghent University, Ghent, Belgium

Simulation in Food Economics
Daniel Thiel, ENITIAA, Nantes, France

Methods and Tools Applied to Food and Bio-Industries
Christoph Hartmann, The German University in Cairo, Cairo, Egypt
Tomás O' Mathúna, Cork Institute of Technology, Cork, Ireland
Pierre-Sylvain Mirade, INRA-Theix, St.Genes Champanelle, France

Simulation and Training
Daniel Thiel, ENITIAA, Nantes, France

FOODSIM 2006

All articles published in this Proceedings have been peer reviewed

EUROSIS-ETI Publications are ISI-Thomson and INSPEC referenced

For permission to publish a complete paper write EUROSIS, c/o Philippe Geril, ETI Executive Director, Ghent University, Faculty of Engineering, Dept. of Industrial Management, Technologiepark 903, Campus Ardoyen, B-9052 Ghent-Zwijnaarde, Belgium.

EUROSIS is a Division of ETI Bvba, The European Technology Institute, Torhoutsesteenweg 162, Box 4, B-8400 Ostend, Belgium

Printed in Belgium by Reproduct NV, Ghent, Belgium
Cover Design by Grafisch Bedrijf Lammaing, Ostend, Belgium

EUROSIS-ETI Publication
ISBN: 90-77381-27-9

PREFACE

Mathematical and computing techniques play an important role in simulation, optimization and management of food processing techniques. Nowadays, as the availability of powerful and cheap hardware/software computational tools is strongly increased, the effectiveness and reliability of modelling procedure has became a valuable alternative and support to traditional experimental approach. In that respect, mathematical simulation is of paramount importance in, describing phenomena, solving problems, test new ideas for a better representation of reality.

This process derives from a sapient mixture of different and heterogeneous components, such as the capability to develop comprehensive and consistent mathematical models which depict with a fairly good degree of approximation food processes development, taking in the proper account the complex phenomena of physical, chemical and biological origin which take place, as well as the fine tuning of computational techniques either specifically devised for those applications or borrowed from other fields. Thus, the solution of these problems requires a strongly interdisciplinary approach in which mathematicians efforts is coupled to the technological needs of the food scientists.

During the last decades several research groups developed mathematical models with increasing relevance for practical application in the food area regarding risk analyses, food safety, fermentation, texture and flavour of food products, plant control, hardware automation, simulation in Food Sciences and Biotechnology, Food Production Management and Economics. The next frontier will be to implement these models to better respond to both R&D and process operation requirements. In doing this, new issues arise such as standardisation and coupling of different simulation models.

The 4th bi-annual FOODSIM conference, conceived in 2000 by Daniel Thiel from ENITIAA in cooperation with the European Simulation Office, will bring together model developers, food experts and (potential) industrial users of model simulation tools. Far from being exhaustive of the very exciting topic, the conference aim is to present a broad overview of the state-of-the-art in using computer models in development and operation of food products and also to give to the researchers in the field a unique opportunity to discuss and exchange ideas.

Finally we would like to thanks to all persons and organisations, which have contributed in making this appointment an international event. A special thanks is due also to Dr. A. Romano for her invaluable technical, scientific and practical help.

The local organizing committee is pleased to welcome all conference delegates and to wish them a nice stay in Naples. We hope that congress has significantly helped the development of mathematical modelling applied to the solution of the many problems in the food area and moreover the international cooperation.

Prof. Paolo Masi and Prof. Gerardo Toraldo

June 15-17, 2006
University of Naples Federico II, Naples, Italy

CONTENTS

CONTENTS

LIQUIDS PRODUCTION SIMULATION

PACKAGED FOODS SIMULATION

SPRAY-DRYING SIMULATION

HEAT TRANSFER SIMULATION

DIFFUSION AND DISPERSION

COMPLEX FOOD PRODUCTS

CONTENTS

FOOD QUALITY SIMULATION

SIMULATION TRAINING

POSTERS

LATE PAPERS

CONTENTS

SCIENTIFIC PROGRAMME

INDUSTRIAL SIMULATION PROCESS MODELS

A MODEL LIBRARY FOR DYNAMIC SIMULATION OF LIQUID FOOD PROCESS LINES

Tomas Skoglund[a,b] and Petr Dejmek[a]
[a]Department of Food Technology, Engineering and Nutrition
Lund Institute of Technology, Lund University
P.O. Box 124, SE-221 00 Lund, Sweden
[b]Tetra Pak Processing Systems
Ruben Rausings gata, SE-221 86 Lund, Sweden

KEYWORDS
Dynamic, Model, Simulation, Liquid Food, Processing

ABSTRACT

Ongoing work in developing a general structure and a comprehensive components library aiming at modelling liquid-food process lines is presented. The dynamic component models were developed in an object-oriented library structure based on the dynamic modelling language Modelica using the object-oriented graphical tool Dymola. The models were based on fundamental conservation laws and can simulate one-dimensional dynamics in liquid-food plants including process control, in terms of flows, pressures, temperatures and compositions. Novel solutions were proposed to handle varying fluid properties during changeover in heat exchangers. Examples of simulations of cream and milk pasteurisation, juice blending and flash boiling for de-aeration of juice are given[1].

INTRODUCTION

For many decades, as a means of cost-efficient development, the industry has taken advantage of dynamic simulation before manufacturing (Åström et al. 1998). In spite of its advantages it has been considered too expensive within the industrial field of engineering of liquid-food process lines. Hence it has been used only occasionally in special cases. However, gradual improvements in hardware and software have brought about increased computational power simultaneously with reduced costs. This has enabled simulation for engineering of liquid-food process lines on a more regular basis. Even though flow-sheeting, i.e. stationary simulation (e.g. NIZO Premia) and full CFD-simulation, e.g. (Straatsma et al. 1999a and Straatsma et al. 1999b) have been performed in food applications, to the best of or knowledge dynamic simulation of full liquid-food process lines has not been carried out before. Furthermore, a dynamic component library for this purpose has never been created before. This paper describes a case where process line dynamic simulation, including process control, is being introduced as a design tool in a process line supplier company. Based on the objective of fast configuration of process lines, a general component library was first created based on the dynamic modelling language Modelica (Skoglund 2003) that enables full time resolution of complete production lines including a full range of the most interesting physical/chemical variables (Skoglund 2003).
To achieve sufficient accuracy with computational efficiency, in-depth studies were undertaken of fluid transitions in heat exchangers (Skoglund et al. 2006) as well as fluid dispersion and chemical reaction (in preparation). In this article an overview of achievements and possibilities are described. The novelty of the work is the over all capacity of the library as well as the separately reported ability to efficiently simulate fluid transitions in heat exchangers.

THE DYNAMIC MODEL LIBRARY

Modern dynamic modelling tools are equation based, i.e. take care of symbolic handling and sorting of the equations and eventually also solves them. These features relieve the modeller from much work that instead can be focused on the mathematical formulations of the phenomena, e.g. physical or chemical. A basic decision was taken to avoid black box models as much as possible. In the present work the equations are a mixture of ordinary differential equations (ODE) and algebraic equations (AE). In liquid-food applications it means that physical/chemical mechanisms are approximated with bulk properties (i.e. lumped models) since no partial differential equations are dealt with. In spite of that, the important flow-direction space coordinate is taken into account by axial discretization of some models, e.g. heat exchangers and pipes.
The design decisions are further influenced by intended users and usage (Skoglund 2003). Also the model builders' aspects need to be considered. Examples of important programming efficiency features are object orientation, heritage and graphical interface.

Physical equations and model variables

The models were described in terms of equations of two types. The first type concerns the fundamental laws of conservation:

- mass conservation
- energy conservation (thermal)
- volume conservation (incompressibility)
- momentum conservation

The other type of equations concerns empirical engineering design correlations, e.g. Fanning friction factor or convective heat transfer coefficient.
Beside these, fluid properties (density, specific heat capacity, viscosity etc.) as functions of temperature and composition (water, carbohydrates, fat, etc) are an integral part of the environment.

[1] A standard PC was used: Dell Optiplex SX270 with Intel® Pentium® 4 CPU 3.2 GHz, 1.0 GB RAM.

With the above set of equations, the system was able to calculate dynamically many physical properties in the system whereof the most fundamental are

- temperatures
- flow rates
- pressures
- concentrations

Library structure

A hierarchical model structure is used, with models and model fragments that are used as building blocks in a "Modeller's area" and parameterized instances of component models representing physical process components in a "User's area", Figure 1.

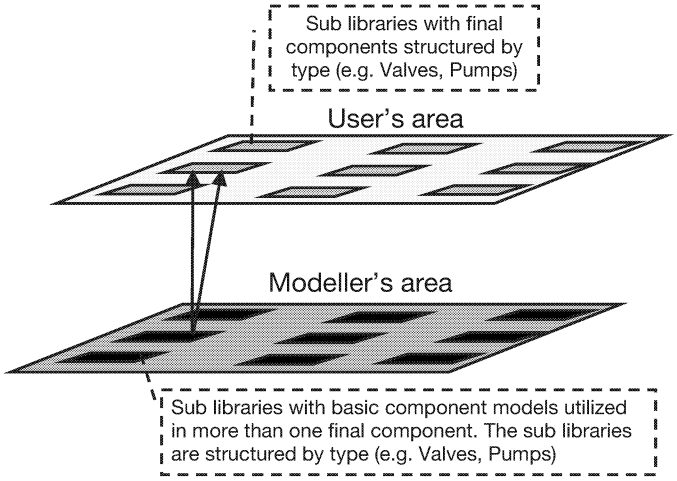

Figure 1: Library Structure

Figure 2 shows how the possibility of building hierarchies with heritage was utilized in the case of some vessels.

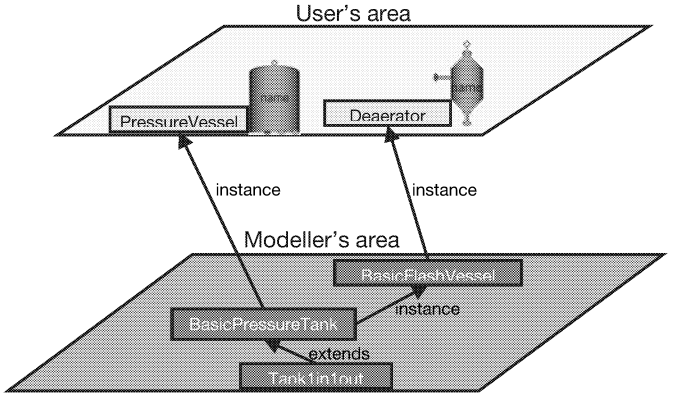

Figure 2: Library Hierarchy to Reuse Common Code

Modelling language

Given the requirement that the modelling tool should support solving of DAEs (system of ODEs and AEs) we have chosen Modelica (Modelica Association; Mattsson et al. 1998; Tiller 2001) that has proven its capacity in some different branches, e.g. thermodynamic systems (Eborn 2001; Elmqvist et al. 2003; Tummseheit 2002). The chosen Modelica platform was Dymola (Supplied by Dynasim AB) that provides graphical interface, compiler and solvers. Figure 3 shows a view of the user interface when accessing the "Food Processing" library.

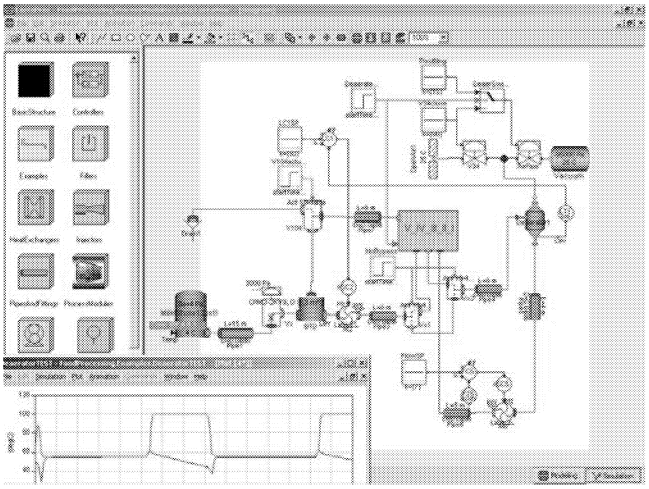

Figure 3: User Interface of the Modelling Tool, Displaying the Library (left), a System Model (middle) together with the Plot of a Simulation (lower left)

From the library of dynamic component models a system is built by graphical "drag-and-drop" and graphical connections. The component characteristics are assigned via parameter lists associated individually to each instance of a component.

HEAT EXCHANGER MODELS

There is a great deal in the literature about dynamic modelling and simulation of heat exchangers e.g. (Lakshmanan et al. 1994; Romie 1984; Romie 1999; Xuan and Roetzel 1993), but a specific requirement of food industry is to predict the transient changes, e.g. when product is changed or product flushed. As an important part of this work dynamic heat exchanger models were developed to deal with arbitrary changes in flow rates, temperatures and fluid compositions (Skoglund et al. 2006).

Model validation

The dynamic heat-exchanger models were validated with pilot plant experiments (Kauhanen 2001). The experiments were conducted with arbitrary changes in flow rate and temperature for counter-current flow as well as for co-current flow. Figure 4 shows the corresponding simulation set-up into which the recorded input values of flow and temperature were fed.

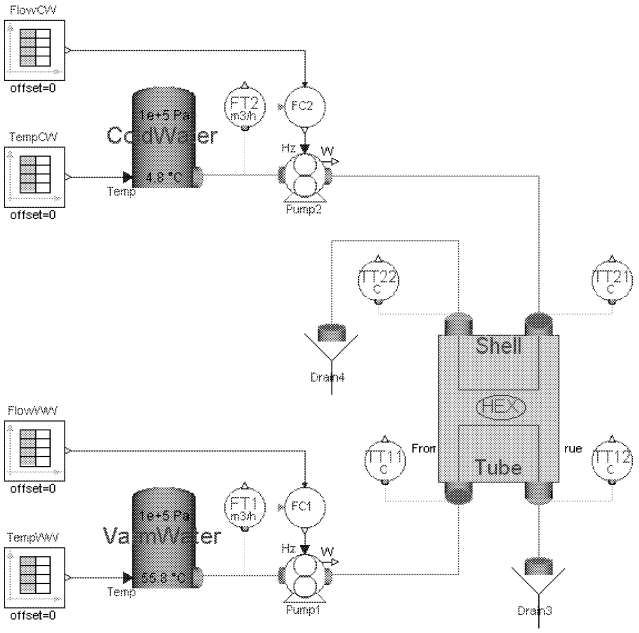

Figure 4: Simulation Set-up of Experiment for Validation of Heat-Exchanger models

Two different experimental results are shown in Figures 5 and 6 together with the result from corresponding simulation.

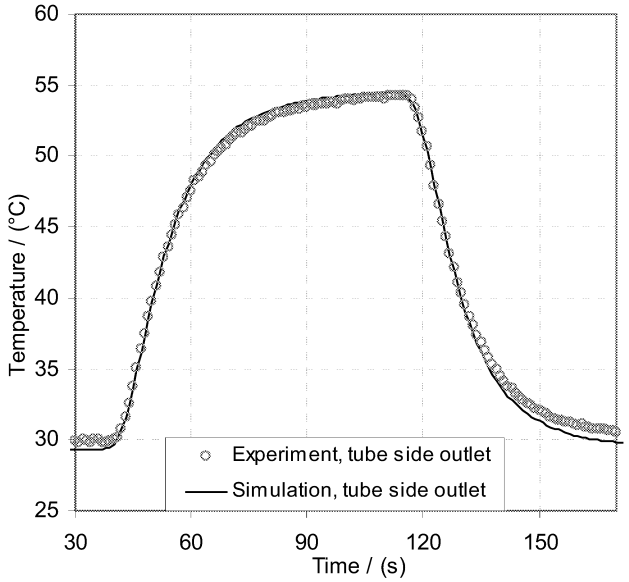

Figure 5: Experimental and Simulated Response of a Temperature Step Up/Down at the Shell Side Inlet of a Co-Current Tubular Heat Exchanger

Also frequency analysis was used to estimate how well the model fits with experimental data over a range of frequencies. This was carried out by process identification based on experimental data as well as on data from simulations. These two identified transfer functions were then used to calculate amplitude and phase shift over a frequency range. Figure 7 shows such a comparison of experiment with simulation, where the simulations were carried out with different discretization (very low; N=2 and medium; N=6). Both the amplitude and the phase shift lies close together over the analysed frequency range.

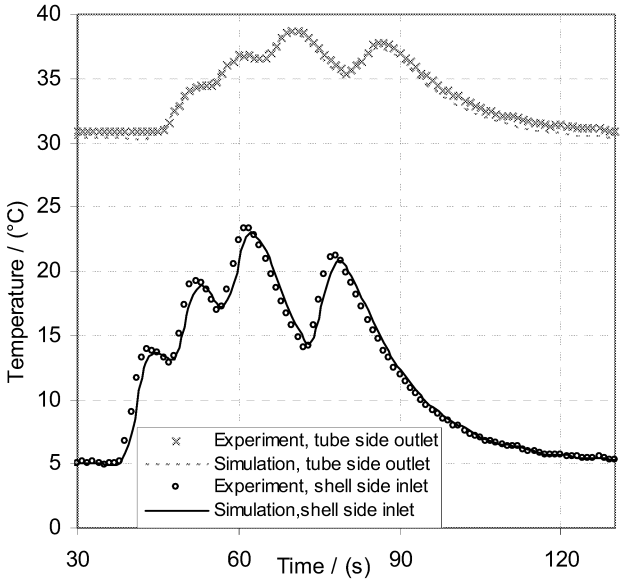

Figure 6: Experimental and Simulated Response of an "arbitrary" Temperature Perturbation at the Shell Side Inlet of a Co-Current Tubular Heat Exchanger

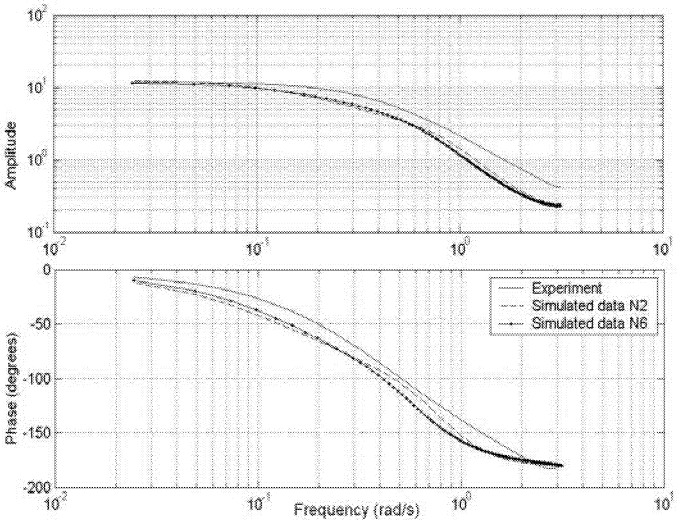

Figure 7: Frequency Analysis of Data from Experiment and Simulation

Fluid transition

With validated heat-exchanger models the work proceeded with introduction of fluid transitions.
The difference between the above heat exchanger model compared with traditional dynamic models was that (i) the heat capacity of the metal separating the cold side from the hot side was included in the model, and (ii) the fluid transport time was handled directly in the model by a true transport delay handling. The latter improved the model performance when simulating fluid transitions with a reasonable computational time increase. Figure 8 shows a system configuration that was applied to simulate this.

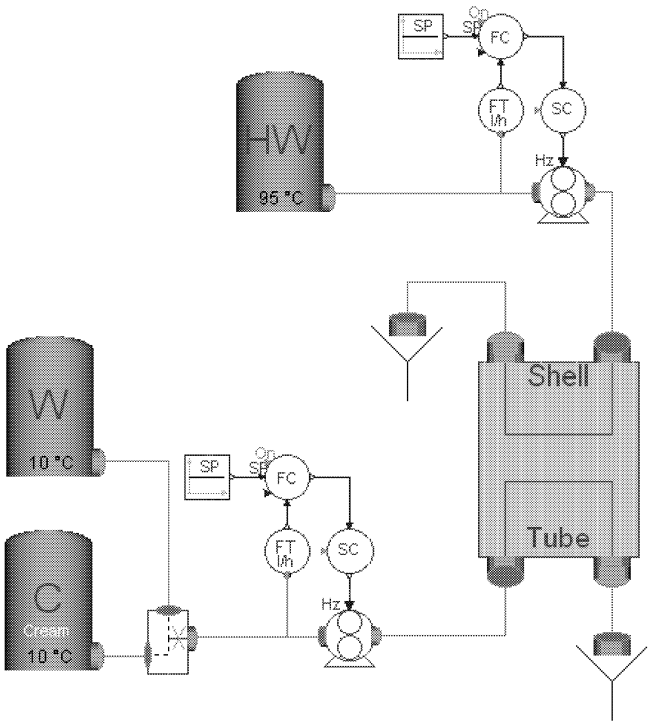

Figure 8: The System Configuration that was applied to Simulate Fluid Transitions Water-Cream-Water

Simulations were performed to prove the model's computational efficiency. An example of such a fluid-transition simulation is shown in Figure 9a. The first transition is when cream (with 15% fat) pushes water, and vice versa in the second transition. The first transition starts at 100 s and the latter starts at 200 s.

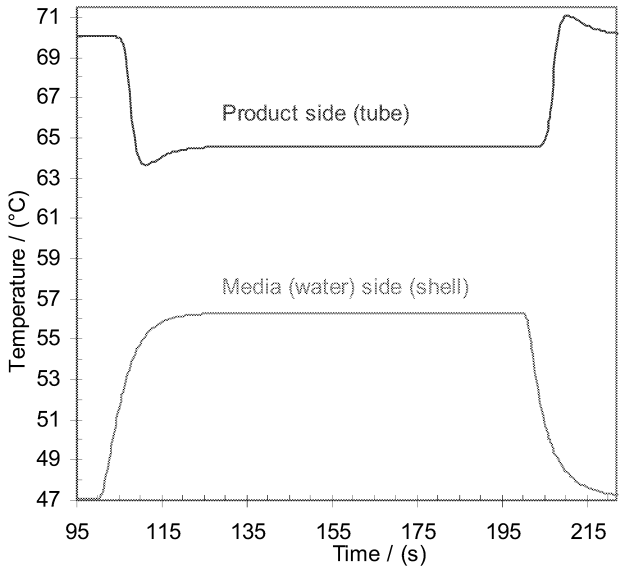

Figure 9a: Outlet Temperatures at Simulated Fluid Transitions in a Heat Exchanger. The Transition from Water to Cream Starts at 100 s and the Transition from Cream to Water Starts at 200 s.

Figure 9b shows a part of Figure 9a including also the simulation result when using a more traditional model. At equal discretization the computational load was approximately the same, but the simulated temperature of the new model was closer to the exact solution. (The number of heat transfer units in the channels varies during the transition and are in the range from 1.1 to 1.7.)

The degree of discretization determines the achieved accuracy. Figure 9b shows simulation results with low discretization (N=5, i.e. 5 control volumes) and high discretization (N=80) for both models. When increasing the discretization, both models converged to the same solution, shown as curves lying close together for N=80. However, at lower discretization the simulation results of the new model were much closer to the convergent solution, which is clearly visible in the figure. Results from more simulations of both models are compiled in Figure 9c. The conclusion from these simulations was that to achieve a certain accuracy the new model required less discretization compared to the traditional model, corresponding to approximately 10 times less computation time.

Further details of the model are reported in (Skoglund et al 2006)

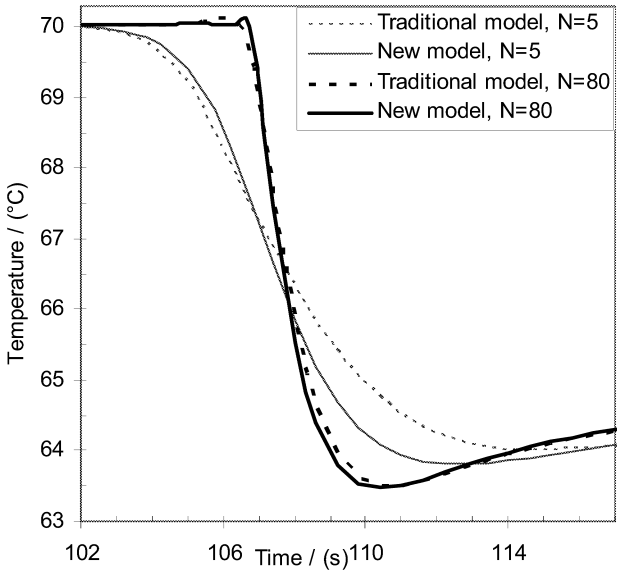

Figure 9b: Expanded View of the Product Temperature (in the Tube) during the first Transition in Figure 9a for both a Traditional Model and the New Model, for Low (N=5) and High (N=80) Discretization. The Curves Clearly Indicates the Faster Convergence of the New Model

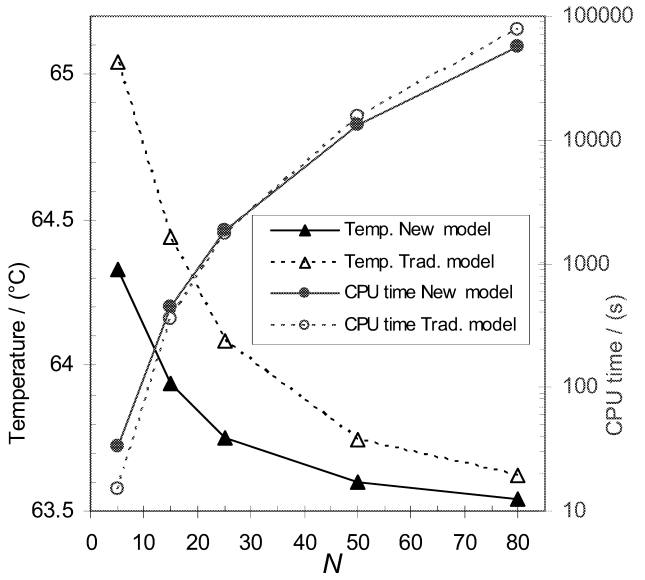

Figure 9c: As an Indication of Convergence, the Temperature at 110 s is Shown for the Traditional and New Model as a Function of Degree of Discretization. The Required CPU Time is also Shown as a Function of Degree of Discretization.

To further analyse the propagation of the cream during the fill-up, the simulated temperature profiles in the heat-exchanger tube were plotted. The result is shown in Figure 10 at different moments in time. The dotted (red) line shows the stationary temperature profile at the beginning of the transition (at 100.0 s) just when the cream enters the tube (channel 1). The dashed (blue) line shows the stationary temperature profile when stable after the transition (at 150.0 s) when channel 1 is filled with cream. Of particular interest is the temperature profile at time 108.8 s in channel 1, which shows an exit temperature lower than the final stationary temperature. It corresponds to the temperature dip visible in Figures 9a and 9b.

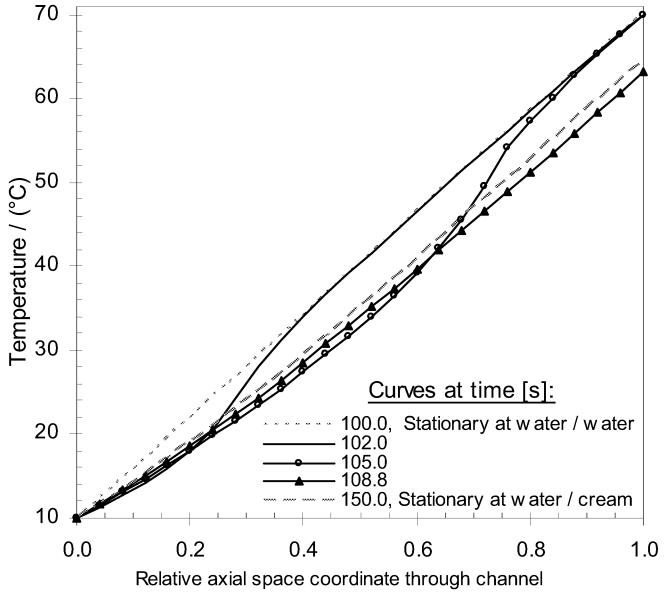

Figure 10: Temperatures along the Heat-Exchanger Tube at Different Moments in Time

SIMULATION OF A MILK PASTEURISER

Based on the created library also full process lines were configured and simulated. An example of that is the milk pasteurizer that is shown in Figure 11a and 11b. Some of the simulated variables are shown in Figures 12a and 12b. They demonstrate the initial 400 s of start-up of the system, which is interesting to simulate for performance reasons.

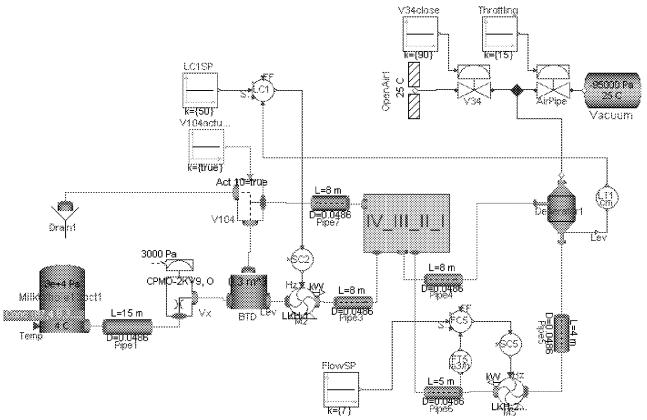

Figure 11a: A Milk Pasteurizer Configured with the Library Component Models. The inner Structure of the Heat Exchanger Model "IV_III_II_I" is shown in Figure 11b

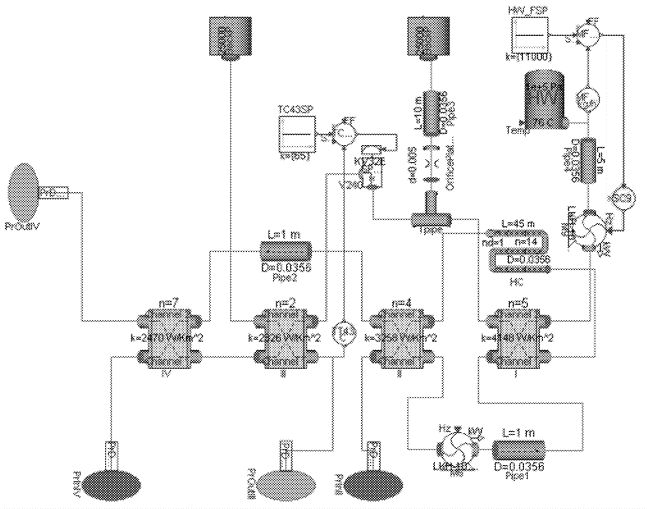

Figure 11b: The Inner Structure of the Heat Exchanger Model that is used in the Pasteuriser in Figure 11a

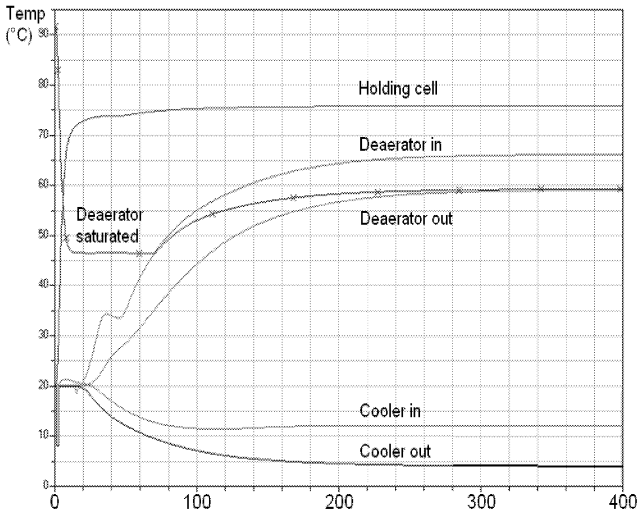

Figure 12a: Some Simulated Temperatures vs. Time (s) during Start-up of the Pasteurizer Shown in Figures 11a-b. The used CPU Time was 436 s whereof 200 s was used for the First 1 s

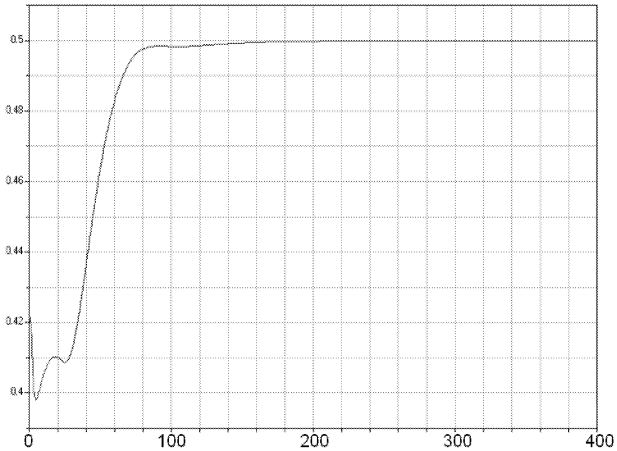

Figure 12b: Level (m) vs. Time (s) as a result of the Same Simulation as in Figure 12a

SIMULATION OF A JUICE BLENDING PROCESS

Most of the orange juice in Europe is blended from orange-juice concentrate and water. Batch systems are common, but in-line systems have advantages. One of the challenges when blending in-line is to blend very accurately with simultaneous capacity adaptation. That is a reason for simulating to verify that the design of the process and control meets the specifications. As with the milk pasteurizer above, a juice blender was configured and simulated (Figure 13). Simulation results are shown in Figures 14a-e, where Figures 14a-b show a badly tuned case, Figure 14c a well tuned, Figure 14d a well tuned and improved process and Figure 14e the same as 14d, but with inaccuracy of sensors included in the simulation. The Figures clearly show how simulation can be used to test and improve design and parameter settings, and eventually get figures on dynamic performance (accuracy) before manufacturing.

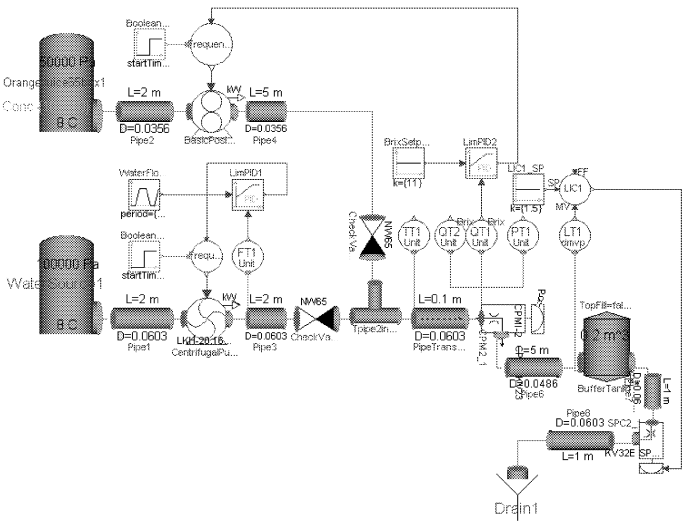

Figure 13: An In-line Juice Blender Configured with the Library Component Models

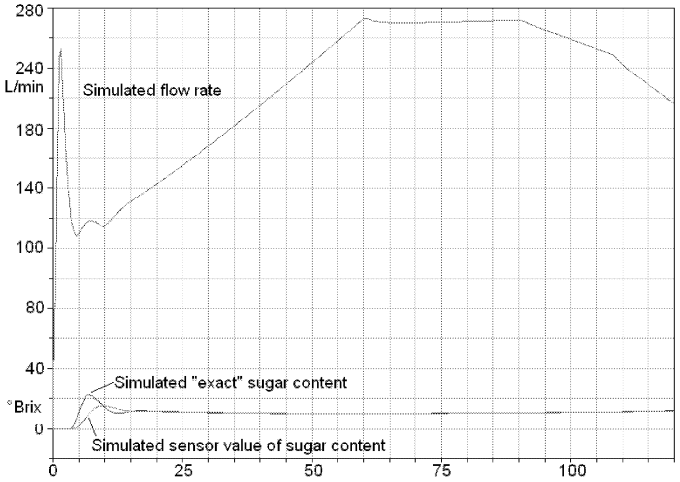

Figure 14a: Simulation of a Badly Tuned In-line Juice Blender. Top Curve shows the varying Flow Rate (l/min). The Bottom Curves shows the Sugar Content (°Brix) where 11 was the Set Point. The x-axis Shows Time (s). The used CPU Time was 1.3 s

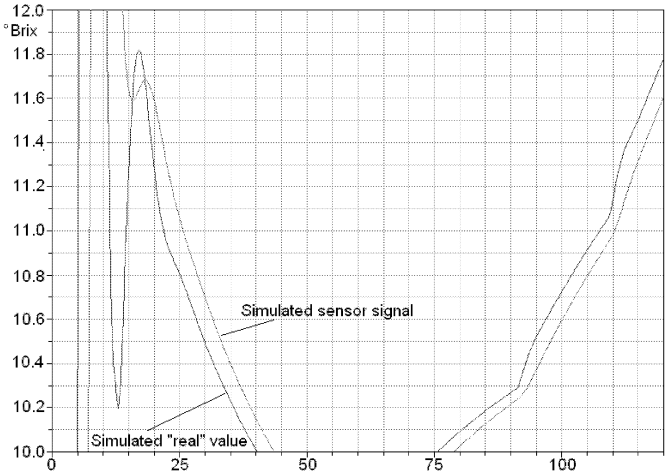

Figure 14b: Expanded View of Concentration Curves in Figure 14a (°Brix). As the Flow Changes the Inaccuracy is here worse than ±1 °Brix. The Time Lag of the Sensor is Clearly Visible

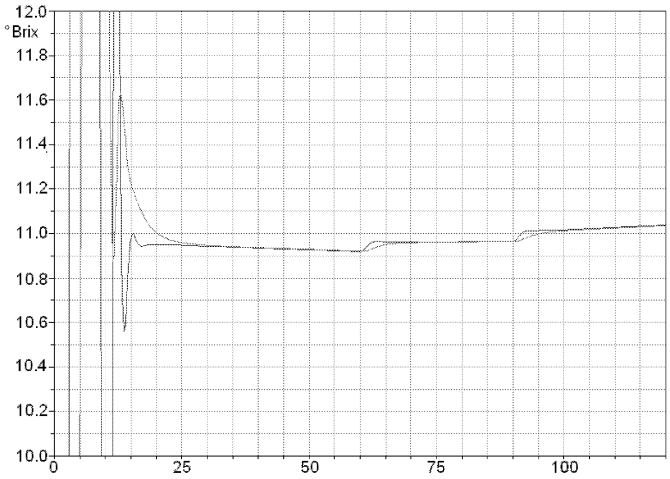

Figure 14c: The same Plot as in Figure 14b but Simulation with a Well Tuned System. The Inaccuracy is here approximately ±0.2 °Brix. The used CPU Time was 4.1 s

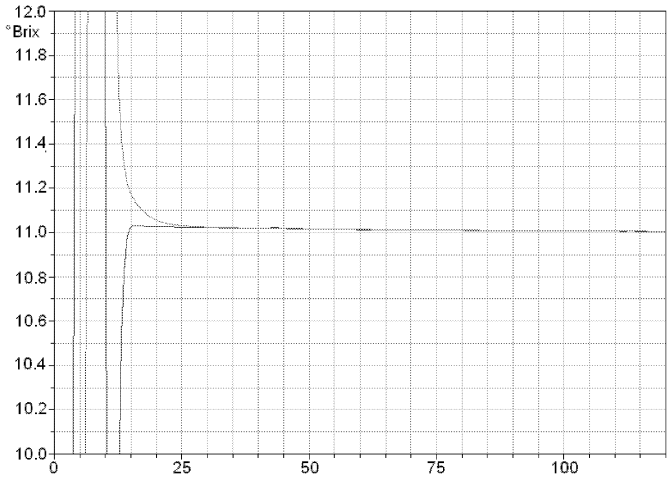

Figure 14d: The same Plot as in Figure 14c but Simulation with an Improved Process Design. The Inaccuracy is here approximately ±0.01 °Brix. The used CPU Time was 2 s

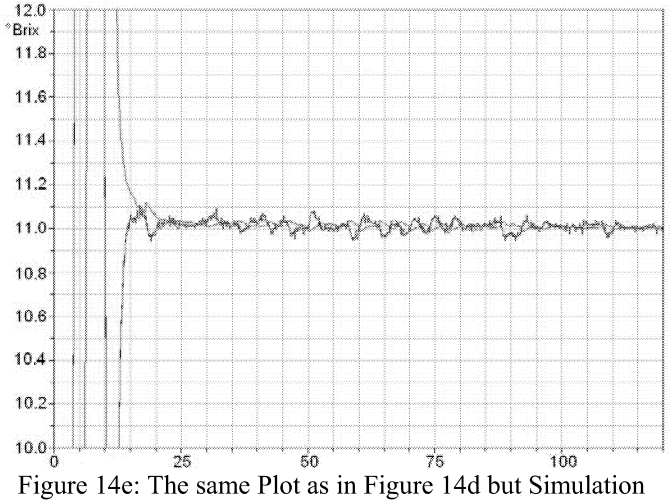

Figure 14e: The same Plot as in Figure 14d but Simulation with a Simulated Inaccuracy of Sensor of 0.22%. The Additional Green Line is a Simulated Lab Analysis (also with 0.22 % Inaccuracy). The system Inaccuracy is here approximately ±0.05 °Brix while the "Lab Analysis" varies ±0.09 °Brix. The used CPU Time was 14 s

SIMULATION OF A FLASH BOILING PROCESS

De-aeration of products is essential to bring down the content of oxygen and by that minimize oxidation of the product. When processing of fruit juices the de-aeration is mostly done by flash boiling of the product in a vacuum vessel where the pressure is below the saturation pressure corresponding to the product temperature at the vessel inlet. Such a process has been simulated. Just as with the above mentioned examples, a juice de-aeration process was configured and simulated (Figure 15). The de-aeration takes place in a vessel included as a part of a pasteurisation line. Figure 16 shows the product temperature at the vessel in- and outlet when vacuum is applied. The control system was designed to control the flash to a constant temperature drop of 2 °C even during varying inlet temperature.
The simulation was used to evaluate and improve the performance of the flash boiling regarding process design as well as control design.

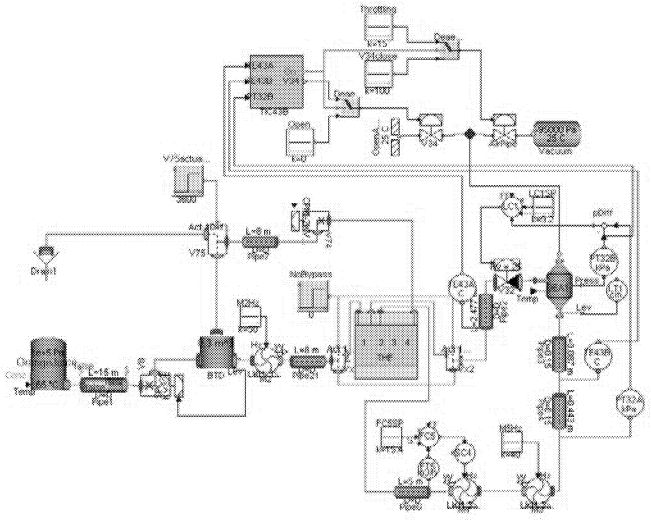

Figure 15: A Juice De-aeration Process Configured with the Library Component Models

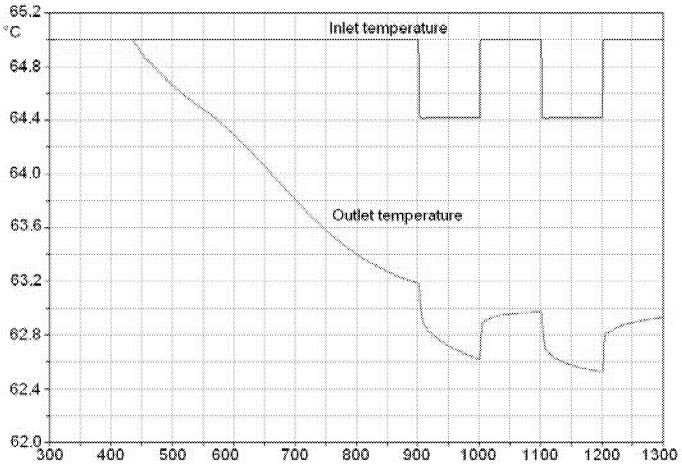

Figure 16: Inlet Temperature and Outlet Temperature vs. Time (s). When Vacuum is applied the Pressure Gradually Drops until Flash Boiling Starts. The Graph Shows The System Response to some Temperature Disturbances of the Product at the Inlet. The used CPU Time was 56 s

CONCLUSIONS

The present work has shown, by examples, a novel and feasible approach to dynamic simulation with full time resolution of the most interesting physical/chemical variables in complete liquid food processing lines by building and using a structured library of dynamic models. The adequacy of using a modern equation-based modelling language like Modelica was evident due to the fact that it enables focus on the modelling rather than on solving DAEs.
Simulation results from a proposed, and recently reported, novel model solution to handle varying fluid properties during fluid changeover in heat exchangers were also shown. The improved computational efficiency of this model was illustrated.
Further modelling work is going on to extend the scope of the present "Food Processing" library to also include fluid dispersion and chemical reaction. This work will be reported elsewhere.

ACKNOWLEDGEMENTS

We would like to express our gratitude to Tetra Pak Processing Systems for the funding of this work.

REFERENCES

Åström, K.J. et al. 1998. "Evolution of continuous-time modeling and simulation". In *Proceedings of the 12th European Simulation Multiconference* (ESM'98, Manchester, UK, June 16-19). Society for Computer Simulation International, pp 9-18.

Eborn, J. 2001. *On Model Libraries for Thermo-hydraulic Applications* PhD thesis ISRN LUTFD2/TFRT - - 1061 - - SE, Department of Automatic Control, Lund Institute of Technology, Lund, Sweden.

Elmqvist, H.; Tummesheit, H.; Otter, M. 2003 "Object-Oriented Modeling of Thermo-Fluid Systems". In *Proceedings of 3rd International Modelica Conference* (Linköping University, Linköping, Sweden, Nov. 3-4, 2003). The Modelica Association and Institutionen för datavetenskap, Linköping University,

Mattsson, S.E.; Elmqvist, H.; Otter, M. 1998. "Physical system modeling with Modelica" *Control Engineering Practice* 6 No 4, 501-510.

Romie, F.E. 1984. "Transient-Response Of The Counterflow Heat-Exchanger" *Journal Of Heat Transfer-Transactions Of The Asme* 106 No.3, 620-626.

Romie, F.E. 1999. "Response of counterflow heat exchangers to step changes of flow rates" *Journal Of Heat Transfer-Transactions Of The Asme* 121 No.3, 746-748.

Lakshmanan, C.C.; Potter, O.E. 1994. "Dynamic simulation of a counter current heat exchanger modelling-start-up and frequency response" *Int Commun. Heat Mass Transfer 21* No 3, 421-434.

Kauhanen, P. 2004. "Verifying the dynamic model of a heat exchanger configuration" M.Sc. thesis. Department of Chemical Engineering, Lund Institute of Technology, Lund, Sweden.

Skoglund, T. 2003. "Simulation of Liquid Food Processes in Modelica". In *Proceedings of 3rd International Modelica Conference* (Linköping University, Linköping, Sweden, Nov. 3-4, 2003). The Modelica Association and Institutionen för datavetenskap, Linköping University, 51-58.

Skoglund, T.; Årzén, K-E.; Dejmek, P. 2006. "Dynamic object-oriented heat-exchanger models for simulation of fluid property transitions" *International Journal of Heat and Mass Transfer* (in press).

Straatsma J.; Van Houwelingen G.; Steenbergen AE.; De Jong P. 1999a. "Spray drying of food products: 1. Simulation model" *Journal of Food Engineering* 42 No 2, 67-72.

Straatsma J.; Van Houwelingen G.; Steenbergen AE.; De Jong P. 1999b. "Spray drying of food products: 2. Prediction of insolubility index" *Journal of Food Engineering* 42 No 2, 73-77.

Tiller, M. 2001. *Introduction to Physical Modeling with Modelica*, Kluwer Academic Publishers, Massachusets, USA, ISBN 0-7923-7367-7.

Tummesheit, H. 2002. *Design and implementation of Object-Oriented Model Libraries using Modelica* PhD thesis ISRN LUTFD2/TFRT - - 1063 - - SE, Department of Automatic Control, Lund Institute of Technology, Lund, Sweden.

Xuan, Y. and Roetzel, W. "Dynamics of shell-and-tube heat exchangers to arbitrary temperature and step flow variations" *Aiche Journal* 39 No.3, 413-421.

Modelica defined by Modelica Association (http://www.modelica.org)

AUTHOR BIOGRAPHY

PETR DEJMEK, with a distant past at Alfa Laval in Sweden and Denmark, has been professor of Food Eng at Lund University for over 15 years. In addition to simulations his interests range widely, from imaging, rheology and electric properties of foods to the effects of pulsed electric fields in plant foods and colloidal aspects of dairy technology. (E-mail: Petr.Dejmek@food.lth.se)

TOMAS SKOGLUND studied engineering physics at the Institute of Technology at Lund University and obtained his degree 1978. Since then he has worked with automatic control engineering (at Volvo Aero), acoustics and vibrations consultations (at Ingemansson Akustik) and with research and education (at the Department of Physics at Lund Institute of Technology). Since 1982 he has been working for Alfa-Laval and Tetra Pak with a range of assignments, e.g. plant and machine automation, project management, technical product management, department management and research & development. Currently his employment includes part-time PhD studies at Lund Institute of Technology, Lund University. (E-mail 1: Tomas.Skoglund@food.lth.se
E-mail 2: Tomas.Skoglund@tetrapak.com)

A NEW MODEL TO PREDICT RESIDENCE TIME DISTRIBUTION IN EXTRUSION PROCESS

Peggy Vauchel[1,2]
Régis Baron[1]
Raymond Kaas[1]
Abdellah Arhaliass[2]
Jack Legrand [2]

(1) IFREMER, rue de l'Ile d'Yeu, BP 21105, 44311 Nantes Cedex 03, France
E-mail : {Peggy.Vauchel|Regis.Baron|Raymond.Kaas}@ifremer.fr
(2) UMR CNRS 6144 GEPEA, 58, rue Michel Ange, BP 420, 44606 Saint-Nazaire Cedex, France
E-mail :{arhalias|legrand}@gepea.univ-nantes.fr

KEYWORDS
Model, twin-screw extrusion, axial dispersion model, length of fully filled channel.

ABSTRACT

In this paper, a simple new model is proposed to predict the residence time distribution (RTD) in fully intermeshing co-rotating twin-screw extruders. This model is based on an extension of an axial dispersion model, including control parameters (screw speed and flow rate) and geometrical parameters, enabling to take into account the screw profile and the die design. Simulations illustrate the large evolution of RTD in the extrusion process for a BC45 extruder. This model should provide a precious help whilst designing installations of industrial size.

INTRODUCTION

The goal of this presentation is to describe a new model predicting the residence time distribution in fully intermeshing twin-screw extrusion process, including all geometrical and control parameters. This process offers many advantages, which have already been largely exploited in the food and polymer industries, and is still very promising. Its flexibility allows to work on a large variety of raw materials, and to get products with a wide range of properties (Baron, 1995 or Baron & al, 1996). Its main advantages, in addition to being a low water demand process, are compactness, modularity and continuity. Nevertheless, up to now, phenomena taking place in the extruder, especially concerning flows and transformation of the material during the process, are not completely understood. Extrusion is still considered as a process which is hard to modelize, simulate, design and control.

Several authors (Ainser, 1996, Puaux & al, 2000) have studied the residence time distribution in twin-screw extruders, by fitting experimental RTD curves with different flow models. Good correlations have been performed, especially with the backflow cell model and the axial dispersion model. Nevertheless those models don't directly take into account the geometrical parameters (screws profile and die design) and the control parameters (screw speed and flow rate). This point limited the prediction value of this modelling approach.

The new model summarily presented here, doesn't aim at improving experimental data fitting, but may be so far interesting in its ability to predict the influence of screws or die design on the residence time distribution. The validation phase is still in progress and will not be discussed here.

Firstly, the physical considerations and hypotheses taken into account for building this model will be described, especially elements developed in a previous simple model of the process (Baron, 1995). Simulations of residence time distribution, in various extreme conditions, will then be presented and discussed. In the last section, some possibilities of future extensions for this model will be outlined.

EXTRUSION MODEL

Length of fully filled channel

A simplified solution of Navier-Stokes equations is used to describe velocity, flow, length of fully filled screw and pressure at steady state in a fully intermeshing co-rotating twin-screw extruder.
This type of extruder consists in two screws, which are parallel, fully-interemeshing, composed of a same sequence of screw elements, and rotating in a barrel. To solve Navier-Stokes equations, this complex geometry is simplified according to common assumptions : the screw channel is unrolled and fixed, the barrel is plane and slides on

the screw channel at V_b velocity (Figure 1). The total length of unrolled channel L_{max} is artificially divided into n zones, corresponding to the number of iterations that will be used to make calculations.

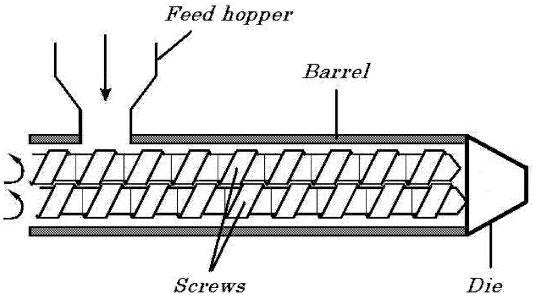

Figure 1: Schema of a twin-screw extruder

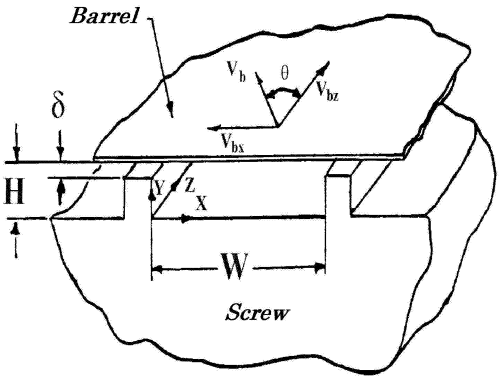

Figure 2: The unrolled channel and the moving plane barrel (Baron, 1995)

The flow rate $Q_{c,i}$ in the zone i of the channel is obtained by solving the steady-state equations, assuming that the length of the extruder is infinite, the fluid is incompressible and Newtonian, the flow is isotherm, laminar and uniform along the channel. It is assumed to be the difference between a pumping flow rate and a drag flow rate (Janssen, 1978 or Tadmor and Klein, 1970) :

$$Q_{c,i}=\alpha_i N-\frac{\beta_i}{\mu L_i}\frac{\partial P_i}{\partial z} \qquad (1),$$

where:
- N (rd/s) is the screw speed,
- μ (Pa.s) is the viscosity,
- L_i (m) is the channel length of the zone i,
- $\frac{\partial P_i}{\partial z}$ (Pa/m) is the pressure gradient for the zone i with respect to the curvilinear abscissa z. Note that for Newtonian fluids this gradient, at its steady state, is linear with respect to z.
- α_i and β_i (m^3 and m^6 respectively) are factors depending on the screw geometry of the zone i,

$$\alpha_i=\frac{\pi D\cos(\theta_i)W_i H_i F_{d,i}}{2},$$

$$\beta_i=\frac{(W_i H_i^2)^2 F_{p,i}}{12},$$

where:
- D is the screw diameter (m),
- θ_i is the pitch angle (rad),
- W_i is the channel width (m),
- H_i is the channel height (m),
- $F_{d,i}$ and $F_{p,i}$ are correcting factors enabling to take into account the narrowness of the channel.

This expression of $Q_{c,i}$ holds true for each type of element, direct or reverse screw pitch for example.

The outflow rate Q_{out} being constrained by the die, it is assumed to follow a Hagen-Poiseuille equation:

$$Q_{out}=\frac{K}{\mu}P_d,$$

with:
- K (m^3) a coefficient depending on the die geometry,
- P_d (Pa) the pressure at the head of the die.

Moreover, the output pressure of the zone n is assumed to be equal to the pressure at the head of the die, and the output pressure of zone i is assumed to be equal to the input pressure of the zone $i+1$. Consequently, pressure gradients can be eliminated in Equation 1 resulting in the following expression of the outflow rate Q_{out} (Baron, 1995):

$$Q_{out}=\left(\frac{a+bl}{c+\frac{d}{K}+l}\right)N$$

where:
- l (m) is the length where the channel is fully filled,
- *a, b, c* and *d* are piecewise constant coefficients depending on the geometry of the screw elements sequence:

$$a=\sum_{i=1}^{n-1}\left(\alpha_i\frac{\beta_n}{\beta_i}-\alpha_n\right)V_i$$

$$b=\alpha_n$$

$$c=\sum_{i=1}^{n-1}\left(\frac{\beta_n}{\beta_i}-1\right)V_i$$

$$d=\beta_n$$

At steady-state, the outflow rate is equal to the input flow rate Q, and l can be estimated by the following equation :

$$l=\frac{-a+\left(c+\frac{d}{K}\right)\frac{Q}{N}}{b-\frac{Q}{N}}$$

Residence time distribution

A largely used approach, is the description of the flow pattern by conceptual models, consisting in combinations of ideal reactors, which represent the overall features of the physical flow. But the residence time distributions commonly encountered in a twin-screw extruder, present intermediate characteristics between those obtained in the two ideal limiting cases, the perfect mixing and the plug flow. Therefore, non-ideal models have to be used, to describe the flow of the material.

The classical tanks-in-series (cell) model and axial dispersion model are one-parameter models. Two parameter structures were obtained by different extensions of the tanks in series model: the Gamma model, the Backflow Cell model, the Fractional Tank Extension model, the Arithmetical Progression model and the Geometric Progression model (Ainser, 1996).

One of the main significant criteria for an extrusion flow model is its ability to describe with sufficient flexibility the axial mixing along the screw. Two models seem to fulfil best this requirement, the one-parameter axial dispersion model and the two-parameter backflow cell model (Puaux & al, 2000).

In this paper, the axial dispersion modelhas been chosen. It consists of a combination between the convective transport and an eddy diffusion mechanism in the axial direction. For a constant fluid velocity v and a constant axial dispersion coefficient D along the flow axis z, the evolution in time and in space of the concentration of a tracer can be described by the following partial differential equation:

$$\frac{\partial C}{\partial t}=D\frac{\partial^2 C}{\partial z^2}-v\frac{\partial C}{\partial z} \qquad (2),$$

where:
- C (mol/m^3 or g/m^3) is the tracer concentration,
- D (m²/s) is the axial dispersion coefficient,
- v (m/s) is the velocity.

We have chosen to extend this equation to the case where D and v are piecewise constant.

The value of v depends on the fully filled length l:
- when the screw channel is partially filled ($0<z_i<L_{max}-l$), the velocity depends on the pumping effect: $v=\frac{\alpha N}{S}$,
- when the channel is fully filled ($L_{max}-l\le z_i\le L_{max}$), the velocity depends on the global outflow rate: $v=\frac{Q}{S}$.

with :
- S (m²) the section of the channel at abscissa z,
- L_{max} (m) the total length of the channel (partially + fully filled).

For the axial dispersion coefficient, two cases (D1 and D2) are described in this paper :

- Case D1:
- for $0<z<L_{max}-l$ (partially filled zone), D=0.002m²/s,
- for $L_{max}-l\le z\le L_{max}$ (fully filled zone), D=0.02m²/s.

These values are arbitrarily chosen, so as to respect the time scale of classical residence time distributions in Clextral BC45 extruders.

- Case D2:
- for $0<z<L_{max}-l$ (partially filled zone), D=0.002m²/s,
- for $L_{max}-l\le z\le L_{max}$ (fully filled zone), the value of D is chosen so as to be proportional to the drag flow:

  $D=\lambda(\alpha N-Q)$, for a direct pitch element,

  $D=\lambda|\alpha N|$ for a reverse pitch element,

λ being a constant (λ=400m^{-1} in this presentation).

The boundary conditions are defined as follow:
- for z=0, $D\frac{\partial C}{\partial z}=v(C-C_{in})$, C_{in} being the input tracer concentration,
- for $z=L_{max}$, $\frac{\partial C}{\partial z}=0$.

A numerical resolution by explicit finite differences is carried out to estimate the output concentration. The derivatives approximations at iteration point i (i=1...n-1) are as follow:

$$\left.\frac{\partial C}{\partial z}\right|_i\approx\frac{C_{i+1}-C_{i-1}}{2\Delta}, \text{ and}$$

$$\left.\frac{\partial^2 C}{\partial z^2}\right|_i\approx\frac{C_{i+1}-2C_i+C_{i-1}}{\Delta^2}, \text{ with } \Delta=z_i-z_{i-1}.$$

SIMULATIONS

All simulations were performed with a pulse of 100 units of tracer concentration from t=0 to t=2 sec.

Three very simple geometry of screw (G1, G2 and G3) for a BC45 Clextral extruder have been considered:
- G1: direct elements of constant pitch p_1 (L_{max}=10m, α=1,1.10^{-5}m^3, β=1.10^{-9}m^6 and S=2.10^{-4}m²), a cylindrical die of 4mm in diameter and 90mm long (K=7.10^{-11}m^3),
- G2: direct elements of constant pitch $p_2<p_1$ (L_{max}=13,33m, α=7,2.10^{-6}m^3, β=7,0.10^{-10}m^6, S=1,5.10^{-4}m² and K=1,5.10^{-10}m^3)
- G3: G1 + a reverse screw element at the end.

Figure 1 illustrates the influence of the number of iterations *n*. An outflow rate of 50kg/h, a screw speed of 400rd/min and an axial dispersion coefficient following case D1 were used in this simulation. A high value of *n* is necessary so as to converge towards a good final estimation. For the next simulations, a value of 250 iterations was retained.

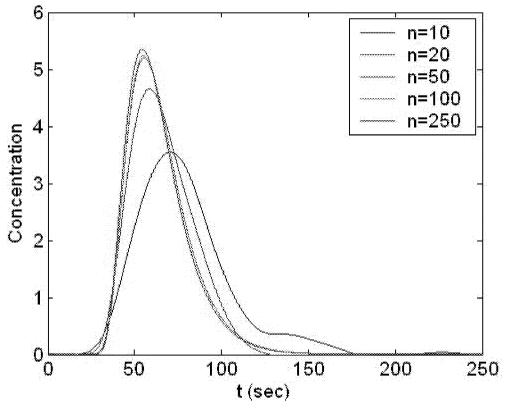

Figure 1 : Influence of n on the numerical resolution of RTD, in the case of a geometry G1 and a axial dispersion D1

Simulation results presented in Figures 2 and 3 were obtained with axial dispersion coefficient values following case D1.
In figure 2, various experimental conditions of flow rate and screw speed were tested for screw geometry G1. For high values of screw speed, almost pure delays depending on values of α, *N, S* and *l* were observed : it corresponded to cases where the channel was partially filled.
In figure 3, the same experimental conditions were tested for screw geometry G2. Decreasing the screw profile pitch amplified the pure delay phenomenon.

Simulation results presented in Figures 4 and 5 were obtained with axial dispersion coefficient values following case D2.
Simulation results for the geometry G1, are shown in Figure 4. Delay and time scale of dispersion revealed to be plausible with most of residence time distributions in the literature.
Figure 5 presents results obtained with the same conditions as presented in figure 4, with the addition of a reverse element at the end of the screw. The accumulation and dispersion of matter induce a larger distribution of RTD, also observed in experimental conditions.

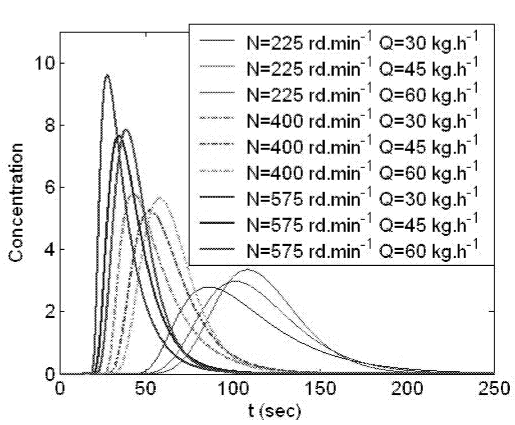

Figure 2 : Simulations of RTD for different values of flow rate and screw speed, in the case of a geometry G1 and an axial dispersion D1

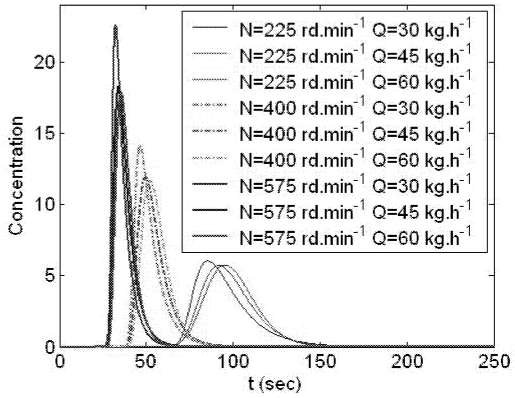

Figure 3 : Simulations of RTD for different values of flow rate and screw speed, in the case of a geometry G2 and an axial dispersion D1

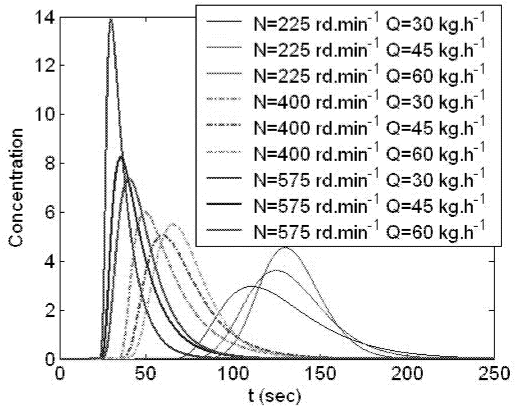

Figure 4 : Simulations of RTD for different values of flow rate and screw speed, in the case of a geometry G1 and an axial dispersion D2

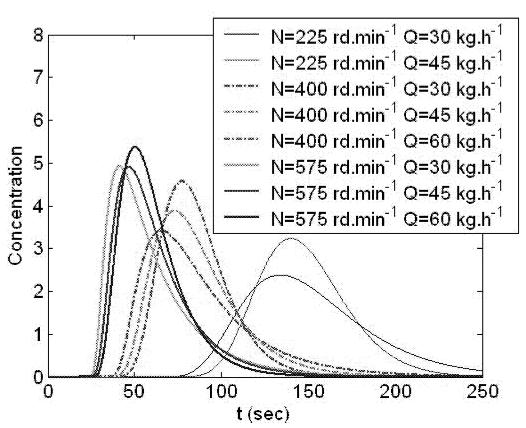

Figure 5 : Simulations of RTD for different values of flow rate and screw speed, in the case of a geometry G3 and a axial dispersion D2

FUTURE EXTENSIONS

In the current model, viscosity is assumed to be constant along the screw axis z. If viscosity evolves in time, it can be taken into account, but the same viscosity is applied instantaneously all along the screw.

If we assume that the local gradient of pressure $\frac{\partial P}{\partial z}$ can be estimated by a finite difference scheme, it seems possible to calculate a new expression of Q_{out} which would associate the length of a fully filled channel and a viscosity function along the screw axis. The fully filled length l is a dynamic variable that can be expressed as the difference between the inflow rate with a pure delay and the outflow rate (Baron, 1995). All these dynamical variables (l, Q_{out}, N…) will be reintroduced in the previous model.

Reactive extrusion could also be simulated by combining Equation 3 with a term describing the kinetics of the reaction.

CONCLUSION

This study shows that the new proposed model is useful to predict the impact of geometrical parameters on the residence time distribution of the twin-screw co-rotating extrusion process. It is a precious tool to help designing industrial installations. Nevertheless, an important work remains to be done to validate, adjust and extend this approach before intensive use.

REFERENCES

Ainser, A. 1996. Etudes des écoulements et réactions chimiques en extrudeuse bi-vis. Approche expérimentale : utilisation de la distribution des temps de séjour. Ph. D. thesis. Université de Saint-Etienne.

Arhaliass, A., J.M. Bouvier and J. Legrand, 2003. Melt growth and shrinkage at the exit of the die in the extrusion-cooking process. *Journal of Food Eng.*, 60 (2), 185-192.

Baron, R.; J. Levine and M. Mastail. 1995. Modelling and Control of a fish extrusion process. *In Proc. 1st Int. Symp. On Mathematical Modelling and Simulation in agriculture and Bio-Industries*, Bruxelles.

Baron, R. 1995. Modélisation et commande d'un procédé d'extrusion de pulpe de poisson. Ph. D. Thesis. Université Paris Sud.

Baron, R. ; M. Mastail ; J.L. Vallet and E. Lukomska. 1996. Texturation de la pulpe de poisson par extrusion à froid. *Sciences des Aliments*, 16(1), 71-78.

Baron, R.; M. Mastail and J. Levine. 1996. Control of a fish extrusion process using flatness. In *Proc. CESA 96 IMACS Multiconference, Symp. On Control, Optimization and Supervision*, (1), 200-205.

Bounie, D. 1988. Modelling of the flow pattern in a twin-screw extruder through residence time distribution experiments. *Journal of food Eng.*, 7, 223-246.

De Pilli, T.; C. Severini; A. Baiano; A. Derossi; A. Arhaliass and J. Legrand. 2005. Effects of operating conditions on oil loss and properties of products obtained by co-rotating twin-screw extrusion of fatty meal: preliminary study. *Journal of Food Eng.*, 70 (1), 109-116.

Ganzeveld, K.J.; J.E. Capel; D.J Van der Waal and L.P.B.M. Janssen. 1994. The modelling of counter-rotating twin screw extruders as reactors for single-component reactions. *Chemical Eng. Science*, 49, 1639-1649.

De Graaf, R.A.; M. Rhode and L.P.B.M. Janssen. 1997. A novel model predicting the residence time distribution during reactive extrusion. *Chemical Eng. Science*, 52 (23), 4345-4356.

Harmann, D.V. and J.M. Harper. 1974. Modelling a forming foods extruder. *J. Food Science*, (39), 1099-1113.

Janssen, L.P.B.M. 1978. Twin-screw Extrusion. Elsevier, Amsterdam.

Janssen, L.P.B.M.; R.W. Hollander; M.W. Spoor and J.M. Smith. 1979. Residence time distributions in a plasticating twin screw extruder. *A.I.Ch. E. Journal*, 25, 345-351.

Kirby, R.B. 1970. Process dynamics of screw extruders. *SPE Journal*, 18 (9), 344-348.

Oberlehner, J.; P. Cassagnau and A. Michel. 1994. Local residence time distribution in a twin screw extruder. *Chemical Eng. Science*, 49, 3897-3907.

Puaux, J.P.; G. Bozga and A. Ainser. 2000. Residence time distribution in a corotating twin-screw extruder. *Chemical Eng. Science*, 55, 1641-1651.

Tadmor, A. and I. Klein. 1970. Engineering Principles of Plasticating Extrusion. Van Nostrand Reinhold Company, New York.

Todd, D.B. 1991. Drag and pressure flow in a twin-screw-extruder. *Int. Polymer Processing*, 5 (2), 143-147.

BIOGRAPHY

Peggy VAUCHEL was born in Le Havre, France and went to the Polytechnical National Institute of Grenoble, where she studied process engineering and obtained her engineer degree in 2004. She started her PhD studies in 2005 both at IFREMER in Nantes and UMR GEPEA in Saint-Nazaire, and is currently in second year.

APPLICABLE MODELS OF INDUSTRIAL PROCESSES BASED ON PROCESS UNDERSTANDING: ACRYLAMIDE PREDICTION

Bo Boye Busk Jensen
Alan Friis
Jens Adler-Nissen
BioCentrum-DTU, Technical University of Denmark
Soltofts Plads, build 221, 2800, Kgs. Lyngby, Denmark
E-mail: bbb@biocentrum.dtu.dk
E-mail: af@biocentrum.dtu.dk
E-mail: jan@biocentrum.dtu.dk

KEYWORDS
Industrial processes, Food, Differential equations, Model analusis, parameter identification

ABSTRACT

Modelling is widely used in food processing, and a large number of papers present a variety of models for the often complex physical, chemical and biological processes going on in food products. This extended abstract presents a modelling approach that focuses on the transparency of the model constants, to give the model robustness and better applicability. Based on a discussion of different modelling approaches an example is given showing that the well known thermal inactivation kinetic model can also be used for predicting the formation of acrylamide as a function of time and temperature in a cereal product in an industrial environment. The model constants (only two) specifically relate to the process investigated.

INTRODUCTION

A wide selection of models for predicting process-product interaction and product changes are found throughout the literature. Many different levels of complexity are proposed, from models based on purely curve fitting (black box models) to models derived from the fundamental equations of the physical, chemical and biological processes taking place in the product during processing (white box models).
Black-box models in principle carry no information about the system studied. This kind of models only gives the numerical modelling of output in relation to input, e.g. change in a particular quality parameter as a function of the process conditions. They are usually established by curve fitting of existing data. The curve-fitting parameters (e.g. the constants in a polynomial fit) have in general no physical meaning. For interpolation these models are often useful, but they are risky to use for extrapolation.
White-box models are in principle informative, but their establishment require many parameters to be estimated. This can be difficult, if not virtually impossible in complex cases, such as in food processing. Furthermore, many of the parameters and the information they carry about details of reaction mechanisms are not of particular interest in for example the optimisation of a process in industry.
Between black-box and white-box models has the *grey-box* model found its place. This type of model is based on fitting equations containing constants that are physically meaningful to the actual process taking place in the product e.g. during heating. All other parameters from the white box approach, that is all those parameters that are intrinsic to the system and therefore carry no information of direct relevance to the process studied, are conveniently lumped together into one empirically determined parameter based on the study of the process under defined process conditions. This makes the model understandable for the users and easier to extend it to include e.g. other products as only a few parameters needs to be re-estimated. Estimation under new conditions is done in the same way as for the original parameters and, finally, using the same type of model over and over again makes it more thrustworthy, easier for users to use and understand and easier to use for different kind of products.
When developing a grey-box model, its robustness should be considered. By this is meant that uncertainties and statistical variations related to the input parameters (e.g. process temperature) should result in a predictable and moderate variation in the output, not to any wild and unpredictable variations in the output. Robustness is assessed by proper design of the mathematical expression; for example differences between two large terms is generally to be avoided when setting up the expression.
This extended abstract introduces the idea behind an on-going study of using a well established model of thermal death of microorganisms as a grey box model for prediction of acrylamide formation in a breakfast cereal.

PROBLEM DESCRIPTION

The objective of our ongoing study of acrylamide formation under industrial conditions is to develop a simple model for various products in the food-processing industry that can be easily applied to the processes with a view of reducing the amount of acrylamide generated in the product through changes in the process.
Three approaches were used to model acrylamide production during the manufacture of a breakfast cereal in an industrial case study. The first model (a white-box model) was

developed from published production pathway research (Mottram et al. 2003, Stadler et al. 2003 and Zyzak et al. 2003) without any restrictions on model parameters, the second similar to the first (white-box model) but with restrictions on the model parameters, while the third was based upon an analogy with thermal death kinetics for microorganisms (grey box model).

EXPERIMENTAL DATA

Data for fitting model parameters were obtained in the factory during production. Acrylamide is generated during the final heating in an oven at a temperature (T_{normal}) with a reference time (t_{normal}). To see the influence of temperature and residence time sampling of product for acrylamide analyses was done at two other combinations: T_{low} at t_{low} and T_{high} at t_{high} with $T_{low} < T_{normal} < T_{high}$ and $t_{high} < t_{normal} < t_{low}$. The combination of T and t were set by trial-and error to give similar water contents at the outlet of the oven.

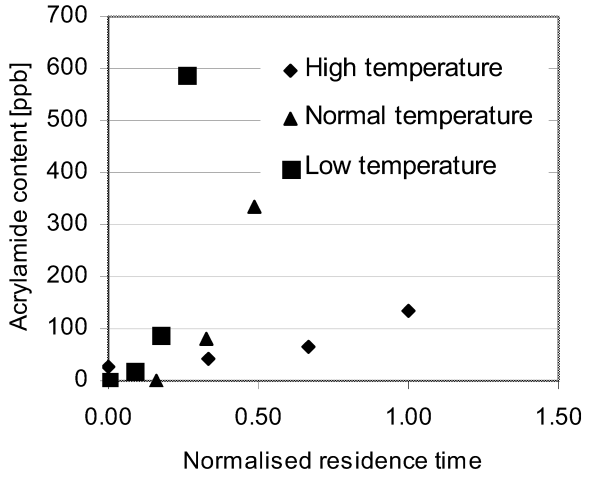

Figure 1: Experimental data used for fitting model constants.

MODELLING APPROACHES

White box modelling, both without and with constraints, is done based on the chemical pathway of acrylamide formation. From the pathway of acrylamide formation from published research (Mottram et al. 2003, Stadler et al. 2003 and Zyzak et al. 2003) an expression was obtained by integrating rate expressions and simplifying the equation from sound assumptions regarding the case study:

$$[Acrylamide] = -\frac{1}{2}\frac{k_2 k_3\left(2e^{-k_4 t} - k_4^2 t^2 + 2k_4 t - 2\right)}{k_4^2}$$

Where, [Acrylamide] is the concentration of acrylamide, k_i are reaction constants for steps in the formation pathway, and t is the time the product is exposed to a roasting process. The temperature-dependence of the reaction constants was estimated using the Arrhenius expression.

$$k_i = A_i e^{\frac{-E_{Ai}}{RT}}$$

Where A_i is the pre-exponential factor, R is the gas constant, T is the temperature and E_{ai} is the activation energy. The changing temperature of the product as it is heated in the process is modelled separately, using the fact that the product had so small dimensions that it could be regarded as an isothermal body in which the average temperature rose fairly rapidly from inlet temperature to the oven temperature. The grey box model approach is based on the well known thermal death equation (F-value equations) based on the time-temperature history of the product:

$$\log\left(\frac{N}{N_0}\right) = -\frac{t}{D} \qquad D = D_{ref} 10^{\frac{T_{ref}-T}{z}}$$

Where N is the number of microorganisms at a specific time (t), N_0 is the initial number of microorganisms, D is the decimal reduction time at a certain temperature (T), D_{ref} is the decimal reduction time at a reference temperature (T_{ref}) and z is the temperature change needed to changes the decimal reduction time a factor of ten. The choice of this model was based on the observation that acrylamide formation data from the process can be linearised by taking the logarithms of the concentrations (Figure 2). The analogy to the inactivation of microorganisms is obvious, except that the concentration *increases* with time for acrylamide while it decreases in the case of microbial inactivation. Thus, the only difference to be made is to change the sign on the slope of the logaritimised curve to turn the classical heat inactivation model into a formation model for acrylamide:

$$\log\left(\frac{C}{C_0}\right) = \frac{t}{a} \qquad a = a_{ref} 10^{\frac{T_{ref}-T}{z}}$$

Where C is the acrylamide concentration a specific time (t), a is the time needed for a ten-fold increase in the acrylamide concentration at a certain temperature (T), a_{ref} is this time at a reference temperature (T_{ref}) and z is the temperature change needed to change the reaction rate by a factor of ten. Following the model for thermal inactivation of microorganisms C_0 should be the initial amount of acrylamide, which is zero. This is not mathematically possible; hence, C_0 is chosen to be the detection limit of the analysis method.

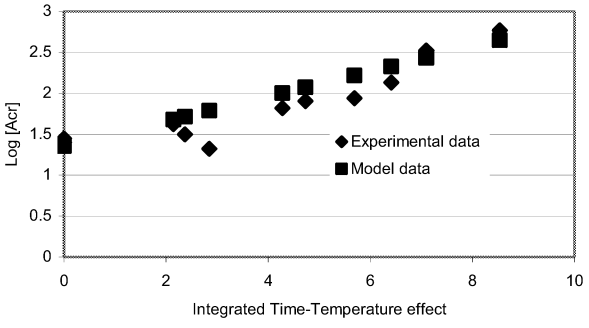

Figure 2: Experimental data and model data plotted versus integrated time-temperature effect calculated based on the thermal death approach.

MODELLING RESULTS AND DISCUSSION

The three approaches were not equally successful. The first white-box approach (pathway without any restriction on constants) produced a good model with good fit to the data but with parameter values having no physical meaning, such as an Arrhenius expression which implies that the reaction rate *decreases* with increasing temperature! Imposing restrictions on the white box model (pathway with restriction on constants) resulted in a very poor model which did not fit the data, however. Finally, the grey box approach (base on the thermal inactivation of microorganisms) gave a good fit.
It became apparent from these model studies that the white box approach could not be developed further without additional kinetic information. Solutions for the parameters exhibited difficulties in converging, especially with regards to parameter identifiability (explained later). Thus the development of this approach was halted until more information from basic kinetic studies of acrylamide formation can be incorporated into the model.
Parameter identifiability problems showed as multiple sets of constants produced a good fit, but several other sets also produced similar good fits. Thus it is impossible to set up a model with constants that are meaningful as the different sets of constants means that the reaction rates depends on what set of fitting constants are used. The grey box approach showed more promise as a feasible correlation, despite some scatter in the experimental data. When scrutinising the data it was discovered that the biggest hindrance to model fitting came from the variability of generated acrylamide levels over time in the examined process. The amount of variability observed was unexpected and quite high. This stressed the need for having a robust model. In this respect, the heat inactivation model is a good choice, due to its simple mathematical expression and its linearity on a logarithmic form.
The two model constants in the thermal inactivation model are the z-value and the a-value. Both are meaningful in the context of the acrylamide formation; a is the time needed for a ten-fold increase in the acrylamide concentration at a certain temperature (T) and z is the change in temperature needed to change a by a factor of ten. Thus based on the units of the parameters one can get information about the process.

CONCLUSION

For a model to be successful (that is quantitative, robust and user friendly) the constants (e.g. temperature dependency) must have a meaning to the user in relation to the process modelled. The grey box model used in this work, based on the well-known thermal inactivation model, gave a model with only two parameters that are explainable by the process the model represents. The model was established from a pragmatic, visual analysis of looking at the trend of experimental data available. The process parameter of primary interest to vary is the temperature, and the effect of this is described by z in the exponential term, which is a well-established way in food technology of modelling the effect of temperature on the reaction rate. The approach may be applied to other reactions, where the concentration of a given component appears to increase exponentially with time. Autocatalytic reactions may be a case of interest in this respect.

REFERENCES

Mottram, D., Wedzicha, B., & Dodson, A. *Nature.*, **419**, 448-449 (2003)

Stadler, R., Blank, I., Varga, N., Robert, F., Hau, J., Guy, P., Robert, M., & Riediker, S. *Nature.*, **419**, 449-450 (2003)

Zyzak, D., Sanders, R., Stojanovic, M., Tallmadge, D., Eberhart, B., Ewald, D., Gruber, D., Morsch, T., Strothers, M., Rizzi, G., & Villagran, M. *J. Agric. Food Chem.*, **51**, 4782-4787 (2003)

AUTHOR BIOGRAPHY

BO BOYE BUSK JENSEN was born in Hou, Denmark and went to Aalborg University, where he studied mechanical engineering with a spiclisation in energy technology and obtained his degree in 1998. After ½ a year of research assistant at Aalborg University in industrial computational fluid mechanics he started his ph.d. in hygienic design of closed processing equipment using computational fluid mechanics at BioCentrum-DTU, Technical University of Denmark. The ph.d degree was obtained in 2003. Upon completion of the ph.d. he was employed at BiC-DTU 3 years as a assistant professor and recently as a associate professor in modeling on industrial food processes.

ANALYSIS OF MASHING WITH A TUCKER3 MODEL

Martin Mitzscherling and Thomas Becker
Department of process analysis and cereal technology
University of Hohenheim
Garbenstraße 23
70599 Stuttgart, Germany
E-mail: mitzsche@uni-hohenheim.de

KEYWORDS
Mashing, Malt Quality, Tucker3, Dynamic Time Warping, Process Analysis

ABSTRACT

A new measurement system is presented, that delivers online data from a mashing process. By Tucker3 decomposition it is shown that the data contain relevant information about the quality of the employed malt. In contrast to bilinear models the Tucker3 preserves the three-dimensional character of batch data. Individual factors for variable, batch and time are obtained and can be analysed separately. An important pre-processing step is the synchronisation of the data. Dynamic Time Warping (DTW) is a suitable method that brings data sets to common length and aligns the data according to its form.

INTRODUCTION

Mashing is a key process during beer production. Endogenous enzymes break down malt components of high molecular weight into smaller, soluble components. As mashing forms the basis of the beer composition a process monitoring would be necessary. However, despite its importance for the subsequent beer quality, no online-monitoring of the mashing has been established. No sensors are available, that could measure the degradation process directly and reliably.

In this paper a new approach is presented. The measurement system consists of an array of unspecific sensors that measure physical and chemical properties of the mash. Each quantity is not a sufficient and reliable measure to categorise the process, but it is shown that the combined, i.e. multivariate, view on all measurement quantities improves the observability.

Batch process data is of three-dimensional nature (Nomikos and MacGregor, 1994). The data can be organised in a three-dimensional array with dimensions time, variable and batch number. These arrays can be analysed by unfolding the data into two-dimensional matrices (Wold et al., 1987; Kosanovich et al., 1996). However, bilinear models, e.g. Principal Component Analysis, lead to models with many parameters and cannot account for the trilinear nature of batch data. As a result, they are more difficult to analyse. Trilinear models, on the other hand, may be more difficult to compute, but have fewer parameters and are easier to interpret. This paper shows how batch data from a mashing process is analysed by a trilinear Tucker3 model (Tucker, 1967).

The paper is organised as follows. First the measurement system applied to a mashing tun will be described. Then the Dynamic Time Warping Algorithm as a means of synchronising batch data and the Tucker3 decomposition for three-way data will be outlined. Finally the results of the analysis of data from the mashing process are presented.

MATERIAL AND METHODS

Mashing

All trials were conducted in a 60 L pilot brewhouse. 10 kg of malt were mashed with 40 L of water. Malt was bought from Weyermann, Bamberg, Germany. Two qualities were available. A regular malt of good quality and a malt produced with a shortened malting process and thus of poor quality. A third quality was obtained by a half and half mixture of both malt batches.

A standardised mashing procedure was defined. It consisted of three rests at 45, 62 and 70 °C. Each rest was held for 30 minutes. This procedure was varied by reducing and extending the rests to 20 and 40 minutes respectively. The heating rate between rests was controlled to be 1 K/min. All three malt qualities were mashed at three rest lengths. Like this 9 mashing experiments were conducted and numbered as shown in Table 1

Table 1: Design of the mashing expreriments

		Malt quality		
		good	50 %/50 %	poor
rest lenght	20 minutes	1	2	3
	30 minutes	4	5	6
	40 minutes	7	8	9

Measurement System

The measurement system was installed in a by-pass configuration. It consisted of a pump, a filtering hydro cyclone and a pipe that contained the sensors (Figure 1).

The filtering hydro cyclone was used to separate the grist from the water. This step was necessary to prevent the

capillary viscosimeters from blocking. The filtering hydro cyclone was first introduced by (Souza et al., 2000) for mining purposes. Unlike usual hydro cyclones, the wall of a filtering hydro cyclone is not solid but made of a permeable material. In this case a 50 µM mesh was used. Instead of using the overflow the filtered liquid downstream the mesh is analysed. Because of the high tangential flow inside the cyclone, the mesh is not blocked.

Downstream the filter all sensors were located. Density and ultrasonic velocity were measured with a DSRn 427 (Anton Paar, Austria), ph-value with InPro pH3200/ pH-transmitter 2100 (Mettler-Toledo), conductivity with InPro 7106/Transmitter 7100 (Mettler-Toledo), viscosity with KV100-25 (Rheotec, Germany) and a self developed viscosimeter for low shear rates (<10/s). Starch degradation was measured by iodine at 578 nm in a flow injection analysis system (FIA).

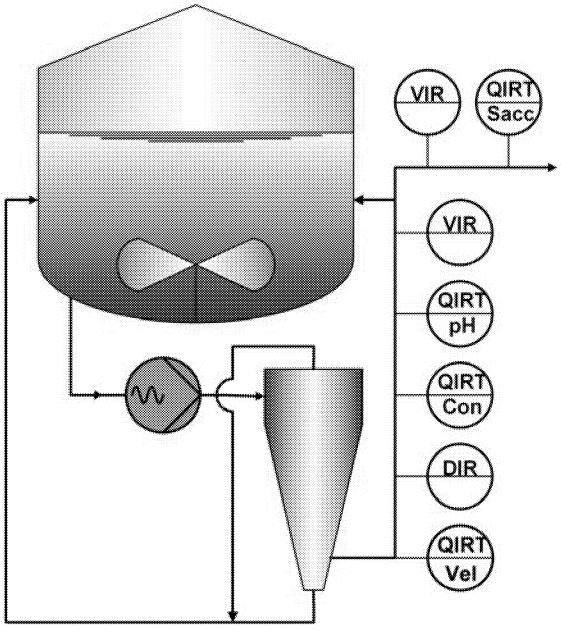

Figure 1: Experimental Setup with Following Sensors QIRT/Vel: Ultrasonic Velocity, DIR: Density, QIRT/Con: Electr. Conductivity, QIRT pH: pH Calue,VIR: Viscosity, QIRT/Sacc: Iodine Value.

The sensors were connected to a personal computer via a PLC and new measurements - when available - were logged every 10 seconds.

DATA PROCESSING

Synchronising Batch Data With Dynamic Time Warping

Many multi-way techniques, including Tucker3, assume that the batch duration and thus the number of data points measured is constant. Only then the data can be arranged in a cuboid. When dealing with process data this is rarely the case. In order to be able to calculate a model data sets from different batches have to be transferred to equal length. This can be easily achieved by interpolating the data. However, interpolating expands or compresses the data evenly over the whole data set. The data sets will have a constant length but most likely they will not be sychronised (Kassidas et al., 1998). That means that variations caused by slight time shifts may completely obscure the process variations.

The goal in process data analysis is to detect differences between batches. Differences in the data can be caused by time shifts (e.g. one step in the process takes some minutes longer). These variations often play a minor role and do not necessarily have an effect on the process and product quality. Consequently variations caused by time shifts should be eliminated whereas variations caused by other parameters like raw materials should be preserved.

Dynamic Time Warping (DTW) is a technique that on the one hand equalises data sets regarding their length. On the other DTW is able to synchronise the data. That is, within one data set DTW can expand and compress the time line where necessary.

DTW was developed for speech recognition in the 1975 (Itakura, 1975). In the 90s it was then adapted to synchronise batch data (Gollmer and Posten, 1996). In this paper only a short introduction will be given. For a more detailed description see (Kassidas et al., 1998).

DTW always synchronises two data sets. If there are more than two sets a reference set is chosen and all other sets are aligned sequentially. Consider two data sets **T** and **R** with *t* and *r* data points respectively. Every data set consists of measurements on n variables. Figure 2 gives a univariate example. Two data sets form a grid of possible pairs. DTW calculates the distances between the data points and determines a sequence of paired data points that represents the minimum accumulated distance.

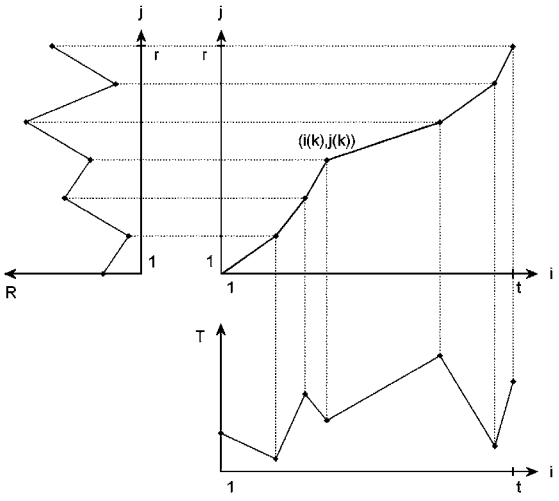

Figure 2: Non-linear Aligning of the Time Line with Dynamic Time Warping

Local constraints are introduced to prevent excessive warping (comp. Figure 3). Every point in the grid is provided with a set of possible predecessors. Example a) does not constrain the slope of the path through the grid and is proposed by Kassidas et al. (1998). As the approach did not perform well in this application, local constraint (b) was chosen, constraining the slope to 2 and 0,5 respectively (Sakoe and Chiba, 1978).

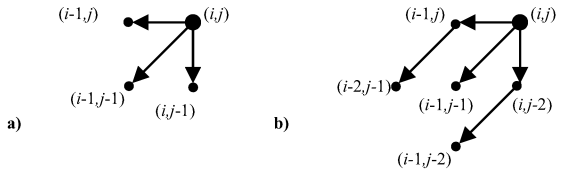

Figure 3: Local Constraints Limiting the Possible Way Through the Grid

For every point in the grid the accumulated distance is calculated only considering the predecessor that minimises the accumulated distance:

$$D_A(i,j) = \min\begin{Bmatrix} D_A(i-1,j-2) + 2\cdot d(i,j-1) + d(i,j) \\ D_A(i-1,j-1) + 2d(i,j) \\ D_A(i-2,j-1) + 2\cdot d(i-1,j) + d(i,j) \end{Bmatrix}$$

Where D_A is the accumulated distance and d is the Euclidian distance $d(i,j) = (\mathbf{t}_i - \mathbf{r}_j)\cdot \mathbf{W} \cdot (\mathbf{t}_i - \mathbf{r}_j)^T$ at the specified grid point using **W** as a weighting matrix. By introducing weights more suitable (e.g. monotonically increasing) variables can be favoured. The indices are used according to Figure 3b. After having calculated all distances, the optimal predecessor is known for every point in the grid. The optimal path through the grid is now determined quite easily. Starting from the last possible pair in the right upper corner (Figure 2) every preceding point is known, leading through the grid to the first pair.

Tucker3 Decomposition

The Tucker3 decomposition was introduced by Tucker (1967) It is an extension of principal component analysis that can handle three-way data, i.e. three dimensional fields. A detailed description of the decomposition and algorithms for its calculation are given by Kroonenberg (1983). In this paper the n-way Matlab toolbox was used (Andersson and Bro, 2000).

The Tucker3 method decomposes a three-dimensional matrix $\underline{\mathbf{X}}$ with size $I \times J \times K$ into three loading matrices **A**, **B**, **C** which are linked through a core matrix **G**. The decomposition can be denoted

$$x_{ijk} = \sum_{p=1}^{P}\sum_{q=1}^{Q}\sum_{r=1}^{R} a_{ip} b_{jq} c_k g_{pqr} + e_{ijk} \qquad (1)$$

Where P, Q and R stand for the number of factors in matrices A, B, C, respectively and e is the residual error. Figure 4 shows a graphical representation of Equation (1).

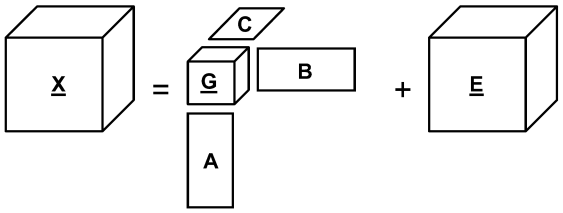

Figure 4: Illustration of the Tucker3 Decomposition of Three-Way Matrix $\underline{\mathbf{X}}$.

Every loading matrix can be seen as a set of principal components for the corresponding dimension of $\underline{\mathbf{X}}$. That is, independent factors for time, batch and measurements are obtained by the decomposition.

The choice of the right factor numbers P, Q, R for a Tucker3 model is not as easy as for the bilinear Principal Component Analysis (PCA), where the factors can be extracted one by one with e.g. the NIPALS algorithm. In a Tucker3 model all factors are calculated simultaneously and a change in the number of factors leads to a new model. That is, the factors in a (1,1,1) model differ from the first factors in a (2,2,2) model.

In this work an alternating least squares model was used that is able to handle missing data. This ability was used to perform cross-validation in order to get the best suited model. 10 % of the data were randomly removed and a model was calculated. Then the model was used to predict the missing data. This procedure was repeated ten times, so that every element of $\underline{\mathbf{X}}$ was removed and predicted exactly once. For every model with P, Q, and R factors the overall Predicted Residual Error Sum of Squares (PRESS) was determined:

$$\mathrm{PRESS}_{PQR} = \sum_{i=1}^{I}\sum_{j=1}^{J}\sum_{k=1}^{K}\left(x_{ijk} - \hat{x}_{ijk}^{PQR}\right)^2$$

Where x is the true and $\hat{x}^{PQR}$ is the predicted value using a (*P, Q, R*)-model.

The determination of a Tucker3 model is rather cumbersome as every factor combination must be calculated separately and calculation time is increased tenfold by the cross-validation procedure. A slight simplification is given by the fact that certain factor combinations are redundant (Louwerse et al., 1999). This is expressed by the following relations:

$$P \le Q \cdot R$$
$$Q \le P \cdot R$$
$$R \le P \cdot Q$$

All combinations that violate the relations are redundant and can be omitted, e.g. a (2,1,3)-model violating the relations does not give a better fit than a (2,1,2)-model. In that way the number of models to be calculated can be reduced significantly. E.g. assuming a maximum of 5 factors for each dimension, only 74 instead of 125 models have to be considered.

RESULTS

Synchronisation with Dynamic Time Warping

The data were autoscaled to ensure a reliable determination of the distance between points. All nine batches were then synchronised using batch number 5 (medium quality, medium rest length) as the reference batch. Before synchronisation batch data vary in length (510, 690 and 870 data points, respectively) and characteristic events like a peak in viscosity due to gelatinization cannot be compared directly as they occur at different points (Figure 5, upper half).

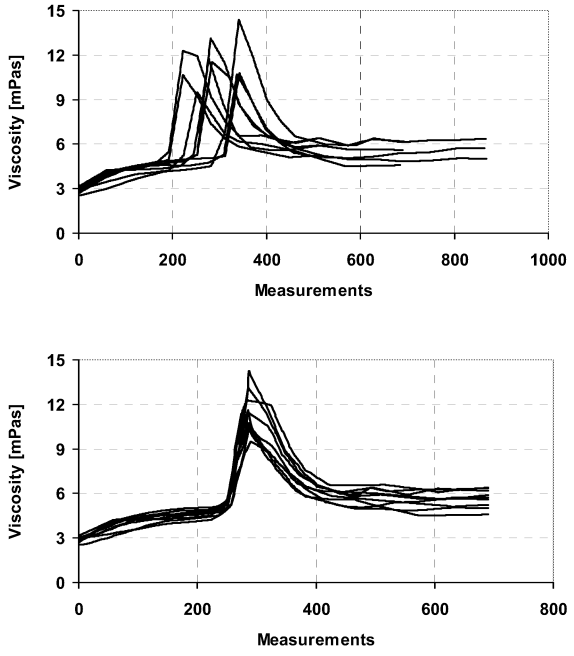

Figure 5: Data Sets Before and After Synchronisation with Dynamic Time Warping.

After synchronisation all batch data sets dispose of the same length (690 data points). At the same time characteristic events are shifted along they time line in order to coincide. Like this batch data become mathematically comparable. Variations between batch data are now based on variations in the process and not on time shifts. In this case a three dimensional array could be built up with 690 measurements, nine batches and seven variables.

Tucker 3 decomposition

The three dimensional data array **X** was autoscaled to allow all variables to have the same weight in the subsequent decomposition. A cross validation was performed to obtain the best combination of factors. PRESS did not show a clear minimum. On the contrary, PRESS decreased with an increasing number of factors. Thus, the number of factors had to be chosen arbitrary. The combination of 4 batch factors, 4 variable factors and 2 time factors was considered a careful and stable choice.

Table 1 shows the entries of the core matrix **C**. The eight highest absolute values are shaded grey. Every element of **C** is assigned to one combination of batch factor, variable factor and time factor. The entries of C can be interpreted as the importance of every factor combination to model the original data array **X**.

Table 2: Core Matrix of the Tucker3 Decomposition

		Variable factor				
		1	2	3	4	
Batch factor	1	-100.63	3.72	18.68	-3.79	Time factor 1
	2	0.70	85.41	-6.66	13.58	
	3	-8.03	-22.42	-10.07	50.04	
	4	-8.68	-4.02	-57.37	-12.96	
	1	-9.86	-4.06	3.55	4.59	Time factor 2
	2	11.63	4.50	26.68	-7.36	
	3	45.21	-0.62	24.88	1.66	
	4	-8.40	-4.22	11.22	5.37	

The 1,1,1-combination possesses the highest absolute weight. It cannot be interpreted technologically. Probably this combination serves as a unspecific scaling quantity that is contrasted by the other entries.

Six of the eight highest elements of the core matrix concern the second and the third batch factor. Apparently, they are important in distinguishing the batch properties. This is shown in Figure 6. Batch factor 2 groups the batches according to the rest length during mashing. Batches with short rests (1, 2, 3) are assigned high values, medium length batches (4, 5, 6) have low values and batches with long rests (7, 8, 9) tend to be centred, with batch 7 being an exception. In contrast, batch factor 3 contains information about the malt quality. Good malt qualities (1, 4, 7) have rather low values and poor malt qualities (3, 6, 9) have high values. Batches with medium malt quality (2, 5, 8) are located in between. This shows that the Tucker3 decomposition is a powerful tool to analyse data and to evaluate the degree of process observability gained by online data. In this case the information of 40000 measurements is compressed into one plane, proving that important process information like raw material quality is hidden in the online data.

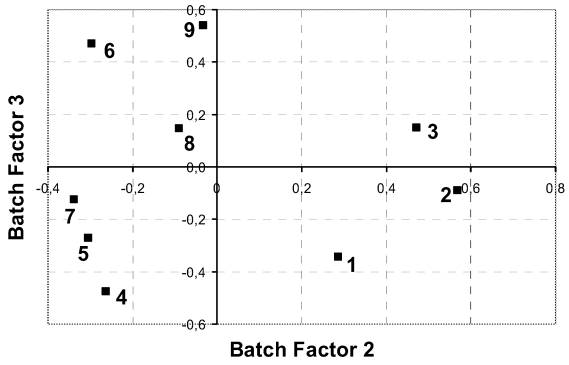

Figure 6: Plot of the second and third batch factor

Another characteristic of the process data is revealed by looking at the time factors (Figure 7). Time factor 1 is represented by the black line and time factor 2 is represented by a grey line. To improve orientation the temperature profile of a mashing process is shown as well.

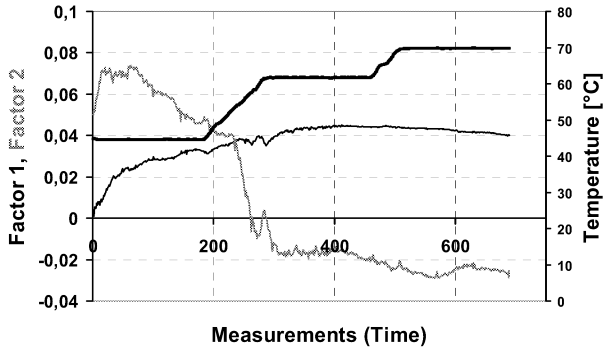

Figure 7: Time Factor 1 (black), Time Factor 2 (grey) and Temperature (bold black) Over Batch Duration.

The first time factor is low at the beginning of the process, rises then and remains rather constant throughout the whole mashing process. It does not differentiate the data very much. The second factor, however, is of almost sigmoid shape. It shows a significant shift around data point 250, corresponding to a temperature of about 55° C. At exactly that time starch gelatinization takes place. Time Factor 2 indicates that correlations between data sets differ before and after gelatinization. The same phenomenon could be observed in a calibration application based on the same data (Mitzscherling et al., 2006).

CONCLUSION

Tucker3 decomposition proves to be a powerful technique to analyse data from batch processes. With this method it is shown, that online data from a mashing process contain relevant information about the product quality of the used raw materials.

ACKNOWLEDGEMENTS

The authors are thankful for the funding by Arbeitsgemeinschaft Industrieller Forschungsvereinigungen (project no. 12552 and no. 13469) and by Wissenschaftsförderung der Deutschen Brauwirtschaft e.V. (project R387).

REFERENCES

Andersson, C. A. and Bro, R., 2000: The N-way Toolbox for MATLAB. *Chemometrics and Intelligent Laboratory Systems,* 52: 1-4.

Gollmer, K. and Posten, C., 1996: Supervision of bioprocesses using a dynamic time warping algorithm. *Control Engineering Practice,* 4: 1287-1295.

Itakura, F., 1975: Minimum Prediction Residual Principle Applied to Speech Recognition. *IEEE Transactions on acoustics, speech, and signal processing,* 23: 67-72.

Kassidas, A., MacGregor, J. F., and Taylor, P. A., 1998: Synchronization of batch trajectories using dynamic time warping. *Aiche Journal,* 44: 864-875.

Kosanovich, K. A., Dahl, K. S., and Piovoso, M. J., 1996: Improved process understanding using multiway principal component analysis. *Industrial & Engineering Chemistry Research,* 35: 138-146.

Kroonenberg, P. M., 1983: *Three-Mode Principal component analysis*. Leiden: DSWO Press.

Louwerse, D. J., Smilde, A. K., and Kiers, H. A. L., 1999: Cross-validation of multiway component models. *Journal of Chemometrics,* 13: 491-510.

Mitzscherling, M., Becker, T., Delgado, A., Kühbeck, F. Krottenthaler, and M., Back, W., 2006: Online monitoring of Gravity, FAN and β-Glucane during mashing. *Journal of the Institute of Brewing* (submitted)

Nomikos, P. and MacGregor, J. F., 1994: Monitoring Batch Processes Using Multiway Principal Component Analysis. *Aiche Journal,* 40: 1361-1375.

Sakoe, H. and Chiba, S., 1978: Dynamic Programming Algorithm Optimization for Spoken Word Recognition. *IEEE Transactions on acoustics, speech, and signal processing,* 26: 43-49.

Souza, F. J., Vieira, L. G. M., Damasceno, J. J. R., and Barrozo, M. A. S., 2000: Analysis of the influence of the filtering medium on the behaviour of the filtering hydrocyclone. *Powder Technology,* 107: 259-267.

Tucker, L. R., 1967: Implications of factor analysis of three-way matrices for measurement of change. *In* Harris, C. W. (ed.), *Problems in Measuring Change*. Wisconsin: The University of Wisconsin Press, 123-137.

Wold, S., Geladi, P., Esbensen, K. H., and Öhman, J., 1987: Multi-way principal components- and PLS-analysis. *Journal of Chemometrics,* 1: 41-56.

BIOGRAPHY

MARTIN MITZSCHERLING was born in Brunswick, Germany and went to the Technical University of Munich to study Brewing Technology. He obtained his degrees in 1999. Then he did doctoral study at the Chair of Fluid Dynamics and Process Automation and received his doctoral degree in 2004. Since 2004 he works at the University of Hohenheim at the Department of Process Analysis and Cereal Technology.

IDENTIFIABILITY OF TIME VARYING PARAMETERS IN A GREY-BOX NEURAL MODEL: APPLICATION TO A BIOTECHNOLOGICAL PROCESS

Gonzalo Acuña
Francisco Cruz
Vicente Moreno
Departamento de Ingeniería Informática, Universidad de Santiago de Chile, USACH
Av. Ecuador 3659 – Santiago - Chile
{gacuna, fcruz, vmoreno}@usach.cl

KEYWORDS
Grey-Box, neural networks, identifiability, time-varying parameters, biotechnological processes.

ABSTRACT

Grey Box Neural Models (GBNM) constitute a real alternative for those processes for which the available *a priori* knowledge is incomplete. In this work an application to a biotechnological process has been performed. Good results of the GBNM acting as a software sensor for the non measured state variables has been shown. However even if the estimation performance is good, correct identification of the time varying parameters is not assured. Identifiability of these parameters has to be tested and some proposed techniques are used in this work showing that the specific growth kinetics and the specific production kinetics can be identified although the last one is more difficult because of its dependence on only one measured variable.

INTRODUCTION

In the development of dynamic system models it is better to take advantage of *a priori* knowledge of a process, generally expressed in terms of sets of ordinary differential equations which represent mass or energy balances. In complex biotechnological processes, the most difficult task is the modeling of time varying parameters, such as the specific kinetics. In order to address this problem, Psichogios and Ungar (1992) proposed to use grey-box models which combine *a priori* knowledge expressed in terms of a phenomenological, or white-box model, with a black-box model such as a neural network. These models have proved to be satisfactory for dynamic systems, they have better generalization characteristics, and they can be identified with a smaller amount of data (Psichogios and Ungar, 1992). Thompson and Kramer (1994) classified these grey-box models into two principal categories: those which deliver intermediate values (of parameters or variables) for use in phenomenological models (serial grey-box models), or those in parallel with the dynamic model, adjusted to compensate for modeling errors (parallel grey-box models). Van Can *et al.* (1996) showed that the series strategy resulted in grey-box models with superior results. More recently Thibault *et al.* (2000), and Acuña *et al.* (1999) have employed and analyzed this type of models demonstrating their performance and their use in complex processes.

Another problem that is often encountered concerns the identifiability of those time varying parameters. This could be a great problem because the aim of grey-box models is not only to minimize the difference between the model output variables and some targets but also to obtain a good model of the unknown time-varying parameters in terms of some relevant variables. So the question is how to know when, even if the outputs are correctly estimated, we can trust in the time-varying parameters values and hence in the determined model. So, the objective of this work is to develop a grey-box neural model for a biotechnological process taking care of the identifiability of the time-varying parameters by using some appropriate indices.

This article is organized as follow: first the biotechnological process is described, then a section is devoted to grey-box modeling. Identifiability methods are then presented followed by some results and conclusions.

BIOTECHNOLOGICAL PROCESS

The bioprocess considered is the production of giberelic acid (a vegetal growth hormone) by the filamentous fungi *Gibberella fujikuroi* growing in a solid state batch culture (SSC) at a laboratory level. A simplified model describing the evolution of the main variables is reported in (Gelmi *et al.*, 2002). This phenomenological model based on material balance laws considers 7 state variables: living Biomass (X), measured Biomass (X_m), urea (U), intermediate nitrogen (N_I), soluble starch (S), giberelic acid (GA_3), produced CO_2 and consumed O_2. Only the last two variables can be directly measured on-line but for including parameter β into the identifiability analysis we will also consider GA_3 as an on-line measured variable. The model equations are the following:

$$\frac{dX_m}{dt} = \mu \cdot X \quad (1)$$

$$\frac{dX}{dt} = \mu \cdot X - k_d \cdot X \quad (2)$$

$$\frac{dU}{dt} = -k \quad (3)$$

$$\frac{dN_I}{dt} = \begin{cases} 0,47 \cdot k - \mu \cdot \left(\frac{X}{Y_{X/N_I}} \right), si\ U \geq 0 \\ -\mu \cdot \left(\frac{X}{Y_{X/N_I}} \right), U(t) = 0, si\ U < 0 \end{cases} \quad (4)$$

$$\frac{dS}{dt} = -\frac{\mu \cdot X}{Y_{X/S}} - m_s \cdot X \quad (5)$$

$$\frac{dGA_3}{dt} = \beta \cdot X - k_p \cdot GA_3 \quad (6)$$

$$\frac{dCO_2}{dt} = \mu \cdot \frac{X}{Y_{X/CO_2}} + m_{CO2} \cdot X \quad (7)$$

$$\frac{dO_2}{dt} = \mu \cdot \frac{X}{Y_{X/O_2}} + m_{O2} \cdot X \quad (8)$$

μ, corresponds to the specific growth rate and its intermediate nitrogen dependence is modeled by a Monod law. β corresponds to the specific production rate of giberelic acid.

$$\mu = \mu_m \cdot \frac{N_I}{k_n + N_I} \quad (9)$$

$$\beta = \frac{\beta_{etam}}{1 + K_i \cdot N_I} \quad (10)$$

The other model parameters were identified on the basis of some specific experiments and experimental considerations. Their values are included in Table I for controlled temperature and water activity conditions (T=25ºC, Aw=0,992).

Table 1: Model parameters

Name/Description		Value
μ_m	Maximum specific growth rate	0.28 [1/h]
β_{etam}	Maximum specific production rate	6.5 10^{-4} [g GA_3/g X h]
k	Urea degradation constant	1.33 10^{-4} [g/h]
k_n	Constant	1.1 10^{-3} [g N_I/g.i.s.]
k_d	Dead constant	0.031 [1/h]
k_p	Giberelic acid degradation rate	4.4 10^{-4} [1/h]
k_i	Intermediate nitrogen production rate	7.86 10^5 [1/g N_I g.i.s.]
m_S	S maintenance coefficient	0.11 [g S / g X h]
m_{CO2}	CO_2 maintenance coefficient	0.11 [g CO_2 / g X h]
m_{O2}	O_2 maintenance coefficient	0.06 [g O_2 / g X h]
$Y_{X/NI}$	Yield coefficient	20.8 [g X / g N_I]
$Y_{X/S}$	Yield coefficient	1.21 [g X / g S]
$Y_{X/CO2}$	Yield coefficient	0.58 [g X / g CO_2]
$Y_{X/O2}$	Yield coefficient	2.11 [g X / g O_2]

GREY BOX NEURAL MODEL

As previously mentioned GBNMs take advantage of the combination of *a priori* knowledge surrounding a given process expressed in terms of a set of differential equations that represent the first principles that govern that process with neural networks. The latter are responsible for the modeling of the interaction between variables that are relevant to the system, and certain parameters whose expressions are difficult to model. It is a well established fact that neural networks are capable of approximating non-linear functions. In particular, it has been demonstrated that perceptrons, with only one hidden layer and an adequate number of neurons in their internal layer, are universal approximators (Hornik *et al*., 1989).

For the purposes of the present work it is important to distinguish between two training modes for neural networks inserted in GBNMs. The first type, also known as the direct learning mode (Acuña *et al*., 1999), uses the error generated at the output of the neural network for the correct determination of its weights (Figure 1).

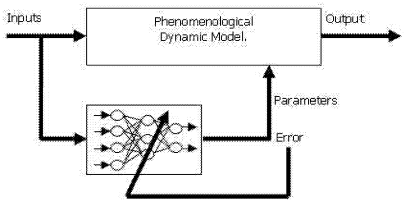

Figure 1: Grey-Box Neural Model in its direct learning mode.

The second type corresponds to an indirect mode by which the error generated at the output of the GBNM is used for the training of the neural network (Acuña *et al*., 1999) (Figure 2).

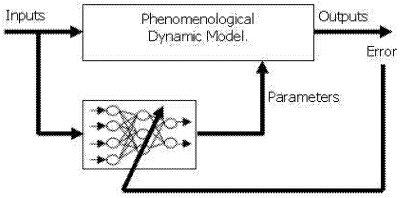

Figure 2: Grey-Box Neural Model in its indirect learning mode.

In the present work the indirect learning mode of the neural network is used. The neural networks used are multi-layered perceptrons with only one hidden layer. The training algorithm is error backpropagation combined with a Levenberg-Marquardt optimization.

The validation of the results obtained is carried out with tests that consist in evaluating the error produced when using the GBNM as a software sensor for the non-measured variables. The error index used is the Index of Agreement (IA), which is presented below :

$$IA = 1 - \frac{\sum_{i=1}^{n}(o_i - p_i)^2}{\sum_{i=1}^{n}(|o_i'| + |p_i'|)^2}$$

Where o_i and p_i are the observed and predicted values respectively, in time i, and N is the total number of data. $p_i' = p_i - o_m$ and $o_i' = o_i - o_m$, where o_m is the median value of the observations.

IDENTIFIABILITY METHODS

The identifiability of model parameters is determined using techniques proposed by (Brun *et al.*, 2002, Reichert and Vanrolleghem, 2001) based on sensitivity and uniqueness analyses. In fact model identifiability will be quantified by measuring the sensitivity of the model output variables to the time varying parameters determined by the neural network part of the grey-box model.

If we considered the measured output variables as $y = \varphi(x, t, \theta)$, where x corresponds to the state variables at time t and θ to the unknown parameter vector then the sensitivity matrix (dimensionless) is:

$$ss_{ij} = \left(\frac{\partial \hat{y}_i}{\partial \theta_j} \right) \theta_j w_i^{1/2} \quad (11)$$

i = 1... number of observations
j = 1... number of parameters

w_i correspond to a scale factor associated with the i^{th} output variable and is defined as the inverse of the measurement error variance.

A dimensionless index of sensitivity, defined by (Brun et al., 2002) is:

$$\delta_j^{msqr} = \sqrt{\frac{1}{N}\sum_{i=1}^{N} s_{ij}^2} \quad (12)$$

Low sensitivity implies low influence of the parameter to the corresponding output hence low identifiability of this parameter.

Uniqueness of the parameters depends on their correlation (Zhang *et al.*, 2003) which is computed from the variance-covariance matrix of the estimated parameters.

$$Corr(\theta_u, \theta_v) = \frac{\text{cov}(\theta_u, \theta_v)}{\sqrt{\text{cov}(\theta_u, \theta_v) \cdot \text{cov}(\theta_u, \theta_v)}}$$

A high correlation between the parameters means that they cannot be uniquely identified from the available observations.

RESULTS

Grey-Box Neural Model

The detailed GBNN considering equations (1)-(8) and the fact that μ and β depend on N_I is shown in Figure 3. It is to notice that the discretized model of eqs. (1)-(8) is represented as a neural network with fixed weights. Only the black-box has variable weights which can be identified by backpropagation considering appropriate activation and transfer functions. 700 data points obtained from simulation of the complete model (eqs (1)-(10)) were used for training purposes while 300 data points were left for validation.

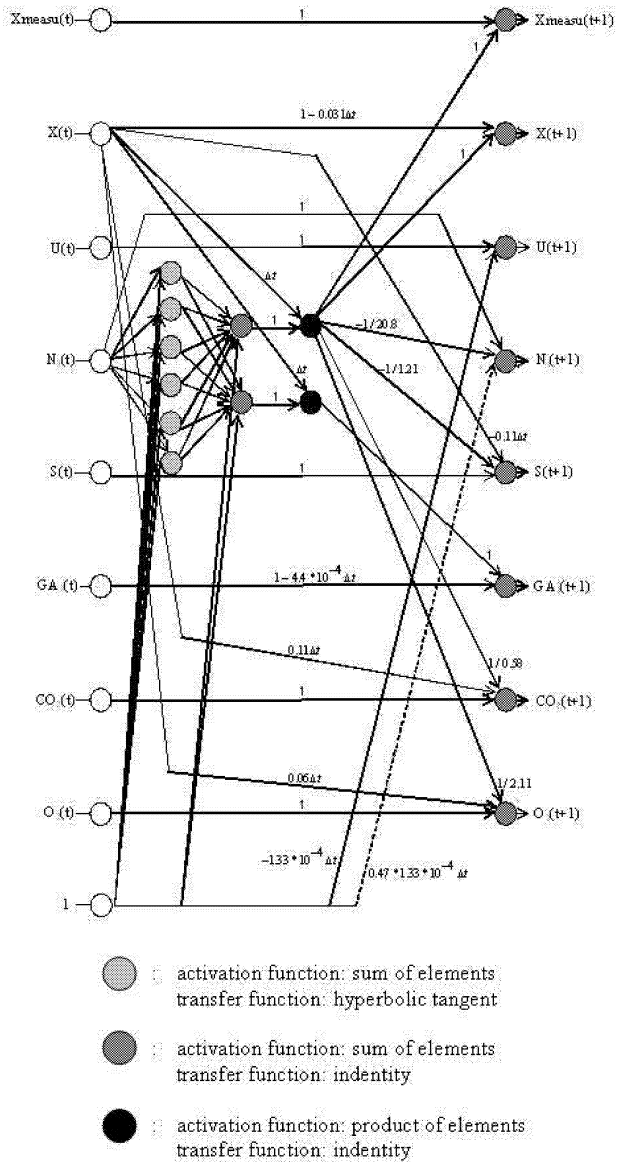

Figure 3: Grey-Box Neural Model for the SSC process.

Two different tests have been built to evaluate the performance and the robustness of the GBNM acting as a software sensor for the first five state variables (eqs (1)-(5)). That means that the GBNM is used in a Model Predictive Output (MPO) mode for those five variables (only from initial conditions) and in an One Step Ahead (OSA) mode

(Billings *et al*., 1992) for the other three variables (eqs (6)-(8)):

1. Results under ideal conditions (0% error and no perturbations).
2. Results with an initial 250% error on the living biomass and affected by a 5% amplitude gaussian noise on all the state variables.

The initial value used for the living biomass (without noise and any perturbation) is 0.01 (gr/gr).

Test 1

For concision reasons only the results on the three most relevant variables or parameters for this analysis will be shown. A very good coherence can be seen between the simulated and estimated values of the living biomass (X) and the specific growth rate as it is shown in figures 4 and 5. Good results are also obtained for the estimation of the other state variables (IA > 0.99). A non as good estimation of the specific production rate can be observed. This is probably due to the exclusive dependence of this parameter to only one output variable (GA_3) as it is shown in Table II.

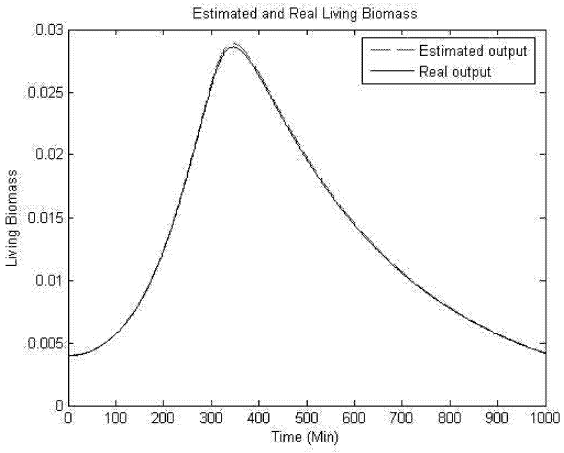

Figure 4: Simulated (Continuous lines) and estimated (dotted lines) living biomass

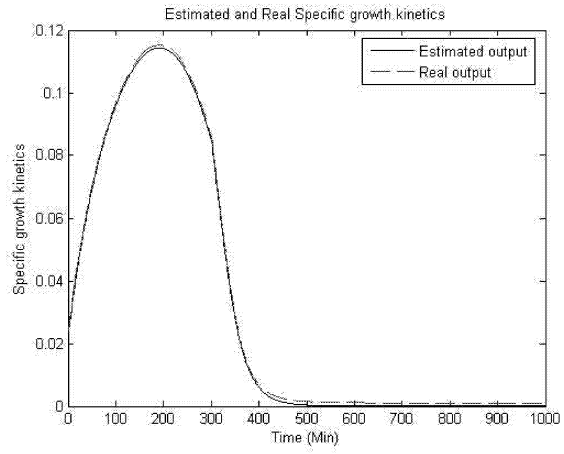

Figure 5: Simulated (Continuous lines) and estimated (dotted lines) specific growth rate.

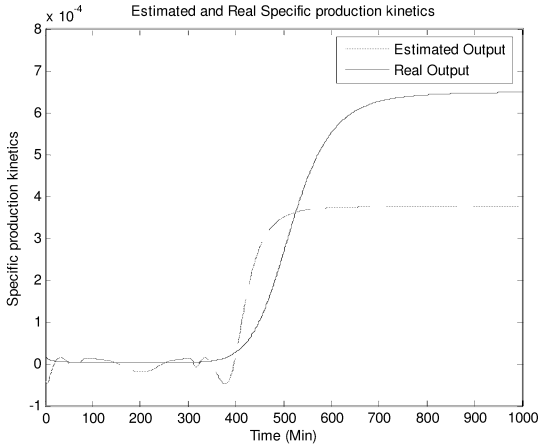

Figure 6: Simulated (Continuous lines) and estimated (dotted lines) specific production rate.

Test 2

A large initial perturbation on the state variable (living biomass) is quickly compensated by the GBNM acting as a software sensor and a 5% noise affecting the output is well filtered by the method. The error of 250% in the initial living biomass, although is not a real case, allows to clearly show the properties of convergence and stability of the method, supposing that in a practical application a great error in the initial conditions is committed, in the presence of noisy measurements. General results are shown in figure 7, 8 and 9. The same above mentioned remark concerning the specific production kinetics β has to be stated

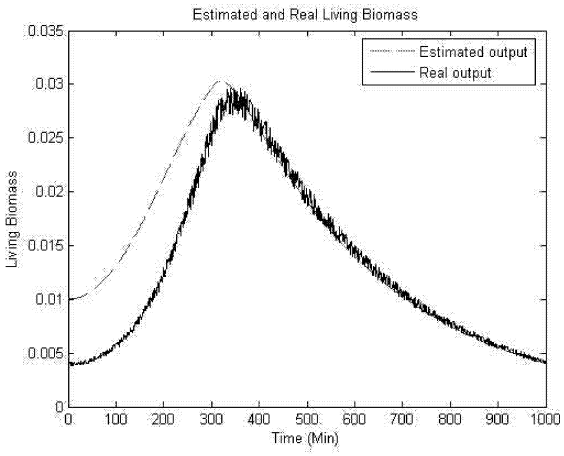

Figure 7: Simulated (Continuous lines) and estimated (dotted lines) living biomass

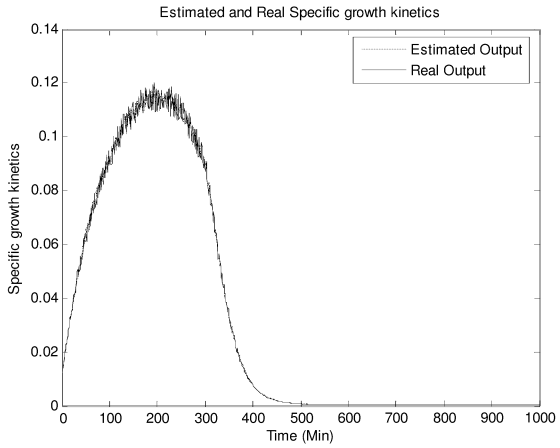

Figure 8: Simulated (Continuous lines) and estimated (dotted lines) specific growth rate.

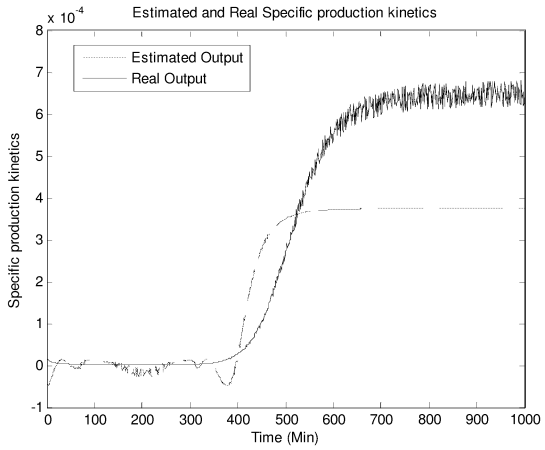

Figure 9: Simulated (Continuous lines) and estimated (dotted lines) specific production rate.

Identifiability Analysis

For computing the sensitivity matrix the derivative of the output to the corresponding parameters was determined from the following finite difference approximation:

$$\frac{\partial y_i}{\partial \theta_j} \approx \frac{y(x,t,\theta_j+\Delta\theta_j)-y(x,t,\theta_j)}{\Delta\theta_j} \quad (13)$$

A small enough parameter perturbation $\Delta\theta_j$ was used in order to assure a small truncation error in the finite difference approximation. The considered outputs and parameters were respectively CO_2, O_2, GA_3 and the specific kinetics μ and β. Hence the sensitivity matrix was constructed from the determination of:

$$\frac{\partial CO_2}{\partial \mu_t}, \frac{\partial CO_2}{\partial \beta_t}, \frac{\partial O_2}{\partial \mu_t}, \frac{\partial O_2}{\partial \beta_t}, \frac{\partial GA_3}{\partial \mu_t}, \frac{\partial GA_3}{\partial \beta_t} \quad (14)$$

In Table II results for the sensitivity index δ_j^{msqr} showing that β has no influence over CO2 and O_2 are presented. It can also be noticed that μ_t has no influence over GA_3.

Table 2: Sensitivity index δ_j^{msqr} for different output variables and parameters.

δ_j^{msqr}	μ_t	β_t
CO_2	0.0020	0
O_2	0.0012	0
GA_3	0	0.1311

Sensitivities of each parameter to the corresponding output variables are shown in Figures 10, 11 and 12. The greater influence of the parameters over the output variables ranges from 100 to 400 (min) which corresponds to the period of greater biomass growth.

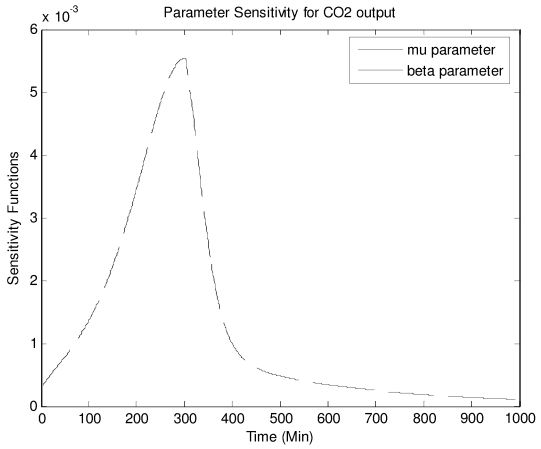

Figure 10: Relative sensitivity for CO2 output.

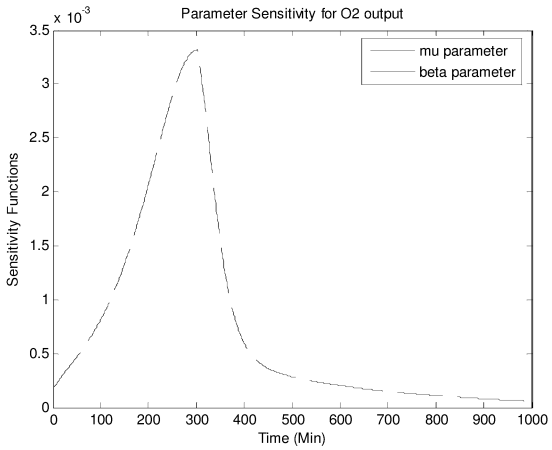

Figure 11: Relative sensitivity for O2 output.

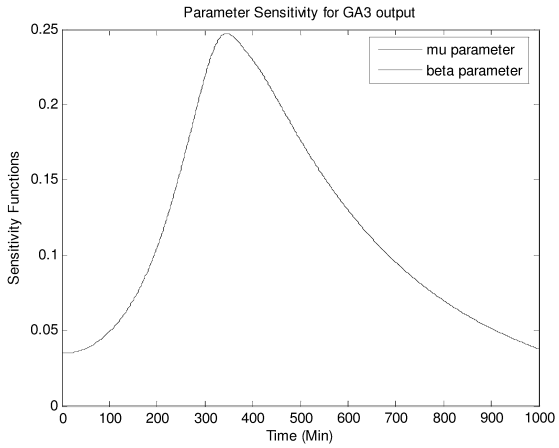

Figures 12: Relative sensitivity for GA3 output.

Uniqueness of parameters was analyzed from the following correlation Table (III).

Table 3: Correlation coefficients between estimated parameters.

$Corr(\theta_u, \theta_v)$	μ	β
μ	1	-0.8554
β	-0.8554	1

It can be seen that the low absolute value of the correlation index between the parameters obtained (< 0.95) allows them to be uniquely determined from an adequately identification procedure.

CONCLUSIONS

GBNM constitute a real alternative for those real world processes for which the available *a priori* knowledge is incomplete, for example in a variety of industrial processes. As in GBNM only some of the physical and/or chemical laws that represent the model are known, and there are unknown parameters that must somehow be estimated, multi-layered perceptron neural networks have been employed for their notable capacity to approximate complex functions on the basis of observed data.

In this work an application to a biotechnological process has been performed. Good results of the GBNM acting as a software sensor for the non measured state variables has been shown. Convergence and noise rejection capacities were also some of the valuable features of this kind of software sensor. However even if the estimation performance is good, correct identification of the time varying parameters is not assured. Identifiability of these parameters has to be tested and some proposed techniques are used in this work showing that both time-varying parameters, the specific growth kinetics μ and the specific production kinetics β can be identified although the last one is more difficult to be correctly identified because of its dependence on only one measured variable (GA_3).

Acknowledgements: The authors would like to acknowledge grants from the Chilean Government (FONDECYT-1040208).

REFERENCES

Acuña A., Cubillos F., Thibault J., Latrille E., 1999, Comparison of Methods for Training Grey-Box Neural Networks Models, Computers and Chemical Engineering Supplement, 23:561-564.

Billings, S., Jamaluddin, B and Chen, S., 1992, "Properties of neural networks with applications to modeling non linear dynamical systems", International Journal of Control, 55(1):193-224.

Brun, R.; Kühni, M.; Siegrist, H.R.; Gujer, W. and Reichert, P. 2002. "Practical identifiability of ASM2d parameters - systematic selection and tuning of parameter subsets". Water Research 36(16):4113-4127.

Gelmi, C., Perez-Correa, R. and Agosin, E., 2002, "Modelling *Gibberella fujikuroi* growth and GA3 production on solid-state fermentation", Process Biochemistry, 37(9):1033-1040.

Hornik, K., Stinchcombre, M. and White, H., 1989, "Multilayer feedforward networks are universal approximators", Neural Networks, 2:359-366.

Psichogios D., Ungar L., 1992, A Hybrid representation approach for modeling complex dynamic bioprocesses. Bioprocess Engineering, 22: 547-556.

Reichert P. and Vanrolleghem P. 2001. "Identiability and uncertainty analysis of the river quality model no.1 (RQM1)". Water Sci Technol, 43(7):329-338.

Thibault, J, Acuña, G., Pérez-Correa, R., Jorquera, H., Molin, P., Agosin, E., 2000, "A hybrid representation approach for modelling complex dynamic bioprocesses" Bioprocess Engineering, 22(6):547-556.

Thompson M., Kramer M., 1994, Modeling Chemical Processes Using Prior Knowledge and Neural Networks, Computer & Chemical Engineering, 40:1328-1340.

Van Can H, Braake H., Dubbelman S., Hellinga C., Luyben K., Heijnen J., 1996, Understanding and Applying the Extrapolation Properties of Serial Gray-Box Models, AIChE journal, 44: 1071-1089.

Zhang, Z.F.; A.L. Ward. and G.W. Gee. 2003. "Estimating soil hydraulic parameters of a field drainage experiment using inverse techniques". Vadose Zone J. 2:201–211.

FOOD PRODUCTION SIMULATION

A model based on factorial design to predict the evolution of *Brettanomyces sp.* population as function of environmental conditions in winemaking

Claudia Castro Martínez
Cédric Brandam
Felipe Ramón Portugal
Pierre Strehaiano
Laboratoire de Génie Chimique, UMR-CNRS 5503
5 rue Paulin Talabot, 31106
Toulouse cedex 1, France
E-mail: Cedric.Brandam@ensiacet.fr

KEYWORDS

Microbial growth, lag phase, *Brettanomyces*, mathematic model, wine

ABSTRACT

Contamination of wines by *Brettanomyces* is an increasing industrial problem. Here, we propose a model able to predict the evolution of a *Brettanomyces* population as function of environmental conditions as temperature, ethanol concentration or dioxide sulfur concentration. Polynomial models obtained from factorial design realized on synthetic medium gave the lag phase, the specific growth rate and the maximal biomass concentration as function of these medium factors. A logistic model was then used with the determined growth parameters to represent the evolution of *Brettanomyces* population.
The factorial design showed that temperature has an important effect on maximal biomass concentration and specific growth rate but a negligible effect on lag phase. Conversely, molecular sulfur dioxide had an important effect on lag phase but a little influence on growth parameters. Ethanol concentration played an important role on the three parameters tested.

INTRODUCTION

In wine industry, the market competition is more and more important with notably the arrival of "wines from new world". Today, the wine quality and the productivity are factors more considered than yesterday in winemaking. Winemaking needs micro-organisms to ferment sugars into alcohol, to decrease acidity of wine (malo-lactic fermentation) or to produce aromas and other sensorial properties. With these objectives, selected strains are used in the beginning of the fermentation. Nevertheless, natural micro-organisms can contaminate the must because it is a not sterilized process. Among these contaminants, the yeast *Brettanomyces/Dekkera* is particularly undesirable. It can be found in must but also in wine (Fulgelsang 1997). Typically, these yeasts grow after alcoholic and malo-lactic fermentation during storage of wine in tanks, barrels, or bottles (Chatonnet et al. 1995). They are considered as organoleptic contaminants of wine because they produce volatile phenols (4-ethylphenol and 4-ethylgaiacol). These components are usually described in sensorial analysis as responsible for "horse sweat" or "mousy taint" flavours (Heresztyn 1986; Chatonnet et al. 1995).
For about twenty years, some works have been realized to understand why *Brettanomyces* appears or not during fermentation and wine storage. However, the influence of the environmental factors has been little studied. Particularly, it is known that growth of yeasts in general is influenced by temperature and ethanol concentration but little and controversial data are available for the genus *Brettanomyces*. In winemaking, sulfur dioxide is often added to avoid all type of contamination, but its effect on *Brettanomyces* growth is not yet really evaluated.
In this context, the aim of this work was to develop a model to predict the evolution of *Brettanomyces* population in wine as function of different factors as ethanol concentration, temperature and sulfur dioxide concentration. A three factorial design was done to evaluate the influence of these three parameters. We obtained polynomial models to determine classical parameters of yeast growth: lag phase, specific growth rate and maximal population. A logistic model was then used to represent the growth phase. Finally, we were able to simulate the evolution of *Brettanomyces* population for a

medium with a known composition in ethanol and sulfur dioxide and for a fixed temperature.

MATERIALS AND METHODS

Yeast strain

The *Brettanomyces bruxellensis* strain used in this work was isolated in a winemaking plant in France. Its identification was made using PCR by IDAC laboratory (Nantes, France).

Culture media

Cultures were made on synthetic medium close to wine. The composition was in g/L: glucose, 10; fructose, 10; $MgSO_4.7H_2O$, 0.4; KH_2PO_4, 5; $(NH_4)_2SO_4$, 0.5; yeast extract, 0.5; citric acid, 0.3; malic acid, 3; glycerol, 6. Sterilization was made during 15 min at 120°C.

Culture conditions

Preculture was prepared in two steps of 35 h each. First, in medium without ethanol; then, 3% (v/v) of ethanol was added in culture medium. The experiments were carried out in cotton plugged Erlenmeyer flasks of 500 mL with a 300 mL working volume at 150 rpm and without aeration. After sterilization, the medium was inoculated with $3x10^6$ cells/mL. Temperature was controlled. Before inoculation, the alcoholic concentration was set to the wanted level by addition of ethanol. The initial pH value was adjusted and the initial free sulfur dioxide concentration was fixed.

Analytical techniques

Biomass concentration was followed by two techniques. A correlation between the optical density of yeast suspension at 620 nm and the cell dry weight gives weight concentration.

Data treatment

Experimental biomass concentrations were smoothed by a cubic spline function. The lag phase was then predefined as the time needed to double the initial biomass ($\lambda=2X_o$). The specific growth rate μ_{max} and the maximal biomass concentration X_{max} were equally obtained from smoothed experimental data.

The statistical software (Statgraphics, Centirion XV) was used to analyze the results of the factorial design. In order to determine the sensibility of the calculated parameters, an analysis of variance (ANOVA) was done.

RESULTS AND DISCUSSION

Role of pH

Preliminary experiments were done to evaluate the effect of the pH on microbial growth and lag phase. The pH values tested were 3.2 and 3.6, with no sulphur dioxide, for two ethanol concentrations (7 and 10% v/v) and two temperatures (18 and 25°C). The results obtained showed that pH had no influence on the lag phase and growth (data not showed). So, pH was not taken into account in the factorial design as individual factor. However, it is well known that pH plays an important role for the action of sulphur dioxide on microbial growth. When SO_2 is added in a medium, a part is combined with other constituents of wine and a part remains free. Depending on pH value, the free SO_2 is partially dissociated and transformed in molecular SO_2. Only the molecular SO_2 is able to enter the cell and act on micro-organism activity. The amount of available molecular SO_2 is function of pH value and free SO_2 concentration. The equation used to calculate the molecular SO_2 is:

$$MolecularSO_2 = \frac{FreeSO_2}{\left(10^{(pH-1.81)}+1\right)}$$

As consequence of this preliminary study, pH value allows adjusting the desired initial molecular SO_2.

Factorial design

A 2^3 factorial design with four central points was used to determinate the significance of individual and interaction effects of the initial ethanol concentration, initial molecular SO_2 concentration and temperature on the maximal growth (X_{max}), maximal specific growth rate (μ_{max}) and lag phase (λ). The value factors are presented in table 1.

Table 1. Coded factor levels and real values for the experimental design

Factor	Low value (-1)	High value (+1)
Ethanol (% v/v)	7	10
Molecular SO_2 (mg/L)	0.16	0.39
Temperature (°C)	18	25

The results of the adjusted models obtained for maximal biomass concentration, maximal specific growth rate and lag phase as function of the more significant variables were:

$\mathbf{X_{max}} = 1.80 - 0.21\ E + 0.16\ T$

μ_{max} = 0.039 - 0.009 EOH + 0.011 T - 0.003 E*SO_2m - 0.004 E*T

λ = 104.8 + 78.3 EOH + 72.5 SO_2m - 10.9 T + 73.2 EOH*SO_2m - 6.0 EOH*T - 4.2 SO_2m*T

Where E is the initial ethanol concentration, SO_2m the initial molecular sulfur dioxide concentration and T the temperature.

The analysis of variance (ANOVA) showed that μ_{max} and λ presented a high correlation coefficient (>0.95) and X_{max} the highest coefficient (0.99). The polynomial models could be considered statistically significant according to the T-test with 95% of confidence.
The figures 1 to 3 show the Pareto charts for the three studied responses. They allow visualizing the significance of each factor on studied responses.

Maximal biomass concentration and maximal specific growth rate.

Figure 1 concerns the maximal biomass concentration and figure 2 the maximal specific growth rate. The ethanol concentration (E) and the temperature (T) had a significant effect on these two factors whereas the molecular SO_2 (SO_2 m) was not significant. For maximal biomass concentration, no interaction factor was significant whereas for maximal specific growth rate ethanol-temperature and ethanol-sulphur dioxide interactions were little significant. Finally, the most important effects were those of ethanol concentration and temperature for these two growth parameters. Ethanol concentration had a negative effect whereas temperature increased the growth rate and the quantity of produced cells.

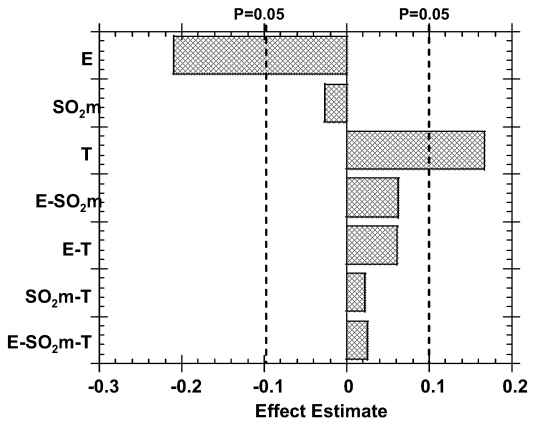

Figure 1. Pareto chart of all effects on maximal biomass concentration.

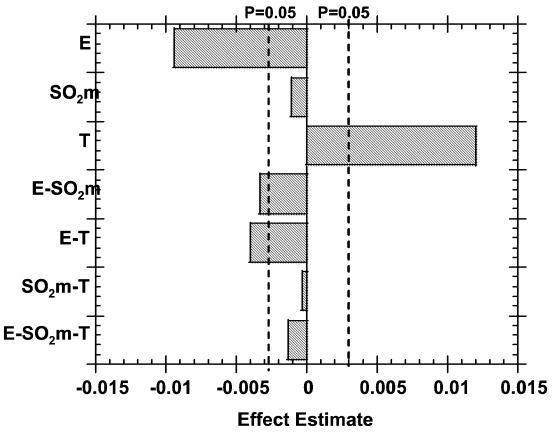

Figure 2. Pareto chart of all effects on maximal specific growth rate.

The inhibitory activity of ethanol can be linked to the cell membrane permeability. Its toxicity is associated with the solubility in membrane lipids (Leao and Van Uden 1982). Moreover, the ethanol was found to inhibit hexokinase and some amino-acid synthesis enzymes and thus metabolic deficiencies on the cell reproduction (Nagodawithana et al. 1977).
On the other hand, the positive effect of the temperature can be related to the increase of the membrane fluidity. It is equally associated to the increase in the affinity of the protein transport for substrates (Nedwell 1999). Silva et al. 2004 showed the same behaviour as regards of temperature and ethanol concentration for *Brettanomyces* and *Dekkera* in wine.

Lag phase

Figure 3 shows that lag phase was mainly affected by ethanol and molecular SO_2 concentrations. These two factors increased the lag phase. The interaction of the ethanol and molecular SO_2 was also very significant with a synergic effect. A slightly negative effect was observed for the temperature. The other interactions were not really significant.
Traditionally, the molecular SO_2 is used as an antimicrobial agent in winemaking (Beech and Thomas 1985). The addition of this compound in wine decreases the specific ATPase activity and as consequence increases lag phase. In the cell, sulphur dioxide may react with proteins, nucleic acids and some cofactors. It can inhibit enzymes and as consequence cells are unable to replicate (Romano et al. 1993).

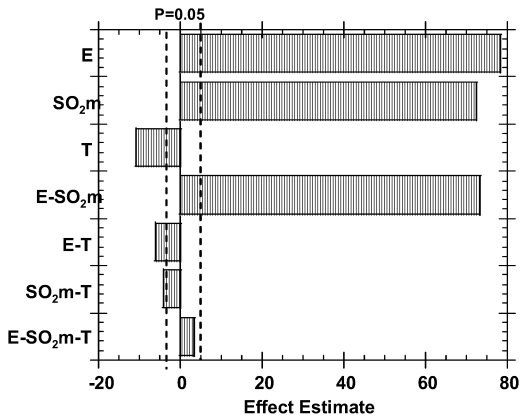

Figure 3. Pareto chart of all effects on lag phase.

Model for *Brettanomyces* growth

The factorial design enabled to determine the main influent factors on *Brettanomyces* growth. It gave three polynomial models to determine λ, μmax and Xmax as function of temperature and medium composition in ethanol and sulphur dioxide.

To represent the evolution of the *Brettanomyces* population, we used the logistic model (Verhulst 1845). These model is known for its "goodness of fit" to describe the dynamic of the biomass in a batch culture.

The general form of the logistic equation is:

$$\frac{dX}{dt} = \mu_{\max} X\left[1 - \frac{X}{X_{\max}}\right] \qquad (1)$$

The integration of equation 1 gives:

$$X(t) = \frac{X_o e^{\mu \max t}}{1 - (\frac{X_o}{X_{\max}})(1 - e^{\mu \max t})} \qquad (2)$$

The parameters Xmax and μmax were calculated for each experiment with the polynomial models. As the logistic model does not allow representing the lag phase, it must be combined with the lag phase polynomial model.

A good correlation between experimental points and modeled values for biomass concentrations was obtained (> 0.95) for all the experiments.

Figure 4 shows examples of biomass profiles for 6 experiments. The temperature increase favoured the growth rate and the maximal population but didn't act on the lag phase (4A). Moreover, the increase of ethanol concentration increased the lag phase and decreased the maximal population obtained (4B). We can equally see the importance of initial molecular SO_2 on the lag phase but also the absence of effect on the growth rate (4C).

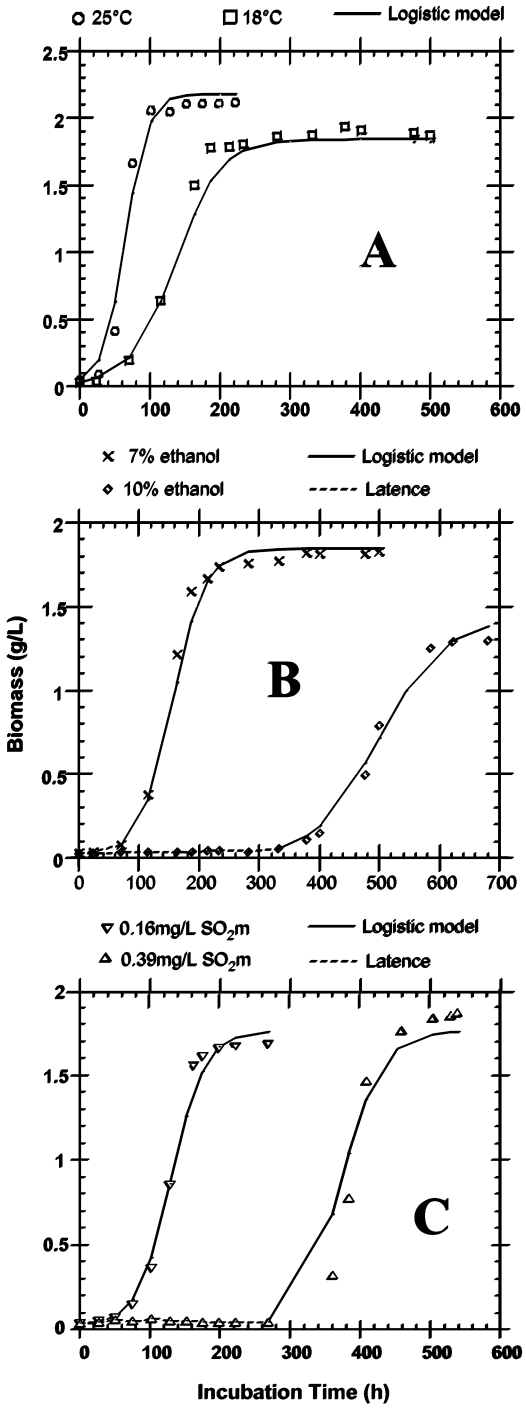

Figure 4. Comparison of experimental biomass values (points) and modelled values (lines). (A) experiment at 7% of ethanol, 0.16 mg/L of initial SO_2 molecular and 25 or 18°C; (B) experiment at 18°C, 0.39 mg/L of initial SO_2 molecular and 7 or 10% of ethanol; (C) experiment at 25°C, 0.39 or 0.16 mg/L of initial SO_2 molecular and 10% of ethanol.

CONCLUSIONS

This work showed that high concentrations in ethanol led to decrease the maximal biomass concentration and maximal specific growth rate. Temperature acted equally on growth but by increasing the maximal specific growth rate and the biomass concentration. For the lag phase, the initial ethanol and molecular SO_2 concentrations had a great effect. The interactions between these two factors were equally very important, increasing the lag phase. These compounds are well known as inhibitors of micro-organisms (Moulin et al. 1984; Du Toit and Pretorius 2000). It is interesting to remark that SO_2 delayed the beginning of the growth but didn't act on the growth rate and on the quantity of final biomass. The mechanism of action of this compound remains still little known. Similar results were obtained by Medawar et al. 2003 on another *Brettanomyces* strain.

In this work, we established a model to predict the evolution of *Brettanomyces* population in a synthetic wine medium. Industrially, the problem is not really the *Brettanomyces* presence but some by-products as ethyl-phenol and acetic acid produced by this yeast. The following of this study is to determine the relation between the growth of *Brettanomyces* and the production of these undesirable compounds.

REFERENCES

Beech, F.W., Thomas, S. 1985. Action antimicrobienne de l'anhydride sulfureux. Bull. d'O.I.V. 58:564-581.

Chatonnet, P., Dubourdieu, D., Boidron, J.N. 1995. The influence of *Brettanomyces/ Dekkera sp.* Yeasts and lactic acid bacteria on the ethylphenol content of red wines. Am Enol Vitic 46:463-468.

Du Toit, M., Pretorius., I.S. 2000. Microbial spoilage and preservation of wine: using weapons from nature's own arsenal-review. South African J. Enol. Vitic. 21:76-96.

Fugelsang, K. 1997. *Brettanomyces*: Dr. Jekyll ou Mr. Hyde des vins? Biofutur 182:22-23.

Heresztyn, T. 1986. Formation of substituted tetrahydropyridines by species of *Brettanomyces* and lactovacillus isolated from mousy wines. Am. J. Enol. Viticult. 37:127-132.

Leao, C., Van Uden, N. 1982. Effects of ethanol and other alkanols on the glucose transport system of *Saccharomyces cerevisiae* suspensions. Biotechnol. Bioeng. 24:2601-2604.

Medawar, W., Strehaiano, P., Délia M.L. 2003. Yeast growth: lag phase modeling in alcoholic media. Food Microbiol. 20:527-532.

Moulin, G., Boze, H., Galzy, P. 1984. Inhibition of alcoholic fermentation. Biotechnol. Genet. Eng. Rev. 1:365-382.

Nagodawithana, T. W., Whitt, J.T., Cutain., A.J. 1977. Study of the feedback effect of ethanol on selected enzymes of the glycolitic pathway. J. Am. Soc. Brew. Chem. 35:179-183.

Nedwell, D.B. 1999 Effect of low temperature on microbial growth: lowered affinity for substrates limits growth at low temperature. FEMS Microbiol Lett 30:101-111.

Romano, P., Suzzi, G. 1993. Sulfur dioxide and wine microorganisms. In Fleet, G. H. (Ed.), Wine Microbiol. and Biotechnol. Harwood Academic, Switzerland, 373-393.

Silva, P., Cardoso, H., Gerós, H. 2004. Studies on the wine spoilage capacity of *Brettanomyces /Dekkera sp.* Am. J. Enol. Vitic. 55:1.

Verhulst, P.F. 1845 Recherches mathématiques sur la loi d'accroissement de la population. Nouv mém de l'Academie Royale des Sci et Belles-Lettres de Bruxelles 18:1-41.

IMPROVED VENTILATION INSIDE A LARGE MEAT CARCASS CHILLER FOLLOWING CFD MODELLING

Laurent Picgirard
Association pour le Développement
de l'Institut de la Viande (ADIV)
2, rue Chappe
63039 Clermont-errand Cedex 2
E-mail: laurent.picgirard@adiv.fr

Pierre-Sylvain Mirade
Institut National de la Recherche
Agronomique (INRA)
CEPIA, QuaPA-C2T, Theix
63122 St Genès Champanelle, France
E-mail: mirade@clermont.inra.fr

KEYWORDS
Ventilation level, Air velocity, CFD, Carcass chiller, Fan.

ABSTRACT

We discuss the application of a computational fluid dynamics (CFD) approach, first to predicting air velocities in a large batch-type meat carcass chiller, and second to designing low-cost technical solutions to increase ventilation levels around the carcasses. Comparisons between calculations and measurements revealed close agreement in the qualitative prediction and some inaccuracies in the quantitative prediction of airflow velocities in both the existing and the modified chiller configurations. Adding two rows of six fans above the fifth and thirteenth rows of carcasses led to a marked increase in air velocity in the volume filled by the meat carcasses as a result of an increase in air change rate. Therefore, compared with experimentation, CFD is a low-cost option well-suited to testing new technical solutions designed for improving the operation of food plants.

INTRODUCTION

Carcass chiller performance is known to be affected by airflow distribution, equally as much in continuous-type systems as batch-type systems.
In continuous chillers, although the movement of each carcass means average air velocity remains the same, the existence of poorly ventilated areas is much more harmful to process efficiency than airflow heterogeneity because potentially large poorly ventilated areas are liable to have a strong and durable impact on chilling kinetics (Daudin and Van Gerwen 1996). Mirade et al. (2002) calculated that increasing ventilation in a continuous-type chiller from a mean velocity of 0.17 $m.s^{-1}$ (with variations ranging from 0.10 to 0.45 $m.s^{-1}$) to 0.39 $m.s^{-1}$ (with variations ranging from 0.10 to 1.02 $m.s^{-1}$) led to a 14% increase in the heat extracted from an 80 kg pork carcass. These authors also indicated that this adjustment in ventilation level shortened the chilling time of the carcass by only 20 min, while increasing its total weight loss from 1.3% to 1.7%.
In batch chillers, the spatial heterogeneity of air velocity is the main source of variations in chilling times and weight losses, which are the two most important economic criteria in terms of process efficiency and homogeneity. Wooton's study (1986) on the relative effects of various parameters (carcass location, carcass weight, fatness, etc.) on deep leg temperature in beef carcasses chilled in a conventional batch plant highlighted variations of over 10°C in the temperatures reached at 24 h after slaughter. A multivariate analysis showed that carcass location (*i.e.* air velocity distribution) in the room was as important as carcass weight in explaining the observed temperature heterogeneity. Kondjoyan and Daudin (1997) calculated that the core temperature and weight losses of 80 kg pork carcasses varied from 1.7°C to nearly 11°C and from 1.8% to 2.8%, respectively, depending on whether the carcasses were located close to a fan refrigerator unit where airflow velocity, temperature and turbulence reached 2.0 $m.s^{-1}$, -1°C and 40%, respectively, or whether they were located in a poorly-ventilated area where air velocity, temperature and turbulence reached 0.5 $m.s^{-1}$, 3°C and 6%.
However, there can be no ideal chiller design and operation since each configuration suffers from specific disadvantages leading to airflow heterogeneity which impairs process efficiency, caused by both the air conditioning system and plant geometry (Mirade and Picgirard, 2001).

Until now, engineers have used practical know-how and rule of thumb in chiller design and operation, with all the inherent risks of making mistakes. However, since Computational Fluid Dynamics (CFD) codes have become commercially available over the last ten years, many authors have investigated the use of CFD as a tool for rationalising design and operation in the food industry (Scott 1994; Mariotti et al. 1995; Scott and Richardson 1997; Mirade and Daudin 1998a; Hu and Sun 2000; Hoang et al. 2000; Foster et al. 2002; Mirade et al. 2002; Xia and Sun 2002; Xie et al. 2006).
General purpose CFD codes such as Fluent or CFX were designed for solving turbulent fluid flow problems coupled with heat and mass transfers in a given geometry by the use of a mesh where all the Navier-Stokes transport equations are solved. The above-mentioned studies highlight how CFD can be applied to improve our understanding of the dynamics and physics of the chilling operation and thus optimise existing equipment and help design new solutions.
Mirade and Picgirard (2001) used CFD techniques to improve air circulation around beef carcasses in a

continuous-type chiller. Based on 2D models, they showed that installing a jet deflector in front of the cooling battery fans offered a good and efficient compromise between airflow patterns and investment costs, but without experimentally checking the beneficial effects of adding this deflector.

The objective of this study was to improve airflow distribution inside a 1,825 m^3 batch-type meat carcass chiller where measurements had pointed out insufficient ventilation levels. Two types of 3-dimensional CFD model were constructed; the first was designed to match calculated air velocities with measurements in order to fit the parameters of the porous media used to represent the rows of carcasses, while the second type was designed to identify a technical solution offering significant improvements in ventilation levels around the carcasses. The solution designed was then installed, and its efficiency in terms of increased ventilation levels was assessed and compared to the previously obtained numerical results.

MATERIALS AND METHODS

Description of the meat carcass chiller

The large batch-type meat carcass chiller investigated in this study is illustrated in Figures 1a (transverse section) and 1b (top view). The chiller was 18.9 m long on one side, 21 m long on other side, 16 m wide and 6 m high, giving an overall volume of over 1,825 m^3. The full airflow rate blown into the plant was 173,000 $m^3.h^{-1}$, *i.e.* an air change rate of about 95 volumes.h^{-1}. The filling capacity of this large carcass chiller was 375 beef carcasses arranged in 15 rows (Figures 1a and 1b).

The air conditioning system was composed of four cooling batteries coupled with 14 fans placed above the rows of carcasses, near the ceiling and approximately at half-width of the chiller (Figures 1a and b). Air was blown through 0.6 m-high openings located on both sides of the four cooling batteries and extracted through the 14 fans set underneath the cooling batteries at 4.1 m from the floor (Figures 1a and b). These figures also include two additional rows of six fans, detailing the change performed in the meat carcass chiller following CFD modelling in order to improve ventilation levels (See section 'Air velocity fields in the modified chiller configuration').

The first row of carcasses was located at 0.62 m from the side wall of the plant, and the last 1.14 m away from the other side wall. Distance between two consecutive rows was 0.9 m, except between rows 6-7 and 10-11 where free space reached 2.37 m and 1.17 m, respectively (Figures 1a and b).

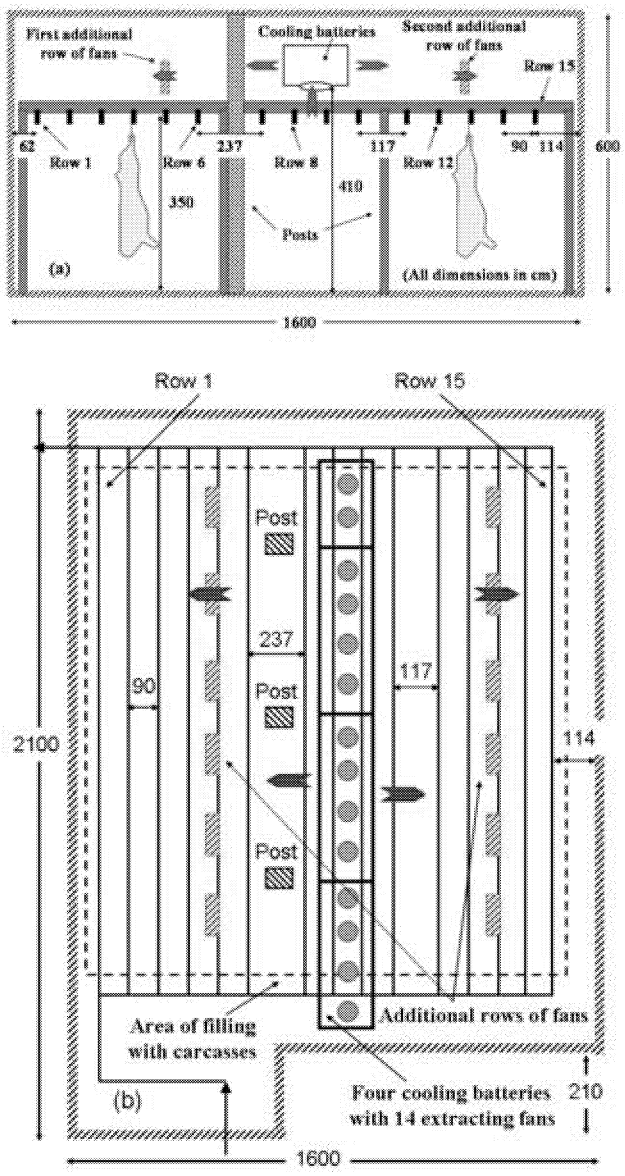

Figure 1: Geometry of the Large Meat Carcass Chiller Studied: (a) a Transverse View, and (b) a Top View (the Arrows Represent Air Inflow and Air Outflow)

Air velocity measurements

An experimental study of air velocity carried out in the chiller yielded a diagnosis of its overall operation (Picgirard and Mirade 2005). This diagnosis was obtained using a method specially developed for measuring velocity by means of a hot-film anemometer in an industrial air flow (Mirade and Daudin 1998b).
This method allows the average air velocity values to be calculated quickly and accurately at up to several thousand points via the following procedure: (i) probes are moved slowly and continuously, and measurements are recorded at regular intervals; (ii) a signal processing technique is applied to the data to eliminate as far as possible any time

variations due to airflow unsteadiness, and thus obtain mean air velocity values *versus* spatial co-ordinates. Measurement accuracy is 0.1 $m.s^{-1}$, *i.e.* equal to the measurement error when using a hot-film anemometer. In addition, this method reduces experiment duration 350-fold compared with the standard procedure which consists in averaging measurements over a long enough time to obtain a constant value for mean velocity (Mirade and Daudin 1998b).

Owing to the batch operating conditions of the meat carcass chiller investigated in this study, a purpose-built cableway-type system (Mirade and Picgirard 2001) was used to hold the measurement devices and automatically move them at a slow and fairly constant velocity, at heights ranging from 66 cm to 311 cm (at 35 cm steps) and for lengths ranging from 273 cm to 1673 cm (at 10 cm steps). The measurement devices were multi-directional hot-film anemometers (model 8465, TSI, St Paul, USA) connected to a data-logger (Squirrel 1000, Grant, Cambridge, England). The travel velocity chosen for the experiments was about 2.3 $cm.s^{-1}$ to be high enough to keep the experimental time short but low enough to be negligible compared with the air velocity to be measured.
A total of 3,480 measurement points were performed inside the large meat carcass chiller.

CFD models

Based on the geometrical configuration presented in Figure 1, we used the CFD code 'Fluent 6.0.20' (Anonymous, 2001) to build two series of numerical models based on unstructured 3-dimensional hybrid meshes of 1,342,000 hexahedral and tetrahedral cells.
The inside of the air conditioning system was considered as being outside the computational domain; therefore, air inflow corresponded to the output from the openings located on both sides of the cooling batteries, and air outflow corresponded to the 14 fans located in the lower part of the air conditioning system.

To simplify the mesh and thus reduce total computation time, the carcasses filling the plant were represented by three anisotropic mega-porous media (the first for rows 1 to 6, the second for rows 7 to 10 and the third for rows 11 to 15) coupled with the Darcy-Forchheimer approach in which viscous resistance, inertial resistance and porosity factors had to be adjusted according to the three spatial directions.
Due to the absence of a rational method for calculating these factors, the first series of models was constructed to identify the factors by visually comparing the measured fields with the air velocity fields determined from a host of CFD calculations, assuming that viscous resistance factor was equal to zero whatever the spatial direction considered. This assumption amounts to neglecting the Darcy term in comparison with the Forchheimer term in the expression of the momentum source term added to the standard fluid flow equations. In other words, it means that the mean static pressure gradient is linear with the squared mean air velocity within the porous medium, and not proportional to the velocity as expressed by the Darcy formulation. This assumption is often made in bioclimatology when assessing airflows in greenhouses or wind circulation in forests (Bartzanas et al. 2002) and was recently verified in a food industry setting (Mirade et al. 2004).
Further to the analysis of the first series of simulations, porosity factor was determined as 90% whatever the spatial direction considered, and values of 10, 2 and 5 m^{-1} were determined for the inertial resistance factors according to the length, height and width of the mega-porous media, respectively.

Once the factors of the porous medium formulation were determined, a second series of 3-D simulations was performed to identify an efficient technical solution for increasing air velocities within the carcass chiller.
All the solutions tested were based on adding fans. Indeed, given the geometry of this large chiller, we decided that adding deflectors just at the output of the air-conditioning blowing areas would be an inefficient solution. We then decided to test the adding of two new rows of fans that would be located at approximately half-distance between the output of the air-conditioning blowing areas and the lateral walls of the chiller. The aim of these new simulations was to optimize the number and location of these fans while assessing the improvement in ventilation levels around the carcasses.

In all the numerical models built, airflow was considered as steady, incompressible, isothermal and turbulent. Main flow turbulence was taken into account using the tried-and-tested standard k-ε model (Launder and Spalding 1972) when far from the walls, which were assumed to be smooth, and where the standard wall function was applied. The Simple algorithm (Patankar and Spalding 1972) was chosen for coupling pressure and velocity and introducing pressure into the continuity equation. A first-order upwind differencing scheme was incorporated into the computational models as discretization scheme for the convection terms of each governing equation. First-order schemes are known to increase numerical diffusion due to discretization errors, especially when the flow is not aligned with the mesh, *i.e.* for triangular and tetrahedral grids (Hirsch 1988). Although they therefore yield less accurate results, first-order schemes give better convergence of calculation than second-order schemes.
For all the calculations performed, an air velocity of 2.3 $m.s^{-1}$ determined based on *in situ* measurements and a turbulence rate arbitrarily valued at 10% were specified in the inlet area corresponding to the output of the openings located on both sides of the air-conditioning system. Outflow-type boundary conditions were applied at the extraction areas corresponding to the 14 fans located underneath the air conditioning system at 4.1 m from the floor. This is the standard type of condition used when details on air velocity and pressure fields are unknown prior to solution of the flow problem; it is obeyed in fully-

developed flows where the diffusion flux for all variables in the exit direction is zero.

Calculations were performed on a 3 GHz P IV PC with 2.0 Go of RAM. Complete convergence of the discretized differential equations required 17 h.

RESULTS AND DISCUSSION

Given the large number of simulations performed both to calculate airflow patterns in the existing configuration and to test technical solutions liable to improve ventilation levels, only significant results are reported in this section, *i.e.* results corresponding to the existing configuration with porous media porosity and inertial resistance factors fitted to 90% and 10, 2 and 5 $m.s^{-1}$, respectively, and results corresponding to the technical solution configuration that most significantly increased the air velocities around carcasses at limited cost.

Air velocity fields in the existing configuration of the chiller

Analysis of the top view located at a height of 206 cm (Figure 2) showed a fairly strong heterogeneous airflow in the existing meat carcass chiller configuration, with air velocities higher than 1.4 $m.s^{-1}$ near the lateral walls, almost certainly resulting from airflow flowing down, and less than 0.2 $m.s^{-1}$ on both sides of the air conditioning system. This uneven airflow distribution almost certainly impaired process efficiency on account of the large poorly ventilated areas illustrated in Figure 2, which highlights a lack of ventilation in the areas filled by the carcasses. Simulation also indicated a more highly ventilated area underneath the extracting fans of the cooling batteries, with air velocities exceeding 0.6 $m.s^{-1}$.

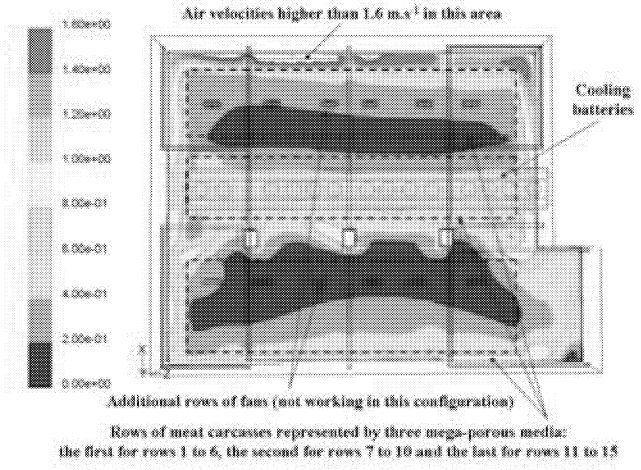

Figure 2: Air Velocity Fields Calculated on a Horizontal Section Located at a Height of 206 cm from the Floor in the Existing Configuration of the Meat Carcass Chiller

Consequently, chilling kinetics had to be altered and variations in chilling times could occur, since beef carcasses placed in low-velocity areas will cool far more slowly than carcasses placed underneath the cooling batteries, particularly if they are of higher weight.

Figure 3, which is a top view located at a height of 66 cm, *i.e.* level with the neck of carcasses, shows higher air velocities than previously (Figure 2), with values exceeding 0.4 $m.s^{-1}$ and peaking at 1.4 $m.s^{-1}$ at many points. There appeared to be unbalanced ventilation levels at this height between the right-hand side of the chiller where air velocities were higher than 1 $m.s^{-1}$ and the left-hand side, where they were closer to 0.6-0.8 $m.s^{-1}$.

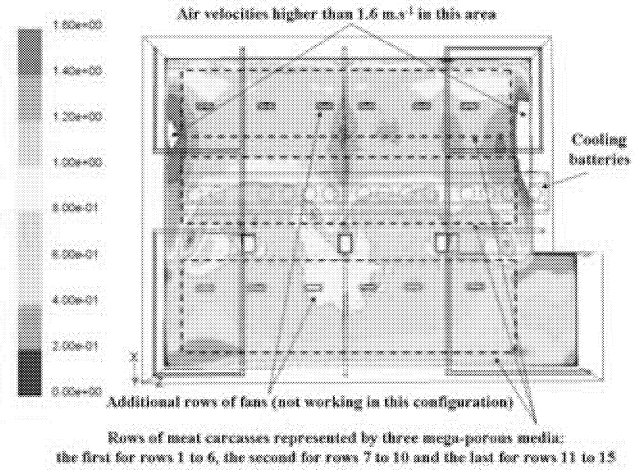

Figure 3: Air Velocity Fields Calculated on a Horizontal Section Located at a Height of 66 cm from the Floor in the Existing Configuration of the Meat Carcass Chiller

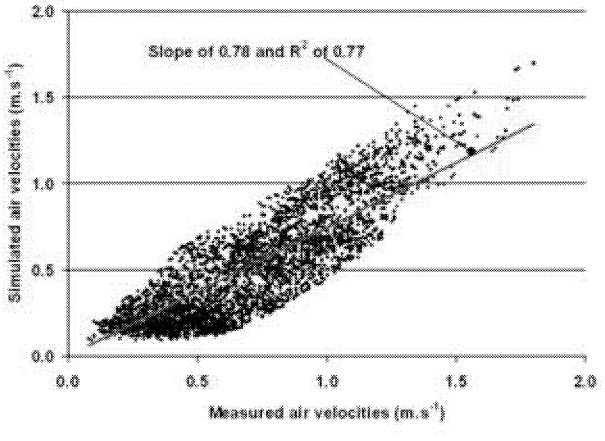

Figure 4: Overall Comparison between Simulated and Measured Air Velocities in the Existing Meat Carcass Chiller Configuration

Comparisons performed between the numerical predictions of air velocities and the 3,480 measurement points in the

existing chiller configuration revealed fairly close agreement and correlation between the two, as indicated by the slope of 0.78 and the coefficient R^2 of 0.77 of the straight line linking velocity simulation and measurement (Figure 4). However, the CFD model underestimated the air ventilation levels inside the chiller, since the slope was not equal to the ideal value of 1. Overall comparison also confirmed the poor ventilation of the full volume filled by the meat carcasses, since all the velocity magnitudes were lower than 1.8 $m.s^{-1}$.

Figure 5, comparing air velocity prediction against carcass row number, shows that poor performance of the CFD model is particularly obvious for rows 5 and 6, with a discrepancy of about 35% on account of strong underestimation of the air velocity predictions in these rows. However, excluding rows 5 to 6, the discrepancy between simulations and measurements of air velocities ranged from less than 4% (row 14) to about 25% (rows 4 and 11), and remained absolutely comparable to the discrepancies commonly reported in 3-D airflow pattern modelling studies performed in large cooling plants (Mirade and Daudin 1998a; Hoang et al. 2000).

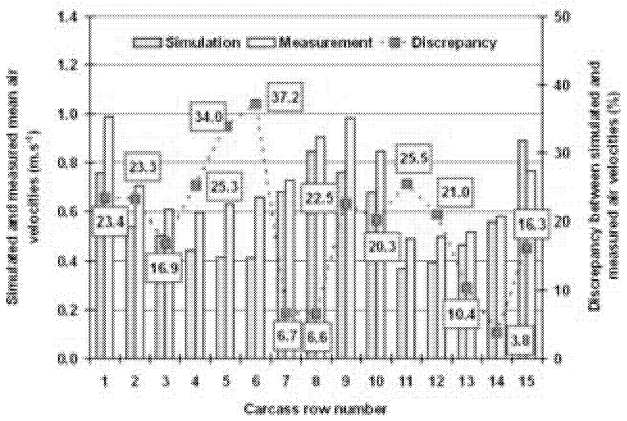

Figure 5: Comparison between Simulated and Measured Air Velocities in the Existing Meat Carcass Chiller Configuration *versus* Carcass Row

The data in Figure 5 confirm the findings illustrated in Figure 2, *i.e.* highly ventilated areas near the lateral walls of the chiller (rows 1 and 15) and underneath the cooling batteries as a result of a suction effect generated by the 14 extractor fans (rows 7 to 10), surrounding more poorly ventilated areas with air velocities lower than about 0.6 $m.s^{-1}$ (rows 3 to 6 and 11 to 14). It appears that the air blown either side of the four cooling batteries mainly follows the ceiling and flows down near each of the lateral walls, before circulating in the free space ranging from the ground to the carcass necks and rising back up towards the 14 extractor fans, thus giving rise to both a clockwise airflow and a counter-clockwise airflow.

Several possible explanations may be put forward to explain the limited accuracy in air velocity prediction, particularly for rows 5 and 6: (i) integration into the CFD model of the standard k-ε model for modelling turbulence and the first-order upwind differencing scheme as discretization scheme for the convection terms in the fluid mechanics equations, which are known to reduce strong gradients and give rise to numerical diffusion (Hirsch 1988); (ii) the use of porous media which only roughly describe the preferential paths for airflow over the meat carcasses into the rows, and possibly (iii) despite steadily increasing computational power and the 1,342,000 cells used for meshing the existing chiller configuration, the potential impossibility of obtaining truly independent results due to an insufficiently fine mesh.

However, given the adequate accuracy in air velocity predictions for the existing configuration, the CFD code 'Fluent' (Anonymous 2001) was then applied in an attempt to identify technical solutions for improving ventilation levels inside the large batch chiller.

Air velocity fields in the modified chiller configuration

As mentioned earlier, the second series of 3-D simulations was performed to identify an efficient and low-cost technical solution to significantly improve ventilation levels. All the solutions were based on adding fans above the carcass rows at half-distance between the blowing areas of the four cooling batteries and the lateral walls. The second series of simulations aimed to optimize the number and location of these fans, while assessing the improvement in ventilation levels around the carcasses.

The efficient and low-cost solution chosen for increasing air velocity magnitudes around the beef carcasses in order to reduce chilling times is depicted in Figures 1a and b. It consisted in adding two rows of six fans above the fifth and thirteenth rows of carcasses, leading to a 50% increase in airflow rate and air change rate inside the plant.

A comparison of Figure 6 with Figure 2 shows that adding 12 fans significantly increased ventilation levels, since large areas with air velocities lower than 0.2 $m.s^{-1}$ have almost disappeared owing to the increase in air change rate. However, on the whole the airflow distribution still followed the same patterns, with the most ventilated areas located near the lateral walls and below the extractor fans surrounding more poorly ventilated areas, on account of there being no jet deflector installed in order to force the air to penetrate the carcass rows. Indeed, given the geometry of this large chiller, we decided that adding deflectors just at the output of the air-conditioning blowing would be an inefficient solution, and too difficult to assess.

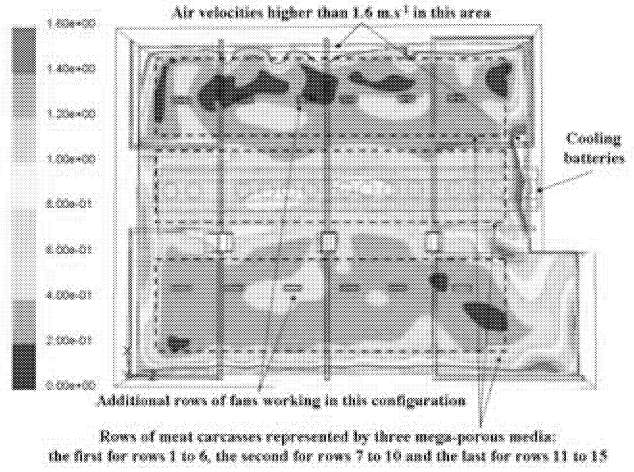

Figure 6: Air Velocity Fields Calculated on a Horizontal Section Located at a Height of 206 cm from the Floor in the Modified Configuration of the Meat Carcass Chiller where Additional Rows of Fans Are Working

Figure 7 illustrates the positive effect generated by the addition of two rows of six fans on ventilation levels in the area filled by the meat carcasses. Comparison with Figure 3 clearly highlights the disappearance of the imbalance in airflow distribution between the right-hand side and left-hand side of the chiller. As previously, ventilation level is higher at levels close to the floor.

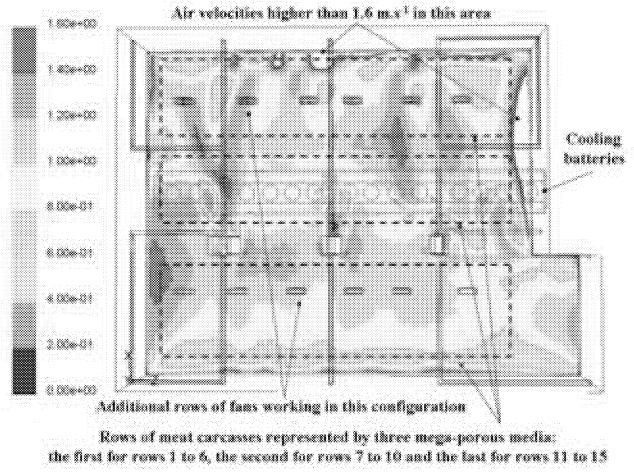

Figure 7: Air Velocity Fields Calculated on a Horizontal Section Located at a Height of 66 cm from the Floor in the Modified Configuration of the Meat Carcass Chiller where Additional Rows of Fans Are Working

From a practical point of view, the solution consisting in adding two rows of six fans above the fifth and thirteenth rows of carcasses represents a particularly interesting compromise between efficient gain in ventilation levels and low investment costs. Furthermore, it also has the advantage of being relatively simple to implement in an industrial large volume configuration.

Validation of the improvements numerically tested

The best solution design following the CFD investigation was installed on-site in the large meat carcass chiller. A second campaign of air velocity magnitude measurements was carried out to assess the real efficiency of the CFD-designed technical modification.

Figure 8 gives a full comparison between the air velocities predicted by the CFD model and the measured values taken from the second campaign of experimental investigation. As in the case of the existing meat carcass chiller configuration (Figure 4), the 3,480 simulated air velocities values were in quite close agreement with the measured velocities; the slope of the straight line reached 0.74, compared to 0.78 previously. However, the coefficient R^2 decreased from 0.77 to 0.71, meaning that the total dispersion of the comparison points increased, probably due to a higher discrepancy between calculation and measurement at several points or in certain areas.

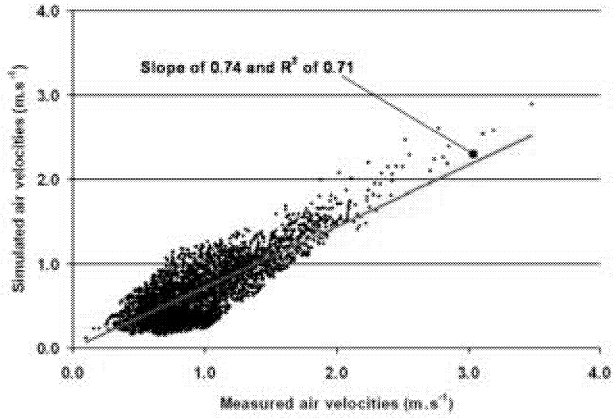

Figure 8: Overall Comparison between Simulated and Measured Air Velocities in the Modified Meat Carcass Chiller Configuration

Even so, the correlation between the predicted air velocities and the measured velocities remained clear. Furthermore, Figure 8 confirms the increase in air velocities shown in Figures 6 and 7, since air velocity magnitudes exceeded 2 $m.s^{-1}$ and even peaked at 3 $m.s^{-1}$ at several points of the modified chiller configuration, whereas all the velocity magnitudes were previously lower than 1.8 $m.s^{-1}$ (Figure 4).

Figure 9 comparing air velocity prediction against carcass row shows that, as was the case with the existing carcass chiller configuration (Figure 5), the CFD model underestimated the air ventilation levels, particularly for rows 2 to 6 where the underestimation exceeded 21% (row 2) and even reached 37% (row 6). Figure 9 also confirms the results of Figure 5, namely a strong ventilation in the middle of the plant and for rows 1 and 15 located in

close vicinity to the lateral walls of the chiller. On the whole, the discrepancy between simulation and measurement was still in agreement with the discrepancies commonly reported in the literature (Mirade and Daudin 1998a; Hoang et al. 2000).

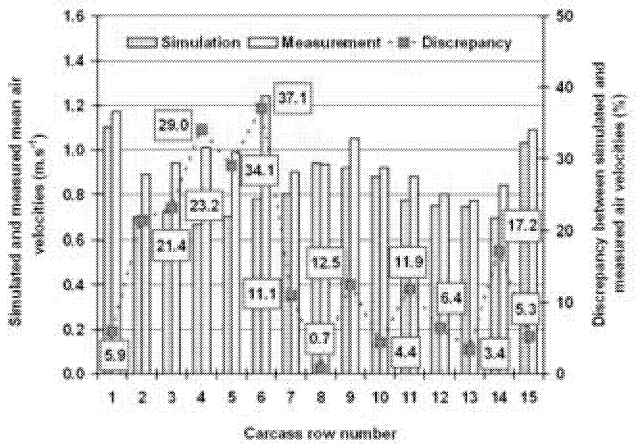

Figure 9: Comparison between Simulated and Measured Air Velocities in the Modified Meat Carcass Chiller Configuration *versus* Carcass Row

The air velocity measurements highlighted a strong increase (about 39%) in mean air velocity magnitudes in the whole volume filled by the meat carcasses following the addition of the two rows of fans, thus corroborating the findings of CFD modelling. In addition to this strong increase in velocity magnitudes, the measurements also indicated a slight decrease of 5% in mean standard deviations.

Several months after the experiment and the installation of the additional rows of fans, the professionals who use this large batch-type chiller have unambiguously noted a marked reduction in mean carcass temperature values on exit from the plant.

CONCLUSION

This study clearly shows that CFD techniques can be very useful tools for both assessing and improving air circulation in industrial meat carcass chillers, and thereby process efficiency, even though the use of porous media represented a major simplification of the filling of the plant in the numerical models.

Following on from a first series of numerical models built to understand air flow patterns in the existing configuration of the large batch-type carcass chiller, a second series of calculations was performed in order to identify a technical solution for improving ventilation levels in the plant. In general, comparison of calculations with measurements revealed close agreement with the predictions of air velocity magnitudes within the chiller.

The results reported here demonstrate that CFD is well suited to evaluating the significance and effects of modifying certain operating parameters or design elements on the performance of food processing apparatuses, and therefore to testing new technical improvement solutions at low-cost while saving time compared with an experimental investigation. Further progress can be expected in years to come as increasingly flexible CFD codes are run on PCs with steadily increasing calculating power.

ACKNOWLEDGEMENTS

The authors are grateful to INTERBEV and the OFIVAL for providing financial support for this project. We would also like to thank the employees of the study slaughterhouse for their friendly co-operation.

REFERENCES

Anonymous. 2001. *Fluent 6: User's Guide.* Fluent Inc, Lebanon, USA.

Bartzanas, T.; T. Boulard; and C. Kittas. 2002. "Numerical Simulation of the Airflow and Temperature Distribution in a Tunnel Greenhouse Equipped with Insect-Proof Screen in the Openings." *Computers and Electronics in Agriculture* 34, No.1-3 (May), 207-221.

Daudin, J.D. and R.J.M. Van Gerwen. 1996. "Air Circulation: How to Cope with this Critical Point?" In *New Developments in Meat Refrigeration 1996*, J.D. Daudin (Ed.). Holland, Utrecht, 30-37.

Foster, A.; R. Barrett; S.J. James; and M.J. Swain. 2002. "Measurement and Prediction of Air Movement through Doorways in Refrigerated Rooms." *International Journal of Refrigeration* 25, No.8 (Dec), 1102-1109.

Hirsch, C. 1988. *Numerical Computation of Internal and External Flows: Computational Methods for Inviscid and Viscous Flows*. John Wiley & Sons Ltd, Chichester, UK.

Hoang, M.L.; P. Verboven; J. De Baerdemaeker; and B.M. Nicolaï. 2000. "Analysis of Air Flow in a Cold Store by means of Computational Fluid Dynamics." *International Journal of Refrigeration* 23, No.2 (Mar), 127-140.

Hu, Z. and D.W. Sun. 2000. "CFD Simulation of Heat and Moisture Transfer for Predicting Cooling Rate and Weight Loss of Cooked Ham during Air-Blast Chilling Process." *Journal of Food Engineering* 46, No.3 (Nov), 189-198.

Kondjoyan, A. and J.D. Daudin. 1997. "Optimisation of Air-Flow Conditions during the Chilling and Storage of Carcasses and Meat Products." *Journal of Food Engineering* 34, No.3 (Nov), 243-258.

Launder, B.E. and D.B. Spalding. 1972. *Mathematical Models of Turbulence*. Academic Press Inc. Ltd, London, UK.

Mariotti, M.; G. Rech; and P. Romagnoni. 1995. "Numerical Study of Air Distribution in a Refrigerated Room." In *Proceedings of the 19th International Congress of Refrigeration* (Den Hague, Holland, Aug. 20-25). International Institute of Refrigeration, Paris, France, 98-105.

Mirade, P.S. and J.D. Daudin. 1998a. "Numerical Simulation and Validation of the Air Velocity Field in a Meat Chiller." *International Journal of Applied Science and Computations* 5, No.1 (Jun), 11-24.

Mirade, P.S. and J.D. Daudin. 1998b. "A New Experimental Method for Measuring and Visualising Air Flow in Large Food Plants." *Journal of Food Engineering* 36, No.1 (Apr), 31-49.

Mirade, P.S. and L. Picgirard. 2001. "Assessment of Airflow Patterns inside Six Industrial Beef Carcass Chillers." *International Journal of Food Science and Technology* 36, No.5 (Jun), 463-475.

Mirade, P.S.; A. Kondjoyan; and J.D. Daudin. 2002. "Three-Dimensional CFD Calculations for Designing Large Food Chillers." *Computers and Electronics in Agriculture* 34, No.1-3 (May), 67-88.

Mirade, P.S.; E. Agabriel; Y. Brunet; and T. Boulard. 2004. "Airflow Modelling by Computational Fluid Dynamics in an Industrial Plant Filled with Food Products." In *Proceedings of the 9th International Congress on Engineering and Food* (Montpellier, France, Mar. 7-11). International Association for Engineering and Food, Paris, France, 50-55.

Patankar, S.V. and D.B. Spalding. 1972. "A Calculation Procedure for Heat, Mass and Momentum Transfer in Three-Dimensional Parabolic Flows." *International Journal of Heat and Mass Transfer* 15, No.10 (Oct), 1787-1806.

Picgirard, L. and P.S. Mirade. 2005. "Validation de la Simulation de l'Aéraulique pour Améliorer et/ou Concevoir les Ressuages de Gros Bovins. " *Viandes et Produits Carnés* 24, No.4 (Jul-Aug), 131-136.

Scott, G. 1994. "Computational Fluid Dynamics for the Food Industry." *Food Technology International Europe*, 49-51.

Scott, G. and P. Richardson. 1997. "The Application of Computational Fluid Dynamics in the Food Industry." *Trends in Food Science & Technology* 8, No.4 (Apr), 119-124.

Wooton, A.E. 1986. "Factors Affecting the Chilling Rate of Beef Sides." In *Recent Advances and New Developments in the Refrigeration of Meat by Chilling 1986*, International Institute of Refrigeration (Ed.). UK, Bristol, 115-121.

Xia, B. and D.W. Sun. 2002. "Applications of Computational Fluid Dynamics (CFD) in the Food Industry: a Review." *Computers and Electronics in Agriculture* 34, No.1-3 (May), 5-24.

Xie, J.; X.H. Qu; J.Y. Shi; and D.W. Sun. 2006. "Effects of Design Parameters on Flow and Temperature Fields of a Cold Store by CFD Simulation." *Journal of Food Engineering*, in press.

BIOGRAPHY

LAURENT PICGIRARD is a specialist engineer in processing techniques and technology services. He has spent the last ten years with the ADIV group in Clermont-Ferrand, which is the French Technical Centre for Meat. The ADIV Group has been providing its support and services to professional organizations in the meat sector since 1975, both in France and worldwide, for SMEs and industrial-scale plants alike, in areas such as product design, manufacturing, organization, sales/marketing and training. It possesses an experimental slaughtering facilities and a 2,000 m^2 pilot plant which is unique in France, enabling the ADIV group to develop products, processes and materials. Their COFRAC-accredited laboratories are used for microbiological and physicochemical analyses, sensory analyses and screening for BSE.
With a strong multi-disciplinary team of 80, including more than 50 engineers and technicians, the ADIV group also enjoys the support of 200 researchers from the Clermont-Ferrand Meat Centre, one of the 3 main world centres specializing in meat industry issues.
(http://www.adiv.fr/en/)

PIERRE-SYLVAIN MIRADE trained at the University of Poitiers, graduating in 1996 with a thesis in Fluid Mechanics and Heat Sciences. In 1997, he joined the Meat Research Laboratory (SRV), and in 2005 joined the Animal Products Quality Unit (QuaPA) of the French National Institute for Agronomic Research (INRA) in Clermont-Ferrand/Theix as researcher in food process engineering.
Since 1995, he has authored over 50 papers on the assessment of airflow patterns and heat and mass transfers inside different types of food plants such as meat carcass chillers, modern meat dryers, biscuit baking tunnel ovens and cheese ripening rooms, based on combining computational fluid dynamics modelling and experimental investigation. Dr. Mirade is a member of the French Society of Chemical Engineering (SFGP). In March 2000, the organizational committee of the French AGORAL meetings awarded him the Marcel Loncin Prize for excellence in scientific and technological research applied to the food industry. He accepted to be a member of the international scientific committee of the FoodSim 2006 conference as an expert in methods and tools applied to food and bio-industries.
(http://www.international.inra.fr/)

COMPUTATIONAL FLUID DYNAMICS ANALYSIS FOR DESIGN OPTIMISATION OF A CONTINUOUS OVEN FOR CONVENIENCE MEAT PRODUCTS

Siegfried Denys
Jan G. Pieters
Biosystems Engineering
Ghent University
Coupure links 653
B-9000 Ghent
Belgium
E-mail: Siegfried.Denys@UGent.be

ABSTRACT

Computational Fluid Dynamics was used to simulate air flow, heat transfer and temperature distribution in a continuous multi-conveyer industrial oven, developed for cooking convenience meat products. A prototype design was evaluated and shown to perform poorly in terms of air flow and temperature uniformity. Based on the results, the oven design was adapted and re-evaluated in order to improve its performance. Adaptations included changes for better controlling the air flow and optimising the position, shape and size of air deflection plates, used for uniformly distributing preheated air over the successive conveyers. Satisfying results were obtained and Computational Fluid Dynamics can be seen as a powerful tool to optimise the design of food process equipment, reducing the need for experimental work.

INTRODUCTION

Computational fluid dynamics (CFD) is a powerful design and analysis tool to optimise processes and equipment. Also in the food and beverage industry, it can be used to provide physical understanding of food processing problems in detail, through flow and thermal field predictions (Scott and Richardson, 1997). Well-considered design of food processing equipment, assisted by CFD studies that help in understanding the dynamics and underlying physics of process operations, can lead to reduced energy requirements, increased product throughput and improved product quality.

CFD was used to optimise the design of a multi-conveyer industrial oven for cooking convenience meat products. The performance of such ovens in terms of product quality largely depends on the uniformity (air velocity and temperature) within the oven. Process uniformity is critical and determines the overall quality of the treated products. In this work, a prototype oven was used as a case study. At the time of the research, the oven was not constructed yet. The output of the study was used to provide guidelines with respect to geometrical design.

OVEN DESCRIPTION

Fig. 1 shows the original design of the oven prototype. The oven consisted of an insulated compartment and eleven belt conveyers for transporting the products in the longitudinal direction through the oven. Products at low temperature enter the oven at the topmost conveyer belt and leave the oven at the bottommost belt (Fig. 1a). The product residence time is determined by the conveyer belt speed. Pre-heated air is circulated in the oven by means of a fan. The stream directions of air and products were perpendicular and air could flow over the successive conveyer belts loaded with product, as well as in the areas between leaving and returning conveyer belts (Fig. 1b). Obviously, the latter air flow will not directly contribute to heat transfer to the products. Furthermore, the oven was provided with an automatic valve (Fig. 1b) that allowed reversing the air flow direction. Air flowed alternately in opposite directions and products that lie on one side of the conveyer belt experience the same process conditions as the ones lying on the other side. For a uniform process, the air should be uniformly distributed over the belt conveyers. For this purpose, air deflection plates with plate linearly increasing from top to bottom were used (Fig. 1b).

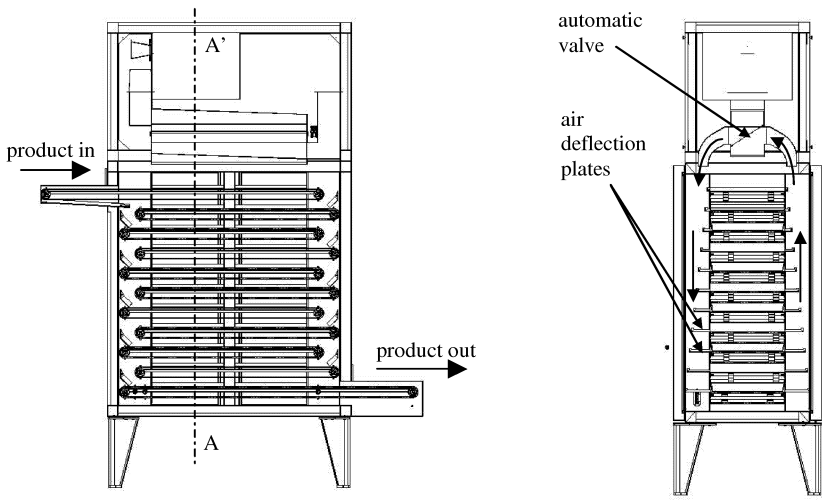

a b

Figures 1: Geometry of the Cooking Oven: (a) Longitudinal Section; (b) Cross Section

CFD ANALYSIS AND DESIGN IMPROVEMENTS

Because the main air flow direction is perpendicular to the conveyer belt direction, a two-dimensional approach was followed, i.e., air flow was simulated in a vertical cross-section (sectional plane AA' in Fig. 1a). Fig. 2a shows the simplified internal geometry for the original oven design. In the generation of the computational mesh, the insulation layer was not included, as the CFD solver used a one-dimensional equation to account for heat transfer through the walls. The complexity of the upper part of the oven, containing the heater, the fan and the valve for reversing the air flow direction, was strongly reduced: only the air inlet and outlet ducts were included in the CFD analysis. Based on the 2D geometry, a computational mesh was generated in Gambit (Fluent Inc., Lebanon, U.S.), the general pre-processor and mesh generator for the CFD solver used in this study. The mesh consisted of ± 140,000 rectangular control cells.

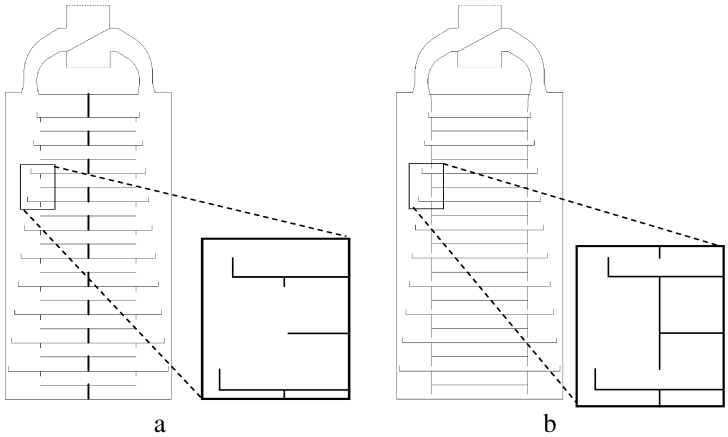

a b

Figures 2: (a) Simplified Geometry used in the CFD Analysis. The bold vertical lines are Surfaces through which Flow Rates were studied; (b) Adapted Design where the Air Inlet Area was reduced by cutting off the Areas between Leaving and Returning Conveyer Belts, and part of the Remaining Surface at the successive Oven Levels

The information contained in the computational grid was imported into the commercial CFD solver Fluent (Fluent Inc., Lebanon, U.S.). The partial differential equations governing mass, momentum, and energy conservation in Cartesian coordinates were solved using a first-order fully implicit numerical algorithm (Tannehill et al., 1997). Turbulent flow was modelled using the standard k-ε turbulence model with enhanced wall treatment (Tannehill et al., 1997).

To account for conductive heat losses through the oven walls, Fluent solves a one-dimensional equation to compute

its thermal resistance. To include this, the thermal conductivity of the insulation material was accounted for (value provided by the manufacturer). The thermal boundary on the outer surface of the oven walls was specified by a uniform convective heat transfer coefficient, which was estimated by means of empirical equations for the local Nusselt number (Janna, 2000). Velocity boundary conditions were used at the inlet and outlet ducts. Inlet velocities of 0.1, 1 and 5 m/s were considered.

In order to improve its performance, adjustments to the original design were suggested and the new design was then re-evaluated by means of CFD. A first adaptation was to reduce the air inlet area in order to have a better controlled flow. This was done by closing the areas between leaving and returning conveyer belts, and reducing the surface available for air inlet at the successive oven levels (Fig. 2b). Secondly, it was attempted to improve the air flow uniformity by adapting the width of the air deflection plates. In the original design, the deflection plate width increased linearly from the top level to the bottom level (Fig. 3). A configuration, where the width of the successive air deflection plates increased according to a quadratic equation was also studied (Fig. 3). Finally, an improved design was studied, where the size of the successive air deflection plates was adapted, based on the CFD results for the case with linearly increasing deflection plate width. Hereto, for each oven level, the percentage difference between the flow rate at the particular level, and the average flow rate (total flow rate divided by the number of levels) was calculated. Based on these results, the deflection plate width was adapted for each level (i.e., decreased when the flow rate over the corresponding belt was lower than the average flow rate and increased in the opposite case), and a new CFD simulation was performed. This optimisation procedure was repeated until additional improvements in terms of flow rate uniformity were minimal, i.e., until further optimisation only led to minimal adaptations (< 1 mm) of the deflection plate width.

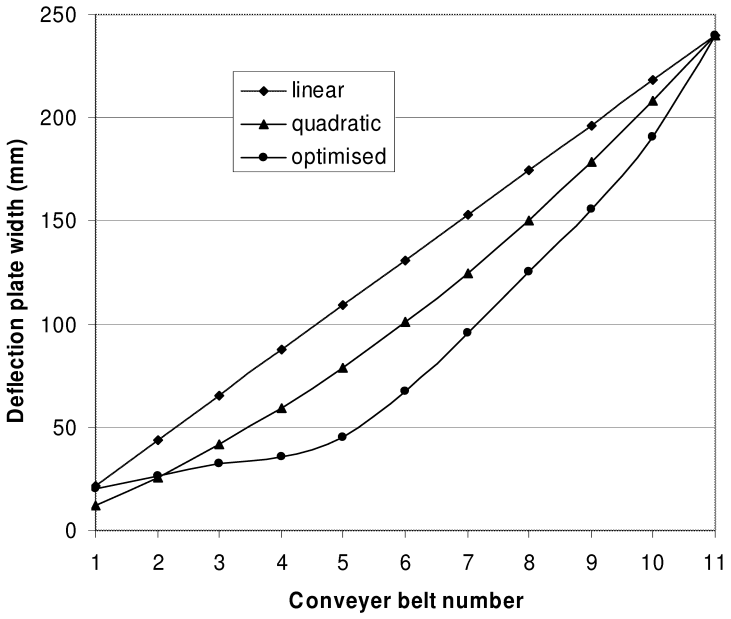

Figure 3: Deflection Plate Width for the successive Oven Levels: Conveyer Belt 1 refers to the Topmost Level; Conveyer Belt 11 is the Bottommost Level

RESULTS AND DISCUSSION

Original design

Fig. 4 shows velocity and temperature distributions in the oven for inlet and outlet velocities of 0.1 and 5 m/s. The temperature distributions indicate that heat losses through the oven walls are better compensated for when the inlet air velocity is higher. An analysis of the flow rates at different levels is shown in Fig. 5. In this figure, the flow rate through a vertical surface between the leaving conveyer belt and the higher level returning belt (surfaces indicated in Fig. 2a), is included for each level. Air flow is not uniformly distributed over the conveyer belts.

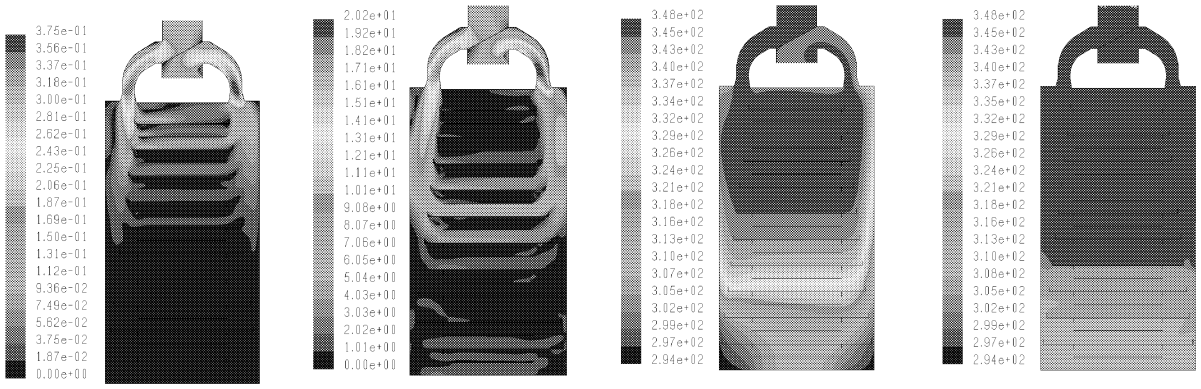

a b c d

Figures 4: Velocity (a and b) and Temperature Distributions (c and d) in the original Oven for Inlet and Outlet Velocities of 0.1 m/s (a and c) and 5 m/s (b and d)

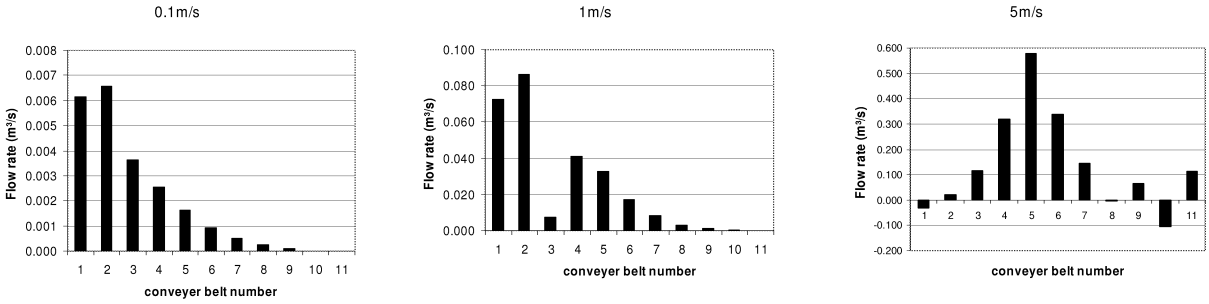

Figures 5: Flow Rates through Vertical Surfaces (Fig. 2a) for each level, for Inlet and Outlet Velocities of 0.1, 1 and 5 m/s (original design)

Improved designs

Based on the above described CFD results, the oven design was adapted and re-evaluated in order to improve its performance. When cutting off the areas between leaving and returning conveyer belts for air flow, and reducing the surface available for air inlet above the leaving belts, undesired air circulation was avoided, as shown in Fig. 6a. in this case, all oven levels were provided with a positive air flow, meaning that no recirculation occurred. A better performance in terms of air flow distribution, as compared to the original design, was observed. The improvement in terms of uniformity can also be seen in the velocity and temperature profiles: for an inlet air velocity of 1 m/s, temperature is quasi uniform in the complete oven (Fig. 7). This effect is even more pronounced at higher inlet air velocities (results not shown).

From Fig. 6a, it can be seen that the highest flow rates were observed at levels 2 to 5, while the flow rates at the upper and lower levels are lower. The amount of air, deflected by a deflection plate, depends amongst others on the difference between the width of the deflection plate and the width of the deflection plate at the higher level. As a consequence, when the dimensions of successive deflection plates is determined by a quadratic relation, rather than a linear one (Fig. 3), less air will be deflected at the upper levels, while the lower conveyer belts will receive a higher flow rate. This effect is shown in Fig. 6b, where the flow rates at successive levels are indicated for a quadratic relation of deflection plate width. In this case, the flow rates were higher at the lower levels, as compared to the case where the deflection plate width increased linearly from top to bottom, while the highest levels received less air flow.

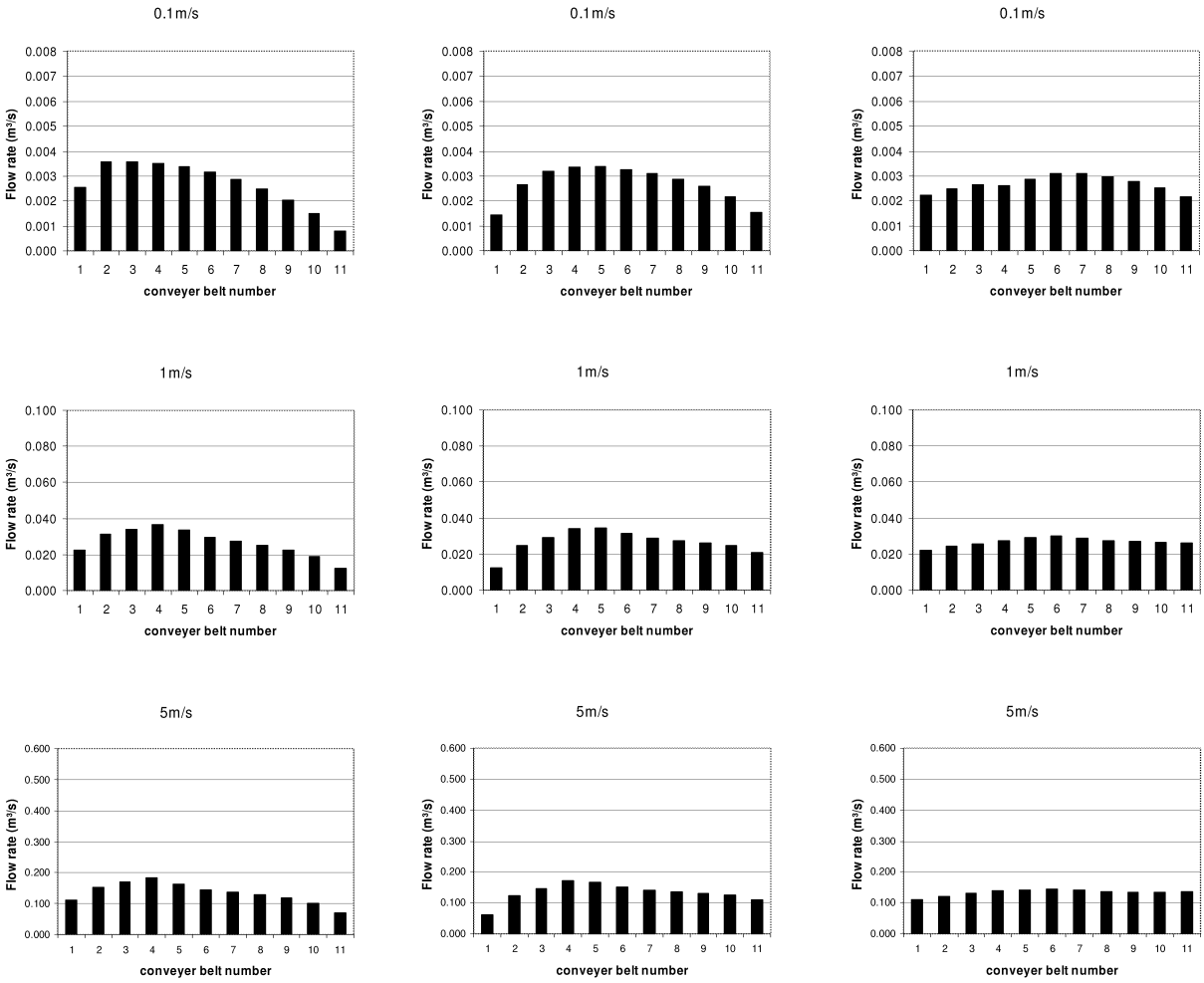

a b c

Figures 6: Flow Rates through Vertical Surfaces (Fig. 2a) for the Improved Designs where the Air Inlet Surface was reduced; results for Inlet and Outlet Velocities of 0.1, 1 and 5 m/s are included. (a) Linearly Increasing Deflection Plate Width; (b) Quadratic Relation; (c) Optimised Case

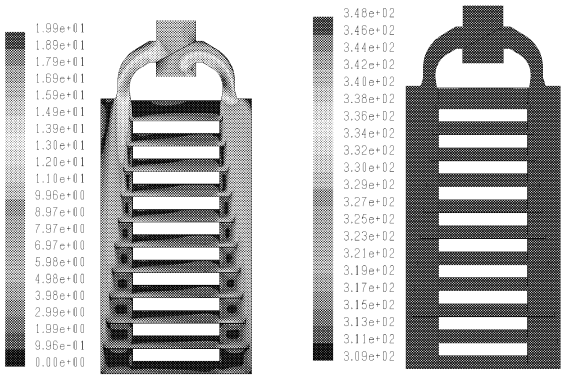

a b

Figures 7: Velocity (a) and Temperature Distributions (b) for an Improved Design where the Air Inlet Surface was reduced (Inlet and Outlet Air Velocity of 1 m/s)

Finally, the deflection plate configuration was optimised, based on successive adaptations, whereby the deviation of the flow rate over the conveyer belts from the average flow rate was evaluated after each adaptation. Using the aforementioned optimisation procedure, satisfying results were obtained after two iterative optimisation routines. A third optimisation only led to minimal adaptations of the deflection plate width and minimal additional improvements in terms of flow rate uniformity. Fig. 3 shows the optimised deflection plate width for the successive levels and Fig. 6c shows the flow rates resulting over the conveyer belts. While the first modification of the design (cutting off the areas between leaving and returning conveyer belts for air flow) could avoid undesired air recirculation, optimising the size of the air deflection plates improved the performance in terms of air flow and temperature uniformity. This is shown in Table 1, where the proportional flow rate deviation —defined as the accumulated deviation of the flow rates (m^3/s) over the conveyer belts from the corresponding average flow rate, divided by the average belt flow rate— is given for the original design (with linearly increasing deflection plate width), and for the improved designs where the areas between leaving and returning conveyer belts were closed for air flow. For the design where the width of successive deflection plates followed a quadratic equation, minor effects were observed, while the optimised case was characterised by a more uniform air flow pattern. It can also be observed that better performance in terms of uniformity was obtained for higher inlet air velocities.

Table 1: Proportional Flow Rate Deviation over the Successive Conveyer Belts from the corresponding Average Flow Rates, both for the Original and Improved Designs

	0.1 m/s	1 m/s	5 m/s
Original design	10.63	10.91	11.50
Improved designs (Reduced air inlet surface)			
linearly increasing deflection plate width	3.00	2.41	2.15
quadratic relation	2.29	1.85	1.71
optimised design	1.04	0.66	0.56

CONCLUSIONS

A prototype oven design was studied with CFD and showed poor performance in terms of air flow and temperature uniformity. Adaptations to the design and re-evaluation by means of a CFD study could improve the expected performance of the oven. Adaptations including cutting off part of the surface, available to air flow through the oven and optimising the size of air deflection plates, used for uniformly distributing preheated air over the successive conveyers, proved successful. By the former modification, undesired air recirculation was avoided. The latter adaptation (optimisation of the air deflection plate width) improved the performance in terms of air flow and temperature uniformity. This was illustrated by an analysis of the flow rates at the different oven levels.

The output of this study can be used as a guideline with respect to geometrical design of this particular oven. Inclusion of the treated food in the performed analysis will obviously lead to better mastering the resulting product quality. Besides, experimental validation of the results — after constructing the prototype— is being carried out. However, it can be concluded that CFD reduces the experimental effort and is a powerful tool to optimise food process equipment.

REFERENCES

Scott, G. and P. Richardson. 1997. The application of computational fluid dynamics in the food industry. *Trends Food Sci. Technol.* 8: 119-124.

Janna, W. S. 2000. In *Engineering heat transfer*, Ed. W.S. Janna, CRC Press, London.

Tannehill; J.C., D.A. Anderson; and R.H. Pletcher. 1997. In *Computational fluid mechanics and heat transfer*, Eds. W.J. Minkowycz and E.M. Sparrow, Taylor & Francis, London.

LIQUIDS PRODUCTION SIMULATION

FLEXIBILITY STUDY OF A LIQUID FOOD PRODUCTION PROCESS

Hongyuan Cheng and Alan Friis
Food Process Engineering, Biocentrum-DTU
Technical University of Denmark
Søltofts Plads, Building 221, DK-2800, Lyngby, Denmark
E-mail: hyc@biocentrum.dtu.dk

KEYWORDS
milk processing, simulation, flexibility.

ABSTRACT

Applying process engineering simulation method to model the processing of liquid food can provide a way to build a flexible food factory that can efficiently offer a wide range of tailored products in short delivery time. A milk production process, as an example, is simulated using a process engineering software to investigate the process operation conditions and flexibility. The established simulation method can be adapted to simulate similar liquid food production processes through suitable modifications.

INTRODUCTION

One of contemporary challenges for food industry is that a food factory has to offer a wide range of tailored products in short delivery time and maintain in a cost efficient way. Food productions become "manufacture to order" rather than "manufacture according to sales prediction". An economic and efficient way in dealing with the similar liquid products is to process all of them in the same production unit by swiftly shifting between different productions. Different liquid food productions have some similarities in many degrees and potentially can be processed in the same production line. To achieve the engineering goals, necessary experiments and calculations for these products processing must be identified and executed systematically and expeditiously through using proper facilities and software tools. Process engineering simulation method is a valuable tool to carry out such calculation and to design and control such multi-task flexible production unit.

Process simulation technology has been widely applied in many industrial areas. It is proven that industrial process design, development and operation have benefited from the application of process simulation technology. With the help of the process simulation technology, engineers can make operational decisions based on profitability by capitalizing on market dynamics, identify future opportunities, manage and optimize plant performance, and act on these decisions in an integrated manner across whole enterprise. Some process simulation tools, such as aspenOne from AspenTech, PRO/II from Simsci-Esscor, have been intensively employed in process engineering applications, especially for liquid material processing. These software tools provide a platform for us to investigate food production processes.

Liquid food processing commonly includes mixing, heating, cooling etc. The manufacture of liquid food products, such as milk-based liquid foods, undergoes more or less the same processing steps but under different conditions. An existing liquid food unit can possibly process all of the similar liquid products. In this work, we select a milk pasteurization unit to investigate the process operability and flexibility under different processing conditions using a process simulation tool. The milk production unit is simulated using the simulation tool under clean or fouling conditions.

Because a milk-based liquid food can be approximately characterized by its fat content and viscosity, the physical properties of a liquid food are used in the simulation to identify different liquid foods. Therefore, through varying the fat content and viscosity for the inlet liquid flow, we can simulate different foods processing behaviours in the existing milk production unit. As the flowsheet simulation tool is very flexible, the built flowsheet simulator for the existing milk process unit can also be modified and changed into another slight different flowsheet simulation. By this way we can explore a broad range of milk-based liquid product productions.

MILK PRODUCTION UNIT SIMULAITON

A market milk production process, as shown in Figure 1, is studied in this work. In the flowsheet a milk inlet flow at 7000kg/h, 13% fat content (wt) and 4°C is processed. Sections 1-5 are five different parts of a plate heat exchanger. The total heat transfer area of the sections in the plate heat exchanger is 10, 9.9, 3.6, 19.6 and 6.9 m^2 for the sections 1-5, respectively.

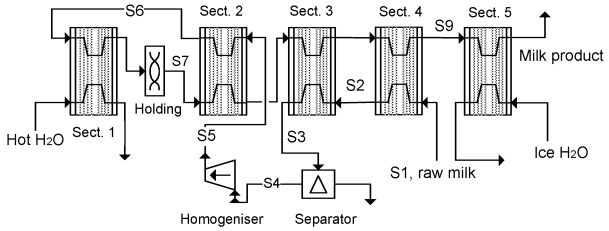

Figure 1: Market milk production process flowsheet

A milk stream S1 (7000kg/h, 13% fat) enters section 4 at 4°C and is heated by a hot water stream in section 3. Milk stream S3 passes a fat standardization system and a homogenisation unit. After the homogenisation (at 21 bar), the milk stream temperature is about 61°C. Milk stream S5 is heated at heat regeneration section 2. In section 1, milk stream S6 is heated

to a pasteurisation temperature 72°C by a hot water stream. Then, milk stream S6 is hold in a holding tube, Holding. After the pasteurisation, the milk stream is continuously cooled in sections 2 and 4. The final product is cooled to 4°C by a 2°C ice water stream in section 5.

Modelling and simulation work has been carried out for the unit operations in dairy production line, especially for plate heat exchanger. Georgiadis at al. (1998) systematically studied the optimal design and operation of heat exchangers under milk fouling (Georgiadis and Macchietto 2000). Gut and Pinto (2003) modeled the plate heat exchanger with generalized configurations. However, our simulation work is not only focus on the modelling heat exchanger but on the operation behaviours of the milk production unit.

Using the process simulation tool, the milk production unit (shown in figure 1) simulation is built. In the simulation, the heat exchange sections of the plate heat exchanger are calculated with simple heat exchanger module. Pressure drop and overall heat transfer coefficient of these sections are calculated through a separated calculator module. The calculation method for the pressure drop and overall heat transfer coefficient of a heat transfer section is taken from HEDH (Schlünder 1995). However, the convective coefficient *N*u and friction factor *f* for milk fluids are calculated using the correlations of Shah and Focke (1988), and Saunders (1988). In the calculation, mean plate spacing of the studied plate heat exchanger has been adjusted from initial estimation to match a set of experimental pressure drop data. A pump module combining with a simple heat exchanger module is used to represent the main physical characteristics of a homogenisation process. In the simulation, the built-in method or topology in the process simulation tool is used to tear a recycle loop and give a converged solution for the whole flowsheet simulator.

To carry out the process simulation, we have to supply the properties of milk for the process simulation tool, because it does not contain the physical properties of milk in its physical property database. The physical properties of milk have been studied and reported. Some thermal property models of milk and milk products have been collected in books of Rahman (1995) and Okos (1985). From literature, we selected a set of temperature and fat content dependent correlations to calculate milk density and thermal conductivity. Two specific temperature and fat content dependent correlations are also developed in this work to model milk enthalpy and viscosity. The use of temperature and fat composition dependent correlations in process simulation will improve the calculation accuracy and enable the simulation to apply for a broad range of milk product productions.

The milk production unit in figure 1 is simulated in the process simulation tool using the flowsheet parameters described above. Comparing to design data, the simulation can satisfactorily represent the temperature program of the process under clean condition.

In the operation of milk or other liquid food production processes, fouling is a problem resulting in significant capital and operating cost. The fouling is developed with process operation time. Consequently, the process operation parameters are adjusted from time to time according to a designed control strategy to maintain the process at its desired objectives. Traditionally, the system adjustment actions depend on the online process parameter measurements, such as temperatures. However, if we can simulate and predict the behaviours of the production operation under fouling, we can study and optimize the corresponding operation adjustments in advance. Through such simulation and prediction for the process behaviours, we can design a predictive operation parameter control strategy for the liquid production process, and to improve the food product quality.

Milk fouling has been studied for some years (Schreier and Fryer 1995; Fryer et al. 1996; Sahoo et al. 2005; De Jong and van Asselt 2006). The equipment in a food production line, such as heat exchanger, starts clean and becomes fouled. In an induction period of the fouling, the heat transfer conditions do not change significantly. After the induction period, it is a fouling period. The heat transfer coefficient of a heat exchanger decreases and the pressure drop increases. Fouling models have been developed for milk fluid on plate and tube heat exchangers (Fryer et al., 1996; Schreier and Fryer, 1995; Sahoo et al. 2005; Nema and Datta 2005). In the study of fouling, a dimensionless number, B_i, is often applied to describe the characteristics of fouling resistance, R_f. For a uniform deposit of thickness x and thermal conductivity λ, the fouling resistance $R_f = x/\lambda$. The product $R_f U_0$ is defined as a Biot number, B_i. Thus, the overall heat transfer coefficient of heat transfer under fouling is given as

$$U = \frac{U_0}{(1+B_i)} \qquad (1)$$

where U_0 and U are the clean and fouled overall heat transfer coefficient. The dimensionless number, B_i, is a function of time and other different fouling factors.

In our simulation for the milk production process, the equation (1) is employed to account for the overall heat transfer coefficient variations with fouling. A series of B_i values are substituted into equation (1) to represent the heat transfer coefficient changes in different milk fouling periods. But, these B_i factors are not calculated from any milk fouling model. Instead, the B_i factors are a series of increased numbers from 0 to 1, 2, 3, etc.

For a plate heat exchanger, an equation can be established to correlate B_i and mean plate spacing. Based on the equation, the pressure drop development of the plate heat exchanger can also be calculated according different B_i values. The equation is given as following descriptions. By the definition of Biot number, B_i, a relationship between Bi and deposit thickness x can be derived as $B_i = \frac{U_0}{\lambda} x$. If the clean overall heat transfer coefficient, U_0, is assumed to be a constant, a linear relationship can be derived for the B_i value and mean plate spacing as follow:

$$B_i = \frac{U_0}{2\lambda}(d_0 - d) \qquad (2)$$

where d_0 and d is the initial and fouled mean plate spacing (mm), respectively, λ is the thermal conductivity of the fouling deposit (W/mK). It should point out that the equation (2) is an equipment dependent correlation because the U_0 is not a constant in practice.

In the industrial operation, a process is operated and controlled at a set of nominated or designed parameters under system disturbance. For the market milk production process, the operation and control parameters are pasteurization and final product temperatures, homogenization pressure, cream separation degree, etc. Among of these operation parameters, the temperatures are controlled from the adjustment of hot water temperature and ice water flowrate. The homogenization pressure and cream separation condition are fixed by pump output pressure and centrifugal degree, respectively. Thus, in our simulation, the operation and control objective for the market milk process is expressed as a minimization of the pasteurisation and cooling temperature deviations from their desired values subject to manipulated variable bounds. The equation is given as follows.

$$\min_{T_H, F_C}\left(\alpha_1\left|\frac{T_p - T_p^0}{T_p^0}\right| + \alpha_2\left|\frac{T_c - T_c^0}{T_c^0}\right|\right) \qquad (3a)$$

$$\text{s.t. } a \le T_H \le b \qquad (3b)$$

$$c \le F_C \le d \qquad (3c)$$

where T_H and F_C are the hot water temperature and ice water flowrate, respectively, T_p and T_c are the pasteurisation and cooling temperature in section 1 and 5, respectively, T_p^0 and T_c^0 are the desired pasteurisation and cooling temperatures in section 1 and 5, respectively, a, b, c and d are the bounds of the manipulated variables, α_1 and α_2 are the weight factors ($\alpha_1 + \alpha_2 = 1.0$). Here, the hot water temperature and ice water stream flowrate are the manipulated variables for the system. A set of typical boundary values for the hot water temperature (T_H) and ice water (F_C) flowrate are $73 \le T_H \le 96$ °C and $9000 \le F_C \le 22000$ kg/hr if the desired pasteurisation and cooling temperatures in section 1 and 5 are 72°C and 4°C, respectively.

Using the operation objective for the market milk unit, we investigate the process operability under the variation of milk fouling and inlet milk flowrate. The minimization problem is solved by an optimizer module in the process simulation tool. The objective function is implemented by a separated calculator module in the process simulation tool. The calculation results are given as figures 2-3.

It can be seen from figure 2 that the hot water temperature and ice water flowrate increase with fouling factor. Figure 3 shows that the hot water temperature and ice water flowrate increase with inlet milk flowrate, where the results are obtained at fouling factor B_i=1.0. However, the calculation shows in figure 3 that the existing milk processing unit reaches its capacity limit around 9500 kg/hr for inlet milk flowrate. As can be seen from figures 2-3, the process simulation can quantitatively describe and predict the process operation behaviours.

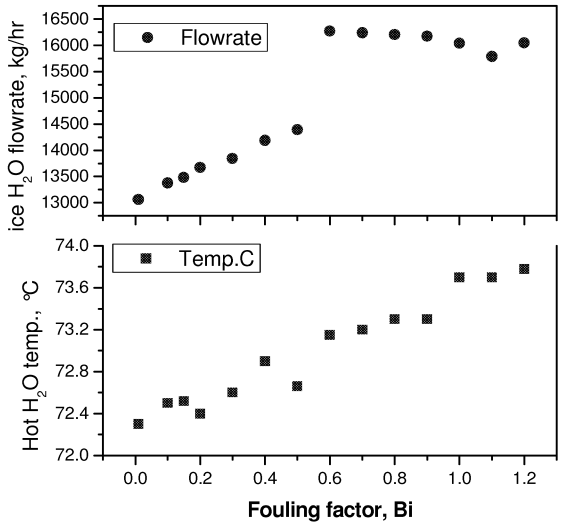

Figure 2: Hot water temperature and ice water flowrate at different milk fouling conditions

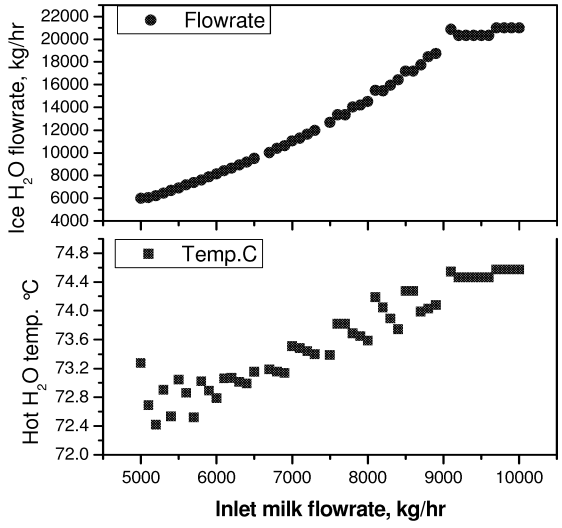

Figure 3: Hot water temperature and ice water flowrate at different milk inlet flowrate

Based on the built simulation for the market milk production unit, the unit can be also investigated in an alternative operation method by replacing manipulated variables from hot water temperature and ice water flowrate to hot water and ice water flowrates, which has been suggested and experimentally investigated by researchers (Yoon and Lund 1994). With the new manipulated variables, the milk processing unit is controlled through the adjustment of hot water and ice water flowrates to reach its operation objective, i.e. equation (3). To change the manipulated variables to hot water and ice water flowrates, the simulation objective equation (3) is needed to be modified. With the two new manipulated variables, we replaced the objective function for the built simulation and simulate the existing

market production unit operations. The simulation results are shown in figure 4.

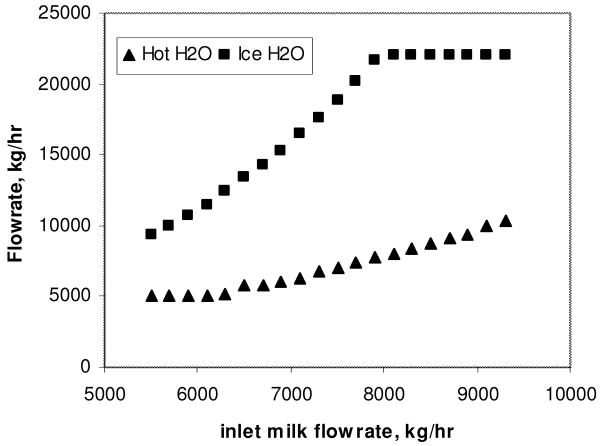

Figure 4: Hot water and ice water flowrates at different inlet milk capacity

In the simulation, the fouling factor of the system is set as 1.0 for the overall heat transfer coefficient calculation equation (1). From figure 4, it can be seen that the market milk unit reaches its limit around 8000kg/hr. The ice water supply cannot support more than 8000 kg/hr milk production for the existing process when the process uses the hot water and ice water flowrates as manipulated variables.

PROCESS FLEXIBILITY ANALYSIS

In our work, the process flexibility illustrates the capability of a process to operate at a range of uncertain conditions that may be encountered during a process operation. For the milk production unit, the uncertain conditions can be milk inlet condition variations and milk fouling, i.e. temperature, flowrate, fat content, heat transfer flux and pressure drop. The variations of fat or water contents in the milk inlet flow also reflect the processing of different milk products. One method to find out the process flexibility is to explore a maximum tolerance or expansion for uncertainties around a set of nominal process operation parameters through experimental or simulation work. In this work, we will take the advantage of process simulation method to study the flexibility of the milk production process.

A widely used investigation concept for the process flexibility is proposed by Grossmann and co-workers (Grossmann et al. 1983), and will be used in our work. From the method of Grossmann and co-workers, the flexibility, δ, is maximized in each vertex direction, ν, belonging the set of all vertex directions, V, (ν∈V) by the following optimization formulation:

$$\delta^{\nu^*} = \max_{u,\delta^\nu} \delta^\nu \qquad (4a)$$

s.t. process mass/energy balance (4b)

$$\theta = \theta^0 + \nu\delta^\nu \qquad (4c)$$

where u is the vector of control or free variables (e.g. the manipulated variables for a process), δ is the non-negative scalar, ν is the vertex directions, -1 or +1 (+ or – indicate variable increase or decrease), θ is the uncertain parameters, θ^0 is the nominal or design value of the uncertain parameter θ. The flexibility index, δ^*, is the smallest one among the solutions of equation (4) as follow:

$$\delta^* = \min_{\nu \in V} \delta^{\nu^*} \qquad (5)$$

The total number of vertex direction for N uncertain parameters is 2^N (ν=1,…, 2^N combinations of the ± directed deviations from the nominal values of the uncertain parameters, θ^0).

In this work, temperature, flow rate, and fat content of the milk inlet flow are selected as uncertain parameters for the process flexibility investigation. The fouling effects are fixed by setting B_i=1.0 for the milk production process, which corresponds to a system pressure drop 240 kPa. In the investigation, we suppose the critical point of the milk production system is a vertex of the hyper-rectangle. Thus, we use vertex enumeration method to implement our calculation in the simulator for the milk production unit.

Based on the built simulator for the milk production unit, we start with a small non-negative scalar to enumerate all vertex directions and run the milk process simulator. We found out that the flexibility index δ* is 0.1 for the studied milk production unit, which means the studied three uncertain parameters can simultaneously expand maximum 10% in all vertex directions. In another way, the flexibility index can be expressed as the norm of uncertain parameter, θ, and nominal value of the uncertain parameter, θ^0, as following.

$$\delta^* = \left\| \frac{\theta - \theta^0}{\theta^0} \right\| \%$$

CONCLUSIONS

In this work, we simulate a milk processing unit using a flowsheet simulation tool. The simulation is focused on the milk process operation parameters, i.e. temperature, flow rate, etc. The simulation results are in good agreement with the design data for the milk production process under clean condition. The simulator for the market milk production process, then, is employed to carry out process operation parameter and flexibility study under milk fouling condition. It is found out that the flexibility of the milk production process is 0.10 (maximum 10% expansion in all vertex direction) based on the selected uncertain parameters, i.e. milk inlet flow temperature, flowrate and fat content.

The established milk processing simulator can be adapted to simulate similar liquid food production units through suitable modifications. From the simulation, it is can be seen that the process simulation tool is very efficient to be used to investigate a new process operation method, to optimize the process operation for different objectives and to design a predictive control strategy for a liquid food processing unit.

REFERENCES

De Jong, P., A. J. van Asselt, 2006. “Review on Fouling Control in the Dairy Industry: What Do We Have and What Need To Be Done”. In *Proceedings Fouling, Cleaning and Disinfection in Food Processing 2006* (Jesus College, Cambridge, 20-22 March). 180-187.

Fryer, P.J.; P.T. Robbins; C. Green; P.J.R. Schreier; A.M. Pritchard; A.P.M. Hasting; D.G. Royston and J.F. Richardson. 1996. “A Statistical Model for Fouling of a Plate Heat Exchanger by Whey Protein Solution at UHT Conditions.” *Transaction of the Institution of Chemical Engineers* 74, 189-199.

Georgiadis, M.C.; G.E. Rotstein and S. Macchietto. 1998. “Optimal Design and Operation of Heat Exchangers under Milk Fouling.” *AIChE Journal* 44, 2099-2111.

Georgiadis, M.C. and S. Macchietto. 2000. “Dynamic Modelling and Simulation of Plate Heat Exchangers under Milk Fouling.” *Chemical Engineering Science* 55, 1605-1619.

Grossmann, I. E.; K. P. Halemane and R.E. Swaney. 1983. “Optimization Strategies for Flexible Chemical Processes.” *Computers & Chemical Engineering* 7, 439-62.

Gut, J.A.W. and J.M. Pinto. 2003. “Modelling of Plate Heat Exchangers with Generalized Configurations.” *International Journal of Heat and Mass Transfer* 46, 2571-2585.

Nema, P.K. and A.K. Datta. 2005. “A Computer Based Solution to Check the Drop in Milk Outlet Temperature Due to Fouling In a Tubular Heat Exchanger.” *Journal of Food Engineering* 71, 133-142.

Okos, M. R. 1985. *Physical and Chemical Properties of Foods*. American Society of Agricultural Engineers, St. Joseph, Michigan, USA.

Rahman, S. 1995. *Food Properties Handbook*. CRC Press, Boca Raton.

Sahoo, P.K.; I.A. Ansari and A.K. Datta. 2005. “Milk Fouling Simulation in Helical Tube Heat Exchanger.” *Journal of Food Engineering* 69, 235-244.

Saunders, E.A.D. 1988. *Heat Exchangers: Selection, Design and Construction*. New York, Longman S. &T. s. 4, 16, 17.

Schlünder, E.U. (ed.) 1995. *HEDH, Heat Exchanger Design Handbook*. Hemishere, New York. section 3.7.

Schreier, P. J. R. and P. J. Fryer. 1995. “Heat Exchanger Fouling: a Model Study of the Scaleup of Laboratory Data.” *Chemical Engineering Science* 50, 1311-1321.

Shah, R.K. and W.W. Focke. 1988. “Plate Heat Exchangers and Their Design Theory”. In *Heat Transfer Equipment Design*, R.K. Shah; E.C. Subbarao and R.A. Mashelkar (Eds.). Hemisphere, New York, Hemisphere Publishing Co., 227-254.

Singh, R.P. and A. G. Medina. 1989. *Food Properties and Computer-Aided Engineering of Food Processing Systems*. Kluwer Academic Publishers.

Tijskens, L. M. M.; M. L. A. T. M. Hertog; and B. M. Nicolai. 2001. *Food Process Modelling*. Woodhead Publishing Limited, Cambridge, England.

Yoon, J. and D. B. Lund. 1993. “Comparison of Two Operating Methods of a Plate Heat Exchanger under Constant Heat Flux Condition and Their Effect on the Temperature Profile during Milk Fouling.” *Journal of Food Process Engineering*, 17, 243-262.

ARTIFICIAL NEURAL NETWORKS FOR PREDICTION OF BEER'S PREFERENCE

Ravipim Chaveesuk and Amarin Saravanee
Program of Agro-Industry Technology Management
Faculty pf Agro-Industry, Kasetsart University
50 Paholyothin Road, Chatuchuck,
Bangkok, Thailand
E-mail: ravipim.c@ku.ac.th

KEYWORDS
Predictive Modeling, Beer Preference Rating, Polynomial Regression, Backpropagation Network.

ABSTRACT

Quality, particularly appearance and flavor of beer, plays a vital role in consumer preference. Study on the relationship between measurable characteristics of the beer and the degree of consumer liking via modeling approach can be very useful. The model can predict the consumer preference of any beer of interest and help identify significant characteristics affecting the preference. This research investigated the use of thirty five beer characteristics as independent variables and ten factors obtained from performing factor analysis on those thirty five variables for their effectiveness in modeling the relationship. Polynomial regression and backpropagation neural network (BPN) were examined and compared. Results indicated that variable reduction by factor analysis slightly improved the performance of the models. The BPN models outperformed the polynomial regression models in terms of prediction accuracy and generalization capability. Significant characteristics affecting the beer preference identified by the best BPN were ethyl hexanoate, ethyl octanoate, 3-methyl-1-butanol, 2-methyl-1-butanol, ethyl butyrate, 3-methyl butyl acetate, isobutyraldehyde, bitterness units, color, and formazin turbidity.

INTRODUCTION

Beer is one of the most popular alcoholic beverages worldwide. The global beer market has experienced a considerable annual growth rate of nearly 7 percent during 1997-2003, reaching US$6.6 billion in 2003 (USDA 2004). The growth was forecasted to continue in the future. The market growth is driven by increasing incomes and demand for more premium prized and specialty beer. Competition among beer breweries for consumer's loyalty is extremely strong. Advertising and promotion play an important role in establishing and maintaining their market share. However, a beer quality happens to be a major factor affecting the buying decision and hence the brewery's long-term competitiveness. Beer quality is in the eyes, nose, mouth and mind of the consumer. Consequently, breweries often conduct a sensory evaluation to compare their existing beers, competitors' beers and newly developed beers on their consumers.

The quality of beer is a function of its appearance and flavor. More than 800 compounds are present in beer (Meilgaard 1982) and approximately 600 of which are volatile (Maarse and Visscher 1989). These volatile compounds influence the flavor, consumer preference and acceptability of the beer. Certain groups of these volatiles are alcohols, esters, organic acids, aldehydes, sulfur compounds, amines, phenols and other mixtures (Pollock 1981). Their concentrations in beer vary depending on raw material such as barley, malt, and hop, yeast strain, fermentation and aging conditions. Alcohols are key volatile compounds in beer. Some of which are produced during the fermentation such as ethanol, 2-methylpropanol, 2-methylbutanol, 3-methylbutanol, and 2-pentanol whereas the others such as 2-octanol, 2-nonanol and 2-decanol are from hop and malt. Esters, produced by enzymatic reaction in yeast cells, provide fruity flavor in the beer. Major esters are ethyl acetate, 2-methylbutyl acetate, and 3- methyl butyl acetate. Organic acids, such as acetic acid, citric acid, 3-methhyl-butanoic acid, and 3-methhyl-oxopentanoic acid, are often associated with sourness, bitterness and astringency in the beer. They may come from malt or be produced during the fermentation. Aledhyde and ketones from raw material and being produced before or after fermentation process, give green leaves, grassy, and fruity flavor. Major amines in beer are pyrazines from malt and wort boiling process. Sulfur compounds generally come from malt and hop.

Since major physical and chemical characteristics that constitute beer appearance and flavor are laboratory measurable, it will be very useful to correlate these characteristics with the consumer preference. Once the relationship is analytically established, the brewers and marketers can use this information for predicting the consumer preference of the beer with a large number of physical or chemical characteristic combinations. Furthermore, if the significant characteristics affecting the beer preference can be identified, they will help support the management decision in the product and process improvement or product development.

This paper reviews two predictive modeling techniques : polynomial regression and artificial neural network and attempts to examine the potential use of both techniques in

approximating the relationship between physical or chemical characteristics and the consumer preference of beers.

MODELING APPROACH

This research compares and contrasts two modeling techniques including polynomial regression and the very popular artificial neural network, namely, the backpropagation network.

Polynomial Regression

Polynomial regression is widely used in modeling the input-output relationship. A polynomial regression model for m input factors, $(x_1, x_2, \ldots, x_m) = \mathbf{x}$, can be expressed as:

$$Y = \sum_{k=1}^{p} \beta_k Z_k(\mathbf{x}) + \varepsilon_p \qquad (1)$$

where there are p power functions $Z_k(\mathbf{x})$, e.g., linear, quadratic, cross terms, etc. β_k are the regression coefficients which are calculated from the observed pairs of data points via least squares estimation. ε_p is a random error term that is distributed according to $N(0,\sigma)$. Although polynomial regression models are straightforward to implement, they requires restrictive assumptions on the error terms and their performance depends on the appropriateness of the polynomial functional forms.

Artificial Neural Network (ANN)

ANN has recently been recognized in modeling applications. It develops a mapping from the input variables to the output variables through an iterative learning process. The model requires little or no prior assumption of functional relationships and is also robust to deviations from traditional statistical assumptions such as normal random errors, common error variance, and no multicollinearity. Typically, an ANN is organized into a sequence of layers: the input, hidden, and output layers (Figure 1).

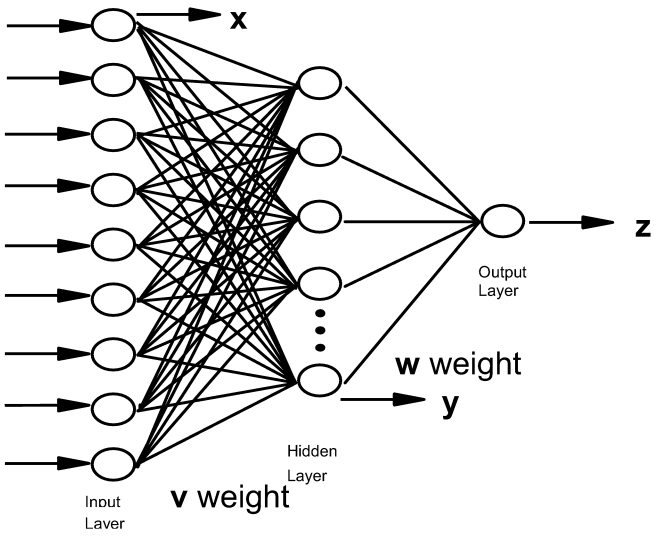

Figure 1: Typical ANN model

The input and output layers contain nodes or neurons that correspond to the input and output variables, respectively. Data flow between layers across weighted connections. Each neuron in the hidden or the output layer sums its input signals from the previous layer weighted by the connection weights, and applies an activation function to determine its output signal. There are several activation functions, ranging from a simple threshold function to complex non linear functions such as sigmoid, hyperbolic tangent and logistic functions. A multi-layer ANN with nonlinear transfer functions can theoretically model any relationship to an arbitrary accuracy and is thus termed a universal approximator (Funahashi 1989; Hornick 1989).

Backpropagation network (BPN) is a feed forward multi-layer neural network trained by gradient descent method (Rumelhart et al. 1986). The training algorithm is based on minimization of total squared error of output computed by the network. The training algorithm involves three stages: the feed forward of input training set, the calculation and backpropagation of error, and the adjustment of the weights. Limitations in the BPN are a slow learning rate due to backpropagating errors and adjusting all weights simultaneously as well as a difficulty in selecting its architectures and training parameters. Due to the data-driven characteristic, all neural network models are also prone to overparameterization, producing a good fit on the model construction data set but poor generalization to others.

METHODOLOGY

Data Collection and Preparation

The beer data of a Canadian brewery from Li and Petkau (1990) were used to develop the models. These data composed of 111 beer samples including house brands, newly developed products, and competitors' products purchased from retail outlets. For each beer sample, 35 measurable physical and chemical characteristics and the corresponding mean consumer preference rating were collected. The preference rating were conducted on a nine-point rating scale ranging from dislike extremely (rating 1) to like extremely (rating 9). The data were then arranged in the input-output pattern with the 35 analytical characteristics as inputs and the mean preference rating as an output. Table 1 lists the 35 beer characteristics.

Effect of Variable Reduction

When there are a large number of input variables to be included in the model, factor analysis may be used to group or combine the variables that are correlated to each other in the same factor. Conducting the factor analysis task leads to a reduction in input variables which in turn facilitates a model builder. This research investigated whether the use of factor analysis on the data would improve the model performance. The beer data were prepared in two patterns : (1) using original data and (2) performing factor analysis on the original data using principal component analysis for factor extraction and orthogonal rotation. Factor analysis was performed using SPSS version 12.0. The model

performance in terms of prediction accuracy was then compared.

Table 1: Thirty Five Analytical Variables

Variable	Name	Description
V1	pH	hydrogen-ion concentration
V2	color	spectrophotometric color
V3	refractive index	
V4	specific gravity	
V5	apparent extract	apparent amount of sucrose in the beer
V6	real extract	actual amount of solids in the beer
V7	extract of original wort	calculated original amount of solids in the wort
V8	alcohol	alcohol content of the beer
V9	remaining flavor extract	amount of yeast fermentable extract remaining in the beer
V10	calories	
V11	bitterness units	amount of bitter substance in the beer
V12	vicinal diketones	concentration of vicinal diketones, mainly diacetyl in the beer
V13	air	volume of air
V14	carbon dioxide	volume of dissolved CO_2 in the beer
V15	formazin turbidity units	degree of turbidity or haziness of the beer
V16	age	days since bottled
V17	foam collapse rate	measured by the sigma value method
V18	sulfur dioxide	quantity of sulfite in the beer
V19	isobutyraldehyde	in ppb
V20	n-propanol	in ppb
V21	ethyl acetate	in ppb
V22	iso-butanol	in ppb
V23	n-butanol	in ppb
V24	ethyl propionate	in ppb
V25	propyl acetate	in ppb
V26	3-methyl-1-butanol	in ppb
V27	2-methyl-1-butanol	in ppb
V28	Iso-butyl acetate	in ppb
V29	Ethyl butyrate	in ppb
V30	3-methyl butyl acetate	in ppb
V31	2-methyl butyl acetate	in ppb
V32	ethyl hexanoate	in ppb
V33	ethyl octanoate	in ppb
V34	2-phenylethyl acetate	in ppb
V35	ethyl decanotate	in ppb

Model Building

The entire data, either in the original pattern or in the pattern resulted from factor analysis, were randomly divided into 3 parts for fitting, testing and validating the models. The fitting data set comprised of 69 data points and the testing data set comprised of 22 data points. These two sets were used to build the model and select proper model parameters. The validation data set comprised of 20 data points for assessing the model's generalization capability.

Polynomial Regression

First, second and third order stepwise regression models were explored to fit the first data set. In order to minimize multicollinearity, each input factor is expressed as a deviation around its mean. Both forward and backward stepwise regressions are employed with the probability to enter and remove of 0.05. The aptness of the polynomial regression model was investigated through residual and normal probability plots and the variance inflation factor (VIF) is calculated to examine multicollinearity. All statistical works were performed by SPSS version12.0. Once the models with different functional forms were constructed, they were used to predict the preference rating of the testing data set to select the proper functional form. The one with the lowest predictive error measures was selected. The error measure used was mean absolute error (MAE) and was defined as follows:

$$MAE = \frac{\sum_{i=1}^{n} |\hat{y}_i - y_i|}{n} \qquad (2)$$

where $\hat{y}_i$ = the predicted response value of data point i

y_i = the actual response value of the data point i

n = the total number of data points

Backpropagation Network (BPN)

One hidden layer BPN models were developed using NeuralWorks Explorer. All variables were normalized between –1 and 1 to be consistent with the range of activation function. Building a useful BPN model requires proper selection of its architecture, the training parameters, and the stopping criteria. Various numbers of hidden neurons (1-4 neurons), activation function (sigmoid and hyperbolic tangent-tanH), learning rates (0.1-0.5), learning rules (delta rule and extended delta bar delta rule), momentum (0.1-0.5), and several sets of initial weights were explored. BPN with various model parameters were constructed using the first data set. In order to avoid overtraining, the learning phase was stopped every 100 learning iterations, and the network was evaluated for its prediction accuracy using the testing data set. Learning was stopped when the error measure of this testing data set continued to increase. The proper architecture and learning parameters were selected based on the MAE of the testing data set.

Model Validation

The generalization capability of both polynomial regression and BPN models were evaluated using the validating data set. The extent of model deterioration and overfit were examined by comparing the MAE from this validation data set with those from other data sets. The superior predictive model should possess good prediction accuracy across all data sets. The generalization capability becomes one of the major criteria in comparing the models.

Identification of Significant Beer Characteristics

In addition to use the developed models for prediction or performing what-if analysis, one can use them to gain insight in the system behavior. The model can be used to identify what input variables significantly affect the response. Chaveesuk and Smith (2003) demonstrated that polynomial regression and backpropagation network could help identify the critical factors in capital project evaluation. For a stepwise polynomial regression model, an inference can be made from the magnitude of the standardized regression coefficients. A large coefficient indicates a significant effect of that variable. In case of BPN model, altering the input variables by a certain percentage and calculating how much the output changes provides the basis for observing the important effects of the input variable. The larger the percentage changes, the greater the effect of that input variable.

RESULTS AND DISCUSSIONS

Factor analysis on the original data has reduced the input variables from 35 beer characteristics to 10 factors as summarized in Table 2.

Table 2: Factor Analysis of 35 Beer Characteristics

Factor	Component
F1	real extract, specific gravity, refractive index, apparent extract, calories, extract of original wort, alcohol
F2	2-methyl butyl acetate, 3-methl butyl acetate, iso-butyl acetate, iso-butanol, 2-phenylethyl acetate, 2-methyl-1-butanol, 3-methyl-1-butanol
F3	ethyl propionate, n-propanol, color, pH
F4	ethyl butyrate, ethyl octanoate, ethyl hexanoate
F5	isobutyraldehyde, n-butanol, ethyl decanoate
F6	sulfur dioxide, formazin turbidity units, bitterness units
F7	age, foam collapse rate
F8	ethyl acetate, propyl acetate
F9	dissolved carbon dioxide, air, vicinal diketones (VDK)
F10	remaining flavor extract

The results has revealed that some characteristics formed a unique group as follows : factor 1 composes of physical characteristics and the amount of solid and alcohol in the beer; factor 2 composes of acetate esters and volatile alcohols which provides banana, pear or fruity flavor and sweet musty odor; factor 4 composes of ethyl ester which provides apple or fruity flavor; factor 8 composes of acetate that provides fruity and solvent like flavor; and factor 9 composes of gas or carbonation and VDK that provide buttery or butterscotch odor.

In fitting various orders of polynomial regression models, the stepwise procedure selected only up to a second-order model for the 35-variable data and up to only a first-order model for the 10-factor data. The first-order polynomial regression model constructed from the 10-factor data showed the highest prediction accuracy in terms of MAE in the testing data set, followed by second-order polynomial regression model constructed from the 35-variable data (Table 3). This result demonstrated that performing variable reduction via factor analysis slightly increased the prediction accuracy of the polynomial regression model. Meanwhile, the BPN model with 4 hidden neurons, learning rate of 0.5, momentum of 0.5, using delta rule and sigmoid activation function, constructed from the 35-variable data, exhibited the highest prediction accuracy of the testing data set among all other combinations of model parameters studied (Table 3). It also appears that the variable reduction via factor analysis did not improve the prediction accuracy of the BPN model.

Table 3: Prediction Accuracy of Polynomial Regression and BPN Models on the Testing Data Set

Data Pattern	Model	MAE
35-vairable data	1st order regression	0.40
	2nd order regression	0.32
	BPN with 4 hidden neurons, learning rate of 0.5, momentum of 0.5, delta rule, sigmoid activation function	0.16
10-factor data	1st order regression	0.31
	BPN with 2 hidden neurons, learning rate of 0.3, momentum of 0.5, delta rule, tanH activation function	0.21

The generalization capability of the polynomial regression and BPN models with proper model parameters are shown in Table 4.

Table 4: Comparison of Model Generalization Capability

Data Pattern	Model	MAE	
		Fitting Set	Validating Set
35-vairable data	2nd order regression	0.08	0.60
	BPN - 4 hidden neurons	0.20	0.33
10-factor data	1st order regression	0.19	0.46
	BPN - 2 hidden neurons	0.19	0.31

It is observed that all models have shown some extent of deterioration in prediction accuracy for the validating data

set. However, the BPN models exhibited superior generalization capability than the polynomial regression models. The BPN prediction accuracy degraded to a lesser degree than that of the polynomial regression. The results also showed that performing variable reduction slightly improved the model accuracy in the validating data set.

Identification of important input variables is a further benefit gained from the accurate models. Table 5 exhibits important variables or factors identified by the polynomial regression and BPN models. It is noted that we can also identify significant interactions among the variables or factors if the regression models is used.

Table 5: Identification of Significant Variables or Factors

Impact	Regression		BPN	
	Variable	Factor	Variable	Factor
1 (highest)	V32	F5*F6	V32	F9
2	V18*V23[1]		V33	F2
3	V20*V26		V26	F5
4	V35*V35		V27	F3
5			V29	F6
6			V30	
7			V19	
8			V11	
9			V2	
10 (lowest)			V15	

[1] indicates interaction between variables

Identification of influential beer characteristics or factors will be based on BPN models since they generally possess superior prediction accuracy as well as generalization capability than polynomial regression models. The BPN models constructed from 35-variable data with 4 hidden neurons, learning rate of 0.5, momentum of 0.5, using delta rule and sigmoid activation function pointed out that the top ten beer characteristics considerably impacted the consumer preference rating were ethyl hexanoate (V32), ethyl octanoate (V33), 3-methyl-1-butanol (V26), 2-methyl-1-butanol (V27), ethyl butyrate (V29) and 3-methyl butyl acetate (V30), isobutyraldehyde (V19), bitterness units (V11), color (V2), and Formazin turbidity (V15). It is obvious that the top five variables are flavoring potent in the beer. These ethyl esters and volatile alcohols are recognized as secondary flavor constituents in the beer (Meilgaard et al. 1975). They together form the bulk of a beer's flavor. Removal any one of these constituents will produce a noticeable change in flavor. One can distinguish one beer from another of the same type by variations in these constituents. Moreover, the results of identifying significant characteristics using 35-variable model was quite consistent with identifying using 10-factor model.

CONCLUSION

The complex relationship between a large number of quantitative beer characteristics and consumer preference rating could be approximated by polynomial regression and backpropagation network models. The backpropagation network model, however, exhibited superior prediction accuracy and generalization capability than polynomial regression model. Performing a variable reduction using factor analysis slightly improved the model accuracy. When the best backpropagation network model was used to identify influential variables or factors affecting the preference rating, it indicated that flavoring constituents were most essential. These included ethyl esters such as ethyl hexanoate, ethyl octanoate, and ethyl butyrate, volatile alcohols such as 3-methyl-1-butanol and 2-methyl-1-butanol, 3-methyl butyl acetate and isobutyraldehyde. Other important characteristics were bitterness from hops, color, and turbidity of the beers.

REFERENCES

Chaveesuk, R., and A.E. Smith. 2003. "Economic Valuation of Capital Projects Using Neural Network Metamodels". *The Engineering Economist*, Vol.48, No.1, 1-30.

Funahashi, K. 1989. "On the Approximate Realization of Continuous Mappings by Neural Networks". *Neural Networks*, Vol.2, 183-192.

Hornik, K.; M. Stinchcombe; and H. White. 1989. "Multilayer Feedforward Networks are Universal Approximators". *Neural Networks*, No.2, 359-366.

Li, B. and A.J. Petkau. 1990. "Case Studies in Data Analysis, No. 6: A Regression Model with Random Effects for Beer Chemistry and Canadian's Beer Preference". *The Canadian Journal of Statistics.* Vol. 18, 98-125.

Maarse, H. and C.A. Visscher. 1989. "Volatile Compounds in Food". *Alcoholic Beverages-Qualitative and Quantitative Data.* TNO-CIVO Food Analysis Institute, Netherlands.

Meilgaard, M.C.; C.E. Dalgliesh; and J.F. Clapperton. 1979. "Beer Flavor Terminology". *Journal of American Society Brewing Chemists.* Vol. 37, No.1, 47-52.

Meilgaard, M.C. 1982. "Prediction of Flavor Differences between Beers from Their Chemical Composition". *Journal of Agricultural Food Chemistry*, Vol. 30, 1009-1017.

Pollock, J.R.A. 1981. *Brewing Science.* Vol. 2. Academic Press, London.

Rumelhart, D.E.; G.E. Hinton; and R.J. Williams. 1986. "Learning Internal Representations by Error Propagation". In *Parallel Distributed Processing: Explorations in the Microstructure of Cognition, Vol. 1: Foundations*, D.E. Rumehart and J.L. McClelland, (Eds.). MIT Press, Cambridge, MA, 318-362.

USDA. 2004. "Prospect in the Global Beer Market". Commodity and Marketing Programs-Agricultural Export Service Division, International Strategic Marketing Group, USA. (Dec).

BIOGRAPHY

RAVIPIM CHAVEESUK is an assistant professor in a Graduate Program of Agro-Industry Technology Management at Kasetsart University, Bangkok, Thailand. She received a B.S. in Agro-Industrial Product Development from Kasetsart University, Thailand, a M.S. in Food Science and Agricultural Chemistry from McGill University in Canada, and a M.S. and a Ph.D. in Industrial Engineering from University of Pittsburgh, USA. Her research interest is in the area of data modeling using statistical methods and computational intelligence, data mining, production economic analysis, and agro-industrial supply chain management.

MICROFLUIDICS MODELLING OF A HIGH-THROUGHPUT MICROCALORIMETRIC BIOSENSOR FOR ASCORBIC ACID QUANTIFICATION

Pieter Verboven
S. Vermeir
B.M. Nicolaï
J. Lammertyn
BIOSYST-MeBioS
Katholieke Universiteit Leuven
W. de Croylaan 42
B-3001 Leuven, Belgium
E-mail: Pieter.Verboven@biw.kuleuven.be

V. Vulsteke
L. Hoflack
B. Baeten
P. Van Gerwen
Vivactis NV
Kapeldreef 60
3001 Leuven, Belgium

KEYWORDS
food quality, functionality, model-based design, enzyme kinetics, heat and mass transfer, finite element method

ABSTRACT

Ascorbic acid (AA) is of great importance in the human diet due to its anti-oxidative properties and its role as vitamin in many biochemical processes. A microcalorimetric biosensor is presented for high-throughput quantification of ascorbic acid in food. The transduction mechanism of the presented method is based on microplate differential calorimetry (MIDICAL^{TM}) technology developed by Vivactis (Leuven, Belgium) using a novel membrane wafer sensor mechanism. A model of the system was developed and used to explain the effect of the physics and reaction kinetics on the sensor signal. The model considered transient diffusion of AA and oxygen, Michaelis-Menten kinetics and the resulting heat transfer. The finite element method was used to solve for concentration profiles and temperature in comparison with the sensor response of the MIDICAL^{TM} system. In a further step, model-based kinetic parameter identification will be possible.

INTRODUCTION

The importance of ascorbic acid (Vitamin C) for the human health is well known, such as its role in biosynthesis of collagen and in the metabolism of amino acids. Fruit and vegetables are the main sources of ascorbic acid in the human diet. The amount of the vitamin in these products is an important objective parameter for nutritional quality evaluation of the fruits. The development of fast, accurate and cheap detection methods is requirement for routine large scale analyses.
In the literature, a wide range of analysis methods have been described, such as chromatography, spectrophotometry and electrochemical methods. A review is given by Antonelli et al. (2002). Other methods (fluorimetry, titration, UV) are also referred to by Zeng et al. (2005).
Microcalorimetry has been presented by Wilson et al. (1995) and Antonelli et al. (2002). The method uses the measurement of enzymatic reaction heat of ascorbic acid with ascorbate oxidase as a detection mechanism and has large potential for high throughput analyses. The speed of the reaction and the specific sensitivity of the sensor to ascorbic acid oxidation still require attention. The role of oxygen has not received attention to date.
Models have rarely been used to simulate the behavior of biosensors. However, such an approach has been shown to improve the understanding of the mechanisms, and offer the possibility for process improvement and design (Lammertyn et al. 2006).
In this paper we present a model-based approach to analyze a novel high throughput microcalorimetric technique for detection of ascorbic acid.

MICROPLATE DIFFERENTIAL MICROCALORIMETRY

Microcalorimetry has proven in the past to be a successful technique for the enzyme-catalyzed measurement of a whole range of analytes but this is the first application of a high-throughput microcalorimetric device using a novel membrane wafer sensor mechanism. The transduction mechanism of the presented method is based on the microplate differential calorimetry (MIDICAL^{TM}) technology developed by Vivactis (Leuven, Belgium).
The microplate contains an array of 96 wells (volume 20 µl) which allow simultaneous ascorbic acid quantification of 48 samples. The transduction principle is based on the measurement of the difference in heat generation between two microfluidic wells, located at the cold and the hot junctions of a thermopile. Initially one well is filled with an enzyme-buffer mixture whereas the other is filled with only buffer. Afterwards the sample (max 4µl) is injected in both wells with a nanodispenser. The exothermic reaction of AA with ascorbate oxidase (E.C 1.10.3.3) is monitored and the AA-content is estimated by integrating the area under the signal curve. A high correlation ($R^2 > 0.99$) was found between this parameter and the AA concentration in the sample. A linearity of calibration curve was observed between 0.5 mM and 100 mM with a limit of detection of 0.5 mM corresponding to a total amount of 0.5 nmol AA in the sample.

BIOSENSOR MODEL FORMULATION

Model Equations

Since the enzymatic conversion of ascorbic acid into dehydroascorbic acid is oxygen dependent, the amount of oxygen dissolved in the buffer strongly influences the signal shape. To study this effect in the microfluidic system and to optimize the sensor a reaction-diffusion model was developed in Femlab 3.1 (Comsol, Stockholm, Sweden),

describing the mass transfer and the heat generation and dissipation in the well:

$$\begin{aligned} \frac{\partial}{\partial t} O_2 &= \nabla D_{O_2} \nabla O_2 - r_{O_2} \\ \frac{\partial}{\partial t} AA &= \nabla D_{AA} \nabla AA - r_{AA} \\ \rho c \frac{\partial}{\partial t} T &= \nabla \lambda \nabla T + q_r \end{aligned} \quad (1)$$

with O_2 the oxygen concentration [mM or mol m^{-3}], AA the ascorbic acid concentration [mM], D_{O2} and D_{AA} the diffusion coefficients of the two species, T is temperature [K], ρc the heat capacity [J m^{-3} K^{-1}] and λ the thermal conductivity [W m^{-1} K^{-1}] of the different materials. The reaction heat generation q_r [W m^{-3}] equals

$$q_r = h_r r_{AA}$$

where h_r (J mol^{-1}) is the change is enthalpy due to oxidation of ascorbic acid. The reaction rates r_{O2} and r_{AA} are calculated from the enzyme kinetics of the following reaction that is mediated by the enzyme ascorbate oxidase *AAO* (Wilson et al. 1995; BRENDA 2006):

$$2AA + O_2 \xrightarrow{AAO} 2H_2O + 2DAA$$

which was modelled in a Michaelis-Menten type reaction rate with an oxygen-dependent rate constant. The model parameters are given in Table 1. The thermal parameters are thermophysical properties of water and the wafer.

Table 1: Model parameters

D_{O2}	2×10^{-9} m^2 s^{-1}
D_{AA}	6×10^{-10} m^2 s^{-1}
V_{max}	0.67*O_2 mol m^{-3} s^{-1} at 0.5U AAO
K_m	0.2 mM
h_r	1.2875×10^5 J/mol

Geometry and Boundary Conditions

The equation system is solved for diffusion-reaction of the species and heat transfer in a single well of the microplate. The geometry of the system (in 2D axisymmetric formulation) is given in Figure 1. The reaction takes place in a microliter drop between the walls of the well. A thermopile in the floor of the well measures the heat generation. The drop is saturated with oxygen in equilibrium with the surrounding air. When the reaction starts, oxygen is consumed and the deficit is supplied by means of diffusion from the surrounding air. Both oxygen and ascorbic acid diffuse through the drop from regions of high concentration to regions of low concentration. The generated heat diffuses through the drop and the well, and is finally removed by the surrounding air.

The species boundary conditions for equation system (1) are axial symmetry conditions for both species on the left boundary, zero flux on the floor and walls of the well, a fixed oxygen concentration (20%) at the top boundary and zero flux of AA at the surface of the drop. The boundary condition for heat transfer is a Neumann condition using a heat transfer coefficient at the surface of the drop and walls, and the thermal resistance of the membrane stack on the floor. The heat transfer coefficient was determined from a model optimization with respect to the measured signals. A constant value of 25 W m^{-2} K^{-1} was used throughout the study. Initial conditions are uniform concentrations of the species and uniform constant temperature.

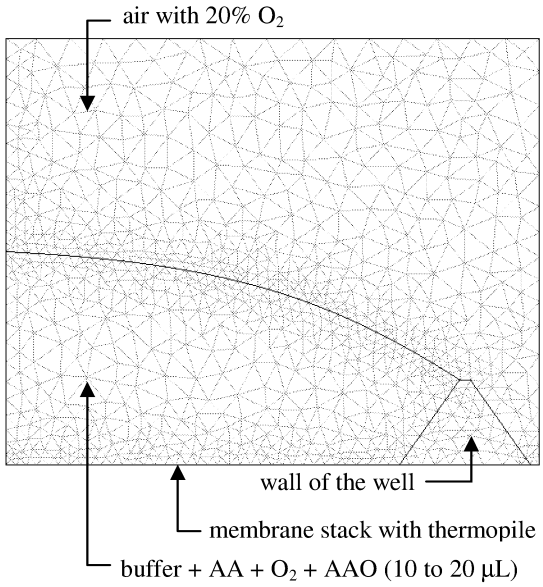

Figure 1: 2D Geometry of a Microplate Differential Microcalorimeter Well with Finite Element Mesh

Finite Element Method Solution

The model is solved using the finite element method, employing FEMLAB 3.1 (Comsol, Sweden). The mesh consists of 1783 triangular elements and is visible in Figure 1. Backward differentiation formulas of 5th order are used for a stable solution of the resulting differential equation system. The transient solution (2000 seconds) is obtained in less than a minute CPU time on a AMD Athlon 2.41 GHz Windows XP workstation with 2Gb RAM.

RESULTS AND DISCUSSION

Profiles of Oxygen and Ascorbic Acid in the Biosensor Well

Figure 2 shows the simulated profiles of oxygen and ascorbic acid in the well of the biosensor for a concentration of 500 mM AA and 0.5U AAO. The available oxygen in the well is consumed very fast and its concentration remains 0 in the lower part of the well for most of the process time, while higher values are maintained towards the surface of the drop. During a first period the oxygen concentration profile remains the same, balancing supply from the air and consumption by the enzyme reaction. At the same time ascorbic acid is steadily transformed at the surface of the

well without pronounced gradients in the well. Note that no transformation takes place at the bottom of the well because oxygen is not available. The transformation of AA is thus balanced by its diffusion. In the second period, when AA has decreased considerably, the demand for oxygen by the reaction decreases. Oxygen then diffuses further into the well where reaction can now take place locally.

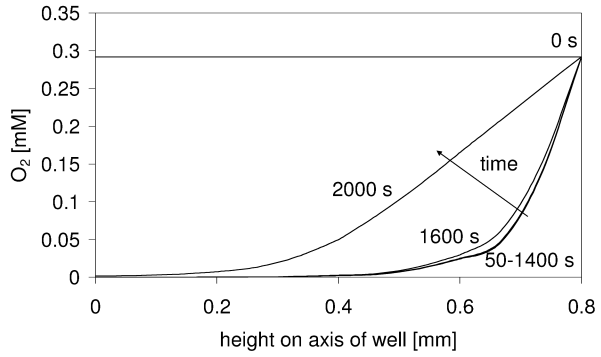

(a)

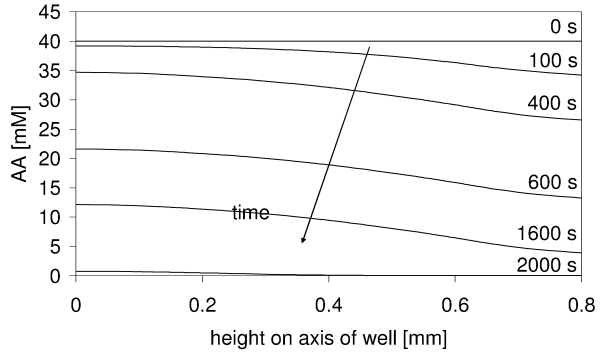

(b)

Figure 2: Model Simulations of Oxygen (a) and AA (b) Concentration on the Height Axis of the Well during Enzyme Mediated Oxidation of Ascorbic Acid (1µl 500 mM AA in a 12.5 µl well)

Figure 3 confirms the above observations. In the figure profiles of oxygen and ascorbic acid are displayed at different points on the floor of the well. Available oxygen depletes very fast and is only replaced by the end of the process. On the other hand, ascorbic acid steadily decreases due to diffusion to upper regions of lower concentration where reaction continues to take place. From figures 2 and 3 it can be clearly observed that the whole reaction process involves important spatial phenomena. The presented approach allows taking these diffusion effects into account.

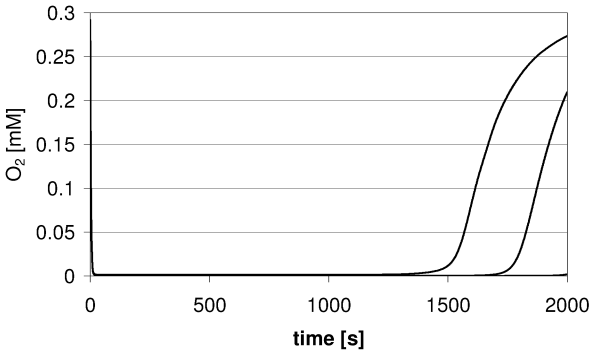

(a)

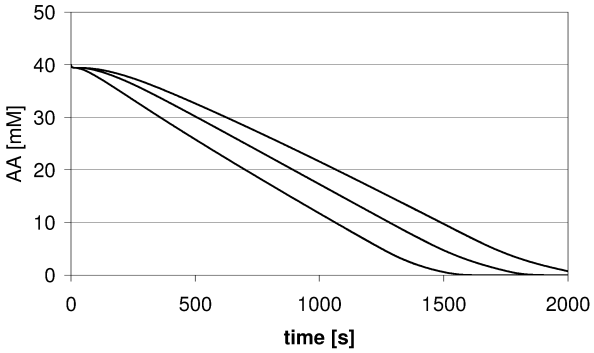

(b)

Figure 3: Model Simulations of Oxygen (a) and AA (b) Concentration in Different Points on the Floor of the Well during Enzyme Mediated Oxidation of Ascorbic Acid (1µl 500 mM AA in a 12.5 µl well)

Figure 4 demonstrates the large effect of oxygen on the reaction. The simulated biosensor response is shown for a reaction that is limited or not by oxygen. In the latter case, it is assumed that the well is continuously saturated with oxygen. Clearly, the reality of oxygen consumption leads to a reaction time that is 4 times longer. The sensor signal shape is also different. In presence of oxygen depletion, the response exposes a shoulder or plateau that indicates a limiting effect of oxygen is manifested.

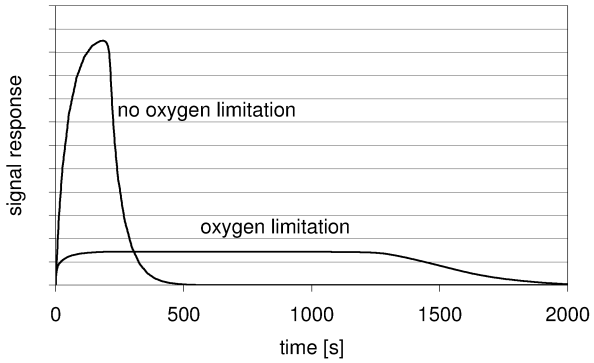

Figure 4: Simulated Biosensor Response as Affected by Oxygen Diffusion (1µl 500 mM AA in a 12.5 µl well)

The effect of oxygen diffusion on the reaction kinetics of AA oxidation was discussed by Wilson et al. (1995). In their study, experiments were conducted with a negligible head space to study the intrinsic effect of oxygen in the reaction solution on the reaction rate. With their results they were able to explain earlier studies where oxygen diffusion was present, but not taken into account the analysis. To our knowledge, the present study is the first to take into account and quantify the effect of oxygen diffusion on kinetic assays of ascorbic acid.

Model vs. Experiment

Figure 5 shows the comparison of the simulated biosensor signal to the measured sensor response. The experimental sensor response is the average of 4 wells. The model predicts correctly the introduction and growth of a shoulder with increasing concentration of ascorbic acid. At the shoulder the transformation rate of ascorbic acid is limited by the supply rate of oxygen from the air into the well (Figures 2 & 3). The oxygen supply limitation ends when the curves start to decrease. This effect does not manifest itself at low concentrations of ascorbic acid, because the oxygen consumption is lower and the supply limitation does not occur. The model also captures the effect of changing the enzyme units of ascorbate oxidase (Figure 6). The peak signal increases and the plateau time shortens with increasing amount of enzyme. With increasing enzyme units, the maximum conversion rate of ascorbic acid increases. As a result, the higher heat production causes a higher peak response. At the same time, the amount of substrate decreases more quickly, which reduces the size of the plateau.
At higher enzyme units, the level of the plateau is over predicted. This may be due to the use of simplified boundary conditions for heat transfer. This, however, does not affect the shape of the signal. More importantly, the model also fails to capture the first peak at higher ascorbic acid concentrations (Figure 5). The peak is also more pronounced at higher enzyme units (Figure 6). Clearly an additional mechanism that comes into play at higher substrate concentrations is missing in the model. This will be subject of further investigations.

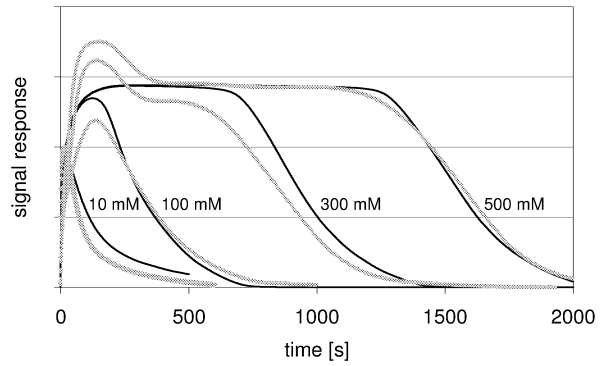

Figure 5: Model (thin lines) vs. Experimental (thick lines) Microplate Calorimeter Biosensor Response with 0.5U AAO

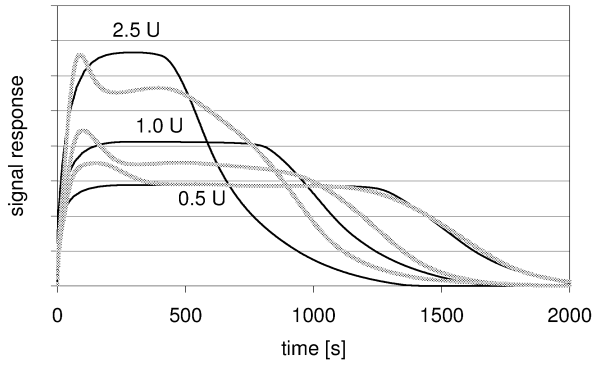

Figure 6: Model (thin lines) vs. Experimental (thick lines) Microplate Calorimeter Biosensor Response (1µl 500 mM AA in a 12.5 µl well)

CONCLUSIONS

For the first time, the mechanism of diffusion-reaction in a microfluidic microcalorimetric biosensor for ascorbic acid detection has been explained. The reaction is limited by oxygen diffusion, and as a result the process has, even on the microliter scale, a strong spatial aspect. The presented model-based approach is a basis for process and sensor design and, due to its reasonably small computational cost, can be used for model-based kinetic parameter estimation.
The simulated sensor response corresponded well with the experimental signal. The effect of enzyme and ascorbic acid concentration was demonstrated.
The presented microplate differential calorimetry (MIDICAL^{TM}) technology was shown to be a promising method for high throughput detection of ascorbic acid.

ACKNOWLEDGEMENTS

This research was made possible by means of the financial support of a research grant of the Fund for Scientific Research–Flanders (Belgium), the Institute for the Promotion of Innovation by Science and Technology in Flanders (IWT), the Katholieke Universiteit Leuven and Vivactis NV. Pieter Verboven is postdoctoral fellow of of the Fund for Scientific Research–Flanders.

REFERENCES

Antonelli, M.L.; G. D'Ascenzo; A. Laganà and P. Pusceddu. 2002. "Food analyses: a new calorimetric method for ascorbic acid (vitamin C) determination." *Talanta* 58, 961-967.

BRENDA. 2005. *The Comprehensive Enzyme Information System*. http://www.brenda.uni-koeln.de/

Lammertyn J.; P. Verboven; E.A. Veraverbeke; S. Vermeir; J. Irudayaraj and B.M. Nicolaï. 2005. "Analysis of fluid flow and reaction kinetics in a flow injection analysis biosensor. *Sensors and Actuators B: Chemical*." In press.

Wilson, R.J.,; A.E. Breezer and J.C. Mitchell. 1995. "A kinetic study of the oxidation of L-ascorbic acid (vitamin C) in solution using an isothermal microcalorimeter." *Thermochimica Acta* 264, 27-40.

Zeng, W.; F. Martinuzzi and A. MacGregor. 2005. "Development and application of a novel UV method for the analysis of

ascorbic acid." *Journal of Pharmaceutical and Biomedical Analysis* 36, 1107-1111.

AUTHORS BIOGRAPHY

PIETER VERBOVEN, STEVEN VERMEIR, BART NICOLAÏ and JEROEN LAMMERTYN are coworkers at the division of Mechatronics, Biostatistics and Sensors (MeBioS) of the Department of Biosystems of the Catholic University of Leuven. The main research theme of the division is the interaction between biological systems and physical processes. Within the Sensor Technology Group, high throughput systems are developed for food quality and safety assessment. A unique approach is followed, where expertises on analytical methods are combined with physical modeling and advanced biostatistics.

PETER VAN GERVEN and coworkers perform R&D at Vivactis NV. Vivactis is a technology platform company pioneering the use of its proprietary Microplate Differential Calorimetry (MiDiCal™) for the rapid identification and parametrization of novel active molecules.

PACKAGED FOODS SIMULATION

MULTISCALE DETERMINATION OF DIFFUSIVE PROPERTIES IN POLYMERS: APPLICATION TO THE PREDICTION OF DESORPTION PACKAGING CONSTITUENTS INTO FOODSTUFFS

Jérôme Lézervant
Olivier Vitrac
Alexandre Feigenbaum
INRA – UMR 614
Moulin de la Housse, BP 1039
51687 Reims cedex 2, FRANCE
E-mail: jerome.lezervant@reims.inra.fr

KEYWORDS
Parameter identification, diffusion, packaging, confocal microscopy.

ABSTRACT

Chemical substances (additives, monomers, residues) from packaging materials can migrate into foodstuffs. Their diffusive properties in packaging materials are required to predict the contamination of food by packaging substances. This work proposes a general and robust methodology for a fast determination of diffusion coefficients (ranged between 10^{-12} and 10^{-17} $m^2 \cdot s^{-1}$) and their activation energies in plastic materials. The methodology, which combines both spatial (1D and 2D) and time information, was tested for spatial scales varying between 5 mm down to 0.3 µm. Experiments in laser scanning confocal microscopy demonstrated, that diffusion coefficients varied significantly at microscopic scale in semi-crystalline polymers such as low density polyethylene. The variation was particularly significant for length scales below 3 µm.

INTRODUCTION

The understanding of transport phenomena, which control the desorption of substances (monomers, additives, residues) of packaging materials into food, is a major concern to reduce the risk of contamination of food products. The recent EU directive 72/2002/EC (EU 2002) dedicated to food contact materials in plastics defines both the list of authorized substances and their acceptable limit of migration. Besides, article 14 specifies that this amount can be either experimentally assessed or derived from appropriated simulations. Predictive approaches are however limited by the availability of diffusive properties as diffusion coefficients (D) and activation energies (Ea) for a large set of polymers, diffusants and thermodynamic conditions. Diffusants of interest have molecular mass ranged between 100 and 1000 $g \cdot mol^{-1}$ and diffusion coefficients (D) typically ranged between 10^{-11} and 10^{-19} $m^2 \cdot s^{-1}$ in plastic materials (EC 2003). Diffusion coefficients are conventionally derived i) from desorption kinetics into food simulants (Aminabhavi and Phayde 1995; Reynier et al. 2002) or ii) from the variation of concentration profiles in the polymer (Roe et al. 1974; Moisan 1980). Both approaches are limited by the duration (from minutes to years) required to detect a significant variation in the measured concentration, respectively in the liquid phase or in the polymer. Activation energies are inferred similarly from the variation of D with temperature.

In order to get faster determinations of diffusion coefficients, several authors proposed to use microscopic methods, which reduces drastically the characteristic time required to assess a detectable effect. First methods were based on the measurement of concentration profiles of UV tracers by micro-spectrophotometry (*e.g.* Dudler and Muiños 1996). As other macroscopic methods, this approach required to put in contact a virgin polymer with a source of dyes. At equilibrium, the measurement cannot be reiterated since there is no more discernible concentration gradient. Alternative methods based on laser-induced photooxidation of fluorescent tracers are more promising. Since the initial concentration profile in the substrate is generated by an in situ chemical reaction in presence of intense light and oxygen, the experiments can be repeated at the same location. This methodology, so-called fluorescence recovery after photobleaching (FRAP), was however developed to assess diffusion coefficients in living cells and biological tissues (Axelrod et al. 1976; Soumpasis 1983), whose values (above 10^{-10} $m^2 \cdot s^{-1}$) are typically far higher than those considered in plastics. First applications to plastic materials were operated by interferometry (Cicerone et al. 1995; Tseng et al. 2000).

This work examines several robust experimental approaches and identification techniques to assess low diffusion coefficients (about 10^{-15} $m^2 \cdot s^{-1}$) from a macroscopic scale (5 mm) to microscopic ones (down to 300 nm) in semi-crystalline polymer such as polyethylene. All techniques involve the characterization of concentration profiles in 1 or 2 dimensions for different diffusion times. General diffusion times or Fourier times, noted Fo, and defined by Equation (1) are used in this study:

$$Fo = \frac{D \cdot t}{l^2} \quad (1)$$

where t and l are the time and the characteristic length of the measurement. Experimentally, the equivalence between time and space according to equation (1) is particularly efficient to generate profiles for a wide range of D values. From the computational point of view, this equivalence lead to new techniques of identification of D based on homothetic solutions of transport equations and likelihood principles.

Indeed, even in complex situations where D was not constant during the experiment (*e.g.* change in temperature set), an equivalent diffusion time may be defined by (Cranck 1975):

$$Fo = \frac{\int_0^t D \cdot d\tau}{l^2} \quad (2)$$

The paper is organized as follow. The theoretical section presents the principles of the identification of D by combining both spatial (1D or 2D) and time information. The third section describes the experimental methodologies to assess concentration profiles at macroscopic and microscopic scales. The fourth section presents the results obtained for different optimized initial concentration profiles. Since semi-crystalline polymers as polyolefins can be considered homogeneous only at scales larger than 50 µm, the proposed time-space methodology is first tested at macroscopic scale with small probes (*i.e.* with high diffusion coefficients). Experiments at microscopic scale were performed with a larger probe (*i.e.* with a lower diffusion coefficient) below the critical length scale of 50 µm. The last section concludes on the feasibility to measure in situ Ea values in anisotropic materials (*e.g.* in oriented polymer) and down to the scale of light diffraction.

THEORETICAL SECTION

Forward Problem

The variation on an initial concentration profile (1D or 2D), $u(x,y,t=0)$ with time was calculated from the dimensionless diffusion transport equation:

$$\frac{\partial u_{(x^*,Fo)}}{\partial Fo} = \Delta^* u = \frac{\partial^2 u_{(x^*,y^*,Fo)}}{\partial x^{*2}} + \frac{\partial^2 u_{(x^*,y^*,Fo)}}{\partial y^{*2}} \quad (3)$$

where u is a dimensionless concentration or a quantity proportional to the concentration, $x^* = \frac{x}{l}$ and $y^* = \frac{y}{l}$ are dimensionless Cartesian coordinates. It is worth to notice that the diffusion coefficient is assumed to be uniform in the material.

Numerical Strategy of Resolution in 1D
In 1D, two particular boundary conditions were considered: impervious boundary condition and infinite geometry (*i.e.* no boundaries), for macroscopic and microscopic experiments respectively. In finite geometries, a numerical solution was discretized onto piecewise second degree polynomials (local interpolants). The solution was based on 100 nodes. In infinite geometries, the solution was expanded as global interpolants based on sinus cardinal functions as described by Weideman and Reddy (2000). This method is particularly intended for solving problems on the real line (-∞,+∞). About 100 equidistant collocation nodes and symmetric with respect to the center of the "center" of the initial profile were used. The collocation was constrained by adding steady conditions close to the boundaries ($\Delta^* u = 0$). All expanded solutions were integrated in time according to a second order implicit difference scheme.

Numerical Strategy of Resolution in 2D
In 2D, the solution at time t was calculated in one step from the bivariate convolution of the initial solution with a bivariate Gaussian kernel, with zero mean and a scaled variance, σ^2, defined by the Einstein Equation:

$$\sigma^2 = 4 \cdot \frac{D \cdot t}{l^2} = 4 \cdot Fo \quad (4)$$

The convolution was calculated by assuming symmetric boundary conditions, which are equivalent to impervious boundary conditions.

Inverse Problem

The inverse problem consisted in finding D from n different measures of u for different $\{t_i/l_i^2\}_{i=1..n}$ values. The whole process was carried out into two stages.
The first stage consisted in finding for each profile different from the initial one the best Fo_i value, which minimizes the criterion:

$$\chi_i^2 = \left\| w_{(x^*,y^*)} \cdot \left[u_{(Fo_i,x^*,y^*)} - \hat{u}_{(Fo_i,x^*,y^*)} \right] \right\|_{x^*,y^*}^2 \quad (5)$$

where $\hat{u}$ is the predicted concentration profile and w a suitable weighting function (1D or 2D Heaviside functions), which controls the importance of each local value.
The second stage consisted in deriving D values from the regression line between identified $\{Fo_i\}_{i=1..n}$ and $\{t_i/l_i^2\}_{i=1..n}$ values. As a result the final D value is estimated in a least square sense. The consistency of individual results is analyzed by the linearity of the data and the absence of significant intercept.
In practice, u was numerically filtered and normalized before identification. A detailed sensitivity analysis of the whole procedure filtering+identification was performed by adding random noise to the initial profiles in the range of experimental errors. Confidence intervals were calculated from at least 100 Monte Carlo trials.

MATERIALS AND METHODS

Virgin and Formulated Polymer

All experiments were carried out on disks (∅ 30 mm, thickness 70-420 µm) of low density polyethylene (LDPE, reference: Lacqtene, Atofina, France). Films were pressed by pressing at 130°C and 6 MPa from powder including or not a tracer. Only the central part of the disks was used in the further experiments.
Fluorescent probes were used as tracers, their main characteristics are summarized in Table 1. The LDPE powder was impregnated with a solution of probe in

dichloromethane (HPLC grade, Acros, France). The powder was used after evaporation of dichloromethane.

Table 1: Main characteristics of the tested probes.

probes	*molecular mass* ($g \cdot mol^{-1}$)	*suppliers*	*analysis scale*
naphthalene	128	Fluka, France	macro
2-ethoxynaphthalene	172	Acros, France	macro
phenanthrene	178	Fluka, France	macro
pyrene	202	Fluka, France	macro
rubrene *	533	Fluka, France	micro

* 6,11,12-tetraphenylnaphthacene

Reference Method at Macroscopic Scale

Macroscopic concentration profiles were obtained by putting in contact with pressure a combination of virgin and formulated films. Our methodology is a modified version of systems previously described by Roe et al. (1974) and Moisan (1980). The stack of films comprised 14 films with 2 formulated films at positions 5 and 10. Experiments occurred at 40°C for contact time varying from 17 to 96 hours. Each film was subsequently extracted in dichloromethane (16 hours at 40°C). The concentration in the extract was determinated by high performance liquid chromatography (HPLC model Agilent 1100 Series, Agilent Technologies, France) with fluorescence detection under the following chromatographic conditions: mobile phase water 40% – acetonitrile 60%; pre-column and column Kromasil C18 (reference 18651155, Alltech, France); flow rate 1 $mL \cdot min^{-1}$; injection volume 10 µL; excitation wavelength 250 nm and multi emission wavelengths analysis.

Microscopic Scale Experiments

Microscopic observations were performed on an inverted laser scanning confocal microscope (model LSCM AOBS SP2, Leica, Germany), with UV and visible lasers. Laser power was controlled by acousto-optical tunable filters. Observations were performed with oil immersion objectives at magnification ×40 and ×63, with numerical aperture of 1.25 and 1.32 respectively. Intensity images (12 bits, 512 ×512 pixels) were obtained by scanning along x and y axes. The z position was accurately controlled with a piezo-electric overstage (model Scan IM 100x100, Märhäuser, Germany).
The initial 2D intensity profile was obtained by a FRAP technique. A predefined region was x-y scanned with the largest scan field as possible and the maximum laser intensity (available power per pixel about 20 mW). It was verified that the bleaching operated also in the z direction so that the thickness of the bleaching region was larger than 10 times the characteristic length in plane x-y. The observations were performed in the z symmetry of the bleached region. These conditions ensured that mass transport might be interpreted in the observation plane. 1D bleach patterns were based on a combination of double and quadruple planes. 2D patterns consisted in a partial chessboard. The variation of concentration profiles were monitored every 2 or 5 minutes with a laser intensity 100 times lower than the bleaching intensity. Each profile was based on the accumulation of 4 or 12 images to reduce Poisson noise. Accumulation was performed in 16 bits to prevent numerical truncation. The effect of possible bias due to a non uniform excitation or emission in the scanned field was corrected from the initial image acquired prior bleaching. All corrections were based on the Beer-Lambert law.

RESULTS AND DISCUSSION

Preliminary simulations and tests demonstrated that the mathematical well-posedness of the identification problem was significantly improved when the concentration profile included a change in modality (*e.g.* from bimodal to monomodal). Initial macroscopic and microscopic profiles were designed to include this feature.
It emphasized that the number of degree of freedom in spatial information was much higher in microscopic experiments than in macroscopic experiments. The number of time samples were almost similar in both approaches. In macroscopic experiments, additional regularization was enforced by assuming the mass conservation in tracers. In microscopic experiments with an infinite medium, the calculated profile was constrained by steady boundary conditions.

Typical Identifications of *D* Values at Macroscopic Scale

Typical results are plotted in figure 1. Figures 1a-1d describes in particular the variation from a bimodal to a monomodal distribution when *Fo* values were higher than 1. Variations of the ratio t/l^2 was obtained by modifying the thicknesses of films (70, 210 and 420 µm) and contact times (between 17 and 96 h).
In our conditions *Fo* varied between 0.3 to 7.2 with determination coefficients higher than 0.99. No significant bias (intercept) was detected and confirmed the reliability of the estimation of *D* since it was based on independent experiments. Identified *D* values were of 3.7 10^{-12}, 2.7 10^{-12}, 2.0 10^{-12} and 9.5 10^{-13} $m^2 \cdot s^{-1}$ for naphthalene, 2-ethoxynaphthalene, phenanthrene and pyrene respectively. Confidence intervals were lower than 10^{-15} s $m^2 \cdot s^{-1}$.

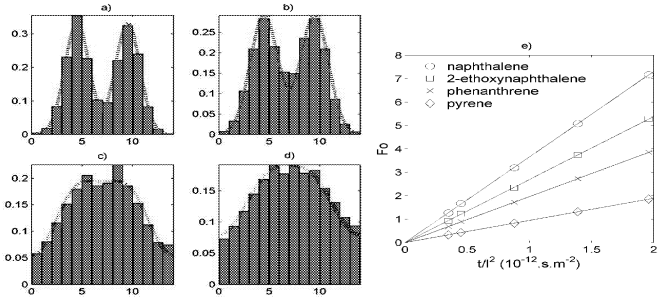

Figure 1: a-d) Typical dimensionless experimental and fitted concentration profiles: a) Fo = 0.7, b) Fo = 0.9, c) Fo = 2.7, d) Fo = 3.9; e) identified Fo values against the scaling ratio t/l^2 for 4 probes in LDPE at 40°C.

Typical Identifications of *D* Values at Microscopic Scale

Typical 1D Intensity Profiles
Typical concentration profiles as observed in confocal

microscopy for rubrene in LDPE are depicted on Figure 2. Images include Poisson and Gaussian noise. For 1D patterns, both noises are significantly removed by the projection operation and no more additional filtering is almost required. In 2D patterns, filtering based on neighborhood is required to remove Poisson noise. Since the same filter (conventionally an Hanning filter) is applied of all images, it does not change the result of the iterative deconvolution algorithm used in this work. The contribution of an heterogeneous illumination of the background was log-subtracted to all filtered images. The fading between images due to additional bleaching during acquisition or possible oscillations in z position was corrected from the average intensity far from the bleach region.

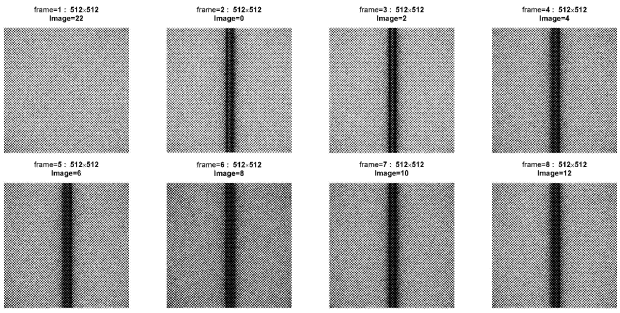

Figure 2: Raw intensity images before and after bleaching. The time interval between each image is of 4 min. Image field is 465×465 µm^2 in LDPE at 21°C.

Projected and filtered intensity profiles corresponding to figure 2 are plotted in figure 3. Filtering was a based on non-causal filter of order 5. Experimental profiles were identified as physically interpretable when a same steady inflexion point was identified for all profiles. It is worth to notice that the profile depicted in figure 3b is almost a negative image of the profile depicted in figure 1a.

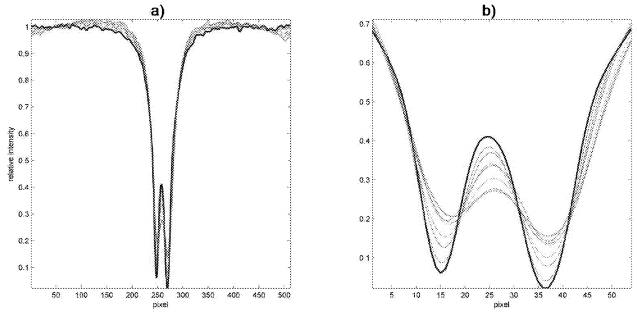

Figure 3: Variations of projected and filtered intensity profiles (corresponding to figure 2) with time: a) whole scanned field, b) details.

Typical Identifications

Experimental data of figure 3 with a weighting window centered between positions 200 and 300. The corresponding variations of the normalized distance criterion with Fo are plotted in figure 4. For all images different from the initial one, a minimum was identified and optimal Fo values were found to increase with time. It was however that confidence intervals were overlapping. This effect was related to filtering, the order of which was close to the typical distance between two consecutive inflexion points (about 10 pixels). The corresponding variation of identified Fo values with t/l^2 are depicted in figure 6c. The relationship was linear and unbiased. The identified D value was of 1.5 $10^{-15} \pm 8\ 10^{-17}$ m^2·s^{-1} for rubrene in LDPE at 21°C. Adding random noise to raw images did not change significantly the result.

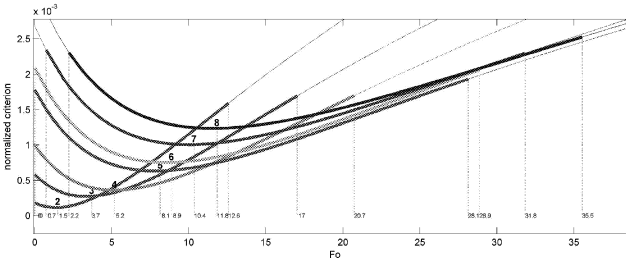

Figure 4: Normalized distance criterion versus theoretical Fo values for each frame in the series depicted in figure 2.

Repeatability of D Measurements

It is emphasized that the regression lines $Fo=D\cdot t/l^2$ obtained from the microscopic method are derived from a same experiment and not from independent experiments (different samples) as in the macroscopic method. So-calculated confidence intervals do not provide any information on the repeatability of the measurement in a different location. Besides, it is underlined that D values derived from 1D profiles were not true local values (*e.g.* 10 µm), since the 1D profiles were obtained from the projection on 2D profiles along a main direction (typical size > 400 µm).

Figures 5 and 6a plot 1D and 2D patterns respectively, the characteristic length scales of which were higher than the one used figure 2. The corresponding regression lines $Fo=D\cdot t/l^2$ are plotted in figure 6c.

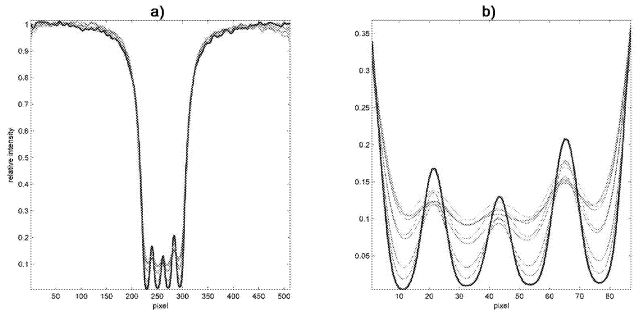

Figure 5: Variation of a 4 bands 1D intensity profile with time: a) whole scanned field, b) details. The time interval between each image is of 4 min with an image field of 465 µm.

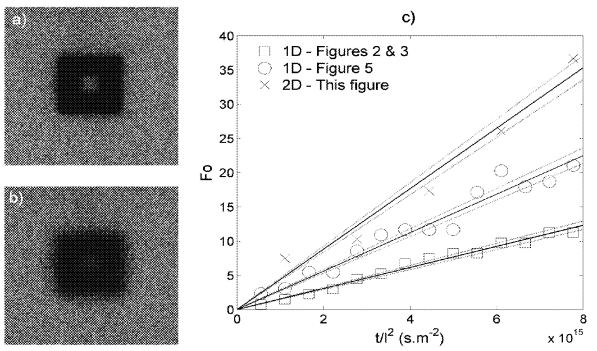

Figure 6: a-b) 2D pattern (field 465×465 µm^2): a) initial, b) after 24 min; c) Fo values versus t/l^2. 95% Confidence intervals of regression are plotted in dotted lines.

The D values were respectively 2.8 $10^{-15} \pm 1\ 10^{-16}$ $m^2 \cdot s^{-1}$ and 4.4 $10^{-15} \pm 2\ 10^{-16}$ $m^2 \cdot s^{-1}$. All results yielded similar magnitude orders for D but whose difference was higher than the confidence intervals on each individual value. The sensitivity analysis showed that combing the information for different t/l^2 reduced the uncertainty in D by a factor 5. It confirmed also that differences obtained from different acquisition series could not be explained by the initial noise in the intensity images.

Variation of *D* Values with the Measurement Length Scale

The dispersion of D values in space and according to the characteristic length scale of initial intensity profile was tested from independent bleach experiments in a same material. The pattern consisted in a single line and its characteristic length (thickness) varied between 0.3 µm and 11 µm. The other bleach dimension was set to 30 times the characteristic length. Results are plotted in figure 7. The values oscillated around 4 10^{-15} $m^2 \cdot s^{-1}$ with a span of 7 10^{-16} $m^2 \cdot s^{-1}$. The amplitudes of oscillations were significantly higher below 3 µm.

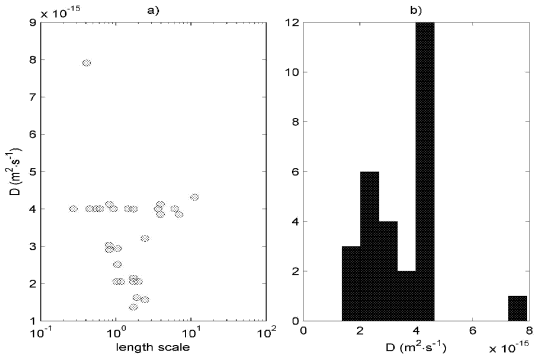

Figure 7: a) variations of D values of rubrene in LDPE at 21°C with bleaching thickness (in µm), b) distribution of D values.

CONCLUSIONS

A general approach was proposed to assess diffusion coefficients from the variation of an initial concentration profile in time and in space. The variation of the scale of measurement was proposed as a possible alternative to diffusion time. This approach makes it possible to reduce drastically the time required to measure diffusion coefficients, as those encountered in plastic materials. This approach was tested on macroscopic and microscopic experiments involving fluorescent tracers.

In particular, diffusion coefficients as low as 10^{-15} $m^2 \cdot s^{-1}$ were measurable under a confocal microscope in less than 10 minutes (see figure 6c). However, in semi-crystalline polymers, these properties were measured at a length scale lower than the typical size of a representative volume of the material. As a result, D values were found to be highly variable with the considered position in the polymer. In the case of rubrene in LDPE, representative D values seemed achievable by combining at least 5 measurements.

The tested combination of different length scales (magnitude up to 5 10^4) makes it possible to assess microscopic mass transport in complex materials as semi-crystalline polymers: accessibility, tortuosity, molecular interactions with the polymer. As an example, current work aims at identifying the distribution of local activation energies in LDPE by monitoring the evolution of a same concentration profile subsequently to different set temperatures. Besides, a direct visualization of the polymer structure after labeling is tested to relate the morphology of crystallites with the values of diffusive properties (D and Ea).

REFERENCES

Aminabhavi, T.M. and H.T.S. Phayde. 1995. "Sorption, desorption, resorption, redesorption, and diffusion of haloalcanes into polymeric blend of ethylene-propylene random copolymer and isotatic polypropylene." *Journal of Applied Polymer Science*, 57(12), 1419-1428.

Axelrod, D.; Koppel, D.E.; Schlessinger, J.; Elson, E. and W.W. Webb. 1976. "Mobility measurement by analysis of fluorescence photobleaching recovery kinetics." *Biophysical Journal*, 16, 1055-1069.

Cicerone, M.T.; Blackburn, F.R. and M.D. Ediger. 1995. "Anomalous diffusion of probe molecules in polystyrene: evidence for spatially heterogeneous segmental dynamics." *Macromolecules*, 28, 8224-8232.

Dudler, V. and C. Muiños. 1996. "Diffusion of benzotriazoles in polypropylene: Influence of Polymer Morphology and Stabilizer Structure." In: *Polymer Durability: degradation, stabilization, and lifetime prediction.* Ed. R.L. Clough, N.C. Billingham, K.T. Gillen, Oxford University Press, Oxford, pp. 441-453.

Cranck, J., 1975. *Mathematics of diffusion*. 2nd edition. Oxford University Press, Oxford.

EC. 2003. *Conclusions of the Project FAIR CT98-4318* "Recyclability: Programme on the recyclability of food packaging materials with respect to food safety considerations – polyethylene terephthalate (PET), paper and board and plastics covered by functional barriers."

EU. 2002. *EU directive 2002/72/EC relating to plastics materials and articles intended to come into contact with foodstuffs*. Official Journal, L220 of 15.08.2002, 18.

Moisan, J.Y. 1980. "Diffusion des additifs du polyethylene – I – influence de la nature du diffusant." *European Polymer Journal*, 16, 979-987.

Reynier, A.; Dole, P. and A. Feigenbaum. 2002. "Migration of additives from polymers into food simulants: numerical solution of a mathematical model taking into account food and polymer interactions." *Food and Additives Contaminants*, 19(1), 89-102.

Roe, R.J.; Bair, H.E. and C. Gieniewski. 1974. "Solubility and diffusion coefficients of antioxydants in polyethylene." *Journal of Applied Polymer Science*, 18, 843-856.

Soumpasis, D.M. 1983. "Theoretical analysis of fluorescence photobleaching recovery experiments." *Biophysical Journal*, 41, 95-97.

Tseng, K.C.; Turro, N.J. and C.J. Durning. 2000. "Molecular mobility in polymer thin films." *Physical Review E*, 61(2), 1800-1811.

Weideman, J.A.C. and S.C. Reddy. 2000. "A MATLAB Differentiation Matrix Suite." *ACM Transaction Mathematical Software*, 26(4), 465-519.

A THERMODYNAMICALLY CONSISTENT DESCRIPTION OF THE DESORPTION OF PACKAGING CONSTITUENTS INTO FOODSTUFFS

Ali Mougahrbel
Olivier Vitrac
Alexandre Feigenbaum

INRA – UMR 614
Moulin de la Housse, BP 1039
51687 Reims cedex 2, FRANCE
E-mail: ali.mougharbel@reims.inra.fr

KEYWORDS
Partition coefficients, food packaging, thermodynamics

ABSTRACT
Simulations may replace experiments to check the compliance of food contact materials and to assess the exposure of consumers to packaging substances. The reliability of simulated results depends both on the availability of physicochemical data (diffusion and partition coefficients) and on the consistency of physical assumptions. This work tests the validity of thermodynamical assumptions implied in common desorption models. The analysis is based on experimental desorption isotherms obtained for low density polyethylene formulated before and after processing with two series of surrogates (linear alkanes, Uvitex OB).

INTRODUCTION

Constituents of packaging materials (additives, monomers etc.) can diffuse into food products. The current EU directive 2002/72/EC (EC 2002a) on plastic materials defines both the list of authorized substances and their specific migration limits (SML). In addition, it makes it possible the use of mathematical modeling based on diffusion and mass balance equations to check the compliance of single layer plastic packaging materials against SML. Besides, probabilistic modeling has been recently proposed to perform sanitary surveys on the contaminants of packed food products (Vitrac and Hayert, 2005a, Vitrac et al., 2005c) and to assess the consumer exposure to packaging substances (Vitrac and Leblanc, 2005).
Previous works were mainly focused on the determination and prediction of diffusion coefficients for different diffusants in different plastic materials and various temperatures (EC 2002b, Helmroth et al. 2002, Reynier et al. 2001a and 2001b and Vitrac et al. 2005b). By contrast, few works have been performed on the determination or prediction of apparent partition coefficients, noted K, between packaging materials, noted P, and food or food simulants, noted F. The importance of this parameter on the prediction of desorption kinetics is discussed extensively in Cranck (1975). The few values, which are available in the literature, were reviewed by Tehrany and Desobry (2004). The current version of the guidance document for the application of the EU directive 2002/72/EC (EC 2003), to which two of us participated, proposes only very rough approximations for K for plastic additives. A value of 1 is proposed for hydrophobic food and a value of 10^{-3} for aqueous food.
In addition to the urge to generate data on partition coefficients and related models of prediction, there is a need to provide a reliable and thermodynamically acceptable description of equilibrium desorption curves for packaging substances. Apparent partition coefficients, K, in closed P+F systems are defined as the ratio of concentrations of the diffusion species i between both phases at equilibrium:

$$K = \frac{C_{i,F}\big|_{eq}}{C_{i,P}\big|_{eq}} \qquad (1)$$

Their values depends how the concentrations are expressed: in mass per mass, in mass per volume or mol per volume. There is an alternative description derived from statistical physics, where the partition coefficient at the PF interface I, noted K_I, is connected to the partition function (i.e. probability of occupation), noted $\left\{ Z_{i,j}\big|_I \right\}_{j=F,P}$, on both side of the interface as:

$$K_I = \frac{Z_{i,F}\big|_I}{Z_{i,P}\big|_I} \qquad (2)$$

Equation (2) describes the local thermodynamical equilibrium between P and F. It is used to express the mass transfer rate at the interface I in physical models of desorption. This description is detailed in Gandek (1989a and 1989b), Vergnaud (1995) and in Vitrac et al. (2006). It is however assumed that K and K_I are equal.
This work examines common assumptions on the thermodynamics of the desorption of packaging substances into foodstuffs. These assumptions include i) the desorption isotherm of packaging substances obeys to Henry law, ii) the sorption isotherm of packaging substances into food obeys also to Henry law, iii) whole of packaging substances could be desorbed into a food with an infinite volume, iv) all packaging substances can diffuse in the whole equivalent volume of the polymer (i.e. homogenized volume which neglect the effect of the crystalline phase) and v) $K=K_I$.
The paper is organized as follows. Section 2 presents how the magnitude of partition coefficients can be derived from the theory of polymer in solutions and from the regular solution theory. Section 3 describes the conditions, which were used to assess K and K_I. The results are presented and discussed in section 4. The main deviations are summarized in the last section.

THEORETICAL SECTION: THERMODYNAMICAL EQUILIBRIUM BETWEEN THE FOOD PRODUCT AND ITS PACKAGING

The true macroscopic equilibrium between the food product and its packaging material would correspond to a situation of minimal free energy of the food-packaging system. This equilibrium is reached by exchanging matter (packaging substances, food substances) between both compartments. This equilibrium has low practical use since the desorption of plastic substances is generally faster than the sorption of food constituents and because the industry prefer polymers which develop low interactions with food (i.e. polymer constant rates are chosen greater than the food product shelf-life).

Local Thermodynamical Equilibrium

In this work, we focus on the local thermodynamic equilibrium (LTE), which controls the desorption of packaging substances at food-packaging interface *I*. For the diffusing packaging constituent *i*, LTE enforces the equality of chemical potentials, noted $\{\mu_{i,j}\}_{j=P,F}$, on both side of the interface *I*.

$$\underbrace{\mu_{i,P}|_I}_{\mu^{ref}_{i,P}|_I+\mu^{excess}_{i,P}|_I} = \underbrace{\mu_{i,F}|_I}_{\mu^{ref}_{i,F}|_I+\mu^{excess}_{i,F}|_I} \quad (3)$$

where $\{\mu^{ref}_{i,j}|_I\}_{j=P,F}$ and $\{\mu^{excess}_{i,j}|_I\}_{j=P,F}$ are respectively the reference and the excess in chemical potential of the diffusant *i* in the phase *j* at the interface.
When the possible mass transport of food constituents into the polymer is neglected, the LTE can be also expressed as the equality of partial free molar energies of the mixtures *P+i* and *F+i*:

$$\left(\frac{\partial G_{P+i}}{\partial n_i}\right)_{T,p,n_P} = \left(\frac{\partial G_{F+i}}{\partial n_i}\right)_{T,p,n_F} \quad (4)$$

where *G* is a Gibbs free energy, n_i, n_P and n_F are the number of molecules i, polymer and food. *T* and *p* are the absolute temperature and the pressure respectively.

Expression of the Chemical Potential on the Packaging Side
The expression of the free energy related to the mixture G_{P+i} can be approximated from the Flory-Huggins theory of polymers in solution. In the case of very cohesive systems such as polymers, it is emphasized that the free energy of the mixture *P+i* is mainly related to the variation in conformational entropy of the polymer itself. Indeed, the presence of small molecules in the polymer reduces the number of achievable conformations for the polymer. According to the Flory and Huggins theory (Flory, 1953), the conformation of the polymer is decomposed on a lattice, whose sites can be occupied either by an equivalent polymer unit or by a small molecule. For a solid polymer, the typical site size is associated to the free volume of the diffusant, which is a very rough approximation of the size of sorption sites in polymer. Thus, the diffusant is assumed to be of length *1* and the polymer of length *r*. The parameter *r* is defined by the ratio of the free volume fractions of the polymer and of the diffusant. The molar entropy of the mixture S_{P+i} is assumed equal to the entropy of the polymer, which is defined by the Boltzmann law:

$$S_{P+i} \approx S_P \approx R \cdot n_P \cdot \ln\left(\underbrace{\frac{n_i + r \cdot n_P}{r \cdot n_P}}_{\text{number of achievable microstates for one macrostate}}\right) = -R \cdot n_P \cdot \ln(\phi_P) \quad (5)$$

where *R* is the ideal gas constant.

The molar enthalpy of the mixture H_{P+i} is mainly related to the excess in enthalpy of the mixture and controlled by the Flory-Huggins interaction parameter $\chi_{i,P}$:

$$H_{P+i} = R \cdot T \cdot \chi_{i,P} \cdot n_i \cdot \phi_P \quad (6)$$

The molar free enthalpy of the mixture G_{P+i} is therefore:

$$G_{P+i} = H_{P+i} - T \cdot S_{P+i} = R \cdot T\left[n_P \cdot \ln(\phi_P) + \chi_{i,P} \cdot n_i \cdot \phi_P\right] \quad (7)$$

The excess in chemical potential of *i* in *P* is finally derived by differentiating Equation (7) with respect to n_i:

$$\mu^{excess}_{i,P} = R \cdot T\left[\left(1-\frac{1}{r}\right)\phi_P + \chi_{i,P} \cdot \phi_P^2\right] \quad (8)$$

Expression of the Chemical Potential on the Food Side
The excess in chemical potential can be expressed similarly on the food side. For liquid food, the regular solution theory for small molecules (Hildebrand and Scott 1964) implies *r=1* in Equation (8):

$$\mu^{excess}_{i,F} = R \cdot T \cdot \chi_{i,F} \cdot \phi_F^2 \quad (9)$$

Approximations of Flory-Huggins interaction parameters
$\chi_{i,P}$ and $\chi_{i,F}$ can be approximated from the solubility parameters, $\{\delta_k\}_{k=i,P,F}$, which are related to the density of cohesive energy of the pure compound *k*:

$$\chi_{i,j} = \frac{V_i}{RT}\left(\delta_i - \delta_j\right)^2 \text{ for } j = P,F \quad (10)$$

$\{\delta_k\}_{k=i,P,F}$ are derived in this work from the quantitative structure property relationship proposed by Van Krevelen (1990).

Thermodynamical Definition of Partition Coefficients

If reference potentials are chosen equal, equation (3) implies that the activities of *i* in P and F are equal. If at infinite dilution, they obey to Henry Law, one gets:

$$\gamma_{i,P} \cdot X_{i,P} = \gamma_{i,F} \cdot X_{i,F} \quad (11)$$

where $\{\gamma_{i,j}\}_{j=P,F}$ and $\{X_{i,j}\}_{j=P,F}$ are respectively the activities coefficients and the molar fraction of *i* in the phase *j*. By expressing the concentration in mass per mass with the molar concentration, the following expression of the partition coefficient, as used in this study, is inferred:

$$K_I = \frac{C_{i,F}\big|_I}{C_{i,P}\big|_I} = \frac{\gamma_{i,P}}{\gamma_{i,F}} \cdot \frac{V_P}{V_F} \cdot \frac{\rho_P}{\rho_F} \quad (12)$$

where $\{\rho_j\}_{j=P,F}$ and $\{V_j\}_{j=P,F}$ are respectively the density of j and the molar volume of j.

TESTED MATERIALS

P was a low density polyethylene (Atofina, France) processed from ground pellets by extrusion in a mono-screw extruder (model Scamia RHED 20.11.D, France; set zone temperatures: 120, 125, 130 and 135°C) and subsequently calendered (final thickness about 100 µm).
F consisted in absolute ethanol (SDS, France).
Five diffusants (i=1..5) were tested, including 4 linear alkanes: dodecane, tetradecane, hexadecane, octadecane; and a plastic additive: 2,5-thiophenediylbis(5-tert-butyl-1,3-benzoxazole (Uvitex OB, Ciba, Switzerland).

EXPERIMENTAL METHODS

Formulation of Plastic Films Before Processing

Reference desorption experiments were carried out on films, whose resin was formulated prior processing. Two formulations were prepared by soaking the powder into two dichloromethane solutions containing either the 4 alkanes or Uvitex OB and octadecane. The solvent was subsequently vaporized. The tested conditions corresponded to almost industrial conditions of formulation of plastic materials.

Formulation of Plastic Films After Processing

Since it was expected that all diffusants could be not available for desorption due to possible trapping in crystalline phases or insufficient dispersion of surrogates in the polymer, a formulation after processing was also performed. It consisted in a sorption stage at 40°C of virgin films in ethanol solutions containing the desired surrogates (here: Uvitex OB and octadecane). After sorption, dried films were stored at ambient temperature during 2 weeks.

Desorption Experiments

Desorption experiments were performed on plastic strips (5× 5×0.1 mm^3) dispersed in ethanol at 40°C. A gentle stirring effect was achieved by rotating vertically the flasks. Tested conditions included several initial concentrations (400-2000 mg·kg^{-1}) and several dilution factors, noted L. L was defined as the phase ratio between F and P; it varied between 1.5 and 14. For all tested surrogates, equilibrium conditions (no detectable further desorption) were obtained after 2 days.

Concentration Measurements

Concentrations in F were measured by gas chromatography with flame ionization detection as described by Vitrac et al. (2006). Residual concentrations in P were measured similarly after extraction in dichloromethane.

RESULTS AND DISCUSSION

Theoretical Prediction of the Partitioning

The approximations of the excess in chemical potential in both phases (equations 8 and 9) at infinite dilution makes it possible to assess where the location of the diffusant i is more likely (e.g. in P or in F), when only a single diffusant is added to the system P+F. Figure 1 plots the ratios of excess in chemical potentials between P and F at 40°C when $\phi_F \to 1, \phi_P \to 1$ and by assuming r>>1 for P.

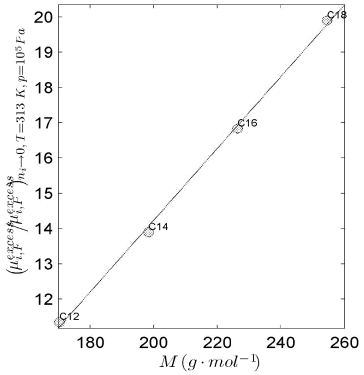

Figure 1: Ratio of the excess in chemical potential between F and P for the 4 tested alkanes (M is the molecular mass).

Since the chemical potential is much higher in F than in P, the presence of 4 tested alkanes is more probable in P than in F at infinite dilution. The partition coefficient K_I can be derived from equation (2) and values at equilibrium by noting: $\left\{Z_{i,j}\big|_I \approx \exp(-G_{i+j}\big|_{eq} / R\cdot T)\right\}_{j=F,P}$. G_{i+j} values corresponding to $\left\{\mu_{i,j}^{excess}\big|_{\eta_i \to 0}\right\}_{j=F,P}$ should be however avoided, because they were not calculated at equilibrium (i.e. for a ratio of chemical potentials equal to 1).

Experimental Assessment of Possible Deviations to Ideality on F Side

The behavior G_{i+F} was tested by assessing the values of K_I and K for different equilibriums obtained for a same initial packaging material (same formulation and subsequently processing). Different equilibriums were achieved by changing the dilution factor L.

Estimation of K_I
The values of K_I were derived exclusively from the values of $C_{i,F}\big|_{eq}^{(L)}$ and by assuming that the maximum amount of i, which should be desorbed, noted $C_{i,P}^{\max}\big|_{t=0}$, was unknown. The principle was based on a mass balance between L and P:

$$C_{i,F}\big|_{eq}^{(L)} = C_{i,P}^{\max}\big|_{t=0} \cdot \left(K_I^{-1} + L\right)^{-1} \quad (13)$$

The unknown $C_{i,P}^{\max}\big|_{t=0}$ was eliminated by plotting the ratio $C_{i,F}\big|_{eq}^{(L)} / C_{i,F}\big|_{eq}^{(Lref)}$ for different L values, where L_{ref} is a reference value for L. K_I and its possible variations with $C_{i,F}\big|_{eq}^{(L)}$ are

analyzed in Figure 2 by comparing experimental $C_{i,F}\Big|_{eq}^{(L)}$ against theoretical ones calculated for different constant K_I values. It is highlighted that experimental and theoretical curves presented slightly different curvatures for the 4 tested alkanes. The equivalent K_I values tended to decrease when the concentration on liquid side was higher. For octadecane, K_I changed from 0.4 towards 0.3.

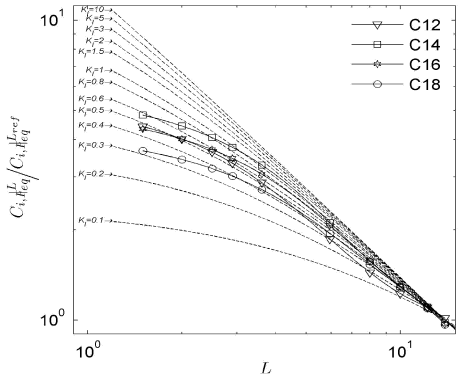

Figure 2: Variations of the normalized concentration in F for different dilution factors L (L_{ref} = 14). All surrogates were included in the same formulation of P. Theoretical curves for constant K_I values are plotted in dashed lines.

Estimation of K

According to equation (1), apparent K values corresponding to figure 2 were calculated from $C_{i,F}\Big|_{eq}^{(L)}$ and $C_{i,P}\Big|_{eq}^{(L)}$ values (figure 2). Since all alkanes were included in the same formulation of the polymer, K values are plotted against the concentration of each diffusant and against the total concentration in F at equilibrium.

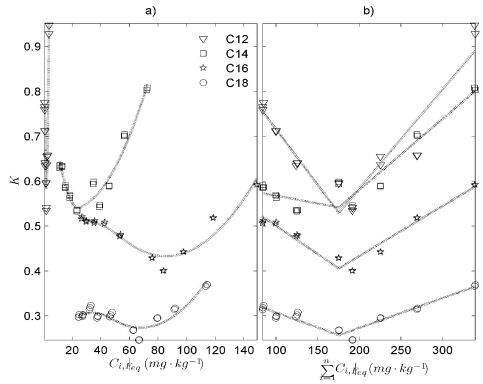

Figure 3: Variations of K values a) with the concentration of each diffusant in P and b) with the total concentration in diffusants in F. All values are measured at equilibrium.

For each diffusant, the assumption of constant K values was acceptable only in a small range of $C_{F,i}\Big|_{eq}^{(L)}$ values. Apparent K values successively decreased and increased with $C_{F,i}\Big|_{eq}^{(L)}$.

The position of the minimum appeared all the earlier than the diffusant was smaller (figure 3a). Figure 3b shows besides that this minimum was related to a same overall concentration in all diffusants about 180 mg·kg^{-1}. Beyond this critical overall concentration, the drastic increase in apparent K values was associated to the solubility limit of our mixture of alkanes in ethanol. A phase separation of the mixture alkanes+ethanol would displace the apparent F+P equilibrium as observed and would increase the desorption rate without leading to a similar increase in K_I values.

Experimental Assessment of Possible Deviations to Ideality on P Side

In previous experiments, the non linear variation of K with $C_{i,F}\Big|_{eq}^{(L)}$ and the deviations between K and K_I were unexpected. Only the increase of K with $C_{i,F}\Big|_{eq}^{(L)}$ could be explained with a deviation to the ideality on F side. A possible deviation to ideality in the previously tested material (i.e. formulated before processing) was analyzed by assessing the cumulative amount of "desorbable" substances after successive equilibriums with ethanol ($L \approx 10$). The "non ideal" behavior of the tested material was also compared with the desorption isotherm related to only "desorbable" substances.

Amount of "Desorbable Substances"

The cumulative amount of "desorbable" substances, which approximates $C_{i,P}^{\max}\Big|_{t=0}$, is plotted in figure 4 for P formulated prior processing with octadecane and Uvitex OB. Desorption yields showed that a significant amount of initial surrogates, between 3 % and 10 % could be not desorbed. It was therefore confirmed that apparent K values derived from Equation (1) underestimated the true partition coefficients below the critical overall concentration. The underestimations were expected to be all the higher than $C_{i,P}\Big|_{eq}^{(L)}$ were lower or equivalently than the $C_{i,L}\Big|_{eq}^{(L)}$ were lower.

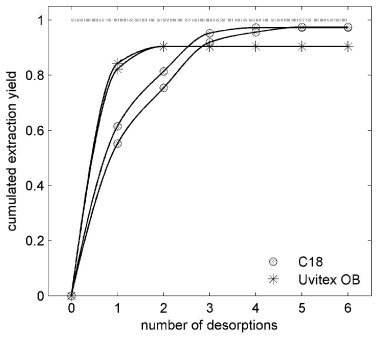

Figure 4: Cumulative extraction yields after successive desorptions ($L \approx 10$) up to equilibrium. Experiments are duplicated.

Desorption Isotherm of "Desorbable Substances"

The desorption isotherm $C_{F,i}\Big|_{eq}^{(L)} = f\left[C_{P,i}\Big|_{eq}^{(L)}\right]$ related to only "desorbable" substances was estimated by performing desorption on materials, which were formulated after processing. The formulation (by sorption in concentrated solutions) and the subsequent desorption experiments were designed to generate equilibrium concentrations in phases P and F higher than those presented in figure 3 and close to the expected critical overall concentration. The isotherm of "desorbable" octadecane is compared with the apparent isotherm obtained with materials formulated prior processing in figure 5.

The isotherm of "desorbable" octadecane was linear and did

not present any bias (i.e. intercept). This ideal behavior would correspond to an equilibrium obeying to Equation (12). The partition coefficient K given by the slope of the desorption curve was about 0.33. This value was not significantly different from the K_1 value obtained in figure 3 for the highest concentration in F.

In formulated materials before processing, the apparent isotherm was not linear. For concentrations in P lower than 180 mg·kg^{-1}, it was almost parallel to the isotherm of "desorbable" substances but the amount of "desorbed substances" was underestimated. This deviation was consistent with a significant amount of "non desorbable" substances, while the equilibrium of "desorbable" substances remained completely reversible. Above 180 mg·kg^{-1}, the amount of desorbed substances tended to be overestimated. From figure 4, the negative deviation was expected to be larger for Uvitex OB, but the results are still pending.

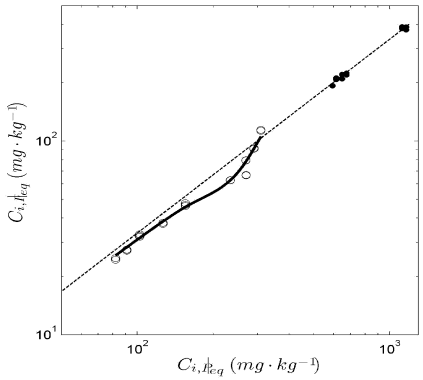

Figure 5: Desorption isotherm of octadecane: for materials formulated after processing (filled symbols) and for materials formulated before processing (open symbols, see figure 3). The dashed line is the regression line fitting the filled symbols and intercepting 0 (slope=0.33±0.01).

CONCLUSIONS

This work examines the physical consistency of assumptions, which are generally implicitly introduced in desorption models to predict the contamination of food products by packaging substances. Significant deviations to Henry law on F side were only identified for concentrations which are far from the maximum concentration authorized in food (60 mg·kg^{-1}). On P side, it was demonstrated that a significant amount of additives (either linear or aromatic) could be trapped in the polymer matrix (here low density polyethylene) and not available for desorption. Current work aims at identifying at microscopic scale the location of fluorescent tracers in polyolefins.

REFERENCES

EC. 2002a. EU directive 2002/72/EC relating to plastics materials and articles intended to come into contact with foodstuffs. Official Journal, L220 of 15.08.2002, 18-55.

EC. 2002b. Conclusions of the thematic network "Evaluation of migration models to be used under directive 90/128/EEC": SMT–CT98–7513.

EC. 2003. Food contact materials: a practical guide for users of European directives. http://europa.eu.int/comm/food/food/chemicalsafety/foodcontact/practical_guide_en.pdf

Flory, P.J. 1953. Principles of Polymer Chemistry. *Cornell University Press*, New York.

Fredenslund, A.; Gmehling, J. and P. Rasmussen. 1977. Group-contribution estimation of equilibrium ratios for multicomponent distillation design. *Proc. Conf. Appl. Chem., Unit Oper. Processes*, 3rd, 15-21.

Gandek, T.P.; Hatton, T.A. and R.C. Reid. 1989a. Batch extraction with reaction: Phenolic antioxidant migration from polyolefins to water. 1. Theory. *Industrial and Engineering Chemistry Research*, 28, 1030-1036.

Gandek, T.P.; Hatton, T.A. and R.C. Reid. 1989b. Batch extraction with reaction: Phenolic antioxidant migration from polyolefins to water. 2. Experimental results and discussion. *Industrial and Engineering Chemistry Research*, 28, 1036-1045.

Helmroth, E.; Rijk, R.; Dekker, M. and W. Jongen. 2002. Predictive modelling of migration from packaging materials into food products for regulatory purposes. *Trends in Food Science and Technology*, 13, 102-109.

Hildebrand, J.H. and R.L. Scott. 1964. The solubility of non electrolytes. *Dover*, New York.

Reynier, A.; Dole, P.; Feigenbaum, A. and S. Humbel. 2001a. Additive diffusion coefficients in polyolefins. II. Effect of swelling and temperature on the D = f(M) correlation. *Journal of Applied Polymer Science*, 82(10), 2422-2433.

Reynier, A.; Dole, P.; Feigenbaum, A. and S. Humbel. 2001b. Diffusion coefficients of additives in polymers. I. Correlation with geometric parameters. *Journal of Applied Polymer Science*, 82(10), 2422-2433.

Tehrany, E.A. and S. Desobry. 2004. Partition coefficients in food/packaging systems: a review. *Food Additives and Contaminants*, 21, 1186-1202.

Van Krevelen, D.W. 1990. Cohesive properties and solubility. Properties of polymer,the correlation with chemical structure; their numerical estimation and prediction from additive group contributions, *3rd edition*, Elsevier (Amsterdam), 189-225.

Vergnaud, J.M. 1995/6. General survey on the mass transfers taking place between a polymer and a liquid. *Journal of Polymer Engineering*, 15(1-2), 57-77.

Vergnaud, J.M. 1991. Liquid transport processes in polymeric materials: modeling and industrial applications. *Polymer science and engineering series*. James E. Mark, series editor, USA, 362p.

Vitrac, O. and J.-C. Leblanc. 2005. Exposure of consumers to plastic packaging materials: assessment of the contribution of styrene from yoghurt pots. *Accepted in Food and Additives Contaminants*.

Vitrac, O. and M. Hayert. 2005a. Risk assessment of migration from packaging materials into foodstuffs. *AIChE Journal*, 51(4), 1080-1095.

Vitrac, O.; Lézervant, J. and A. Feigenbaum. 2005b, Decision trees applied to the robust estimation of diffusion coefficients in polyolefins. *Accepted in Journal of Applied Polymer Science, in press.*

Vitrac, O.; Challe, B.; Leblanc, J.-C. and A. Feigenbaum. 2005c. Risk of contamination of packed foods by substances from plastic contact layer: a generic quantitative methodology at the scale of private households. *Accepted in Food and Additives Contaminants*.

Vitrac, O.; Mougharbel, A. and A. Feigenbaum. 2006. Interfacial mass transport properties which control the migration of packaging constituents into foodstuffs. *Journal of Food engineering*, in press.

FOOD PACKAGING OPTIMIZATION BY MEANS OF INTEGRATED CAD/CAE AND STATISTICAL TECHNIQUES

Mario Antonio Francese and Domenico Livio Francese
DEVELPACK srl – Packaging Development
89053 Catona, Reggio Calabria,
Italy
E-mail: mfrancese@develpack.it

KEYWORDS
Computer Aided Design (CAD), Computer Aided Engineering (CAE), Optimization.

ABSTRACT

Packaging innovation, finalized to configure food in terms of product/service, is crucial in satisfying consumers' needs: pleasure, practicalness, health.
Furthermore, also in such sector, time reduction between the R&D activity and the industrial exploitation of the results becomes more and more strategically important.
In such scenery, "Steam Pack", an innovative disposable pack, has been developed for pressure cooking of food in microwave ovens.
The development in short times of "Steam Pack", winner of the Oscar dell'Imballaggio 2005 ("Technology" section) and of a World Star Packaging Award 2005, was possible thanks to integrated CAD/CAE and statistical techniques.
The study has been carried out according to a DOE of FEM analyses aimed to optimize the geometry of the membrane spring, the geometry of the steam vent and the thickness of the bowl walls.
The use of integrated CAD/CAE and statistical techniques made possible the simultaneous handling of several parameters, enabling optimization in short times. This allowed to realize prototypes and start the testing stage after just two weeks from the beginning of the design activity.

DEVELOPMENT OF "STEAM PACK", A DISPOSABLE PACKAGE FOR MICROWAVE COOKING

Steam Pack is realized in polypropylene and consists of two parts (Figure 1) :
• an oval-shaped bowl subdivided into two concentric compartments, to keep food components separated until use;
• a valve, which characterizes the pack and acts also as a plug for the central compartment. By means of such valve, through a cyclic "open/close" process, the outflow of the steam generated during the cooking process is optimized, with a remarkable reduction in preparation times.

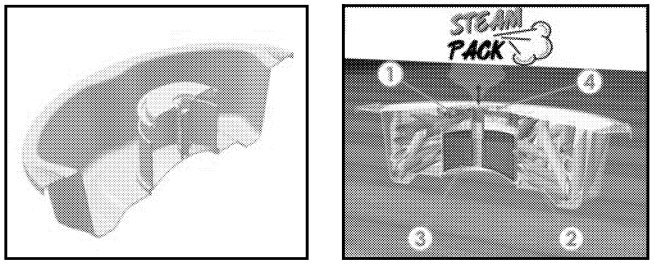

Figure 1: sectional view of the bowl (blue) of the valve (green) and the finished package

The bottom of the central chamber features a spring membrane (3), which lifts the valve (1) when such valve desengages from the dispenser (2) due to the build up of steam generated during cooking. The valve performs open and close cycles dragged by the thermowelded film (4) inflating and deflating thanks to the steam. Such device represents the key element for the correct performance of the pack.
The development of Steam Pack called for optimization in terms of costs, functionality, practicality of use and handling.
As the product needs to be industrialized, further limitation derive from the production process, logistics, and needs resulting from the packaging of the final product.
The entire optimization process can be simplified in the following steps:
• brainstorming, to evaluate all factors contributing to obtain satisfying results for all requirements
• factor screening to individuate the most influential factors for each individual requirement. Regarding this last issue we referred to a DOE performed using reduced factorial plans and trough the analysis of the related Pareto diagrams and ANOVA tables
• full factorial plans and response surface method performed on the most influential factors for each requirement with the aim of researching optimal values for each factor (goal driven optimization)
Following is a report on the most critical aspects, with regards to the optimization of the spring-valve, the exit hole diameter and thickness of the bowl wall.

Optimization of the spring-membrane

Following the factor screening performed on the membrane operation, the three most influential factors have been pin pointed as being: radius, height, thickness. (Figure 2)

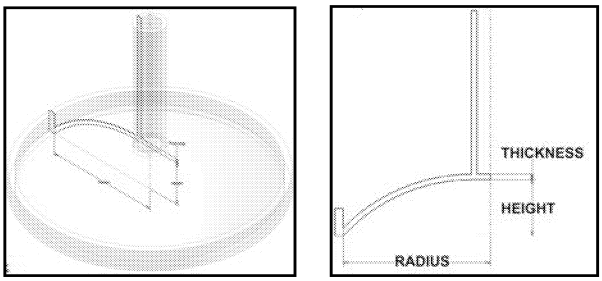

Figure 2: parameters influencing the geometry of the spring membrane (radius, height, thickness)

We analysed, in particular, the influence of the three parameters on the value of the third buckling mode, needed to deform the membrane during packaging. The first and second buckling mode have been overlooked as they are considered not influential during product packaging.
The referred load environment and the three buckling modes are shown in Figure 3.

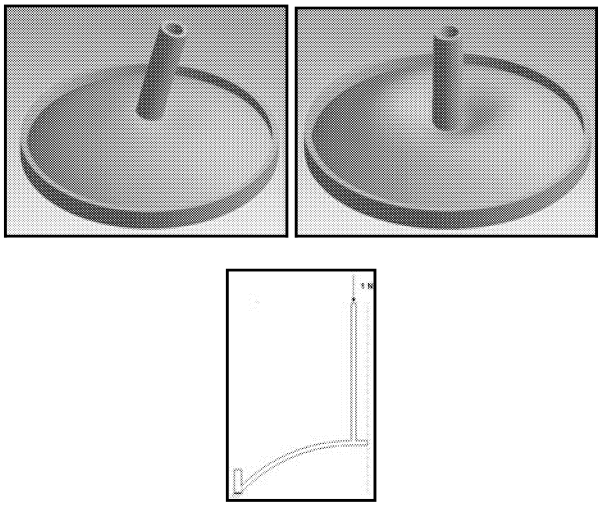

Figure 3:1°-2° buckling mode, 3° buckling mode, load environment

With the benefit of previous experience in designing and adopting the principles of hybrid modelling, the target was set for the 3rd buckling mode, for the goal driven optimization, with relation to the value of the buckling mode multiplier for a previously created product . During analysis we considered the non-conservative buckling nature.

Design of experiment and results
The parameters manager of Ansys Workbench Simulation 9.0 and the integration betweeen Ansys Workbench and the modelling software used (Autodesk Inventor Series 10) allowed for the rapid implementation of a full factorial plan 33 (Table 1), performed during advanced optimization of the three influential parameters for the 3rd buckling mode identified during factor screening (radius, height and thickness).

Table1: Parameters and levels for full factorial

Parameter	Low Value	Center Value	High Value
Radius (mm)	25	27.5	30
Height (mm)	5	7.5	10
Thickness (mm)	0.4	0.6	0.8

Following is the response surface for the 3rd buckling mode with relation to height and thickness (Figure 4).

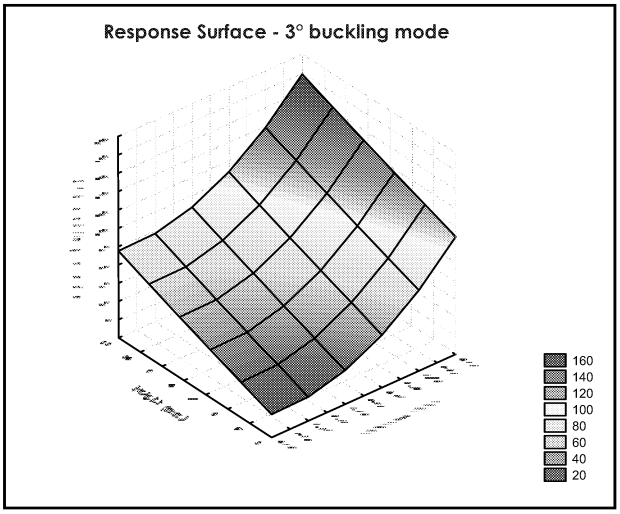

Figure 4: response surface of 3rd buckling mode in function of height and thickness of the full factorial DOE

Assigning a value of 60, resulting from the buckling analysis performed with Ansys Workbench Simulation 9.0 on a existing membrane with similar features to the desired ones, to the 3rd buckling mode load multiplier ,as the target of optimization , and imposing as desirable conditions of the 3 examined factors, values resulting from considerations of economic and functional nature, we managed to determine a set of optimal values of the three factors (radius = 28.5 mm, thickness = 0.56 mm, height = 8.4 mm).

Optimization of the exit hole diameter

Determining the optimal diameter of the exit hole is very important as it determines the level of the pack internal pressure, directly influencing the final results in terms of preservation of the nutritious substances and cooking time. In addition it's important to determine the existing relation between the diameter and the generated internal pressure, to be able to choose the best diameter for each food product.
A stationary fluidodynamic analysis has been arranged, which boundary conditions are shown in picture 5.
In order to reduce the computational effort, the pack symmetric properties have been exploited.

Boundary Conditions
Fluid: Water Vapour at 100°C
Inlet: Mass Flow Rate = 0.303 gr/sec
Outlet: Relative Pressure = 0 mbar

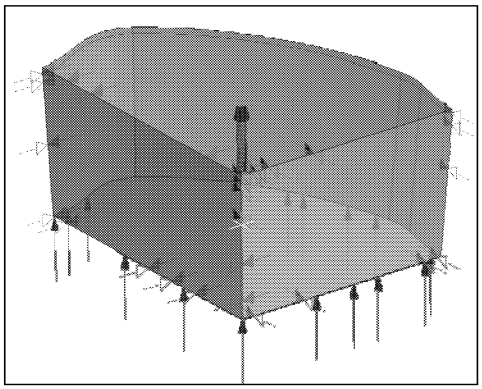

Figure 5: boundary conditions for fluidodynamic analysis

The values of the boundary conditions parameters result from simple thermodynamic evaluations, together with the results of a cooking test in a microwave oven performed using a simplified prototype of the packaging.
Using a parametric CAD file, having as a sole parameter the diameter of the steam exit hole, various fluidodynamic analysis have been performed for different values of the diameter. Finally, the flow of the average pressure in relation to the diameter was outlined. (Fig. 6)

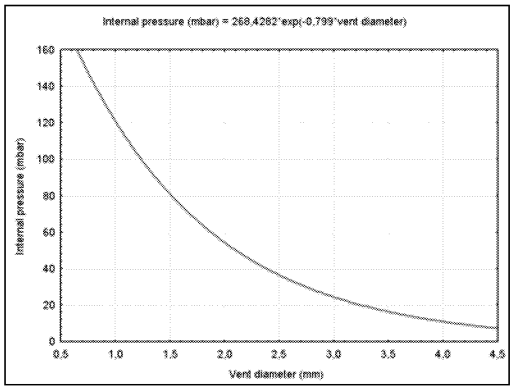

Figure 6: diameter-pressure chart obtained through fluidodynamics simulations

Optimization of the wall thickness

Once the pack internal pressure had been established, the optimal thickness of the pack walls was determined. Determination of minimum wall thickness of the oven bowl is fundamental to make the pack as light as possible (improving cost cut and recyclability), compatibly with needs of production by means of injection molding and the admissible deformations during cooking (positive internal pack pressure) and in a cooling off phase (negative internal pack pressure), for a correct operation.
To evaluate deformation we used Ansys/Workbench Simulation 9.0, using the parameters manager to vary the only used parameter: the wall thickness.
To evaluate compatibility of the wall thickness with the production process, we used a program simulating the injection molding process, considering different thickness of the pack.
Analysing results from the different analysis performed , we determined the desired thickness.

In Figure 7 the load environment considered through the study of deformation with Ansys Workbench Simulation 9.0 and the the results for fill analysis for injection molding process.

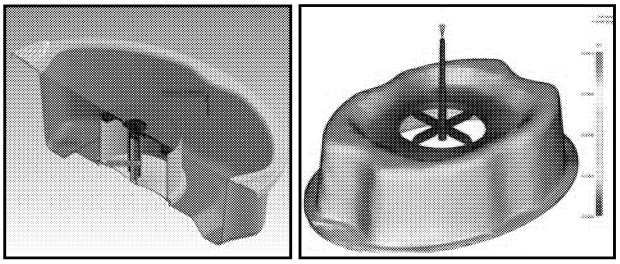

Figure 7 : load environment of simulations with Ansys Workbench 9.0 and CAD model for injection molding process simulation

The optimal wall thickness resulted in 0.8 mm.

FURTHER FEM APPLICATIONS FOR STEAM PACK

FEM analysis have also been performed, to determine the strength needed to keep the film and the dish together during operation in order to individuate an optimal film and to determine the optimal geometry of the snap fits keeping all the pack components together. (Fig. 8)

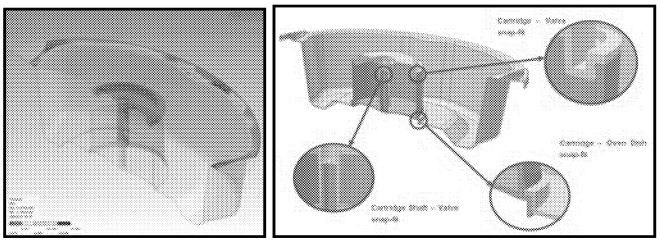

Figure 8 : contact pressure analysis between the film and the bowl (on the right) and the snap fits optimized through FEM analysis

REFERENCES

Douglas C. Montgomery 1996. “Introduction to statistical quality control.” *John Wiley & Sons Inc.*

AUTHOR BIOGRAPHY

MARIO ANTONIO FRANCESE is a project engineer at Develpack srl, Reggio Calabria, Italy. Develpack, the most innovative young company in Italy, focuses on “hi-tech food packaging research”. He joined Develpack in 2005 and together with the whole work team has promoted the use of numerical simulation tools and integrated CAD/CAE technologies in the field of food packaging. He graduated in 2003 at Politecnico di Bari, Bari – Italy ,in mechanical engineering and has worked as a researcher in plastics engineering and rapid prototyping for ISRIM, Terni – Italy.
e-mail: mfrancese@velpack.it, mario.francese@libero.it.

GENERAL QUALITY AND RED DISCOLORATION OF MODIFIED ATMOSPHERE PACKAGED, FRESH-CUT ENDIVE AS AFFECTED BY TEMPERATURE AND OXYGEN FRACTION

Hajo Rijgersberg
Agrotechnology & Food Sciences Group
Wageningen University and Research Centre
P.O. Box 17, NL-6700 AA, Wageningen
The Netherlands
E-mail: hajo.rijgersberg@wur.nl

Jan L. Top
Vrije Universiteit Amsterdam
Faculty of Sciences, Computer Science
De Boelelaan 1081A, NL-1081 HV, Amsterdam
The Netherlands

KEYWORDS
Fresh-cut endive, Quality, Modified atmosphere packaging, Simulation model, Flow-through system.

ABSTRACT

The dependency of modified atmosphere (MA) packaged, fresh-cut endive on storage conditions was investigated. For this purpose the product was stored at different temperatures, oxygen fractions and carbon dioxide fractions. The general quality and red discoloration were observed. Two composite Arrhenius models, incorporating the effects of both temperature and oxygen fraction on the rates of general quality change and red discoloration of the product were successfully evaluated. The chosen model integrates the temperature and oxygen effects and gives a reasonable idea of the empirical relations underlying the development of quality aspects of MA-packed, fresh-cut endive.

INTRODUCTION

Fresh-cut vegetables and fruit are packed in modified atmosphere packages (MAPs), mainly to prevent dehydration of a product that is already damaged (Jongen, 2003). Additionally, altered gas conditions develop in the packaging as a result of respiration processes of the product and a specific selectivity of the packaging film. These altered gas conditions on turn affect (i.e., slow down) these same respiration processes (Peppelenbos 1996). Respiration is identified as one of the most important processes in the senescence of vegetables and fruit (Peppelenbos 1996). However, what the relations exactly are is difficult to say and can be different per product, cultivar, batch, growing conditions, season, climate, origin, etc.
In this paper we model the dependence of the behavior of MA-packaged, fresh-cut endive on (distribution) chain conditions. How do the quality variables depend on the combination of temperatures and gas fractions? What proportions do the effects of anaerobic conditions and high temperatures on the product bear to one another? In order to answer these questions we have examined the effect of a matrix of temperatures and oxygen and carbon dioxide fractions on the product quality variables. The hypothesis that we will test in this paper is that the dependency of the rate constants of the quality variables on temperature and gas components can be characterized using composite Arrhenius relationships for the effects of temperature and oxygen fraction.

MODEL DEVELOPMENT

MA-Packed, Fresh-Cut Endive Quality Variables: General Quality And Red Discoloration

The quality of MA-packed, fresh-cut endive is considered to decompose in (i) general quality Q and (ii) red discoloration R. General quality generalizes the properties “freshness”, “voluminousness”, “crispiness”, “vivid greenness of the green parts” and “bright whiteness of the white parts (in contrast to brown parts)” of the product. These are properties that are generally kept under control by a low oxygen fraction, but not zero, because of the *risk* of growth of unwanted microbes (pathogens) or the occurrence of fermentation of the product. Red discoloration, on the other hand, is prevented most under anaerobic circumstances. Other aspects, such as general microbial activity, are recognized to be important in a later stage of product life, and are not considered further in this work.
It is generally known that both high oxygen levels and low oxygen levels can affect the general quality of MA-packed fruits and vegetables. As these two effects cannot take place at the same time, and the general quality is a very general variable decomposing in a range of subvariables, we have formulated this as an addition:

$$Q(t) = Q_{\mathrm{O}_2,\mathrm{low}}(t) + Q_{\mathrm{O}_2,\mathrm{high}}(t) \qquad (1)$$

However, as we will see in the observations (Section 4.1), effects due to high oxygen levels were not observed. As a consequence, Q and $Q_{\mathrm{O}_2,\mathrm{low}}$ “merge” to one and the same variable:

$$Q(t) = Q_{\mathrm{O}_2,\mathrm{low}}(t) \qquad (2)$$

Primary Models: Logistic General Quality And Red Discoloration Models

Quality variables of vegetables and fruit can be described using logistic models (Tijskens 2004; Eccher Zerbini *et al.* 2006). Accordingly, we propose to describe general quality change $\mathrm{d}Q/\mathrm{d}t$ and red discoloration change $\mathrm{d}R/\mathrm{d}t$ as

dependent on rates k_Q and k_R, general quality Q, red discoloration R, maximum general quality Q_{max}, and maximum red discoloration R_{max}, as:

$$\frac{dQ}{dt} = k_Q Q(1 - \frac{Q}{Q_{max}}) \quad (3)$$

$$\frac{dR}{dt} = k_R R(1 - \frac{R}{R_{max}}) \quad (4)$$

Secondary Models: Composite Arrhenius Relationships

The temperature dependency of the rate constants in Eqs. 3 and 4 is usually described using Arrhenius' law. The activation energy E_a can be seen as the amount of energy required for a reaction to proceed. The thought behind Arrhenius' law is that chemical reactions "need energy to "prepare" their reagents for reaction" (Nobel 1983; Tijskens *et al.* 1996). Yet, Arrhenius' law does not take other parameters, such as the oxygen fraction, into account. Here, we propose composite Arrhenius relationships, incorporating the effects of temperature and other parameters, in our case, the oxygen fraction:

$$k_Q = k_{ref} e^{\frac{E_a^T}{R}(\frac{1}{T_{ref}} - \frac{1}{T})} e^{\alpha(x_{O_2,Q}^{ref} - x_{O_2})} \quad (5)$$

$$k_R = k_{ref} e^{\frac{E_a^T}{R}(\frac{1}{T_{ref}} - \frac{1}{T})} e^{\beta(x_{O_2} - x_{O_2,R}^{ref})} \quad (6)$$

Anaerobic oxygen levels are known to have a great effect on the general quality of the product, in general. This is formulated in Eq. 5. The effects of high oxygen levels on general quality are, as discussed earlier, excluded in the model. Low oxygen levels are known to inhibit red discoloration of fresh-cut endive, which is formulated in Eq. 6. R is the universal gas constant (8.314 J/mol K), T_{ref} is the Arrhenius referential temperature, and $x_{O_2,Q}^{ref}$ and $x_{O_2,R}^{ref}$ are referential oxygen fractions. α and β are fit parameters. This kind of composite Arrhenius approach is seen before in the fields of microbiology (Geeraerd *et al.* 1998), paper chemistry (Vance Best 1968) and applied physics (Mizuishi *et al.* 1979). By means of this approach the effects of temperature and oxygen fraction are incorporated in comprehensible models. The effects of the different conditions have become comparable, and therefore their *relation* has become better interpretable and debatable. Questions like "which factor has more influence: temperature or oxygen fraction?" can be answered now, by comparing the temperature and oxygen fraction terms in the equations. This may lead to a deeper understanding of the sensitivity of the product to the different conditions in the end.

MATERIALS AND METHODS

MA-Packaged, Fresh-Cut Endive

The product that was observed was endive, cv. Natacha, origin Spain. After harvest, the endive was transported to The Netherlands, where it was washed, dried (spin-drying and warm air) and packaged in bags of 0.4 kg, using an OPP film. For a short period, the product was stored at 2-4 °C and next transported, under cooling conditions. The experiments were prepared at 11 °C and subsequently carried out.

General Quality Scale

Six classes of general quality were distinguished, from 0 ("excellent") to 5 ("very bad") representing states of freshness, voluminousness, crispiness, bright-greenness, and bright-whiteness as indicated in Table 1. These sub-variables were considered to be taken together. Product of class 2 general quality was considered still acceptable to sell; class 3 general quality endive was considered not acceptable anymore. The measurements took place in a destructive way, by emptying the bags and spreading out the endive parts, in order to obtain a good overview and, as a consequence, adequate judgment. The judgments were done by trained product experts.
The general quality measurement scale was considered to be an interval scale.

Red Discoloration Scale

Five classes of red discoloration were distinguished, from 0 ("all parts bright white") to 4 ("all parts red") as defined in Table 2. Class 1 red discolored product was considered still acceptable, class 2 not anymore. The measurements took place together with the general quality measurements, which were destructive). The judgments were carried out by the same trained product experts.

Table 1. General Quality Scale Classes

Class	Name	Freshness	Voluminousness	Crispiness	Bright-greenness	Bright-whiteness
0	excellent	fresh	voluminous	crispy	bright-green parts	bright white parts
1	-	fresh	voluminous	crispy	some green parts are dark-green	bright white parts
2	-	fairly fresh	fairly voluminous	fairly crispy	some green parts are dark-green	bright white parts
3	-	not fresh	not voluminous	slack	many green parts are dark-green	some white parts are brown
4	-	not fresh	not voluminous	slack	most green parts are dark-green	many white parts are brown
5	very bad	not fresh	not voluminous	slack	most green parts are dark-green	most white parts are brown

The red discoloration scale was assumed to be an interval scale.

Table 2. Red Discoloration Scale Classes

Class	Description
0	bright white parts
1	some white parts are red/brown
2	fairly many white parts are red/brown
3	many white parts are red/brown
4	nearly all white parts are red/brown

Experimental Design

The product was observed for a maximum of 17 days. Combinations of different temperatures (4 °C, 7 °C, 11 °C and 20 °C) and oxygen fractions (0 mol/mol, 0.005 mol/mol, 0.025 mol/mol and 0.07 mol/mol) were imposed. The packages of endive were opened up and placed in the containers of our flow-through system. The product was left in the package film, yet the experimented (gas) conditions were imposed inside the package. Assessments of general quality and red discoloration were made at the beginning of the experiment ($t = 0$), and after 4, 7, 10, 14 and 17 days. The number of replicates was four.

Repeated extreme values at the end of the logistic curves were excluded, as they are considered to weigh too much in the fit. Moreover, these measurements have to be handled with special care as they violate the fitting assumption that all variances are normally distributed.

The flow-through system was developed at Wageningen UR and has often been employed to experiment product in different imposed gas compositions. The system consists of a number of small containers. In each of these containers, different gas conditions can be imposed. The temperature and the relative humidity (100% in our experiments) can be set in every storage cell that contains the containers.

Statistical analyses

Matlab® was used for all model fits and statistical analyses. The ODE23 solver routine was used to solve the ordinary differential equations. The *lsqcurvefit* routine was used to fit the models to the measured data.

RESULTS

General Quality Measurements

The general quality of the fresh-cut endive depended strongly on temperature and oxygen levels (Fig. 1). The measured data fitted well to the proposed logistic model with composite Arrhenius relationship (Table 3).

The measurements were carried out at two carbon dioxide levels: 0.1 and 0.2 mol/mol. However, no significant differences were observed between these measurements.

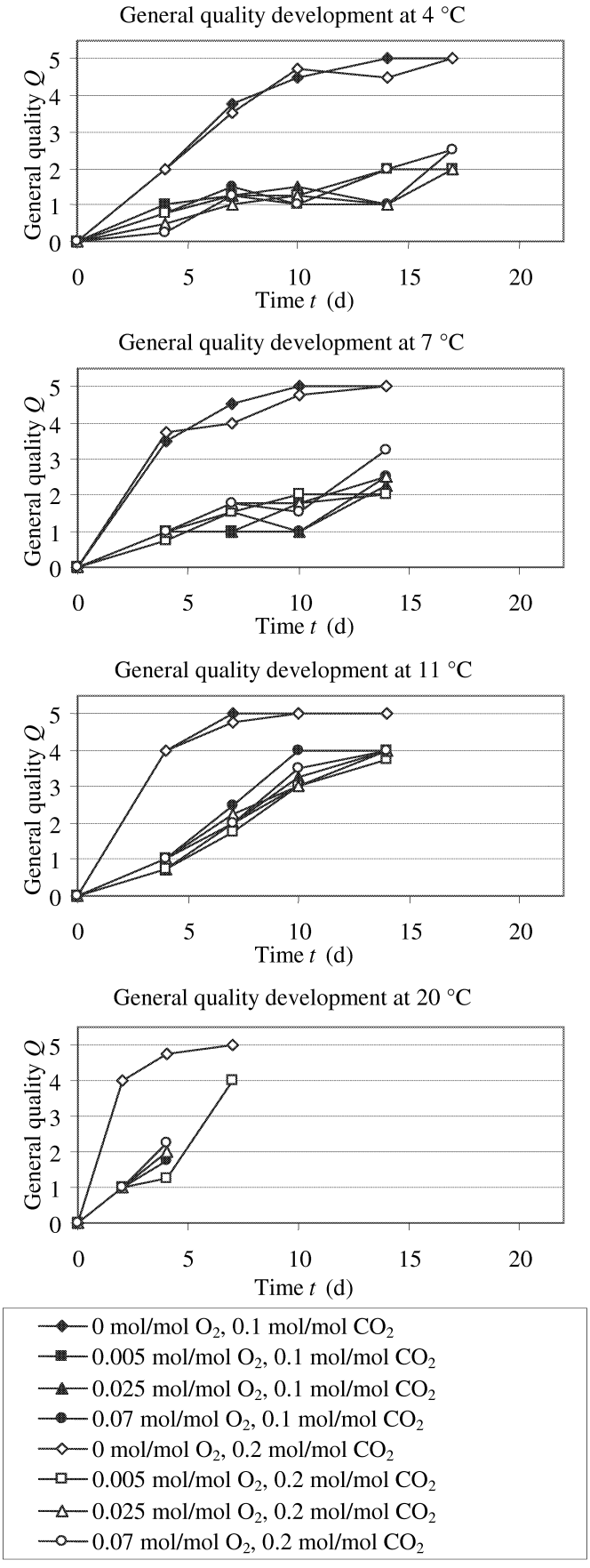

Figure 1: General Quality at Different Temperatures (4, 7, 11 and 20 °C) and Oxygen Levels (0, 0.005, 0.025 and 0.07 mol/mol) During Time

Table 3. Fitting Results ($T_{ref} = 284.15$ K and $x^{ref}_{O_2,Q} = 0.005$ mol/mol)

Quantity	Fitted value	Standard error
$Q_{t=0}$ ([0,5])	0.42	0.11
k_{ref} ([0,5]/s)	3.7×10^{-6}	0.41×10^{-6}
E_a (J/mol)	5.5×10^{4}	0.62×10^{4}
α (1)	9.6	2.2

Red Discoloration Measurements

The red discoloration of the fresh-cut endive depended strongly on temperature and oxygen levels (Fig. 2). The measured data fitted well to the proposed logistic model with composite Arrhenius relationship (Table 4).

Table 4. Fitting Results ($T_{ref} = 284.15$ K and $x^{ref}_{O_2,R} = 0$ mol/mol)

Quantity	Fitted value	Standard error
$R_{t=0}$ ([0,4])	0.42	0.09
k_{ref} ([0,4]/s)	2.4×10^{-6}	0.33×10^{-6}
E_a (J/mol)	3.0×10^{4}	0.61×10^{4}
β (1)	11.2	1.7

The measurements were carried out at two carbon dioxide levels: 0.1 and 0.2 mol/mol. However, no significant differences were observed between these measurements.

DISCUSSION

From the standard errors in Tables 3 and 4 it can be concluded that general quality and red discoloration of MA-packed fresh-cut endive were well described by the proposed models, logistic models including composite Arrhenius relationships. However, it remains important to see this in the light of the following issues.

As can be seen in Figures 1 and 2, the measurements were sometimes broken up too early. The quality variables of most samples did not reach their maximum values.

The standard errors of the initial general quality and initial red discoloration are relatively large, as compared to the other fit parameters. We expect this to be due to the natural variance of these parameters across batches.

The grid of oxygen fractions was quite coarse and the interval was quite narrow (the highest oxygen fraction was 0.07 mol/mol). Because of the fact that the "anaerobic zone" appeared to be so narrow, we recommend the inclusion of an oxygen fraction between 0 and 0.005 mol/mol, e.g. 0.0025 mol/mol, and at least one higher fraction, e.g. 0.2 mol/mol, in future experiments. A similar issue applies to the imposed carbon dioxide levels.

The oxygen effects could not be divided in effects due to low oxygen levels and effects due to high oxygen levels, as the latter effects could not be observed in the experiments. As a consequence, the low level oxygen effects may be overestimated, as, likely, there will be an "overlap" between the two effects on the general quality variable.

A disadvantage of the logistic primary models is that they lack a mechanistic ground. There is no clue in terms of the

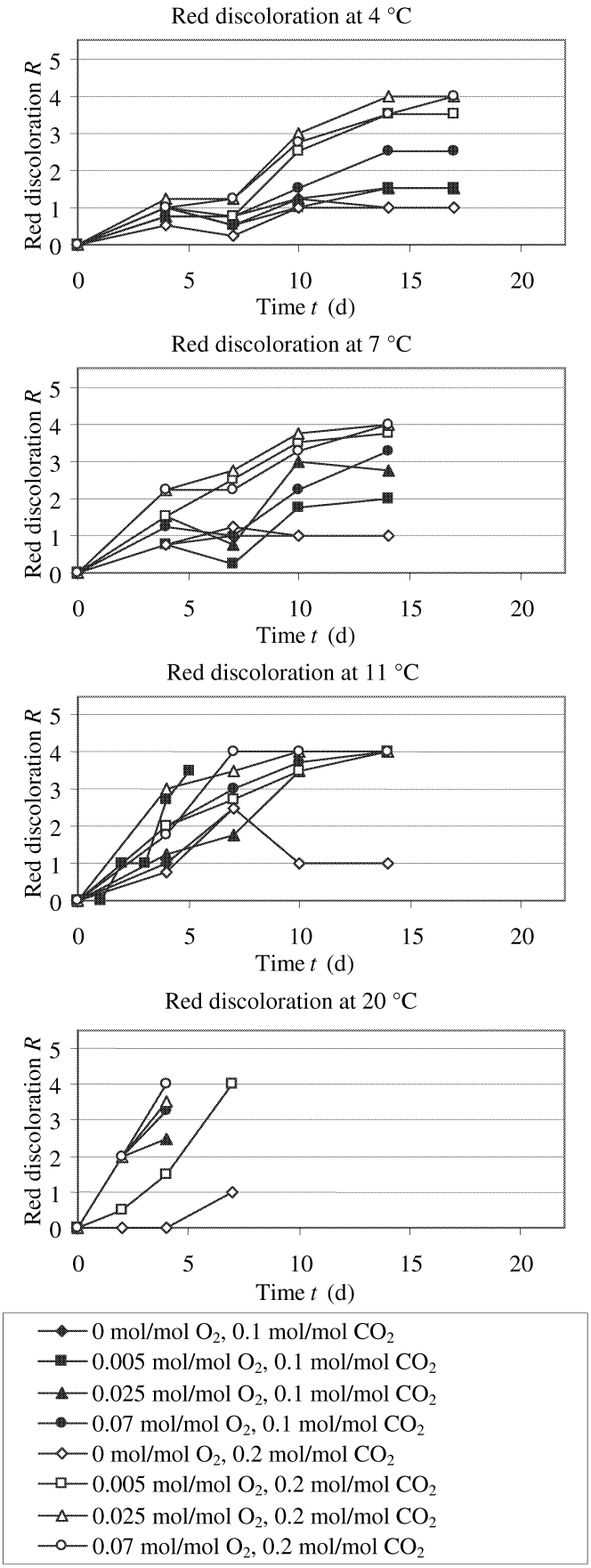

Figure 2: Red Discoloration at Different Temperatures (4, 7, 11 and 20 °C) and Oxygen Levels (0, 0.005, 0.025 and 0.07 mol/mol) During Time

underlying kinetics why quality attribute rates should be dependent on their maximum values.
Also the composite Arrhenius relationships currently still lack physiological ground. However, as a first step in acquiring new knowledge, we argue that one could look for direct relationships between independent and dependent variables that are at least "statistically" meaningful (which is what we have done in this work).

CONCLUSIONS

The dependency of modified atmosphere packaged, fresh-cut endive on storage conditions was investigated. For this purpose the product was stored at different temperatures (4, 7, 11 and 20 °C), oxygen fractions (0, 0.5, 2.5, 7 mol/mol) and carbon dioxide fractions (0.1 and 0.2 mol/mol). The general quality and red discoloration were observed. Two composite Arrhenius models, incorporating the effects of temperature and oxygen fraction on the rates of the general quality and red discoloration of the product were successfully fitted. The chosen model integrates the temperature and oxygen effects and gives a reasonable idea of the empirical relations underlying the development of quality aspects of MA-packed, fresh-cut endive.
When calibrated, the model can be used to optimize package and transport conditions to specific demands. Computer simulations can be carried out to evaluate the effect of temperature peaks in the (distribution) chain on the quality variables of the product. In co-operation with a MAP model, the effects of temperature on product quality and the oxygen fraction in the package (which, in turn also affects product quality) can be evaluated.
In the future we would like to fit this model to data where both low oxygen level effects and high oxygen level effects were observed in a quality variable.

ACKNOWLEDGEMENTS

This work was carried out in the context of the project "Reststroomreductie in de gesneden-groenteketen", 2003-2005, funded by Agro Keten Kennis (AKK), The Netherlands. The project was financially supported by SenterNovem and the Stichting Agro Keten Kennis. We gratefully acknowledge M. Sanders and R. Vernède for their valuable comments.

REFERENCES

Eccher Zerbini, P.; M. Vanoli; M. Grassi; A. Rizzolo; M. Fibiani; R. Cubeddu; A. Pifferi; L. Spinelli; and A. Torricelli. 2006. "A model for the softening of nectarines based on sorting fruit at harvest by time-resolved refelectance spectroscopy". Postharvest Biology and Technology 39.

Geeraerd, A.H.; C.H. Herremans; L.R. Ludikhuyze; M.E. Hendrickx; J.F. van Impe. 1998. "Modeling the kinetics of isobaric-isothermal inactivation of Bacillus subtilis α-amylase with artificial neural networks". Journal of Food Engineering 36.

Jongen, W. (Ed.). 2003. "Fruit and Vegetable Processing: Improving Quality". CRC Press, Boca Raton, Boston, New York, Washington DC and Woodhead Publishing Limited, Cambridge, England.

Mizuishi, K.; N. Chinone; H. Sato; and R. Ito. 1979. "Acceleration of the gradual degradation in (GaAl)As double-heterostructure lasers as an exponent of the value of the driving current". Journal of Applied Physics 50(11).

Nobel, P.S. 1983. "Biophysical plant physiology and ecology". Freeman, San Francisco.

Peppelenbos, H.W. 1996. "The Use of Gas Exchange Characteristics to Optimize CA Storage and MA packaging of Fruits and Vegetables". Ph.D. thesis, Agricultural University of Wageningen, The Netherlands.

Tijskens, L.M.M. 2004. "Discovering the future: modelling quality matters". Ph.D. thesis, Agricultural University of Wageningen, The Netherlands.

Tijskens, L.M.M.; M. Sloof; E.C. Wilkinson; W.G. van Doorn. 1996. "A model of the effects of temperature and time on the acceptability of potted plants stored in darkness". Postharvest Biology and Technology 8.

Vance Best, E. 1968. "Kinetics of Hot Alkaline Cleavage of the Glycosidic Bonds of Methyl β-D-Glucoside and Methyl β-Cellobioside". Ph.D. thesis, Lawrence University, Appleton, Wisconsin.

SPRAY DRYING SIMULATION

MODELLING AGGLOMERATION IN SPRAY DRYERS

Maykel Verschueren
Ruud Verdurmen*
Han Straatsma
Michiel Gunsing
NIZO food research
PO Box 20, 6710 BA Ede
The Netherlands
maykel.verschueren@nizo.nl
*current affiliation: Numico Research
PO Box 7005, 6700 CA Wageningen
The Netherlands

Ruud van Ommen
John Nijenhuis
Delft University of Technology
Product & Process Engineering,
DelftChemTech
Julianalaan 136, 2628 BL Delft
The Netherlands
J.R.vanOmmen@tudelft.nl

Ton Backx
IPCOS Technology Netherlands
Bosscheweg 145a
5282 WV, Boxtel
The Netherlands
ton.backx@ipcos.com

INTRODUCTION

Spray drying is an essential unit operation for the manufacture of many products with specific powder properties. It is characterized by atomization of a solution or suspension into droplets, followed by subsequent drying of these droplets by evaporation of water or other solvents. Spray drying is used for the manufacture of many consumer and industrial products such as instant food products, laundry detergents, pharmaceuticals, ceramics and agrochemicals. The best known example of an instant food product is milk powder. Consumers desire a quick dissolution or dispersion of such powders in water or milk without the formation of lumps. But also manufacturers have their wishes. They require free flowing powders and absence of dust in such a way that it facilitates the handling of the powders. Both requirements are met by applying agglomeration of food powders (Hansen, 1980; Retsina, 1988; Pietsch, 1999).

Agglomeration is a size enlargement process of powders, where small particles combine to form large relatively permanent masses, in which the original particles are still identifiable, see also figure 1. In this way the characteristics of a single particle are maintained while the bulk powder properties are improved by the creation of the larger agglomerates.

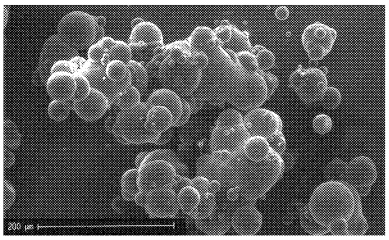

Figure 1: SEM-photograph of spray dried and agglomerated powder (from Verdurmen et al., 2004)

In a spray dryer agglomeration can take place within the spray of an atomizer, between sprays of various atomizers and between sprays and dry material being introduced into the drying chamber (e.g. by fines return, see figure 2). The latter technique is often the most effective way to achieve and control agglomeration in spray dryers.

Agglomeration takes place when two sticky particles, or a sticky and a dry particle, collide and form a liquid bridge that is strong enough to resist mechanical deformations, while the integrity of the particles is maintained. Various researchers have calculated the critical viscosity for sticking during contact times of a few seconds by applying various models. As a result the critical viscosity appears to be in the range of 10^6 – 10^8 Pa·s. This value has been confirmed experimentally by various investigators (Wallack and King, 1988; Downton et al., 1982; Aguilera et al., 1995; Bhandari and Howes, 1999). At lower viscosities the particles will coalesce upon collision, at higher viscosities the particles will not stick together (see also next chapter).

The critical viscosity occurs at a temperature that is called the sticky point temperature. Roos and Karel (1991) related the sticky point temperature to the glass transition temperature which is characteristic for each material. For skim milk solids for example, the stickiness and caking zone is positioned at about 10 °C or higher above the T_g measured by DSC (Hennings et al., 2000; Roos, 2002). Sticky points can further deviate from glass transition points, for instance because also the dynamics of colliding particles are also relevant. It would therefore be better to measure sticky points directly under dynamic conditions. However, the classical measurement techniques (Lazar, 1956) are not very accurate and show poor reproducibility when the examined powder is not free-flowing.

In this paper a new method to measure stickiness under dynamic conditions is presented. The method is based on a technique called attractor comparison, which was developed by Delft University. It can detect small hydrodynamic changes in fluid beds by analyzing high frequency pressure measurements by attractor comparison methods. For details concerning attractor comparison the reader is referred to Van Ommen et al. (2000). The method has been implemented in an industrial software package called DyMonT (Dynamics Monitoring Toolkit) and is successfully being used as an early warning system for agglomeration of sand particles in fluidised beds for biomass combustion and gasification. In this paper it is used to monitor the stickiness of food powder particles in a fluidized bed while changing the conditions of the inlet air (temperature and relative humidity). Since DyMonT is very sensitive to small changes in the hydrodynamics it is much

more suitable for monitoring stickiness than by conventional parameters such as the pressure drop over the bed or visual inspection. In this paper we present some results of stickiness measurements by attractor comparison. The results are compared to results obtained by conventional techniques, both statically and dynamically.

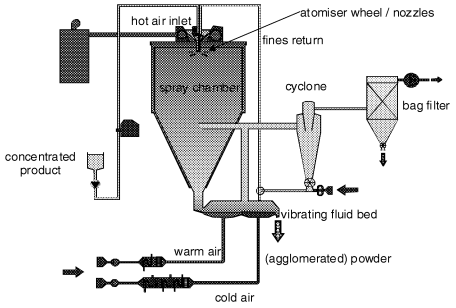

Figure 2: An industrial 2-stage spray dryer with fines return (source: Anhydro A/S, Denmark)

Agglomeration during spray drying is considered to be a difficult process to control. The main cause of this is the complex interaction of the process variables: the atomization process, the mixing of spray and hot air, the drying of suspension droplets and the collision of particles which might lead to coalescence or agglomeration. As a consequence, agglomeration during spray drying is operated by trial-and-error. In 2001 an EC-sponsored project started, coordinated by NIZO food research, entitled EDECAD (Efficient DEsign and Control of Agglomeration in spray Drying machines, www.edecad.com). The EDECAD project aimed at developing an industrially validated computer model, using computational fluid dynamics (CFD) technology, to predict agglomeration processes in spray drying machines. In this paper some CFD simulation and validation results are presented.

STICKINESS MEASUREMENTS

The sticky-point of a powder (i.e. the combination of temperature and relative humidity of the outer layer of the powder leading to sticky particles) can be measured using a stagnant layer of powder. This so-called "static sticky-point" is of relevance for storage of powders and to determine when build-up of a powder layer can occur at the chamber wall or cone of spray driers.

The static sticky-point is determined by filling an open container (d=85mm) with some powder (h=5 mm). This container is exposed to a constant temperature in a controlled air cabinet. The relative humidity of the circulating air will be step-wise increased (leaving at least 6 hours between such steps) until an visual change in powder structure is observed. This change in structure is regarded as the static sticky-point. By repeating this procedure at different temperatures, a static stickiness line can be constructed.

The dynamic sticky-point of a powder can be determined by fluidizing a powder in an experimental fluid bed (Bloore, 2004). This fluid bed is composed of a sintered distributor plate and a cylinder, see figure 3.

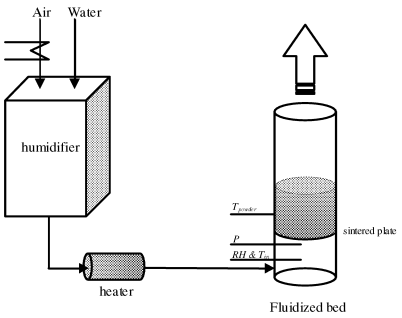

Figure 3: Schematic set-up of the test rig to determine the dynamic sticky-point.

The air that is fluidizing the powder can be heated up to 100 °C and the maximum air humidity is 50 g·kg^{-1}. Air pressure, temperature and relative humidity are measured below the sintered distribution plate. Also the powder temperature is measured. The pressure is measured every 5 seconds and the temperatures and relative humidity every 5 minutes. The amount of powder added is 500 grams. At a constant air flow (adjusted to achieve sufficient fluidization) and temperature, the relative humidity of the air is step-wise increase every 5 minutes until the fluidization characteristics are changed (visual observation). To determine the dynamic sticky-point, visual observations and measurements of air pressure and powder temperature are used. By repeating this procedure at different temperatures, a dynamic stickiness line can be constructed.

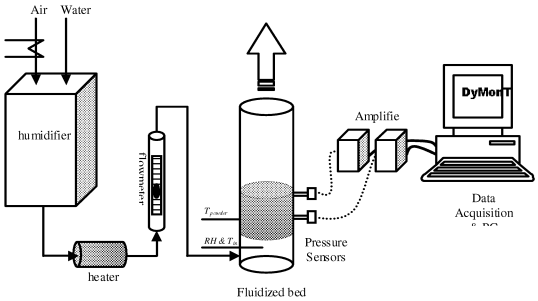

Figure 4: Schematic set-up of the test rig to determine the dynamic sticky-point using DyMonT

The experimental set-up for the dynamic sticky-point measurements by attractor comparison is schematically depicted in figure 4. The set-up consists of the set-up shown in figure 3 with two additional pressure probes each containing a high frequency pressure sensor. The sensors are connected to a data acquisition system which is used to analyse the pressure signals. As in the conventional stickiness experiments skim milk powder was used. The bed height used in the experiments is approximately 15 cm in non-fluidised state. The pressure probes are located at 5 and 10 cm from the sintered plate. An inletair flow of 133 l/min is used in the experiments, which corresponds to a superficial gas velocity of 0.125 m/s (5.5*u_{mf}). Experiments are carried out at inlet an inlet air temperature of 60ºC. The humidity of the inlet air is step-wise increased, using time

intervals of 1 to 2 hours to let the system equilibrate after each increase.

MODELLING SPRAY DRYING

Predictive computer models are helpful tools to maximize the production capacity of available installations, to minimize fouling of equipment and to reduce energy consumption. These models also reduce the number of costly and time-consuming production trials needed for the development of new products or processes. By Verdurmen et al. (2004) an overview has been given how different modelling approaches can be applied to spray drying equipment. Currently, CFD is regarded as on of the best approaches to simulate spray drying process in detail (Huang et al. 2003; Huang et al., 2004; Kievit, 1997; Oakley, 2004; Straatsma et al., 1999a; Verdurmen et al., 2004; Xia and Sun, 2002). The airflow field, the local temperature and the local humidity inside the spray dryer can be computed by using CFD techniques, taking into account the coupling for mass, momentum and energy.

The difference from standard (e.g. diesel sprays used in the automotive industry) spray calculations mainly concerns the drying part: stickiness primarily depends on the drying state of the outer layer of the particles. Additional sub-models for moisture diffusion inside the particles (Straatsma et al., 1999a) and for the relation between the drying state and stickiness (Roos, 2002) are therefore required to be able to compute the drying and fouling behavior of spray drying systems.

Some powder properties (e.g. insolubility) can be related to the moisture content and the temperature-time history of the particles (Straatsma et al., 1999b). For these properties the modelling techniques described above can be used. The majority of relevant powder quality properties, however, are related to the degree of agglomeration.

The aim of the EDECAD project has been to develop an industrially validated CFD model, a so called Design Tool, to predict agglomeration processes in spray drying machines. The project has focused on agglomeration that takes place at the upper part of the spray chamber, i.e. between sprays and between sprays and fines return. The modelling technique used is an extension of the Euler-Lagrange model for the drying and fouling behaviour of spray dryers described above.

The initial spray conditions were measured and the sub-models for drying, collision and agglomeration were developed and validated by the academic partners in the project (Blei, 2003; Blei and Sommerfeld, 2004a; Blei and Sommerfeld, 2004b; Menn, 2005; Nhumaio et al., 2004). For a detailed description of the CFD model and its sub-models and pilot-plant validation work carried out by the industrial partners we refer to Verdurmen et al. (2004).

RESULTS AND DISCUSSION

Stickiness measurements

The results of both the static and dynamic stickiness measurements for skim milk powder are presented in Figure 5 as a function of relative humidity of the air in the fluid bed. The glass transition temperature of skim milk solids as determined by DSC is also plotted in figure 5 and is taken from literature (Vuataz, 2002).

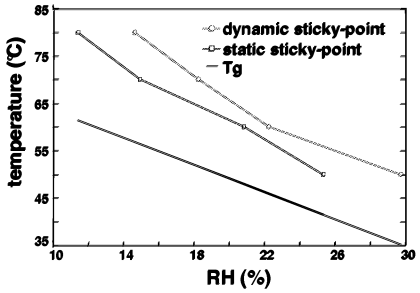

Figure 5: Results of the static and dynamic stickiness measurements of skim milk powder (blue and red lines respectively), as compared to the glass transition temperature (black line)

These results confirm earlier observations (Hennings et al., 2002; Roos and Karel, 1991; Roos, 2002) that the sticky point temperature and glass transition temperature are related, also when sticky points are measured under dynamic conditions. The average offset between the glass transition temperature and the static sticky-point is 13 °C, whereas the average off-set between the glass transition temperature and the dynamic static point is 18 °C. These observations are also in line with a recent study by Paterson *et al.* (2005), who found that for amorphous lactose, being the dominating carbohydrate in skim milk solids, a temperature exceeding the glass transition temperature by 25 °C or more leads to instantaneous stickiness, even under very short contact times, such as those experienced in industrial fluid bed dryers. The sticky-point curves obtained are used as input for the agglomeration sub-model of the Design Tool, as is described by Verdurmen *et al.* (2004).

Figures 6 to 8 show the results of the dynamic stickiness measurements by attractor comparison. Figure 6 is a plot of the inlet air temperature, the powder temperature and the relative humidity of the inlet air as measured during the experiments. The step-wise increase of the relative humidity can be clearly observed in figure 6.

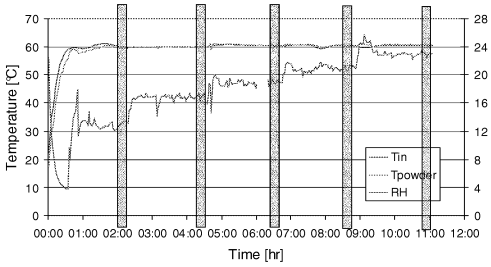

Figure 6: Inlet air temperature and humidity and the powder temperature during the experiment

Figure 7 shows the S-value for the two pressure sensors during the experiment, using the attractor at the end of the first increase in relative humidity as a reference (indicated by the first green bar in figures 6 and 7).

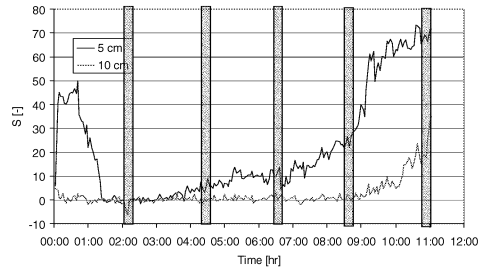

Figure 7: The S-value during the experiment

Figure 7 shows S as a function of the relative humidity of the inlet air. The S values shown in figure 7 are obtained at the end of each step-wise increase in relative humidity (indicated by the green bars in figure 5), using the attractor at RH = 12% as a reference.

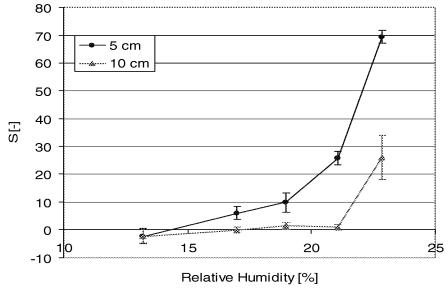

Figure 8: S-value as a function of the relative humidity of the inlet air (evaluation periods used are indicated by the green bars in figures 6 and 7)

Both curves in figure 8 show a steep increase at a relative humidity of approximately 22%, which corresponds well to the dynamic sticky-point measured by the conventional approach at 60°C (see figure 5). There is a clear difference between the two curves, however. The sensor located at 10 cm does not show a significant change in S (<3) until RH=22%, whereas the sensor at 5 cm already shows a significant change at RH=17%. Since skim milk powder is a polydisperse system, this might be due to stratification effects in the fluidised bed. An early change in S before the conventional dynamic sticky point is reached, as observed by the sensor at 5 cm, is not unlikely, however. Glass transition at 60°C occurs at RH=12% (see figure 5). Therefore, for RH>12% there will be a change in the physical state of the outer layer of the powder particles, which causing a change in the collision behaviour. This small change in hydrodynamics can results in changes in S, even though no change can be observed visually or in pressure drop over the bed.

Modelling spray drying

Figure 9 shows a typical simulation result for the particle trajectories in the pilot plant dryer which was also used for the validation trials. The size of the particles shown in figure 9 is a measure for the particle diameter. The results clearly show that the smaller particles (fines) leave the dryer through the air outlet, whereas the majority of the larger particles leave the dryer through the bottom of the dryer. The results also show large recirculation pattern in the dryer, which is not unusual especially for relatively small particles.

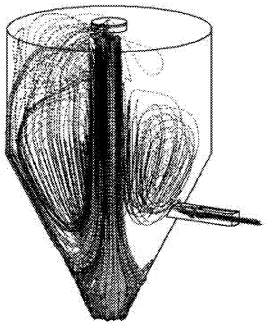

Figure9: Simulated particle trajectories (the shown size is a measure of the particle diameter and the colours represent the particle temperature in K)

Figure 10 shows the initial particle size distribution at the nozzle and the computed size distribution at the bottom of the dryer corresponding to the calculation shown in figure 9.

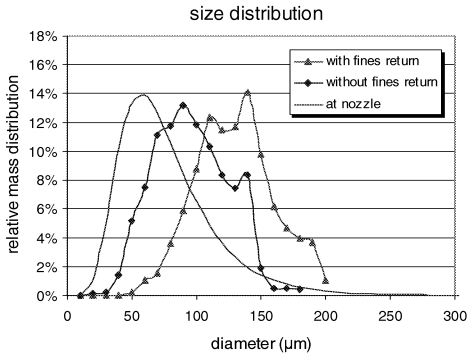

Figure 10: Particle size distribution at the nozzle (measured) and at the bottom of the dryer (simulated)

Two cases have been simulated: production of infant formulae without and with fines return. An increase in the particle size of the powder is observed when using a fines return configuration. This is in correspondence with experimental observations. In Table 1 the experimental and simulated average particle sizes are compared.

Table 1: Comparison of powder particle size distributions of simulations and validating spray drying trials.

		Model prediction	Measured (directly at dryer)	Measured (after transport)
without fines return	average diameter d (v, 0.5) [µm]	95	103	92
	relative span [-]*	1.0	2.7	2.0
with fines return	average diameter d (v, 0.5) [µm]	130	164	103
	relative span [-]*	0.6	2.3	2.0

* relative span is defined as (d (v, 0.9) – d (v, 0.1))/ d (v, 0.5)

It can be concluded that the simulations are giving results in the correct order of magnitude. However, there is still a need for further fine-tuning. Moreover, special attention has to be paid to experimental determination of model input parameters, especially parameters for which the model is sensitive such as viscosity and stickiness.

ACKNOWLEDGEMENTS

This work has partly been sponsored by the European Commission in the frame of the EC Fifth Framework Programme within the research programme "Competitive and Sustainable Growth" (contract G1RD-CT-2000-00340, http://www.edecad.com). The authors would like to thank the other project partners Armor Protéines, Royal Numico, Anhydro A/S, University of Manchester, Bremen University, TU Darmstadt and Martin-Luther-Universität Halle-Wittenberg. Johan van der Knaap is acknowledged for his assistance in the experimental work.

REFERENCES

Aguilera, J.M., J.M. Del Valle and M. Karel (1995), Caking phenomena in amorphous food powders, Trends in Food Science & Technology Vol. 6, pp. 149-155.

Bhandari, B.R. and T. Howes (1999), Implication of glass transition for the drying and stability of dried foods, Journal of Food Engineering, Vol. 40, pp. 71-79.

Blei, S. and M. Sommerfeld (2003), Lagrangian modeling of agglomeration during spray drying processes, Proceedings of the 9th International Conference on Liquid Atomization and Spray Systems, Sorrento, Italy, 13-17 July 2003, paper no. 1604.

Blei, S. and M. Sommerfeld (2004a), Computation of agglomeration for non-uniform dispersed phase properties – an extended stochastic collision model, Proceedings of the 5th International Conference on Multiphase Flow, ICMF'04, Yokohama, Japan, 30 May-4 June 2004, paper no. 438.

Blei, S. and M. Sommerfeld (2004b), Investigation of droplet collisions of viscous process fluids by imaging techniques, Proceedings ILASS Europe 2004, 19th Annual Conference on Liquid Atomization and Spray Systems, Nottingham, United Kingdom, 6-8 September 2004.

Bloore, C. (2004). Dairy Industry Systems Consultant, Dunedin, New Zealand. Personal communication.

Downton, G.E., J.L. Flores-Luna and C.J. King. (1982), Mechanism of stickiness in hygroscopic, amorphous powders, Ind. Eng. Chem. Fundam., Vol. 21, pp. 447-451.

Hansen, P.S. (1980), Production of agglomerated fat-filled milk powder, J. Soc.Dairy Technology, Vol. 33, pp. 9-23.

Hennings, C., T.K. Kockel and T.A.G. Langrish. (2000), New measurements of the sticky behaviour of skim milk powder, Proceedings of the 12th International Drying Symposium IDS2000, Noordwijkerhout, The Netherlands, 28-31 August 2000.

Huang, L., K. Kumar and A.S. Mujumdar (2003), Use of computational fluid dynamics to evaluate alternative spray dryer chamber configurations, Drying Technology, Vol. 21, pp. 385-412.

Huang, L., K. Kumar and A.S. Mujumdar (2004), Simulation of a spray dryer fitted with a rotary disk atomizer using a three-dimensional computer fluid dynamic model, Drying Technology Vol. 22, pp. 1489-1515.

Kievit, G.K. (1997), Modelling quality in spray drying, Thesis Eindhoven University of Technology, The Netherlands.

King, C.J., ed. (1984). Transport processes affecting food quality in spray drying, Engineering and food, Processing applications G. Vol. 2, pp. 559-574.

Lazar, M.E., A.H. Brown, G.S. Smith, F.F. Wong and F.E. Lindquist (1956), Experimental production of tomato powder by spray drying, Food Technology Vol. 10, pp. 129-137.

Menn, P. (2005), Charakterisierung von Sprays. Thesis Bremen University, Shaker Verlag, Aachen, Germany.

Nhumaio, G.C.S., A.P. Watkins and A.J. Yule (2004), Experiments and CFD predictions of two overlapping water sprays issued from air-assist atomizers, Proceedings ILASS Europe 2004, 19th Annual Conference on Liquid Atomization and Spray Systems, Nottingham, United Kingdom, 6-8 September 2004.

Oakley, D.E. (2004), Spray dryer modelling in theory and practice, Drying Technology Vol. 22, pp. 1371-1402

Pietsch, W. (1999), Readily engineer agglomerates with special properties from micro-and nanosized particles, Chemical Engineering Progress Vol. 95 (8), pp. 67-81.

Paterson, A.H.J., G.F. Brooks, J.E. Bronlund and K.D. Foster (2005), Development of stickiness in amorphous lactose at constant T-Tg levels, International Dairy Journal, Vol. 15, pp. 513-519.

Retsina T. (1988), Agglomeration: a process to improve fine powder handling, Food Technology International Europe, pp. 37-39.

Roos, Y.H. and M. Karel (1991), Plasticizing effect of water on thermal behaviour and crystallization of amorphous food models, Journal of Food Science, Vol. 56 (1), pp. 38-43.

Roos, Y.H. (2002), Importance of glass transition and water activity to spray drying and stability of dairy powders, Le Lait, Vol. 82 (4), pp. 475-484.

Straatsma, J., G. van Houwelingen, A.E. Steenbergen and P. de Jong (1999a), Spray drying of food products: 1. Simulation model, J. Food Eng., Vol. 42, pp. 67-72.

Straatsma, J., G.van Houwelingen, A.E. Steenbergen and P. de Jong (1999b). Spray drying of food products: 2. Prediction of insolubility index, J. Food Eng., Vol. 42, pp. 73-77.

Van Ommen, J. R., Coppens, M.O., Van den Bleek, C.M., Schouten, J.C., 2000. 'Early warning of agglomeration in fluidized beds by attractor comparison'. *AIChE J.*, 46, 2183-2197.

Verdurmen, R.E.M., P. Menn, J. Ritzert, S. Blei, G.C.S. Nhumaio, T. Sonne Sørensen, M. Gunsing, J. Straatsma, M. Verschueren, M. Sibeijn, G. Schulte, U. Fritsching, K. Bauckhage, C. Tropea, M. Sommerfeld, A.P. Watkins, A. Yule and H. Schønfeldt (2004), Simulation of agglomeration in spray drying installations: the EDECAD project, Drying Technology Vol. 22, pp. 1403-1461.

Verdurmen, R.E.M., M. Verschueren, M. Gunsing, H. Straatsma, S. Blei and M. Sommerfeld (2005), Simulation of agglomeration in spray dryers: the EDECAD project, Le Lait , Vol. 85, pp. 343-351.

Vuataz, G. (2002), The phase diagram of milk: a new tool for optimising the drying process, Le Lait, Vol. 82, pp. 485-500.

Wallack, D.A. and C.J. King.(1988), Sticking and agglomeration of hygroscopic, amorphous carbohydrate and food powders, Biotechnology Progress, Vol. 4(1), pp. 31-35.

Xia, B. and D-W. Sun. (2002), Application of computational fluid dynamics (CFD) in the food industry: a review, Computers and Electronics in Agriculture, Vol. 24, pp. 5-24.

MODELLING SPRAY DRYING LOSSES IN BATCH, TOP-SPRAY FLUIDISED BED COATING PROCESSES

Frederik Ronsse[a,b], Jan G. Pieters[a] and Koen Dewettinck[b]
[a] Biosystems Engineering
[b] Food Technology and Engineering
Ghent University
Coupure Links 653
B-9000 Ghent, Belgium
E-mail: Frederik.Ronsse@UGent.be

KEYWORDS

Fluidisation, Mass transfer, Heat transfer, Simulation, Coating mass distribution, Spray drying.

ABSTRACT

A thermodynamic model is presented for the top-spray fluidised bed coating process. The model is based on the bed's discretisation into horizontal layers (or control volumes). In each control volume, both particle population balances and heat and mass balances for the solid, gas and droplet phases are constructed. Model-predicted spray drying losses were compared against experimentally determined coating efficiencies.

INTRODUCTION

Fluidised bed coating is a process in which a particulate solid material is encapsulated by spraying a coating polymer directly onto a fluidised bed (Abe et al. 1998; Dewettinck and Huyghebaert 1999). The coating polymer to be applied could be an aqueous or organic solvent-based solution or even a melt and is continuously sprayed into the fluidised bed, usually by means of a pneumatic nozzle which may be submerged in or positioned above the bed (Jozwiaskowski et al. 1990; Link and Schlünder 1997; Zank et al. 2001; Nasr et al. 2002). Depending on the position of the nozzle with respect to the fluidised bed, distinction is made between top-spray, bottom-spray and tangential-spray (Jones 1985).

The use of compressed air in a binary nozzle results in very strong shear forces at the liquid-gas interface, producing droplets with a size ranging from 10 to 40 µm (Guignon et al. 2002). The droplet size distribution of a spray produced by a pneumatic nozzle is characterised by the nozzle's specific construction, the liquid flow rate, the rheology of the coating and, the flow rate and pressure of the atomising air (Schæfer and Wørts 1977; Lefebvre 1988; Liu and Litster 1993; Juslin et al. 1995; Guignon et al. 2002). It is important that a certain ratio of droplet-to-particle size is to be respected during fluidised bed coating. According to Liu & Litster (1993), this ratio should be at least 10.

Due to the complex thermodynamic interactions between the droplet phase, the particles and the gas phase, the coating process is prone to unwanted yield-reducing or quality-degrading side effects, such as agglomeration (Dewettinck et al. 1998; Kage et al. 1998; Saleh et al. 1999; Nakano and Yuasa 2001), premature droplet evaporation (Smith and Nienow 1983; Jones 1985), attrition of friable particles (Guignon et al. 2002) and degradation of heat-sensitive core or coating materials (Kröber and Teipel 2005).

The exhaust air of a fluidised bed coating process is usually not saturated and consequently, premature droplet evaporation is likely to occur before the coating solution droplet adheres onto the particle surface (Jones 1985; Hemati et al. 2003). The spray-dried coating material could either be elutriated from the bed or, in case of heavier dry fines, the spray-dried fines are entrapped within the coating film, resulting in coating imperfections (Smith & Nienow 1983). Besides the reduced coating quality, spray drying losses increase production costs due to the loss in coating material and the increased processing times required to reach the same degree of coating compared to a process where spray drying losses are absent (Gouin 2004).

Premature droplet evaporation is the result of a complex interaction between several factors including the evaporative capacity of the bed, the droplet travel distance and velocity, the droplet impingement efficiency and the droplet adhesion probability (Jones 1994; Dewettinck and Huyghebaert 1998; Heinrich et al. 2003). Spray drying losses and agglomeration are two side effects occurring at each other's opposite end of the bed's drying capacity range which implies that fluidised bed coating is often characterised by a narrow operational region as illustrated in Figure 1.

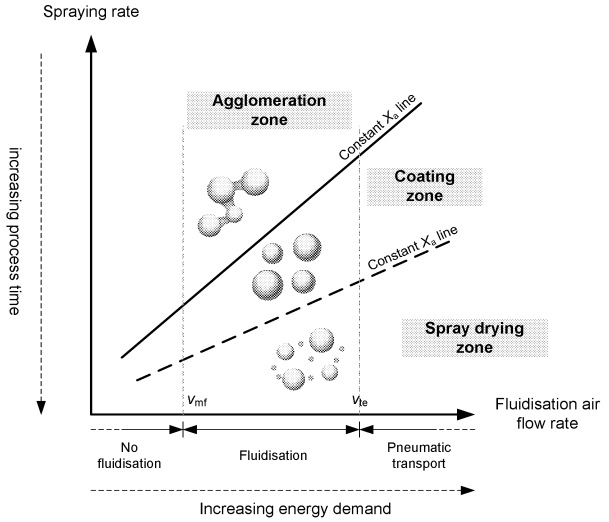

Figure 1. Relationship between particle growth kinetics in fluidised bed coating and the spraying rate and fluidisation air flow rate process variables (after Guoin 2004).

Currently, the knowledge on the different microprocesses that are involved, such as droplet penetration, impingement,

spreading and evaporation, as well as the interactions between the droplets and the particle-laden gas flow, is limited. This study's aim is the development of a mass- and heat transfer model capable of predicting the extent to which side-effects during fluidised bed processing occur. This paper will be focused on the spray drying loss or premature droplet evaporation phenomenon.

NOMENCLATURE

Symbols

a, b	Coefficients in impingement efficiency calculation
d	Diameter, m
DM	Dry matter content, dimensionless
G	Air flow rate, kg dry air/s
J	Mass flow rate, kg/s
n	number of control volumes
r	Particle exchange rate, Hz
S	Control volume
St	Stokes number, dimensionless
T	Temperature, K
v	Linear velocity
W	Particle moisture content, kg water/kg core
X	Absolute air humidity, kg water/kg dry air
Y	Coating mass fraction, kg coating/kg core

Greek Letters

ε	Voidage, dimensionless
η	Viscosity, Pa.s
θ	Droplet/particle contact angle
φ	Air relative humidity, dimensionless
Φ	Heat transfer rate, W
ρ	Density, kg/m^3
χ	Impingement efficiency, dimensionless

Subscripts

a	Fluidising air
at	Atomisation air
crit	Critical
dp	Droplet phase
p	Particles
sol	Coating solution
sd	Spray dried

MODEL DESCRIPTION

Main model

The model used in this study is an evolved version of the fluidised bed coating model presented by Ronsse et al. (2004; 2006a, b). However, whereas the original model only included two phases – being the gas and solid phases – the presented model is a fully developed three-phase model, including the droplet (spray) phase. Both models are based on the horizontal discretisation of the bed into n control volumes (or layers, S_i), each having a constant volume and containing a constant number of particles. A schematic overview of the model is given in Figures 2 and 3.

In modelling these 3 phases within the fluidised bed, the following assumptions were made:

- All three phases (droplets, gas and solids) are perfectly mixed within each control volume S_i.
- The mass flow of dry air, G_a, is constant and is equal for all control volumes (plug flow assumption)
- The continuous particle transport between the different control volumes (layers) is expressed by the variable r_i, as the fraction of the particle population exchanged per time unit from S_i towards S_{i+1}.
- Particles are non-porous and mechanically inert; there is neither agglomeration nor attrition.
- The droplet phase only moves downward through the particle bed. If no successful adhesion occurs before complete droplet evaporation, dry fines are produced. Dry fines are assumed to elutriate completely from the bed by the fluidising air.

In each control volume S_i, the population balance for the particles along with the dynamic heat and mass balances for the fluidising air (characterised by the air temperature, $T_{a,i}$, and air humidity, $\varphi_{a,i}$ or $X_{a,i}$), the particles (characterized by the particle temperature, $T_{p,i}$, particle moisture content, $W_{p,i}$, and particle coating content, $Y_{p,i}$) and the droplet phase (using the droplet temperature, $T_{dp,i}$, droplet phase mass, $M_{dp,i}$, and droplet dry matter content, $DM_{dp,i}$) are constructed. A detailed description of the numerical method to solve the model is given by Ronsse et al. (2006a)

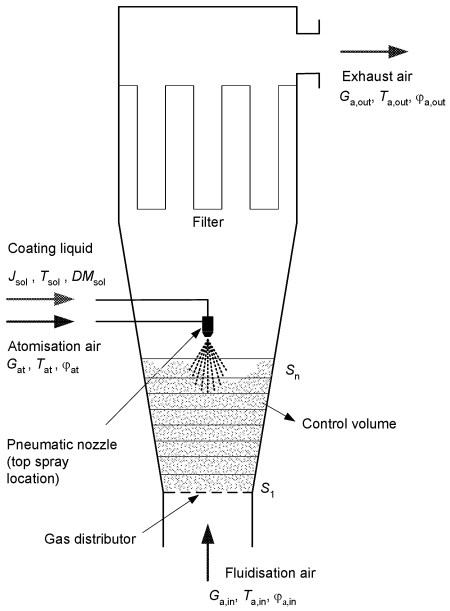

Figure 2. Schematic overview of the top-spray fluidised bed coater.

In order to complete the modelling of the fluidised bed coating process, the following variables had to be quantified:

- The heat and mass transfer rates at the air/particle and the air/droplet interface. Using the Whitaker equation, the dimensionless Nusselt and Sherwood numbers to estimate heat and mass transfer rates. This equation applies to forced convection around spherical bodies, being both droplets and particles (Sparrow et al. 2004).
- The particle exchange rate can be calculated using Rowe's (1973) correlation for the calculation of particle

circulation times as a function of gas velocity (G_a) in bubbling fluidised beds.

- Heat is exchanged from the bed to the environment either by convection of the gas (air) at the inner reactor wall ($\Phi_{loss,a,i}$ in Figure 3), or through contact between the particles and the reactor wall ($\Phi_{loss,p,i}$ in Figure 3). For an extensive overview of the different mechanisms of heat transfer between submerged surfaces (i.e. reactor wall) and bubbling fluidised beds, the reader is referred to Kunii and Levenspiel (1991).
- Finally, the droplet collection rate per control volume is unknown. In order to quantify the local droplet collection rate, a separate droplet submodel was designed, of which the details are given in the next section.

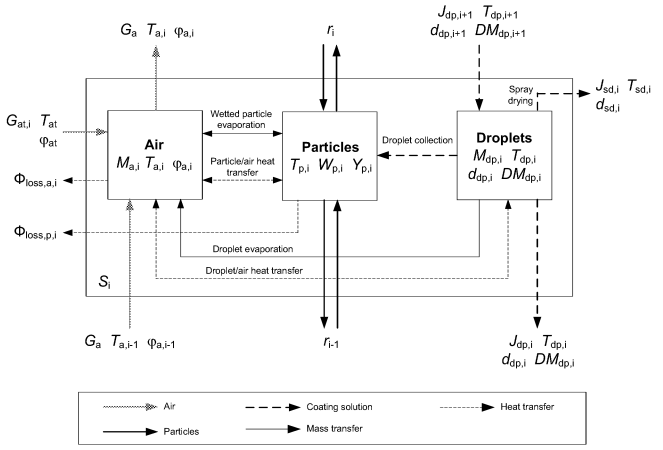

Figure 3. Detail of a single modelled control volume.

Droplet Submodel

In the droplet submodel, spatial droplet distribution and local droplet/particle collection rates are determined by tracking the trajectories of individual droplets throughout the computational domain. Individual droplet trajectories are calculated based on the forces acting on each individual droplet (gravitational and drag forces).

Assuming that the gas velocity profiles produced by the release of compressed air in the pneumatic nozzle are similar to a free axisymmetric jet (Donadono et al. 1980; Becher and Schlünder 1997; Zank et al. 2001), drag force calculation is based on the velocity profiles given by Schlichting et al. (2004) and the empirical drag coefficient equations of Turton and Levenspiel (1986), and Mostoufi and Chaouki (1999). The size distribution of the droplets produced at the nozzle is calculated according to the droplet size correlations described by Lefebvre (1988).

Droplet-particle collision occurs when the droplet trajectory is separated from the fluid streamline (Figure 4). The probability of droplet trajectory separation from the fluid streamline or the so-called 'impingement efficiency', χ, is obtained through the following empirical equation with St being the particle dimensionless Stokes' number, a and b being coefficients depending on the flow regime around the receiving particle (Löffler 1988; Zank et al. 2001; Heinrich et al. 2003):

$$\chi = \left(\frac{St_{dp}}{St_{dp} + a} \right)^{b} \tag{1}$$

Depending on the kinetic energy of the droplet and the wettability of the particles substrate, droplets remain adhered or bounce off the particle surface once initial particle-droplet contact has been made (Link and Schlünder 1997). Various authors use the concept of critical impingement velocity, above which the droplets are reflected on the particle surface (Link and Schlünder 1997; Zank et al. 2001; Heinrich et al. 2003). The critical impingement velocity for flat, non-porous and dry surfaces was deduced by Link (Zank et al. 2001),

$$v_{crit} = \frac{4\eta_{dp}\left(3\tan(\theta/2) + \tan^3(\theta/2)\right)^{2/3}}{d_{dp}\rho_{dp}\tan^2(\theta/2)} \tag{2}$$

By combining the impingement efficiency with the critical impingement velocity the overall droplet collection efficiency is calculated. By simulating a representatively large number of individual droplet trajectories, the spatial distribution in the bed of the droplet/particle collection rate can be derived and used to solve the heat and mass balances of the main coating model.

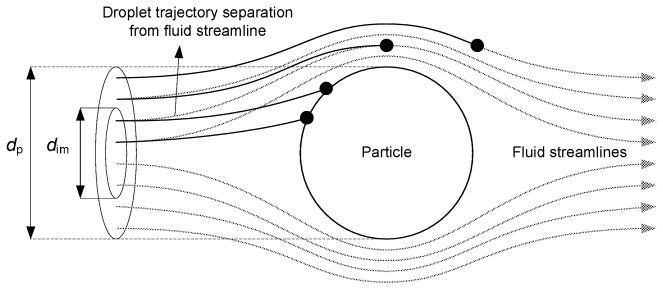

Figure 4. Droplet collision mechanism and the concept of impingement efficiency.

EXPERIMENTAL SET-UP

For the determination of the coating mass and coating efficiency, experimental data by Dewettinck (1997) were used. In this research work, the core material used was 1 kg of NaCl crystals which were coated with a 5 *w%* sodium caseinate solution. The adhered sodium caseinate, which is a protein, was then quantitatively determined using the Lowry. The coating efficiency was subsequently calculated as the amount of protein retrieved on the particles, compared to the total amount of coating material injected into the bed throughout the batch coating process.

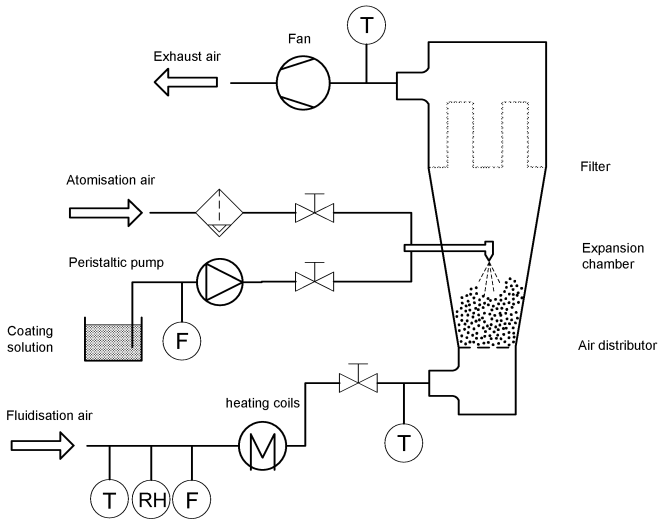

Figure 5. Schematic overview of the Glatt GPCG-1 fluidised bed coating unit.

All coating experiments were performed in the Glatt GPCG-1 fluidised bed unit (Figure 5) using the top-spray insert with the nozzle in the upper position (h = 0.225 m). In each coating experiment, the spraying rate and the inlet air flow rate were kept constant (J_{sol} = 7 g min^{-1}, $G_{a,in}$ = 1.34 × 10^{-2} kg s^{-1}), while the particle diameter, d_p, atomisation air pressure, P_{at}, and the inlet air temperature, $T_{a,in}$, were varied between different experiments as is shown in Table 1. Each coating experiment was terminated when the total amount of coating solution introduced into the bed was equal to 0.5 kg. After finishing the coating process, coating efficiency was determined by means of the Lowry-method.

Table 1. Studied process variables

Variable	Values studied				
Particle diameter (μm)	250	–	350	–	450
Corresponding bed height (m)	0.092	–	0.086	–	0.081
Corresponding particle exchange rate (Hz)	2.48	–	2.34	–	2.14
Inlet air temperature (°C)	70	–	78	–	86
Atomisation air pressure (bar)	1.5	–	2.5	–	3.5
Corresponding atomisation air flow rate (g/s)	1.45	–	2.04	–	2.38

Also, during each experiment, the steady-state bed temperature was recorded by means of a shielded T-type thermocouple suspended in the fluidised bed approximately 0.06 m above the air distributor. The bed temperature was used as an additional validation of the model.

RESULTS AND DISCUSSION

Thermodynamic validation

The measured bed temperature during steady state coating regime was compared with the model-predicted bed temperature. The results are shown in Figure 6, while the regression analysis results are given in Table 2. In each simulation, a total of 24 control volumes and 10000 particles were used, while the submodel simulated a total of 5000 droplet trajectories. More details concerning the effect of the sample size and the number of control volumes on the model-predicted results is given in Ronsse et al. (2006a).

From the results of the regression analysis, it could be deduced that a good correlation was attained between the experiment and the model, although the model tended to overestimate the bed temperature as can be seen by the asymmetric 95%-confidence interval of the intercept. Previous thermodynamic validation (Ronsse et al. 2005) revealed that the model tended to underestimate the air temperature – and ultimately, the bed temperature – in the lower sections of the fluidised bed. However, the method of measuring the bed temperature by means of a shielded probe suspended in the bed is likely to result in lower temperatures due to evaporative cooling due to probe wetting. Indeed, visual inspection of the temperature probe after conducting coating experiments using coloured coating solutions often revealed a clearly distinguishable layer of coating material sticking on the probe. This indicates that part of the coating material somehow must have contacted the probe in a dissolved state, either by direct droplet contact or by collision of wetted particles resulting in evaporative cooling of the probe tip.

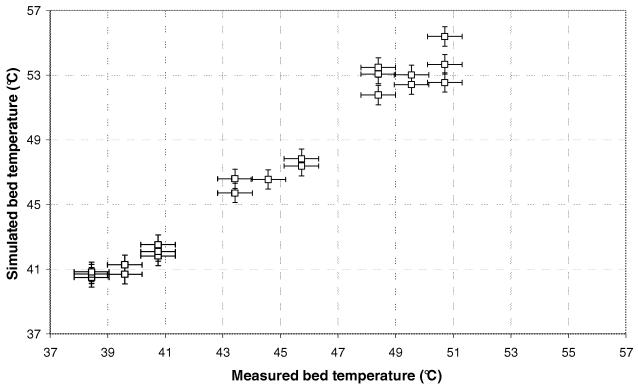

Figure 6. Measured bed temperature during steady state coating versus the model-predicted bed temperature.

Table 2. Regression analysis between model-predicted and experimental bed temperature

$T_{bed,exp} = a T_{bed,mod} + b$	
R^2	0.972
SSR	164.5
Slope, a	1.160
95% confidence interval of slope	[1.065; 1.257]
Intercept, b	-4.564
95% confidence interval of intercept	[-8.814; -0.313]

Validation of coating efficiency

The experimental spray drying losses were compared with the model-predicted spray drying losses and the results are graphically represented in Figure 7, while the regression analysis is summarised in Table 3.

From these results it can be concluded that modest correlation was achieved, given the complex thermodynamic nature (multivariateness) of the spray drying effect. As can be seen from the regression analysis, the model tended to underestimate the spray drying loss (slope = 0.769), but this could be due to the fact that any loss in coating material throughout the process was assumed to be solely the result of the spray drying of the coating solution. In reality, however, effects such as attrition of deposited coating material and subsequent entrainment of coating material in the filter will contribute in decreasing the overall coating efficiency and thus, the experimental spray drying losses may be significantly smaller than the overall loss in coating material during the process, possibly explaining the underestimation in the model.

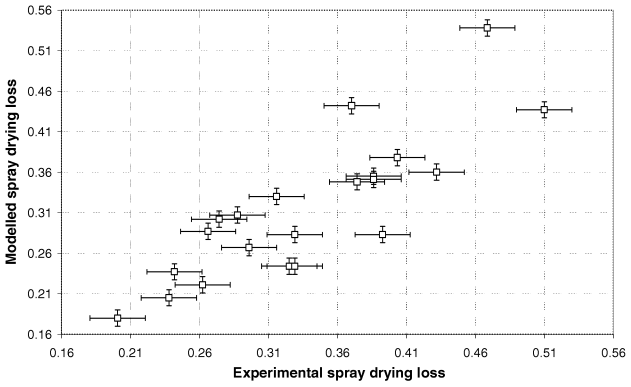

Figure 7. The measured spray drying loss (expressed as the spray-dried weight fraction of the total amount of dry matter introduced in the coating process) during steady state coating versus the model-predicted spray drying loss.

Table 2. Regression analysis between model-predicted and experimental spray drying loss

$J_{sd,exp} = a\,J_{sd,mod} + b$	
R^2	0.701
SSR	0.058
Slope, *a*	0.769
95% confidence interval of slope	[0.528; 1.010]
Intercept, *b*	0.096
95% confidence interval of intercept	[0.017; 0.175]

CONCLUSIONS

A model has been presented to calculate the dynamic behaviour of a top-spray fluidised bed coater. The model combines the one-dimensional discretised representation of the fluidised bed with a spraying submodel which serves to calculate the individual droplet trajectories. Although the model has shown to be quite reliable in predicting the overall bed thermodynamics, it also has proven to be capable of roughly estimating the spray drying losses. An additional difficulty in this kind of validation experiments is that not the spray drying in se is measured, but the overall process efficiency. The latter is also affected by attrition and entrainment; effects which are still not implemented into the model. As a consequence there is an underestimation of the model-predicted spray drying losses.

REFERENCES

Abe, E., Yamada, N., Hirosue, H., Nakamura, H. 1998. "Coating mass distributions of seed particles in a tumbling fluidized bed coater." *Powder Technology*, 97, 85-90.

Becher, R.D. and Schlünder, E.-U. 1997. "Fluidized bed granulation: Gas flow, particle motion and moisture distribution." *Chemical Engineering and Processing*, 36, 261-269.

Dewettinck, K. 1997. "Fluidized bed coating in food technology: process and product quality." PhD dissertation, Ghent University, 309p.

Dewettinck, K. and Huyghebaert, A. 1998. "Top-spray fluidized bed coating: Effect of process variables on coating efficiency." *Lebensmittel-Wissenschaft und Technologie*, 31, 568-575.

Dewettinck, K. and Huyghebaert, A. 1999. "Fluidized bed coating in food technology." *Trends in Food Science and Technology*, 10, 163-168.

Dewettinck, K., De Visscher, A., Deroo, L. and Huyghebaert, A. 1999. "Modeling the steady-state thermodynamic operation point of top-spray fluidized bed processing." *Journal of Food Engineering*, 39, 131-143.

Donadono, S., Mareca, A. and Massimilla, L. 1980. "Gas injection in shallow beds of fluidized, coarse solids." *Ingenieria Chimica Italiana*, 16, 1-10.

Guignon, B., Duquenoy, A., Dumoulin, E.D. 2002. "Fluid bed encapsulation of particles: principles and practice." *Drying Technology*, 20, 419-447.

Guoin, S. 2004. "Microencapsulation: industrial appraisal of existing technologies and trends." *Trends in Food Science and Technology*, 15, 330-347.

Heinrich, S., Blumschein, J., Henneberg, M., Ihlow, M., Peglow, M. and Mörl, L. 2003. "Study of dynamic multi-dimensional temperature and concentration distributions in liquid-sprayed fluidized beds." *Chemical Engineering Science*, 58, 5135-5160.

Hemati, M., Cherif, R., Saleh, K. and Pont, V. 2003. "Fluidized bed coating and granulation: influence of process-related variables and physicochemical properties on the growth kinetics." *Powder Technology*, 130, 18-34.

Jones, D.M. 1985. "Factors to consider in fluid-bed processing." *Pharmaceutical Technology*, 9, 50-62.

Jones, D. 1994. "Air suspension coating for multiparticulates." *Drug Development and Industrial Pharmacy*, 20, 3175-3206.

Jozwiaskowski, M.J., Jones, D. and Franz, R.M. 1990. "Characterization of a hot melt fluid bed coating process for fine granules." *Pharmaceutical Research,* 7, 3–10.

Juslin, L., Antikainen, O., Merkku, P. and Yliruusi, J. 1995. "Droplet size measurement: I. Effect of three independent variables on droplet size distribution and spray angle from a pneumatic nozzle." *International Journal of Pharmaceutics*, 123, 247-256.

Kage, H., Takahashi, T., Yoshida, T., Ogura, H., Matsuno, Y. 1998. "The coating surface and agglomeration of seed particles in a fluidized bed coater." *Advanced Powder Technology*, 9, 245-259.

Kröber, H. and Teipel, U. 2005. "Microencapsulation of particles using supercritical carbon dioxide." *Chemical Engineering and Processing*, 44, 215-219.

Kunii, D. and Levenspiel, O. 1991. "Fluidisation Engineering (2nd ed.)." Butterworth-Heinemann, Stoneham, 491p.

Lefebvre, A.H. 1988. "Atomization and sprays." Taylor and Francis, New York, 421p.

Link, K.C. and Schlünder, E.-U. 1997. "Fluidized bed spray granulation. Investigation of the coating process on a single sphere." *Chemical Engineering and Processing*, 36, 443-457.

Liu, L.X., Litster, J.D. 1993. "Spouted bed seed coating: the effect of process variables on maximum coating rate and elutriation." *Powder Technology*, 74, 215-230.

Löffler, F. (1998). "Staubabscheiden." Thieme verlag, Stuttgart.

Mostoufi, N. and Chaouki, J. (1999). "Prediction of effective drag coefficient in fluidized beds." *Chemical Engineering Science*, 54, 851-858.

Nakano, T. and Yuasa, H., 2001, "Suppression of agglomeration in fluidized bed coating. IV. Effects of sodium citrate concentration on the suppression of particle agglomeration and the physical properties of HPMC film." *International Journal of Pharmaceutics*, 215, 3-12.

Nasr, G.G., Yule, A.J. and Bendig, L. 2002. "Industrial sprays and atomization – Design, analysis and applications." Springer-Verlag, London. 501p.

Ronsse, F., Pieters, J.G. and Dewettinck, K. 2004. "Combined thermodynamic and population balance model of the batch top-spray fluidised bed coating process of inert spheres." *Proceedings of FOODSIM'2004, 3rd International Conference on Simulation in the Food Industry*, 16-18 June 2004, Wageningen, The Netherlands, 37-40.

Ronsse, F., Pieters J.G. and Dewettinck, K. 2006. "Combined population balance and thermodynamic modelling of the batch top-spray fluidised bed coating process. Part I – Model development and validation." *Journal of Food Engineering*, in press.

Ronsse, F., Pieters J.G. and Dewettinck, K. 2006. "Combined population balance and thermodynamic modelling of the batch top-spray fluidised bed coating process. Part II – Model and process analysis." *Journal of Food Engineering*, in press.

Ronsse, F.; Dewettinck, K. and Pieters, J. 2005. "Modelling the dynamic temperature and humidity distributions in fluidised bed coating processes." *Proceedings of the Fourth International Conference on Heat Transfer, Fluid Mechanics and Thermodynamica (HEFAT2005)*, 19-22 September 2005, Cairo, Egypt, HEFAT2005-RF1, 6p

Rowe, P.N. 1973. "Estimation of solids circulation rate in a bubbling fluidized bed." *Chemical Engineering Science*, 28, 979-980.

Saleh, K., Cherif, R., Hemati, A. 1999. "An experimental study of fluidized-bed coating: influence of operating conditions on growth rate and mechanism." *Advanced Powder Technology*, 10, 255-277.

Schæfer, T. and Wørts, O. 1977. "Control of fluidized bed granulation. III. Effects of inlet air temperature and liquid flow rate on granule size and size distribution." Control of moisture content of granules in the drying phase. *Arch. Pharm. Chemi. Sci. Ed.*, 6, 1-13.

Schlichting, H., Gersten, K., Krause, E., Oertel, H. and Mayes, C. 2004. "Boundary layer theory, 8th edn." Springer-Verlag, Berlin.

Smith, P.G. and Nienow, A.W. 1983. "Particle growth mechanisms in fluidized-bed granulation. I. The effects of process variables." *Chemical Engineering Science*, 38(8), 1223-1231.

Sparrow, E.M., Abraham, J.P., Tong, J.C.K. 2004. "Archival correlations for average heat transfer coefficients for non-circular and circular cylinders and for spheres in cross-flow." *International Journal of Heat and Mass Transfer*, 47, 5285-5296.

Turton, R. and Levenspiel, O. 1986. "A short note on the drag correlation for spheres." *Powder Technology*, 47, 83-86.

Zank, J., Kind, M. and Schlünder, E.-U. 2001. "Particle growth and droplet deposition in fluidised bed granulation." *Powder Technology*, 120, 76-81.

BIOGRAPHY

FREDERIK RONSSE was born in Kortrijk, Belgium on November 3rd, 1978. He graduated from the Ghent University in 2001 with a M.Sc. in Biological Engineering Sciences. Currently he is a doctoral researcher at the Ghent University in the Faculty of Agricultural and Applied Biological Sciences. His current research deals with the process optimisation and control of fluidised bed systems in the food industry, a joint project between the Biosystems Engineering Research Group (Department of Agricultural Engineering) and the Food Technology and Engineering Research Group (Department of Food Technology and Nutrition). Among his prime research interests are food microencapsulation, population balance modelling in powder technology, industrial automation and machine prototyping.

HEAT TRANSFER SIMULATION

MODELLING OF HEAT TRANSFER IN GLASS JARS WITH PARTICULATED FOODS IMMERSED IN A LIQUID MEDIUM

Alejandro R. Lespinard
Pablo R. Salgado
Luis A. Roche
Rodolfo H. Mascheroni
Centro de Investigación y Desarrollo en Criotecnología de Alimentos (C.I.D.C.A.)
47 y 116 – (B1900AJJ) La Plata, Argentina
E-mail: alespinard@cidca.org.ar

KEYWORDS
Modelling; Heat Transfer; Glass Containers, Particulated Foods

ABSTRACT

A sigmoid model is proposed for the simulation of food temperature evolution during the processing of preserves in low capacity sterilizers. Predicted results are compared against a formula method (exponential), widely used in the simulation and control of industrial processes.
The proposed model resulted to be simple and accurate for the prediction of thermal histories of foods of different shapes and sizes sterilized in glass jars, and may be very useful for low volume processors. The exponential model did not provide accurate predictions for these processing conditions.

INTRODUCTION

Sterilization is widely used for food preservation. Notwithstanding, only processing of foods packaged in cans or plastic containers and continuous aseptic processing (without containers) have been studied in depth for the heat transfer point of view. Almost no attention has been devoted to food processing in glass containers (Maroulis and Saravacos 2003).
During the last years there has been in Argentina a steady increase in the processing of low volumes of vegetable and fruit preserves at commercial level (home-made, organic, specialties, etc.), due to their much higher value. All these products are presented in transparent glass containers. In these cases, visual quality (appearance) of the products (normally whole or sliced fruits or vegetables) is the main quality index that costumers count on. So, it is mandatory to provoke the minimal changes in colour, shape and overall appearance, compatible with the destruction of microrganisms. That is why it is necessary to count on simple and accurate methods to predict product temperature evolution during thermal treatment, so as to minimize the usual thermal abuse due to overprocessing. An additional complexity is that retort temperatures – in these low volume batches – generally vary during processing, increasing up to a constant value.
Few references to this subject can be found in literature. Bimbenet and Michiels (1974) presented an initial theory for heat transfer in these systems (particulated foods in a liquid medium packaged in glass containers). Some later papers that dealt with the simulation of particular cases can be found (Akterian and Fikiin 1994; Akterian 1995; Abril et al. 1998; Márquez et al. 1998, 2001, 2002, 2003).
In this work an easy-to-use approximate calculation method to predict heat penetration in particulated foods immersed in a liquid medium and packaged in glass containers is proposed. The method is especially useful for heat treatments with time variable process conditions (come-up period) and enables to relate the variation of heating medium temperature to food temperature and to link it to microbe destruction and loss of quality kinetics.

MATERIALS AND METHODS

Containers and Samples

To perform the tests cylindrical glass containers of 360 cm^3 (external diameter 0.069m), were used. The containers were filled with cylinders, cubes or spheres of 0.010, 0.015 and 0.020 m of characteristic length L (diameter, side and diameter, respectively). These shapes and sizes were selected according to those of products found in the markets. As the objective was to simulate the pasterization and sterilization of fruits and vegetables, a test material of thermal properties similar to those of fruits and vegetables was used for the samples, in this case high-density polyethylene. The amount of test material filled to each container was calculated considering 45% of porosity. As covering liquid a 4% solution of NaCl was added, completing 90% of the total volume of the container.

Retort System

Tests were performed in a vertical batch retort built in stainless steel (Figure 1.a), with a holding capacity of 27 containers of 360 cm^3 each. The retort is furnished with an automatic security valve that opens at the overpressure of 1 atmosphere, reaching and maintaining a final temperature of approximately 118 ºC. This type of retort and working temperature are typical to little-volume processors.

Data Acquisition

Temperature within the retort and at the geometric center

of the sample placed in the coldest spot of the container (determined in exploratory runs) were measured each 15 seconds, using Type T copper-constantan (Cu-CuNi) thermocouples. To this end, the metallic lids of the containers were drilled in the centre to let the passage of the thermocouple (Figure 1.b). A high-temperature resistant seal was used to secure hermeticity around the thermocouple in the lid. Thermal histories were measured and registered using a multi-channel data acquisition system KEITHLEY model AS-TC.

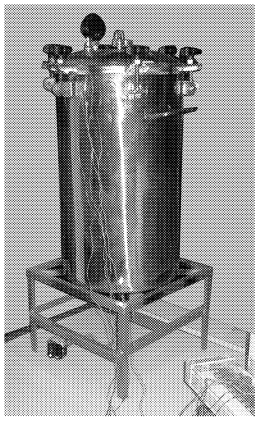

(a)

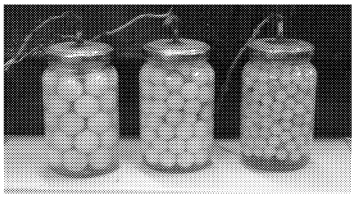

(b)

Figure 1: (a) Retort System, (b) Containers and Samples, Showing the Insertion of Thermocouples through the Lids

Thermal Processing

Thermal processing of the simulated preserves consisted of an initial heating stage of approximately 30 minutes, where retort temperature increases from the initial (ambient) temperature up to a final temperature of about 118 ºC, regulated by the security valve set to approximately one atmosphere. This stage is followed by a second period during which temperature maintains practically constant during 14 minutes.
Experiments were performed by triplicate. The proposed calculation methods – described later - were adjusted to each thermal history, and the values of the regression parameters were averaged for each shape and size.

Modelling of heat penetration

A) Heat penetration was modelled by means of a standard *Formula Method* (Ball 1923; Ball and Olson 1957; Holdsworth 1997). This exponential model, widely used in industrial processing of preserves, is defined through two parameters: f_{he} and j_h.

$$Tc^* = \frac{T_r - T_c}{T_r - T_0} = j_h \cdot e^{-2.303 \cdot t / f_{he}} \qquad (1)$$

Being f_{he} the time the system needs to traverse a natural logarithm cycle in the semilogarithmic plot of Equation (1) and depends on product thermal properties, shape and size and heat transfer conditions, meanwhile j_h is mainly related container and food shapes and sizes.
Their values were calculated by linear regression of the semilogarithmic plot of T* vs. time, being j_h and f_{he}, respectively, the intercept and the slope of the linear plot.

B) After the study of the shapes of the experimental heating curves (see Figures 3 and 4) a sigmoid model, defined by Equation (2) and characterized by four parameters: A_1, A_2, x_o, and dx, is proposed.

$$T_c = \frac{(A_1 - A_2)}{1 + e^{(t - x_0)/dx}} + A_2 \qquad (2)$$

Being A_1 the pseudo-initial temperature of the slowest heating point (ºC), A_2 the final retort temperature (ºC), x_0 the time the slowest heating point needs to reach the temperature $(A_1+A_2)/2$ and dx a parameter related to the first derivative of Tc evaluated in x_0. To calculate the parameters, a nonlinear fitting of experimental data to Equation (2) was done using the software Origin 7.0, prescribing parameter A_2 as the final retort temperature.

Calculation of Microbial Lethality

Acumulated lethalities were calculated in the usual way, by means of Equation (3), as the integral of the lethal rate L along the processing time. Experimental thermal histories and those predicted by both models were used. As reference microrganims *Clostridium pasteurianum* ($D_{120ºC}$ = 0.01 and z_e = 10ºC), were used.

$$F = \int_0^t L dt = \int_0^t 10^{(Tc(t) - Tref)/z_e} dt \qquad (3)$$

Acumulated lethality values F were calculated by approximate integration of Equation (3) with a second-order Newton-Cotes method, using Excel 7.0.

Validation of the Model

Both prediction methods were validated comparing simulated temperatures against experimental ones. To perform these comparisons average absolute percent residues, as defined in Equation (4), were used:

$$R = \frac{1}{m} \sum_{i=1}^{m} \frac{|T_s - T_e|}{T_e} 100\,(\%) \qquad (4)$$

Calculated values of acumulated lethality F were also compared, using the relative percent absolute difference DF:

$$DF = \frac{|F_s - F_e|}{F_e} 100\,(\%) \qquad (5)$$

RESULTS AND DISCUSSION

Figures 2.a, 2.b and 2.c show the thermal histories of cylinders, cubes and spheres, respectively, during thermal processing with variable external medium temperature. In these figures an initial period during which food product temperature remains constant (time lag) can be observed. This lag is a function of the material and thickness of the container and of the size of the products (higher thickness implies higher delay), as has been previously shown (Márquez et al. 2003). Respect to retort temperature, it shows two characteristic periods: one initial with continuous increase (firstly steady, later with lower slope)

and a second period of constant temperature, regulated by internal pressure in the retort.

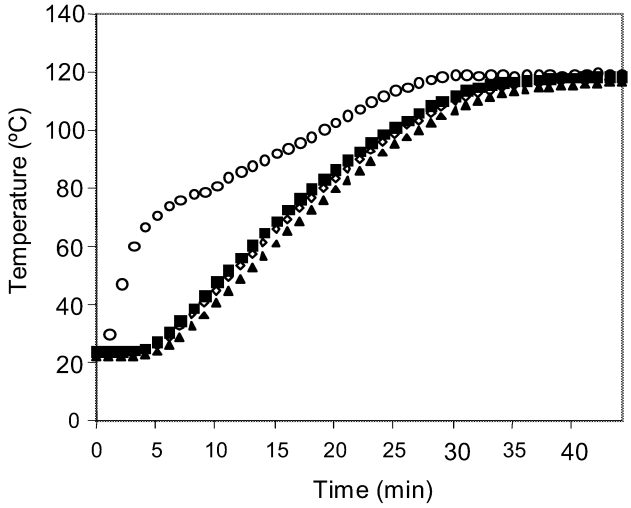

Figure 2.a: Experimental Thermal History in Cylinders. (○) Retort, (■) 0.01 m, (◊) 0.015 m, (▲) 0.02 m

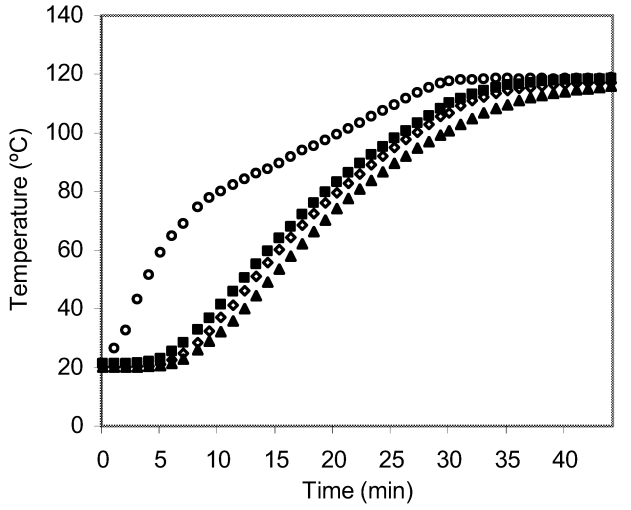

Figure 2.b: Experimental Thermal History in Cubes. (○) Retort, (■) 0.01 m, (◊) 0.015 m, (▲) 0.02 m

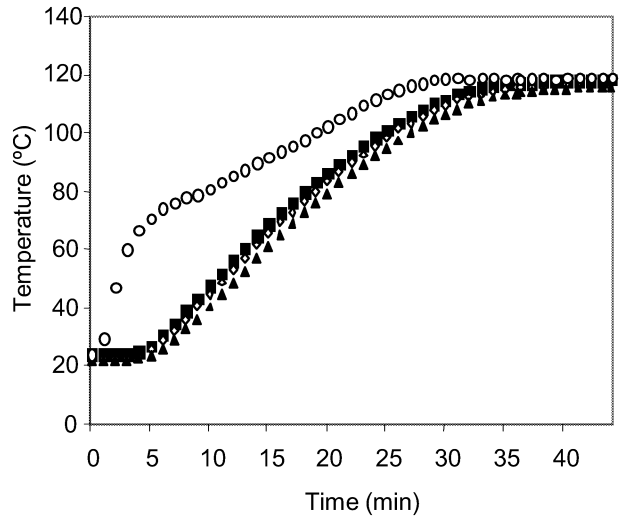

Figure 2.c: Experimental Thermal History in Spheres. (○) Retort, (■) 0.01 m, (◊) 0.015 m, (▲) 0.02 m

Parameters calculated from the respective thermal histories are presented in tables 1 and 2. In the sigmoid model, parameter x_o (min) is related to the delay of the system and is defined as the time that the slowest heating point in the system reaches a temperature $(A_1+A_2)/2$ ºC, increasing with the characteristic length L. Similarly, parameter j_h lowers with the increase of L (lower heating rate). Meanwhile, dx and f_h increase with L, being related to the increase of process time with product size (higher L means lower heating rate).

Table 1: Parameters of the Exponential Model

Shape	L (m)	j_h	f_{he}
Cylinders	0.010	2.37	22.75
	0.015	1.78	29.29
	0.020	1.35	36.60
Cubes	0.010	2.81	19.76
	0.015	1.52	27.98
	0.020	1.06	38.50
Spheres	0.010	2.14	20.79
	0.015	1.30	29.54
	0.020	0.85	38.80

Table 2: Parameters of the Sigmoid Model

Shape	L(m)	A_1	A_2	x_o	dx
Cylinders	0.010	13.58	118.08	20.39	5.51
	0.015	12.08	118.08	20.83	6.07
	0.020	11.42	118.08	21.69	6.61
Cubes	0.010	9.34	118.56	15.59	5.97
	0.015	8.11	118.56	16.48	6.19
	0.020	6.94	118.56	17,88	6.61
Spheres	0.010	11.05	118.52	14.36	6.11
	0.015	9.20	118.52	14.90	6.44
	0.020	8.60	118.52	15.95	6.69

Figure 3 shows the experimental and simulated – by both methods – thermal history for cubes with 0.015 m of side. As can be seen, the exponential model only works satisfactorily at long processing times (when retort temperature T_r is constant), but at short process times deviations are considerable. This model could be useful for low acidity foods, were process times are long and the initial error in predicted temperature has no weight on overall calculated lethality.

Meanwhile, the sigmoid model predicts temperatures with high accuracy at short and large processing times, because it adequately considers the variation in T_r. This means that this model is also useful for short processing times, as in the case of high acidity foods. These behaviours of the models were the same for the different shapes and sizes.

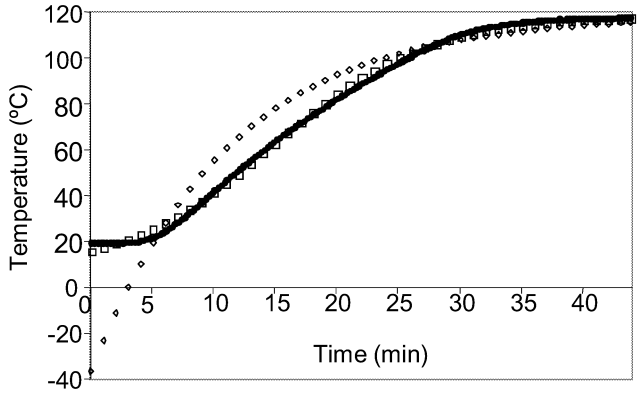

Figure 3: Experimental and Simulated Thermal History of a Cube of 1.5 cm Side. (◊) Exponential Model, (□) Sigmoid Model, (-) Real

Residues calculated according to Equation (4) are shown in Table 3. In all cases, those of the sigmoid model were much lower than for the exponential one, always less than 10 %, showing the accuracy of the sigmoid model.

Table 3: Calculated Residues for Predicted Temperatures

		L (m)		
Shape	Model	*0.010*	*0.015*	*0.020*
Cylinders	*Sigmoid*	4.56	5.13	4.94
	Exponential	74.01	48.17	37.23
Cubes	*Sigmoid*	2.87	3.38	3.96
	Exponential	75.91	27.44	32.09
Spheres	*Sigmoid*	9.86	9.05	9.37
	Exponential	152.72	69.49	152.68

Acumulated lethalities F for all shapes and sizes, both real and calculated, are presented in Table 4. In most cases predicted values for both models were lower than true values. This is good for microbiological security of predicted work conditions, meanwhile deviations from real values be low. This is so for predicted F by the sigmoid model, but those from exponential model show a low degree of accuracy, implying high quality losses and energy consumption. These trends are reflected in predicted relative differences (DF), which were much lower for the sigmoid model (Table 4).

The parameters of the sigmoid model (x_o and dx) obtained through the fitting of experimental thermal histories can be related to product size (L), as previously expressed. This is shown in Figures 4.a and 4.b.

Figure 4.a shows that x_o increases in exponential manner with L for the three shapes, meanwhile dx increases in a linear way, as shown in Figure 4.b. These figures allow to interpolate for calculating their values for intermediate sizes.

Table 4: Acumulated Lethalities F (min) and Relative Percent Absolute Differences

		Model				
Shape	L (m)	Real	Sigmoid		Exponential	
		F(min)	F(min)	DF(%)	F(min)	DF(%)
Cylinders	*0.010*	3.21	3.15	1.91	2.80	12.90
	0.015	1.94	2.21	14.07	1.19	38.56
	0.020	1.12	1.37	22.70	0.56	50.03
Cubes	*0.010*	6.90	5.15	25.36	4.62	33.02
	0.015	4.74	4.22	10.91	2.19	53.68
	0.020	2.40	2.86	19.24	0.86	64.06
Spheres	*0.010*	7.44	5.61	24.66	5.01	32.71
	0.015	5.20	4.64	10.77	2.27	56.28
	0.020	3.55	3.67	3.28	1.42	59.90

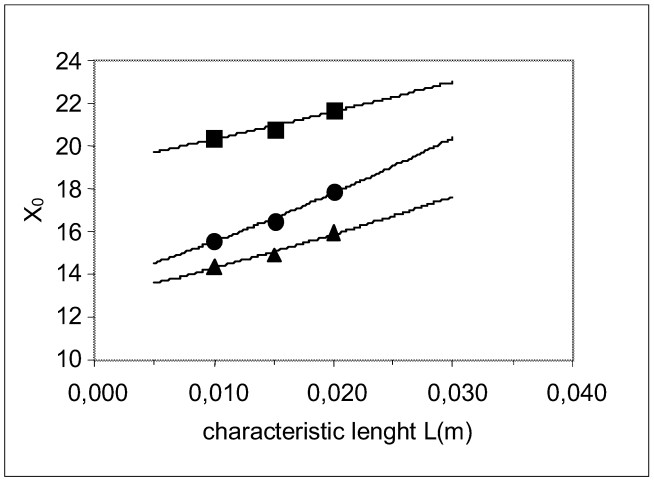

Figure 4.a: Variation of x_o with L for the Different Shapes. (■)Cylinders, (●)Cubes, (▲)Spheres

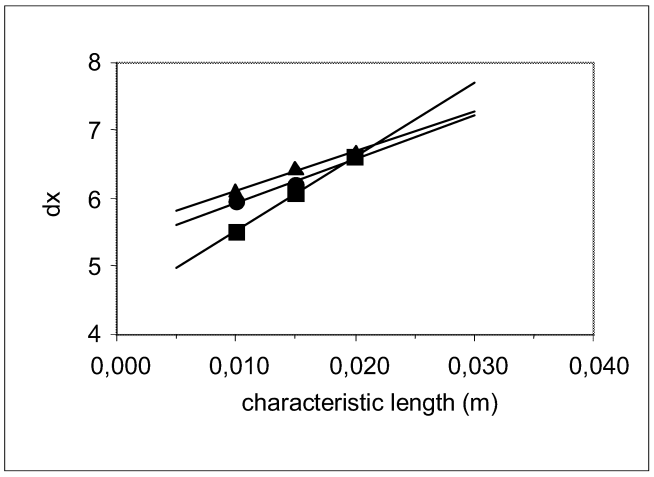

Figure 4.b: Variation of dx with L for the Different Shapes. (■)Cylinders, (●)Cubes, (▲)Spheres

CONCLUSIONS

A sigmoid model has been proposed for the prediction of thermal histories in particulated foods (of different shapes and sizes) packaged in glass containers, that can be very practical for calculation of low-volume productions. The also tested formula method (exponential) – normally very useful for industrial processing conditions where constant retort temperatures are reached almost instantaneously – does not provide accurate results for the initial variable retort temperature of the tested working conditions.

The proposed model predicted with good accuracy the thermal evolution of all the tested cases, with average relative absolute differences lower than 10%, fulfilling the usual technical requirements.

Besides, it was found that model parameters x_o and dx can be easily related to food size for each shape, which enables to use the model to simulate process conditions for food sizes different from the tested ones.

Simulated acumulated lethalities were, in most cases, lower than real ones, which is adequate from the point of view of microbial security. The model allows to calculate the sterilization time needed to secure microbial inactivation and – at the same time – assuring the minimal quality loss due to overprocessing.

NOTATION

A_1 Pseudo-initial temperature of the slowest heating point (ºC)

A_2 Final retort temperature (ºC)

DF Relative percent absolute difference between calculated F using real and simulated temperatures (%)

D Decimal reduction time (min)

dx Constant in sigmoid model related to the first derivate ($\frac{dT_c}{dt} = \frac{A_2 - A_1}{4d_x}$) evaluated in x_0 (min)

F Acumulated lethality (min)

f_{he} Time to dimensionless temperature to traverse a natural logarithm cycle (min)

j_h Lag factor

L Characteristic dimension (m)

m Number of experiment temperatures compared

R Percent residue (%)

T Temperature (ºC)

t Time (min)

x_0 Time the slowest heating point needs to reach the temperature $(A_1+A_2)/2$ (min)

z_e Thermal resistance factor (ºC)

Subscripts

c Thermal center of the slowest heating product

e experimental

h heating phase

o initial

r retort

ref reference

s simulated

Superscripts

* dimensionless

ACKNOWLEDGMENTS

Authors acknowledge the financial support of CONICET, UNLP and ANPCyT from Argentina.

REFERENCES

Abril, J.; P. Vírseda; and J. Moure. 1998. "Modelización de la penetración de calor en conservas vegetales". In *II Congreso Iberoamericano de Ingeniería de Alimentos (CD)*. Bahía Blanca, Argentina, Paper IV.11.

Akterian, S.G. and K.A. Fikiin. 1994. "Numerical simulation of unsteady heat conduction in arbitrary shaped canned foods during sterilization process". *Journal of Food Engineering* 21, 343-354.

Akterian, S.G. 1995. "Numerical simulation of unsteady heat transfer in canned mushrooms in brine during sterilization process". *Journal of Food Engineering* 25, 45-53.

Ball, C.O. 1923. "Thermal process time for canned food". Bulletin No. 37, National Research Council, Washington DC.

Ball, C.O. and F.C.W. Olson. 1957. *Sterilization in food processing – Theory, Practice and Calculations*. Mac Graw-Hill, New York.

Bimbenet, J.J. and L. Michiels. 1974. "Transferts de chaleur par convection au cours de la stérilisation des conserves". In *Proc. IV Int. Congress Food Sci. & Technol.,* Vol. IV, 361-379.

Holdsworth, S.D. 1997. *Thermal processing of packaged foods*. London, Ed. Chapman Hall, 146-155.

Maroulis, Z.B. and G.D. Saravacos. 2003. *Food Process Design* , Marcel Dekker Co., New York, 380-388.

Márquez, C.A.; A. De Michelis; V.O. Salvadori; and R.H. Mascheroni. 1998. "Application of transfer functions to the thermal processing of particulate foods enclosed in liquid medium". *Journal of Food Engineering* 38, 189-205.

Márquez, C.A.; V.O. Salvadori; A. De Michelis; and R.H. Mascheroni. 2001. "Predicción y ajuste de tiempos de pasterización en conservas de cereza y guinda envasadas en recipientes de vidrio. Método simple y rápido". In *Actas del 8 Congreso Iberoamericano de Transferencia de Calor y Materia*, 207-213.

Márquez, C.A.; M. Vullioud; A. De Michelis; V.O. Salvadori; and R.H. Mascheroni. 2002. "Parámetros que caracterizan la transferencia de calor durante la esterilización de conservas de frutas en frascos en función de los tamaños de los frascos y de las frutas". In *IX Congreso Argentino de Ciencia y Tecnología de Alimentos,* Buenos Aires, 7-9 Agosto de 2002, Paper 12.23.

Márquez, C.A.; V.O. Salvadori; R.H. Mascheroni; and A. De Michelis. 2003. "Application of transfer functions to the thermal processing of sweet and sour cherries preserves: influence of particle and container sizes". *Food Science and Technology International* 9 (2), 69-76.

FOULING OF HEAT EXCHANGERS IN THE DAIRY INDUSTRY BY COUPLING FLOW AND KINETICS MODELLING

Maria Valeria De Bonis, Caterina Calamello and Gianpaolo Ruocco
CFD*food*, DITEC
Università degli studi della Basilicata
Campus Macchia Romana, Potenza 85100, Italy
e-mail: CFD*food*@unibas.it

KEYWORDS
Biology, Production, Partial differential equations, Industrial processes, Continuous simulation.

ABSTRACT

Thermal treatment of milk represents a major unit operation in the dairy industry, to ensure the product's microbiologic safety and shelf-life increase. But during the thermal treatments of such sensible fluids in common Plate Heat Exchangers, proteins are often degraded and precipitated to form fouling that greatly affect the treatment efficiency and alter the product's desired features. Computational Fluid Dynamics simulations can then be successfully exploited, bringing forth temperature and velocity information, that yield for deposit distributions when coupled to biochemical notations for thermal denaturation of fluid constituents.
The present work exploits such modelling of a heat exchanger single channel during pasteurization of milk. The model applies for the first time a large, consistent system of differential equations to a corrugated plate to combine the flow, heat transfer and local transport of β-LactoGlobulin, the protein responsible of the subject problem. A preliminary, 2D computation has been performed with a commercial Finite Element Method software, showing the potential of application to optimized geometries (different corrugation shape and orientation) and for a variety of products of known biochemical evolution.

INTRODUCTION

The increasing attention on safety and quality of medium and long time shelf–life has stimulated the application of various and optimized thermal treatments, in order to get flavors and nutritional values closer to those of untreated foods.
Thermal treatment of milk and the like is one of the most important unit operation in the dairy industry, to ensure microbial safety and extend storage. Energy delivery is a paramount parameter (through temperature) in controlling the alterations among the milk constituents during its biochemical evolution, but it must be coupled with time exposure, that measures the ultimate energy level. It is evident therefore that an adequate temperature–time coupling is the most important feature to be optimized in the dairy industry.
The device generally entitled to realize an indirect heating of milk is the Plate Heat Exchanger (PHE), depicted in Fig. 1, which features a number of favorable aspects: flexibility to allow different fluid treatment, safety, high thermofluid efficiency, high turbulence to enhance heat transfer and low weight/surface ratio (Shah et al. 1988). Nevertheless, during its working cycles, the PHE is subject to a complex phenomenon which causes undesired material accumulation along its working surfaces: fouling. Fouling formation and control represents one of the unresolved operating problems affecting a variety of industries, causing an increase of capital costs, energy and maintenance time, and a loss of production, together with a meaningful environmental impact. Indeed, the plant is heavily affected as fouling causes increased pressure drop, reduction of working efficiency through the reduction of the heat transfer, and increased down–time due to the frequent cleaning stage, with environmentally offensive chemicals, to ensure stable processing (Burton 1988).
The fouling biochemical mechanism has been long stud-

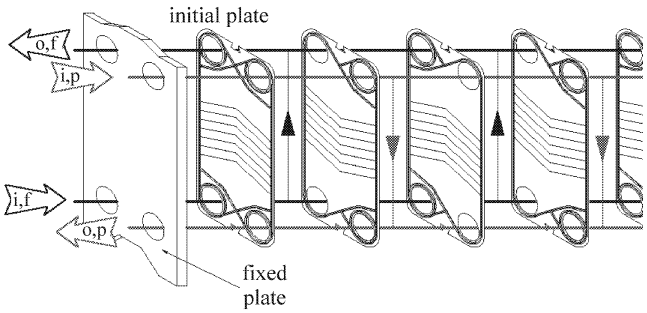

Figure 1: The stacked PHE arrangement, with indication of streams. The product line with gray lines and arrows (p), and the auxiliary fluid (thermal carrier) with black lines and arrows (f) are reported, respectively, at inlet (i) and outlet (o).

ied, but only partially understood due to its complex nature. As shown by (Georgiadis et al. 1998; Georgiadis and Macchietto 2000; Grijspeerdt et al. 2004) the denaturation of β-LactoGlobulin (βLG), a serum protein, is responsible for fouling for thermal treatment close to 90 °C, while several additional parameters influence such dynamics: milk composition, pH, plate geometry and entrained air.
Nowadays the optimization of technological process and their operating conditions are often looked upon with the aid of numerical modelling of transfer phenomena. Integration of governing Partial Differential Equations (PDEs) allows for a fundamental and quantitative way to understand complex phenomena which is complementary to the traditional approaches of theory and experiment. This approach is becoming increasingly widespread in basic research and advanced technological applications, cross cutting the fields of physics, chemistry, mechanics, engineering, and biology.
(Georgiadis and Macchietto 2000) proposed a mathematical model by integrating a plug–flow model with the heat convection along the flow direction and the effects of dispersion. Fouling is considered as mono–dimensional and steady–state, and different heat exchanger configurations are compared by using a specific software to quantify the fouling distribution in the whole device. The deposit varies linearly with time, specially at the beginning of treatment, and is non–uniform in the different channels considered being more localized in the first flow passages, where temperature is higher. Then (Jun and Puri 2006) have improved their model by a two–dimensional geometry, though still idealized (plates have no corrugations) showing that the temperature distribution and related fouling can be more accurately analyzed. A validation has been also carried out, which compare favorably with tests, for several thermal and fluid flow conditions. It is confirmed that the deposit is strongly dependent on operating conditions.
Well within this framework, in the present research line the modelling and simulation approach has been chosen, integrating the governing PDEs by the Computational Fluid Dynamics (CFD). Even when dealing with complex phenomena, the detailed flow field study coupled to many other transport phenomena notations, offer a potential of improved performance, better reliability, more confident scale-up, improved product consistency, and higher plant productivity. All these aspects will give plant scientists and managers a much better and deeper understanding of what is happening in a particular process or system: it makes it possible to evaluate geometric changes with much less time and cost than would be involved in laboratory testing, it can answer many "what if" questions in a short time and, finally, it is particularly useful in simulating conditions where it is not possible to take detailed measurements.
In the present work, CFD has been exploited to study the fouling formation on the PHE surfaces, during pasteurization of milk. All governing PDEs and related biochemical notations have been solved by a Finite Element Method (FEM) commercial solver, in order to determine the temperature distribution, the velocity profile and the distribution of the proteic deposit, for the first time on a simplified corrugated plate channel. Such model can be extended and used to show all operating and geometry conditions such that the fouling be minimized, i.e. by modifying corrugation shape and orientation. The application of the model could be beneficial to the food and biotechnology industry, suggesting the application of specific heat exchanger geometries for a specific product or process.

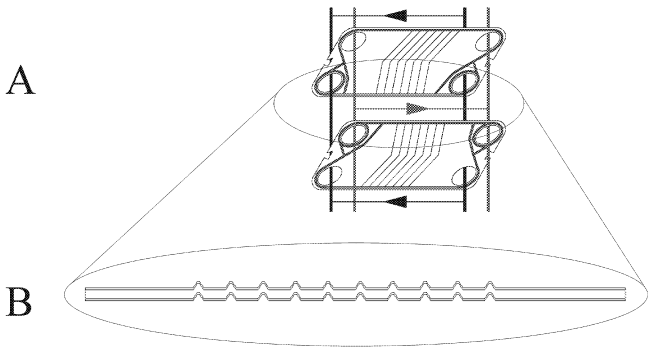

Figure 2: The PHE's selected channel: a sector of PHE depicted in Fig. 1 (A); the close–up of the simplified corrugate plate channel (B).

PROBLEM FORMULATION

In the present work a pasteurization treatment of milk in the first channel passage of a PHE has been studied (Fig. 2), to analyze the βLG's denaturation and subsequent aggregation, responsible for PHE fouling. The transfer phenomena at hand are based on the βLG's local kinetics mechanisms and related time evolution, depending on the adopted thermal regime and flow geometry. The subject control volume in Fig. 2.B is formed by 2 AISI 4340 steel, 25 cm–long and 1 mm–thick, parallel plates. These form a channel whose height is 4 mm; the inferior trapezoidal corrugations have long side, short side and height equal to 5, 1 and 3 mm, respectively, are spaced by 2 cm and are associated to specular superior vanes.
The following considerations have been adopted:

1. The product flow is two–dimensional, in rectangular Cartesian coordinates, laminar with channel Re = 2700 and incompressible (negligible pressure work and kinetic energy).

2. The milk flow with constant properties enters the channel at 60 °C with a native βLG mass concentra-

tion of 5 g/l; the auxiliary flow is counter–current saturated vapor at 97 °C.

3. The viscous heat dissipation is neglected.
4. Due to the adopted flow regime, no body force is accounted for.
5. No–slip is enforced at every solid surface.
6. Mass diffusivities of species have been computed by following (Jun and Puri 2006) specifications.

Furthermore, as the present work is focused on the evolution of βLG, it is suitable to present here its inclusion in the CFD formalism. The (Jun and Puri 2006) reaction scheme is adopted:

1. Proteins react in both the bulk fluid and a thermal boundary layer. Native protein N is transformed to denaturated unfolded protein D by a first order reaction. The unfolded protein then reacts to give an aggregated protein A by a second order reaction.
2. Mass transfer between the bulk and the thermal boundary layer takes place for each protein form.
3. An aggregated protein F only fouls the channel wall. The rate of deposition is proportional to the concentration of protein A in the thermal boundary layer.
4. The fouling resistance to heat transfer is proportional to the thickness of the deposit F.

This scheme can be summarized by the following:

$$N \xrightarrow{k_{ND}} D \xrightarrow{k_{DA}} A \xrightarrow{k_{AF}} F \tag{1}$$

Combining all this in a full multi–dimensional CFD framework, the standard unsteady–state governing Navier–Stokes, energy and mass conservation PDEs are enforced, in conservative form and for primitive variables, to yield for velocity components, pressure, mass fractions distributions in the fluid sub–domain, and temperature distribution in both sub–domains:

$$\nabla \cdot \mathbf{v} = 0 \tag{2}$$

where $\mathbf{v}$ is the milk velocity;

$$\frac{\partial \mathbf{v}}{\partial t} + \mathbf{v} \cdot \nabla \mathbf{v} + \frac{1}{\rho} \nabla P = \nu \nabla^2 \mathbf{v} \tag{3}$$

where P is the pressure, t is the time and ρ and ν are the milk density and kinematic viscosity, respectively;

$$\frac{\partial T}{\partial t} + \mathbf{v} \cdot \nabla T = \alpha \nabla^2 T \tag{4}$$

where T is the temperature and α is the milk thermal diffusivity;

$$\frac{\partial c_{ir}}{\partial t} + \mathbf{v} \cdot \nabla c_{ir} = D \nabla^2 c_{ir} + R'_{ir} - R''_{ir} \tag{5}$$

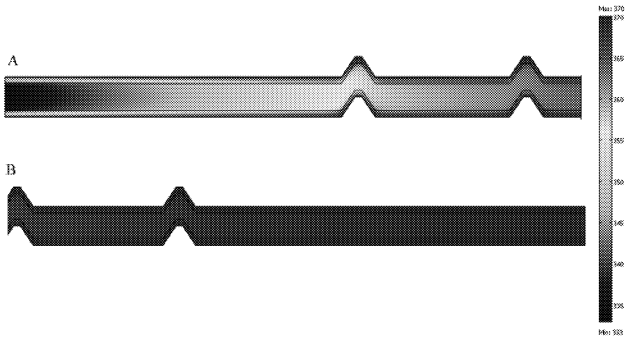

Figure 3: T distribution in the channel's inlet (A) and outlet (B) sections.

where c_{ir} is the molar concentration of the species i (either native N, denaturated D, aggregated A or deposited F βLG), in the topological region r (in the bulk fluid b or in the thermal boundary layer l); moreover, R' and R'' are its molar rates of creation and destruction, respectively. For sake of brevity, the interested reader is referred to (Jun and Puri 2006) for R'_{ir} and R''_{ir} values, in terms of Arrhenius expressions and their combinations.

RESULTS

The problem has been attacked by using COMSOL Multiphysics v.3a, with a grid of over 5400 finite elements and a Lagrange–Quadratic shape function, for a total of over 71400 degrees of freedom. The number of mesh elements and shape function type determine the accuracy of the final solution and the solver speed. The large number of degrees of freedom is justified by the 9 differential equations to be simultaneously integrated in space and advanced in time. A grid–independency analysis was not possible due to the instability of the solver for this study. The run has taken under five minutes of computing time for an elapsed time of 15 h simulation, on a Xeon server (3GHz CPU, 2GB RAM) running under Windows XPPro.

Heat transfer and fluid dynamics

Temperature and velocity distributions help understand the fouling distribution. Figure 3.A first shows the temperature distribution at channel inlet, in the flow and in the confining plates. Temperature readily changes from its initial value of 60 °C in milk, while the walls are being cooled–off by the fresh fluid, whereas at channel outlet, in Fig. 3.B, due to the combined heating by the channel walls and streamwise convection, the temperature is finally uniform at 97 °C.

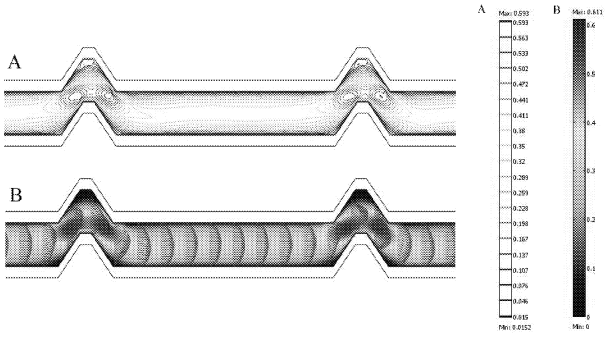

Figure 4: Streamlines (A) and **v** (B) distribution.

Then the flow field is reported, as streamlines, and vector velocity distribution in Fig. 4.A and B respectively. Fluid acceleration is caused by the corrugations, and small stagnation regions are evident down–wind from extruding corrugations and in the corresponding vanes, along all of the channel length.

Mass transfer

βLG denaturation (i.e the thermal damage) is initiated in those regions where the fluid is slowed down and the contact time with heating walls is longer. Computations show that there is species uniformity across the channel height (no gradient by passing from b to l regions) therefore results relative to b region will be presented only. In

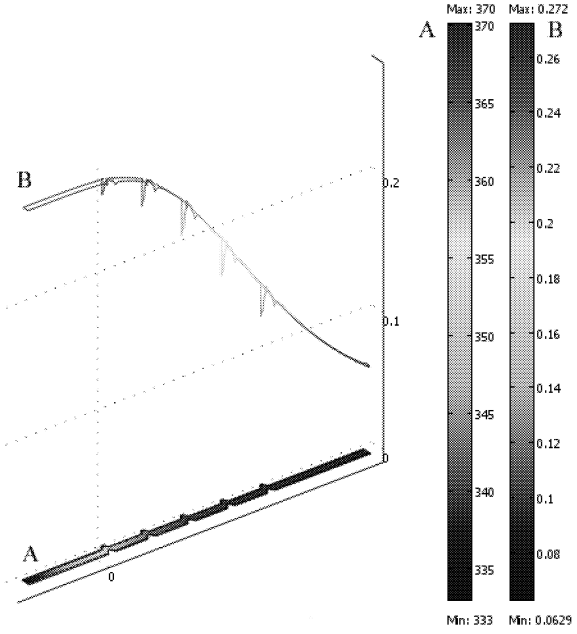

Figure 5: Effect of T (A) on c_{Nb} (B).

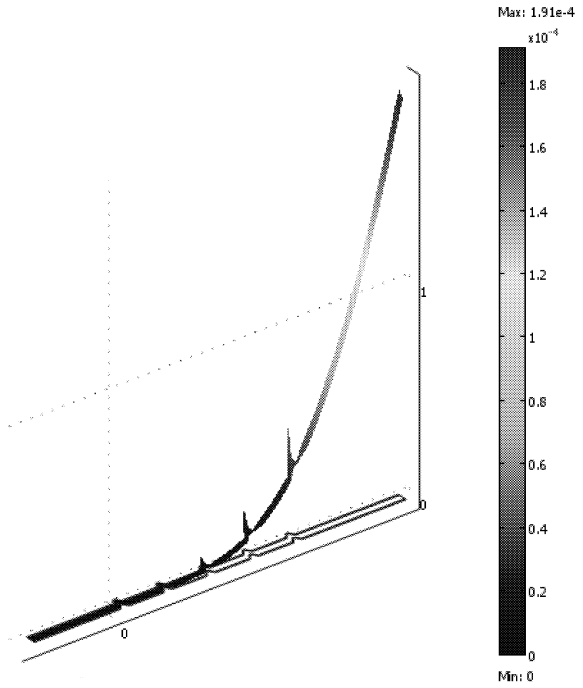

Figure 6: c_{Ab} distribution.

Fig. 5.A the temperature increase is clearly correlated to the depletion of βLG$_N$ in Fig. 5.B: at channel outlet, but also locally in each superior vane, due to the aforementioned fluid flow effect. In Fig. 5 two colored scale are also provided, to allow quantification of temperature (from 60 to 97 °C), and molar concentration c_{Nb} (from 0.06 to 0.27 mol/m^3).

Figure 6 evidences the nonlinearity of the phenomena: from comparison with Fig. 5, it is seen that the c_{Ab} is not simply complementary to the c_{Nb}.

Finally, it is seen that the most of the fouling is created in the outlet section of the channel, Fig. 7.A, while it appears also downwind of last corrugation (1), as well

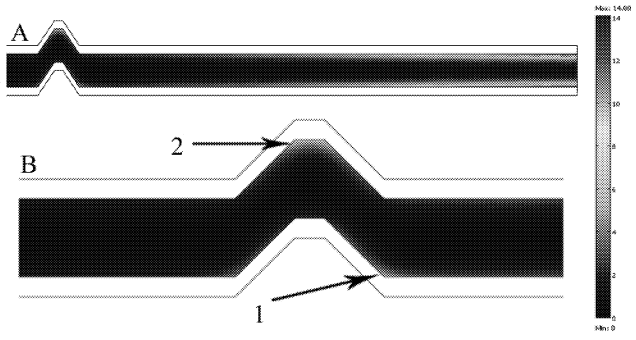

Figure 7: c_{Fb} distribution at outlet (A) and last corrugation (B), with different zones 1 and 2.

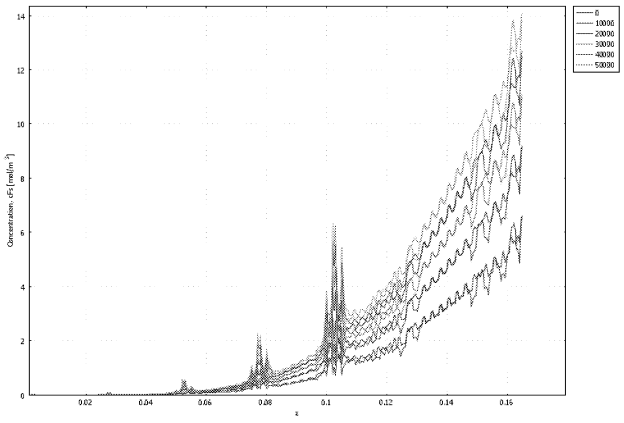

Figure 8: c_{Fb} evolution along the channel length, during a 14 h period.

as its corresponding vane (2) in Fig. 7.B. In Fig. 8 the fouling's time evolution is reported along the channel, for 5 times from PHE start–up. The formation of the deposited protein is nonlinear with time, as accretion rate decreases. This Figure also serve as preliminary validation with both (Georgiadis and Macchietto 2000) and (Jun and Puri 2006), as converting from molar concentration to volume fraction, and integrating the curve at 7 h, the total value of about 5 g of fouling is calculated, which compare favorably.

FUTURE IMPLEMENTATIONS

It is then confirmed that the fouling formation is strictly dependent upon the wall temperature distribution, but also on flow deceleration that impede solid deposition by fluid abrasion. As mentioned earlier, fouling results in expensive down–time and cleaning of heat exchanger devices in industrial systems. In biotechnology applications, plate profiles have never been studied so far to lengthen the down–time due to protein, enzyme, microbial kinetics interaction with heat and fluid flow. An interesting potential exists, therefore, to find optimal PHE geometries, for each working fluid, that may extend PHE working cycles. In particular, NURBS representations (nonuniform rational B-spline) will be employed to investigate on the potential of geometry optimization.
Also, Navier-Stokes equations interdependence with biochemistry can more more intriguing than the results shown so far. In particular, NS equations can be perturbed by localized fouling. The resulted velocity distribution can alter nonlinearly the biochemistry: favoring excess fouling and/or favoring inadequate heating load and sensory (Non–enzymatic browning) and functional features of fluid food. The perturbation of flow due to fouling accretion can be done by increasing in some finite element of the mesh the viscosity of flow, to a very large value which will result in a representation of a solid, with negligible velocity values. The cut–off condition to vary the viscosity can be set as a condition of maximum molar concentration in the given finite element. Local over–heating can then be accounted for, depending on the increase of wall conductive resistance due to fouling accretion.

CONCLUSIONS

CFD modelling can prove useful in product, process and system design, and in real–world problem resolution in the food and biotech industry. In this work the fouling by βLG has been attacked by a commercial Finite Element solver, applying a well-established modelling to corrugated–plate heat exchanger during pasteurization of milk. Local species concentration, velocity and temperature can be described to test new corrugation shapes and orientations, to minimize fouling. In this way, innovative configurations and designs can be inferred and proposed.

ACKNOWLEDGEMENT

Dr. G.L. Zanotelli of COMSOL s.r.l. is gratefully acknowledged for his help with the software.

REFERENCES

[1] Burton, H. 1988. Ultra–high temperture processing of milk and milk products. Elsevier Applied Science, London, UK.

[2] Georgiadis, M.C., G.E. Rotstein and S. Macchietto. 1998. "Modelling and Simulation of Complex Plate Heat Exchanger Arrangements under Milk Fouling." Computers Chemical Engineering 22, 331-338.

[3] Georgiadis, M.C., and S. Macchietto. 2000. "Dynamic modelling and simulation of plate heat exchangers under milk fouling." Chemical Engineering Science 55, 1605-1619.

[4] Grijspeerdt, K., L. Mortier, J. De Block and R. Van Renterghem. 2004. "Application of Modelling to Optimise Ultra High Temperature Milk Heat Exchangers with Respect to Fouling." Food Control 15, 117-130.

[5] Jun, S. and V.M. Puri. 2004. "Fouling models for heat exchangers in dairy processing: a review." Journal of Food Process Engineering 28, 1-34.

[6] Shah, R.K., E.C. Subbarao and R.A. Mashelkar. 1988. Heat transfer equipment design. Hemisphere Publishing Corporation, Washington, DC.

EFFECT OF REDUCED TEMPERATURE DURING EVAPORATION AND CRYSTALLISATION ON SUGAR QUALITY AND ENERGY DEMAND AT SUGAR PRODUCTION – MODEL BASED SIMULATIONS

Quido Smejkal
Arash Bagherzadeh
Rudolf Schick
Lutz-Günther Fleischer
Tomas Kurz
Department of Food Process Engineering
Technische Universität Berlin
Amrumer Str. 13, 13353 Berlin
Germany
E-mail: Tomas.Kurz@tu-berlin.de

KEYWORDS

Sugar Production, Model, Optimisation, Temperature Dependency, Energy Demand, Quality.

ABSTRACT

The industrial crystallisation of sugar is usually carried out in 3 or 4 stages. While applying a 3-product sugar end scheme only sugar from the first stage is sold. If a 4-product scheme is assumed only sugar from the first two stages can be traded due to limitations on sugar colour in solution. Because of quality regulations sugar from all the other stages should be dissolved and crystallised again which leads to elevated engineering and energy costs and also to extensive sucrose loss.
The decrease in quality between particular crystallisation steps depends on the enrichment of non-sucrose components in the mother liquor. Among all these non-sucrose substances the colorants are of peculiar importance since their concentration in the final product (sugar) is strictly limited. A close and statistically proven dependence between colour concentration in magma and sugar colour was found. This function shows that an improvement in sugar quality could be only realised by decreasing the colour loading of magma solution.
The results of the presented study show that the reduction of temperature in evaporation and crystallisation is feasible and technologically reasonable. The purpose of the project is achieved - the proposed reduction of temperature results in improved sugar yield, better sugar quality and lower steam consumption.

INTRODUCTION

The most important factors influencing colour formation and sucrose degradation are time and temperature. Furthermore, also pH value and amount of reduced sugars and amino acids play a considerable role. The colour formation depends linear on time and exponential on the temperature. Due to the application of falling-film evaporators the reduction of residence time in evaporation is already exploited and thus, sucrose degradation and colour formation could be minimised mostly by temperature decrease. However, lower temperature in evaporation influences the energy utilisation of a sugar factory. Therefore the influence of reduced temperature during evaporation and crystallisation on sucrose losses, colour formation and crystallisation rate on the one hand and energy requirements on the other hand was investigated in more detail at Berlin Sugar Institute. Based on these results the aim of this work was to develop a model based simulation tool based on the commercial software SUGARS™ which allows a preevaluation and optimization of different processing strategies in the sugar production.

EXPERIMENTS

Sucrose degradation and colour formation

For better understanding of sucrose degradation the invert sugar formation was investigated and the kinetics of the sucrose degradation were determined. Hence, the formation of invert sugar at given reaction conditions (temperature, residence time) could be calculated.
The activation energy of sucrose degradation of 108,9±14 kJ/mol follows from the kinetic measurements. This value is in a very good agreement with previous results (Bohn 1970).
Based on the kinetic experiments the dependence of reaction rate on the temperature was determined by colour formation. The experiments gave a time-dependence of a colour index for any reaction temperature. It is a linear function for short time periods (Westphal et al, 1996). That means, the colour formation could be described as a first-order reaction for the initial conditions of the non-enzymatic browning reaction (Smejkal et al., 2005). The reaction rate is derived from the slopes of colour increase *dF/dt* (1):

$$\frac{dF}{dt} = k \qquad \text{[IU/min]} \qquad (1)$$

The formal kinetic constants ***k*** [IU/min] have been determined for all experimental conditions. The reaction rates for different temperatures enable the calculation of the activation energy E_a according to the theory of the reaction kinetics, see Equation (2):

$$\frac{\partial \ln k}{\partial \vartheta} = \frac{E_a}{RT^2} \qquad (2)$$

The integrated form of this equation is the Arrhenius equation, which describes the dependence of kinetic constants k on temperature:

$$k = k_\infty . \exp\left(\frac{-E_a}{RT}\right) \quad \ln k = \left(\frac{-1}{RT}\right) E_a + \ln k_\infty \qquad (3)$$

where k_∞ is the frequency factor. If the natural logarithm of kinetic constant is plotted against *-1/RT*, the slope of this curve represents the activation energy of the overall chemical reaction for a given temperature interval.

At temperatures below 100°C, the activation energy of colour formation is equal to 76,8±3 kJ/mol ($\ln k_\infty$=26,85±0,9). The activation energy at temperatures above 100°C reaches 112,1±2,7 kJ/mol ($\ln k_\infty$=38,9±0,8). The kinetic constants k were measured with a residual from 0,068 below 100°C to 0,083 above 100°C. The standard deviation amounts 0,0768. The experimental data are within a confidence interval of 95%.

Furthermore, from results presented in Figure 1 could be derived that the final reaction step of the colour formation consists of two different mechanisms. The intersection of the reaction mechanism occurs at 100,4 °C.

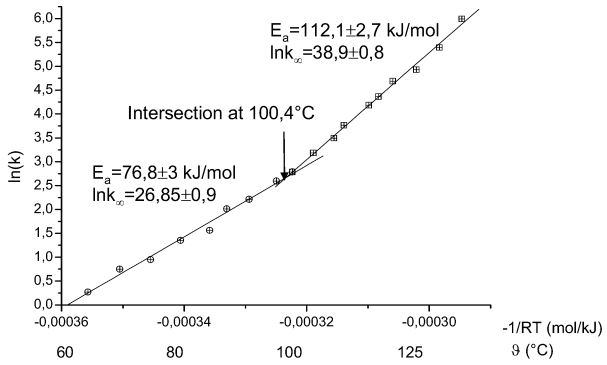

Figure 1: Kinetic constant k as a function of -1/RT

The influence of temperature and residence time on colour formation was also described by the equivalent heat effect times method founded by Vukov und Patkai, 1981. This simplified kinetic method enables to compare roughly the sugar degradation and therewith the connected colour formation at different temperatures. It is defined as an equilibrium heat effect time t_e, which is coupled with residence time and reference temperature of 100°C by equation 4:

$$\log \frac{t_e}{t} = \frac{(\vartheta - 100)}{Z} \qquad [\theta]=°C \qquad (4)$$

where Z-Parameter is a pseudo-kinetic constant and amounts for temperatures below 100 °C 24K and above 100 °C 27 K. The application of this method is limited to temperatures from 80 to 120°C. The original kinetic method of Vukov was modified using own kinetic data and the period of validity was extended to 60-135°C. The reaction mechanism of colour formation is changing at 100,4 °C (see above Figure 1). Indeed, a modification of original reference temperature of 100,0 °C in the equation 1 has almost no influence on the calculation.

The analysis of own kinetic data results for temperature interval 65-100°C to the Z-Parameter of 31 K. This value was evaluated from experiments with four different types of juices (two thick juices, two types of A-sugar run-off). For temperatures from 100 to 130°C Z-value corresponds to 26 K.

Crystallisation

Reduced temperature in evaporation influences crystallisation rate. Therefore, the influence of temperature on the crystallisation was investigated. The cooling crystallisation experiments were performed in isothermal mode. The dependence of crystallisation rate on supersaturation between 1,08 and 1,15 for thick juice crystallisation is roughly linear. The experimental results are presented in Figure 2. The standard deviation is equal to 0,02 and experimental data lie within a confidence interval of 93%.

The results from Figure 2 show that the decrease of crystallisation temperature from common 70°C to modified 60°C at chosen supersaturation of 1,1 causes reduction of crystallisation rate of approximately 30%. That is in a good agreement with previous published results (Ekelhof 1997). Moreover, from the results presented in Figure 2 it can be concluded that the decrease of crystallisation rate at lower temperature could be compensated by slight increase of the supersaturation (see dashed line in Figure 2). E.g. crystallisation rate remains almost constant for conditions demonstrated in Figure 2 (crystallization temperature 70°C and supersaturation of 1,1 or 60°C and 1,13, respectively).

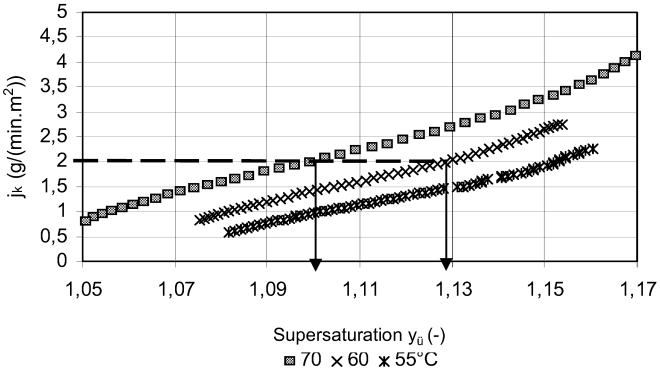

Figure 2: Evaluation of experimental results for thick juice crystallisation experiments (purity 93 %) at temperatures of 55, 60 und 70 °C

Similar dependence was also found at crystallisation from A-sugar run-off.

ENERGY ORIENTED PROCESS SIMULATIONS

To analyse the technological and economical influence of changed temperature profiles on the energy requirements energy-oriented process simulations were performed. A modified process variant with lower temperature in evaporation (maximal juice temperature of 110 °C) and crystallisation (A-sugar station working at 60 °C, B-sugar at 65 °C, see also Figure 2) was presented and compared to the basic process variant (maximal juice temperature of 129,7 °C, A-sugar station 70°C, B-sugar station 75 °C). At modified process variant the sugars from both A- and B-

stations were blended together in EG 2 quality. Slicing capacity in both process variants is equal to 12 000 t/d.
Crystallisation was performed in three stages. The available temperature difference in all crystallisation steps amounts at least 15 K. This demands in the condensation a pressure of approx. 0,1 bar.
The process parameters of both process simulation variants are summarised in Table 1.

Table 1: Process parameters of the simulation

	basic variant	modified variant
Heat consumption (kg/100 kg beet)	19,26	18,81
Heating surface area– juice preheating (m^2)	2100	3400
Heating surface area– evaporation (m^2)	26000	27000
Condenser losses (%)	<0,1	<0,1
Thick juice dry substance (%)	73,07	73,0
Maximal juice temperature (°C)	129,7	109,9
No. of evaporation effects	5	6
Exhaust steam pressure (bar)	3,1	1,85

The calculation of k-Values [W/(K*m^2)] in falling-film tube-bundle evaporators, including its temperature dependence, was made based on GEA-Wiegand equation. The formation of colour in sugar production was calculated using for this purpose developed kinetic model (see above).
Juice pre-heating and purification were performed in the same manner, the juice was pre-heated in three heat exchangers. The results of juice purification and pre-heating by process simulations from SUGARS^{TM} program are presented in Tables 2 and 3.

Table 2: Temperature profile in basic variant

Medium	$\dot{m}$	ϑ_{in}	ϑ_{out}	Heating medium	ϑ_{in}	A	k-value
	t/h	°C	°C		°C	m^2	W/(K.m^2)
Press water	225,2	64,9	70,0	Vapour 5	96,4	25	2100
Circulation juice	350	64,1	78,0	Vapour 5	96,4	112	1900
Raw juice I	572,98	27,8	41,6	Falling water	52,0	340	1800
Raw juice II	572,98	41,6	49,6	Falling water	55,8	330	1800
Raw juice III	572,98	49,6	55,0	End condensate	67,6	152	2000
Prelimed juice 2-I	587,9	54,8	74,0	End condensate	100,0	320	2000
Prelimed juice 2-II	587,9	74,0	80,0	Vapour 5	96,4	99	2000
Prelimed juice 2-III	587,9	80,0	83,0	Vapour 4	105,9	51	2000
Juice to filtration	619,3	82,5	88,0	Vapour 4	105,9	102	2400
Thin juice I	555,38	86,3	93,0	Vapour 4	105,9	170	2400
Thin juiceIII-1*	461,9	96,4	104,0	Vapour 3	116,6	77	3400
Thin juice III-2	461,9	104,0	115,0	Vapour 2	123,9	126	3400
Thin juice III-3	461,9	115,0	125,0	Vapour 1	129,7	184	3400
				Total heating surface area		2088	m^2

*Heating after pre-evaporation in 3 stages

Table 3: Temperature profile in modified variant

Medium	$\dot{m}$	ϑ_{in}	ϑ_{out}	Heating medium	ϑ_{in}	A	k-value
	t/h	°C	°C		°C	m^2	W/(K.m^2)
Press water	225,2	64,6	70,0	Vapour 6	76,0	290	2100
Circulation juice	350	64,1	78,0	Vapour 5	80,7	320	1900
Raw juice I	572,98	27,8	39,9	End condensate	68,0	160	1900
Raw juice II	572,98	39,9	55,0	Vapour 6	76,0	220	1900
Prelimed juice I	587,9	54,8	65,9	End condensate	87,0	190	2200
Prelimed juice II	587,9	65,9	79,0	Vapour 5	80,7	750	2000
Prelimed juice III	587,9	79,0	83,0	Vapour 4	89,9	220	2000
Juice to filtration	619,3	82,5	88,0	Vapour 3	97,4	140	2400
Thin juice I	555,38	86,3	93,0	Vapour 3	97,4	290	2400
Thin juiceIII-1*	479,2	80,7	95,0	Vapour 3	97,4	410	3400
Thin juice III-2	479,2	95,0	100,0	Vapour 2	103,6	160	3400
Thin juice III-3	479,2	100,0	107,0	Vapour 1	109,9	210	3400
				Sum of heating surface area		3360	m^2
				Heating surface area increase		1272	m^2

*Heating after pre-evaporation in 3 stages

The function of A-sugar and B-sugar VKTs in sugar house was fitted based on crystallisation rate measurements (see also assumptions of process simulations). C-sugar station was not modified and it worked in both process variants at comparable conditions. Schemes of evaporation and crystallisation in the basic as well as in the modified process variant are given in Figure 3 and 4.

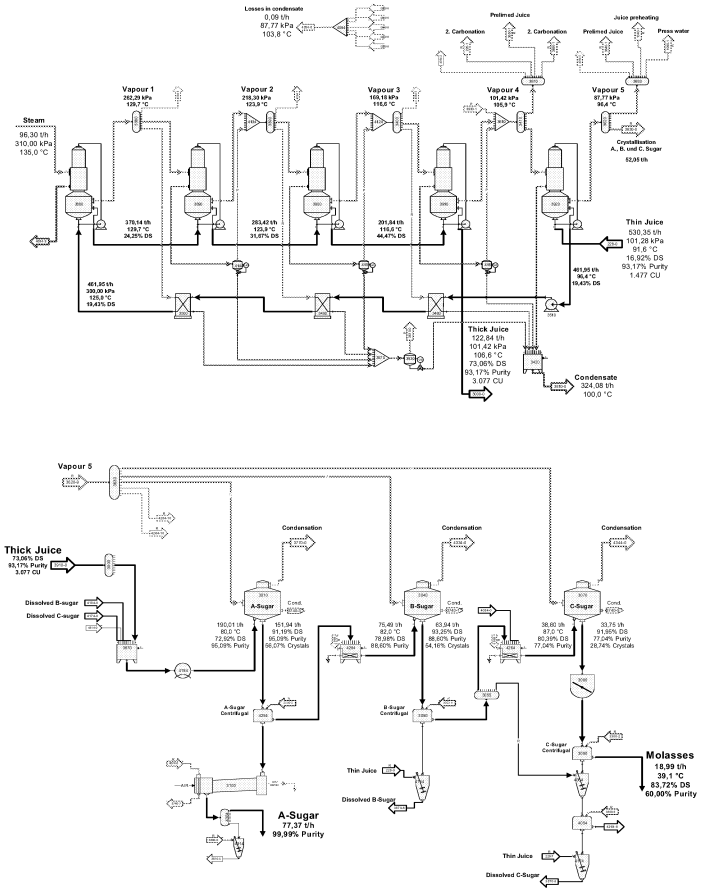

Figure 3: Scheme of evaporation and crystallization in the basic process variant

Economical consequences

Due to the lower water evaporation in the crystallisation is the steam consumption in the modified variant decreased by 0,45 kg/100 kg beet compared to the basic variant. Moreover, the blending of A-sugar together with B-sugar enables a significant reduction of A-sugar station loading. The mass flow from the A-station will be about 39 % lower than in the basic variant. At reduced temperature in both first crystallisation steps the decrease of the crystallisation rate in modified process variant could be compensated by slight increase of supersaturation in evaporating crystallisers. Thus, an extension of the crystallisation unit is not necessary. However, the heating surface area for evaporation and juice pre-heating should be increased by approx. 2300 m^2 compared to the basic variant, see Table 1.
Also, steam pressure from turbine entering first evaporation effect is reduced in the modified process variant. It is apparent that electricity production at almost same fresh steam consumption (compared to basic process variant) could be increased. Using fresh steam of 80 bar and 500°C the difference remains 2800 MWh for 90-days campaign and could be treated as an additional benefit of the modified process variant.

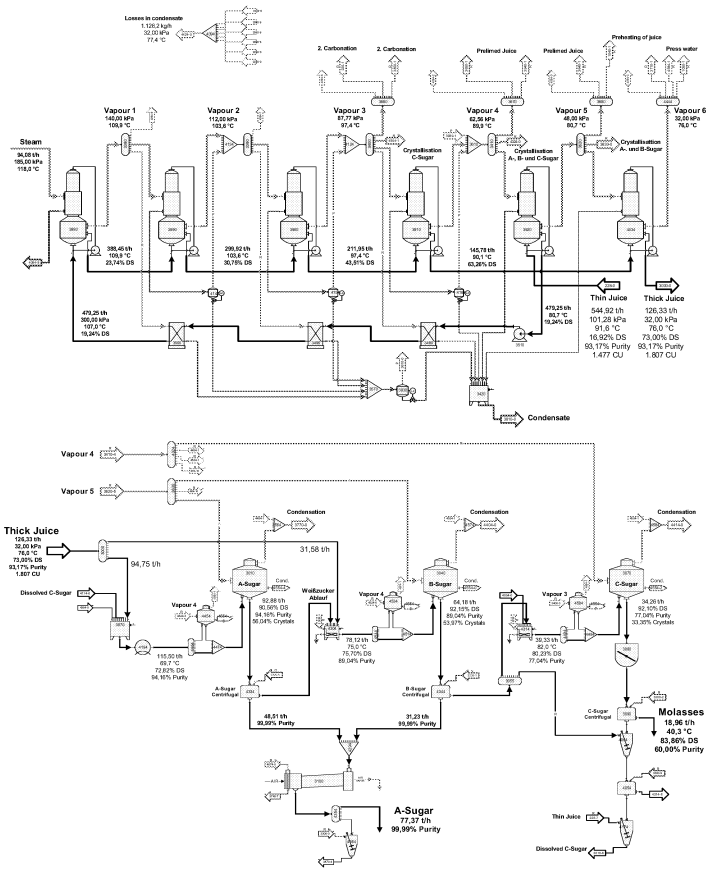

Figure 4: Scheme of evaporation and crystallization in the modified process variant

The sucrose losses are from economical point of view the most important parameter in the discussion of benefits of modified process variant. They amount (based on own kinetic calculation) in the evaporation 0,076 kg/100 kg beet in the basic variant and 0,015 kg/100 kg beet in the modified variant. In sugar house sucrose losses according to Vukov, 1972 are equal to 0,056 kg/100 kg beet in the basic variant and 0,033 kg/100 kg beet in the modified variant. The difference of 0,084 kg Sucrose/ 100 kg beet represents the benefit of the modified variant. Thus, the non-sucrose in the molasses will be also reduced by 0,0848 kg / 100 kg beet. Assuming sugar/non-sucrose ratio of 1,5, the sucrose content in molasses will be decreased of 0,126 kg/100 kg beet. The yield of the production will be therefore increased of 0,210 kg/100 kg beet. However, the dry substance in molasses will be reduced of the same amount.

CONCLUSIONS

During the non-enzymatic browning experiments with a technical aqueous sucrose solution was found that the reaction rate of overall reaction depends very strongly on temperature. At lower temperature between 65° - 100 °C is the colour formation suppressed. For higher reaction (exposition) temperature increases the rate of non-enzymatic browning reaction. At temperatures below 100°C, the activation energy of colour formation is equal to 76,8±3 kJ/mol ($\ln k_\infty$=26,85±0,9). The activation energy at temperatures above 100°C amounts 112,1±2,7 kJ/mol ($\ln k_\infty$=38,9±0,8).

From crystallisation experiments is apparent that the decrease of crystallisation rate at lower temperature could be compensated by means of slight increase of supersaturation in crystalliser.

Based on the results from above mentioned experiments a model based simulation tool could be established which allowed the evaluation of different processing schemes in sugar production. In particular, the reduction of temperature levels during sugar production promises an improvement in sugar quality (colour) and sugar losses. However changes in processing are strongly related to the energy demand in different steps of the sugar production. The exemparily presented modified process variant shows an essential appreciable increase of required heating surface area at reduced loading of A-sugar crystalliser. On contrary, it can be shown that the undefined sucrose losses could be reduced and the overall yield of the sugar factory can be thus slightly increased. Moreover, significantly reduction of colour formation results in high quality of B-sugar which could be sold together with A-sugar. Therefore was additionally reduced also loading of A-sugar station of about 39% in the modified variant. Finally, it can be stated that the simulation tool allows the prediction of the complex relations between qualitative, energetic, apparative and conomical aspects in sugar production.

ACKNOWLEDGEMENT

The financial support from

- German Federation of Industrial Cooperative Research Associations “Otto von Guericke” No.: 13584N
- Nordzucker AG
- Pfeifer & Langen KG

is gratefully acknowledged.

REFERENCES

Bohn, K. 1970, „Untersuchungen über den Saccharoseabbau in alkalischer Lösung bei Temperaturen über 100° C“, Dissertation B, Humboldt Universität zu Berlin.

Ekelhof, B. 1997, „Gesamtmodell der Kristallisation der Saccharose in reinen und unreinen Lösungen“, Dissertation, Braunschweig

Smejkal, Q., Schick, R., Fleischer, L.-G. 2005 “Influence of reduced temperature during evaporation and crystallization on sugar quality”, SIT Conference Dubai, VAE, Book of Abstracts, Paper 873

Vukov, K. 1972, „Physik und Chemie der Zuckerrübe als Grundlage der Verarbeitungsverfahren“, Akademia, Budapest

Vukov, K., Patkai, G. 1981, „Rechnerische Methode zur Ermittlung von äquivalenten Wärmeeinwirkungszeiten für den Zuckerabbau in Säften“, Zuckerindustrie, 106, pages 314-318

Westphal, G., Buhr, H., Otto, H. 1996, „Reaktionskinetik in Lebensmitteln“. Springer Verlag, Berlin

BIOGRAPHY

QUIDO SMEJKAL studied chemical engineering at Prague university and obtained his PhD in 1999. Between 1999 and 2005 he was engaged in different projects at TU Berlin Dep. of Catalysis and Dep. of Food Process Engineering. Since

2006 he is working as a self-employed project engineer in Berlin.

RUDOLF SCHICK
studied Sugar Technology at Humboldt University in Berlin from 1961-1966. Afterwards, he worked in industry until he became a scientific assistant at Humboldt University in 1970. He obtained his PhD

LUTZ-GÜNTHER FLEISCHER Head of the Dep. of Food Process Engineering TU Berlin since 1995. Professor for Food Process Enginnering at Humboldt University Berlin since 1979.

TOMAS KURZ studied Brewing and Beverage Technology at TU München. He worked at the Dep. of Fluidmechanics and Process Automation of TU München as head of process automation group from 1997 to 2003. He obtained his PhD in 2002. In 2003 he obtained a junior-professorship at TU Berlin Dep. of Food Process Engineering.

DIFFUSION AND DISPERSION

ESTIMATION OF THE EFFECTIVE DIFFUSION COEFFICIENT OF WATER IN FRESH VEGETABLES

Maria Aversa
Stefano Curcio
Vincenza Calabrò
Gabriele Iorio
Department of Chemical Engineering and Materials
Ponte P.Bucci - Cubo 45/a
University of Calabria, Rende (CS) ITALY
Tel. +39 0984496 670/711/703/709 – Fax +39 0984496655
E-mail: maria.aversa@unical.it; stefano.curcio@unical.it; vincenza.calabro@unical.it; gabriele.iorio@unical.it

KEYWORDS

Diffusivity, Water, Eggplants, Drying, Halogen.

ABSTRACT

Food process modelling involves the resolution of balance equations defined in terms of chemical, physical and transport properties. These properties are difficult to evaluate since they depend on food structure and composition that change during processing. Some food properties, i.e. the density and the specific heat, obey the rule of additivity (Lewiki 2004): this assumption, however, is not valid for other properties such as thermal conductivity and mass diffusivity (Lewiki 2004, Maroulis, Krokida., Rahman 2002). Water diffusivity is one of the most important transport properties since food drying rate strongly depends on how water moves through food structure. During drying, both food moisture content and temperature change significantly, thus affecting diffusion coefficient values. The aim of this work is to determine, on the basis of the so-called drying method, a relationship between water diffusivity, food temperature and food moisture content for an eggplant slab and to test a novel experimental procedure that allows obtaining the drying curves by means of a Halogen Moisture Analyzer.

INTRODUCTION

The mass transfer mechanism in a solid material is less well understood than in fluid systems, so that empirical approaches are often used to estimate the transport properties. Food structure changes during processing and storage, for this reason diffusivity of water is mainly determined by experimental techniques.
There are several methods for diffusivity estimation involving defined geometries, and well-defined experimental conditions (steady state or transient conditions).
The permeability method consists in placing a thin sheet of solid material between two environments at constant water concentration and temperature. When steady state conditions are attained and a linear concentration gradient develops, diffusivity (or permeability) can be determined by applying the first Flick's law (Bird, Stewart, Lightfoot 1960).
The concentration–distance curve method consists in measuring, as a function of time, the moisture concentration profile developing within the sample. The diffusion is supposed to occur essentially along one dimension and the solute concentration profile along this dimension is estimated by slicing and weighing the samples (Saravacos, Maroulis 2001).
In sorption /desorption methods the sample weight is measured at regular times in order to evaluate the moisture increase/ loss. The moisture increase/ loss is estimated under constant and controlled air conditions (temperature, velocity and humidity). In the drying method, only the falling rate period, i.e. the period when the drying rate is controlled by water transport within the material, is considered. The analytical solution of Flick's diffusion equation provides the value of diffusivity (Saravacos, Maroulis 2001).
It is important to note that all the above methods are based on the assumption that the external resistance to moisture transfer is negligible. None of them is a standard method. The published values present a huge variability which is due either to the different experimental methods available, or to the variability of structure and composition of the tested products (Panagiotou, Krokida, Maroulis, Saravacos 2004).
The "drying" method is more suitable for food drying process, whereas sorption method is applicable to moisture adsorption during food storage.
The aim of this work is to determine, on the basis of the drying method, a relationship between water diffusivity, food temperature and food moisture content and to and test a novel experimental procedure that allows obtaining the drying curves by means of a Halogen Moisture Analyzer.

THEORY

Three main stages can be distinguished in drying process. During the first stage, called the *constant rate period*, the

process is controlled by external mass transfer; the water leaving the sample is not bounded to food structure *(free water)* and drying rate attains its maximum value. Afterwards, during the so called *falling rate period*, the process rate is controlled by internal mass transfer and a progressively decrease of drying curve slope can be observed. In the third period, drying rate attains a value approaching zero because the evaporation front moves from food surface towards the food centre increasing mass transfer resistance. Drying methods can be distinguished in two types: methods evaluating a constant diffusivity and methods evaluating a variable diffusivity.

Drying Method for water diffusivity estimation

The determination of moisture diffusivity is carried out during the falling rate period by the application of the diffusion equation to the food sample of known initial dimensions (Hassini, Azzouz, Belghith 2004).
Flick's diffusion equation applies under the hypothesis of mono-dimensional moisture transport:

$$\frac{\partial C}{\partial t} = \frac{\partial}{\partial z}\left(D \frac{\partial C}{\partial z} \right) \qquad (1)$$

the diffusion coefficient D of water in solids is actually an effective diffusivity (m^2/s), that is to be considered as an overall transport property, accounting for all the transport mechanisms. C is the moisture concentration in food (mol/m^3), t is the time (s) and z is the dimension (m). Equation (1) is solved assuming uniform initial moisture distribution, negligible external resistance, isothermal conditions and constant diffusivity (Crank, 1975, Hassini , Azzouz , Belghith 2004). Therefore, for a very thin slab the moisture transport is described by the equation:

$$\frac{X - Xe}{Xo - Xe} = \frac{8}{\pi^2} \sum_{n=0}^{\infty} \frac{1}{(2n+1)^2} \exp\left(-\frac{(2n+1)^2 \pi^2 Dt}{4L^2} \right) \qquad (2)$$

where X is the mean moisture content (-) at time t, X_o is the initial moisture content (-), X_e is the equilibrium moisture content (-), and L is the sample thickness (m). The moisture content X is expressed on dry basis, i.e. as kg water/kg dry matter.
Another simplified approach to predict drying kinetics, has been introduced by the so called "thin layer equation" (Ertekin & Yaldiz (2004), Doymaz (2004), Krokida, Karathanos, Maroulis & Marinos-Kouris 2003))

$$-\frac{dX}{dt} = K(X - Xe) \qquad (3)$$

The above equation is valid when the material is thin enough, and/or the air velocity is high enough, so that the drying conditions are constant throughout the material. Integration of thin layer equation leads to

$$\frac{X - Xe}{Xo - Xe} = \exp(-Kt) \qquad (4)$$

Where K is an empirical constant (a combination of several transport properties) called the "drying constant" (s^{-1}). Comparing Equation (4) and the first term of the series solution of Equation (2), the drying constant K can be related to the moisture diffusivity by the relation

$$K = \frac{\pi^2 D}{L^2} \qquad (5)$$

Where the term $\frac{8}{\pi^2}$ is considered approximately equal to unity. Equation (5) relates the empirical drying constant K, to the observed diffusion coefficient of water in the solid matrix. Considering Xe=0, the K value is the slope (Equation (3)), of lnX versus t plot that can be calculated from the *drying curves,* i.e. from the food weight versus t curves obtained during drying process.
During drying process, changes in food structure actually take place; for this reason, moisture diffusivity changes significantly with moisture content, food temperature and its structure. Different drying methods can be applied to account for diffusion coefficient variability, the approach used in this work is the so-called *method of drying constants.* It is based on the assumption that the drying curve can be subdivided into linear parts in order to apply the *method of constant diffusivity* to each of them.

MATERIALS AND METHODS

In this work, instead of a traditional convection oven, a Halogen Moisture Analyzer ((HB43, Mettler Toledo)) was used to obtain the drying curves. It consists of a small chamber, where the food to be dried is placed. The weight loss of the product subject to drying is monitored during the process by a precision balance. The heat necessary for water evaporation is provided by a halogen lamp. The proposed method is cheaper than a convection oven; moreover it is much simpler to obtain the experimental drying curves necessary to estimate moisture diffusion coefficient. The material under investigation was the eggplant since literature data about this vegetable are rather poor. The application of the above-described drying methods is based on the assumption that both external heat and mass transfer resistances are negligible. In convective oven this is guaranteed by the high values of air velocity; in the present case, the curves were processed to select the actual range of drying process in which external transfer resistance is negligible. This conditions has been verified analyzing the semi-logarithmic plots of (X/Xo) versus t: low (negative) slopes of drying curve indicate that external resistance to mass transfer prevails, whereas high (negative) slopes of drying curve characterize internal resistance (Mulet, 1994, Saravacos Maroulis 2001).

Eggplant purchased in local market were peeled and sliced. All the slices necessary for experimental tests had the same dimensions (radius and thickness) A single slice was submitted to drying into the Halogen Moisture Analyzer at fixed air temperature conditions.
Two different values of initial slab thickness were investigated: 0.6 cm and 0.8 cm , each thickness value was submitted to drying experiments under the following conditions

- air relative humidity : 45%
- air temperature : 60°C, 70°C, 80°C, 90°C

Each measure was repeated twice.
It should be observed that the drying cell was open so to attain air recycle inside the drying chamber. Air humidity was, therefore, monitored with an external hygrometer assuming that the air humidity in the drying chamber equals to the external air humidity. The sample weight was registered by the balance on which eggplant was placed while drying proceeded.
In this way the curves *X* versus *t* were obtained and the method of drying constant was used. The application of Equation (5) in variable diffusivity method requires a measure of the actual eggplant thickness. This was attained removing periodically the slab from the chamber and measuring its radius and thickness during drying in the shorter time possible.

RESULTS AND DISCUSSION

Figures 1 and 2 show the drying curves (X/Xo) versus time for 0.6 cm and 0.8 cm slab thickness, respectively . In both figures the effect of temperature on drying time can be observed, an increase in air temperature decreases the time necessary to reach a predefined value of final moisture content. All the curves in figures 1 and 2 show the above mentioned three stages, characteristic of a drying process; each curve includes the c*onstant rate period*, the *falling rate period* and the "*approaching zero" rate period*, but only the falling rate period was used for moisture diffusivity estimation. In figures 3 and 4 the values of drying constant K versus time for 0.6 cm and 0.8 cm slab thickness are, respectively, shown. Temperature has a positive effect on K value; in fact an increase in temperature determines an increase in K value and also in moisture diffusivity value (since K and D are proportional according to equation (5)).

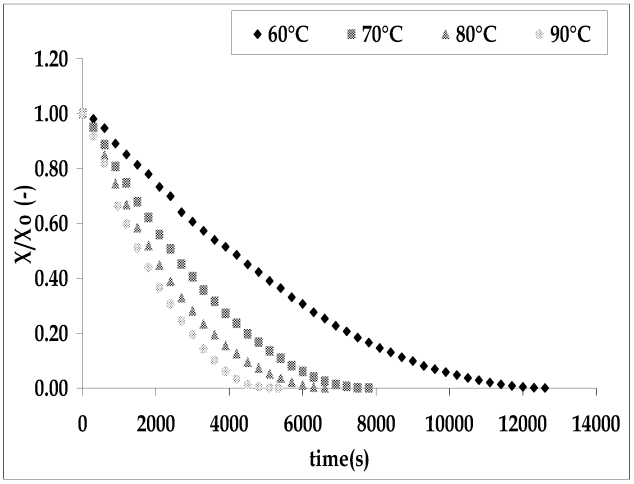

Figure 1: Normalized Eggplant Moisture content X/X_o versus Time at different Air Temperatures. (Slab thickness= 0.6 cm)

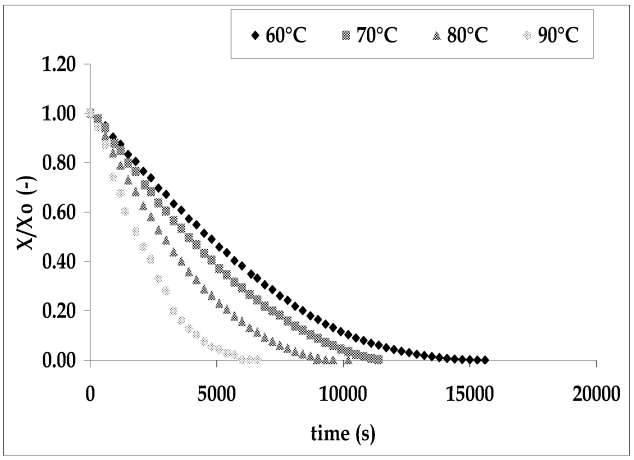

Figure 2: Normalized Eggplant Moisture content X/X_o versus Time at different Air Temperatures. (Slab thickness= 0.8 cm)

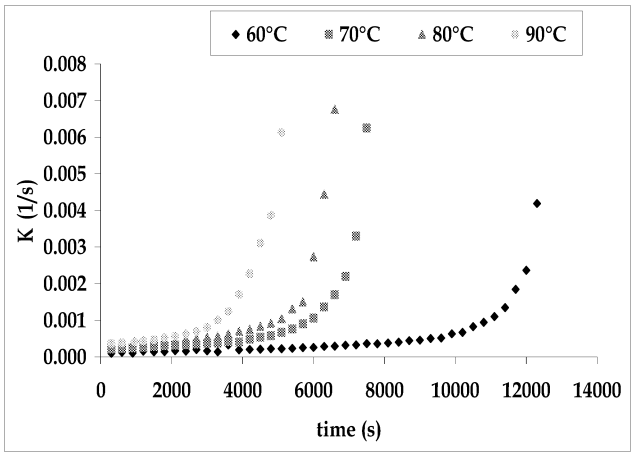

Figure 3: Drying Constant value versus Time at different Air Temperatures. (Slab thickness= 0.6 cm)

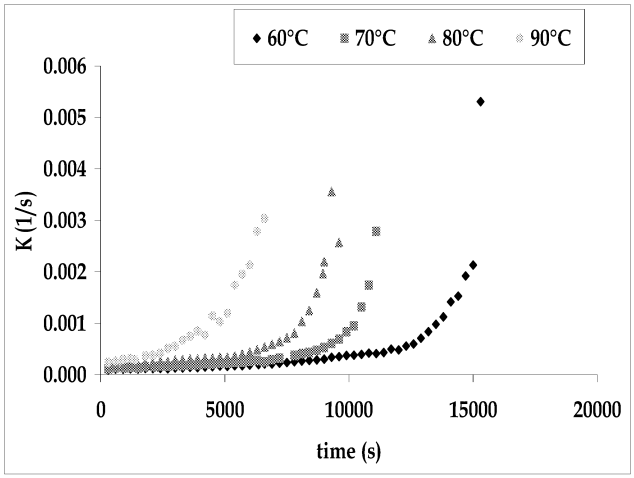

Figure 4: Drying Constant value versus Time at different Air Temperatures. (Slab thickness= 0.8 cm)

All the values of D, evaluated by Equation (5), at different temperature and moisture content, were finally fitted using the well known model proposed by Maroulis et al. 2001.

$$D=\frac{1}{1+X}\cdot Do\exp\left[-\frac{Eo}{R}\left(\frac{1}{T}-\frac{1}{Tr}\right)\right]+\frac{X}{1+X}\cdot Di\exp\left[-\frac{Ei}{R}\cdot\left(\frac{1}{T}-\frac{1}{Tr}\right)\right] \quad (6)$$

where D (m^2/s) the effective moisture diffusivity, Do (m^2/s) the moisture diffusivity of the dried material, Di (m^2/s) the moisture diffusivity of the wet material, X (-) the material moisture content, T (K) the material temperature, Tr (K) a reference temperature, Eo (kJ/mol) the activation energy for diffusion of the dried material, Ei (kJ/mol) the activation energy for diffusion of the wet material and R= 0.0083143 kJ/mol K the ideal gas constant. Figure 5 represents an example of regression analysis performed according to Equation (6), on the experimental data shown in Figure 1. Only the points belonging to the falling rate period were considered so to estimate the model parameters reported in Tab 1. For both the tested thickness it can be observed that activation energy for the dried material diffusion is higher than that of the wet material; this is an evidence that the interactions between water and food are stronger for a lower moisture content. Moreover the moisture diffusivities of both wet and dried material have the same order of magnitude even though effective diffusion coefficient is higher for the wet material For the thicker slab the values of Do and Di are higher than for the thinner one; the higher value of moisture diffusivity could represent an higher porosity development during drying since an increase in porosity is related to an increase of water diffusivity.
These results are in good agreement with those obtained for other vegetables (Saravacos, Maroulis 2001).

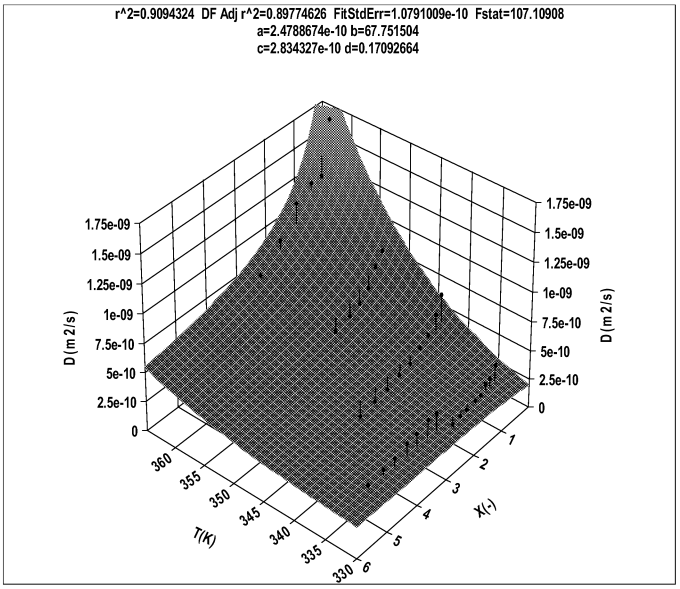

Figure 5:Experimental Data Regression Analysis (Initial eggplant thickness 0.6 cm)

Table 1: Model parameters in equation (6)

	Do(m^2/s)	Di (m^2/s)	Eo (kJ/mol)	Ei (kJ/mol)
Eggplant 0.6 cm	2.48e-10	2.83e-10	68	0.2
Eggplant 0.8 cm	3.47e-9	4.76e-9	100	11.4

CONCLUSIONS

Effective diffusion coefficient of water in eggplants was estimated at different conditions of moisture content and temperature. Drying curves were obtained by a Halogen Moisture Analyzer and the drying constants method was used to evaluate D value from experimental curves. The model parameters obtained after a regression analysis are

in good agreement with other vegetables (Saravacos, Maroulis 2001). These results confirm that the use of a Halogen Moisture Analyzer is a good experimental technique to obtain drying curves for diffusivity calculation. Furthermore, it is a simpler and cheaper tool for this purpose than convective drying ovens. The future prospective of this work regards the possibility of applying the above-described technique also to other food products. This will allow the estimated diffusion coefficients to compare with those obtained by more traditional, but also more expensive and time-consuming methods so to validate the proposed procedure.

REFERENCES

Bird, R.B., Stewart, W.E., Lightfoot, E.N. (1960). "Transport Phenomena" John Wiley & Sons, London, UK. Pag 511.

Crank J.. 1975 "The Mathematics of diffusion" 2nd ed. Oxford:Oxford Univ. Press. Page 48.

Doymaz, İ. (2004). "Convective Air Drying Characteristis Of Thin Layer Carrots" *J. Of Food Engineering*, 61, 359-364.

Ertekin, C., Yaldiz, O. (2004). "Drying Of Eggplant And Selection Of A Suitable Thin Layer Drying Model" *J. Of Food Engineering*, 63, 349-359.

Hassini L., Azzouz S., Belghith A 2004. "Estimation Of The Moisture Diffusion Coefficient Of Potato During Hot-Air Drying". *Proceedings of the 14th International Drying Symposium. IDS. San Paulo, Brazil, 22-25 August 2004, vol.B, pp1488-1495*

Hernàndez, J.A., Pavòn, G., Garcìa, M.A. (2000). "Analytical Solution Of Mass Transfer Equation Considering Shrinkage For Modeling Food-Drying Kinetics". *Journal Of Food Engineering*, 45, 1-10.

Krokida, M.K., Karathanos, V.T., Maroulis, Z.B., Marinos-Kouris, D. (2003). "Drying Kinetics Of Burdens Vegetables". *Journal Of Food Engineering*, 59, 391-403.

Lewicki P.P 2004. "Water as determinant of food engineering properties. A review". *Journal of food engineering* 61 (2004) 483-495

Maroulis Z.B., Krokida M.K., Rahman M.S 2002. **"**A structural generic model to predict the effective thermal conductivity of fruits and vegetables during drying". *Journal of food engineering* 52 (2002) 47-52

Mulet, A.1994. "Drying Modeling of water diffusivity in Carrots and Potatoes". *Journal of food engineering* 22:324-348

Panagiotou N.M., Krokida M.K., Maroulis Z.B., Saravacos G.D.2004." Moisture Diffusivity: literature data compilation for foodstuff". *International journal of food properties* 7 (2): 273-299 jul 2004.

Saravacos G.D., 2001 Maroulis Z.B."Transport properties of food" . *Dekker* . (cap 5 pp14, 41, cap 6 pp 200, 202)

BIOGRAPHY

Maria Aversa was born in Crotone, Italy in 1977. She obtained her degree in Chemical Engineering at the University of Calabria in 2003. She is currently Ph.D student at the Department of Chemical Engineering and Materials. Her research interests are the food process modelling by finite elements method and the determination of physical and transport properties in foods.

TAXONOMY OF RECENT POPULATION DYNAMICS MODELS OF ANIMAL INFECTIOUS DISEASES

Thi Le Hoa Vo and Daniel Thiel
University of Nantes and E.N.I.T.I.A.A. Nantes, LARGECIA-CRGNA
Rue de la Géraudière - BP 82225
44322 Nantes Cedex 3
France
E-mail : thilehoa.vo@enitiaa-nantes.fr

KEYWORDS

Epidemic dynamic modeling, Animal Diseases, Food contamination, Simulation models, Taxonomy.

ABSTRACT

It is in a PhD research framework which consists in modeling the whole poultry supply chain confronted to bird flu crisis that this paper will focus on the downstream chain, particularly on the supplying problems resulted from such epizooties. Moreover, in order to develop our future supply chain system dynamics model, it is necessary to record different population dynamics models of animal infectious diseases that result in food safety crisis. We recognized that mathematical modeling of epidemics is a very active field of research that crosses different theoretical areas. Hence, grounding on miscellaneous models types, we attempt to present taxonomy of some current epidemic simulation models basing on well-judged categorizations: deterministic *versus* stochastic models, spatial and temporal treatments. Given the result of this work, we have justified a multiagent model for chicken influenza spread.

INTRODUCTION

Nowadays, the study of complex systems involving epidemics modeling is investigated seriously. Propagation of infection in a population is complex as the system changes and adapts to exogenous (e.g., seasonal variations in the contact rate) as well as endogenous factors (e.g., herd immunity, prevalence of cases). Actors (individuals) in complex systems are interdependent and institute a dynamics that cannot be represented by static or linear statistical models. It seems that epidemic simulation models allow us to approach moderately complex systems and understand the interdependence between the individuals that constitute the system.

It is important to underline that this paper is justified by a new PhD research which tackles on food supply chain behavior and cooperation between economic deciders in a context of sanitary crisis, mostly in bird flu impact on the supply chain management (SCM). To analyze the dynamics of this chain, we needed to determine the major models that centralize such type of exogenous fluctuations and combine an epidemic simulation model with our systems dynamics model. Therefore, we will present different modeling approaches of similar animal diseases spread resulted from a direct contact within the animals.

Historically, Kermack and A. McKendrick proposed in 1926 a simple *Susceptible–Infected–Recovered* (SIR) model for epidemic spread based upon a system of nonlinear ordinary equations. It deals with an epidemiological model to investigate the theoretical number of people infected with a contagious illness in a closed population over time. Current modeling works encompass epidemiological theory, population genetics, landscape ecology and economic modeling. The principal challenge is to capture the essential feature of an epidemic in a sufficiently rigorous mathematical formulation that allows us to analyze the spatial and temporal dynamics of the system in order to understand why do epidemics occur, how do they spread, why does disease occur in some regions and not in others, etc. This model can be considered as an archetype of such dynamic models. We will now analyze and classify some particular and recent dynamics models applied to population evolution of animal infectious diseases.

PROPOSAL OF AN EPIDEMIC MODELLING TAXONOMY

We observed in the literature that there is no agreed classification system for such models. Many authors have focused on different aspects of models that may distinguish them from each other. According to the aim of this paper and our PhD research work, we propose to classify the models in two important aspects: deterministic *versus* stochastic models, spatial and temporal treatments.

Deterministic *versus* Stochastic Models

The deterministic models categorize individuals into different subgroups (compartments). The SEIR model, for example, includes four compartments: *Susceptible, Exposed (Infected), Infectious, and Recovered* (immunized). Most models of infectious disease processes used until now, are deterministic because they require less data, are relatively easy to set up.

These models are based on system of common or partial differential equations. *See examples in table 1.*

Disease	Type of model	Authors	Model short description	References to other works
SARS Influenza	Deterministic	Tuen Wai Ng *et al.* , 2003	Based on standard model SIR, this model is developed with two superimposed epidemics to study the recent spread of the SARS in wide regions. Especially, in this model, the authors used the differential equations and numeric simulations basing on SARS data to predict the evolution and the future development of the epidemics.	Dye & Gay, 2003, Donnelly *et al.*, 2003, Lipsitch *et al.,* 2003, Brauer, 2003, Shi, 2003, Liu *et al.* 2005.
Brucellosis	Stochastic and deterministic	England *et al..*, *2002*	A stochastic within herd model and simple deterministic mathematical model for between herd spread. The model was used to evaluate the risk of brucellosis spreading from an insertion in a single herd to other herds, under different frequencies of testing. The aim is to provide a tool to examine the consequences of varying testing frequency, not necessarily to pinpoint the exact optimum.	Hugh-Jones *et al.,* 1976
Foot and Mouth Disease (FMD)	Deterministic	Ferguson *et al..*, 2001	The *Imperial group* produced a deterministic, state-transition type model based on differential equations. In the model, farms within the population could be in one of several states: susceptible, infected but not infectious, infectious but not reported, reported, slaughtered (assumed uninfectious). However, the model did not explicitly represent the spatial relationships within the UK farm population but complex mathematical techniques were used to represent local spread of disease.	Kao, 2002, Keeling *et al.,* 2001, Haydon *et al.,* 1997

Table 1: Recent deterministic diseases spread models

Stochastic models, by explicitly including variability and chance, appear to be more realistic than deterministic models. These models are based on stochastic differential equation or Markov modeling by interval process. Stochastic models include allowance for:

Demographic Stochasticity

Chance effects in transmission from infected to susceptible individuals under otherwise identical conditions.

Environmental Stochasticity

when transmission parameters are influenced by local or global changes in environmental variables.

See an example in table 2.

Disease	Type of model	Authors	Model short description	References to other works
Brucellosis	Stochastic and deterministic	England *et al.*, 2002	A stochastic within herd model and simple deterministic mathematical model for between herd spread. The model was used to evaluate the risk of brucellosis spreading from an insertion in a single herd to other herds, under different frequencies of testing. The aim is to provide a tool to examine the consequences of varying testing frequency, not necessarily to pinpoint the exact optimum.	Hugh-Jones *et al.,* 1976

Table 2: Recent stochastic diseases spread model

Temporal and Spatial Treatment in Epidemic Modeling

Temporal models are mostly based on compartmental SEIR models for epidemics but with additional complexities of:

- Dual sources of inoculums;
- Quenching as hosts become resistant to infection;
- And host dynamics that depend upon infection load.

These models may treat time as continuous or progressing in discrete intervals. This leads to quite distinct methods by which the model result is calculated.

See examples in table 3.

Disease models represent the behavior of disease in population of animals. In real life those animals exist in space. Models may or may not attempt to represent the spatial relationships of animals in the modeled population. More recently the spatial dimension has been incorporated into models. This requires refinements particularly in models of contagious disease such as FMD, avian influenza…, when data describing the « contact structure » of the population are required. The term « contact structure » refers to the fact that contacts between animals

are no longer completely random, but are determined by their relative positions in space. These models include:

Spatially-Implicit Models

Seek to capture some of the spatial aspects of epidemics within a temporal model by using non-linear mixing terms between susceptible and infected or Moment closure and pair-approximation methods.

Spatially-Explicit Models Include Individual-Based

For example, for susceptible on a lattice, often with local mixing, there are Reaction-advection-diffusion and dispersal-kernel models or Metapopulation models that comprise coupled sub-populations such as fields or different regions.

See below examples in table 4.

Disease	Type of model	Authors	Model short description	References to other works
Classical Swine Fever (CSF)	Stochastic-spatial	Mangen *et al.,*, 2003	Based on the model *InterSpread* of Jalvingh A.R.W. et al., this model is built for simulating daily disease spread from infected farms through three contact types: animal, vehicles, persons and through local spread in one region of 2km. The main disease-control mechanisms that influence the disease spread in the model are: diagnosis of the infected farms, depopulation of infected farms, movement controls within quarantine areas, tracing and preventive slaughter.	Stegeman *et al.,* 1999, Jalvingh *et al.,* 1999 Nielen *et al.,* 1999, Van Klink *et al.*1999,
Influenza	Spatial stochastic	Dargatz & Georgescu, 2004	By applying an observation-driven approach, the authors tried to build realistic models for space-time interactions on discrete irregular spatial graphs. Particularly, all of neighboring areas observations enters directly as explanatory variables. The main focus lie on the demonstration of the spread of influenza in the region, obtained through the design and simulation of a spatial extension of the classical SIR model.	Knorr-Held, 2000 Lagazio *et al.,* 2001 Lagazio et al., 2003 Schmid & Held, 2004, Hufnagel *et al.,* 2004, Rue & Held, 2005

Table 3: Recent stochastic spatial diseases spread model

Example of a Stochastic Model with Spatial Extension of SEIR Model.

Dargatz *et al.* (2005) used an observation-driven approach, where past observed counts in neighboring areas enter directly as explanatory variables. The demonstration of spread of influenza is obtained through the design and simulation of a spatial extension of the classical SEIR model.

Stochastic Model at Local Level

$$\frac{ds}{dt} = -\alpha sj + \frac{1}{\sqrt{N}}\sqrt{\alpha sj}\,\xi_1(t)$$

$$\frac{de}{dt} = -\alpha sj - \varepsilon e - \frac{1}{\sqrt{N}}\sqrt{\alpha sj}\,\xi_1(t) + \frac{1}{\sqrt{N}}\sqrt{\varepsilon e}\,\xi_3(t)$$

$$\frac{dj}{dt} = \varepsilon e - \beta j - \frac{1}{\sqrt{N}}\sqrt{\varepsilon e}\,\xi_1(t) + \frac{1}{\sqrt{N}}\sqrt{\beta j}\,\xi_2(t)$$

where : *s, e, j, r* are denoted the fractions of susceptible, exposed (infected), infectious, and recovered (removed) and r = 1 – *s* – *e* – *j*.

$\xi_1(t)$, $\xi_2(t)$, $\xi_3(t)$ are independent Gaussian white noise forces, modeling fluctuations in transmission and recovery matters, and noise in the duration of the latent period.

Stochastic Model at Regional Level

The authors introduce a network of subregions 1… *n* of the primarily observed area, each region I having a population N_i being composed of S_i, I_i, R_i susceptible, infectious and recovered individuals. Whilst the local infection dynamics within a subregion is given by the stochastic SIR model, the global dispersal between the knots of the network is rated in a connectivity matrix $\gamma = (\gamma_{ij})_{ij}$. The system of stochastic differential equations now changes to:

$$\frac{ds_i}{dt} = -\alpha s_i j_i - \sum_k \gamma_{ik} s_k + \frac{1}{\sqrt{N_i}}\sqrt{\alpha s_i j_i}\,\xi_1^{(i)}(t) + \frac{1}{\sqrt{N_i}}\sqrt{\sum_k \gamma_{ik} s_i}\,\xi_4^{(i)}(t) - \frac{1}{\sqrt{N_i}}\sqrt{\sum_k \gamma_{ki} s_k}\,\xi_5^{(i)}(t)$$

$$\frac{dj_i}{dt} = \alpha s_i j_i - \beta_i - \sum_k \gamma_{ik} j_i - \sum_k \gamma_{ki} j_k - \frac{1}{\sqrt{N_i}}\sqrt{\alpha s_i j_i}\,\xi_1^{(i)}(t) + \frac{1}{\sqrt{N_i}}\sqrt{\beta_i}\,\xi_2^{(i)}(t) + \frac{1}{\sqrt{N_i}}\sqrt{\sum_k \gamma_{ik} j_i}\,\xi_4^{(i)}(t)$$

$$\frac{1}{\sqrt{N_i}}\sqrt{\sum_k \gamma_{ki} j_k}\,\xi_5^{(i)}(t)$$

$$\frac{dr_i}{dt} = \beta j_i - \frac{1}{\sqrt{N_i}}\sqrt{\beta j_i}\,\xi_2^{(i)}(t)$$

Where $i = 1 \ldots n$;

$\xi_1(t) = (\xi_1^{(1)}{}'(t), \ldots, \xi_1^{(n)}{}'(t))$, $\xi_2(t)$, $\xi_4(t)$, $\xi_5(t)$: are independent vector-valued white noise forces which stand for fluctuations in transmission, recovery, and outbound and inbound traffic, respectively.

Disease	Type of model	Authors	Model short description	References to other works
Avian influenza	Cellular automata	Hokky, 2004	The author showed an application of cellular automata computational analysis as the dynamic model of spatial epidemiology. In this study of avian influenza disease in Indonesia, a computational model is built and a map-based simulation is performed using several simplified data of transportation, poultry industries and avian influenza infected area. The result of simulation demonstrates the spreading rate of influenza and possible preventive action through isolation of infected areas.	Hatta & Kawaoko, 2002, Piyawong *et.al.,* 2003, Wolfram, 1983, Chopard & Droz, 1998, Brown, 2001, Capua & Alexander, 2002
Foot and Mouth Disease (FMD)	Spatial simulation	Garner & Beckett, 2002	The authors used three approaches: pathway, spread rate and hybrid approaches to build a model of transmission of the virus FMD.	
FMD	InterSpread	Morris *et al.*2001	*InterSpread* is a very detailed simulation model which attempts to represent transmission of disease by specific contact routes and also include the effects on transmission of differences between species and other farm level factors. The model therefore includes many epidemiological parameters. Parameterization of the model can be simplified by aggregating some of the farm types.	Morris *et al.,* 2002
FMD	Cambridge/ Edinburgh	Keeling *et al.,* 2001	The model is a spatially explicit, stochastic, individual farm based model. The model was populated with geo-referenced real farms on the basis of the UK census data of 2000. This model did not attempt to mechanistically represent different modes of disease transmission. The model related the probability of infection passing from an infectious to a susceptible farm to the distance between them and the species and number of animals on the two farms.	Keeling *et al.,* 2003 Ferguson *et al.,* 2001
BSE	Simulation	Wilesmith *et al.,* 1988.	A simulation model was constructed on a spreadsheet platform to examine the time of onset and duration of exposure to the causal agent, the incubation period and the age classes of animals exposed. The model consisted basically of an age-banded population turnover model. Values for the unknown parameters (time and duration of exposure and incubation period) could be imposed on the model with goal of reproducing the observed age and time distribution of actual cases.	Richards *et al.,* 1993 Donnelly *et al.,* 1997; Ferguson *et al*., 1997; 1999; Medley & Short, 1996; Anderson *et al.,* 1996

Table 4: Recent spatial and temporal treatments in diseases spread models

CONCLUSION

Epidemic mathematical modeling can help us to understand better the spread of infectious diseases and to verify control strategies. This study has presented some basic mathematical models as the origin of much of mathematical epidemiology. In fact, models may serve different purposes and this means that different models are often made to suit a particular purpose. Different models may also be developed which concentrate on certain details of epidemic. Epidemiologists, computer scientists and social scientists share a common interest in studying spreading phenomena and make use of very similar models for the description of the diffusion of viruses, knowledge and innovation. Epidemic modeling relies also on the knowledge of the underlying population structure in which the spreading is occurring. In this perspective, the increased power of computers and informatics tools is having a large impact on epidemic modeling by allowing the gathering and handling of large data sets for a variety of contact networks of practical interest in social sciences, critical infrastructures and epidemiology.

For our PhD research, we will build a multiagent model for chicken influenza evolution coupled with a continuous system dynamics model. The dynamics of the cellular automata network will create instabilities like limit cycles or chaos attractors which will influence the input continuity for the supply chain dynamics model.

REFERENCES

Abbey, H. 1952. "An examination of the Reed-Frost theory of epidemics", *Hum. Biol.* vol.3, 201-233.

Ackleh, A.S. and Allen, J.S.L. 2005. "Competitive exclusion in SIS and SIR epidemic models with total cross immunity and density-dependent host mortality", *AIMS*, *Discrete and*

Continuous Dynamical Systems-Series B, vol. 5, No. 2, 175-188.

Anderson, R. M. and Robert, M. M. 1992. *Infectious diseases of humans: Dynamics and Control*, Oxford Univ. Press.

Arino, J. and Driessche, P.V.D. 2003. "The basic reproduction number in a multi-city compartmental epidemic model", *Lecture Notes in Control and Information Sciences, Springer-Verlag Berlin Heidelberg 2003*, vol. 294, 135-142.

Ball, F.; O'Neill, P.D. and Pike, J. 2005. "Stochastic epidemic models in structured populations featuring dynamic vaccination and isolation", *Applied Probability Trust, Advances in Applied Probability,* vol. 3, No. 1, 99-123.

Dargatz C.; Georgescu V. and Held L. 2005. "Stochastic modeling of the spatial spread of Influenza in Germany", *Austrian Journal of Statistics (to appear), Discussion Paper 450, SFB 386.*

England, T.; Jones, R.; Kelly, L. and Wooldridge, M. 2002. "A simulation model to estimate the rate of spread of Brucellosis within the national cattle herd under a variety of testing strategies", *Poster presented at conference of Society for Veterinary Epidemiology and Preventive Medicine, Cambridge, UK.* http://www.svepm.org.uk/posters/index.php

Ferguson N. M.; Donnelly C. A. and Anderson R. M. 2001. "The foot-and-mouth epidemic in Great Britain: pattern of spread and impact of interventions", *Science Express, Science,* vol. 292, issue 5519, 1155-1160.

Frost, W.H. 1976. "Some conceptions of epidemics in general", *Oxford Journals, Am. J. Epidemiol.* vol. 103, No. 2, 141-151.

Gani, R. and Leach, S. 2000. "Transmission potential of smallpox in contemporary populations", *Nature Publishing Group, International Weekly Journal of Science*, vol. 414, No. 6865, 748-751.

Garner, G. and Beckett, S. 2002. "Representing Disease Spread in Spatial Simulation Models", *Department of Agriculture, Fisheries and Forestry, Autralian Government,* http://www.epicentre.massey.ac.nz/acvsc/scwk_05/Beckett_representing_spread.pdf.

Gaver, D. P.; Jacobs, P.A. ; Bullock, G. and Simons, R. 2004. "Models for transmission and control of bioterroristic epidemics", *Naval Postgraduate School Monterey, CA 93943-5000, Report prepared for: Office of Domestic Preparedness Department of Homeland Security.*

Grenfell, B.T.; Smith, G.; Anderson, R.M. 1987. "A mathematical model of the population biology of Ostertagia ostertagi in calves and yearlings", *Elsevier, Parasitology,* vol. 95, No. 2, 389-406.

Hethcote, H.W. 2000. "The mathematics of infectious diseases", *Society for Industrial and Applied Mathematics, SIAM Review,* vol. 42, No. 4, 599-653.

Hokky, S. 2004. "Epidemiology through cellular automata, case of study: Avian Influenza in Indonesia", W*orking Paper WPE2004 Dept. Computational Sociology, Bandung Fe Institute,* http://www.arxiv:nlin.CG/0403035.

Hötzendorfer, H.; Popper N. and Breitenecker F. 2004. "Temporal and spatial evolution of a SIR-type epidemic" – *ARGESIM comparison C17 – Definition, Simulation News Europe*, Issue 41/42, 1-3.

Jalvingh, A. W.; Nielen, M.; Maurice, H.; Stegeman, A. J.; Elbers A.R. and Dijkhuizen A. A. 1999. "Spatial and stochastic simulation to evaluate the impact of events and control measures on the 1997-1998 classical swine fever epidemic", in *The Netherlands 1-Description of simulation model*, Elsevier, Preventive Veterinary Medicine, vol. 42, 271-317.

Keeling, M. J.; Woolhouse, M.E.; Shaw, D.J.; Matthews, L.; Chase-Topping, M.; Haydon, D.T.; Cornell, S.J.; Kappey, J.; Wilesmith, J. and Grenfell, B.T. 2001. "Dynamics of the 2001 UK Foot and Mouth Epidemic – stochastic dispersal in a heterogeneous landscape", *Science Express, Science* vol. 294, No. 5543, 813-817.

Kermack, W.O. and McKendrick, A.G. 1997. "A Contribution to the Mathematical Theory of Epidemics", *The Royal Society, Proceedings of the Royal Society of London. Series A, Containing Papers of a Mathematical and Physical Character,* vol. 115, No. 772, 700-721.

Liu, R.; Shuai, J.; Wu, J. and Zhu, H. 2006. "Modeling spatial spread of West Nile virus and impact of directional dispersal of birds", *AIMS and Beihang University, Mathematical Biosciences and Engineering,* **3**, *1*, 145-160.

Lurz, P.W.W.; Rushton, S.P.; Wauters, L.A., Bertolino, S.; Currado I.; Mazzoglio P. and Shirley M.D.F. 2001. "Predicting greys quirrel expansion North Italy: a spatially explicit modelling approach", *Springer Netherlands, Landscape Ecology,* vol. 16, No. 5, 407–420.

Mangen, J.J.; Nielen, M. and Burrell, A.M. 2003. "Simulated epidemiological and economic effects of measures to reduce piglet supply during a classical swine fever epidemic in the Netherlands", *OIE 2003*, *Rev. Sci. tech. Off. Int. Epiz*., vol. 22, No. 3, 811-822.

Mooney, J.D.; Holmes, E. and Christie1, P. 2002. « Modélisation en temps réel des épidémies de grippe : une analyse de régression linéaire », *Rapport de surveillance, Eurosurveillance Monthly*, vol 7, No. 12, 184-187.

Morris, R.S.; Wilesmith, J.W.; Stern, M.W.; Sanson, R.L. and Stevenson M.A. 2001. "Predictive spatial modelling of alternative control strategies for the foot and mouth disease epidemic in Great Britain", *The British Veterinary Association, The Veterinary Record,* vol.149, issue 5, 137-144.

Ng, T.W..; Turinici, G. and Danchin, A.. 2003. "A double epidemic model for the SARS propagation", *BioMed Central, BMC Infectious Diseases*, vol. 3, No. 19, 1-16.

Taylor, N. 2003. Review of the use of models in informing disease control policy development and adjustment, *A report for DEFRA, Veterinary Epidemiology and Economics Research Unit, VEERU, http://www.defra.gov.uk/science/documents/publications/2003.*

Trottier, H. and Philippe, P. 2001. "Deterministic modeling of infectious diseases: Theory and methods", *Internet Scientific Publications*, *The Internet Journal of Infectious Diseases*, **1** *2*.

Wilesmith, J.W.; Wells, G.A.H.; Cranwell, M.P. and Ryan, J.B.M. 1988. "Bovine spongiform encephalopathy: Epidemiological studies", *The British Veterinary Association, The Veterinary Record* vol.123, issue 25, 638-644.

SIMULATION OF THE DIETARY EXPOSURE TO ACRYLAMIDE FROM FRENCH FRIES FOR IRISH CONSUMERS

Enda Cummins
Francis Butler
Biosystems Engineering
School of Agriculture, Food Science and Veterinary Medicine
University College Dublin
Earlsfort Terrace
Dublin 2
Ireland
E-mail: Enda.Cummins@UCD.ie

Ronan Gormley
Nigel Brunton
The Ashtown Food Research Centre
Ashtown
Dublin 15
Ireland

ABSTRACT

This study develops a farm-to-fork risk assessment model for acrylamide formation in French fries in Ireland. The model was developed in Microsoft Excel with the @Risk add-on package. Probability distributions were used to simulate the impact of each process stage on potato reducing sugar levels and final acrylamide formation. The model was run for 10,000 iterations using Latin Hypercube sampling. The simulated mean acrylamide level in French fries was calculated to be 317 µg/kg. It was found that in Ireland, females are exposed to smaller levels of acrylamide than males (mean exposure of 0.20 µg/kg bw/day and 0.27 µg/kg bw/day, respectively). Transposing the exposure assessment through a dose-response model yields an uncertainty distribution for a lifetime probability of illness resulting from exposure to acrylamide from French fries for both males (mean value –3.78 log lifetime probability of illness, i.e. a probability of approximately 1 in 10,000) and females (-3.92 log probability of illness). A sensitivity analysis revealed that controlling the initial reducing sugar levels in the raw potato (correlation coefficient of 0.54 for glucose and 0.52 for fructose) may be the most effective means of reducing human exposure. This may include initial selection of appropriate cultivars or altering storage conditions to ensure minimal reducing sugar levels. The model represents an initial attempt to create a farm-to-fork risk assessment model for acrylamide in French fries encompassing all available scientific information.

INTRODUCTION

Worldwide concern about acrylamide occurred in 2002 when researchers in Sweden first reported that high levels (>1000 µg/kg) of the group 2a carcinogen existed in many foods which were heated to high temperatures. Subsequent research found that acrylamide may be formed by the heating of many starchy foodstuffs (Rosen and Hellenas 2002; Tareke et al. 2000). This study has focused on the potential risks from acrylamide in French fries and represents an initial, and currently only, farm –to-fork study of human exposure to acrylamide.

Acrylamide is formed during the Maillard reaction (Coughlin 2003; Mottram, Wedzicha and Dodson 2002). Asparagine, glucose and fructose are considered to be the main precursors to acrylamide formation (Yaylayan et al. 2003). The reaction only appears to occur at temperatures above 100 °C (Friedman 2003). Reducing sugars and asparagines are also precursors for flavour and browning formation which means acrylamide is generated in parallel with flavours and browning (Amrien et al. 2003). The model generated in this paper models the reducing sugar levels in potatoes during critical process stages and links the final reducing sugar levels to an estimate of the likely acrylamide level in French fries and corresponding risk to consumers.

MATERIALS AND METHODS

Model development

While there has been previously published risk assessment models on the risks of acrylamide from an overall consumption perspective (Dybing et al. 2005; Matthys et al. 2005), there has been no published attempts to model acrylamide formation for any food product from "farm-to-fork", highlighting the originality of this work. This study models acrylamide formation in French fries using largely empirical data to model potato growth, storage, subsequent processing and cooking procedures. This is achieved by means of Monte Carlo simulation techniques. A flow diagram of the process modelled is given in Figure 1.

Model inputs

Glucose and fructose levels were found to be the main determinant factors in acrylamide formation (Amrein et al. 2003; Becalski et al. 2004; Amrein et al. 2004). Given this extensive scientific evidence, the initial focus of the model is on levels of reducing sugars in raw potatoes and the effect the various processes have on reducing sugar levels during potato chip production.

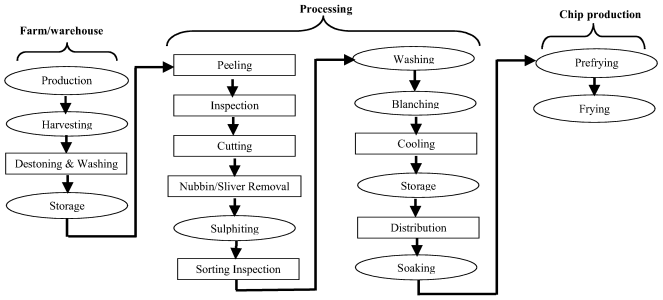

Figure 1: Flow diagram of the production of French fries.

To model the initial glucose and fructose in fresh potato a distribution was fitted to the data presented by Brunton et al. (2006) who gave glucose and fructose levels in Maris Piper potatoes stored under Irish conditions. The resulting distributions were lognormal with mean values of 176 mg/kg and 180 mg/kg for glucose and fructose respectively. Glucose and fructose are not independent variables i.e. they are strongly correlated. An analysis of the data given by Amrein et al. (2003), reported a strong correlation between glucose and fructose sugar levels (r^2 = 0.9495). Similarly a study by Brunton et al. (2006) found a strong correlation between glucose and fructose (r^2 = 0.93) in Irish Maris Piper potatoes. These correlations were taken into account in the model by means of a correlation matrix, Storage temperatures below 8 – 10 °C results in the release of reducing sugars from starch resulting in an increase of reducing sugars to 3-15 g/kg (fresh weight). To model the effect of storage on sugar levels the model simulated several time and temperature combinations. To account for variability a triangular distribution was used to model storage temperature with a minimum temperature of 8 °C, a mode of 8.5 and maximum value of 9 °C. Storage time was modelled using a triangular distribution with a minimum of 3 days, mode of 90 days and maximum of 186 days. This was based on typical storage conditions used in Ireland. To model the impact of storage conditions a cumulative distribution was fit the data provided in Table 1 which shows the expected increase in sugar levels based on various scientific studies.

Table 1: Data used to model the increase in sugars in potatoes stored at temperatures greater then 8 °C

Storage time (Days)	Factor increase in sugars	Reference
1	1.00	Brunton *et al.*, 2006a
25	1.20	Brunton *et al.*, 2006a
39	2.92	Brunton *et al.*, 2006a
70	2.43	Brunton *et al.*, 2006a
85	6.97	Brunton *et al.*, 2006a
93	9.45	Coffin *et al.*, 1987
114	12.33	Brunton *et al.*, 2006a
114	12.01	Brunton *et al.*, 2006a
156	5.44	Brunton et al., 2006a
156	5.09	Haase and Weber 2003

Reconditioning of cooled potatoes at ambient temperature for 1-2 weeks can result in a reduction in the reducing sugars levels (Grob et al. 2003). However, reconditioning will not reduce sugar levels to their original levels prior to being refrigerated (EFSA 2003). The reconditioning stage was modelled by means of a triangular distribution with a minimum of 1 (i.e. no change) a mode of 2 (i.e. 50% reduction) and a maximum of 3 in line with published data.

There is no scientific evidence to suggest that the sulphiting process significantly influences the level of reducing sugars in potatoes. Blanching removes glucose and asparagines from potato tissue leading to lower acrylamide formation in fried potato slices (Pedreschi and Moyano 2004; Pedreschi et al. 2004). To account for this uncertainty a continuous empirical distribution, in the form of a cumulative distribution, was fitted to the data sets from Wicklund et al. (2005) and Pedreschi et al. (2004) and used to simulate the effect of blanching on reducing sugars. The resulting distribution is given in Figure 2.

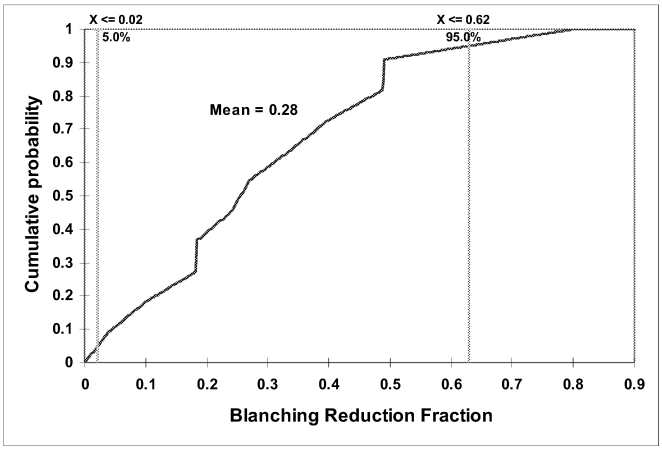

Figure 2: Cumulative probability distribution for the effect of blanching on reducing sugar levels in raw potato chips.

There is some degree of uncertainty about the effect of soaking on sugar levels and acrylamide formation in potatoes. Some researchers suggest that the effect of soaking in water prior to frying does not appear to have a significant effect on acrylamide formation (Williams 2004). Yet others note quite significant changes and maintain that water soluble components, such as glucose and fructose, are washed out from the external layer of the potato (Matthaus et al. 2004). To model the uncertainty about this parameter a continuous empirical distribution was fit to the data in the form of a cumulative distribution. The resulting distribution is given in Figure 3.

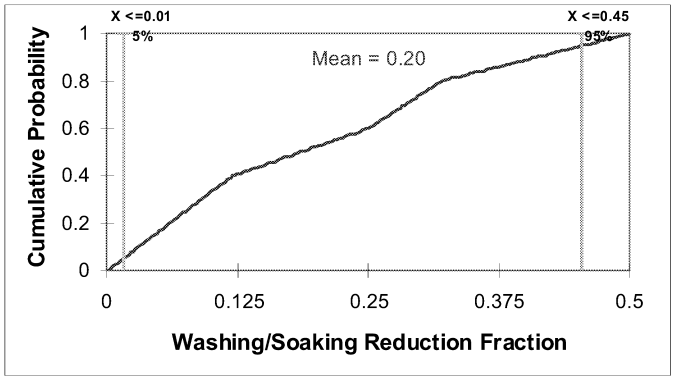

Figure 3: Cumulative probability distribution for washing/soaking reduction fraction.

Frying time and frying temperature can greatly affect acrylamide formation (WHO 2002). When the potato chip is pre-fried the main frying time is greatly reduced. The pre-frying stage was incorporated by simulating its effect on acrylamide levels. Uncertainty about the parameter was incorporated by means of a uniform distribution with a minimum reduction of acrylamide of 40% and a maximum of 62%, in line with published data (Grob et al., 2003). There is still considerable uncertainty about the formation of acrylamide and the reaction which takes place following frying. The model assumes a linear relationship between total reducing sugar levels (i.e. glucose plus fructose) and acrylamide level for a particular time and temperature combination. This assumption is supported by previous research conducted by Amrein et al. (2003, 2004). Thus, based on previous scientific studies, a cooking prediction curve was created which enables an estimation of acrylamide formation following cooking to be made, based on the reducing sugar levels of the raw French fries and the cooking conditions used.

A consumption survey carried out on the island of Ireland (IUNA 2001) give details of the various food products consumed by Irish consumers and the corresponding intake amounts (g/day). The daily consumption of French fries was estimated from this survey (74 g/day and 44 g/day for males and females, respectively). This data can thus be used to calculate the daily intake of acrylamide from French fries given the simulated acrylamide content of French fries. A linear dose-response model for acrylamide (Dybing and Sanner 2003) was used in accordance with best scientific information. Using this dose-response model and transposing the simulated exposure results in the calculation of a lifetime cancer risk related to daily intake of acrylamide from French fries. The dose-response used is conservative, thus the true risk to consumers may be lower. A table of distributions and summarised inputs are given in Table 2.

RESULTS AND DISCUSSION

The input parameters were combined onto a spreadsheet (Microsoft Excel 2000) running the @Risk add-on package (Palisade Software, Newfield, N.Y.) and the simulation was performed using Latin Hypercube sampling. The simulation was performed using the parameters and calculations presented and the model run for 10,000 iterations. A table of the simulated outputs are given in Table 3.

The simulated probability density distribution describing the uncertainty about the acrylamide level in French fries is given in Figure 4. The simulated mean acrylamide level was 317 µg/kg. However, there was a large uncertainty distribution generated around this (90th percentile range 36 - 1003 µg/kg). The simulated levels and range are comparable with reported acrylamide levels in French fries (WHO 2002) where the mean acrylamide level was found to be 537 µg/kg with (minimum of <50 µg/kg and maximum of 3500 µg/kg in samples from Norway, Sweden, Switzerland, the UK and the USA). A study in Sweden found a mean acrylamide level in French fries of 540 µg/kg with a range between 300 to 1100 µg/kg. Heated food can contain concentrations in excess of 1000 µg/kg (Tareke et al. 2002).

Table 2: Table of model distributions and inputs.

Symbol	Description	Mean value	Distribution	Units
	Harvesting data			
G	Glucose in raw potato	176	Lognormal, standard deviation 77	mg/kg
F	Fructose in raw potato	180	Lognormal, standard deviation 86	mg/kg
CF	Correlation factor	0.9495	Fixed value	
H_f	Harvest date factor	1	Exponential, beta value of 1	factor
G_{ph}	Glucose in harvested potato		$G \times H_f$	mg/kg
F_{ph}	Fructose in harvested potato		$F \times H_f$	mg/kg
	Storage			
S_{tim}	Storage time	90	Triangular, minimum 3, maximum 186	days
S_{temp}	Storage temperature	8.5	Triangular, minimum 8, maximum 9	°C
S_f	Storage factor		From table	factor
G_{ps}	Glucose post storage		$G_{ph} \times S_f$	mg/kg
F_{ps}	Fructose post storage		$F_{ph} \times S_f$	mg/kg
R	Reconditioning	1	Fixed value	factor
G_{pc}	Glucose post conditioning		G_{ps} / R	mg/kg
F_{pc}	Fructose post conditioning		F_{ps} / R	mg/kg
	Processing			
W	Washing reduction		Cumulative, based on data	fraction
B	Blanching reduction		Cumulative, based on data	fraction
S	Soaking reduction		Cumulative, based on data	fraction
G_{pp}	Glucose post processing		$G_{pc} \times (1-W) \times (1-B) \times (1-S)$	mg/kg
F_{pp}	Fructose post processing		$F_{pc} \times (1-W) \times (1-B) \times (1-S)$	mg/kg
TS_{pp}	Total sugars		$G_{pp} + F_{pp}$	mg/kg
	Main Frying			
F_{time}	Time		Discrete, all 10%	min (5-10 min only)
F_{temp}	Temperature	180	Triangular, minimum 160,maximum 190	°C
IP	Intercept		Uniform(0,60)	µg/kg
RSL	Reference sugar level		From data, see text	µg/kg
RAL	Reference acrylamide level		From data, time & temp dependent, see text	µg/kg
M	Slope		(IP-RAL)/(0-RSL)	
A	Acrylamide		$M \times TS_{pp} + IP$	µg/kg
PF	Pre-fry reduction		Uniform, minimum 0.41, maximum 0.62	fraction
	Exposure assessment			
M_m	Males mean weight (18-64y)	82.9	Fixed value	kg
IPDM	Intake of product per day	74	Lognormal, standard deviation 69	g/d
M_f	Females mean weight (18-64yr)	67.5	Fixed value	kg
IPDF	Intake of product per day	44	Lognormal, standard deviation 44	g/d
LH	Life time hazard after lifelong exposure to 1ug acrylamide per kg body weight per day	1.60E-03	Fixed value	Risk of illness

Table 3: List of simulated model outputs.

Symbol	Description	Distribution	Units
A_{final}	Final Acrylamide in Chips	$A \times (1-PF)$	µg/kg
$IPDM_{bw}$	Intake of acrylamide per day (males)	$A_{final} \times IPDM / M_m$	µg/kg bw/day
$IPDF_{bw}$	Intake of acrylamide per day (females)	$A_{final} \times IPDF / M_f$	µg/kg bw/day
LPI_m	Log prob of illness (males)	$LH \times IPDMbw$	lifetime risk
LPI_f	Log prob of illness (females)	$LH \times IPDF_{bw}$	lifetime risk

It has been reported that fried and baked potato products such as French fries, crisps, baked potatoes and hash browns can have concentrations in excess of 3000 µg/kg (Tareke et al. 2002, Becalski et al. 2003, Ros and Hellen 2002). A study by Brunton et al. (2006) found a range of between 60 - 720 µg/kg for acrylamide levels in French fries made from Irish Maris Piper potatoes cooked under laboratory conditions simulating commercial chip frying. This range validates the models estimate.

A probability density distribution describing the uncertainty about daily exposure to acrylamide following the consumption of French fries is provided in Figure 5. It is noticeable that females are exposed to smaller levels of acrylamide (0.20 µg/kg bw/day) than males (0.27 µg/kg bw/day). This is mainly due to the greater consumption levels for males when compared with females. This observation is consistent with previous studies (Norwegian Food Agency 2002).

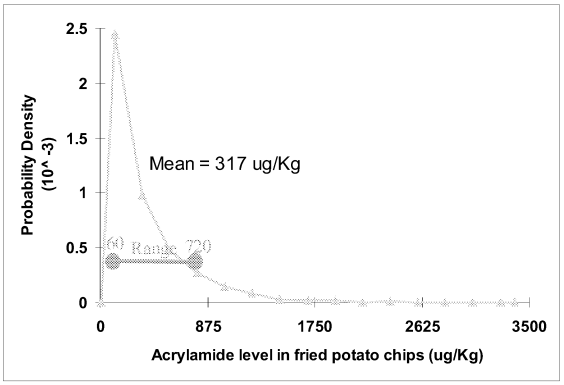

Figure 4: Probability distribution for the acrylamide level in French fries arising from the Monte Carlo simulation including experimental range from Brunton et al. (2006)

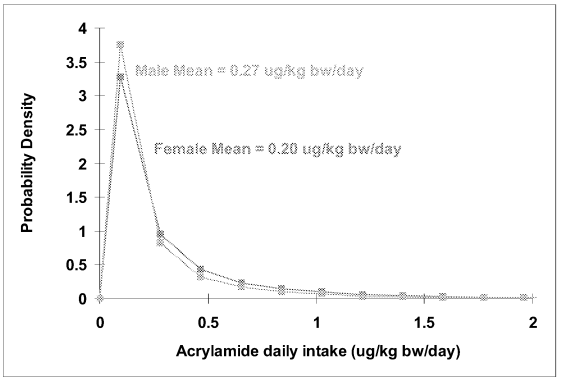

Figure 5: Acrylamide daily exposure for males and females resulting from the consumption of French fries in Ireland.

The limit of exposure to acrylamide, as suggested by WHO, is 1 µg/kg bw/day (WHO 2002; Grob and Biedermann 2003). The mean simulated exposure levels for males and females from French fries are well below this limit, indicating that eating French fries does not constitute a significant risk to human health on its own. It should be pointed out that French fries are only one source of acrylamide. Other sources may include coffee, bread and biscuits. Cumulating all of these sources of acrylamide may result in an individual exceeding the recommended 1 µg/kg bw/day suggested by WHO.

Transposing the exposure assessment through a dose-response model (Dybing and Sanner 2003) yields an uncertainty distribution for a lifetime probability of illness resulting from exposure to acrylamide from French fries for both males and females. The mean risk for males was found to be higher than the risk experienced by females (-3.78 (i.e. approximate probability of 1: 10,000) and –3.92 log lifetime probability of illness for males and females, respectively), corresponding to a reduced exposure for females. The simulated risks are less than the risks estimated for the Norwegian population (Dybing and Sanner 2003) where the average lifetime risk of illness for males and females was estimated to be –3.22 log.

The model allows a sensitivity analysis to be performed. The analysis is shown here is the form of a tornado plot. A sensitivity analysis for the level of acrylamide in French fries is presented in Figure 6. The analysis revealed the parameter having the biggest impact on model predictions was the level of reducing sugars present in the potatoes (correlation coefficient 0.54 and 0.52 for glucose and fructose, respectively). The analysis indicated that process stages such as blanching, cooking time and temperature are also having a significant impact on the final acrylamide formation and resulting human exposure. The sensitivity analysis is supported by experimental research conducted by Williams (2004) who indicated that cooking time/temperature and soaking had the biggest impact on acrylamide levels.

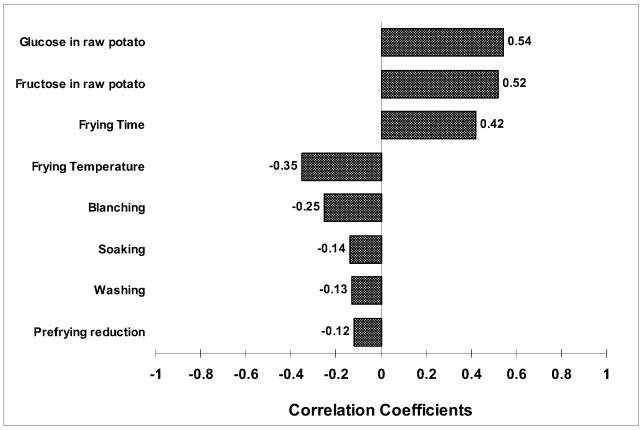

Figure 6: Sensitivity analysis for level of acrylamide in French fries.

The analysis indicated that by careful selection of cultivars with low concentrations of reducing sugars, significant reductions in acrylamide can be achieved.

CONCLUSION

The model developed during this study is an initial attempt to model acrylamide formation by modelling reducing sugar levels from farm-to-fork. As such the model is unique, as no previous attempts have been made to model this complicated process. The model indicated that the mean level of acrylamide in French fries is likely to 317 µg/kg. In addition, daily exposure to acrylamide from French fries for males and females was estimated to be relatively low (0.27 µg/kg bw/day and 0.20 µg/kg bw/day, respectively) and well below the limit of 1 µg/kg bw/day as suggested by WHO (WHO 2002). Transposing the exposure assessment through a linear dose-response model yielded an estimate of the risk of human illness following the consumption of French fries. The mean values were –3.78 and –3.92 log lifetime probability of illness for males and females, respectively.

The most effective means of limiting acrylamide formation is to control reducing sugar concentrations as highlighted in the uncertainty analysis. This may involve initial selection of appropriate cultivar or altering storage condition to ensure minimal reducing sugar levels. The sensitivity analysis will be of interest to risk managers trying to devise possible risk reduction strategies. Cooking temperature was also found to have a significant influence on the level of acrylamide formation. The model provides a systematic approach to modelling acrylamide formation and human exposure/risk and enables a closer analysis of the parameters influencing human risk from acrylamide.

ACKNOWLEDGEMENTS

The authors wish to acknowledge the Irish Department of Agriculture and Food for their funding of this project under the Food Institute Research Measure.

REFERENCES

Amrein, T. M., Schönbächler, B., Rohner, F., Lukac, H., Schneider, H., Keiser, A., Escher, F. and Amadò, R. 2004. “Potential for acrylamide formation in potatoes: data from the 2003 harvest”. European Food Research and Technology. 219: 572-578.

Amrein, T.M., Bachmann, S., Noti, A., Biederman, M., Barbosa, M.F., Biedermann-Brem, S., Grob, K., Keiser, A., Realini, P., Escher, F. and Amado, R. 2003. “Potential of acrylamide formation, sugars, and free asparagine in potatoes: a comparison of cultivars and farming systems”. Journal of Agricultural and Food Chemistry. 51(18): 5556-60.

Becalski A., Lau B.P.Y., Lewis D. and Seaman, S.W. (2003). “Acrylamide in foods: Occurrence, sources and modelling”. Journal of Agricultural and Food Chemistry. 51: 802-808.

Brunton et al. 2006. Unpublished data on Trial B: Chip trials. Available from The Ashtown Food Research Centre, Ashtown, Dublin 15.

Coughlin, J.R. 2003. “Acrylamide: What we have learned so far”. Food Technology. 57(2): 100.

Dybing, E. and Sanner, T. 2003. “Risk assessment of acrylamide in foods”. Toxicological Sciences. 72(1): 144-144.

Dybing, E., Farmer, P.B., Andersen, M., Fennell, T.R., Lalljie, S.P.D., Muller, D.J.G., Olin, S., Petersen, B.J., Schlatter, J., Scholz, G., Scimeca, J.A., Slimani, N., Tornqvist, M., Tuijtelaars, S. and Verger, P. 2005. “Human exposure and internal dose assessments of acrylamide in food”. Food and chemical toxicology. 43(3): 365-410.

EFSA 2003. European Food safety Authority, workshop on acrylamide formation in food, 17 November Brussels. Report of the workshop. AF 06.04.2004-10

Friedman, M. 2003. “Chemistry, Biochemistry and safety of Acrylamide. A review”. Journal of Agricultural and Food Chemistry. 51(16): 4504-4526.

Grob, K. and Biedermann, M. 2003. “French fries with less than 100 ug/kg acrylamide. A collaboration between cooks and analysts”. European Food Research and Technology. 217: 185-194.

Hasse, N.U. 2003. “Ways to reduce acrylamide in potato chips (crisps)”. Available at : www.ifst.org/euwkshp4.pdf.

IUNA 2001. Irish Universities Nutrition Alliance, North/south Ireland food consumption survey, summary report, Published by: Food Safety Promotion Board, Abbey Court, lower Abbey Street, Dublin 1, ISBN: 9-9540351-0-0.

Matthaus, B., Hasse, N.U. and Vosmann, K. 2004. “Factors affecting the concentration of acrylamide during deep-fat frying of potatoes”. European Journal of Lipid science Technology. 106: 793-801.

Matthys, C., Bilau, M., Govaert, Y., Moons E, De Henauw, S., and Willems, J.L. 2005. “Risk assessment of dietary acrylamide intake in Flemish adolescents”. Food and Chemical Toxicolog. 43(2):271-8.

Mottram, D.S., Wedzicha, B.L., and Dodson, A.T. 2002. “Acrylamide is formed in the Maillard reaction”. Nature. 419: 448 –449.

Norwegian Food Agency. 2002. Available at :http://www.snt.no/nytt/tema/Akrylamid/analyseresultater.htm.

Pedreschi, F. and Moyano, P. 2004. “Color changes and acrylamide formation in fried potato slices”. Food Research International. 38: 1-9.

Pedreschi, F., Kaack, K. and Granby, K. 2004. Reduction of acrylamide formation in potato slices during frying. Lebensmittel-Wissenschaft and Technologie. 37: 679-685.

Rosen, J. and Hellenas, K.E. 2002. “Analysis of acrylamide in cooked foods by liquid chromatography tandem mass spectrometry”. Analyst. 127: 880 –882.

Tareke, E., Rydberg, P., Karlsson, P., Eriksson, S. Tornqvist, M. 2002. “Analysis of acrylamide, a carcinogen formed in heated foodstuffs”. Journal of Agricultural and Food Chemistry. 50: 4998 –5006

Tareke, E., Rydberg, P., Karlsson, P., Eriksson, S., Tornqvist, M. 2000. Acrylamide: a cooking carcinogen? Chemical Research in Toxicology. 13: 517–22.

WHO. 2002. FAO/WHO consultation on the health implications of acrylamide in food. Summary report of a meeting held in Geneva, Switzerland; 25-27 June 2002. Available from: http://www.who.int/fsf. Accessed 5 Oct. 2004.

Wicklund, T., Østlie, H., Lothe, O., Knutsen, S.H., Bråthen, E. and Kita, A. 2005. “Acrylamide in potato crisp—the effect of raw material and processing”. Food Science and Technology, In Press, Corrected Proof, Available online 3 May 2005

Williams, J.S.E. 2004. “Influence of variety and processing conditions on acrylamide levels in fried potato crisps”. Food Chemistry. 90(4): 875-881.

Yaylayan, V.A., Wnorowski, A., and Perez Locas, C. 2003. “Why asparagine needs carbohydrates to generate acrylamide”. Journal of Agriculture and Food Chemistry. 51: 1753 –1757.

COMPLEX FOOD PRODUCTS

HOW STATISTICAL PHYSICS CAN HELP TO PREDICT MASS TRANSPORT PROPERTIES IN COMPLEX FOOD PRODUCTS

Olivier Vitrac
INRA – UMR 614
Moulin de la Housse, BP 1039
51687 Reims cedex 2, FRANCE
E-mail: olivier.vitrac@reims.inra.fr

Murielle Hayert
ENITIAA – UMR CNRS 6144
La Géraudière
44322 Nantes cedex 3, FRANCE
E-mail: hayert@enitiaa-nantes.fr

KEYWORDS
effective transport properties, diffusion, homogenization, statistical physics

ABSTRACT

This work illustrates how principles of statistical physics including random walks, micro-reversibility and partition functions can be used to derive effective transport properties in complex materials such as food materials. A general formulation based on continuous Langevin Dynamics is proposed to calculate effective diffusivities in emulsions up to the percolation threshold. Interface conditions assuming either reflections or transmissions are used to account for possible partitioning between phases and could be extended to the interactions with macromolecules. The effective properties simulated in 2D emulsions for a wide range of conditions are compared with the analytical core-shell model proposed by Kalnin and Kotomin (1998) for low dense emulsions. The effects were classified in decreasing importance order as follows: ratio of diffusion coefficients, $r_D = \left[10^{-2}, 10^{2}\right]$, partition coefficients between the continuous and disperse phases, $K = \left[10^{-2}, +\infty\right[$, globule densities, $d = [0.1, 0.4]$, and morphologies. The effects of r_D, K and d were nonlinearly coupled in a way that depended on the morphology of the emulsion: heterogeneity in the size of globules, packing of globules, quasi-continuity between globules.

INTRODUCTION

Foodstuffs consist generally in a mixture of several phases, because their constituents are at different physical states (solid, liquid, gas) or because they have a different chemical affinity (e.g. between lipophilic and hydrophilic constituents). Although Fickian diffusion is strictly limited to ideal mixtures (Nauman and He 2001), it is generally more convenient to represent transport properties even in very complex food by effective diffusion coefficient (Doulia et al. 2000). This approach is physically consistent if both the equivalent transport properties and the equivalent driving force (e.g. concentration gradient) are averaged over a representative volume (Busch and Soukoulis 1995). In practice, this typical volume must be representative of the local composition and detailed microstructure. In particular cases such as in polymer systems or when a specific interaction with a macromolecule is expected, the equivalent description should also take into account small and possibly rare traps, which govern the slowdown of random walks in random environments (Sznitman 2001).

This paper proposes a general methodology based on statistical physics to calculate effective diffusivities of small molecules dispersed at very low concentrations (e.g. additives, active substances, aroma, contaminants...) in simulated or digitized microstructures of foodstuffs. By conception, the formulation accepts i) as many phases as needed and ii) complex thermodynamical descriptions on a wide range of space scales. Since the proposed methodology is a simplified version of Molecular Dynamics, which can be easily updated to multi-rate processes involving several local equilibria of sorption/desorption or association/dissociation, it is thought to be more general than other off-lattice approaches involving lattice gas models (Küntz et al. 2001) or high order spectral approximations (Zhu et al. 2001).

The whole approach is applied to the calculation of effective diffusion coefficients in bi-dimensional emulsions, where the density in globules is up to the percolation threshold and when the ratio between the radius of the smallest and the largest is above 10^3. There is no general model available in the literature to predict effective diffusion coefficients from i) the diffusion coefficients in the continuous and in the discontinuous phase, ii) the partition coefficient between each phase and iii) from the morphology of the emulsion. There is a significant literature on the subject by taking into account only obstacle effects (i.e. impenetrable globules) or by neglecting the possible partition of the diffusing species between both phases (see for example: Riley et al. 1994; Belova and Murch 2003). Earlier results including the Maxwell-Garnett equation are recapitulated in Cranck (1975). The partition effect was first analyzed in details by Ronis (1986). More recently, an algebraic equation, which extends the Maxwell-Garnett equation to cases with partitioning, has been proposed by Kalnin and Kotomin (1998) and discussed further in Kalnin et al. (2002). The equation is based on the solution for a core-shell (or coated sphere) model. It takes into account both the effect of partitioning and different transport properties between both phases. In a general case with several globules, the geometric parameter, Φ, in Equation (29) in Kalnin and Kotomin (1998), is however an adjustable parameter. The value of this parameter is expected to vary significantly with the arrangement and morphology of the emulsion. Besides, since the equation is based on a 1D solution in radial coordinates, some deviations are expected to occur when the connectivity of globules is significant or when globules packing is enough significant to modify the mean free path of particles.

To provide a more general formulation, scaled Langevin dynamics applied to arbitrary microstructures and thermodynamically consistent are developed in the first section. Then the way to determine the effective diffusivities

from the mean square distance visited by our "virtual" diffusants is detailed. The following section recapitulates the scaled results obtained for a wide range of conditions including the effect of diffusion coefficients ratio, partition coefficients, emulsion density and emulsion morphology. The reliability of our results is compared to the analytical model of Kalnin and Kotomin (1998).

LANGEVIN DYNAMICS APPLIED TO EMULSIONS

Equation of motions

As a result of thermal fluctuations, dispersed molecules at very low concentrations are self-moving particles without interacting with themselves. This transport mechanism that aims at homogenizing the density in dispersed molecules in a homogeneous phase is known as tracer diffusion or molecular diffusion. On a lattice, this random motion on mesoscopic length scales is described with preferred turning angles. We prefer here a continuous model based on the stochastic equations of motions in two dimensions and which assumes the conservation of momentum and of angular momentum. In absence of external force field, the trajectory of molecules is governed by a stochastic differential equation obtained by adding a Gaussian white noise to a first order linear system:

$$\frac{d}{dt}\left[\vec{r}(t)\right] = -\alpha \cdot \vec{r}(t) + \vec{\xi}(t) \quad (1)$$

where α is a reciprocal correlation time and $\vec{\xi}(t)$ is a random vector with orthogonal components, $\xi_x(t)$ and $\xi_y(t)$. Each component is normally distributed with zero mean and are uncorrelated for different times t and t' so that its autocorrelation obeys to the Einstein relation:

$$\left\langle \xi_i(t) \cdot \xi_i(t') \right\rangle = 2 \cdot D_i \cdot \delta(t - t') \qquad \text{for } i = x, y \quad (2)$$

where D_i is the diffusion coefficient in the direction i and $\delta(t)$ is the delta or Dirac function.

For $\alpha > 0$, the corresponding trajectory includes some low frequency deterministic behavior with a correlation time $1/\alpha$. Above this correlation time, the trajectory keeps in memory its previous positions (e.g. due to bulk convection).

In practice, Equation (1) is integrated with a fixed time step, δt, according to an explicit Eulerian discretization scheme:

$$\vec{r}(t + \delta t) = \vec{r}(t) + \delta t \cdot \left[-\alpha \cdot \vec{r}(t) + \vec{\xi}(t)\right] \quad (3)$$

If $\delta t \ll 1/\alpha$ so that the diffusion length during δt is higher than the typical distance traveled as a result of bulk inertia, the condition of low Peclet values ($Pe \ll 1$) is verified. It entails:

$$\vec{r}(t + \delta t) = \vec{r}(t) + \widetilde{d\vec{r}} \quad (4)$$

where $\widetilde{d\vec{r}} = \delta t \cdot \vec{\xi}(t)$ is a random increment of the Wiener process, whose orthogonal components are random numbers sampled from a normal distribution with zero mean and a standard deviation defined by $\sqrt{2 \cdot D_i \cdot \delta t}$. As a result, the trajectory is obtained from the cumulation of independent increments or moves along each direction. Since all increments increase as $\delta t^{1/2}$, the integration scheme defined by Equation (4) has a global order of 0.5. It is emphasized that this algorithm with low integration order requires long-term iterations to sample the trajectory in space and in frequency. Since only the second moments of the stochastic trajectory interested ourselves, a parallel implementation would be possible by integrating m independent trajectories including each n steps.

Equation (4) was applied to both the continuous phase, noted "c", and the dispersed phase, noted "d", with a different diffusion tensor (with principal components D_x and D_y). In this work, the diffusion coefficient was assumed isotropic so that $D_x^c = D_y^c = D^c$ and $D_x^d = D_y^d = D^d$. In this work, $m \times n$ was chosen higher than 10^7.

Interface conditions in biphasic systems

In a biphasic medium, additional assumptions are required to account for different chemical affinities of the diffusant for phases c and d. If sorption and desorption processes are reversible and conveniently approximated by a Henry'like relationship in each phase, the macroscopic equilibrium between c and d is completely determined by a partition coefficient, K, defined by:

$$K = \frac{C_{eq}^c}{C_{eq}^d} \quad (5)$$

where $\left\{C_{eq}^k\right\}_{k=c,d}$ is the concentration of diffusants in the phase k at equilibrium. Concentration are expressed in amount (mass or number of molecules) per volume unit so that there are related to the density in molecules in each phase.

If the trajectories are calculated at equilibrium, they may verify the condition of local thermodynamical equilibrium at the c-d interface, noted $d\Omega$, which connects the partition function in each phase, noted $\left\{Z^k\big|_{d\Omega}\right\}_{k=c,d}$, to the macroscopic partition coefficient via:

$$K = \frac{Z^c\big|_{d\Omega}}{Z^d\big|_{d\Omega}} \quad (6)$$

At the interface, the probability of crossing the interface in the direction $c \to d$ and in the direction $d \to c$, noted $pr(c \to d | d\Omega)$ and $pr(d \to c | d\Omega)$, are given by

$$\begin{cases} pr\left(c \to d\middle|d\Omega\right) = \dfrac{Z^d\big|_{d\Omega}}{Z^c\big|_{d\Omega} + Z^d\big|_{d\Omega}} = \dfrac{1}{1+K^{-1}} \\ pr\left(d \to c\middle|d\Omega\right) = \dfrac{Z^c\big|_{d\Omega}}{Z^c\big|_{d\Omega} + Z^d\big|_{d\Omega}} = \dfrac{1}{1+K} \end{cases} \quad (7)$$

Since $pr\left(c \to d\middle|d\Omega\right) + pr\left(d \to c\middle|d\Omega\right) = 1$, Equation (7) verifies the principle of mass conservation on both sides of the interface. Besides, for consistency, if the diffusant does not cross the interface, it stays in the initial phase so that:

$$\begin{cases} pr\left(c \to c\middle|d\Omega\right) + pr\left(c \to d\middle|d\Omega\right) = 1 \\ pr\left(d \to d\middle|d\Omega\right) + pr\left(d \to c\middle|d\Omega\right) = 1 \end{cases} \quad (8)$$

When they are applied with a constant time step of integration, it is straightforward to demonstrate that Equations (7) and (8) comply the principle of detailed balance in the direction normal to the interface, $\vec{n}_{d\Omega}$:

$$\underbrace{\frac{1}{\delta t}\cdot\left[pr\left(c \to c\middle|d\Omega\right) + pr\left(d \to c\middle|d\Omega\right)\right]\cdot\vec{n}_{d\Omega}}_{\text{normal probability flux towards the c side}} = \underbrace{-\frac{1}{\delta t}\cdot\left[pr\left(d \to d\middle|d\Omega\right) + pr\left(c \to d\middle|d\Omega\right)\right]\cdot\vec{n}_{d\Omega}}_{\text{normal probability flux towards the d side}} \quad (9)$$

The detailed balance condition also known as microreversibility is a sufficient but not necessary condition to ensure a Gibbsian equilibrium state (Marsh and Coveney, 1998).

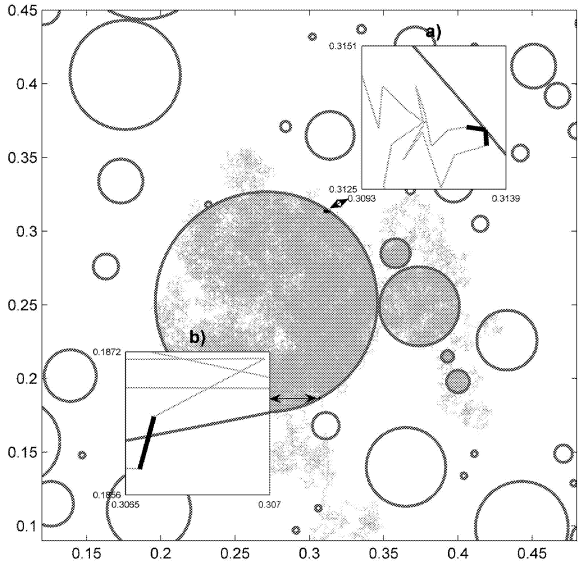

Figure 1: Illustration of interface conditions: a) reflection ($d \to d\big|_{\partial\Omega}$), b) transmission ($d \to c\big|_{\partial\Omega}$). The depicted conditions correspond to $K = 10, r_D = 2, d = 0.3$.

For stability and convergence purposes in the integration scheme, stronger constraints are applied at the interface by forcing the time-reversibility of the trajectory for the four possible transitions at the c-d interface: $c \to c\middle|d\Omega$, $d \to d\middle|d\Omega$, $c \to d\middle|d\Omega$ and $d \to c\middle|d\Omega$. Since the current transport equations do not conserve the energy, the propose interface conditions also allow to dissipate energy. The applied boundary conditions are illustrated on practical cases in Figure 1 and detailed as follows.

Reflective boundary conditions for transitions $c \to c\middle|d\Omega$ *and* $d \to d\middle|d\Omega$

A specular reflective boundary condition was applied to the "internal" transitions $c \to c\middle|d\Omega$ and $d \to d\middle|d\Omega$. During δt, the local trajectory before and after the collision with the interface at a position I was therefore microreversible and symmetric to $\vec{n}_{d\Omega}$.

Transmitting boundary conditions for transitions $c \to d\middle|d\Omega$ *and* $d \to c\middle|d\Omega$

When the trajectory crosses the interface in straight line at a point I from a point A to a point B, the time-reversibility principle implies that the normal flux at the position of I emitted by A and reaching B is the same than the flux emitted by B and reaching A. Since the random increments, $\widetilde{d\vec{r}}$, are not equivalently distributed between each phases, the distance IB after the interface (for $\left\|\widetilde{d\vec{r}}\right\| > AI$) must be rescaled to verify similar probabilities for the transitions A→B and B→A during δt. Since $\widetilde{d\vec{r}}$ increases as the square root of the diffusion coefficient, IB is obtained by:

$$IB = \sqrt{\frac{D^a}{D^b}}\cdot AI \quad (10)$$

where D^a and D^b are the diffusion coefficients in the positions A and B respectively.

It follows from Equation (10) that only the direction $\overrightarrow{AB}$ and the interface crossing are chosen randomly at time $t + \delta t$. The distances IA and IB depend on the previous position at time t and on the local environment (closeness of interfaces).

When IB is higher than the distance between objects or higher than the distance between the interfaces within a same object, the ballistic trajectory is recursively segmented into subsequent reflections and transmissions which follow the rules detailed in the following section. In the current formulation, a maximum of reflections was set to 10. The integration step was updated so that the mean free path was at least 10 folds larger than the typical distance between objects and the smallest object.

SIMULATED CONDITIONS

Scaled 2D emulsions

2D emulsions were represented as randomly dispersed globules, possibly in contact, on a scaled periodic cell on $[0,1[\times [0,1[$, corresponding to an infinite medium of

periodicity l_0. The size of each globule was sampled from a log-normal distribution with arithmetic average, $\mu_\emptyset$, and standard deviation, $\sigma_\emptyset$. The positions of each globule were fixed during dynamics. The effect of globule dynamics is discarded since its time constant is expected to be much higher than the dynamics of diffusants.

The tested conditions are summarized in Table 1. Two extreme morphologies were studied: a monodisperse emulsion, denoted E_0, and a very heterogeneous emulsion, denoted E_1. The effect of tortuosity was tested by varying the density, d, between 0.1 and 0.4. To reduce possible bias due to the construction of emulsions, all simulations were performed on a small set including between 4 and 7 sampled structures. According to the set density, each morphology included between 70 and 800 globules.

Table 1: Tested morphologies of emulsions. Mean and standard deviations are based on sampled values.

morphology		***E_0***	***E_1***
globule diameter	$\mu_\emptyset \times l_0$	4×10^{-2}	$2\times10^{-2} \pm 4\times10^{-3}$
	$\sigma_\emptyset \times l_0$	3×10^{-8}	$2.8\times10^{-2} \pm 6\times10^{-3}$
number of repetitions	d=0.1	4	7
	d=0.2	4	7
	d=0.3	4	7
	d=0.4	4	7

Examples of emulsions and their corresponding size distributions are given in Figure 2.

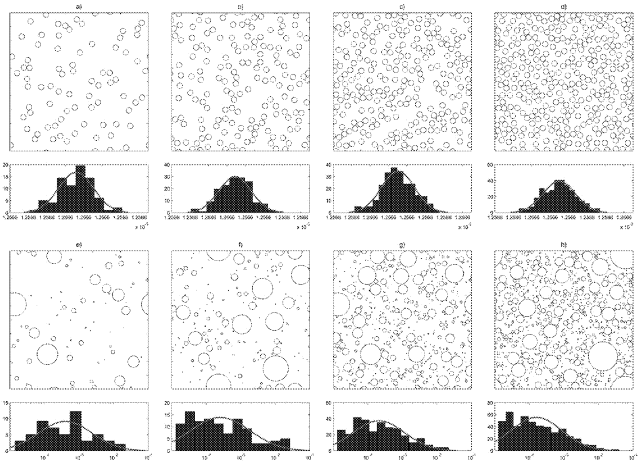

Figure 2: Typical 2D emulsions on a same domain for a,e) , b,f) , c,g) and for d,h). Histograms plot the distributions of surface area of droplets fitted with a continuous normal and a log-normal distribution for E_0 (a-d) and E_1 (e-h) respectively.

Tested range of physico-chemical properties

The diffusion coefficient in the dispersed phase, D^d, was arbitrary chosen as reference. The simulations were performed for different ratios $r_D = D^c/D^d$ between 10^{-2} and 10^2. This range was assumed to fit with generally needs. By contrast, partition coefficients, K, were tested on the whole scale from 0 (no affinity for the continuous phase) to $+\infty$ (no affinity for the dispersed phase). A particular care was brought to the developed code to verify the equilibrium properties defined by Equation (7) even for the most extreme conditions. Reliable results were obtained by describing accurately multiple reflections in dense regions or within small globules. In practice, a search procedure including three levels was used to track interfaces.

Identification of diffusion coefficients

In absence of confinement on long time scales, the diffusion is expected to be linear in the long time limit and large length scales (i.e. larger than the typical length of globules). This limit hydrodynamic regime implies that the mean square displacement is proportional to the diffusion time, τ:

$$D = \frac{1}{2\cdot \dim}\cdot \lim_{\tau\to\infty}\frac{\partial}{\partial \tau}\left\langle \left\| \vec{r}(t+\tau) - \vec{r}(t) \right\|^2 \right\rangle_{t,i=1\ldots m} \qquad (11)$$

Equation (11), known as Einstein equation, relies on the central limit theorem and assumes that the trajectory observed during the typical time scale τ is centered on average on all possible starting positions $\vec{r}(t)$. dim is the number of dimensions. $\langle\ \rangle_{t,i=1\ldots m}$ is the average operator over all possible initial times and diffusing molecules. Since momentum is conserved in Langevin dynamics, the center of mass chosen as reference frame is fixed and no correction due to a possible moving reference frame (e.g. flowing emulsion) is required. It is however assumed that the typical time scale responsible for the modification of the distances between globules is longer than the time scale required to reach the asymptotic regime.

For the particular value $K = 0$, a confinement in the dispersed phase occurs over all time scales. The mean square displacement or equivalently the total variance of the position vector converges towards the maximum surface of the dispersed phase $d\cdot l_0^2$. The equivalent diffusivity is zero since no transport between globules is allowed. In practice, a non-zero diffusion coefficient was achievable even for low K values when a sufficiently large number of $c \to d|d\Omega$ and $d \to c|d\Omega$ transitions were sampled.

RESULTS AND DISCUSSION

Typical trajectories and mean-square displacements

Trajectories

The effect of r_D and K on the trajectory of 5 diffusants is depicted in Figure 3 for $r_D = 2$ and $K = \{0.1,1,10\}$ in an heterogeneous emulsion with $d = 0.3$. The corresponding cumulated diffusion time was set to $m\cdot t = 5\cdot 10^6\cdot \delta t$ to get a partly ergodic system but without reaching the equilibrium. As a result, the distribution of corresponding residence times were not uniform in each phase and the details of the trajectories were discernible. Residence times averaged over all diffusants were calculated on a 50×50 grid and plotted as

filled regions with iso-residence times based on 2D cubic interpolants.

Raising the affinity for the dispersed phase ($K \to 0$) led to a winding of the trajectories (Figure 3a) inside the globules and increased the residence time in the globules (Figure 3b). For $K = 1$, the trajectories were spread over all the simulated domain without any distinction between both phases (Figure 3c). In details, the residence times looked higher inside the globules than in the continuous phase (Figure 3d). This effect is related to a twice lower diffusion coefficient in the disperse phase. The situation $K = 10$ led to a more rapid uniform filling of the continuous space between globules (Figure 3e) but with a low visiting rate inside globules (Figure 3f). It is however underlined that the transient trajectories appeared also concentrated between globules, particularly in regions were the density in globules was high or led to tortuous paths.

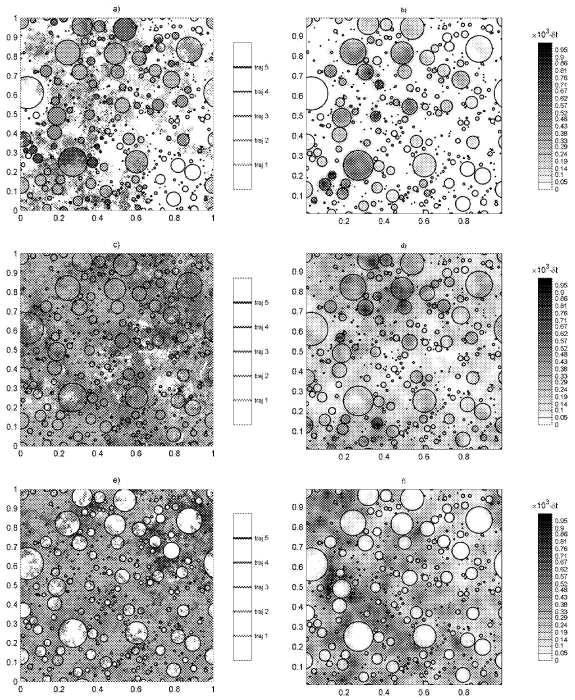

Figure 3: a,c,e) Five typical trajectories during $10^6 \cdot \delta t$ and b,d,f) corresponding residence times in the emulsion plotted in Figure 2g ($d = 0.3$) for $r_D = 2$ and a-b) $K = 0.1$, c-d) $K = 1$, e-f) $K = 10$.

Mean square displacements

The typical dimensionless mean-square displacements (msd) versus the dimensionless diffusion time ($t \cdot D^d \cdot l_0^{-2}$) are plotted for a counter-intuitive situation: E_1, $d = 0.3$ and $r_D = 0.1$ and wide range of K values in Figure 4. The msd values of each curve were averaged over the trajectories of 100 diffusants. The theoretical curves corresponding to a scaled asymptotic diffusion coefficient, D/D^d, equals to the scaled diffusion coefficient in the continuous phase, r_D, are also indicated. On a log-log scale, the asymptotic regime is identified by an unitary slope and the corresponding diffusion coefficient is given by its intercept.

In the depicted situation, the transport in the continuous phase is the limiting factor on short time scales so that msd values are lower when the affinity for the dispersed phase (low K values) is higher. By contrast, on long time scales and for low K values, the trend is reverse and the limiting factor is the confinement in the dispersed phase. The change in behavior is identified by a change in the slope of the scaling relationship of msd with diffusion time. For all morphology, there is always an optimal K value, lower than 1, which leads to the shortest paths between all possible combinations on short and long time scales. This value is all the lower than d is higher.

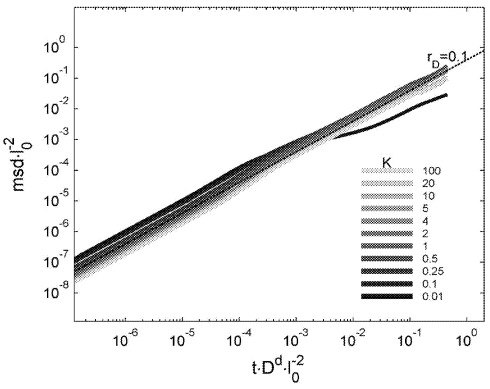

Figure 4: Scaling relationship of msd with diffusion time for E_1, $d = 0.3$ and $r_D = 0.1$.

Variation of the asymptotic diffusion coefficient with studied properties (2042 tested conditions)

The effects of all tested parameters were analyzed as least-square bi-variate cubic spline approximations of D/D^d versus r_D and K for all tested d values and morphologies. Each model consisted in 4 continuous piecewise approximations along each variable (r_D and K). The positions of nodes were optimally calculated to minimize the deviation to calculated results. Boundary conditions were applied to fit asymptotic behavior for $r_D = \{0, +\infty\} \times K = \{0, +\infty\}$. The 8 derived abacus are plotted in Figure 5 as contour plots for common D/D^d values.

The contour plots exhibit a half square shape which confirms the predominance of r_D effects for K values higher than 1. For a same r_D value, a variation of K between 10^{-2} and $+\infty$ generates a variation in of D/D^d up to 5 folds. A greater effect is expected for values lower than 10^{-2}.

The effect of K is significant mainly for values lower than 1. When the diffusivity is higher in the discontinuous phase, the asymptotic diffusion coefficient does not vary monotonously with K (Figure 5d) and reaches a maximum close to $K = 1$. The maximum is only located at $K = 1$ only for $r_D = 1$ (Figure 5e). It is obtained for K values slightly lower than 1 for $r_D < 1$ and above 1 for $r_D > 1$ (Figure 5f-j). $K \to \infty$ yields never a maximum.

Oscillations observed for certain contours are not an artifact and are related to non-linear combined effects between r_D

and K. They are connected to non monotonous variations of D/D^d with K for r_D values around 1. The effects of d and of the morphology consist mainly in modifying the location of this maximum on the K scale and consequently the amplitude of the oscillations.

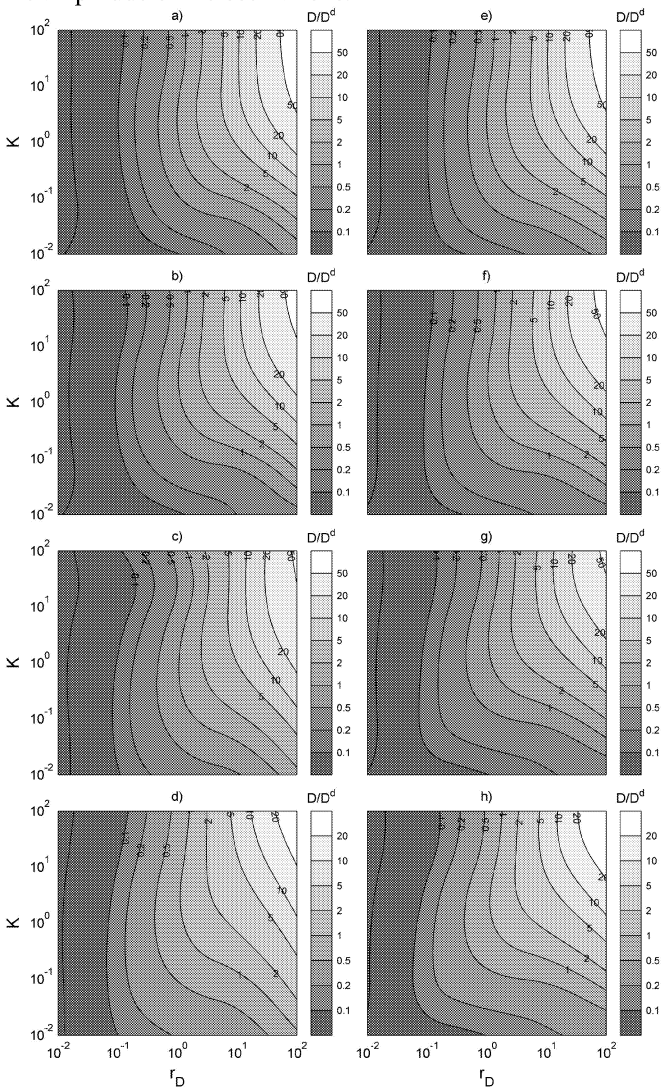

Figure 5: Bi-variate cubic spline approximations of the asymptotic diffusion coefficient with K and r_D for a,e) $d = 0.1$, b,f) $d = 0.2$, c,g) $d = 0.3$, d,h) $d = 0.4$ and for a-d) morphology E_0, e-h) morphology E_1.

Comparison of simulated results with the model proposed by Kalnin and Kotomin (1998)

In our notations, the model proposed by Kalnin and Kotomin (1998) is written in 2D with $0 \le \Phi \le 1$:

$$\frac{D}{D^d} = \frac{r_D}{1 - \Phi - \frac{\Phi}{K}} \cdot \left[1 + 2 \cdot \left(\frac{1}{K} - r_D \right) \cdot \frac{\Phi}{r_D + \frac{1}{K} - \left(\frac{1}{K} - r_D \right) \cdot \Phi} \right] \quad (12)$$

Equation (12) admits a free parameter, Φ, which must be fitted to either experimental or simulated results to predict the effective diffusion coefficient in emulsions. Since, it is originally related to the volume ratio of concentric regions, Φ was first fitted to results obtained for a same d value and morphology.

The results are depicted in Figure 6 for all conditions reliably tested in this study.

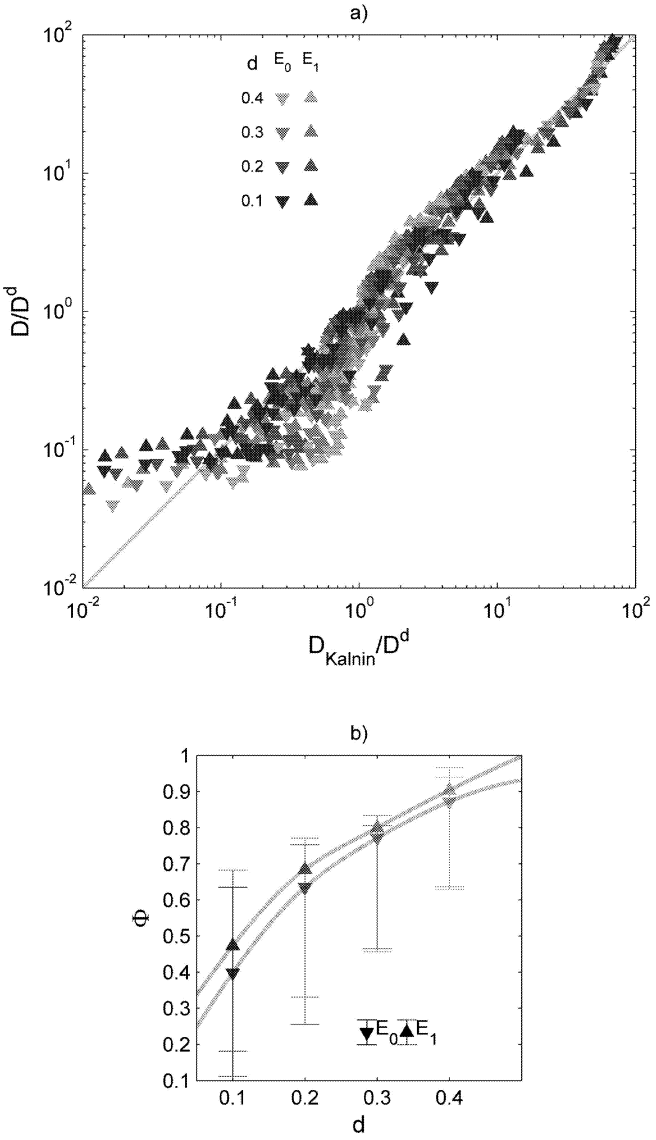

Figure 6: a) Comparison between simulated results and the fitted algebraic model proposed par Kalnin and Kotomin (1998). The curve y=x is plotted in dotted line. b) Values of the fitted parameter Φ in the Kalnin and Kotomin model by assuming it varies only with d. 80% confidence intervals plotted as error bars were calculated by considering possible effects of K and r_D.

The two estimates of the effective diffusion coefficient were in good agreement. Significant negative deviations were nonetheless observed for the most heterogeneous morphology (E_1). Besides, a higher bias was identified for small D/D^d values related to either low K or r_D values (Figure 6a).

To test whether observed discrepancies could be related to possible variations of Φ with K or r_D, Figure 6b plots the previously identified values of Φ versus d and their 80%

confidence intervals (based on 10th and 90th percentile values) calculated by adjusting independently Φ from results simulated for similar K and r_D values. Φ was found to increase significantly and non-linearly with d. The contribution of d was however as high as the other variations due to K or r_D. As a result, Φ should be envisioned as a nonlinear function of d, K, r_D and of the morphology. This possible extension of the model proposed by Kalnin and Kotomin (1998) was related to the possible contacts between globules and the confinement generated by globule aggregates.

CONCLUSIONS

This work illustrates how the simulation of random walks in the general framework of Langevin Dynamics can be used to calculate efficiently effective transport properties in complex systems as food products. The proposed methodology was applied to the calculation of effective diffusion coefficients in emulsions for a wide range of conditions $K = \left[10^{-2}, \infty\right[\times r_D = \left[10^{-2}, 10^{2}\right] \times d = [0.1, 0.4] \times [E_0, E_1]$.

Only approximations exist for this general problem and only simulations make it possible to assess the subtle effects related to the morphology (density, connectivity) of the emulsion or to the transition between the Fickian regime and Knudsen regime in dense emulsions. The continuous implementation of motion equations and their interface conditions made it possible to handle in single formulation all phenomena. The reliability of the whole approach was examined in very detailed microstructure with variations between the smallest and the largest globules up to 4 magnitude orders.

The simulated results showed that r_D had a major effect and controlled the magnitude order of D/D^d, while K was not too small. For very low K values, K had a drastic effect and led to a confinement of trajectories on long terms. The effects of r_D and K did not commute since very low r_D values restricted the trajectories within globules only during short or middle terms. For r_D values lower than 1, the possible connectivity between globules or the trapping of the continuous phase at high concentration of globules modified the diffusion paths so that the maximum D/D^d value occurred for a K value lower than 1. The core-shell model proposed by Kalnin and Kotomin (1998) was compared to our simulated results by adjusting the parameter Φ and could be proposed as a phenomenological estimate of effective diffusivities in emulsions. The background theory of this model should be however modified to account for variations of Φ not only with the globule densities but also with the complex morphologies and distributions of globules. Indeed, close to the percolation threshold, the local variations in the globules concentration modifies the effective diffusion coefficient even for monodisperse emulsions.

Since our results rely on simplifications, which may be unrealistic for true macroscopic emulsions, further work is desirable to account for i) relative displacement or reordering of globules (e.g. due to Brownian motions) and ii) possible specific interactions at the globule interface due to the presence of surfactants. A 3D version of our code is yet available.

REFERENCES

Belova, I. V. and G.E. Murch. 2003. The effective diffusivity in two-phase material. Defect and diffusion forum, 218-220, 79-89.

Busch, K. and C. M. Soukoulis. 1995. Transport properties of random media: a new effective medium theory. Physical Review Letters, 75(19), 3342-3445.

Cranck, J. 1975. "Chapter 12: Diffusion in heteregeneous media." In The mathematics of diffusion, 2nd Edition, Oxford University Press, 266-285.

Doulia, D.; Tzia, K. and V. Gekas. 2000. A knowledge base for the apparent mass diffusion coefficient (D_{eff}) of foods. International Journal of Food Properties, 3(1), 1-14.

Kalnin, J.R.; Kotomin, E. A. and J. Maier. 2002. Calculations of the effective diffusion coefficient for inhomogeneous media. Journal of Physics and Chemistry of Solids, 63, 449-456.

Kalnin, J.R. and E. Kotomin. 1998. Modified Maxwell-Garnett equation for the effective transport coefficients in inhomogeneous media. Journal of Physics: Mathematical and General, 31, 7227-7234.

Küntz, M.; van Mier, J.V.M. and P. Lavallée. 2001. A lattice gas automation simulation of the non linear diffusion equation: a model for moisture flow in unsaturated porous media. Transport in porous media, 43, 289-307.

Marsh, C.A. and P.V Coveney. 1998. Detailed balance and H-theorems for dissipative particle dynamics. Journal of Physics A: Mathematical and General, 31, 6561-6568.

Nauman, E.B. and D.Q. He. 2001. Nonlinear diffusion and phase separation, Chemical Engineering Science, 56, 1999-2018.

Riley, M.R.; Muzzio, F.J.; Buettner, H.M. and S.C. Reyes. 1994. Monte Carlo calculation of effective diffusivities in two- and three-dimensional heterogeneous materials of variable structure. Physical Review E., 49(4), 3500-3503.

Ronis, D. 1986. Diffusion in random two phase media. Physical Review A, 36(4), 1908-1928.

Snitzman, A.-S. 2001. On a class of transient random walks in random environment. The annals of Probability, 29(2), 724-765.

Zhu, J.; Chen, L.-Q.; Shen, J. and V. Tikare. 2001. Computing the effective diffusivity using a spectral method. Materials Science and Engineering, A311, 135-141.

MATHEMATICAL MODELLING THE EFFECT OF LIPIDS ON DOUGH DEVELOPMENT DURING LEAVENING

Annalisa Romano
Silvana Cavella
Paolo Masi
CAISIAL - Facoltà di Agraria
DSA - Facoltà di Agraria
Università di Napoli Federico II
Portici (NA), Italy
anromano@unina.it

Gerardo Toraldo
DIAAT - Facoltà di Agraria
Università di Napoli Federico II
Portici (NA), Italy
toraldo@unina.it

KEYWORDS: lipid, bread dough, leavening, non linear regression models.

ABSTRACT

Knowledge of the functional role of ingredients in complex foods may provide guidelines for approaching problems in the production process. Fats and oils have been important bakery ingredients for centuries, maize oil, palm oil and butter were chosen for their different fatty acids composition and percent of fat that is solid at various temperatures. The aim of this study was to select a suitable mathematical model that describes the effects of lipid content and origin on fermentation kinetic of wheat flour doughs. A descriptive growth model of the fermentation kinetic of wheat flour doughs was considered. The fermentation kinetic was investigated by monitoring the variation of the dough volume in time by means of Image Analysis. Fermentation process is a nonlinear and time-dependent process; thus a kinetic model was chosen in order to describe the process. Quite good agreement was observed between experimental data and model parameters.

INTRODUCTION

Leavening is the heart of all processes to produce raised bread, inflating the bubble size distribution produced during mixing, to give a raised loaf of good volume.
Dough is a multiphase and multicomponent system mainly composed of proteins, lipids, carbohydrates, water and air. It has a foam structure, with continuously growing gas bubbles dispersed in a viscoelastic dough phase. As the volume fraction of the gas increases during fermentation, the foam structure becomes increasingly unstable. To obtain a loaf of bread with a good volume and a fine and even crumb texture, it is crucial to promote the stability of the foam during bread dough processing.
The effect of added fats and oils in baking has been investigated by several authors (Bell *et al.*, 1981; Moore and Hoseney, 1986; Watanabe *et al.*, 2002). In particular, Giannou and co-workers (2003) have demonstrated that the lipids embedded into protein matrix are important as they interact with proteins during dough mixing and contribute to the viscoelastic properties of the gluten network, which in turns governs the gas expansion and retention during proofing. Moreover, it is known that the presence of lipids can increase the stability of dough because it helps to maintain the continuity of the gas/liquid interface in the course of the dough expansion process (Gan *et al.*, 1995). Gas cells stabilization and gas retention are of considerable technological interest as both determine the final volume of the loaf. The functional effect of lipids in breadmaking depends on the type of lipid used and the interactions with other dough components (Erazo-Castrejòn *et al.*, 2001). The structural and crystalline properties of fats determine their functionality in food.
Mahdi *et al.* (1981) speculated that plastic solid fat such as shortening aids air incorporation during dough mixing, which leads to more air cells. On the other hand, oil forms spherical droplets with minimal surface-to-volume ratio, thus making it impossible to increase the fat-water interface (Bell *et al.*, 1981). Leissner (1988) regarded dough as a foam and suggested that the effect of lipids was related to stabilization of the aqueous gas interface. There is still a lack of agreement and no satisfactory explanation of why only fats and oils increases the loaf volume. The dough leavening process involves biochemical, rheological and thermodynamic phenomena, which are nonlinear distributed-parameter processes. The description of a fermentation process will always be a rough simplification of reality, since detailed picture of the various biological and physical phenomena responsible for bubbles growth during the leavening process is not fully elucidated yet.
The objective of the present work is to analyze how the presence of lipids in the dough affects the leavening process, depending on their levels and structural features, such as solid fat content (SFC), through the use of a suitable mathematical model.

MATERIALS AND METHODS

Materials

Samples were prepared by using soft wheat flour (Barilla®, Italy: 7.5% proteins, 0.1% fat, 13.5% moisture content), deionised water, salt, sugar and yeast (Mastro Fornaio, Paneangeli®), and different lipids as follows: butter (Yma®, Italy), maize oil (Star®) and palm oil (Master Martini- Unigrà S.p.A.).

Dough-making procedure

All doughs were prepared in a Brabender farinograph (Duisburg, Germany), equipped with a 50 g bowl, by mixing commercial soft wheat flour (43.75g), water (25ml), salt (1.25g), sugar (0.5g) and yeast (0.75g).
Lipids concentrations investigated were 0.0 -3.0 -6.6 -9.0 -12.3 -14.13% (w/w).

Image analysis

45g of dough were taken just after mixing (3min) and incubated at 36 ± 1°C, 70% U.R., monitored by means of a data logger (Logger Escort mod. 10D8, Gamma Instrument s.r.l., Naples, Italy), for 2.5 hour. Dough was continuously photographed during leavening with a MV450 digital camera (Canon INC, Japan). By assuming axial symmetry, the loaf was interpreted as a solid of revolution generated by the revolution of a lamina around the symmetry axis, and its volume V was calculated using the following formula (second theorem of Pappus):

$$V = 2 \pi A r_g \quad (1)$$

where A is the lamina surface and r_g the distance of the center of the mass of the lamina from the axis. The area and centre of the mass were determined by a computer assisted image analyser (Jandel Sigma Scan®Pro Version 2.0, Jandel Corporation, 1995). Each average value represents the mean of 3-7 independent measurements.

Measurement of Solid Fat Content (SFC)

The solid fat content (SFC) was determined by low-resolution pulsed NMR spectroscopy using a NMR – minispek (Bruker S.r.l, Milano, Italy).
Lipid sample (4-5 g) were weighted into a glass test tube of 10 mm in diameter, sealed and placed into the magnet module of the NMR analyzer for testing.
The temperature range used in the NMR experiment was 0 -50°C. Each sample was measured at five temperature points. At every temperature point, the sample was allowed to equilibrate for 1 min the change in the sample temperature during this period was within ± 1°C before measurements were taken. SFC determinations were carried out in duplicate and averaged.

Fitting of the data

The leavening data from each experiment were fitted to the modified Gompertz equation using the curve fitting system for Windows CurveExpert 1.3 (Hyams, 1995). The modified Gompertz equation has the following formula:

$$y(t) = \alpha \exp\left(- \exp\left(\frac{\mu e}{\alpha}(t_{lag} - t) + 1 \right) \right) \quad (2)$$

where α represents the maximum relative volume expansion ratio of the loaf; μ the maximum specific volume growth rate, t_{lag} the time lag of the leavening process and e the Neper number. The independent and dependent variable are t and y, respectively.
Parameters μ, α and t_{lag} were determined using a nonlinear regression procedure (Romano *et al.*, 2005).
The parameters of each model were obtained by minimizing the sum of squares of the prediction errors.

Statistical analysis

Analysis of variance (SPSS v11.0) was performed in order to evaluate the effect of lipids on leavening. Significant differences between the treatment means were compared by means of Duncan's multiple comparison test at the 95% confidence level ($p \leq 0.05$).

RESULTS AND DISCUSSION

By proving the samples at times varying between 0 and 2.5 hour, the effect of lipids on volume expansion was investigated. Figure 1 shows a typical evolution of dough volume during leavening in terms of volume expansion ratio (overrun):

$$\Delta V = \left(\frac{V_t - V_0}{V_0} \right) \quad (3)$$

where V_t is volume at time t and V_0 volume at time 0.

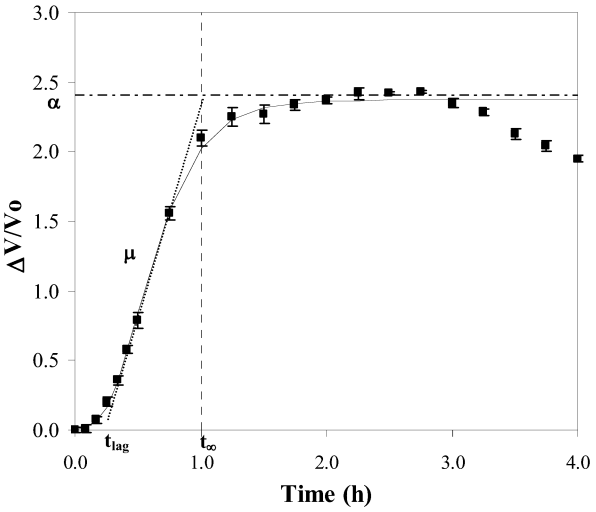

Figure 1: Volume expansion on time of doughs during leavening with model parameters

The typical shape curve of volume expansion ratio is characterized by three distinct regions: (a) induction phase; (b) growth phase; (c) stationary phase (Romano et al., 2004). Such a behavior is accurately described by a sigmoid shaped curve, which increases with a growth

rate monotonically reaching an inflection point and then decreases to zero while the curve approaches asymptotically a constant value.
The model proposed in this work derives from the model originally used for describing the bacterial growth in pH-controlled batch cultures (Schepers *et al.*, 2000). A former study (Romano *et al.*, 2005) demonstrated that the Gompertz model appears very suitable as descriptive of the fermentation kinetic of wheat flour doughs.
The model fits very well to the observations (Tab. 1) and it shows good agreement with the different experimental data set with correlation coefficient greater than 0.98.

Table 1: Fitting results

Lipid content	Maize oil		Butter		Palm oil	
(%w/w)	RSS	standard error	RSS	standard error	RSS	standard error
0.00	0.048	0.058	0.048	0.058	0.048	0.058
3.00	0.015	0.035	0.069	0.070	0.032	0.052
6.60	0.018	0.039	0.021	0.039	0.039	0.057
9.00	0.017	0.037	0.019	0.037	0.033	0.053
12.30	0.022	0.042	0.013	0.030	0.006	0.023
14.13	0.021	0.042	0.017	0.035	0.011	0.030

Our model depicts leavening more accurately and it is an useful tool to describe the effects of fat content and origin on fermentation kinetic of wheat flour doughs.
In Table 2 the parameter values obtained from the fitting curves for the experimental data sets are shown.

Table 2: Parameters

Lipid content (%w/w)	Lipid type	α	μ (h^{-1})	t_{lag} (h)
0.00	none	2.81	2.68	0.28
3.00	Maize oil	2.87	2.85	0.33
	Butter	2.44	3.11	0.38
	Palm oil	2.27	2.77	0.40
6.60	Maize oil	2.74	2.91	0.27
	Butter	2.39	3.24	0.24
	Palm oil	2.14	3.21	0.30
9.00	Maize oil	2.38	2.84	0.30
	Butter	1.99	3.16	0.32
	Palm oil	1.93	2.95	0.32
12.30	Maize oil	2.15	3.09	0.35
	Butter	1.90	2.91	0.29
	Palm oil	1.76	2.66	0.31
14.13	Maize oil	1.72	2.48	0.45
	Butter	1.57	2.45	0.37
	Palm oil	1.43	2.43	0.34

The parameter a which accounts for the maximum volume expansion shows a strong dependence on lipid content and type.
A negative effect of lipids on maximum relative volume expansion ratio of the loaf can be noted. In fact, it decreases with the increase in the lipid content. In particular, the maximum final volume is obtained for 3.0% of added maize oil while the minimum is obtained for 14.13% of butter and palm oil added.
The parameter μ, which accounts for the maximum specific volume growth rate, varies in a not monotonically manner, whilst the time lag t_{lag} remains rather stable (about 0.3) at all concentrations of lipid and for all lipid type.
It is interesting to note that all the observed behaviours are congruent with the influence that lipids exerts on physical and biological processes taking place during dough leavening. With increasing the lipid content the gas production rate does not increase and the model parameters which are all, with except the parameter a, related to gas formation process varies accordingly.
Maize oil, palm oil and butter were chosen for their different plasticity at room temperature. The plastic range, or the fat's consistency at different working temperatures, is of major importance to the fat's performance in several bakery applications. The plastic character of the shortening is influenced by several factors, such as the ratio of solid to liquid components (SFC), the size and form of the individual crystals, the persistence of crystal nuclei, the melting point of the solid phase, etc. (Vieira, 1999). The solid fat contents of maize oil, butter and palm oil are shown in Table 3.

Table 3: Solid Fat Content of lipids used in doughs

T (°C)	MAIZE OIL	BUTTER	PALM OIL
0	0.5	42.5	45.4
10	0.5	13.0	14.7
25	0.3	3.5	5.7
36	0.1	1.1	1.9
40	0.0	0.6	2.1
50	0.0	0.3	0.4

The solid fat content (SFC) is related to the percentage of shortening that is solid at various and selected temperatures. The SFC of a given lipid is characteristic of that lipid and in large measure governs its physical and functional properties. The solid content of different lipid varies widely with origin lipid and different temperatures.
About effects of fats on dough leavening, some studies (Brooker, 1996; Autio and Laurikainen, 1997) have reported that added liquid oils do not increase the loaf volume as solid fats do and suggested that fat crystal are adsorbed at the air-water interface. But there is no satisfactory explanation for how the solid fat increases the loaf volume.
In our experiments, a negative linear correlation was observed between the solid fat content (SFC) of three lipids at leavening temperature (36°C) and the a parameter in all single-sample methods (see figg. 2-6).
The highest correlation and lowest correlation were respectively observed with the maximum (14.13%) and medium (9.0%) lipid content.

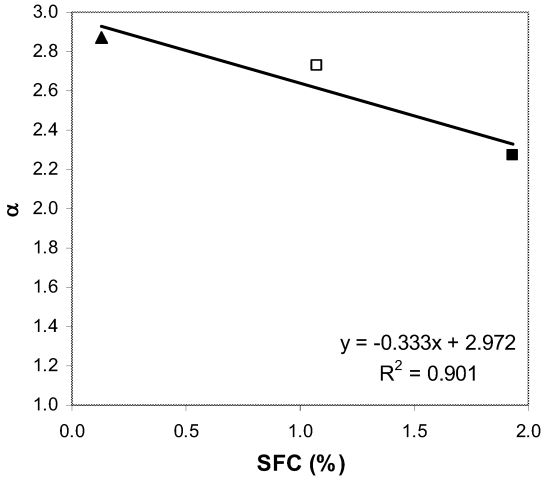

Figure 2: Regression between SFC (%) of maize oil (▲), butter (□), palm oil (■) and α of doughs with 3.0% lipid content.

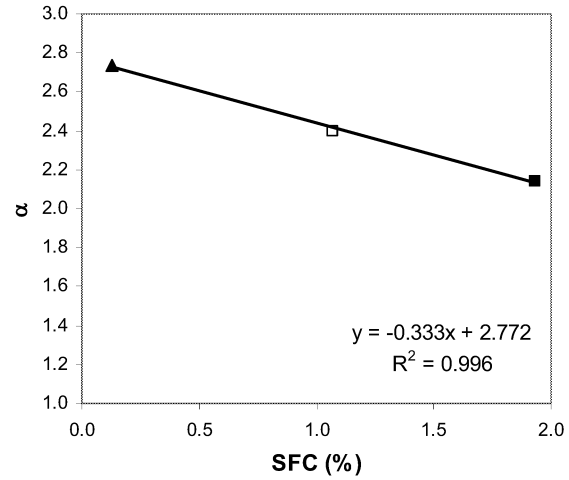

Figure 3: Regression between SFC (%) of maize oil (▲), butter (□), palm oil (■) and α of doughs with 6.6% lipid content.

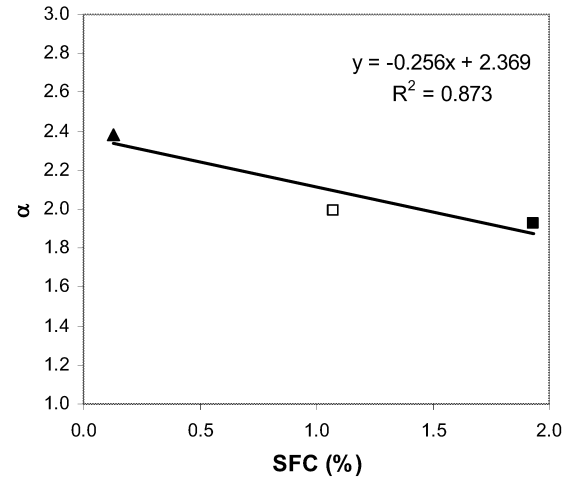

Figure 4: Regression between SFC (%) of maize oil (▲), butter (□), palm oil (■) and α of doughs with 9.0% lipid content.

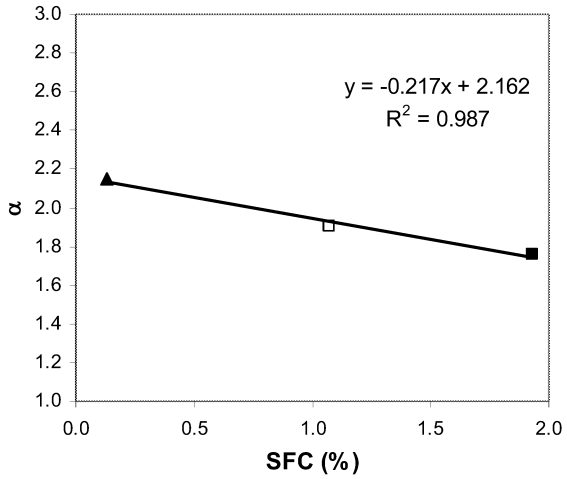

Figure 5: Regression between SFC (%) of maize oil (▲), butter (□), palm oil (■) and α of doughs with 12.3% lipid content.

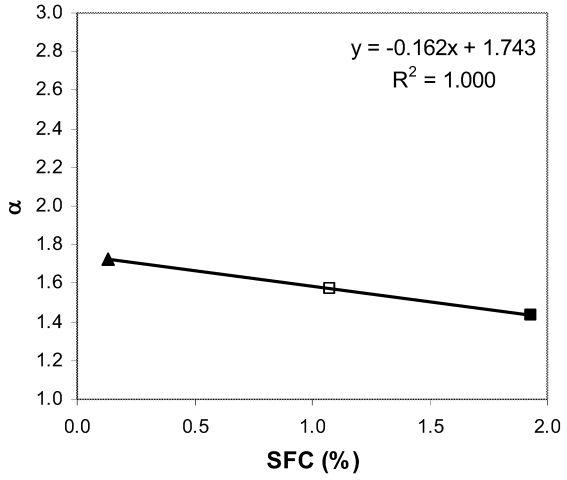

Figure 6: Regression between SFC (%) of maize oil (▲), butter (□), palm oil (■) and α of doughs with 14.13% lipid content.

The influence of type lipid is more relevant for smaller amount of lipids. With the increase of the added lipids, doughs show more elastic behaviour, which resulted in a lower volume expansion of the loaf. Especially the added lipid is absorbed in the gluten structure, causing the aggregation of the gluten. The fats and oils containing gluten tends to stick together. Doughs with elevated level of lipid could thus give the lowest volume because they require higher stress to expand and has a tendency to contract after expanding.

CONCLUSIONS

This study proves that the leavening behaviour of dough is strongly dependent on both lipid contents and type.
The three-parameter model proposed in this work appears very suitable as descriptive of fermentation kinetic of wheat flour doughs with lipids.
Meaningful parameters such as maximum specific growth rate (μ), lag time (t_{lag}), the maximum relative

volume expansion ratio of loaf (α) were estimated from the fitting curves. Their behaviour with varying the lipid concentration is congruent with physicochemical and biological phenomena responsible for the development of the sponge structure of leavened dough. In fact, only α parameter shows a strong dependence on lipids.
The main advantage of this model is that the whole process is described by means of only one experimental measure (volume). The obtained quantitative information can be advantageously used to describe the relationships among physical structure and bread quality.

BIBLIOGRAPHY

Autio K., and Laurikainen T. (1997). Relationships between flour/dough microstructure and dough handling and baking properties. *Trends Food Science & Techn.*, 8, 181-185.

Bell B.M., Daniels D.G.H. and Fisher N. (1981). Vacuum expansion of mechanically devepolment doughs at proof temperature: Effect of shortening. *Cereal Chem.*, 58, 182-186.

Brooker B.E. (1996). The role of fat in the stabilisation of gas cells in bread dough. *J. Cereal Sci.*, 24, 187-198.

Erazo-Castrejon S.V., Doehlert D.C., D'Appolonia B.L. (2001). Application of oat oil in breadmaking. *Cereal Chem.,* 78 , 243-248.

Gan Z., Ellis P.R., & Schofield, J.D. (1995). Mini review: Gas Cell Stabisation and Gas Retention in Wheat Bread Dough. *J. Cereal Sci.,* 21, 215-230,

Giannou V., Kessoglou V., and Tzia C. (2003). Quality and safety characteristics of bread made from frozen dough. *Trends Food Science & Techn.*, 14, 99-108.

Hyams D. 1995-2003. CurveExpert® version 1.3: A comprehensive curve fitting system for Windows.

JANDEL SIGMA SCAN®PRO Version 2.0 1995, Jandel Corporation.

Leissner O. (1988). A comparison of the effect of different polymorphic forms of lipids in breadmaking. *Cereal Chem.*, 65, 202-207.

Mahdi J.G., Varriano-Marston E. and Hoseney R.C. (1981) The effect of mixing atmosphere and fat crystal size on dough structure and bread quality. *Baker's Dig.*, 55, 28-36.

Moore R. and Hoseney R.C. (1986). Influence of shortening and surfactants on retention of carbon dioxide in bread dough. *Cereal Chem.*, 63, 67-70.

Romano A., Bencivenga S., Cavella S., Toraldo G. and Masi P. (2004). The influence of lipids on dough development during mixing and fermentation process. *International Conference on Engineering and Food* ICEF9*,* Montpellier (France), 7-11 March, 620-625.

Romano A., Toraldo G., Cavella S. and Masi P. (2005). Mathematical modelling of bread dough fermentation. *Innovation in Traditional Foods* INTRADFOOD2005*,* Valencia (Spain), 25-28 october, 775-778.

Schepers A.W., Thibault J., Lacroix C. (2000). Comparison of simple neural networks and nonlinear regression models for descriptive modeling of Lactobacillus helveticus growth in pH-controlled batch cultures. *Enzyme Micr. Tech.*, 26, 431-445.

Vieira E.R. (1999). Fats and oils. In *Elementary Food Science*, An Aspen Publication, Aspen Publishers Inc., Gaithersburg, Maryland, 337-346.

Watanabe A., Larsson H. and Eliasson A.C. (2002). Effect of physical states of non-polar lipids on rheology and microstructure of gluten-starch and wheat flour dough. *Cereal Chem.*, 79, 203-209.

FOOD QUALITY SIMULATION

A COMSOL SIMULATION OF THE OSMOTIC DEHYDRATION OF MANGO

Juliane Floury
UMR 1253 STLO - INRA - Agrocampus
65 rue de Saint Brieuc CS 84215
35042 Rennes, France
juliane.floury@agrocampus-rennes.fr

Q. Tuan Pham
School of Chemical Engineering and Industrial Chemistry
University of New South Wales
Sydney 2052, Australia
tuan.pham@unsw.edu.au

Alain Le Bail
UMR CNRS GEPEA
(6144 SPI) - ENITIAA
Rue de la Géraudière BP 82225
F-44322 NANTES cedex 3
lebail@enitiaa-nantes.fr

INTRODUCTION

Osmotic dehydration is widely used for the partial removal of water from plant tissues by immersion in a hypertonic (osmotic) solution. During the process, the food product is in contact with a concentrated sugar solution and a two-way mass transfer is established: (i) water is transferred from the product to the solution, often accompanied by natural substances (sugars, vitamins, pigments, flavours) and (ii) in the opposite direction, solute is transferred from the solution to the fruit pieces (Agnelli et al. 2005).

This paper presents a mathematical model for simulating the mass transfer during osmotic dehydration process of mango cubes. The model was implemented in *COMSOL Multiphysics* using a 3D geometry. The mass balance equation for the transport of each constituent (water and sucrose) is established separately for intracellular and extracellular volumes but taking into account the mass exchanges across the cell membrane between the intracellular and extracellular volumes.

STATE OF THE ART

The existence of two simultaneous and opposite mass fluxes is one of the main difficulties arising when modeling the internal mass transfer in osmotic dehydration. Moreover, these fluxes take place in strong non-equilibrium conditions, accompanied by very important shrinkage and deformation of the vegetable/fruit piece (Geurst et al., 1974; Lenart & Flink, 1984) and, possibly, by interactions between the different fluxes (Biswal & Le Maguer, 1989; Raoult-Wack et al., 1991). Spiazzi and Mascheroni (1997) identified in the literature a number of mathematical models capable of representing the experimental data (Hawkes and Flink 1978; Magee et al. 1983; Rahman et Lamb 1990; Hough et al. 1993), but their use is limited to certain cases and they do not take into account the mechanisms on which the results depend. Other models (Toupin et al. 1989; Marcotte et al. 1991, Yao et Le Maguer, 1996) which are much more elaborate, allow the above-mentioned complexity to be described but their experimental validation is extremely difficult owing to the number of parameters that have to be known in order to solve the equations.

MATHEMATICAL MODEL

With the aim of finding a model that is well founded and yet easy to use, a diffusional model inspired by the models of Toupin et al. (1989); Marcotte et al. (1991) and Spiazzi and Masheroni (1997) was developed in the FEMLAB finite element softtware using a three-dimensional geometry. This model is based on mass transfer through cellular membranes and the diffusion of different species through intercellular spaces.

Parenchymatous cells are the main cell type encountered in osmotic dehydration processes and will be considered to consist of three parts: an intracellular volume (V_c), an extracellular volume (V_e) and a cell membrane located between the two volumes.

Equation of mass balance

The two simultaneous, counter-current flows are the solute flow from the concentrated solution into the tissue and the water flow out from the tissue into the solution. The three paths are the transport within the intracellular volume, namely *symplastic transport*, the transport within the extracellular volume, namely *free-space transport*, and the transport across cell membrane, namely *apoplastic transport*. Mangos were here assumed to be composed of water and sucrose only. The equations of mass balance for each species i within the referenced frame can then be expressed as:

- in the intracellular volume ($i = s$, sucrose and w, water):

$$\frac{\partial\left(V_c\, c_i^{\text{int}}\right)}{\partial t}=\nabla\left(V_c\, D_{eff}^{\text{int}}\nabla c_i^{\text{int}}\right)+A_m J_i \qquad (1)$$

- in the extracellular volume ($i = s$, w):

$$\frac{\partial\left(V_e\, c_i^{\text{int}}\right)}{\partial t}=\nabla\left(\frac{V_e}{\tau}D_{w-s}^{ext}\nabla c_i^{ext}\right)-A_m J_i \qquad (2)$$

where t is the time, c_i^{int} and c_i^{ext} are the concentrations of species i in the intracellular and extracellular volumes (mol.m^{-3}). V_c and V_e are the intracellular and extracellular volumes per m^3 initial total volume. D_{eff}^{int} is the effective diffusion coefficient in the intracellular volume, D_{w-s}^{ext} is the binary water-sucrose diffusion coefficient in the extracellular volume (m^2.s^{-1}) and τ is the tortuosity factor in the extracellular volume. J_i is the molar flux of species i from the intracellular volume into the extracellular volume through the cell membrane (mol.m^{-2}.s^{-1}) and A_m is the interface area between intra- and extracellular phases per m^3 initial total volume (m^2.m^{-3}).

During the mass transport the intracellular and extracellular volumes vary with both time and position. Assuming that the change of the intracellular and extracellular volumes volume is directly proportional to the sum of sugar and water volumes, i.e. ignoring the volume of the other components, the volume fractions of each phase are:

$$V_c=\frac{c_w^{\text{int}}\nu_w+c_s^{\text{int}}\nu_s}{c_{w,0}^{\text{int}}\nu_w+c_{s,0}^{\text{int}}\nu_s}V_{c,0}\;;\; V_e=\frac{c_w^{ext}\nu_w+c_s^{ext}\nu_s}{c_{w,0}^{ext}\nu_w+c_{s,0}^{ext}\nu_s}V_{e,0} \qquad (3), (4)$$

where v_s , v_w are the molar volume of sugar and water ($m^3.mol^{-1}$), $c_{i,0}^{int}$ and $c_{i,0}^{ext}$ are the initial concentrations of species i in the intracellular and extracellular volumes ($mol.m^{-3}$) and $V_{c,0}$ and $V_{e,0}$ are the initial cell and extracellular volumes per m^3 initial total volume ($m^2.m^{-3}$).

Note that the gradient operator in Eqs (1) and (2) has to be expressed with respect to transient coordinates in order to take into account the swelling of the cells and the volume change. If we note S the linear expansion ratio of the cells and assume isotropic expansion then:

$$S = (V_T)^{1/3} = (V_c + V_e)^{1/3} \quad (5)$$

where V_T is the present total volume per m^3 initial total volume, i.e. the total volumetric expansion. Thus the equations (1) and (2) become:

$$V_c \frac{\partial c_i^{int}}{\partial t} = \frac{1}{S}\nabla\left(\frac{V_c}{S} D_{eff}^{int} \nabla c_i^{int}\right) + A_m J_i - c_i^{int}\frac{\partial V_c}{\partial t} \quad (6)$$

$$V_e \frac{\partial c_i^{ext}}{\partial t} = \frac{1}{S}\nabla\left(\frac{V_e}{S} \frac{D_{w-s}^{int}}{\tau} \nabla c_i^{ext}\right) + A_m J_i - c_i^{ext}\frac{\partial V_e}{\partial t} \quad (7)$$

Diffusion coefficients

Predictions of the rate of intracellular and extracellular diffusion requires knowledge of the diffusion constant for the cytoplasmic and the extracellular aqueous sucrose solutions. The extracellular liquid was approximated as a binary solution of water and sucrose. The binary diffusion coefficient can then be estimated from the Stokes-Einstein equation, knowing the solute apparent hydrodynamic radius and the viscosity of the solution (Saravacos, 2005). The viscosity of the extracellular media, considered as binary sucrose and water solutions was evaluated from the sugar concentration and the temperature using an empirical equation proposed by Chenlo et al (2002).

Mass exchange across cell membrane

The driving force for the apoplastic transport of solutes and water across the cell membrane is the chemical potential difference between the solutions in the intracellular and extracellular volumes, which can be characterised using irreversible thermodynamics with the phenomenological equations (Toupin, 1986):

$$J_i = L_{m,i} \cdot \Delta\mu_i \quad (8)$$

where $L_{m,i}$ is a macroscopic phenomenological coefficient describing the permeability characteristics of the membrane to solute i, $\Delta\mu_i$ is the difference in chemical potential of water and sucrose across the membrane The thermodynamic force is given, by definition, for a plant cell environment:

$$\Delta\mu_i = RT\,\Delta \ln a_i + v_i\,\Delta P \quad (9)$$

where R is the universal gas constant, T is the absolute temperature of the system, a_i is the activity of species i, v_i is its partial molar volume and P is the hydrostatic pressure in the phase considered. Because of the difficulty of determining the difference of hydrostatic pressure, which is in relation to the unknown change of cellular volume (Toupin et al. 1989), ΔP was assumed to be negligible in the present study. The macroscopic phenomenological coefficient $L_{m,i}$ was here assumed to vary with concentration (Toupin, 1986) as

$$L_{m,i} = P_{m,i} * \tilde{c}_i \quad (10)$$

where $P_{m,i}$ is a macroscopic permeability coefficient to species i ($mol.N^{-1}s^{-1}$), assumed to be concentration independent. and $\tilde{c}_i$ is the average concentration of solute i across the membrane for which a difference in chemical potential is considered. The water activity values in both the intracellular and extracellular volumes were estimated thank to the Norrish equation (1966), knowing the sucrose concentration in each volume.

The interface area between intra- and extracellular phases per m^3 initial total volume was estimated knowing the average diameter d of the cells:

$$A_m = \frac{6V_c}{d} \quad (11)$$

The intracellular volume fractions V_c of the material was determined by digitally measuring the area occupied by the void phase in the binary image of the plane section.

The second type of transport to consider is the transfer of water from cell to cell, which requires that the molecules cross both the cell membranes and the cell wall. Most of this transport is facilitated thanks to the presence of small channels, known as the symplastic pathway. This transport was included in the effective diffusion coefficient of water, D_{eff}^{int}, characterising the overall cytoplasmic diffusion process:

$$D_{eff}^{int} = \left(\frac{1}{D_{w-s}^{int}} + \frac{A_m}{6K_{wall}}\right)^{-1} \quad (12)$$

where K_{wall} is the overall mass transfer coefficient through walls of two adjacent cells ($m.s^{-1}$). The symplastic effective mass transfer coefficient (K_{wall}) may be globally of the same order of magnitude as the plasmalemmatic mass transfer coefficient (Spiazzi & Masheroni 1997).

EXPERIMENTAL

Mangoes were procured from a local super market. The mango, after peeling, was cut into 10 mm cubes. Commercial sucrose was used as the osmotic agent. The samples were subjected to osmotic dehydration in a sucrose solution (40° or 50° Brix) at 40°C. The temperature was controlled using a constant temperature stirred water bath. The ratio of the volume of the pieces to that of the medium was maintained at 1:25 in order to ensure that the concentration of the osmotic solution did not change significantly during the experiment. Once the immersion time was reached, the samples were taken from the vessel, washed with distilled water, blotted with absorbent paper and weighed. The evolution of mass transfer was calculated from that of moisture content and soluble solids contents (sucrose). The determination of these parameters was done in triplicate as follows: the moisture content was determined in a vacuum oven at 70°C for 18 h and the sucrose concentration was measured with a refractometer (Atago Co, Ltd, Japan).
All the osmotic dehydration experiments were done in duplicate.

IMPLEMENTATION IN COMSOL

The model was implemented in *COMSOL Multiphysics* using a 3D geometry and 4 transient equations of mass

transfer. Due to symmetry considerations, an eighth of the cube was modelled, using a mesh with 192 quadratic elements. In order to avoid very sharp concentration changes at the boundaries, which caused instabilities during the calculations due to the quadratic interpolation method, a mass transfer coefficient k_c equal to 3.10^{-7} m.s^{-1} was implemented to the boundaries in contact with the sucrose solutions, giving an estimated Biot number of about 10. Since Biot >> 1, this reproduces conditions of negligible resistance to mass transfer at the surface.

There is no data for the permeability of membrane to sucrose. It cannot be assumed to be zero, due to possible denaturation of the membrane. Therefore, the trans-membrane flux of sucrose was assumed to be a function of the water flux across the membrane as follows:

$$J_s = -r\frac{v_w}{v_s}J_w \qquad (13)$$

where r, termed the "volume flux ratio", is a variable parameter, which has to be determined by fitting the experimental data. The volume flux ratio r should not be larger than about 1, to ensure that excessive swelling of the cell does not occur, since $r = 1$ means that for any volume of water leaving the cell an equal volume of sugar enters it. Microscopic examination of the processed mango suggests that the total volume of the cells have decreased significantly, therefore a value of r < 1 is assumed. All the others parameters employed in the numerical computation are given in Table 1.

Table 1. Parameter Values Data Used in Calculations

Parameter	Value	Unit
Cell diameter	$d = 87$	µm
Tortuosity factor	$\tau = 1$	-
	$V_{c0} = 0.74$; $V_{e0} = 0.26$	-
Initial volumes	$c_{w,0}^{int} = c_{w,0}^{ext} = 49442$	mol.m^{-3}
Initial concentrations	$c_{s,0}^{int} = c_{s,0}^{ext} = 398$	
Boundary concentrations (40°B)	$C_w^{sol} = 38867$	mol.m^{-3}
	$C_s^{sol} = 1362.5$	
Molar volumes	$v_w = 1.8E\text{-}5$	m^3.mol^{-1}
	$v_s = 21.1E\text{-}5$	
Permeability coefficient	$P_{m,i} = 5.8E\text{-}11$	mol.N^{-1}s^{-1}
Volume flux ratio	$r = 0.35$	-

RESULTS AND DISCUSSION

Comparison with experimental data

Figure 1 provides a comparison between the present numerical simulation and the experimental results obtained from osmotic dehydration of 10 mm mango cubes in 40°Brix and 50°Brix sucrose solutions using the parameters in Table 1. It can be seen that the numerical results are very well consistent with the experimental data. However, the numerical simulation that allowed to fit the best the experimental data were obtained with a tortuosity parameter set to 1, meaning that the mass transfer of the species in the extracellular volume may not be significantly hindered by the presence of the cells.

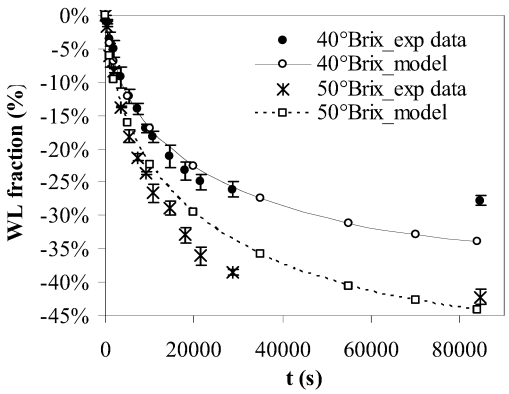

(a)

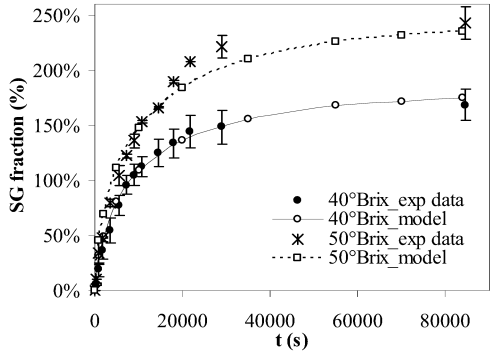

(b)

Figure 1. Experimental (● 40°Brix * 50° Brix Sucrose Solution) and Calculated Evolution of the (a) Water Loss Fraction; (b) Sugar Gain Fraction.

Parametric sensitivity analysis

The performance of the numerical model is highly dependant upon the values employed for the parameters describing diffusion in the intracellular and extracellular volumes, and above all upon the values of the membrane constants describing the fluxes of solutes and water flow over the cell membrane. Indeed, it is generally accepted that the most important organ controlling the osmotic phenomena is the plasmalemma membrane. The selective permeability of cell walls and membranes controls the quantity and the rate of mass transfer. Any destruction or disruption of the cell structure during osmotic treatment will result in poor dehydration and undesired mass transfer behaviour (Shi & Le Maguer, 2002).

Moreover, during osmotic dehydration processing, the solute diffuses into the extracellular volume. Depending on the characteristics of the solute, the solute may or may not penetrate the cell membrane and enter the intracellular volume. According to some authors, solute penetration is confined to extracellular spaces (Hawkes & Flink, 1978). The penetration of the solute creates a chemical potential difference across the cell membrane and draws the water out into the extracellular volume (Yao and Le Maguer 1996). As a consequence of this exchange, the product will lose some weight and it will shrink. However, some maintains that the sucrose may also penetrate into the intracellular volume, because of the denaturation of the membrane cell wall during the dehydration process. For Rastogi & Raghavarao (2004), the state of the cell membrane can change from being

partially permeable to being totally permeable and this can lead to significant changes in tissue architecture.

The influence of specific variables on the overall behaviour of the model can be illustrated effectively by using the model to predict the response of the system studied to changes in values of these variables. The major difficulty was here to find a reliable value for $P_{m,w}$ in the literature, because of the fact that each cell species possesses distinct biophysical properties characteristic of its biological function and structure. The numerous published data of plant membrane water permeability ranged over more than three orders of magnitude, depending on the plant cell specie. The membrane permeability of potato cells was reported equal to 5.8 10^{-9} mol.N^{-1}.s^{-1} (Yao and Le Maguer 1996).

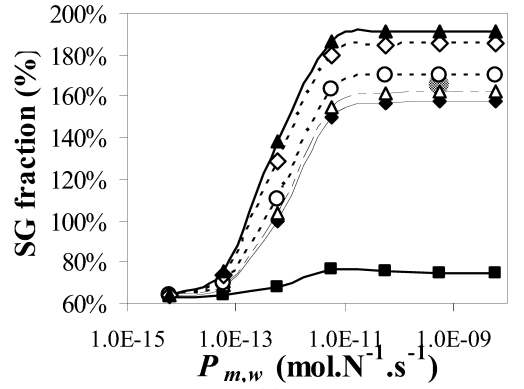

(a)

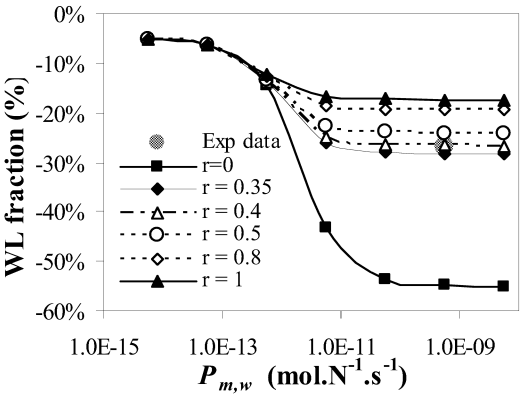

(b)

Figure 2. Influence of the Water Permeability $P_{m,w}$ and Trans-Membrane Flux Ratio r on (a) Sucrose Gain Fraction (b) Water Loss Fraction, both at t = 84000s

Figure 2 shows the influence of both the water permeability coefficient ($P_{m,w}$) and the trans-membrane flux of sucrose (volume flux ratio) on the efficiency of the dehydration process at the equilibrium (t = 84000s), i.e. the sucrose gain and water loss fractions. It can be observed that the water loss and sugar gain reached at the end of the dehydration process do not change much when the membrane permeability coefficient is greater that 1.10^{-11} mol.N^{-1}.s^{-1}. A value of $P_{m,w}$ equal to 5.8.10^{-11} instead of 5.8.10^{-9} mol.N^{-1}.s^{-1} has then been chosen in the present simulations.

When sugar is able to enter the cell, less water will have to leave it before equilibrium is reached. Thus water loss will decrease as sugar gain increases, as shown in Figure 3. We can also note that for a given volume flux ratio r, all points in Figure 3 fall on the same straight line, to a very good approximation, irrespective of the permeability value. This unexpected result allows the volume flux ratio to be estimated from experimental data, since the fractional changes in sugar and water can be easily determined. The sucrose/water trans-membrane volume flux ratio that fitted best the experimental data was $r \approx 0.35$ to 0.40.

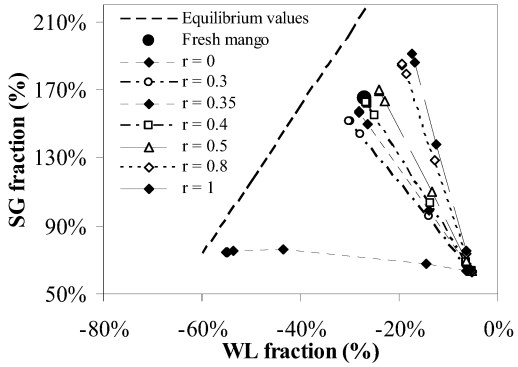

Figure 3. Sucrose Gain Fraction versus Water Loss Fraction

Figure 4 illustrates the variations of the water and sugar concentrations with variations in membrane permeability.

CONCLUSIONS

The osmotic dehydration of mango cubes has been modelled using the COMSOL finite element software. A good quantitative agreement was obtained between the experimental and calculated results for the sugar and water loss, provided the correct value is chosen for the cell membrane permeability to water and the ratio of water to sugar fluxes across the membrane. This flux ratio determines the amount of shrinkage, and hence the overall sugar gain and water loss. When fractional sugar gain is plotted against fractional water loss, the model predicts that all points corresponding to a given trans-membrane volume flux ratio value fall on a straight line. This allowed the volume flux ratio to be easily estimated from the experimental data. The data could be fitted only if it is assumed that the sucrose flux into the cell is about 35%-40% of the water flux out of the cells, in volumetric terms.

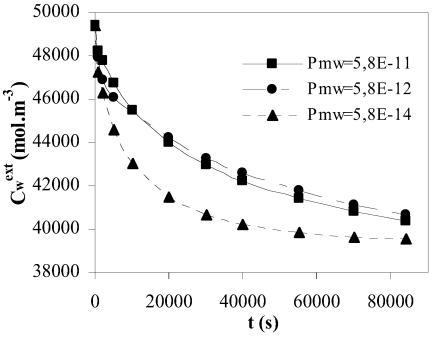

(a)

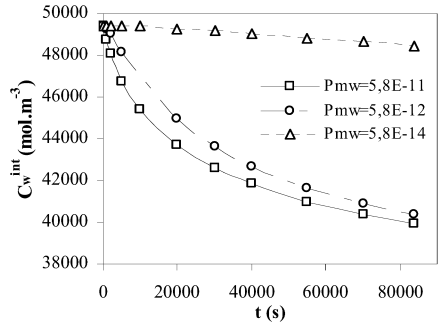

(b)

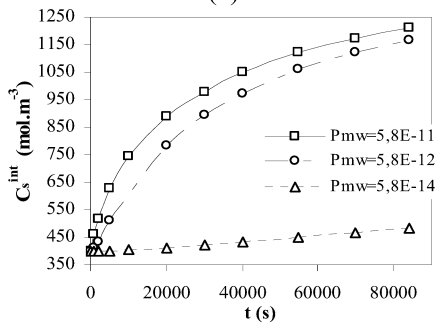

(c)

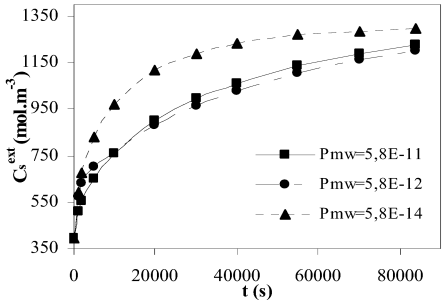

(d)

Figure 4. Influence of the Membrane Permeability $P_{m,w}$ ($mol.N^{-1}.s^{-1}$) on the Concentration Evolution of (a) Extracellular Water, (b) Intracellular Water, (c) Extracellular Sucrose and (c) Intracellular Sucrose.

REFERENCES

Agnelli, M.E., Marani, C.M. and Mascheroni, R.H. 2005. "Modelling of heat and mass transfer during osmodehydrofreezing of fruits". *Journal of Food Engineering*. 69, 415-424.

Biswal, R.N. and Le Maguer, M. 1989. "Mass transfer in plant material in contact with aqueous solutions of ethanol and sodium equilibrium data." *Journal of Food Process Engineering*. 11, 159-176.

Hawkes, J. and Flink, J.M. 1978. "Osmotic concentration of fruit slices prior to osmotic dehydration". *Journal of Food Processing and Preservation.* 2: 265-284.

Hough, G., Chirife, J. and Marini, C. 1993. "A simple model for osmotic dehydration of fruit." *Lebensmittel-Wissenschaft und Technologie*, 26, 151-156.

Lenart, A. and Flink, J.M. 1984. "Osmotic dehydration of potatoes. II. Criteria for the end point of the osmotic process." *Journal of Food Technology*, 19, 45-63.

Magee, T.R., Hassaballah, A.A. and Murphy, W.R. 1983. "Internal mass transfer during osmotic dehydration of apple slices in sugar solutions". *International Journal of Food Science and Technology,* 7, 147-155.

Marcotte, M., Toupin, C.J. and Le Maguer, M. 1991. "Mass transfer in cellular tissues. Part I: The mathematical model." *Journal of Food Engineering*, 13, 199-220.

Norrish, R.S. 1966. "An equation for the activity coefficient and relative humidities of water in confectionary sypup". *Journal of Food Technology*. 1, 25-28.

Rahman, M.S.and Lamb, J. 1990. "Osmotic dehydration of pinapple". *Journal of Food Science and Technology,* 7, 150-152.

Raoult-Wack, A.L. and Guilbert, S. 1990. "La déshydratation osmotique ou procédé de déhydratation-imprégnation par immersion dans les solutions concentrées". *Les Cahiers de l'ENSBANA, « L'eau dans les procédés de transformation et de conservation des aliments »,* 7 : 171-192.

Rastogi, N.K. and Raghavarao, K.S.M.S. 2004. "Mass transfer during osmotic dehydration of pineapple: considering Fickian diffusion in cubical configuration". *Lebensm.-Wiss. u.-Technol.* 37: 43–47

Saravacos, G.D. "Mass Transfer Properties of Foods". in Chap 8. Rao, M.A., Rizvi, S.S.H., Datta, A.K., *Engineering Properties of Foods*, 3rd Ed. CRC Press, Taylor and Francis Group pp. 327-380. 2005.

Shi, J. and Le Maguer, M. 2002. "Analogical Cellular Structure Changes in Solid–Liquid Contacting Operations*". Lebensm.-Wiss. u.-Technol.,* 35, 444–451.

Spiazzi, E. and Mascheroni, R. 1997. "Mass Transfer Model for Osmotic Dehydration of Fruits and Vegetables-I. Development of the Simulation Model". *Journal of Food Engineering*, 34, 387-410.

Toupin, C.J. 1986. "Osmotically Induced Mass Transfer in Biological Systems : the Single Cell and Tissue Behavior". Ph.D. Thesis, department of Food Science, University of Alberta, Edmonton.

Toupin, C.J., Marcotte, M. and Le Maguer, M. 1989. "Osmotically-Induced Mass Transfer in Plant Storage Tissues : A mathematical Model. Part I". *Journal of Food Engineering*. 10; 13-38.;

Yao, Z. and Le Maguer, M. 1996. "Mathematical modelling and simulation of mass transfer in osmotic dehydration processes. Part 1: Conceptual and mathematical models." *Journal of Food Engineering,* 29, 349-360.

A COMPREHENSIVE MODELLING APPROACH FOR YEAST GROWTH AND PHYSIOLOGY

Tomas Kurz
Department of Food Process Engineering
Technische Universität Berlin
Amrumer Str. 32, 13353 Berlin
Germany
E-mail: Tomas.Kurz@TU-Berlin.de

KEYWORDS
Yeast Growth, Physiology, Metabolic Model, Temperature-Dependency, MatLab

ABSTRACT

Propagation of Saccharomyces sp. yeast represents a central step in the production of food or beverages, for example in brewing or bakers' industry. In these industries yeast propagation aims at the provision of an adequate inoculum for subsequent fermentations concerning amount and physiology of the propagated biomass. Referring to this, the present work introduces a deterministic model as a basis for an active process control. The developed model emprises varying propagation strategies, e.g. batch-, sequencing batch, fed-batch- or continuous propagations, which usually are applied, as well as different metabolic states, temperature and oxygen dependency of growth, actual feed rates or varying growth media. Simulations and measured data for biomass and substrate concentrations deviated below 8% for the regarded applications out of the field of brewer's and bakers' yeast propagation. In addition a first approach is presented to correlate simulated growth rates and physiological parameters.

INTRODUCTION

Saccharomyces cerevisiae is one of the best-examined microorganisms in biotechnology. To describe the growth and the ethanol formation in the bakers' yeast propagation process many structured and unstructured modelling approaches are known from literature. Structured approaches consider balanced growth or are specified to describe particular biochemical pathways inside structured models and therefore represent the basis for the modelling approach introduced in this work (Sweere et al. 1988).
In most cases the validity of these approaches, however, is limited to defined states of the metabolism (oxidative, oxidoreductive, fermentative). Temperature dependency and maintenance energy are not considered. Also, a lag-time function to describe the adaptation of the microorganisms to the surrounding growth medium, including the time for formation of enzymes, is merely included in single approaches using different equations (Pham et al. 1998, Zhang et al, 1997). The maintenance energy of the microorganisms is only considered in single approaches, e.g. Pham et al. 1998. However, this approach is only valid if oxygen is available. Most of the reports in literature used full media as a growth medium to avoid undesired limitation effects during the growth process. This is not possible in industrial applications, e.g. if industrial produced beer wort is used as growth medium. Combined limitation and inhibition effects, e.g. caused by high ethanol concentrations, are usually not considered. Therefore, the applicability of the mentioned approaches for industrial purposes, in particular considering the usage of nutrient deficient, limiting or inhibiting media, is not guaranteed without qualifications. So, with a comprehensive modelling approach considering the aforementioned inhibition and limitation effects, knowledge can be gained towards a process control tool for industrial applications.
In particular, for the bottom fermenting brewing yeast strain Saccharomyces uvarum var. carlsbergensis (W34/70) no comprehensive modeling approach is available, which takes into account flocculation as well as the very limiting composition of the specific growth medium, i.e., brewer's wort.
In addition almost no approach is available which combines yeast physiological aspects as stress metabolites storage carbohydrate or biochemical markers and growth related aspects like growth rate in a modeling approach.
This work introduces a metabolic modelling approach, which represents the basis for the development of control strategies during research and industrial applications. The first objective of this work was to develop a metabolic modelling approach for yeast growth considering limiting and inhibiting effects of industrial media and to validate it with literature and experimental data from brewery and bakery applications. The second target was to show the potential of a model based predictive simulation to evaluate process control strategies for Saccharomyces cultures and to extract the limits of controllability using practice relevant case scenarios. Beyond this, exemplarily, relations between specific growth rate and trehalose and glycogen content, respectively are presented.

MATERIALS AND METHODS

A 150 litre (net volume) propagator with an integrated continuous aerator (Frings TRG) and defoamer unit was used. The propagator was equipped with online measurement devices for temperature (PT 100) and dissolved oxygen (Mettler-Toledo, InPro6100). Underlying control loops guaranteed accurate control of the manipulated

variables temperature (+/- 0.1°C) and dissolved oxygen (+/- 0.1 ppm).
A bottom fermenting brewery yeast strain Saccharomyces uvarum var. carlsbergensis W34/70 was used for the experiments. For the propagator experiments, yeast suspension was taken from the aforementioned propagator system. For the experiments industrial wheat beer wort (OG 12.5 w/w%) was used as growth medium. Zinc (0.2 ppm) was added to avoid limitation effects. The initial concentration of free amino acids was nearly constant over all trials at about 220 ppm. Yeast fermentable extract was determined using the SCABA measurement system.
Cell counts were made with a haemocytometer. For the simulation software, biomass concentration was calculated using the dry weight of the yeast, the yeast count, and the molecular weight of the biomass was set to 25.01 g/mol, according to the literature (Sonnleitner and Käppeli, 1986).
Glycogen content: Yeast cells were fixed in 70 % ethanol at 4 °C. The yeast pellet was incubated in 1 ml 1 N HCl for 50 min. HCl was removed by centrifugation and the pellet was stained with acriflavine solution for 1 h (excitation: 488 nm).
Trehalose content: Sample preparation was similar to Glycogen determination. The pellet was stained with ConA-FITC (excitation: 488 nm) (Hutter et al. 2000).
Flow-cytomtric analysis was caried out with a PAS from Partec (Münster, Germany). The flow device from Partec was fitted with a mercury high presure lamp, HBO 100, and an argon laser at 488 nm (Hutter and Eipel, 1978).
Modelling and simulations were carried out using the software package MATLAB 6.5®. For each simulation the starting conditions including concentrations of biomass, gravity, nitrogen, ethanol and dissolved oxygen in the growth medium as well as the progression of the manipulated variables were required. During the parameter estimation procedure, in a first step f_{temp} (temperature coefficient for the substrate uptake rate) and t_{lag} (lag time coefficient) were fitted to the reference data of substrate concentrations. In a second step, the maximum specific oxygen uptake rate $q_{O2,max}$ was fitted to all reference data (substrate-, ethanol- and biomass concentrations).

MATHEMATICAL MODELLING

In this work a metabolic modelling approach is introduced, that describes the states of metabolism dependent on the surrounding medium following literature approaches (Heijnen 1996; van Gulik and Heijnen 1995; Krzystek and Ledakowicz 1998). Considered substances and defined turnover rates were r_S (substrate as glucose equivalent), r_X (biomass equivalents), r_n (nitrogen source), r_o (dissolved oxygen), r_c (carbon dioxide), r_w (water), r_e (ethanol), r_{gly} (glycerol), r_{NADH2} ($NADH/H^+$) and r_{ATP} (ATP). Biomass composition was adopted from Sonnleitner and Käppeli (1986) with $CH_{HX}N_{NX}O_{OX}$ (s. Table 2 Parameters).
As the metabolic pathways were known, stoichiometric relationships were formulated with eight reactions r_1-r_8 as shown in Table 1.
The rate of metabolic turnover of one substance can be formulated as the sum of the turnover in the single reactions. So, it is possible to define linear equations for the relation between the turnover of all substances and the rates of all reactions r = A • v with r representing the vector for the turnover of the single substances. A the matrix of stoichiometry and v the vector for reaction rates (s. eq. 1).
It was assumed, that $NADH/H^+$ and ATP are neither accumulated in the cell nor excreted ($r_{NADH2} = 0$ and $r_{ATP} = 0$). Therefore, for this modelling approach a linear equation system with 10 equations and 16 unknown rates (r_s, r_x, r_n, r_o, r_c, r_w, r_e, r_{gly}, r_1, r_2, r_3, r_4, r_5, r_6, r_7, r_8) was formulated:

$$r=\begin{bmatrix} r_s \\ r_x \\ r_n \\ r_o \\ r_c \\ r_w \\ r_e \\ r_{gly} \\ r_{NAHDH2} \\ r_{ATP} \end{bmatrix} A=\begin{bmatrix} -1 & 0 & -g & -1 & -1 & 0 & 0 & 0 \\ 0 & 0 & 1 & 0 & 0 & 0 & 0 & 1 \\ 0 & 0 & -0{,}15 & 0 & 0 & 0 & 0 & -0{,}15 \\ 0 & -0{,}5 & 0 & 0 & 0 & 0 & 0 & 0 \\ 6 & 0 & c & 2 & 0 & 0 & 2 & c_e \\ -6 & 1 & w & 0 & 0 & 0 & -3 & -w_e \\ 0 & 0 & 0 & 2 & 0 & 0 & 0 & 0 \\ 0 & 0 & 0 & 0 & 2 & 0 & 0 & 0 \\ 12 & -1 & n & 0 & -2 & 0 & 6 & n_e \\ 2 & \delta & -K & 2 & -2 & -1 & 0 & -K_e \end{bmatrix} v=\begin{bmatrix} r_1 \\ r_2 \\ r_3 \\ r_4 \\ r_5 \\ r_6 \\ r_7 \\ r_8 \end{bmatrix} \quad (1)$$

The coefficients δ, K and K_e were calculated using the known yield coefficients for purely aerobic growth on glucose, purely anaerobic growth on glucose and aerobic growth on ethanol ($\delta = 1.5$, $K = 2.2$ and $K_e = 5.1$). Coefficients in the same order of magnitude are presented in literature (Heijnen 1996; van Gulik and Heijnen 1995; Krzystek and Ledakowicz 1998).

Table 1: Description of the relevant metabolic pathways for the yeast propagation process

(1)	**Oxidative degradation of glucose r_1** $C_6H_{12}O_6 + 6\,H_2O \rightarrow 6\,CO_2 + 12\,NADH_2 + 2\,ATP$
(2)	**Respiratory chain r_2** $NADH_2 + ½\,O_2 \rightarrow \delta\,ATP + H_2O$
(3)	**Formation of biomass of glucose r_3** $g\,C_6H_{12}O_6 + 0{,}15\,NH_3 + K\,ATP \rightarrow CH_{1,79}O_{0,57}N_{0,15} + c\,CO_2 + n\,NADH_2 + w\,H_2O$
(4)	**Formation of ethanol of glucose r_4** $C_6H_{12}O_6 \rightarrow 2\,C_2H_5OH + 2\,CO_2 + 2\,ATP$
(5)	**Formation of glycerol of glucose r_5** $C_6H_{12}O_6 + 2\,NADH_2 + 2\,ATP \rightarrow 2\,C_3H_8O_3$
(6)	**Maintenance r_6** $ATP \rightarrow ADP$
(7)	**Oxidative degradation of ethanol r_7** $C_2H_5OH + 3\,H_2O \rightarrow 2\,CO_2 + 6\,NADH_2$
(8)	**Biomass formation of ethanol r_8** $e\,C_2H_5OH + 0{,}15\,NH_3 + K_e\,ATP + w_e\,H_2O \rightarrow CH_{1,79}O_{0,57}N_{0,15} + c_e\,CO_2 + n_e\,NADH_2$

Yield coefficients were assumed to be constant. Table 2 shows the final applied parameters taken from the literature. So, the stoichiometry of this modeling approach is fixed.
In order to solve the equation system six rates have to be determined first. Kinetic equations for the characterisation of the different metabolic states have to be taken into account. Known are rates for oxidative growth OG ($r_e=r_{gly}=r_7=r_8=0$), oxidoreductive growth ORG ($r_{gly}=r_7=r_8=0$) and fermentative growth FG ($r_O=r_1=r_7=r_8=0$) on sugar and for oxidative growth on ethanol OGE ($r_1=r_3=r_4=r_5=0$), respectively. Merely four different rates remain unknown including r_S, r_6, r_O (for oxidative growth on glucose) and r_O (for oxidative growth on ethanol). The missing rates for OG (r_S, r_6), ORG (r_S, r_O, r_6), FG (r_S, r_6) and OGE (r_S, r_6) must be calculated for the different metabolic states using kinetic equations describing rates for substrate turnover and maintenance.

Table 2: Stoichiometric and kinetic parameters used in the modelling approach

Parameter	Value	Unit	Reference
Stoichiometric parameters			
$Y_{X/SOX}$	3,527	mol/mol	Sonnleitner and Käppeli 1986
$Y_{x/sf}$	0,72	mol/mol	Heijnen 1996
$Y_{X/c}$	1,12	mol/mol	Heijnen 1996
HX	1,79	mol/mol	Sonnleitner and Käppeli 1986
NX	0,15	mol/mol	Sonnleitner and Käppeli 1986
OX	0,57	mol/mol	Sonnleitner and Käppeli 1986
C	0,095	mol/mol	Krzystek and Ledakowicz 1998
c_e	0,266	mol/mol	Heijnen 1996
Kinetic parameters			
m_{ATP}	0,013	mol/(mol*h)	Heijnen 1996
$q_{s,max}$	0,4863	mol/(mol*h)	Sonnleitner and Käppeli 1986
K_S	2,8	mmol/L	Sonnleitner and Käppeli 1986
K_O	0,00121	mmol/L	Hartmeier 1972
$K_{i,eth}$	500	mmol/L	Hutter and Oliver 1998
$K_{i,eth,o}$	1000	mmol/L	Sonnleitner and Käppeli 1986
K_{eth}	2,2	mmol/L	Sonnleitner and Käppeli 1986
K_n	2	mmol/L	Cartwright et al. 1989

Kinetics for substrate uptake and oxygen uptake are expressed by Monod-Terms. Monod kinetics are only suitable to describe the exponential and the stationary state of the propagation. After inoculation, the yeast cells need a certain time (lag-time t_{lag}) to get adapted to the surrounding medium. For a description a lag-time coefficient L_t is introduced as a sigmoid function of time t. Summarising, the specific substrate uptake rate can be formulated as (valid for growth on glucose during OG, ORG, FG):

$$q_S = q_{S,max} \cdot \min\left(\frac{S}{S+K_s}, \frac{N}{N+K_n}\right) \cdot \frac{K_{i,eth}}{K_{i,eth}+E} \cdot f_{temp} \cdot L_t \qquad (2)$$

The specific oxygen uptake rate, q_{O2}, is limited by the oxygen concentration and inhibited by the ethanol concentration in the growth medium with $K_{i,eth}$ = 1000 mmol/L (Sonnleitner and Käppeli 1986) and K_o = 0.00121 mmol/L Hartmeier 1972). The value of q_{O2} is limited by a maximum specific oxygen uptake rate $q_{O2,max}$, which is a measure for the oxidative capacity of the yeast cell.

$$q_{O2} \le q_{O2,max} \frac{O}{O+K_O} \cdot \frac{K_{i,eth,o}}{K_{i,eth,o}+E} = q_{O2,lim} \qquad (3)$$

At a critical specific substrate uptake rate q_S ,the oxidative capacity of the cell is reached. With an increase of q_S the metabolism changes from pure oxidative to oxidoreductive metabolism, that means that the glucose is no longer degraded using only the oxidative pathway, but a portion is degraded fermentatively as well. At the critical substrate uptake rate, q_{O2} reaches its limit $q_{O2,lim}$. This phenomenon is known as the Crabtree effect.

For yeast growth on ethanol (OGE) the specific oxygen uptake rate is different from equation 3. As no metabolism regulation effects such as the Crabtree effect have to be considered, a sufficient description of the metabolism can be achieved with one specific uptake rate. Therefore, additionally to equation 3, the specific oxygen uptake rate is limited by available ethanol and nitrogen sources. In addition, as glucose is the preferred substrate, growth on ethanol is only possible if the glucose concentration is very low. According to Sonnleitner and Käppeli (1986), this aspect was expressed by an extra inhibition term ($K_{iS} = K_s$). During growth on ethanol equation 4 describes the kinetics for the specific oxygen uptake rate $q_{O2,e,lim}$.

$$q_{O2e,lim} = q_{O2e,max} \cdot \min\left(\frac{O}{O+K_O}, \frac{E}{E+K_e}, \frac{N}{N+K_n}\right) \cdot \frac{K_{i,etho}}{K_{i,etho}+E} \cdot \frac{K_{i,S}}{K_{i,S}+S} \cdot L_{t,eth} \qquad (4)$$

It is assumed that the specific demand on maintenance energy of yeast cells is constant. If the energy demand m_{ATP} is known (s. Table 2), the rate r_6 can be calculated.

The kinetic is herewith determined for each metabolic state. Reaction rates r_i are calculated by means of $r_i = q_i * x_i$. The switch between the different metabolic states is realised at the critical specific substrate uptake rates for oxidative, oxidoreductive and fermentative metabolism. Critical rates are calculated by combining conditions of two states and solving the equations for q_s.

Model identification and sensitivity analysis

A first rough validity of the developed modelling approach could be verified with literature data from bakers' yeast batch propagations (Sonnleitner and Käppeli 1986; Barford 1981; Barford 1990) and with experimental data from brewery propagations. Reference data on biomass, substrate and ethanol concentrations were compared to model based simulation runs. For the regarded propagations yield coefficients, maximum specific oxygen uptake rate $q_{O2,max}$ and temperature coefficient f_{temp} were extracted as parameters with a high influence on the progression of the considered concentrations in a sensitivity analysis. Sensitivity analysis was performed according to equation 5.

$$\delta = \frac{\max(\partial y)}{\partial p} \cdot \frac{p}{\max(y)} \text{ , with } \partial p = \frac{p}{1000} \qquad (5)$$

Every parameter p was changed by 1/1000 and the relative sensitivity was calculated by dividing the maximal deviation max(δy) during the simulation run (compared with the unchanged parameter) by the maxium value max(y) of substrate or biomass concentration and scaling with p . Equation 5 can be interpreted as the relative change of y per 100 % change of the parameter p (assuming linearity).

In this work, only maximum specific oxygen uptake rate $q_{O2,max}$ and temperature coefficient f_{temp} were intended for the parameter estimation procedure in order to fit model based simulation runs on experimental data. On the other hand, yield coefficients and parameters with low sensitivity were assumed to be constant (s. Table 2).

The accuracy of the simulation concerning the biomass concentration was validated with the deviation between simulation and reference values. A mean value for the deviation of 5.6% could be reached (not shown). Considering the measurement error of yeast count of ±5%, it can be stated that the simulation represents the reference values accurately, which could be reproduced also with different propagation plants and different yeast strains with a conventional discontinuous aeration system (not shown). So,

the validity of the modelling approach for industrial applications could be proven.

PROCESS MANAGEMENT

Temperature and oxygen dependency

Concerning the influence of temperature, in the field of bakers' yeast propagation work was done on a comparably small scale. In contrast to this, several authors described the temperature dependence of microbial growth in general or for specific bacteria. The most common approaches were exponential following the Arrhenius equation or parabolic Belehrádek-type equations.

The main objective of this work is to replace the variable parameters by model equations of their temperature dependency in order to allow a predictive simlation of non isothermal propagation runs. Figure 1 presents the observed temperature dependency of the estimated parameters $q_{O2,max}$ and the temperature coefficient f_{temp} of the specific sugar uptake rate (dots).

Four different modelling approaches were tested, a square-root approach, a potential approach of Belehrádek, the Schoolfield model and an Arrhenius approach of Mohr and Krawiec, to describe the temperature dependency of the parameters f_{temp} and $q_{O2,max}$.

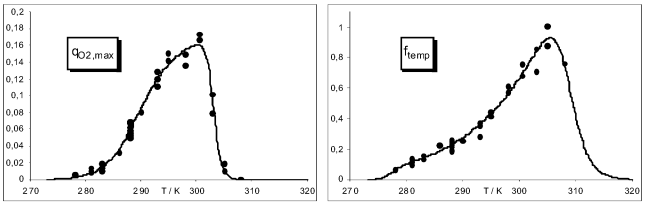

Figure 1: Schoolfield model (lines) fitted on data sets (dots) of the specific oxygen uptake rate $q_{O2,max}$ and the temperature coefficient ftemp of the specific sugar uptake rate.

The Schoolfield model (see equation 6 and lines in Figure 1) could describe the temperature dependency of both parameters best along the entire temperature range.

$$f(T)=\frac{r_{(15°C)}\cdot\frac{T}{288K}\cdot\exp\left[\frac{\Delta H°}{R}\cdot\left(\frac{1}{288K}-\frac{1}{T}\right)\right]}{1+\exp\left[\frac{\Delta H_T^{\circ}}{R}\cdot\left(\frac{1}{T_{0,5\,T}}-\frac{1}{T}\right)\right]+\exp\left[\frac{\Delta H_H^{\circ}}{R}\cdot\left(\frac{1}{T_{0,5\,H}}-\frac{1}{T}\right)\right]} \quad (6)$$

with r(15°C) specific growth rate at 15°C [h^{-1}], $\Delta H°$ activation enthalpy of the limiting enzyme reaction [$Jmol^{-1}$], $\Delta H_T°$ change of the activation enthalpy by inactivation of the enzyme at low temperatures [$Jmol^{-1}$], $T_{0,5\,T}$ temperature [K], when half of the enzymes are inactivated by low temperatures, $\Delta H_H°$ change of the activation enthalpy by inactivation of the enzyme at high temperatures [$Jmol^{-1}$] and $T_{0,5\,H}$ temperature [K], when half of the enzymes are inactivated by high temperatures. The rate of the enzyme catalysed reaction (growth rate) is modelled only by the numerator, if all enzymes are active. The exponential expression in the denominator model the transition in an inactive form caused by high or low temperatures. Belonging values for the parameters are given in Table 3.

Table 3: Final parameters of the Schoolfield model. Units are given in the text.

	$r_{15°C}$	ΔH^0	ΔH_H^o	$T_{0,5H}$	ΔH_T^o	$T_{0,5T}$
f_{temp}	0.22	61742.66	513434.54	308.57	-713399.45	277.20
$q_{O2,max}$	0.14	6695.79	1100795.40	303.11	-236498.15	289.09

Other approaches could not reach the accuracy of the Schoolfield description. Especially the transition from the sub-optimal to the superoptimal temperature range could not be represented by the other three aproaches with an adequate accuracy. Hence, the variable parameters of the applied metabolic modelling approach was replaced by the Schoolfield temperature model.

For the regarded experiments already adapted yeast, inoculated in an exponential state, was used for the propagation. Less than one hour for the lag time resulted by the parameter estimation for all experiments. Therefore the parameter lag time was fixed to zero. Experiments with dried yeast (not presented here) yielded a temperature dependency of the lag-time similar to trials described in literature. However the results could not be confirmed statistically.

Practice relevant concentrations of dissolved oxygen in the required range of 0.1 to 0.8 ppm for experiments at 15°C exerted only a minor influence on the biomass growth compared to the temperature. However, lower dissolved oxygen concentrations than 0.1 ppm decreased the specific growth rate due to oxygen limitation effects, e.g. to 70% at 0.05 ppm dissolved oxygen concentration. This confirmed results of Hartmeier (1972) or Cho and Wang (1990) and therefore is not presented in more detail. An implementation of the dissolved oxygen dependency in the specific growth rate was not necessary, because the relation was represented by the temperature dependent maximum specific oxygen uptake rate $q_{O2,max}$ and the fixed half saturation constant K_o without an individual adaptation.

Flocculation and Sedimentation

During industrial fermentations applying bottom fermenting yeast strains (brewing strains) the available sugar is metabolised totally anaerobic using only the fermentative pathway. However, a physiologically reasoned sedimentation during the fermentation is known and desirable, in order to be able to harvest a sufficient amount of yeast for further inoculation in brewing practice.

In industrial cylindroconical fermentation tanks (CCF) this phenomenon is not of practical relevance for simulation as the sedimentation process is too slow and biomass concentration seemed to remain constant after finishing the growth phase. However, in small CCF or in horizontal tanks a decrease in biomass concentration can be observed.

Mean values for sizes of yeast cells are known to be around 10 µm. However, cell diameters of a bottom fermenting yeast strain W34/70 were measured to be distributed between 7 and 25 µm. Cells with a diameter between 7 and 15 µm had 72% of the cell mass. The rest was inbetween 15 and 25 µm. These data allowed to calculate for each yeast diameter the belonging portion of the whole cell population

concerning volume or weight. Assuming yeast cells to be globular particles, which are sedimenting in a fluid, bigger particles would sediment faster. If all particles of one size passed the sampling level of a CCF, they were not longer detectable and the concentration of suspended particles decreased. To allow a simulation of the yeast fermentation in small or horizontal tanks the modelling approach was extended by a sedimentation model. For this model several assumption were made:

- The yeast is suspended ideally at the beginning of the fermentation
- No convection or mixing is occuring
- Yeast cells are particles with a certain size distribution
- Density and viscosity of the medium is constant during the fermentation

An adjusted size distribution was integrated in the sedimentation model after classification in 10 cell size classes (s. Table 4).

Table 4: Classes of cell sizes and belonging mass portions for the sedimentation model. Sedimentation velocities and sedimentation times were calculated according to equations 6 and 7. A remaining portion of 3% remains in suspension.

Class	Mass portion [%]	Mean diameter [µm]	Sedimentation velocity [m/s]	Sedimentation time [h]
1	12	25	1.6944E-05	24.59
2	7	23	1.434E-05	29.05
3	6	21	1.1955E-05	34.85
4	7	19	9.7867E-06	42.57
5	8	17	7.8348E-06	53.18
6	8	15	6.0997E-06	68.31
7	9	13	4.5816E-06	90.94
8	21	11	3.2803E-06	127.02
9	15	9	2.1959E-06	189.75
10	4	7	1.328E-06	313.66

According to Stokes, sedimentation velocity w_f was calculated as

$$w\_f = \frac{(rho\_Y - rho\_F) * g * d^2}{18 * dyn\_F} \quad (7)$$

with rho_Y = 1080 kg/m^3 (density of the yeast cell), rho_F = 1005.6 kg/m^3 (density of beer at 20°C, g = 9.81 m/s^2 (gravitational acceleration), dyn_F = 1.556 mPas (dynamic viscosity of beer at 20°C and d representing each diameter of the cell classes in Table 4. Sedimentation time t is calculated as

$$t = \frac{h}{w\_f} \quad (8)$$

with h = level height and w_F calculated in equation 7.
After each of these sedimentation times the cell concentration calculated with the model was reduced by the mass portion of the belonging cell class.

Case scenarios

With the formulation of the variable parameters f_{temp} and $q_{O2,max}$ as $f_{temp}(T)$ and $q_{O2,max}(T)$, respectively, and a fixed set of stoichiometric and kinetic parameters, a predictive simulation of the yeast propagation process was possible even for the application of temperature and dissolved oxygen profiles.

Herewith a prerequisite for the realisation of an active process control and evaluation tool for control strategies could be established. In order to show this potential, case scenarios were carried out, which simulate a delay in a preliminary production step. Figure 2 presents a case scenario for a brewery.

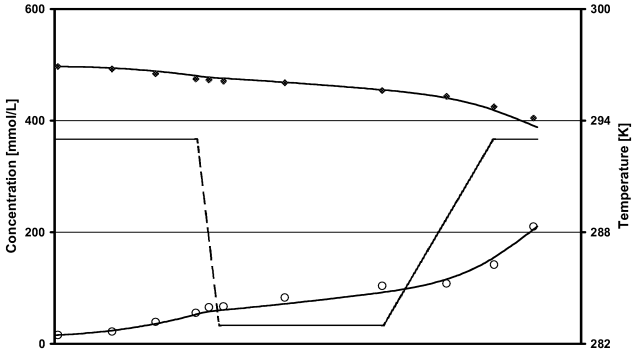

Figure 2: Application of a temperature scenario for the yeast propagation process. A temperature profile (293-283-293 K) was applied (dotted line). Reference values for the progressions of biomass (o) and substrate (♦) and belonging simulations (lines) are shown.

Here, the yeast propagation has to be delayed for several hours due to a disturbance in a preliminary production step. Progressions of reference values (dots) and model based predictive simulations (lines) of the concentrations of biomass and substrate (as glucose equivalents) for the given temperature profile are presented. The change of temperature caused a deceleration and acceleration, respectively, of the propagation process, which can be found in the progressions of the reference values as well as in the belonging predictive simulation runs. The deviation between measurement and simulation was around 6%. Also in other scenarios applying temperature and/or dissolved oxygen as manipulated variable it could be shown, that with a precise adjustment of trajectories the crop time of the inoculum could be varied within a period of 7 to 50 hours by maintaining a high fermentation activity for the subsequent anaerobic fermentation. The results could also be confirmed at industrial propagations in a 200 hL propagation plant as well as with other yeast strains in the described 150 L pilot plant. Similar to aerated and stirred yeast propagation anaerobic batch fermentations could be simulated with a satisfying accuracy after implementation of the discrete sedimentation model.
Figure 3 presents exemplarily a fermentation run in the pilot fermenter. Presented are measurement values for biomass and substrate as well as simulation results including the sedimentation model. For simulation parameters f_{temp} and $q_{O2,max}$ were adopted from a determined temperature function (parameters at 10°C), as the same yeast strain was inoculated. It can be seen, that the biomass concentration was reduced stepwise at the sedimentation times calculated by the sedimentation model for the different cell classes (s. Table 4). Inbetween these times biomass growth and sugar degradation was computed by the model each time based on a new „initial“ concentration. In this way the model could be extended by the sedimentation model without influencing the core of the yeast metabolism model. The accuracy of the

simulation was not evaluated statistically. However, a splined curve through the measurement values fitted well the simulated data at each time after sedimentation of a cell class. This could be verified in several fermentations for the regarded fermentation tank size and yeast strain.

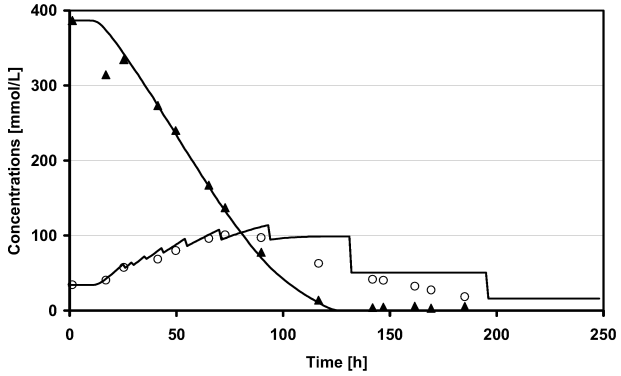

Figure 3: Fermentation run in a 10 hl CCF. Presented are measurement values for biomass (○) and substrate (▲). Lines indicate simulation results.

Additionally, the sedimentation model was extended by functions for viscosity and density of the growth medium according to literature data. However, no improvement in performance could be achieved. A further increase in accuracy could have been reached by a extension of the number of classes or even the implementation of a density function of cell size distribution. Fluid dynamic aspects as convection and CO_2 bubbles affecting the sedimentation process were not considered in this work.
Summarising, it can be stated, that with the sedimentation model in combination with modelling approach fermentations could be simulated with an accuracy sufficient for practice. An additional feature of a sedimentation model lies in an estimation of the amount of sedimented yeast for harvesting in industrial CCF. Besides, with the sedimentation model an important prerequisite for modelling of biochemical substances as diacetyl was created. For example in the implementation of diacetyl formation and degradation kinetics from Engasser et al. (1981) or Votruba et al. (1995) a great potential was found and further research was initiated.

MODELLING OF YEAST PHYSIOLOGY

Physiological parameters

In this chapter, active physiological reactions should be exemplified by formation and degradation of the carbohydrates glycogen and trehalose during different yeast propagation strategies. The latter carbohydrates are regarded as influential determinants of fermentation performance (Boulton 2000); Boulton et al. 2000). A relation of these results to the specific growth rate is examined.
Glycogen is a high molecular weight polymer of α-D-glucose, which is synthesised from glucose-6-phosphate using UDP as a carrier. Glycogen accumulation occurs where growth is limited by a nutrient other than carbon (Lillie and Pringle 1980). Yeast glycogen stores function as a reserve of carbon and energy, which is utilised during periods of starvation or when the cells are undergoing adaptation to a new growth phase, e.g. diauxic shift. In brewing yeast glycogen may account for up to 25-40 % of the cell dry weight (Boulton and Quain 2001).
Trehalose is a dimer of α-D-glucose. It is supposed to be a reserve material as well, but more important is its function as a stress protectant. Thus, it has the ability to increase the thermotolerance of proteins and is capable of stabilising cellular membranes. Levels of trehalose are up to 10 % but usually below 5 % in brewing yeast (Lillie and Pringle 1980; van Dijck et al. 1995). The higher values indicate a response on different kinds of stress as heat-, cold-shock, osmotic stress, or starvation (Boulton and Quain 2001).

Experiments on yeast physiology

Propagations were run at 30, 25, 20, 17 and 12 °C with a dissolved oxygen concentration of 0.5 ppm and at 20 °C without any aeration or dissolved oxygen concentrations below 0.1 ppm. Figure 4 shows the progressions of glycogen, trehalose, gravity and specific growth rate of three different yeast propagations at 30 °C and 20 °C (0.5 ppm dissolved oxygen concentration and at 20 °C without any aeration. It can be seen, that glycogen and trehalose increase to a maximum content and decrease during the exponential state of the propagation.
The maximum peak of glycogen and trehalose contents comes along with the progression of the specific growth rate. At lower temperatures (12 °C) this effect could only be observed for trehalose and glycogen remained nearly constant (see Figure 4, 2nd diagram). The velocity of glycogen degradation decreased at a remaining gravity of 5 to 7 ww % and glycogen started to accumulate.
This comes along with literature results (Lillie and Pringle 1980; Roy and Samson 1988; Parrou et al. 1999) which report that glycogen accumulates before the fermentable sugars are exhausted or in the transition phase between exponential and stationary state of yeast growth, respectively.
A lack of dissolved oxygen did not cause an alteration of the typical progressions of trehalose and glycogen, except for a higher peak maximum for both substances (see Figure 4, 3rd diagram). This could be proved by propagation runs with dissolved oxygen concentrations below 0.1 ppm, which showed higher levels as well.
Similar to the propagations in Figure 4 trehalose is degraded after a maximum peak, which comes along with the maximum specific growth rate. With the lower temperature growth rate decreases rapidly and trehalose accumulation was induced. The same tendency could be observed for glycogen contents (both not shown). Similar progressions could be observed for different propagations with temperature profiles applied.

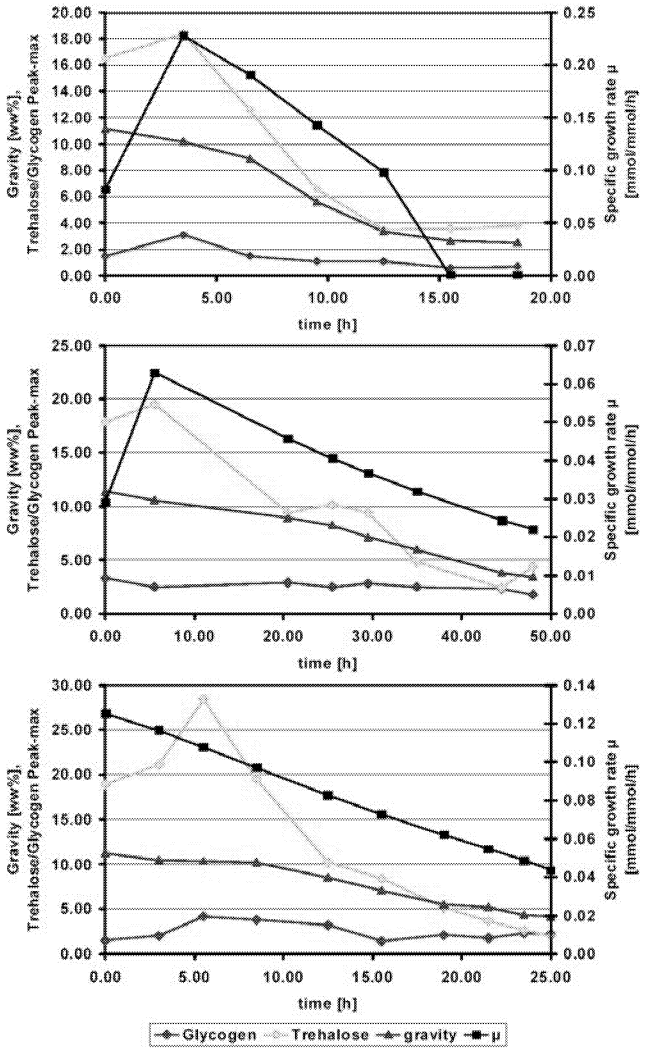

Figure 4: Progressions of trehalose, glycogen, gravity and specific growth rate propagations at 30 °C and 12°C with 0.5 ppm dissolved oxygen concentration (top and middle) and 20 °C without aeration (bottom).

Mathematical description of physiological parameters

A relation of the specific growth rate and trehalose and glycogen contents, respectively is examined in Figure 5.

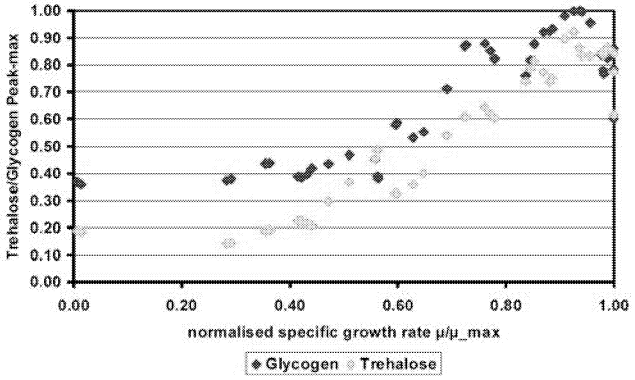

Figure 5: Relations between normalised trehalose or glycogen contents and the normalised specific growth rates during yeast propagations with different temperatures and dissolved oxygen concentration are shown.

This approach was introduced by Paalman et al. (2003) who found that the growth rate controls the trehalose and glycogen synthesis.

In order to compare propagations at different temperatures the specific growth rate, which was calculated by the process model, is normalised by the maximum specific growth rate occurring at each belonging propagation run. Also trehalose and glycogen peaks are normalised by the maximum content occurring in each propagation. It can be seen that with decreasing normalised growth rates the contents of both substances are decreasing as well. A linear approach could describe the relation sufficiently above normalised growth rates of 0.3. Below this value not enough measurement data was available. Paalman et al. (2003) detected an inverse relation for yeast continuous cultures at very low dilution rates or groth rates. This could explain the higher level of trehalose and glycogen at very low normalised growth rates compared to the level at a normalised growth rate of 0.3. So, the induction of carbohydrate synthesis should lie inbetween the range of normalised growth rates of 0-0.3.

CONCLUSIONS

A reasonable modelling approach for research and industrial yeast propagation was developed and validated with literature data and experiments. Model based simulations matched experimental data very well and the validity of the modelling approach for the required brewery propagations could be proven. Therefore, an automatic adaptation of the parameters of the model, as it is proposed in other works to reach a higher accuracy of the model-based simulation, was not indicated in the required application. With only three variable parameters an easy manageable simulation tool is provided for the engineer.

The benefit for the engineer from this work, lies in the gain of process knowledge about both the influence of manipulated variables and the growth medium on biomass growth and resulting biomass activity as well as about the limits of controllability. Though using an industrial growth medium, process control strategies can be simulated and evaluated. The knowledge gained about the process behaviour allows the employment of optimisation algorithms, e.g. genetic algorithms, in order to plan propagation strategies more efficient than before. Mistakes in process strategies can be avoided and active yeast can be provided for inoculation even considering practice relevant scenarios.

Beyond this, an approach for the description of specific physiological parameters (glycogen and trehalose) is introduced. Fuurther work is in progress to confirm these data and to expand the validity of the approach to other physiological parameters as intra-cellular pH-values or enzyme activities.

The applicability of the developed system is not limited to the considered case. Conceivable are applications for fed-batch and continuous cultures as well as industrial fermentations, where economical or traditional aspects prohibit the usage of customised growth media, such as for the production of vinegar, wine, single cell proteins or secondary metabolites.

REFERENCES

Boulton, C. (2000) Trehalose, Glycogen and Sterol. In: Brewing Yeast Fermentation Performance. Katherine Smart (editor). Blackwell Science Ltd., 10-19.

Boulton, C., Clutterbuck, V. & Durnin, S. (2000) Yeast oxygenation and storage. In: Brewing Yeast Fermentation Performance. Katherine Smart (editor). Blackwell Science Ltd., 140-151.

Boulton, C. & Quain, D. (2001) Brewing Yeast and Fermentation. Blackwell Science Ltd.

Cartwright, C.P., Rose, A.H., Calderbank, J., Keenan M.H.J. Solute Transport, In:The Yeasts, Vol. 3, 2nd edn., A.H. Rose and J.S. Harrison Eds., Academic Press: London, pp.5-56, 1989.

Cho, M.H., Wang S.S. Practical method for estimating oxygen kinetic and metabolic parameters. Biotechnology Progress, , 6, 164-167, 1990.

Engasser, J.M., Marc, I., Moll, M., Duteurtre, B. (1981) Kinertic modelling of beer fermentation. Proc. EBC Congress, Vol. 18, 579-586.

Hartmeier, W. (1972) Untersuchungen über die Kinetik der mikrobiellen Sauerstoff-Aufnahme und den Einfluß des Sauerstoff-Partialdruckes auf den Stoffwechsel von Saccharomyces cerevisiae, PhD-thesis, Fachbereich Lebensmitteltechnologie und Biotechnologie, Technische Universität Berlin.

Heijnen, J.J. (1996) Macroscopic approach and mathematical modelling of microbial processes. In: BODL-Advanced Course Microbial Physiology and Fermentation Technology, Delft, 1996.

Hutter, A., Oliver, S.G. Ethanol production using nuclear petite yeast mutants. Applied Microbiology and Biotechnology, 49, 511-516, 1998.

Hutter, K.-J., Remor, M. & Müller, S. (2000) Biomonitoring der Betriebshefen in praxi mit flluoreszenzoptischen Verfahren. VII. Mitteilung: Untersuchungen zur flusszytometrischen Bestimmung des Glykogengehaltes der Btriebshefe, Monatsschrift für Brauwissenschaft, 53(5/6), 68-76.

Hutter, K.-J. & Eipel, H.E. (1978) DNA determination of yeast by flow cytometry, FEMS Microbiol. Lett., 3, 35-38.

Krzystek, L., Ledakowicz, S. Yield and maintenance coefficients in s. cerevisiae cultures. Journal of Chemical Technology and Biotechnology, 71, 197-208, 1998.

Lillie, S.H. & Pringle, J.R. (1980) Reserve carbohydrate metabolism in S. cerevisiae: responses to nutrient limitation, Journal of Bacteriology, 143, 1384-1394.

Müller, S., Hutter, K.J., Bley, T., Petzold, L. & Babel, W. (1997) Dynamics of yeast cell states during proliferation and non proliferation periods in a brewing reactor monitored by multidimensional flow cytometry, Bioprocess Engineering, 17, 287-293.

Paalman, J.W.G., Verwaal, R., Slofstra, S.H., Verkleij, A.J., Boonstra, J. & Verrips, C.T. (2003) Trehalose and glycogen accumulation is related to the duration of the G1 phase of Saccharomyces cerevisiae, FEMS Yeast Research, 3, 261-268.

Parrou, J-L., Enjalbert, B., Plourde, L., Bauche, A., Gonzalez, B. & Francois, J. (1999) Dynamic Responses of Reserve Carbohydrate Metabolism Under Carbon and Nitrogen Limitation, Yeast, 15, 191-203.

Pham, H.T.B., Larsson, G., Enfors, S.-O. Growth and Energy Metabolism in Aerobic Fed-Batch Cultures of Saccharomyces cerevisiae: Simulation and Model Verification. Biotechnology and Bioengineering, 4, 474-482, 1998.

Roy, D. & Samson, R. (1988) Investigation of growth and metabolism of Saccharomyces cerevisiae (bakers' yeast) using microcalorimetry and bioluminetry, Journal of Biotechnology, 8, 193-206.

Sonnleitner, B., Käppeli, O. (1986) Growth of Saccharomyces cerevisiae is controlled by its limited respiratory capacity: formulation and verification of a hypothesis. Biotechnology and Bioengineering, 28, 927-937.

Sweere, A.P.J., Giesselbach, J., Barendse, R., de Krieger, R., Honderd, G., Luyben, K.C.A.M. (1988) Modelling the dynamic behaviour of Saccharomyces cerevisiae and its application in control experiments. Applied Microbiology and Biotechnology, 28, 116-127.

Van Dijck, P., Colavizza, D., Smet, P. & Thevelein, J.M. (1995) Differential importance of trehalose in stress resistance in fermenting and nonfermenting Saccharomyces cerevisiae cells, Applied and Environmental Microbiology, 61(1), 109-115.

Van Gulik, W.M., Heijnen, J.J. A metabolic network stoichiometry analysis of microbial growth and product formation. Biotechnology and Bioengineering, 48, 681-698, 1995.

Votruba, J., Kminek, M., Palatova, M. (1995) Education of Beer Brewing Physiology and Technology Using PSI Simulation Language. In: Preprints of the 6th Int. Conference on Computer Applications in Biotechnology, Garmisch-Partenkirchen, Germany, May 14-17, 1995.

Zhang, Z., Scharer, M., Moo-Young, M. (1997) Mathematical model for aerobic culture of recombinant yeast. Bioprocess Engineering, 17(4), 235-240.

BIOGRAPHY

TOMAS KURZ studied Brewing and Beverage Technology at TU München. He worked at the Dep. of Fluidmechanics and Process Automation of TU München as head of process automation group from 1997 to 2003. He obtained his PhD in 2002. In 2003 he obtained a junior-professorship at TU Berlin Dep. of Food Process Engineering.

Thermal Conductivity Estimation of Sandwich Bread Using Inverse Method

Jean-Yves Monteau
GEPEA, UMR CNRS 6144
École Nationale d'Ingénieurs des Techniques des Industries Agricoles et Alimentaires
rue de la Géraudière, B.P. 82225, 44322 Nantes cedex 3
monteau@enitiaa-nantes.fr

KEYWORDS
Inverse method, thermal conductivity, sandwich bread.

ABSTRACT

Nowadays, study of processes needs computer studies. Parameters of models used have to be determined, in experiments or with identification methods called inverse methods. The aim of this paper is to present an inverse method for sandwich bread thermal conductivity, using a temperature recording during a convection chilling after baking. A sensitivity study shows that the temperature probe has to be placed in center. The estimated thermal conductivity is given as a temperature and local water content polynomial.

INTRODUCTION

Nowadays, study of processes needs computer studies. For these studies, models are developed which rely on the knowledge of thermophysical parameters. Methods were developed to measure thermophysical parameters in food materials. However it is not always easy. For instance, the measurement of effective thermal conductivity of bread just after baking, whereas there is at this time an intense heat transfer by evaporation and during a short time, does not seem realizable. About the measurement of thermal conductivity there are methods such as line heat source method or the flash method. For foodstuffs, the line heat source method was used, in particular by Sweat and Haugh (Sweat and Haugh 1974). Thermal conductivity is very temperature and local water content dependant (Nesvadba 1982). Its determination according to these two variables requires a series of measurements which takes a considerable time. An inverse method can be an alternative for its determination. Inverse methods can be used to estimate an initial state of the system, for instance a temperature field, to estimate unknown parameters, to estimate boundary conditions, or the geometry of a system (Jarny and Maillet 1999). These methods depend on a model of the system, and thus on parameters. The idea is to use the model to compute the output variables (direct problem) according to the sought parameters initialized to given values, and, comparing the output computed variables with these ones get in experiments, to act on the parameters sought, until the computed and experimental variables are "as close as possible". To this end, a function representing the difference between the measured and the computed variables is build. This function is dependant on the unknown parameters, and its minimum is sought with a minimization algorithm (inverse problem). The objectives of the work presented here are to develop an inverse method to estimate bread thermal conductivity, to determine where the temperature probe to record the experimental temperature curve has to be placed, and to find an analytical expression of the sandwich bread thermal conductivity according to temperature and local water content.

MATERIALS AND METHODS

Experiments are achieved on sandwich bread manufactured in laboratory, and chilled by convection after baking.

Follow-up of chilling

Ambient temperature and relative humidity during chilling were logged with a data acquisition system Datalog 20 (AOIP, France), K-type thermocouples and data logger Hygrolog (Rotronic, Switzerland). Chilling was carried out in a room where ambient temperature and relative humidity were measured. During these tests, center temperature variation was logged and mass loss determined by difference before and after chilling. The mass was measured with a balance Sartorius U 3600 S (Sartorius GmbH, Germany). Seven tests were achieved with various ambient conditions.

Thermal conductivity estimation method

The thermal conductivity estimation method rests on the minimization of the sum of squares of the differences between the experimental temperature and the temperature computed with a model, in a point of the product (least squares method). The optimization variables are the coefficients of a 1st degree polynomial in temperature and local water content modeling the thermal conductivity:

$$\lambda = a\,T\,W + b\,T + c\,W + d \qquad (1)$$

For each test a polynomial was obtained. The mean polynomial was then computed. The simulations of heat and mass transfers are performed with the finite element

software Femlab 3.1. A half slice of sandwich bread is considered (Figure 1).

The model of the system is based on the second Fourier's law for the heat transfer, and on the second Fick's law for the mass transfer.

$$\rho Cp\frac{\partial T}{\partial t} = \nabla \bullet (\lambda \nabla T) \quad (2)$$

$$\frac{\partial W}{\partial t} = \nabla \bullet (D\nabla W) \quad (3)$$

The surface boundary conditions take into account transfers by convection, radiation and evaporation.

$$n \bullet (\lambda \nabla T) = L_w k_i (P_a - P_s) + h_i (T_a - T) + \varepsilon\sigma(T_a^4 - T^4) \quad (4)$$

$$n \bullet (D\nabla W) = -k_i (P_s - P_a)/\rho_{dm} \quad (5)$$

with

$$P_a = RH \cdot P_{sat}(T_a) \quad (6)$$

$$P_s = a_w \cdot P_{sat}(T_a) \quad (7)$$

Saturated pressures are given by Antoine's law:

$$P_{sat}(T) = 133.3e^{8.3036 - \frac{3816.44}{T-46.13}} \quad (8)$$

The water activity is given par sorption isotherms (Hamdami et al. 2003).

An insulation condition on the left boundary is imposed to ensure symmetry.

Evaporation flow is integrated on surface and in time to compute the mass loss.

$$p = \int_0^t \int_S k_i (P_s - P_a) dS\, d\tau \quad (9)$$

Mass diffusivity is fitted to adjust the computed mass loss and the measured one. Other model parameters, except thermal conductivity, either were measured, or computed, or estimated.

Initial conditions are homogeneous temperature and local water content.

The criterion function J of the inverse method is carried out with a sequential quadratic programming (SQP) method of the Matlab 7.0 optimization toolbox.

Sensitivity equations set-up

Comparison of experimental and computed temperature values is achieved in a point. To know what point has to be chosen, sensitivity of the temperature field at the thermal conductivity was studied. In this aim, sensitivity equations were set-up by derivation of the model equations with regard to the thermal conductivity:

$$\rho Cp\frac{\partial X_T}{\partial t} = \nabla \bullet (\nabla T + \lambda \nabla X_T) \quad (10)$$

$$n \bullet (\nabla T + \lambda \nabla X_T) = -L_w k_i \frac{\partial P_s}{\partial \lambda_s} - h_i X_T - 4\varepsilon\sigma T^3 X_T \quad (11)$$

$$X_T\big|_{t=0} = 0 \quad (12)$$

$$\frac{\partial X_W}{\partial t} = \nabla \bullet (D\nabla X_W) \quad (13)$$

$$n \bullet (D\nabla X_W) = -k_i \frac{\partial P_s}{\partial \lambda}/\rho_{dm} \quad (14)$$

$$X_W\big|_{t=0} = 0 \quad (15)$$

with

$$\frac{\partial P_s}{\partial \lambda} = 133.3\frac{3816.44 a_w X_T}{(T-46.13)^2} e^{18.3036 - \frac{3816.44}{T-46.13}} + 133.3\frac{\partial a_w}{\partial W} X_W \quad (16)$$

RESULTS AND DISCUSSION

On Figure 1 is drawn the surface sensitivity $X_T(x,y,t)$ at time 6000 s of a chilling. The layout of the sensitivity surface shows that center (0,0.026) is the point where temperature is the more thermal conductivity dependant (Figure 1): matter is necessary so that thermal conductivity has an influence on temperature. Values are negative. The more significant the thermal conductivity, the more the temperature decreases. Values are close to zero in surface and go increasing in absolute value toward the product center. Thus it is at center the temperature probe has to be placed.

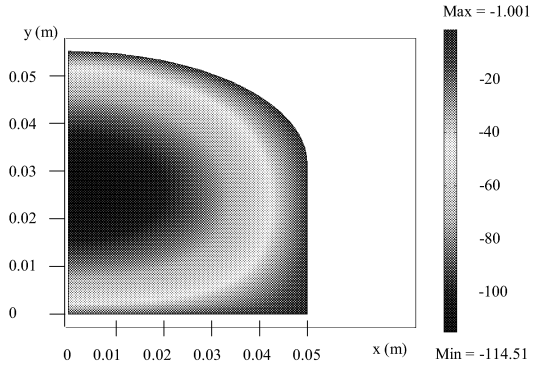

Figure 1: Sensitivity Study. T_a = 19 °C, HR = 50 %

The polynomials obtained for the whole of the tests present a certain scattering (Figure 2). This scattering is an image of the experiments repetitivity. Only the surfaces $\lambda(T,W)$ obtained for two tests are distinguished from the others. These differences must have their origin in experiments. The greatest control of experimental conditions has to be searched. Computed and experimental curves are close for each test. A typical example of

difference between experimental and computed center temperature is shown on figure 3.

The mean polynomial for the seven tests is:

$$\lambda = 4.8382\times10^{-3}TW + 7.304\times10^{-4}T - 1.3678W - 0.1926 \quad (17)$$

It is an increasing function of temperature and local water content.

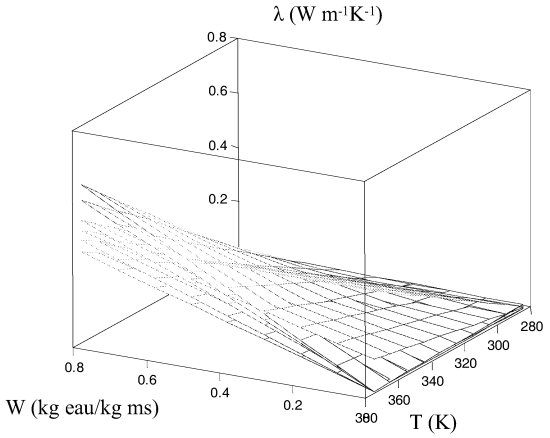

Figure 2: Surfaces λ(T,W)

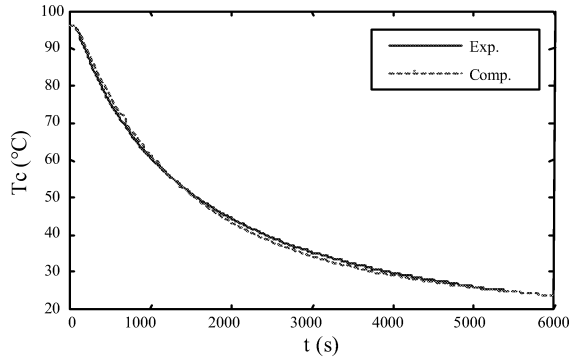

Figure 3: Experimental and Computed Center Temperature

CONCLUSION

This inverse method enables to estimate thermal conductivity versus temperature and local water content, for a time varying product, with a simple temperature recording. Inverse methods were not used until now to estimate the bread thermal conductivity, and in a general way to estimate bread thermophysical parameters. This work thus constitutes an original approach in the determination of these parameters. Extending this approach, this type of method can be used to study the influence of others variables on the variable considered.

NOMENCLATURE

a_w	water activity
D	mass diffusivity, $m^2\ s^{-1}$
Cp	specific heat, $J\ kg^{-1}\ K^{-1}$
h	heat transfer convection coefficient, $W\ m^2\ K^{-1}$
k	mass transfer convection coefficient, $s\ m^{-1}$
L_w	latent heat of water vaporization, $J\ kg^{-1}$
n	normal to the surface, towards outside
p	water loss, kg
P	vapor pressure, Pa
RH	relative humidity
S	bread surface area, m^2
t	time, s
T	temperature, K
W	local water content, kg water/ kg dm
x , y	coordinates, m
X_T	sensitivity coefficient $\frac{\partial T}{\partial \lambda}$, $m\ K^2\ W^{-1}$
X_W	sensitivity coefficient $\frac{\partial W}{\partial \lambda}$, m K kg water /kg dm

Greek Symbols

ε	emissivity
λ	thermal conductivity, $W\ m^{-1}\ K^{-1}$
ρ	density, $kg\ m^{-3}$
σ	Stéfan-Boltzmann constant, $5.67051\times10^{-8}\ W\ m^{-2}\ K^{-4}$

Subscripts

a	ambient
comp	computed
dm	dry matter
exp	experimental
i	index for the geometry faces: 1 right side 2 bottom side 3 upper side
s	surface
sat	saturated
0	initial

REFERENCES

Hamdami, N., Monteau, J.-Y. and Le Bail, A. 2003, "Moisture diffusivity and water activity of part baked bread at above and sub-freezing temperatures." In *International Journal of Food Science and Technology* 41, pages 33-44

Jarny, Y. and Maillet, D. 1999. "Problèmes inverses et estimation de grandeurs en thermique". *Métrologie thermique et techniques inverses, Ecole d'hiver Metti'99, Odeillo - Font-Romeu*, pages 1-50. Presses Universitaires de Perpignan, 1999

Nesvadba, P. 1982, "Methods for the measurement of thermal conductivity and diffusivity of foodstuffs." In *Journal of Food Engineering* 1, pages 93-113

Sweat, V. E. and Haugh, C. G. 1974, "A thermal conductivity probe for small food samples." In *Transactions of the ASAE*, pages 56-58

Determination of Thermal Conductivity of Frozen Meat by Finite Element Modelling

Q.T. Pham (1)*, M.R. Sutjiadi (1), Y. Sagara (2) and G.-S. Do (2)
(1) School of Chemical Engineering and Industrial Chemistry,
University of New South Wales, Sydney, Australia,
email tuan.pham@unsw.edu.au
(2) Department of Global Agricultural Science,
University of Tokyo, Yayoi 1-1-1 Bunkyo-ku, Tokyo 113-8657, Japan
asagara@mail.ecc.u-tokyo.ac.jp

INTRODUCTION

The thermal conductivity of frozen food is needed for calculating their freezing times and other design parameters of freezing processes. It can be measured by various methods: steady state methods such as the guarded hot plate, or transient methods such as the line probe. For materials for which experimental thermal conductivity data have not yet been determined, it would be desirable to be able to calculate them from the constituents. Pham (1989) and Pham & Willix (1989) compared their data for lamb meat, fat and offals against various equations. Tarnawski, Cleland, Corasaniti, Gori,& Mascheroni (2005) repeated the comparison against eight models commonly used for frozen soil.

The different predictions between models result from the geometry assumed for the microstructure. For example, the parallel model assumes parallel layers along the direction of heat flux, the Maxwell model assumed spheres suspended in a continuous medium, etc. In real frozen foods, the constituents are unlikely to be in any such idealized configuration, so agreement with any mode is likely to be fortuitous. There has been previous work on using the finite element method to calculate the effective thermal conductivity on inhomogeneous materials (Carson, Lovatt, Tanner,& Cleland, 2003) using circular inclusions. A more realistic calculation should be based on real life geometry. In particular, the shape, distribution and orientation of ice crystals should be accurately modelled, since ice makes up about half of the mass of the food, and its thermal conductivity is nearly an order of magnitude higher than those of the other components.

Recently, Do, Sagara, Tabata, Kudoh, & Higuchi (2003) obtained detailed and sharp pictures for ice crystals in frozen beef for the first time, using a micro-slicer image processing system. These pictures are sufficiently sharp to be digitized and used for a finite element heat conduction model. We therefore set out to do this to calculate the thermal conductivity of frozen beef, and at the same time verify the accuracy of various simplified models.

THEORY

When heat flows through a composite material, as long as the scale of the inhomogeneities is much smaller than the dimensions of the object, a uniform effective thermal conductivity k_e can be defined, so that on average Fourier's conduction law will hold:

$$q = -k_e \frac{\Delta T}{\Delta x} \quad (1)$$

Many expressions for calculating the effective thermal conductivity has been proposed. Most start from some assumption about an idealised geometry of the microstructure of the composite. An upper bound estimate for k_e is given by the parallel model, which assumes that the components exist as layers parallel to the heat flux:

$$k_{parallel} = \sum_i \phi_i k_i \quad (2)$$

A lower bound is provided by the series model, which assumes that the layers are normal to the heat flux:

$$k_{series} = \left[\sum_i \frac{\phi_i}{k_i} \right]^{-1} \quad (3)$$

A popular model is the Maxwell-Eucken model (Eucken, 1940), which assumes that the composite consists of a sparse suspension of spheres (the dispersed or d-phase) in a continuous (c) phase:

$$k_{ME} = k_c \frac{1 + 2k_c/k_d + 2\phi_d(1 - k_c/k_d)}{1 + 2k_c/k_d - \phi_d(1 - k_c/k_d)} \quad (4)$$

Levy (1981) proposed an empirical model based on Maxwell-Eucken which has the advantage that it is symmetrical with respect to the disperse and continuous phases. The Maxwell-Eucken equation is used with ϕ_d replaced by f:

$$f = \frac{1}{\sigma} - \frac{1}{2} + \phi_d - \frac{1}{2}\sqrt{\left(\frac{2}{\sigma} - 1 + 2\phi_d\right)^2 - 8\frac{\phi_d}{\sigma}} \quad (5)$$

$$\sigma = \frac{(\delta - 1)^2}{(\delta + 1)^2 + \delta/2} \quad (6)$$

$$\delta = k_d / k_c \quad (7)$$

Another well-known model is the Effective Medium Theory (EMT) (Landeauer, 1952; Davis et al 1975):

$$\sum_j \phi_j \cdot \frac{k_j - k_{EMT}}{k_j + 2k_{EMT}} = 0 \quad (8)$$

These models can be termed zero-parameter models, since no inputs other than the component conductivities and volume fractions are required, and hence no parameter curve-fitting. Several other such models were tested by Pham (1989), Pham & Willix (1989) and Tarnawski et al (2005) but none proved better than either Levy, EMT or Maxwell-Eucken, so they will not be mentioned here. Tarnawski et al (2005) found that De Vries's (1963) model is better than Levy's, but it contains a parameter that has to be optimised by curve fitting.

MATERIALS AND METHODS

The micrographs had been obtained by Do et al (2003) by repeatedly shaving off 1μm slices of a piece of frozen beef and reconstructing the 3-D structure from micrographs of the cross-sections by computer. Sectional views were generated in directions parallel and perpendicular to the heat flux, however we will use only the former. 3-D micrographs of two samples were shown: a slowly frozen sample at -15^0C, and a fast frozen sample at -120^0C. The slow frozen sample had large oblong or columnar ice crystals about 100 μm across, while the fast frozen sample had thinner crystals, around 20 μm across. The crystals were irregular and not completely aligned with the heat flux, so a parallel model would not be expected to hold.

The micrographs in Do et al. (2003) were shown in perspective, each face being a parallelogram, with ice crystals being darker than the surrounding matrix (Figure 1). The longer faces are those to be modelled since they lie parallel to the heat flux. Using Adobe Photoshop, they were first subjected to axis skewing and rotation to straighten the angles and make each face into a rectangle, which gives a 2-D model of the heat flow path (Figure 2). The colour pictures were transformed into grayscale, then imported into MATLAB and transformed into black and white. The transformation was done by comparing the brightness of each pixel with an arbitrary threshold value: darker than threshold is ice and brighter is the non-ice matrix. Obviously, the value of the threshold affects the apparent ice content (Figure 3). A range of threshold was used to give a range of ice contents, while making sure that the microstructure remains visually close to the original pictures. The resulting monochrome bitmap images were imported into AutoCAD then traced (later on we discovered that this could have been done automatically using MATLAB). The resulting AutoCAD geometry object is then imported into FEMLAB for the heat conduction simulation (Figure 4).

The sample was modelled as a rectangle, with the upper side at a given temperature T_1 (set at 0) and the lower side at T_2 (set at 1), while the other sides were assumed to be adiabatic. The actual temperature values are immaterial due to the linearity of the problem. Density and specific heat are not needed since the problem is steady-state. A steady state simulation was carried out, then the total heat flow through either face was calculated by integrating the flux numerically. The effective diffusivity was then calculated from Fourier's law.

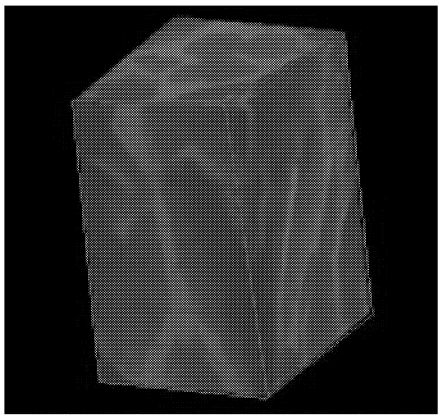

Figure 1. Original 3-D Reconstructed Picture of Frozen Sample

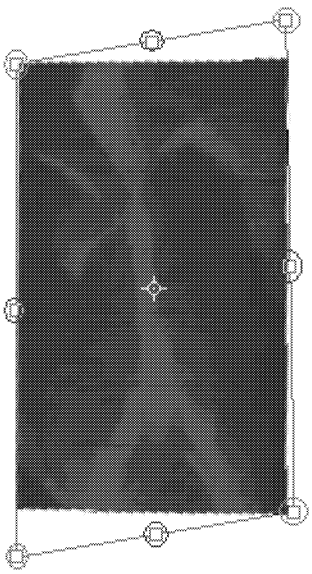

Figure 2. Left Face after Straightening of Angles and Transformed into Grayscale

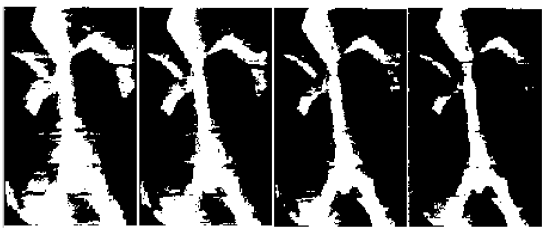

Figure 3. An Illustration of How Different Thresholds Will Yield Different Apparent Ice Contents

The parameters needed for the simulation were the thermal conductivities of ice and the non-ice phases. The thermal conductivity of ice varies with temperature over a range of 2.2 $Wm^{-1}K^{-1}$ at 0^0C to 10 W/mK at -196^0C (Fletcher, 1970), but a constant value of 2.21 $Wm^{-1}K^{-1}$ was chosen. The non-ice phase is a mixture of protein (k = 0.20 $Wm^{-1}K^{-1}$), fat (k = 0.18 $Wm^{-1}K^{-1}$), minerals (k = 0.26 $Wm^{-1}K^{-1}$) and unfrozen water (k = 0.50 $Wm^{-1}K^{-1}$). Normally about 10-20% of the original water remains unfrozen. The composition of the unfrozen mixture can be estimated (Pham, 1987), and its thermal

conductivity calculated by the Levy model is 0.276 W/mK. The ratio of ice to non-ice thermal conductivities was thus 8.0. Some variation in this ratio will not affect the rankings of the agreements between the various models, including the FEMLAB model of this paper.

Figure 4. AutoCAD Tracing Imported into FEMLAB

RESULTS AND DISCUSSION

Figure 5 shows finite element mesh around the circled region near the upper left corner of the previous figure, greatly expanded to illustrate the fineness of the mesh. Figure 6 shows a typical temperature contour plot generated by FEMLAB, with heat flowing from top to bottom.

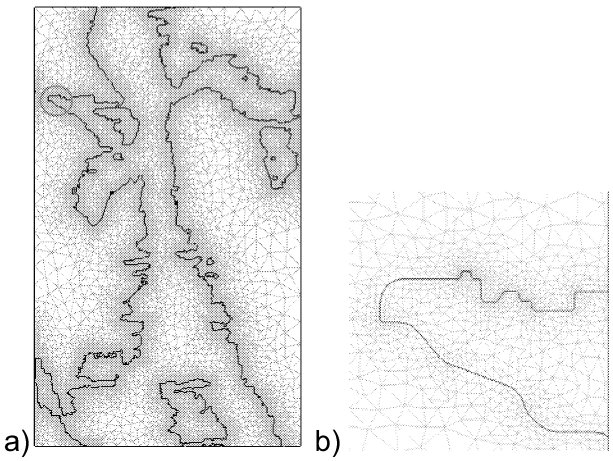

Figure 5. Finite Element Mesh (a) Whole Sample (b) Expanded Circled Region

Figure 7 shows the thermal conductivity results predicted by the Maxwell-Eucken, Levy, EMT, series and parallel models (curves), and the FEMLAB results (points) for various ice contents. The Maxwell-Eucken models give different predictions depending on whether ice is taken as the continuous or disperse phases, so two curves are shown. It can be seen that the Levy model agrees best with the FEMLAB results over the whole range of ice content, except at the lowest point (ϕ_{ice} = 0.44). Inspection of the FEMLAB geometric model at this ice content shows that the ice has indeed become a disperse phase consisting of many unconnected crystals, therefore the assumptions behind the Maxwell-Eucken model are partly satisfied (the assumption of spherical particles is not satisfied, however). For the remaining points, the FEMLAB results and Levy's model show excellent agreement, with an average relative error of 0.13% and standard deviation of 3.1%. This corroborates the results Pham (1989) who found that Levy's model gives best prediction of experimental thermal conductivity data for frozen animal tissues. The results are roughly equidistant from the two versions of the Maxwell-Eucken model.

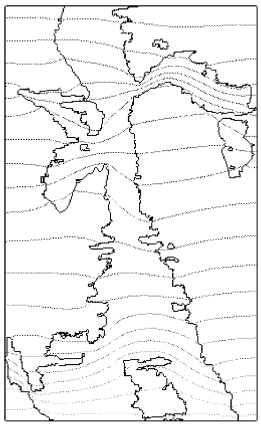

Figure 6. Typical Temperature Contour Plot Generated by FEMLAB

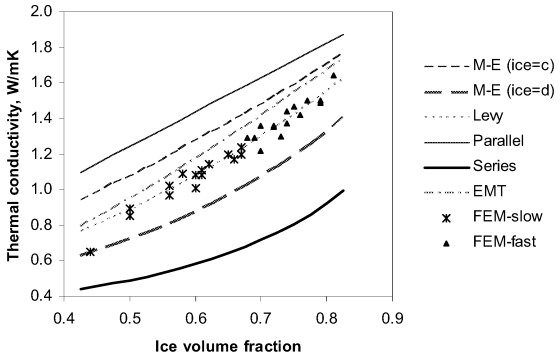

Figure 7. Thermal Conductivities Calculated from FEMLAB and Various Idealized Models

CONCLUSIONS

For frozen lean beef, the equation of Levy agrees very well with thermal conductivity predictions by two-dimensional finite element modelling. This result corroborates earlier comparison of various simplified models with experimental data for animal tissues. Levy's equation was proposed as an empirical correlation without physical justification, but recently a sound physical interpretation has been provided by Wang *et al.* (2006). In this interpretation, the material is a mixture of two substructures with equal volumes and equal thermal conductivities, one consisting of component A dispersed in component B and the other of B dispersed in A. Micrographs of frozen beef obtained from micro-slicing show that, in fact, both the ice and non-ice phase are basically continuous.

The main limitation of the present work was that it was carried out with a 2-D model of the ice crystal structure. It will be useful to carry out a full 3-D finite element model using a computed tomography micro-scan of the frozen food, if possible.

Nomenclature

k	thermal conductivity, $Wm^{-1}K^{-1}$
q	heat flux, Wm^{-2}
ΔT	temperature, K
x	distance, m
ϕ	volume fraction

Subscripts

c	continuous phase
d	disperse phase
e	effective
i	component i

REFERENCES

Carson, J.K., S.J. Lovatt, D.J. Tanner and A.C. Cleland. 2003. "An Analysis of the Influence of Material Structure on the Effective Thermal Conductivity of Porous Materials Using Finite Element Simulations." *International Journal of Refrigeration*, 26, No.8, 873-880.

Davis, T.H., L.R. Valencourt and C.E. Johnson. 1975. "Transport Processes in Composite Media." *Journal of the American Ceramic Society* 58, 447-452.

DeVries, D. A. 1963. "Thermal Properties of Soils." In *Physics of Plant Environment*, 1963, W.R. van Wijk (Ed.), John Wiley & Sons Inc., New York, p. 210-235.

Do, G.-S., Y. Sagara, M. Tabata, M., K.-I. Kudoh, and T. Higuchi. 2004. "Three-dimensional Measurement of Ice Crystals in Frozen Beef with a Micro-Slicer Image Processing System." *International Journal of Refrigeration* 27, 184–190.

Eucken, A. 1940. "Allgemeine Gesetzmassigkeiten fur das Warmeleitvermogen verschiedener Stoffarten und Aggregatzustande." *Forschung und Gebiete Ingenieur (Ausgabbe A)* 11, 6.

Fletcher, N.H. 1970. *The Chemical Physics of Ice*. Cambridge, UK: Cambridge University Press, p.144.

Landeauer, R. 1952. The Electrical Resistance of Binary Metallic Mixtures. *Journal of Applied Physics* 23, 779-784.

Levy, F.L. 1981. "A Modified Maxwell-Eucken Equation for Calculating the Thermal Conductivity of Two-Component Solutions or Mixtures." *International Journal of Refrigeration* 4, 223-225.

Pham, Q.T. 1987. "Calculation of Bound Water in Frozen Foods." *Journal of Food Science* 52, 210-212.

Delgado, A.E., D.-W. Sun, and A.C. Rubiolo. 2005. Thermal Physical Properties of Foods. In *Thermal Food Processing: New Technologies and Quality Issues*, pp. 1-32, D.-W. Sun, ed. Florida, USA: Dekker/CRC Press.

Pham, Q.T. 1990. Prediction of Thermal Conductivity of Meats and Other Animal Products from Composition Data. In *Engineering and Food*, vol. 1, pp. 408-423, W.E.L. Spiess & H. Schubert, ed. London, UK: Elsevier Applied Science.

Pham, Q.T. and J. Willix. 1989. "Thermal Conductivity of Fresh Lamb Meat, Offals and Fat in the Range –40 to +30°C: Measurements and Correlations." *Journal of Food Science* 54 No.3, 508-515.

Tarnawski, V.R., D.J. Cleland, S. Corasaniti, F. Gori and R.H. Mascheroni. 2005. "Extension of Soil Thermal Conductivity Models to Frozen Meats with Low and High Fat Content." *International Journal of Refrigeration* 28, 840-850.

Wang, J.F., J.K. Carson, M.F. North and D.J. Cleland. 2006. A new approach to modelling the effective thermal conductivity of heterogeneous materials. *International Journal of Heat and Mass Transfer*, In Press.

APPENDIX

Ice Fraction	Femlab	Max-well	Parallel	Series	Levy
Slow freezing					
0.615	1.084	0.902	1.465	0.597	1.106
0.700	1.219	1.072	1.630	0.712	1.296
0.759	1.421	1.215	1.744	0.822	1.443
0.794	1.496	1.313	1.811	0.904	1.537
0.609	1.114	0.892	1.454	0.591	1.094
0.651	1.198	0.970	1.535	0.641	1.184
0.687	1.287	1.044	1.605	0.693	1.266
0.739	1.443	1.164	1.706	0.782	1.392
0.583	1.089	0.848	1.404	0.564	1.041
0.704	1.356	1.082	1.638	0.720	1.307
0.772	1.505	1.251	1.770	0.851	1.478
0.814	1.636	1.373	1.850	0.959	1.593
0.556	1.021	0.804	1.352	0.538	0.989
0.660	1.167	0.987	1.552	0.653	1.203
0.730	1.302	1.141	1.687	0.764	1.369
0.795	1.493	1.315	1.813	0.906	1.539
Fast freezing					
0.436	0.649	0.640	1.120	0.446	0.780
0.558	0.966	0.807	1.355	0.540	0.992
0.656	1.172	0.979	1.544	0.648	1.194
0.738	1.370	1.163	1.704	0.780	1.391
0.495	0.892	0.716	1.234	0.487	0.878
0.598	1.078	0.872	1.432	0.579	1.071
0.669	1.241	1.006	1.570	0.666	1.224
0.723	1.349	1.125	1.674	0.751	1.352
0.500	0.849	0.721	1.242	0.490	0.885
0.595	1.015	0.868	1.427	0.576	1.066
0.672	1.202	1.012	1.575	0.670	1.230
0.744	1.366	1.176	1.715	0.791	1.404
0.619	1.136	0.910	1.474	0.603	1.115
0.676	1.289	1.021	1.584	0.676	1.241
0.717	1.361	1.111	1.663	0.741	1.337
0.753	1.470	1.200	1.733	0.810	1.428

Table A1. Ice Fractions and calculated k values. Each sub-table of four rows is for a different micrograph.

SUBSTRATE AND METABOLITE DIFFUSION WITHIN SOLID MEDIUM IN RELATION TO GROWTH OF *GEOTRICHUM CANDIDUM*

Abdeltif Amrane*
Mazen Aldarf
Florence Fourcade
Yves Prigent

Equipe Chimie et Ingénierie des Procédés - Université de Rennes 1 / ENSCR
UMR CNRS 6226 "Sciences Chimiques de Rennes"
ENSCR, Campus de Beaulieu, avenue du Général Leclerc, 35700 Rennes, France.
E-mail address: abdeltif.amrane@univ-rennes1.fr

ABSTRACT

Geotrichum candidum was cultivated at the surface of solid model media containing lactate and glutamate or peptone, to simulate the composition of Camembert cheese. The surface growth of *G. candidum* induced the diffusion of substrates from the core to the rind and the diffusion of produced metabolites from the rind to the core.
Growth kinetics were described using the Verlhust model and both substrates consumption and ammonium production were considered to be partially linked to growth. The experimental diffusion gradients of substrates (lactate and glutamate) and ammonium recorded during *G. candidum* growth were fitted. The diffusion / reaction model was found to match with experimental data until the end of growth, except with regards to ammonium concentration gradients during *G. candidum* growht on peptone – lactate based medium. Indeed, *G. candidum* preferentially assimilated peptone over lactate as a carbon source, resulting in an almost cessation of ammonium release before the end of growth.
On peptone – lactate based medium, both lactate consumption and ammonium release gradients corresponded well to the proton transfer gradients, confirming that both components are responsible for the pH increase observed during the ripening of soft Camembert cheese.
On glutamtate and lactate, significant substrate concentrations (glutamate and lactate) always remained at the top of the gel, showing the absence of diffusional limitation of growth; in addition to the absence of substrate limitation. An absence of diffusional limitation when the medium contained peptone instead of glutamate was also indirectly deduced from the comparison of both media. Indeed, peptone is too complex for a possible identification of diffusional limitation from gradients analysis.

KEYWORDS

Geotrichum candidum, Growth kinetics, Solid-state fermentation, Diffusion, Modelization.

INTRODUCTION

The yeast *Geotrichum candidum* is involved in the ripening of white soft cheeses (Ribadeau-Dumas 1984; Fox et al. 1993). The growth of this fungi at the surface of the cheese accounts for the neutralization of the curd; this step plays an important role in the development of texture (Vassal and Gripon 1984; Fox et al. 1990; Molimard et al. 1994) and the further growth of surface bacteria populations (Karahadian and Lindsay 1987; Fox et al. 1993).
The assimilation of lactic acid by *G. candidum* (and *P. camembertii*) growing at the surface of the curd induces a diffusion of this specie from the core to the rind resulting in a concentration gradient. In a similar way, ammonium release at the surface of the curd induces a diffusion of this component from the rind to the core. These diffusional mechanisms appear therefore as one of the main factors in soft cheese manufacturing.
To our knowledge, no work concerning the diffusional mechanisms, resulting from the concentration gradients of mineral elements, substrates or metabolites, induced by fungal growth are available in the literature. Only few studies concerning the mineral migration of calcium and phosphorus (Le Gräet et al. 1983) and some salts (Le Gräet and Brulé 1988; Gaucheron et al. 1999), all under pH control, can be found. These authors have examined the mineral distribution between the rind, the under-rind and the center of cheeses or model cheeses.

The main purpose of this paper is to study the diffusional mechanisms and to propose a theoretical approach that can be subsequently applied to curd during ripening for its monitoring and control. In this aim, a diffusion / reaction model has been developed: the diffusion of lactate from the bottom of the gel to the upper surface or that of ammonium from top to bottom induced by their respective consumption and production at the surface of the gel due to fungal growth. Pure cultures of *Geotrichum candidum* have been chosen as an example to validate the model.
Obviously, a soft cheese during ripening is a rather complex system (Gaucheron et al. 1999). For a better understanding of the fundamental phenomena, it appears

therefore more suitable, in a first approach, to mimic the real system (lactic curd) by cultivating *G. candidum* on model media. Interesting results were previously obtained in solid (Aldarf et al. 2002a) and liquid (Adour et al. 2002) cultures on media containing, among others, tryptic casein peptone and lactate to simulate the aqueous phase of Camembert cheese (Boutrou et al. 1999). The kinetics of carbon and nitrogen substrates consumption, as well as that of metabolites production (carbon dioxide and ammonium) recorded for *G. candidum* were examined (Adour et al. 2002; Aldarf et al. 2002a).

Mean proton, substrate and product concentrations in the gel were considered in previous studies (Aldarf et al. 2002a). However, the diffusional phenomena resulting from the concentration gradients of consumed nutrients or produced metabolites induced by the fungal growth at the surface of the cheese appear to be key-factors in soft cheese manufacturing (Stephan et al. 2004). Another objective of this work was therefore to examine the contribution of lactate and ammonium concentration gradients to the proton transfer gradients, during pure cultures of *G. candidum* on peptone and lactate.

However, peptone, the nitrogen (and carbon) substrate, is too complex for a fine identification of the nutritional mechanisms, especially those related to amino acids metabolization. Moreover, the peptone concentration gradients can only give global information; possible diffusional limitation cannot be pointed out. Growth of *G. candidum* on simple media, containing lactate and a single amino acid as nitrogen (and carbon) source may give more reliable information. Analysis of growth in relation with the diffusion of the assimilated substrates (glutamic acid and lactate) and the produced metabolite (ammonium) were therefore examined in this work. The chosen amino acid must be a convenient carbon and nitrogen sources for both *G. candidum* and *P. camembertii*. The majority of the amino acids are convenient nitrogen sources for both fungi, while some of them can also be metabolized as carbon sources (Plihon et al. 1998). Among the amino acids which lead to a significant growth for *G. candidum* when used as the sole carbon and nitrogen sources (Plihon et al. 1998), glutamic acid was chosen.

MATERIALS AND METHODS

Microorganisms

The strains *Geotrichum candidum* Geo17 and *Penicillium camembertii* LV2 (Danisco, Dangé St Romain, France) were used. Freeze-dried spores were maintained at + 7 °C.

Media

The composition of the peptone based medium was (g l^{-1}) (Aldarf et al. 2004): agarose, 20 (Biokar Diagnostics, Beauvais, France); tryptic casein peptone or glutamate, 10 (Prolabo, Paris, France); Sodium L(+)-lactate (Acros, Geel, Belgium), 10; KH_2PO_4: 6.26; Na_2HPO_4, $2H_2O$: 0.71; EDTA chelated trace elements (Trinci 1969). The pH was then adjusted to 4.5 with HCl 1M.

Culture conditions

Solid-state cultures were carried out in Petri dishes of 18 cm (internal diameter), at 12 °C and 98 % relative humidity, to simulate the operating conditions in a salting room during the ripening of Camembert cheese, in a cooling incubator Friocell MMM 111 l (Bioblock, Illkirch, France). The presence of a saturated solution of K_2SO_4 in the cooling incubator allowed maintaining the relative humidity at 98 %. 500 ml of medium were sterilized (121°C, 20 min) and poured into the Petri dish. After gelling, the surface of the medium was inoculated with 10 ml of the spore suspension, left 1 h in sterile medium at room temperature for spore hydration and germination.

Analysis

During the fermentation, cores were sampled by stamping out the culture with a sterile hollow punch. By means of tweezers, the thin layers of biomass on the top of the cores were peeled off, dried and weighted; the total biomass concentration was expressed in gram of dry weight per litter of gel.

The remainder of the solid samples was set in a microtome; slices of approximately 3 mm were then cut with a razor and weighted. Every slice was put down into an Eppendorf tube and the pH was measured by sticking a 5 mm diameter combination pH electrode (Mettler Toledo, Viroflay, France) into the solid sample after homogenization. For lactate and ammonium analysis, every slice was dissolved by heating in 10 ml distilled water; L(+)-lactate was then determined enzymatically (Sigma Diagnostics, St Quentin Fallavier, France) and ammonium by the Nessler method (Rodier 1975). Total nitrogen was determined on a core by the Nessler method (Rodier 1975), after mineralization of the sample. The subtraction of ammonium concentration in the core from the total nitrogen led to the peptone concentration at each time. The glutamic acid concentration corresponded to its primary α-amino group measured by the TNBS method (Satake et al. 1960).

The buffer capacity of the medium used was measured by titration of 25 ml of medium by 1M NaOH using an automatic system (Titrino Metrohm 702 SM, Switzerland) (Aldarf et al. 2002a).

THEORETICAL ASPECTS

Determination of the diffusion coefficient

Considering a cylindrical core sample of length *L*, displayed below in longitudinal section:

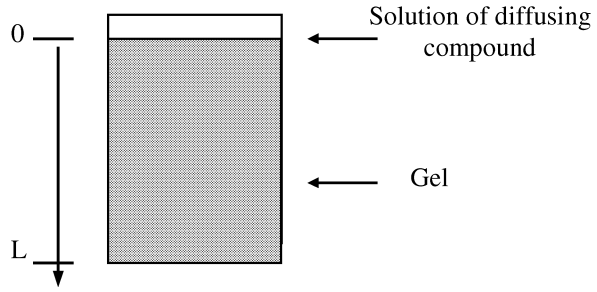

Initially, an aliquot (25 mL) of a solution of diffusing compound was put into contact with the surface of the gel (y = 0) (500 mL of gel) for some minutes (5 min for ammonium and 30 min for glutamate and lactate respectively). The solution was then eliminated from the gel surface, which was rinsed several times with distilled water. During contact-time, only part of the diffusing compound was transferred into the gel, but not sufficiently long enough to allow for diffusion on the whole longitudinal section; most of the diffusing compound remained at the surface of the gel at the end of the allotted time of contact. Therefore, it was assumed that this protocol induced an instantaneous source of the diffusing compound.

The diffusion was plane and one-dimensional. The flux was nil on all the other limits of the gel: the bottom face of the Petri dish was impermeable (y = L) and there was no concentration gradient through the side faces.
Therefore the following partial derivative equation had to be solved (second Fick relation with a constant coefficient diffusion *D*):

$$D * \frac{\partial^2 s}{\partial y^2} - \frac{\partial s}{\partial t} = 0 \qquad (1)$$

With the following initial condition: $t = 0$, $s\ (0,\ 0) = C$ (amount of diffusing compound deposited at time $t = 0$ in the plane $x = 0$).
With the initial time corresponding to the end of the contact-time, and the following limit conditions: y = 0, $\frac{\partial s}{\partial y} = 0$, and a nil flux on the other sides of the gel.
According to Crank (Crank 1975), with regards to a plane and one-dimensional diffusion, induced by an instantaneous source, after a given time *t*, the concentration gradient of the investigated component is given by the following relation:

$$s = \frac{C}{\sqrt{\Pi * D * t}} * exp(-\frac{y^2}{4 * D * t}) \qquad (2)$$

This equation satisfies the condition that the total amount of diffusing substance remains constant and equal to *C* since there was no reaction between the investigated component and the culture medium.
D was determined by minimization of the sum of the deviation squares between the calculated (Eq. 2) and the experimental values of the concentrations. All the concentration gradients were minimized simultaneously to optimize *D* in the given physico-chemical conditions (12 °C, 98 % relative humidity and pH 4.5 or 7.5). This optimization was conducted using the Matlab software package.

The selected pHs for diffusion coefficient determination were 4.5 and 7.5, chosen since they corresponded to the pH at the beginning and at the end of G. candidum cultures. For all components, the pH effect appeared negligible in the range of pH tested. However, one should bear in mind that, between 4.5 and 7.5, the main species present in the medium were glutamate, lactate and ammonium, since glutamic acid, lactic acid and ammonia remained mainly dissociated (pKa = 3.22, 3.8 and 9.25, respectively). Consequently, constant diffusion coefficients were considered throughout this work for the three components, which were 0.56 ± 0.03 $cm^2\ day^{-1}$ for glutamate (Aldarf et al. 2005), and 0.40 ± 0.03 and 0.80 ± 0.05 $cm^2\ day^{-1}$ for lactate and ammonium (Aldarf et al. 2004), respectively.

Determination of the concentration gradients

Mycelial growth can be described using the widespread logistic or Verlhust relation (Moraine and Rogovin 1966; Norton et al. 1994; Diaz et al. 1999; Pandey et al. 2000):

$$\frac{dx}{dt} = \mu_m * x * (1 - \frac{x}{x_m}) \qquad (3)$$

where x and x_m are the biomass concentrations (g L^{-1}) at a given time t and its maximal value respectively, μ_m is the maximal specific growth rate (day^{-1}).
This relation can be solved directly resulting in the following solution:

$$x = x_0 * x_m * \frac{e^{\mu_m * t}}{x_m - x_0 + x_0 * e^{\mu_m * t}} \qquad (4)$$

With x_0 the initial biomass concentration.

As previously shown (Aldarf et al. 2002b), substrate consumption is assumed to be involved in cellular biosynthesis as a carbon source and in energy supply for growth and cellular maintenance. From this, its consumption would appear as partially linked to growth:

$$-\frac{dv}{dt} = A * \frac{dx}{dt} + B * x \qquad (5)$$

Where *A* and *B* are the coefficients for the substrate consumption resulting from cellular biosynthesis and maintenance, respectively.
During growth on glutamate and lactate based medium, it was found that growth was limited by the alkaline pH at the surface of the gel. From this, an additional term has been introduced to account for the pH inhibition of growth:

$$-\frac{dv}{dt} = A * \frac{dx}{dt} + B * x * (1 - \frac{h}{h_f}) \quad (6)$$

With h and h_f the concentration of protons uptake and its final value. Protons uptake values were deduced from pH by means of the buffer capacity of the medium used, measured in the pH range recorded during cultures. Experiments were carried out in a sterile liquid medium under culture conditions.

On the other hand, in order to take into account the substrate limitation observed at the end culture on peptones and lactate based medium, an additional term was added:

$$-\frac{dv}{dt} = A * \frac{dx}{dt} + B * x * (1 - \frac{s_{res}}{s}) \quad (7)$$

With s_{res} being the residual lactate concentration.

The additional term in the above equation (7) was previously introduced to account for cessation of lactate production due to substrate limitation (Amrane 2001).

Amino acids contain excess nitrogen in relation to their carbon content (Deacon 1997). The excess nitrogen is released as ammonium, after amino acid deamination (Hemme et al. 1982; Cerning et al. 1987). As for substrate consumption, ammonium production resulted from both biosynthesis and viable cell maintenance, and appears therefore partially linked to growth:

$$\frac{dm}{dt} = A * \frac{dx}{dt} + B * x \quad (8)$$

Where m corresponded to the metabolite (ammonium) concentration.

In order to take the pH inhibition recorded on glutamate and lactate and similarly to substrate consumption, an additional term was added to the above equation (8):

$$\frac{dm}{dt} = A * \frac{dx}{dt} + B * x * (1 - \frac{h}{h_f}) \quad (9)$$

During growth on peptones and lactate, the following expression was considered for ammonium production:

$$\frac{dm}{dt} = A * \frac{dx}{dt} + B * x * (1 - \frac{z_{res}}{z}) \quad (10)$$

Where z_{res} was the residual peptone concentration. The additional term ($1 - \frac{z_{res}}{z}$) in the above equation (10) was added to account for cessation of ammonium production due to nitrogen substrate limitation (peptone).

In the above equation (8, 9 and 10), A and B were the coefficients for substrate consumption or metabolite production associated and non-growth associated respectively.

Coefficients A and B (Eqs. 6 and 7) were optimized using the EXCEL solver system.

Initially, lactate and glutamate or peptone were uniformly distributed in the gel at a concentration s_0 and z_0 respectively. From the initial time t = 0, the biomass grew uniformly at the surface of the gel (y = 0) following Eq. (4); at the upper surface of the gel (low y), lactate and glutamate concentrations decreased, while ammonium concentration increased but remained constant in a cross section of the gel (plane one-dimensional diffusion). The flux of glutamate and lactate consumption (Eqs.6 and 7), as well as that of ammonium production (Eqs.9 and 10), across a section of 1 cm^2 of gel (at y = 0) are given by the following relation:

$$Flux = L * \frac{dv}{dt} \quad (11)$$

$$Flux = L * \frac{dm}{dt} \quad (12)$$

The flux were nil on all the other limits of the gel: the under side of the Petri dish was impermeable (y = L) and there was no concentration gradient through the side faces.

Therefore the following partial derivative equation had to be solved (second Fick relation with constant coefficient diffusion D):

$$D * \frac{\partial^2 s}{\partial y^2} - \frac{\partial s}{\partial t} = 0 \quad (13)$$

With the following initial conditions:

For lactate and glutamate: t = 0, $v(y, 0) = v_0$, $0 \le y \le L$,

For ammonium: t = 0, $m(y, 0) = 0$, $0 \le y \le L$

The following limit conditions:

For lactate and glutamate: y = 0,

$$Flux = -L * \left(A * \frac{dx}{dt} + B * x * \left(1 - \frac{s_{res}}{s} \right) \right) \quad (14)$$

or $$Flux = -L * \left(A * \frac{dx}{dt} + B * x * \left(1 - \frac{h}{h_f} \right) \right) \quad (15)$$

For ammonium: y = 0,

$$Flux = L * \left(A * \frac{dx}{dt} + B * x * \left(1 - \frac{z_{res}}{z} \right) \right) \quad (16)$$

or $$Flux = L * \left(A * \frac{dx}{dt} + B * x * \left(1 - \frac{h}{h_f} \right) \right) \quad (17)$$

And a nil flux on the other sides of the gel.

The numerical resolution of the above systems was carried out using the Galerkin Finite Element Method (PDease software) to give the concentration profiles $v(y)$ of lactate and ammonium at different times.

RESULTS AND DISCUSSION

The fit using the logistic model (Eq. 4) shows a good agreement with the experimental biomass data for *G. candidum* growing on the two media tested (Fig.1).

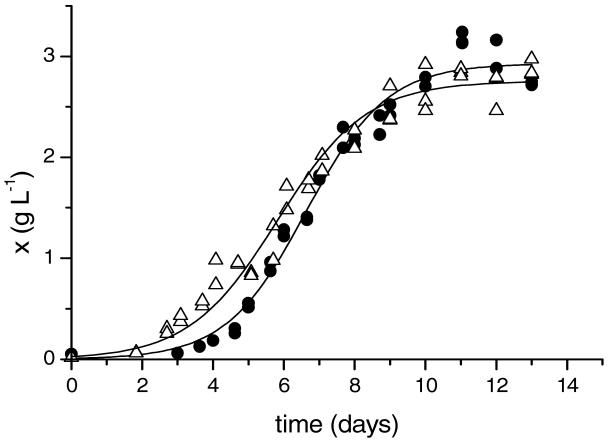

Figure 1. Kinetics of growth for *G. candidum* growing on glutamate – lactate (●), and peptone – lactate (Δ) based media. Continuous line: growth modelization using the Verlhust model (Eq. 4).

Assimilation of lactate and glutamate by *G. candidum* growing at the surface of the gel induces their diffusion from the core to the rind. Therefore, the lactate and glutamate diffusion gradients (Figs.2a and b), namely the concentration between the top and the bottom of the gel, were expected to be linked to growth, as experimentally supported. Indeed, after 7 days for glutamate and 6-8 days for lactate, the maxima for the diffusion gradients were recorded; the maximum rates of consumption were recorded after similar times of culture, as well as the maximum growth rates (Fig.1). This was also the case for ammonium production, since the maximum for diffusion gradients was recorded after 7 days of *G. candidum* growth (Fig.1). Indeed, ammonium resulted from the use of glutamate as a carbon source.

An inhibitory pH effect on growth cannot be deduced from the examination of the kinetics (Aldarf et al. 2005). Indeed, at the end of the linear growth, namely 9 days of *G. candidum* growth, the mean pH value in the gel was 7.8, which was obviously not inhibitory (Amrane and Prigent 2001). However, examination of the pH gradients showed a significant gradient at the end of the linear growth: 0.65 between the first (top) and last (bottom) slice of the gel, with a pH of the first slice (top of the gel) of 8.2. From this, the high pH values recorded at the top of the gel induced a decrease of the growth rates until cessation of growth for surface pH of 8.5 after 10 days of *G. candidum* growth.
Substrates consumption and ammonium production were considered as partially linked to growth (Eqs.5 and 8). An additional term has been therefore introduced to account for the inhibition of growth by the pH (Eqs.6 and 9). The additional term $\frac{h}{h_f}$ (Eqs.6 and 9) involved the concentration of protons exchanged instead of the pH, since this term must be negligible in the beginning of growth and close to unit at the end of culture.
Fig.2 shows that in most cases, the calculated gradients matched with the experimental gradients.

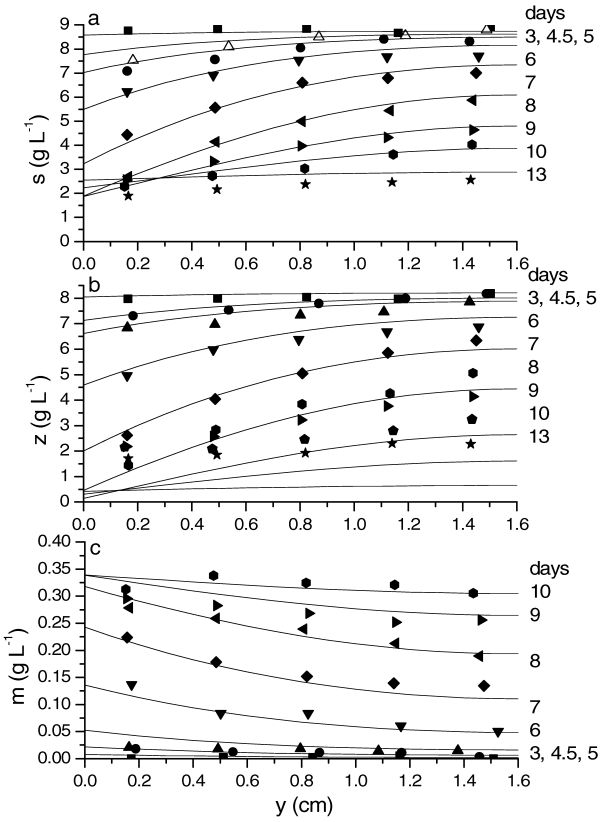

Figure 2. Lactate (a), glutamate (b) and ammonium (c) concentration gradients induced by their consumption or production by *G. candidum* growing at the surface of the glutamate – lactate based medium. Symbols: experimental data points; continuous lines: recalculated diffusion gradients (Eq.13) with the biomass parameter values x_0 = 0.002 g L^{-1}, x_{max} = 2.8 g L^{-1} and μ_{max} = 1.0 day^{-1} (Eq.4 – Fig.1), and A = 2.5, B = 0.2 day^{-1} and D = 0.40 cm^2 day^{-1} for lactate, and A = 1.9, B = 0.2 day^{-1} and D = 0.56 cm^2 day^{-1} for glutamate, and A = 0.12, B = 0.001 day^{-1} and D = 0.80 cm^2 day^{-1} for ammonium.

The contributions of the processes possibly involved in proton transfer had to be examined, namely lactic acid metabolization and ammonia release in relation to growth (Karahadian and Lindsay 1987; Lucey and Fox 1993). Experiments were therefore conducted on lactate and peptones in place of glutamate to simulate the aqueous phase of Camembert cheese (Boutrou et al. 1999). Lactate consumption and ammonium production have been considered to be partially linked to fungal growth and substrate limitation, lactate (carbon) and peptone (nitrogen) limitation respectively (Aldarf et al. 2002a), accounted for

cessation of production or consumption at the end of growth (Eqs.7 and 10).

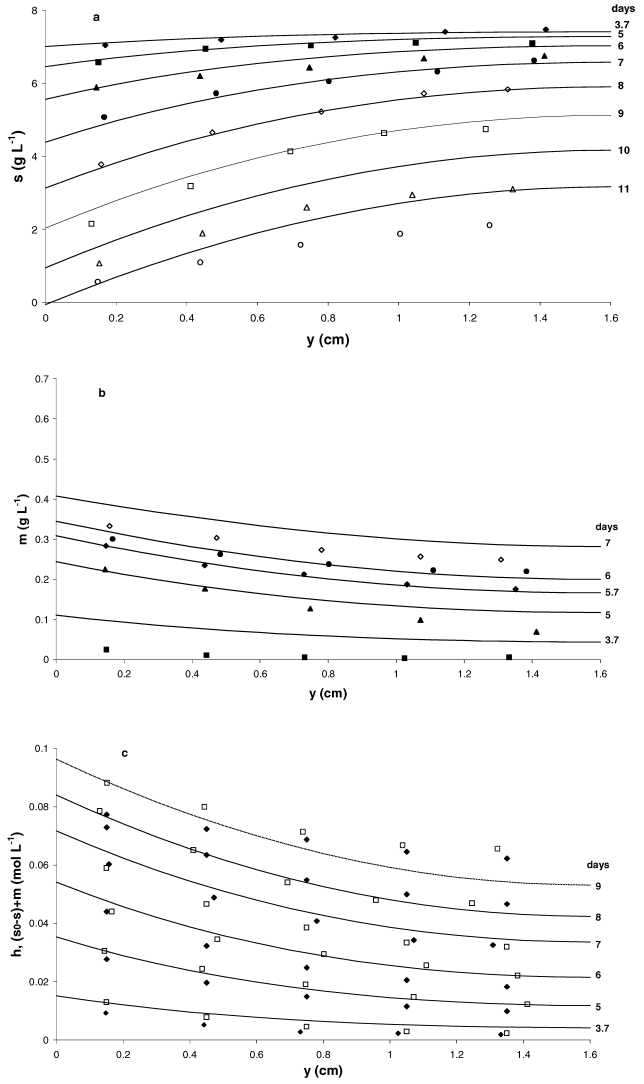

Figure 3. (a) Lactate and (b) ammonium concentration gradients induced by their consumption or production by *G. candidum* growing at the surface of the peptone – lactate based medium. Symbols: experimental data points; continuous lines: recalculated diffusion gradients (Eq.13) with the biomass parameter values x_0 = 0.03 g L^{-1}, x_{max} = 2.75 g L^{-1} and μ_{max} = 0.8 day^{-1} (Eq.4 – Fig.1), and A = 0.40, B = 0.41 day^{-1} and D = 0.40 cm^2 day^{-1} for lactate (Eq.7), and A = 0.185, B = -0.007 day^{-1} and D = 0.80 cm^2 day^{-1} for ammonium (Eq.10). (c) The sum of both gradients of lactate consumption and ammonium release: experimental data (open symbols) and recalculated gradients (—), and experimental gradients of proton uptake (closed symbols) induced by the growth of *G. candidum* at the surface of the medium.

Fig.3 displays the evolution of ammonium and lactate concentration gradients through the gel during the culture of *G. candidum* in peptone and lactate based medium. The overestimation of the ammonium concentration gradients in the beginning of growth (Fig.3b) was due to an overestimation of growth-associated ammonium production at the beginning of growth. Indeed, the Verlhust model (Eq.4) resulted in slight growth during the lag phase (Fig.1), and consequently an overestimation of the ammonium produced during this period of time.

Since peptone was the preferred carbon substrate during *G. candidum* growth (Aldarf et al. 2002a), its assimilation as both carbon and nitrogen sources up until about 6 days of culture, resulted in high consumption rates and consequently high ammonium production rates. A decrease in the rate of ammonium production followed, until production cessation after nearly 8 days of culture, while growth have not ceased yet (Fig.1). The Reaction – Diffusion model developed above (cf. Theoretical Aspects), which is based on a partial linking of ammonium production with growth (Eq.10), can not therefore account for cessation of ammonium production before that of growth. The model matched the experimental gradients well as long as ammonium was produced, namely up until 6 days of culture. After this time, the model overestimated the ammonium concentration gradient, since growth continued at a constant rate.

Peptone was assimilated as a carbon source, in addition to be a nitrogen source, until nearly 7 days of culture. From this time, lactate was the sole carbon substrate, resulting in its maximal rate of consumption (recorded after 9 days of growth), inducing the maximal diffusion gradient (Fig.3a). At the end of growth (10 days), the model underestimated the biomass concentration (Fig.1), resulting in an underestimation of the lactate consumption, and then an overestimation of the lactate concentration gradients (Fig.3a).

Proton transfer gradients were found to correspond to the sum of lactate consumption and ammonium release gradients until 8 days of growth (Fig.3c). This result demonstrated on solid model medium is in accordance with previous ones concerning the neutralization of curd during ripening, which is known to result from lactic acid assimilation (Lenoir 1984; Fox et al. 1990) and ammonia release due to amino acids deamination (Karahadian and Lindsay 1987; Lucey and Fox 1993).

CONCLUSION

Before considering the complex system of soft cheese during ripening (Gaucheron et al. 1999), growth of each microorganism was examined in solid-state culture, on media containing peptone as a nitrogen source, but also as a carbon source, to simulate the aqueous phase of Camembert cheese (Boutrou et al. 1999). Lactate consumption and ammonium release accounted for medium neutralization, since the sum of their gradients corresponded rather well to the proton transfer gradients throughout growth, in agreement with previous work concerning *P. camembertii* (Aldarf et al. 2006), the second microorganism involved in

the ripening of soft Camembert cheese (Fox et al. 1993), and confirming that both components are responsible for the pH increase observed during the ripening.
This preliminary work has to be followed by a similar work on the real medium, lactic curd during ripening, in view of the comprehension of the mechanism of curd neutralization, responsible for texturization development.

REFERENCES

Adour, L., Couriol, C., Amrane, A. and Prigent, Y. 2002. Growth of *Geotrichum candidum* and *Penicillium camemberti* in liquid media in relation with the consumption of carbon and nitrogen sources and the release of ammonia and carbon dioxide. *Enzyme and Microbial Technology* 31: 533-542.

Aldarf, M., Amrane, A. and Prigent, Y. 2002a. Carbon and nitrogen substrates consumption, ammonia release and proton transfer in relation with growth of *Geotrichum candidum* and *Penicillium camembertii* on a solid medium. *Journal of Biotechnology* 95: 99-108.

Aldarf, M., Amrane, A. and Prigent, Y. 2002b. Reconstruction of the biomass history from carbon and nitrogen substrate consumption, ammonia release and proton transfer during solid cultures of *Geotrichum candidum* and *Penicillium camembertii*. *Applied Microbiology and Biotechnology* 58: 823-829.

Aldarf, M., Fourcade, F. and Amrane, A. 2005. Solid-state culture of *Geotrichum candidum* and *Penicillium camembertii* on a glutamate and lactate based medium. *Enzyme and Microbial Technology* 36: 159-167.

Aldarf, M., Fourcade, F., Amrane, A. and Prigent, Y. 2004. Diffusion of lactate and ammonium in relation to growth of *Geotrichum candidum* at the surface of solid media. *Biotechnology and Bioengineering* 87: 69-80.

Aldarf, M., Fourcade, F., Amrane, A. and Prigent, Y. 2006. Substrate and metabolite diffusion within solid medium in relation to growth of Penicillium camembertii. *Journal of Industrial Microbiology and Biotechnology* DOI: 10.007/s10295-006-0093.4: 1-8.

Amrane, A. 2001. Batch cultures of supplemented whey permeate using *Lactobacillus helveticus*: unstructured model for biomass formation, substrate consumption and lactic acid production. *Enzyme and Microbial Technology* 28: 827-834.

Amrane, A. and Prigent, Y. 2001. Growth of *Geotrichum candidum* and *Penicillium camembertii* cultivated on liquid media correlated with ammonia and methanethiol emission. *Acta Biotechnology* 21: 283-290.

Boutrou, R., Gaucheron, F., Piot, M., Michel, F., Maubois, J.L. and Léonil, J. 1999. Changes in the composition of juice expressed from Camembert cheese during ripening. *Le Lait* 79: 503-513.

Cerning, J., Gripon, J.C., Lamberet, G. and Lenoir, J. 1987. Biochemical activities of *Penicillium* used in cheese making. *Le Lait* 67: 3-39.

Crank, J. 1975. *The mathematics of diffusion.* 2nd edition Oxford: Clarendon Press. 414 p.

Deacon, J.W. 1997. *Modern Mycology*. 3 ed. Oxford: Blackwell Science Ltd. 303 p.

Diaz, C., Lelong, P., Dieu, P., Feuillerat, C. and Salome, M. 1999. On-line analysis and modelling microbial growth using a hybrid system approach. *Process Biochemistry* 34: 39-47.

Fox, P.F., Lucey, J.A. and Cogan, T.M. 1990. Glycolysis and related reactions during cheese manufacture and ripening. *Critical Reviews in Food Science and Nutrition* 29: 237-253.

Fox, P.F., Law, J., Mc Sweeney, P.L.H. and Wallace, J. (1993) Biochemistry of cheese ripening. In: *Cheese: Chemistry, Physics and Microbiology, Major cheese groups*. Fox, P.F. (ed). Glasgow: Chapman & Hall. p 389-438.

Gaucheron, F., Le Gräet, Y., Michel, F., Briard, V. and Piot, M. 1999. Evolution of various salt concentrations in the moisture and in the outer layer and centre of a model cheese during its brining and storage in an ammoniacal atmosphere. *Le Lait* 79: 553-566.

Hemme, D., Bouillanne, C., Metro, F. and Desmazeaud, M.J. 1982. Microbial catabolism of amino acids during cheese ripening. *Science des Aliments* 2: 113-123.

Karahadian, C. and Lindsay, R.C. 1987. Integrated roles of lactate, ammonia, and calcium in texture development of mold surface-ripened cheese. *Journal of Dairy Science* 70: 909-918.

Le Gräet, Y. and Brulé, G. 1988. Macro and trace elements migration in Camembert soft cheese during ripening. *Le Lait* 68: 219-234.

Le Gräet, Y., Lepienne, A., Brulé, G. and Ducruet, P. 1983. Mineral migration in soft cheese during ripening. *Le Lait* 629-630: 317-332.

Lenoir, J. 1984. The surface flora and its role in the ripening of cheese. *International Dairy Federation Bulletin* 171: 3-20.

Lucey, J.A. and Fox, P.F. 1993. Importance of calcium and phosphate in cheese manufacture, a review. *Critical Reviews in Food Science and Nutrition* 76: 1714-1724.

Molimard, P., Lesschaeve, I., Bouvier, I., Vassal, L., Schlich, P., Issanchou, S. and Spinnler, H.E. 1994. Bitterness and nitrogen fractions of mold ripened cheese of Camembert type: impact of the association of *Geotrichum candidum* and *Penicillium camembertii*. *Le Lait* 74: 361-374.

Moraine, R.A. and Rogovin, P. 1966. Kinetics of polysaccharide B-1459 fermentation. *Biotechnology and Bioengineering* 8: 511-524.

Norton, S., Lacroix, C. and Vuillemard, J.C. 1994. Kinetic study of continuous whey permeate fermentation by immobilised *Lactobacillus helveticus* for lactic acid production. *Enzyme and Microbial Technology* 6: 457-466.

Pandey, A., Soccol, C.R. and Mitchell, D. 2000. New developments in solid state fermentation: I -bioprocesses and products. *Process Biochemistry* 35: 1153-1169.

Plihon, F., Le Doujet, S., Amrane, A. and Prigent, Y. 1998. Effect of amino acids on the growth of submerged cultures of *Geotrichum candidum* and *Penicillium camembertii*. *Journal of Food Mycology* 1: 203-210.
Ribadeau-Dumas, M. 1984. Studies on the control of the ripening of Camembert type cheeses. *Le Lait* 64: 448-468.
Rodier, J. (1975) Ammoniacal nitrogen analysis. In: *Water analysis.* Paris: Dunod. p 116-120.
Satake, K., Okuyama, T., Ohashi, M. and Shinoda, T. 1960. The spectrophotometric determination of amine, amino acid and peptide with 2,4,6-trinitrobenzene 1-sulfonic acid. *Journal of Biochemistry, Microbiology, Technology and Engineering* 47: 654-660.
Stephan, J., Couriol, C., Fourcade, F., Amrane, A. and Prigent, Y. 2004. Diffusion of glutamic acid in relation to growth of *Geotrichum candidum* and *Penicillium camembertii* at the surface of a solid medium. *Journal of Chemical Technology and Biotechnology* 79: 234-239.
Trinci, A.P.J. 1969. A kinetic study of the growth of *Aspergillus nidulans* and other fungi. *Journal of General Microbiology* 57: 11-24.
Vassal, L. and Gripon, J.C. 1984. Bitterness of cheeses of the camembert type: role of rennet and *Penicillium caseicolum*, means of its control. *Le Lait* 643-644: 397-417.

BIOGRAPHY

Abdeltif AMRANE was born in Algiers (Algeria), obtained his degree in chemical engineering at the university of Algiers (1987) and then went to the university of Rennes 1 for PhD thesis (1991). Since 1992, he worked as an associate professor at the university of Rennes 1, and then as a professor since 2001.

MILD HOMOGENIZATION AND VORTICITY CONTROL

Sarghini F.
DIIAT, UNIVERSITY OF NAPLES FEDERICO II
Via Universitá 100, 80055 Portici (NA) , Italy
e-mail:*sarghini@unina.it*

Masi P.
DSA, UNIVERSITY OF NAPLES FEDERICO II,ITALY
Via Universitá 100, 80055 Portici (NA) , Italy
e-mail:*pmasi@unina.it*

KEYWORDS

Industrial engineering, Model analysis, Computational Fluid dynamics

ABSTRACT

Homogenization in food processing is often obtained by using an high pressure mechanism with related high shear and drop sollicitations. In some cases, a milder mechanism is preferable, and in this paper the possibility of using controlled shear devices is numerically investigated

INTRODUCTION

is a mechanical treatment of drops immersed in an emulsion brought about by passing the mixture under high pressure and through a tiny orifice, which results in a decrease in the average diameter and an increase in number and surface area of the dispersed secondary phase.

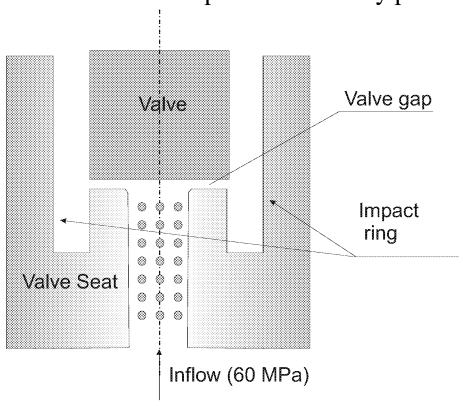

Figure 1. Geometry of a general emulsion dispersion valve

In food industry, droplets size reduction is usually carried out by using multi stage high pressure homogenizers; in classical configurations, a fluid or granular emulsion containing secondary phase droplets is pushed through one or more valves at high pressure, varying from 20 to 200 MPa, and the general configuration schematic is shown in fig. 1.

The radial channel (valve gap) size connecting the inner valve chamber with the external impact ring space where microsizing takes place, is usually very small, and the flow field resulting from the high pressure at the valve inlet is an high speed jet radially impinging on the surface of the external impact ring. The flow field in the external zone is a mixture of complex fluid dynamics phenomena (instabilities, turbulence and sometimes cavitation), producing a dramatic droplet size reduction of many orders of magnitude (i.e. from 200 μm up to 1 or 2 μm).

Such disruption mechanism is sometimes too strong, depending on the emulsion type, and a milder approach combining droplet size control and low pressure could be preferable. The complexity of fluid dynamics phenomena involved and the very small volume in which they take place represents a very challenging task for an experimental investigation, and for this reason the simulation support provides a very useful tool in order to gain a better insight of the homogenization process.

DROP BREAK-UP IN AN EMULSION DISPERSING VALVE

Numerical fluid dynamics has been used by many authors to investigate transient drop deformation and orientation, for example to validate non-equilibrium thermodynamics based models of a single drop in an arbitrary homogeneous flow field using the Boundary Elements Method (Feigl *et al.* (2003)). In real cases , like in a high pressure multi stage homogenization valve, the situation is quite more complicated, due to many factors affecting the

final result: the rheology of the mixture, secondary phase concentration, drop-drop interactions causing drop coalescence and simultaneously break-up, and all these factors are superimposed on a turbulent flow field with a significant pressure drop at the exit of the valve gap and a mean flow velocity which can reach hundred of m/s. Numerical simulations become more challenging and computationally expensive, and different approaches are required depending on the point of view; nonetheless, it is still possible to investigate numerically such a strong mixing mechanism affecting droplet break-up by using a combination of numerical tools. In this work the first simulation was obtained by using a Volume of Fluid (VOF) approach to investigate the break-up mechanism of glycerine droplets of 200 μm diameter immersed in water,fed into an homogenizing valve at 60 MPa. In the VOF method the interface of two immiscible fluids is tracked through a marker concentration function Φ . The advection of Φ is governed by

$$\frac{\partial \Phi}{\partial t} + V \cdot \nabla \Phi = 0 \tag{1}$$

where t is the time and V is the velocity vector, obtained by solving the complete set of Navier Stokes equation. The two fluids are represented by the volume concentration function Φ

$$\Phi = \left\{ \begin{array}{ll} 1 & for fluid1 \\ 0 & for fluid2 \end{array} \right) \tag{2}$$

The value of Φ varies between 0 and 1, the interface location is represented by steep gradients in the marker concentration; as a consequence, high resolution grids are required in order to properly track shape deformations. Average properties are obtained through interpolation; for example, density ρ is computed by

$$\rho = \rho_1 \Phi + \rho_2 (1 - \Phi) \tag{3}$$

while other fluid properties, such as viscosity or thermal conductivity k, are calculated in the same way. The use of VOF approach is justified by the fact that the VOF method mass is conserved and it still maintains a good representation of the interface, depending on the grid resolution (Li *et al.* (2000), Tryggavson *et al.* (2001)). A control volume commercial code (Fluent 6.2) was used in this simulation and a locally third-order numerical scheme was chosen to discretize continuity and momentum equations. The valve gap was set to 50 μm as an average value reported in literature for an emulsion dispersion homogenizer, and a $9 \cdot 10^5$ control volumes computational domain was used, with a grid size resolution of 0.2 μm in order to reduce numerical errors in the droplets interface tracking.

The deformation of an immiscible drop in a liquid suspension will depend on the motion of the fluid immediately surrounding the drop. If the bulk flow is turbulent, drops will experience both inertial forces arising from velocity fluctuations and viscous shear forces. The first studies of the break-up of liquid drops in agitated dispersions (Shinnar (1961),Shinnar and Church (1960),Hinze (1955)) generally invoked the theory of locally isotropic turbulence developed by Kolmogoroff. However, it seems highly unlikely that the turbulence is isotropic in view of the steep velocity gradients both transversely and axially in the entrance to the valve slit, and as a consequence shear effects are considered dominating the drop break-up mechanism. Phipps (Phipps (1975)) wrote that the degree of elongation and break-up of a primary drop will depend not only on its size, but also upon its trajectory into the gap. More recently Maffettone and Minale (Maffettone and Minale (1998)) developed a transient single drop deformation and orientation model in an arbitrary homogeneous flow field, qualitatively described in fig 2 and results were numerically and experimentally validated (Feigl *et al.* (2003))

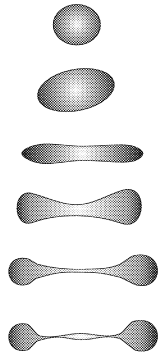

Figure 2. A sketch of a single drop deformation and break-up mechanism is a homogeneous shear flow

Basically the drop shape is first elongated, and then the shear effects shrink the intermediate zone before the drops separates in two or more parts. It is not clear whether the flow in the valve inlet is turbulent or not, due to the presence of a strong pressure gradient whose effect results in a flow regularization; assuming laminar condition at the flow inlet, simulation results show that the drop break-up mechanism seems to be confined in the external annular zone near the impact ring. In fig. 3 two snapshots of volume fractions of glycerine bubbles at different computational times are shown. In the inner zone of the valve inlet, the fluid flow field basically represents a pressure driven flow subjected to a section restriction, while in the radial channel (the valve gap) the flow is basically regularized by the pressure gradient, and no instability appears. The real mixing takes place in the external annular zone, where quite complex high shear zones are present due to the interaction between the jet instabilities (the initial Kelvin-Helmholtz instability of the high speed jet surrounded by a fluid almost at rest) and the impinging mechanism of the jet on the impact ring wall. The droplet is first elongated and entrained into a vortex (see fig. 3 b) and then broken according to the transient viscous mechanism previously mentioned. The main effect of high pressure appears mainly to accelerate the fluid in the valve gap, generating an high speed impinging jet in the external zone. Inside the valve gap, the drop shape is elongated, floating on the water boundary layer developing at the wall; at the

exit the drop is entrained by vortical structures and then broken by the effect of the shear, according to the previously described mechanism. In the impact ring zone a 2D simulation is not appropriate (the Re number based on the channel height and the mean velocity is 6250), and a 3D simulation is required, as turbulence is an intrinsically three dimensional phenomena, and the vortex stretching mechanism, which is the base of turbulence generation can be described only in a 3D framework.

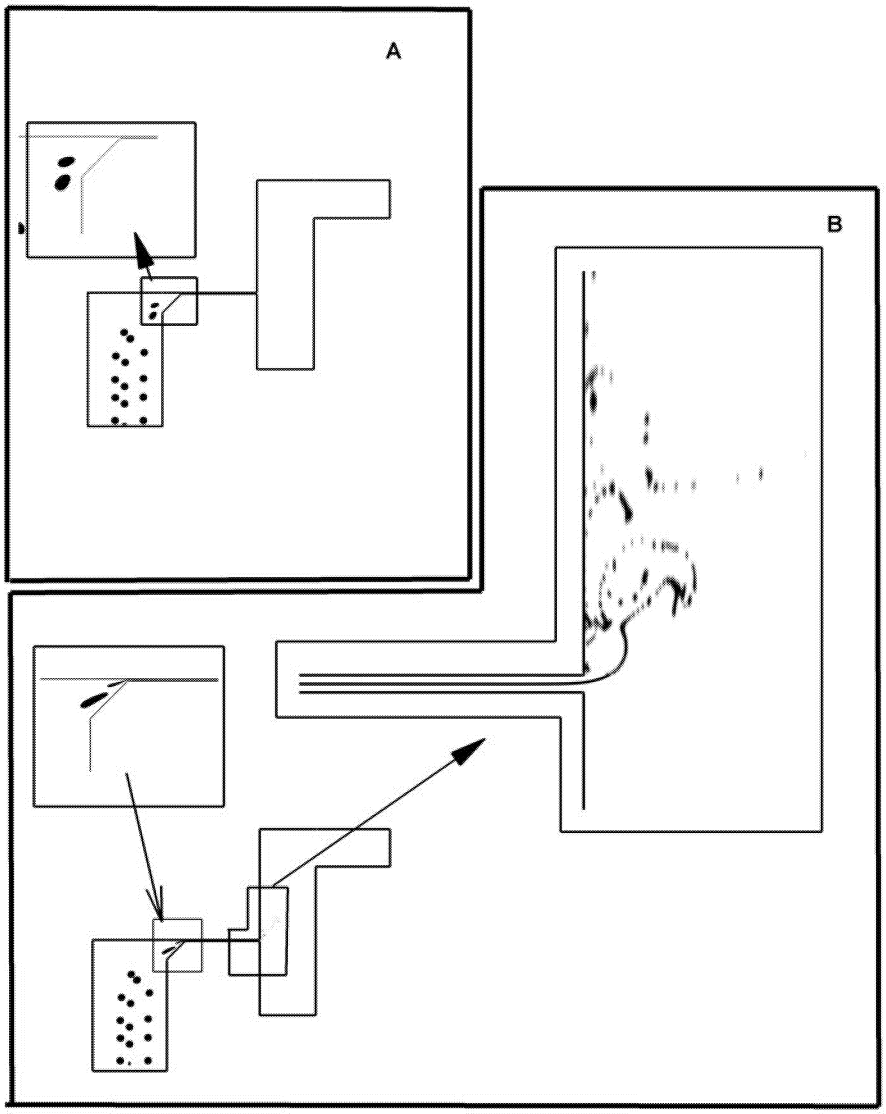

Figure 3. Droplet deformation and breakup at two different time steps

LARGE EDDY SIMULATION OF THE IMPINGING JET ON THE IMPACT RING

A better understanding of vortex dynamics in the impact ring zone can achieved by using the Large Eddy Simulation. Large-eddy simulation (LES) is a technique intermediate between the direct simulation of turbulent flows and the solution of the Reynolds-averaged equations. In LES the contribution of the large, energy-carrying structures to momentum and energy transfer is computed exactly, and only the effect of the smallest scales of turbulence is modeled. Since the small scales tend to be more homogeneous and universal, and less affected by the boundary conditions than the large ones, there is hope that their models can be simpler and require fewer adjustments when applied to different flows than similar models for the RANS equations. In the following simulations a dynamic scale-similar model was adopted for the subgrid scales dissipation terms, which is more appropriate for non-equilibrium flows (in statistical sense), using a box filtering procedure (Sarghini *et al.* (1999)) For this purpose, the flow solver was coupled with an *ad-hoc* routine

for the SGS model, using a box filtering procedure. The simulation of a pure water jet was obtained by using $2 \cdot 10^6$ control volumes, and a computational time step of 10^{-5} s was required.

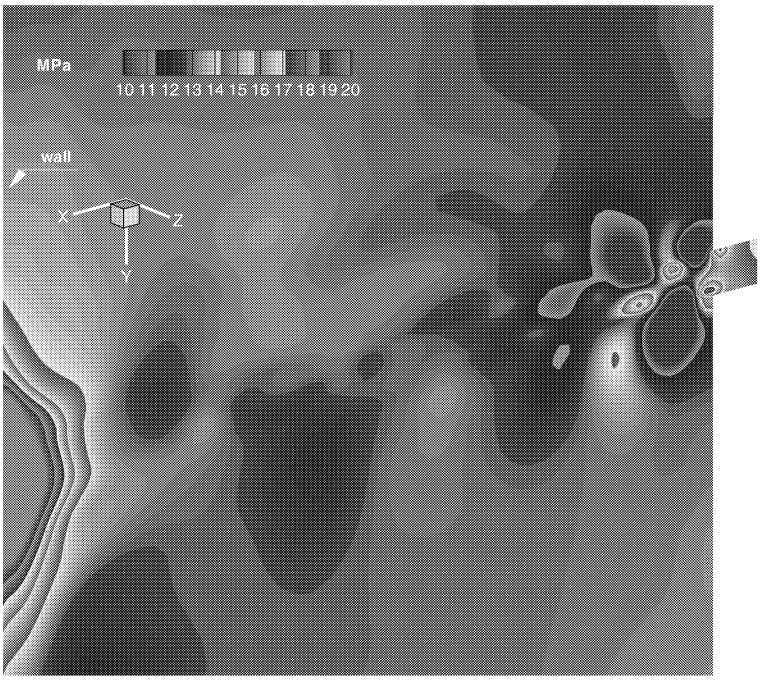

Figure 4. Pressure contours of the impinging jet on a mid-channel wall normal section

In fig. 4 a pressure contour plot on a wall normal section taken in mid-channel position is shown; the fluid dynamics flow field is dominated by an array of vortices developing at the channel exit, like in a double backward facing step configuration, and advancing toward the impact ring. The effect of these vortices is to instabilize and bend the jet core, which is like floating and constrained to pass through the vortices advancing at lower speed, as highlighted in fig 5.

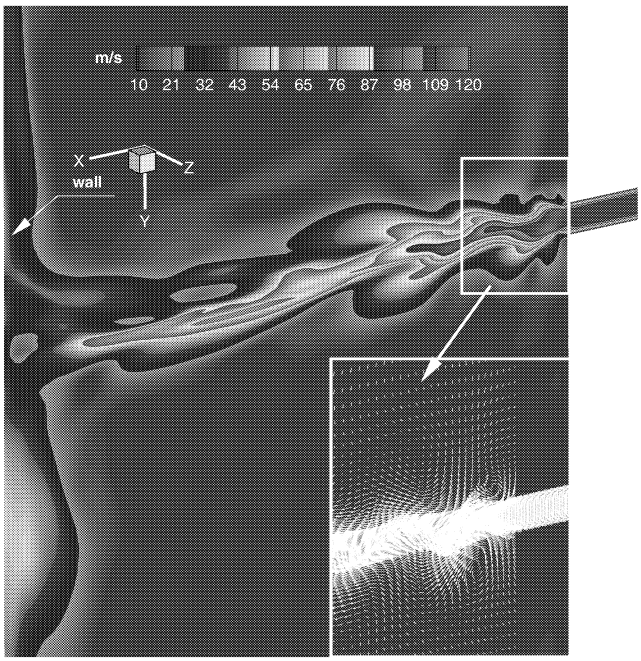

Figure 5. Velocity magnitude contours and velocity vectors of the impinging jet on a mid-channel wall normal section

Simulation results obtained by LES stress the effect of turbulence three-dimensionality, which is missing in resluts obtained with the VOF approach described in the previous paragraph, suggesting that a major effect in drops disruption is played also by the impinging jet on the wall

VORTEX INTERACTIONS IN A DOUBLE RIBLET GEOMETRY

It is possible to reproduce "artificially" the previously described vortex-jet interactions by using riblets. Riblets has been extensively studied in fluid dynamics drag reduction; in particular, the riblets proved to work as a constraint to the production of the Reynolds stresses associated with the growth and eruption of the eddies in the the low-speed regions of the boundary layers. A number of studies of zoologic nature was added to the original fluid dynamic problem, by studying the characteristics of fast-swimming sharks and dolphins, from where some ideas were first derived. In our case, a double reversed riblets configuration for the channel gap was investigated, trying to use the stationary vortices developing behind triangular riblets peaks as rollers to develop a controlled strain rate in inner flow field (see fig. 6), as vorticity generation can be controlled by setting riblet height, peak to peak module and flow velocity. To this purpose, a 3D multiphase simulation coupling together LES and VOF was performed, using a $1.5 \cdot 10^6$ control volumes mesh. The pressure drop ΔP was set to $20MPa$, and after a transient time period to develop the internal flow field (see fig.7 a and b), an ellipsoidal glycerine drop was introduced, as shown in fig. 8

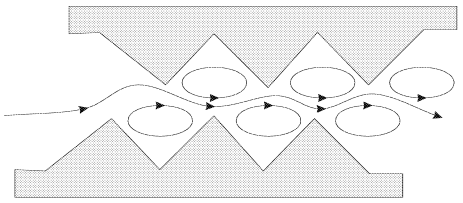

Figure 6. Double riblets configuration for the channel gap

The combined effect of shifted co-rotating vortices generates an high shear internal region, where the drop is firstly deformed and then fragmented in multiple part as shown in fig. 8 c The simulations shown in this work introduce the possibility of using controlled vorticity and strain shear rate to obtain droplet microsizing at moderate pressure, and can be considered a preliminary analysis of an experimental setup. The proposed configuration was obtained by using a series of 2D simulation to find proper riblets geometrical properties.

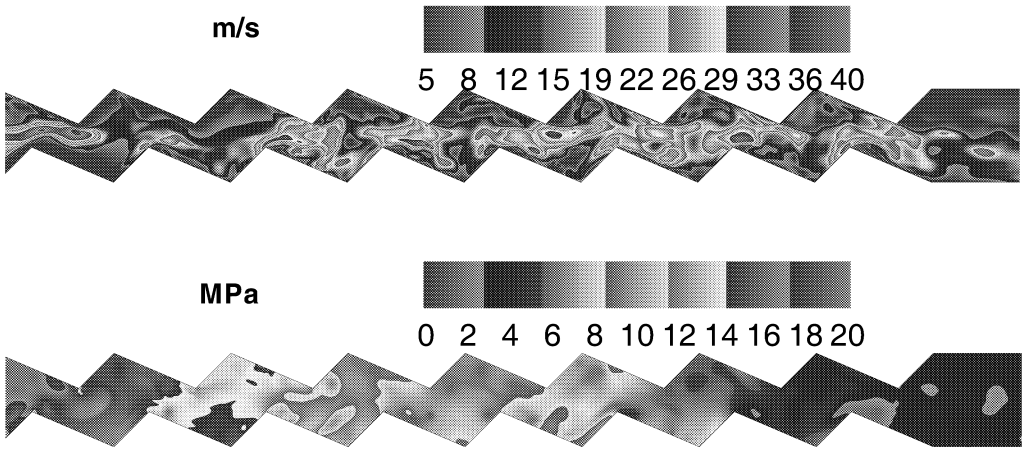

Figure 7. Velocity and pressure instantaneous contours inside the riblet-like channel gap

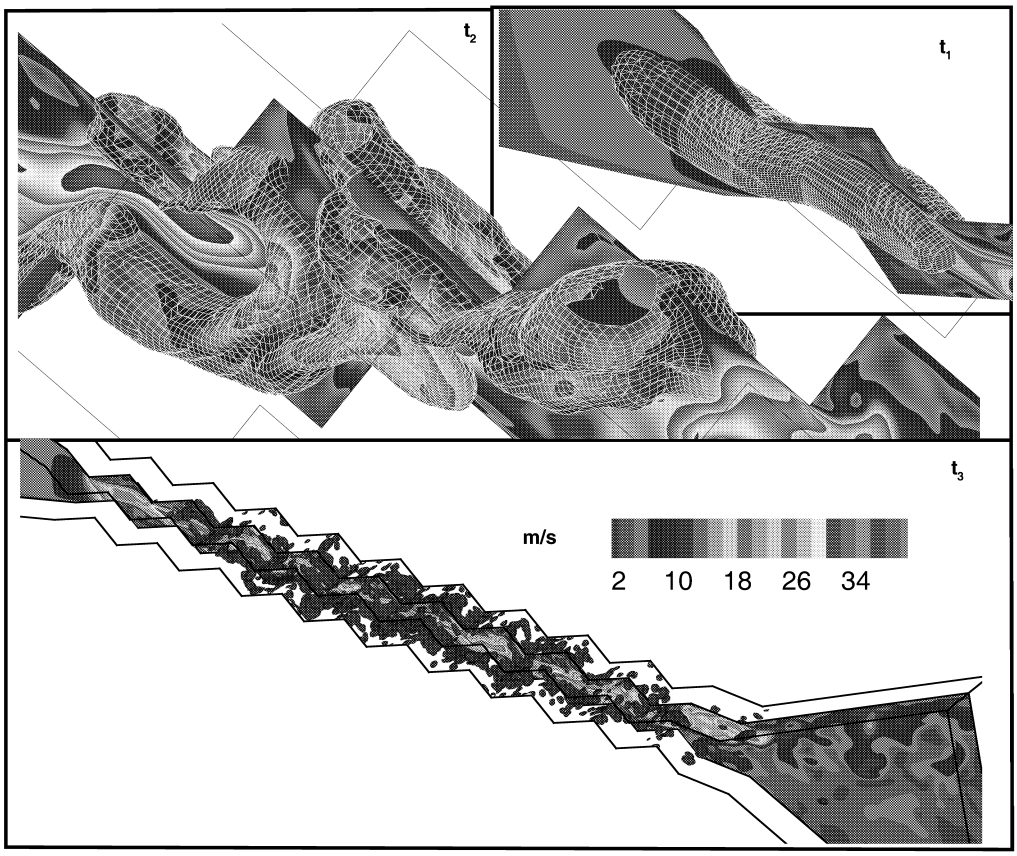

Figure 8. Drop deformation and fragmentation at three different computationa times

References

Feigl, K., Kaufmann, S., Fisher, P., and Windhab, E. (2003). A numerical procedure for calculating droplet deformation in dispersing flows and experimental verfication. *Chem. Eng. Sci.*, **58**, 2351–2363.

Hinze, J. (1955). Fundamentals of the hydrodynamic mechanism of splitting in. dispersion processes. *AIChE J.*, **1**, 289–295.

Kleinig, A. and Middelberg, A. (1996). Fundamentals of the hydrodynamic mechanism of splitting in. dispersion processes. *Chemical Eng. Science*, **23**, 5103–5110.

Li, J., Renardy, Y., and Renardy, M. (2000). Fundamentals of the hydrodynamic mechanism of splitting in. dispersion processes. *Phys. Fluids*, **12**, 269–282.

Maffettone, P. and Minale, M. (1998). Equation of change for ellipsoidal drops in viscous flow. *J. Non-newtonian Fluid Mech.*, **78**, 227–241.

Phipps, L. (1975). Fundamentals of the hydrodynamic mechanism of splitting in. dispersion processes. *J. Phys. D: Appl. Phys.*, **8**, 448–462.

Sarghini, F., Piomelli, U., and Balaras, E. (1999). Scale-similar models for large eddy simulation. *Physics of Fluids*, **11**, 1596–1607.

Shinnar, R. (1961). On the behaviour of liquid dispersions in mixing vessels. *J. Fluid Mech.*, **10**, 259–275.

Shinnar, R. and Church, J. (1960). Statistical theories of turbulence in predicting particle size in agitated dispersions. *Ind. and Eng. Chem.*, **52**, 253–265.

Tryggavson, G., Bunner, B., Esmaeeli, A., Juric, D., Rawahi, N. A., Tauber, W., Han, J., and Jan, Y. N. (2001). A front tracking method for the computations of multiphase flow. *J. Comput. Phys.*, **169**, 708–759.

SIMULATION TRAINING

A methodological guideline for the expert-operator knowledge management in the food industry

Nathalie Perrot*,Irène Allais**, Roch-Boris Edoura-Gaena**, Irina Ioannou+, , Gilles Trystram**,
*UMR GMPA , 78850 Thiverval Grignon, France; nperrot@grignon.inra.fr
**UMR Genial24 Avenue des Landais 63170 Aubière cedex, BP 50085, France
+ENSAIA, INPL Nancy

Gilles Mauris
LAMII Université de Savoie 74000 Annecy
gilles.Mauris@esia.univ-savoie.fr

KEYWORDS: Decision, Industrial processes, Expert system, Man-machine interfaces

ABSTRACT

In the food industry, managing the properties at the manufacturing stage with the aim of controlling them is not an easy task. In practice, operators often play an important role and cooperate with automation. Integrating operator and expert skill in a control framework is thus a relevant direction. In this framework, the aim of this paper is to provide a methodological guideline, integrating adapted mathematical tools, to manage the expert-operator knowledge as to control the food quality and to develop decision support systems. This guideline has 4 steps : selection of the operators-experts, formalization of the variables of interest, modelling of the operator-expert judgment, assessment of the model. The methodological guideline proposed in this paper has been used in 10 applications of control linked to the food industry. Among them, we have chosen to describe 2 applications particularly illustrative : the control of a process of sausage drying and the control of a process of sponge fingers batter aeration. Results are relevant since matching between the model and the real test points is higher than 80%.

1. INTRODUCTION: THE CONTROL OF THE PRODUCT QUALITY IN THE FOOD INDUSTRY

In the food industry, end-products must satisfy a compromise between several properties, including sensory, sanitary, technological properties. Among the latter, sensory and sanitary properties are essential because they influence consumer choice and preference. Nevertheless, managing these properties at the manufacturing stage with the aim of controlling them is not an easy task for several reasons described for example in (Curt, 2004; Ioannou, 2004; Davidson, 1996)). In this context, despite the fact that the design of standards and reliable procedures for controlling the quality of products is a major objective for the food industry (Goyache, 2001), automation is limited. A recent study (Ilyukhin et al., 2001) showed that 60% of food manufacturing plants are not fully automated, and that automatic controllers and human operators are both involved in food processes control. As underlined by (Mc Grath, 1998), many production processes rely to a great extent on the skill and experience of the operator. Consequently, in practice, operators often play an important role and cooperate with automation to: (1) make on-line evaluations of the sensory properties of the product and/or (2) adjust the on-line process. Moreover, experienced operators make macroscopic interpretations of the physicochemical phenomena that appear during processing, which can act in synergy with classical engineering knowledge on the process. Integrating operator and expert skill in a control framework is thus a relevant direction, especially for traditional processes.

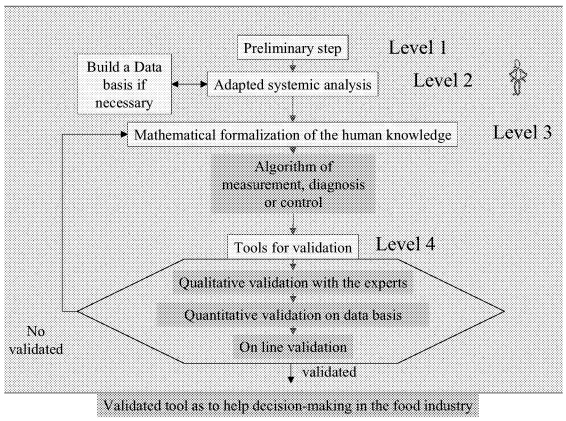

Figure 1: schematic view of the methodological guideline

In this framework, the aim of this paper is to provide a methodological guideline, integrating adapted mathematical tools, to manage the expert-operator knowledge (as) to control the food quality and to develop decision support systems.

2. METHODOLOGICAL GUIDELINE

In the frame of an integration of the expert-operator knowledge, we propose a methodologic guideline presented figure 1 (Perrot, 2004). This guideline is made up of four levels.

2.1. The first level

The aims of the first level are (1) to have a global understanding of the physical, chemical and biological phenomena involved in the processes encountered and (2) to select the operators-experts that will be involved in the work. This step is achieved under conceptual analysis from the KADS approach (KADS, 1994).

2.2. The second level

The second level refers to the systemic analysis proposed by (Foulard, 1994) including a unified formalization of the variables of interest. The first aim is to define the limits of the studied system and the hypothesis associated to the study. The second aim is to unified the formalization of the different variables involved in the problem.

We propose in our methodology to unify the different formats using the theory of fuzzy sets (Zadeh, 1971) and

more specifically the concept of fuzzy symbolic sensor. Since 1971, Zadeh and later Dubois (Dubois and Prade, 1980) have shown the relevance of fuzzy sets to establish a link between a set of words and a universe of "discourse". Applied to the measurement of perceptive "magnitudes", the fuzzy subset theory led to the development of a new concept proposed by (Mauris et al., 1994) in 1994: the fuzzy symbolic sensor. Fuzzy techniques are used to define a language such as a relation between a set of words (L) and a numerical set (N). This relation is characterized by a membership function, μRF, which represents the degree or the strength of the link between the symbols and numbers. This fuzzy relation can be described by two projections that take their values from the set of fuzzy numerical subsets F(N) and from the set of the fuzzy symbolic subsets F(L): Meanings and Descriptions.

Meanings (MF) and Descriptions (DF) can be defined as follows (Eq. 1 and 2):

MF: $L \to F(N),$

(1)

$$\forall a \in L, \forall x \in N, \mu_{M(a)}(x) = \mu RF(a,x)$$

Fuzzy meaning allows representing the symbols manipulated by operators in the form of words. For example this notion can be used to represent, after expert handling, a projection in a numeric space of the symbolic way used by operators to qualify for example a biscuit in terms of moisture content of the product: "dry, normal, humid" (figure 2).

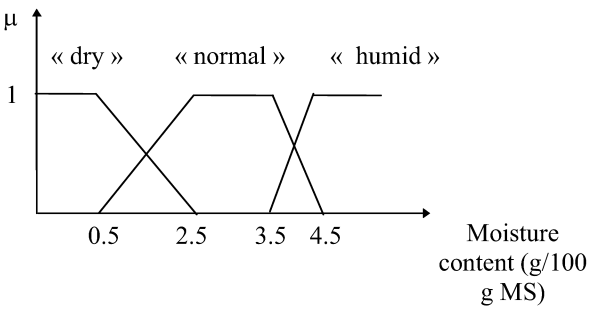

Figure 2: Example of a fuzzy meaning of the moisture content of a biscuit

DF: $N \to F(L),$

(2)

$$\forall x \in N, \forall a \in L, \mu_{D(x)}(a) = \mu RF(a,x)$$

The fuzzy description is a simple way of describing a measurement with words. For example, in figure 2 a moisture content of 4 g/100gMS can be described like this:

μD(4) ("dry")= 0;μD(4) ("normal")= 0.5;μD(4) ("humid")= 0.5

We can also note:

D (4) = 0 /dry + 0.5 /normal + 0.5 /humid.

To conclude, the symbolic sensor approach provides a tool for processing the different symbolism used to represent a physical entity like operator's measurement on a linguistic scale or on an ordonated scale and sensor measurements expressed on a numerical scale.

2.3. The third level

The third level aims to model the operator-expert judgement, it involves two adapted mathematical approaches : classical expert systems and an adapted fuzzy symbolic approach.

2.3.1 Classical expert system

Stock (1989) defined an ES as "an intelligent automation environment comprised of traditional and heuristic methods to solve a particular problem". The problem area to be treated by ESs must meet several requirements : it must be well defined, complex but structured, primarily cognitive and a recognised expertise must be available (Stein and Miscikowski, 1999). Moreover, for process control, ES are suitable when the problem cannot be solved by conventional algorithms and when there is a perceived need or desire for an ES (Davidson, 1994). An ES is first composed of a knowledge base, containing the domain knowledge in the form of facts and rules or another form of heuristics. Rule-based programming is one of the most commonly used techniques for developing expert systems. In this programming paradigm, rules are used to represent heuristics, or "rules of thumb," which specify a set of actions to be performed for a given situation. The second element of an ES is the inference engine which automatically matches facts against patterns and determines which rules are applicable.

2.3.2 The fuzzy symbolic approach

For the fuzzy symbolic approach, associated to the symbolic sensor approach described below, tools for aggregation of the membership degrees to the symbol manipulated are implemented. The fuzzy function used for fusion are created on the basis of an expert explanation of the logical links between the symbols. These links between the symbols, incorporate the global aim of the merging. The inference is made by Zadeh's compositional rule of inference, applied to the fuzzy symbolic descriptions of the inputs, which is explained below.

Let us consider that LX = {A1, ..., Ai, ..., Al}, LY = {B1, ..., Bj, ..., Bm} and LZ = {C1, ..., Ck, ..., Cn} three sets of linguistic terms and let us consider a set of rules with the generic form:

If X is Ai and Y is Bj Then C is gi, j,1/C1 + ... + gi, j, k/Ck + ... + gi, j, n/Cn.

This set of rules defines a fuzzy relation RF on the Cartesian product LX×LY×LZ, with a membership degree μR. The generic rule provides the membership degrees μR(Ai, Bj,

C1) = gi, j, 1, ..., μR (Ai, Bj, Ck) = gi, j, k, ..., μR(Ai, Bj, Cn) = gi, j, n. Obviously, this relation is crisp if no weighting is used (i.e. gi, j, k is equal to 0 or 1).

Let us consider E to be a fuzzy subset of LX and F a fuzzy subset of LY, defined by:

E = a1/A1 + ... + ai/Ai + ... + al/Al and F = b1/B1 + ... + bj/Bj + ... + bm/Bm.

The image of ExF from the fuzzy relation R is a fuzzy subset G of LZ whose membership degrees are presented Eq. 3.

$$\forall k \in \mu G(Ck) = \sup \min(\mu E \times F(Ai, Bj), \mu R(Ai, Bj, Ck)) \quad (3)$$

$$= \sup_{(i,j)} \min(\mu E \times F(Ai, Bj), gi, j, k)$$

with I = {1, ..., l}, J = {1, ..., m} et K = {1, ..., n}

According to the definition of the fuzzy Cartesian product (Eq. 4) :

$$\mu ExF(Ai, Bj) = \min(\mu E(Ai), \mu F(Bj)) = \min(ai, bj) \quad (4)$$

The equation giving G is the direct application of Zadeh's compositional rule of inference. It can be generalized by replacing the min operator by a triangular norm. In other respects, since the the sets are finite, the supremum can be replaced by the maximum, and even generalized by a triangular co-norm. The generalized equation thus becomes (Eq. 5) :

$$\forall k \in K \; \mu G(Ck) = s(i, j) \in IxJ \; t1(t2(ai, bj), gi, j, k) \quad (5)$$

with t1 and t2 being two triangular norms, often similar while and s is a triangular co-norm.

This tool of fusion described below, manipulated at a linguistic level (linguistic inputs, linguistic outputs) is coupled to a TAKAGI-SUGENO constant output type fuzzy controller (Takagi and Sugeno, 1985) when it is necessary to calculate a numeric output. Thus the numerical control (c) is directly calculated with the activation grades (αj) and the constant output parameters (pj) of each rule j (Eq. 6). The Tnorme operator is the minimum one.

$$c = \frac{\sum_j \alpha j pj}{\sum_j \alpha j} \quad (6)$$

2.4. The fourth level

Finally, the fourth level proposed mathematical tools to validate the algorithms built in a context of manipulation of linguistic variables . Three steps define this last level. The first step is a qualitative validation of the algorithm with the experts. Structuration of the fuzzy meanings and descriptions as well as the symbolic rules of fusion implemented are qualitatively validated. The second step is a validation on a data basis constituted for this aim and representative as much as possible of the whole functioning points of the system. The output of the model (Rm) is compared to the registered answer of the operator (Ro) and the number of compatible answer (C) is calculated upon the equation 7. The third step could not always be achieved but is relevant especially if the problematic is the on-line control of a process. It allows, in particular, to adjust the time activation of the control loop which should be fixed with attention.

$$C = \sum_{i=1,2,3}^{n} d$$

$$d = 1 \quad \text{si} \quad Di \le St \quad \text{avec} \quad Di = |Rm - Ro|$$

$$d = 0 \quad \text{si} \quad Di > St \quad (7)$$

where St is the sensibility level of the human perception for the considered sensory measurement

To conclude, the methodological guideline proposed in this paper is a result of an inductive scientific approach and has been established through a confrontation to 10 applications of control linked to the food industry (baking, drying, mixing,…). Among them, we have chosen to describe 2 applications particularly illustrative : the control of a process of sausage drying and the control of a process of sponge fingers batter aeration.

3. HELP THE DECISION MAKING APPLIED TO THE CONTROL OF THE QUALITY OF THE SAUSAGE IN A DRYING PROCESS AND TOTHE CONTROL OF THE QUALITY OF BISCUIT IN AN AERATION PROCESS

3.1. Example of a sausage drying process

3.1.1 Introduction

The aim of the present study was to help the operator to control the drying process as to maintain the sausage quality. After a first work with two experts of the factory managed upon the levels 1 and 2 described in chapter 2, a first structuration of the expertise was captured and formalized in two months of work. The inputs were three linguistic sensory (for example the sausage firmness evaluated by the operator on an ordinated linguistic scale) and the time of measurement. The output of the decision system is constituted with two numeric outputs : moisture and temperature of the drying chamber new set points.

3.1.2 Description and validation of the state model

The heart of the state model is implemented with the fuzzy symbolic approach described in chapter 2. Fusion of the sensory inputs are achieved through a decision tree reasoning, structured after expertise handling. Figure 3 presents this decision tree. At each level of this decision tree, logical equations are implemented and calculus is achieved

using equations 1, 2, 5. Thus, on the basis of a standard trajectory of each sensory inputs expressed by the operators and registered in our state model, a standard deviation of each sensory inputs is calculated using the fuzzy description function (equation 2). On the basis of the result of this step, the three standard deviation of the three inputs are fused using equation 5. Programming of this structured knowledge is achieved using Matlab v 6.5.

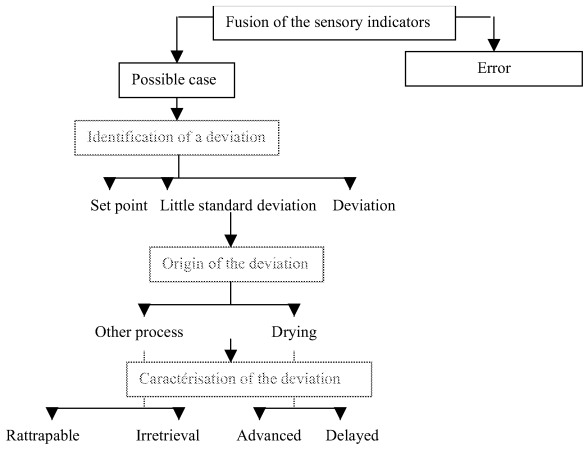

Figure 3: Decision tree of the drying support system

The state model is validated (1) on a data basis of 40 test points and (2) on line in the manufacturing drying chambers. For the validation on the data basis, 97% of compatible answer were found for for the identification of the deviation and the origin of the deviation if drying is concerned and 87.5% for the other levels. For the on line validations, 2 days of validation were achieved with 27 different cases tested and results were pertinent with a percentage of compatible answer of 89 % for the identification of the deviation and the characterisation of the deviation if drying is concerned and 100% for the two other levels of the tree.

3.1.3 Description and validation of the decision help model

Upon the state of the product evaluated on a linguistic format by the model state, a calculus is achieved using a logical table built with the experts. This logical table ensures the link between the output of the model state and the numerical output of the decision help model using equation 6.

Like for the state model, validations are achieved (1) on a data basis of 40 test points and (2) on line in the drying chambers For the first validation on a data basis, the number of compatible answers at a sensitivity of 1% is 92%. For the on line validations, 2 days of validation were achieved with 54 different set points tested and results were pertinent with a percentage of compatible answer of 94 % .

3.2. Example of aeration process

3.2.1 Extraction of the expertise

The aim of the present study was to develop a decision support system in order to help the operator to control the aeration of sponge finger batters. The development of the system was based on a knowledge extraction and formalization. It is a high level supervisory system designed to control the aeration, with the ability to integrate instrumental and sensory measurements performed at different stages of the entire sponge finger production process. The knowledge extracted here was the measurements and the rules used by the operators for the feedback control of the process. Because no relevant sensor are available to measure it, several batter and sponge fingers properties are evaluated by the operators, with their own senses, and directly on the production line.

At first, knowledge extraction was carried out with each of the four operators involved in the management of the process line. Since the plant runs 24 hours a day, one operator was in charge of the entire line for eight hours. This allowed the determination of the measurements and the decision rules commonly used by all the operators. When several experts are involved on a production line, a global expertise can be defined on the basis of a compromise between knowledge extracted from the different experts; but this is rarely totally satisfying (Benkirane, 1991). As an alternative, a single reference expert can be chosen. In this case, the expertise of this expert must be shared with the other experts. In the present study, only one operator was selected as a reference. This operator has been controlling the process for 13 years and his skill was acknowleged. The knowledge extraction required 55 days in the plant.

The operators generally follow a heuristic resolution process to determine the actions suited to correct a quality defect. An appropriate corrective action is associated with a given situation. These heuristics are classically represented using "if-then" type rules. To collect these rules, we used scenarios based on the product's properties hierarchy : the strategy consisted in asking the operator what corrective actions were appropriate when a defect was observed for a given property. Then, the considered situation was progressively complicated by combining gradually other properties defects. These latter were combined by following the order of importance of all the properties established during the measurements formalization

3.2.2. Decision support system

This decision support system was designed to accurately emulate the control of the process as it is performed by the operator. The system was developed using an expert systems shell named CLIPS (C Language Integrated Production System, version 6.2 released in spring 2002) which provides a complete environment for the building of rule and/or object based expert systems and reduces the effort and cost involved in developing expert system. CLIPS provides three different programming paradigms: rule-based, object-oriented and procedural for knowledge representation. We used the rule-based programming which allows knowledge to be represented as heuristics, or "rules of thumb," which specify a set of actions to be performed for a given situation. The inputs of the system are the 10 sensory measurements

and the 4 instrumental measurements used on the production line by the operators to characterize the batter and the sponge fingers. The outputs are the corrective actions suited to the current situation. The current setting values of the actuators are ignored by the system.

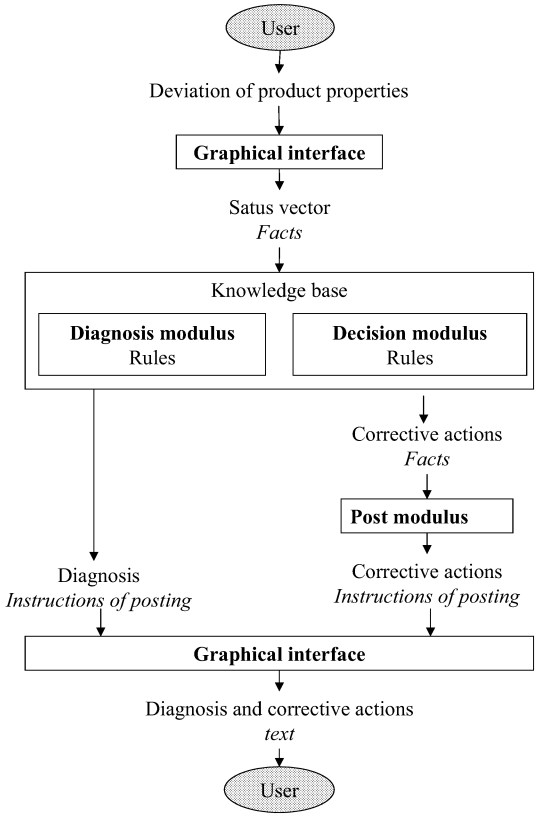

Figure 4 : Functional structure of the decision support system.

The system includes three sets of rules: hierarchical rules, which deal with the organization into a hierarchy of the quality defects observed by the operator; control rules, which determine the suitable corrective actions; interfacing rules which deal with data capture and display.

Control and hierarchical rules sets were directly issued from the knowledge extraction. The control rules set is composed of 47 rules split into 14 modules. A module of rules was built for each of the properties set, each module containing 2 to 8 rules. Each rule is composed of a premise and a conclusion. The premise contains the values of the different relevant properties which describe the current situation and the conclusion contains the suitable corrective actions. The inference engine was provided by CLIPS, it determines whether the conditions of activation of a given rule are satisfied or not. The functional structure of the system is represented in Figure 4.

3.2.3. Evaluation of the system

Two complementary approaches were used to assess how accurately the system could emulate the operator in controlling the process: real disturbed situations collection (the running of the process was monitored 4 times during 8 hours) and simulated disturbed situations: 30 disturbed situations frequently or less frequently encountered were simulated to cover a wide range of cases. For both approaches, the outputs of the system and the corrective actions proposed by an expert operator were compared. The corrective actions applied or proposed by the operator and the system can differ in their total number, the selected actuator(s), their directions (increase or decrease) and their magnitudes. We considered as matching cases, the situations where the operator considered that the system corrections were able to correct the defect(s). Matching was obtained in 21 cases out of the 27 tested.

3.2.4. Interface

Despite the fact that an interface is not the core of a support decision system, the key importance of user-friendly, colour graphical interface in developing advanced computer-aided process control systems cannot be neglected. That's why, a user-friendly interface was developed. Since CLIPS doesn't provide any graphical tool, the interface was developed in C++. In case of quality defect, the high rate of the production line (600 kg per hour) can lead to heavy losses of product. Thus, a requirement for the system was to quickly give the appropriate corrective action when a defect is observed. So, data entry was reduced as much as possible. The user only has to enter the levels of the properties which present a defect, it is done with drop-down menus for sensory measurements or edit box for instrumental measurements; the other properties are considered to be at their standard levels. The system's reasoning is only based on the information entered, no question is asked to the user, so the duration of a session is minimized and a decision aid is provided instantaneously. The decision aid which consists of a diagnosis and proposition(s) of corrective action(s), is presented in a dialog box (Edoura-Gaena et al., in press). The interface was considered as easy to use and the system was well received by the operators.

Two main difficulties have been encountered in this study. First, the operators availability was low and uncertain because their task was first and foremost devoted to the industrial production. Thus, much time was spent to collect expertise (55 days for the aeration process study). Second, the real disturbed situations encountered on the line were not varied enough and, from a statistical point of view, they were not numerous enough to validate a system. Indeed, in an industrial production context, the aim of the control of the process is precisely to avoid variations of production conditions.

4. CONCLUSION

The reason for developing a decision support system was at first, to improve the control of the process. But additional interests arise during the development of the approach, both for managerial staff and operators. For managerial staff, the interests were :

- sharing the knowledge between different operators and standardizing practices between several operators who take turns to control the line;
- transmitting the knowledge and training new operators;

- perpetuating knowledge which is a huge issue for the firm;
- traceability of the measurements for use in quality insurance.

For operators, the interests were :

- an improved image of their role as experts;
- facilitating of their tasks, the decision support system being viewed not as a competitor but as an help which can provide history on the operators actions and reinforce their actions.

To conclude, our team has capitalized a savoir faire in the use of the operator-expert judgement in the food industry. Nevertheless questions keep raised especially on the genericity of such approaches and on a more cognitive dimension, the evaluation of the quality of the answers proposed by the operator-experts.

REFERENCES

Benkirane, M. 1991. Contribution à la méthodologie d'extraction des connaissances dans le domaine du diagnostic technique. In Thesis Automatique Industrielle et Humaine. Valenciennes. p. 177.

Curt, C. ; N. Perrot ; L. Agioux ; I. Allais ; I. Ioannou ; R.B. Edoura-Gaeana; G. Trystram; J. Hossenlopp. 2004. Formalization of at-line human evaluations to monitor product changes during processing: the concept of sensory indicator. « Intelligent Sensory Evaluation - Methodologies and Applications », Editors: Da Ruan, Xianyi Zeng, Publisher: Springer.

Davidson V. J. 1994. Expert systems in process control. Food Research International, 27(2), 121-128.

Davidson, V. 1996. Fuzzy control of food processes, in: G. Mittal (Eds), Computerized Control Systems in the Food Industry. New York, Basel, Hong Kong, 179-205.

Dubois, D. and H. Prade. 1980. Fuzzy Sets and Systems: Theory and Applications. Academic Press, Inc.

Edoura-Gaena, R.B.; I. Allais; J.B. Gros; G. Trystram. 2006. A decision support system to control the aeration of a sponge finger batter. Food Control. 17, 585-596.

Foulard, C. 1994. La modélisation en entreprise, Paris, éditions Hermès, 215 pages.

Goyache, F.; A. Bahamonde; J. Alonso; S. Lopez; J.J. Del Coz; J.R. Quevedo; J. Ranilla; O. Luaces; I. Alvarez; L.J. Royo; J. Diez. 2001. The usefulness of artificial intelligence techniques to assess subjective quality of products in the food industry, Food Science and technology, 12, 370-381.

Ioannou, I, N. Perrot; C. Curt; I. Allais; R.B. Edoura-Gaeana; G. Mauris; G. Trystram; 2004. The fuzzy symbolic approach for the control of sensory properties in food processes. « Intelligent Sensory Evaluation - Methodologies and Applications », Editors: Da Ruan, Xianyi Zeng, Publisher: Springer.

Kads, 1994. CommonKads library for expertise modelling, Breuker J. Van der VeldeIOS Press Amsterdam.

McGrath, M.J.; J.F. O'Connor; S. Cummins. 1998. Implementing a process control strategy for the food processing industry, Journal of food engineering, 35, 313-321.

Iiyukhin, S.V.; T.A. Haley; R.K. Singh2001. A survey of automation practices in the food industry, Food Control, 12, 285-296.

Mauris, G.; N. Perrot; P. Lambert; J. Philippe. 2000. Fuzzy techniques evaluate sausage quality, IEEE Instrumentation and measurement, 3, 14-17.

Perrot, N. 2005. De la maîtrise des procédés alimentaires par intégration de l'expertise humaine – le formalisme de la théorie des ensembles flous comme support. Rapport d'HDR, Université Blaise Pascal, Clermont-Ferrand, 85 pages

Stein E. W. and D. K. Miscikowski. 1999. Supporting product quality with knowledge-based systems. Expert Systems with Applications, 16(4), 365-377.

Stock M. 1989. Glossary. AI In Process Control, (pp.201). New York, USA: M. Graw-Hill.

Takagi T. and M. Sugeno, 1985. Fuzzy identification of systems and its application to modeling and control, IEEE Transactions on Systems Man and Cybernetics, 15 116-132.

Zadeh L. 1971. Quantitative fuzzy semantics, Inf. Sci., 3, 159-176.

POSTERS

MYCOTOXIN TRANSFER ALONG THE FEED TO FOOD CHAIN: A SIMULATION APPROACH

Enda Cummins
Rory Coffey
Shane Ward
School of Agriculture, Food Science and Veterinary Medicine
University College Dublin
Earlsfort Terrace
Dublin 2
Ireland
E-mail: Enda.Cummins@ucd.ie

ABSTRACT

Mycotoxins are secondary metabolites produced by fungi when cereals or animal feed are colonised by moulds. Toxins may be excreted from milk produced by bovines which have been fed mycotoxin contaminated feed; this may represent a human health risk. The objective of this study was to develop a quantitative risk assessment model for mycotoxins in dairy milk and to assess the potential risks to consumers. Monte Carlo simulation techniques were used to account for parameter uncertainty and variability. The model indicates that human exposure to mycotoxins through dairy milk is likely to be well below recommended EU guidelines. There is a deficiency in data for the carryover rate between mycotoxins in feed and milk produce, thus suggesting the need for further research in this area. Ongoing research will try to fill these data gaps in order to reduce model uncertainty and to create performance objectives for the feed industry.

INTRODUCTION

Quantitative Risk Assessment (QRA) is a methodology used to analyse scientific information in order to estimate the probability and severity of an adverse event. This methodology was applied to model the human health risk associated with mycotoxin contamination of dairy feed and, subsequently, dairy milk for human consumption. Excretion of such toxins in bovine milk has been documented (Yiannikouris et al. 2002; Blüthgen et al. 2004) and their carryover to dairy produce represents a potential threat to human health. Studies have demonstrated that human dietary exposure to mycotoxins may lead to severe illness and can lead to liver cancer (Marquardt 1996; Notermans 2003). This assessment specifically focused on six mycotoxins of concern to humans (Aflatoxin B1/M1, Ochratoxin A, Deoxynivalenol, Fumonisin B1, Zearalenone and T-2 toxin) and involved analysing data on the occurrence of these mycotoxins in three dairy feed ingredients (barley, wheat and maize), on inclusion rates in dairy feed, on carryover rates to milk and on subsequent human exposure. By combining the estimated individual mycotoxin concentrations in milk with available consumption data for the Irish population, the daily intake of mycotoxins from milk by individuals was calculated. The exposure was characterised by the probability that viable mycotoxin concentrations were in milk at the time of consumption. Information and data for the development of the model were obtained from Irish studies and expert opinion and, when not available, from research in other countries. The basic model structure is given in Figure 1.

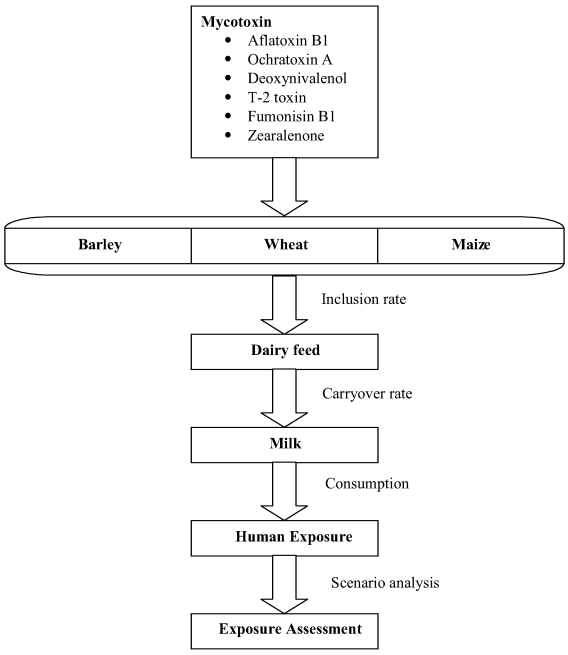

Figure 1: Model structure for simulating feed to food transfer of mycotoxins in bovine milk.

MATERIALS AND METHODS

Model inputs

A summary of model inputs and distributions is provided in Table 1 and discussed in more detail in this section.

Cereal inclusion rates in feed

In order to gain a comprehensive insight into the inclusion rates of barley, wheat and maize/maize products in dairy cow

concentrate feeds, various feed formulations used within Ireland were examined and assessed. This included feeding studies conducted by Teagasc (2001) on sample dairy cow concentrate rations, maximum inclusion levels of feed components in concentrate mixes and concentrate feeding to balance grass/silage based diets.

Mycotoxin contamination in feed ingredients

From the literature reviewed, it was considered that there was only a remote chance of Aflatoxin B1 (AFM1) contamination in feed ingredients (barley, wheat) produced within Ireland (D'Mello et al. 1999; Larsen et al. 2004). This was due to the fact that the Irish climate does not favour the formation of Aflatoxins in cereals. However, because a lot of the components of bovine concentrate feed are imported, maize from other countries was identified as a possible source of Aflatoxin B1 contamination of dairy cow concentrate feeds. To assess the presence of Aflatoxin B1 in maize, data from a survey by The Ministry for Agriculture, Food and Fisheries (MAFF 1999), which analysed maize imported into the UK intended for use in animal feed, was used. 139 samples in total were analysed with the limit of detection (LOD) being 0.1 µg/kg. Out of the 139 samples, 51 proved positive for Aflatoxin B1 with the highest concentration being 16.4 µg/kg. To estimate the typical concentrations of Ochratoxin (OTA) in barley, a survey of stored grain by Prickett et al. (1999) was examined. Out of 106 barley samples analysed, 20 proved positive for OTA with a minimum concentration of 0.3 µg/kg and a maximum concentration of 117 µg/kg. The probability of OTA being present in barley was modelled using a beta distribution (n = 106, s = 20).

The survey carried out by Prickett et al. (1999) also tested stored barley and wheat for Deoxynivalenol (DON). In relation to barley there were 75 positive samples out of the total of 106. The minimum recorded positive concentration was 20 µg/kg and the maximum was 370 µg/kg. To account for this variability, the level of DON in barley was modelled using a cumulative distribution based on the data collected by Prickett et al. (1999). From the literature reviewed, it was concluded that the only real risk from Fumonisin (FB1) in bovine feeds would be from maize and maize products. This was due to the fact that the occurrence of FB1 in barley and wheat was rare and represented a negligible risk. Data from the MAFF survey (1999) was used to assess the risk of FB1 occurring in maize.

Zearalenone (ZEN) in barley was surveyed in the UK by Tanaka et al. (1984). 4 (13%) out of 31 samples contained traces of ZEA with the mean concentration being 1 µg/kg. To represent this uncertainty, the probability of the presence of ZEN in barley was modelled using a beta distribution (n = 34, s = 4). A study by the HGCA (Home Grown Cereals Authority UK) in 2004 revealed a mean concentration of 3 µg/kg, a maximum surveyed value of 21 µg/kg and a 95th percentile of 10 µg/kg. The uncertainty in the mean level of ZEN in barley was modelled using a triangular distribution with the minimum and maximum values corresponding to those given by Tanaka et al. (1984) and the mean equal to that given in the survey work by the HGCA (2004).

Table 1: Model distributions and inputs for mycotoxin contamination level, carry over rate and concentration in dairy milk.

Symbol	Description	Distribution	Units
	Mycotoxin		
	A=Aflatoxin M1/B1 (AFM1)		
P_{Amz}	Probability of AFB1 presence or absence in maize	Beta (n=134, s=51)	fraction
L_{Amz}	Level of AFB1 contamination in maize	Uniform, minimum 0.1, maximum 2	ug/kg
AV_A	Average AFB1 concentration in feed	$I_{mz} \times L_{Amz}$	ug/kg
CO_A	AFM1 carry over rate to milk	Exponential, mean 1.61	percentage
CM_A	Concentration of AFM1 in milk	$AV_A \times CO_A$	ug/kg
	B= Ochratoxin A (OTA)		
P_{Bb}	Probability of OTA presence or absence in barley	Beta (n=106, s=20)	fraction
P_{Bw}	Probability of OTA presence or absence in wheat	Beta (n=201, s=32)	fraction
P_{Bmz}	Probability of OTA presence or absence in maize	Beta (n=139, s=14)	fraction
L_{Bb}	Level of OTA contamination in barley	Cumulative (based on Prickett et al. 1999)	ug/kg
L_{Bw}	Level of OTA contamination in wheat	Cumulative (based on Prickett et al. 1999)	ug/kg
L_{Bmz}	Level of OTA contamination in maize	Uniform	ug/kg
AV_B	Average OTA concentration in feed	$(I_b \times L_{Bb})+(I_w \times L_{Bw})+(I_{mz} \times L_{Bmz})$	ug/kg
CO_B	OTA carry over rate to milk	Fixed value, 0.01%	percentage
CM_B	Concentration of OTA in milk	$AV_B \times CO_B$	ug/kg
	C= Deoxynivalenol (DON)		
P_{Cb}	Probability of DON presence or absence in barley	Beta (n=106, s=75)	fraction
P_{Cw}	Probability of DON presence or absence in wheat	Beta (n=201, s=198)	fraction
P_{Cmz}	Probability of DON presence or absence in maize	Beta (n=41, s=32.52)	fraction
L_{Cb}	Level of DON contamination in barley	Cumulative (based on Prickett et al. 1999)	ug/kg
L_{Cw}	Level of DON contamination in wheat	Cumulative (based on Prickett et al. 1999)	ug/kg
L_{Cmz}	Level of DON contamination in maze	Triangular, minimum 3, maximum 3700	ug/kg
AV_C	Average DON concentration in feed	$(I_b \times L_{Cb})+(I_w \times L_{Cw})+(I_{mz} \times L_{Cmz})$	ug/kg
CO_C	DON carry over rate to milk	Fixed value, 0.22%	percentage
CM_C	Concentration of DON in milk	$AV_C \times CO_C$	ug/kg

70 samples of barley were collected in the UK in 2004 and tested for the presence of T-2 toxin (HGCA, 2004). 70% of the samples (49) were less than the limit of quantification (<10 µg/kg) with 30% (21) proving to have T-2 contamination. This uncertainty in the probability of a positive sample of T-2 in barley was modelled using a beta distribution (n = 70, s = 21). The average concentration of T-toxin in the barley was 12 µg/kg, the 95th percentile was 37 µg/kg and the mean was 12 µg/kg. To account for this variability, the level of T-2 in barley was modelled using a normal distribution with a mean of 12 µg/kg and a standard deviation calculated such that the 95th percentile corresponded to 37 µg/kg as suggested by the HGCA (2004).

Mycotoxin carry over rates

The extent to which AFM1 is carried over to milk has varied greatly. Jones et al. (1994) reported the carry over rate to be circa 1.7 % while studies by the European Food Safety Authority (EFSA) in 2004 suggested a mean carry over rate of 2 % increasing to 6 % for high yielding cows. Henry et al. (2004) suggested ranges from 0.2 – 4 %. An approximate carry over of 0.1% was suggested by Bluthgen et al. (2004). To

account for the uncertainty in the percentage carry over of AFM1 to milk, the individual rates described above were fitted to an exponential distribution.

Due to the fact that OTA is degraded by rumen microflora in bovines, it has been suggested that the carry over rate to milk is minimal. A study by Galtier (1998) calculated that if a cow was fed an oral dose of 1g/day, it would result in 100 µg/kg of OTA in milk. This results in a carry over rate of 0.01% and was taken as a fixed value to represent OTA carry over to milk in the model.

Table 1: Continued.

Symbol	Description	Distribution	Units
	D= Fumonisin B1 (FB1)		
P_{Db}	Probability of FB1 presence or absence in barley	Fixed value, 0	fraction
P_{Dw}	Probability of FB1 presence or absence in wheat	Fixed value, 0	fraction
P_{Dmz}	Probability of FB1 presence or absence in maize	Beta (n=139, s=139)	fraction
L_{Db}	Level of FB1 contamination in barley	Fixed value, 0	ug/kg
L_{Dw}	Level of FB1 contamination in wheat	Fixed value, 0	ug/kg
L_{Dmz}	Level of FB1 contamination in maize	Uniform	ug/kg
AV_D	Average FB1concentration in feed	$(I_b \times L_{Db})+(I_w \times L_{Dw})+(I_{mz} \times L_{Dmz})$	ug/kg
CO_D	FB1 carry over rate to milk	Fixed value, 0.05%,0.11%	percentage
CM_D	Concentration of FB1 in milk	$AV_D \times CO_D$	ug/kg
	E= Zearalenone (ZEA)		
P_{Eb}	Probability of ZEA presence or absence in barley	Beta(n=31, s=31)	fraction
P_{Ew}	Probability of ZEA presence or absence in wheat	Beta (n=317, s=164.4)	fraction
P_{Emz}	Probability of ZEA presence or absence in maize	Beta (n=139, s=135)	fraction
L_{Eb}	Level of ZEA contamination in barley	Triangular, minimum 1, mode 4.3 maximum 21	ug/kg
L_{Ew}	Level of ZEA contamination in wheat	Cumulative, (ased on Vrabcheva et al. 1996)	ug/kg
L_{Emz}	Level of ZEA contamination in maize	Cumulative (based on	ug/kg
AV_E	Average ZEA concentration in feed	$(I_b \times L_{Eb})+(I_w \times L_{Ew})+(I_{mz} \times L_{Emz})$	ug/kg
CO_E	ZEA carry over rate to milk	Cumulative, based on data	percentage
CM_E	Concentration of ZEA in milk	$AV_E \times CO_E$	ug/kg
	F= T-2 toxin (T-2)		
P_{Fb}	Probability of T-2 presence or absence in barley	Beta (n=70, s=21)	fraction
P_{Fw}	Probability of T-2 presence or absence in wheat	Beta (n=921, s=321.2)	fraction
P_{Fmz}	Probability of T-2 presence or absence in maize	Beta (n=57, s=53)	fraction
L_{Fb}	Level of T-2 contamination in barley	Cumulative (based on Galtier, 1998; Yiannikouris and Jouany, 2002)	ug/kg
L_{Fw}	Level of T-2 contamination in wheat	Exponential	ug/kg
L_{Fmz}	Level of T-2 contamination in maize	Uniform, minimum 1.3, maximum 6	ug/kg
AV_F	Average T-2 concentration in feed	$(I_b \times L_{Fb})+(I_w \times L_{Fw})+(I_{mz} \times L_{Fmz})$	ug/kg
CO_F	T-2 carry over rate to milk	Uniform minimum 0.5, maximum 2	percentage
CM_F	Concentration of T-2 in milk	$AV_F \times CO_F$	ug/kg

Similarly with DON, transfer to bovine milk is estimated to be small; however, there is very little research in the area. A carry over of 0.22% was calculated from figures of dose and resulting concentration in milk (Galtier 1998). Again this was taken as a fixed value in the model. For the carry over of FB1 to milk, two values were identified. The first was a value of 0.11% reported by the EFSA (2005). A transfer rate of 0.05% was reported as the average carry over rate for a single administration of 3 mg of toxin per kg of feed by Yiannikouris and Jouany (2002). A uniform distribution (minimum = 0.05, maximum = 0.11) was used to account for this uncertainty.

Transfer of ZEN to milk has revealed varying carry over rates. Yiannikouris and Jouany (2002) reported transfer rates of 0.06%, 0.016% and 0.008%, depending on the dose of the toxin administered. Rates of 0.00625% and 1.924 % were estimated from other feeding studies (Galtier 1998). A cumulative distribution was used to model the uncertainty surrounding ZEN carry over to milk using the transfer rates reported by Yiannikouris and Jouany (2002) and Galtier (1998). The presence of T-2 residues in cows milk was reported to have been found in the range of 0.05 - 2% (Yiannikouris and Jouany 2002). Research by Galtier (1998) found a carry over rate in milk of between 0.02 and 0.32% for dairy cows fed 50,000 µg/kg of body weight. The variability in the transfer of T-2 toxin to milk was modelled using a cumulative distribution fitted to the carry over data suggested in the literature.

Consumption Data

Data on the quantities of milk consumed by Irish consumers was obtained from the Irish Universities Nutritional Alliance Survey (IUNA 2001). The mean consumption of whole milk, low fat skimmed and processed milks for adult males (18-64 years) was 195 g/day, 80 g/day and 5 g/day, respectively and 110 g/day, 95 g/day 5 g/day for females, respectively. A normal distribution corresponding to the given mean and standard deviation for milk consumption of each product was used to account for uncertainty.

Model simulation

The risk model was developed using Monte Carlo simulation techniques with Latin hypercube sampling. This approach permits a quantification of the risk of contamination occurring. The @RISK software package, version 4.0 (Palisade, USA), in combination with Microsoft Excel 2000 (Microsoft, USA) was used to run the simulation. The simulation was run for 10,000 iterations and reflects the inherent variability in the production of bovine feed, milk consumption and in the uncertainty of the mathematical process. The probability of a toxin in milk, the level of the toxin in milk and the probability of human exposure were outputs of the mathematical model.

RESULTS AND DISCUSSION

For each toxin, the risk assessment model produced a probability density distribution (representing the uncertainty about the true mean value) of the potential level of these toxins in bovine milk consumed by humans. A summary of the simulation results, including uncertainty analysis and comparison with EU regulations for each analysed mycotoxin, is given in Table 2.

The mean level of AFM1 in milk was found to be 0.0161 µg/kg. This level is below the allowable limit of 0.05 µg/kg for bovine milk in the EU (Commission Regulation 2003/2174/EC). For OTA the concentrations estimated are very low and underline that only small amounts of OTA escape rumen metabolism and are absorbed into bovine milk. The simulation showed a mean value for DON of 1 µg/kg with a

95th percentile value of 4 µg/kg. These results were slightly higher than expected given that the carry over rate to milk was small (0.22%) and were the highest recorded values by the model for an individual toxin.

Table 2: Simulated level of mycotoxins in bovine milk including uncertainty analysis

	AFM1 (ug/kg)	OTA (ug/kg)	DON (ug/kg)	FB1 (ug/kg)	ZEN (ug/kg)	T-2 (ug/kg)
Mean	0.016	0.0002	1	0.36	0.39	0.072
5th percentile	0.0002	8.84E-07	0.0049	0.0093	0.0002	0.0006
95th percentile	0.83	0.0009	4	1.44	2.55	0.29
Limit	0.5[a]	3[b]	500[c]	400[d]	50[c]	[e]

[a]EU limit for AFM in milk (Commission Regulation 2003/2174/EC)
[b]EU limit for cereal based food (Commission Regulation (EC) 472/2002)
[c]EU limits for cereal based foods (no limits exist for milk) (Commission Regulation (EC) No 856/2005)
[d]EU limits for maize based products (no limits exist for milk) (Commission Regulation (EC) No 856/2005)
[e]No limit for the presence of T-2 in milk/food products exists (Commission Regulation (EC) No 856/2005)

The reason for this was the high and frequent contamination of DON in the analysed crops (maize, barley and wheat) in comparison to the other mycotoxins. Given that FB1 was only considered in maize (rarely occurs in barley and wheat) the result were relatively high. The high FB1 contamination of maize (according to analysed data) was the likely reason for this. The mean level of ZEN in milk calculated by the exposure model was 0.39 µg/kg. A value equal to 2.55 µg/kg was estimated for the 95th percentile. Within the EU a limit of 50 µg/kg has been set for cereal based foods (Commission Regulation (EC) No 856/2005) but no limit exists for the presence of ZEN in milk. AFM1 was the only mycotoxin where the 95th percentile exceeded the selected EU guidelines. All other simulated mycotoxins values were well below recommended values.

CONCLUSION

As natural and unavoidable contaminants of important agricultural commodities, mycotoxins have continued to severely impact animal health and consequently human health, which may have implications for livestock production, crops production and the economy. The risk is well recognised, but at present it has not been quantified accurately. The quantitative risk assessment developed here tries to address this deficiency in the scientific literature and serves as an initial attempt to link the animal feed chain and the human food chain. The model assesses the potential human exposure to six mycotoxins in dairy milk. Mean levels for the mycotoxins assessed in milk all fell below EU limits. Aflatoxin M1 was singled out as the toxin of greatest concern. In certain circumstances, its concentration exceeded the EU limit of 0.05 µg/kg in milk. It was found that mycotoxins can never be completely removed from the feed-to-food chain but that current exposure levels are likely to be small in dairy milk and well below EU guidelines.

REFERENCES

Blüthgen, A., Hammer, P. and Teufel P. 2004. "Mycotoxins in milk production. Occurrence, relevance and possible minimization in the production chain feeds-milk". *Kieler Milchwirtschaftliche Forschungsberichte*. 56(4): 219-263.

D'Mello, J.P.F, Placinta, C.M. and Macdonald, A.M.C. 1999. "A review of worldwide contamination of cereal grains and animal feed with Fusarium mycotoxins". *Journal of Animal Feed Science and Technology*. 78(1-2): 21-37.

EFSA 2004. "Opinion of the Scientific Panel on Contaminants in Food Chain on a request from the Commission related to Aflatoxin B1 as undesirable substance in animal feed". *The European Food Safety Authority Journal*. 39: 1-27.

Galtier P. 1998. "Biological fate of mycotoxins in animals". *Revue du Médicine Véterenaire*. 149: 549-554.

Henry, S.H., Whitaker, T., Rabbani, I., Bowers, J., Park, D., Price, W., Bosch, F.X., Pennington, J., Verger, P., Yoshizawa, T., van Egmond, H., Jonker, M.A. and Coker, R. 2004. "Aflatoxin M1", Available From:http://www.inchem.org/documents/jecfa/jecmono/v47je02.htm Accessed 16/02/06.

Home Grown Cereals Authority (HGCA) 2004. "Investigation of fusarium mycotoxins in UK barley and oat production". Available from:http://www.hgca.com/content.template/4/0/About%20HGCA/About%20HGCA/About%20HGCA%20Home%20Page.mspx Accessed 15/02/06.

IUNA 2001. "Irish Universities Nutritional Alliance North/South Ireland Food Consumption Survey". Report Available from Food Safety Authority, Dublin, Ireland.

Jones, F.T., Genter, M.B., Hagler, W.M., Hansen, J.A., Mowrey, B.A., Poore, M.H. and Whitlow, L.W. 1994. "Understanding and coping with the effects of mycotoxins in livestock feed and forage" Available from: http://www.ces.ncsu.edu/disaster/drought/dro-29.html. Accessed 12/12/05.

Larsen, J.C., Hunt, J., Perrin, I. and Ruckenbauer, P. 2004. "Workshop on trichothecenes with a focus on DON: summary report". *Toxicology Letters*. 153(1): 1-22.

MAFF 1999. Ministry for Agriculture Food and Fisheries UK- "Survey for aflatoxins, ochratoxin A, fumonisins and zearalenone in raw maize". Available from: http://archive.food.gov.uk/maff/archive/food/infsheet/1999/no192/192afla.htm . Accessed 21/01/05)/

Marquardt, R.R. 1996. "Effects of molds and their toxins on livestock performance: a western Canadian perspective". *Animal Feed Science and Technology*. 58(1-2): 77-89.

Notermans S. 2003. "Food authenticity and traceability, ensuring the safety of animal feed". Available from: www.foodmicro.nl/ensuringsafety.pdf Accessed 23/11/05.

Prickett, A.J., Macdonald, S. and Wildley, K.B. 1999. "Survey of mycotoxins in stored grain from the 1999 harvest in the U.K". Home-Grown Cereals Authority. Available from: http://www.hgca.com/publications/documents/cropresearch/230_complete_final_report.pdf. Accessed 04/10/05.

Tanaka, T., Hasegawa, A., Matsuki, Y., Lee, U.S. and Ueno, Y. 1986. "A limited survey of Fusarium mycotoxins nivalenol, deoxynivalenol and zearalenone in 1984 UK harvested wheat and barley". *Food Additive Contamination*. 3(3): 247-52.

Teagasc 2001. "Fodder and feed events". Available from: http://www.teagasc.ie/publications/2001/fodderandfeed/fodderandfeed2001.pdf. Accessed 05/12/05.

Yiannikouris, A. and Jouany, J.P. 2002. "Mycotoxins in feeds and their fate in animals: a review". *Animal research*. 51: 81-99.

AN INTEGRATED EUROPEAN APPROACH TO TSE RISK ASSESSMENT

Enda Cummins
School of Agriculture, Food Science and Veterinary Medicine
University College Dublin
Earlsfort Terrace
Dublin 2
Ireland
E-mail: Enda.Cummins@ucd.ie

Larry Paisley
Danish Institute for Food and Veterinary Research
Mørkhøj Bygade 19, DK-2860 Søborg
Denmark

Aline de Koeijer
Thomas Hagenaars
Wageningen University and Research Centre
Lelystad
The Netherlands

Franck Guarnieri
Deirdre Murray
Ecole des Mines de Paris – ARMINES
France

Amie Adkin
Centre for Epidemiology and Risk Analysis
Veterinary Laboratories Agency
Weybridge, Surrey, UK.

Christine Jacob
Unity of Applied Mathematics and Informatics
INRA
France

ABSTRACT

Mathematical models and risk assessments have been used as a basis for Transmissible Spongiform Encephalopathy (TSE) risk management and control options and much of the legislation regarding the control and eradication of TSEs within the European Union (EU). The NeuroPrion Risk group (European Commission FP6) consists of 8 risk assessment experts representing 6 different European Institutions. These experts have collaborated with the goal of assessing current trends in TSEs across Europe while facilitating an exchange of knowledge and data between research groups on risk management and control of TSEs in addition to establishing a world-wide reference network on the risk assessment of TSE diseases. The research network aims to highlight the benefits of computer simulation and risk assessment methodologies in assessing risks from TSE diseases. Such procedures enable policy makers to make effective legislative decisions while accounting for system uncertainty and ensuring the integrity of the food chain.

INTRODUCTION

Bovine Spongiform Encephalopathy (BSE) is a TSE disease of bovine animals which remains prevalent in many European countries (Liechti 2004), although scientists agree that the disease is on the decrease in the UK and most European countries (Heim and Mumford 2005). The negative impact of the BSE crisis included damage to public confidence and trust in both risk management capabilities and the legitimacy of scientific judgment. Mathematical models and risk assessments have been used as a basis for BSE risk management options and much of the legislation regarding the control and eradication of BSE. The NeuroPrion Risk group have collaborated with the goal of assessing current risk assessment and management procedures with regard to TSEs (including BSE) in animals and to review current state of the art in Europe. The European collaboration highlights the application of different risk assessment procedures and current data gaps with regard to infectivity of CNS and non-CNS tissues, the development of BSE infectivity during the incubation period and the bovine-human species barrier. The work highlights the need for exchange of knowledge and data between countries and the importance of collaboration between international scientists. This study enables a closer analysis of the role risk assessment and management plays in the control of TSEs with a truly European perspective.

MATERIALS AND METHODS

Review procedures

The Neuroprion Risk group has peer reviewed relevant data and risk assessment models used across Europe, ensuring comparisons between countries are justified and generating a consensus on risk assessment procedures for TSE risk assessment (Cummins et al. 2005; Pasiley et al. 2006). Adherence to the Codex Risk Analysis Framework (Figure 1) for effective risk management, and transparency for all stakeholders, has been highlighted. In addition, maintenance of risk management procedures and improved risk communication has been identified as being vital in ensuring consumer confidence across Europe with regard to food safety. The Neuroprion Risk network will facilitate this communication exchange by increasing visibility beyond the scientific community with regard to TSE risk analysis including a continuous review of new scientific findings and opinions on TSE risks as they arise.

Ongoing research

Ongoing research by the group also includes the construction of a systematic inventory of all TSE risk factors, including disease prevalence, transmission dynamics, host susceptibility and tissue infectivity levels. The group will also assess the influence of uncertainty in risk models focusing on un-quantified uncertainty due to assumptions, approximations and modeling techniques, as opposed to parameter uncertainty quantified in the model as calculated by probability distributions. The group also aims to increase the visibility beyond the scientific community with regards to TSE risk analysis highlighting the significant role risk analysis continues to play in controlling TSE diseases.

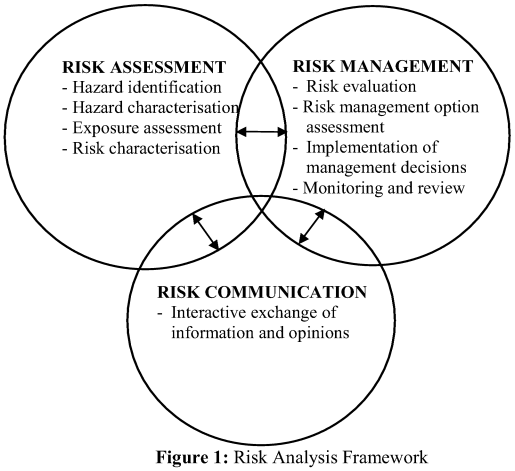

Figure 1: Risk Analysis Framework

CONCLUSION

The Neuroprion Risk groups work highlights the need for an exchange of knowledge and data between countries and the importance of collaboration between international scientists. The role risk assessment plays in the control of BSE has been highlighted resulting in a favourable trend in the BSE prevalence across Europe. Not withstanding this, any proposed relaxation in control measures needs to be looked at in context food safety and risk communication for all stakeholders. Any relaxation should be risk based and carried out in accordance with a risk analysis framework. New measures should be in line with current technology and new evolving scientific knowledge. It is argued that an all-encompassing risk analysis approach, including risk management and risk communication to all stakeholders, would build public confidence in risk analysis practices and help to allay consumer health fears.

ACKNOWLEDGEMENTS

This work is funded by the **NeuroPrion Network of Excellence**, Project nr. FOOD-CT-2004 -506579.

REFERENCES

Cummins, E., Paisley, L., de Koeijer, A., Hagenaars, T., Murray, D., Guarnieri, F., Adkin, A. and Jacob, C. 2005. “European perspective on BSE risk assessment”. In Proceedings of 35th research conference Food, Nutrition and Consumer sciences, University College Cork. 62.

Paisley, L. de Koeijer, A. Hagenaars, T. Murray, D. Guarnieri, F. Adkin A. and Jacob C. 2006. “Risk analysis of TSEs in animals: State-of-the-art”. International Journal of Risk Assessment and Management. Inpress.

Heim, D. and Mumford E. 2005. “The future of BSE from the global perspective”. Meat Science. 70: 555-562.

Liechti R. 2004. “The international conference on bovine spongiform encephalopathy and food safety, April 17–18, 2002” .Food Control. 15(1) : 71-77.

LATE PAPERS

COMBINED TRANSFER PHENOMENA IN 3D MODELLING OF PACKAGED FOODS

Maria Valeria De Bonis°*, Giuseppe Altieri*, Maria Cefola+ and Gianpaolo Ruocco°*
°CFD*food*, *DITEC, Università degli studi della Basilicata, Campus Macchia Romana, Potenza 85100, Italy
+Istituto di Scienze delle Produzioni Alimentari–CNR, Via Amendola, 122/O, Bari 70126, Italy
e-mail: CFD*food*@unibas.it

KEYWORDS
Biology, Production, Partial differential equations, Random number generation, Continuous simulation.

ABSTRACT

Innovative packaging configurations for fresh produce can allow for shelf–life increase, without organoleptic alterations. By using a Modified Packaging Atmosphere (MAP) produce respiration rate and related biochemistry is controlled: in particular, by raising CO_2 and/or reducing O_2 concentrations in packaging (protective atmosphere) or in refrigerated storage (controlled atmosphere).
Heat and mass transfer can be analyzed for conditions that may limit shelf–life: with this target, the purpose of the present work is the development of a general model which is applicable in a large variety of packaging configurations, food products and environmental conditions. To this end, a commercial Finite Elements software is exploited for the first time in a full 3D geometry; time evolution of respiration rate has been included in the model with a constant temperature enzymatic kinetics notation, with an auxiliary formulation for its dependence on temperature. Local and average gas concentrations in the food matrix and in the head space have been preliminary compared for a thermal boundary condition typical of a passive storage configuration. The presented procedure can be exploited by the post–harvest industry to pin-point on the optimal packaging configuration, to ensure the maximum product shelf–life.

INTRODUCTION

Packaging food products in a gas atmosphere (MAP – Modified Atmosphere Packaging), coupled to low temperature storage, results in a prolonged shelf life of the fresh–cut fruit and vegetables (Zagory and Kader 1988) and at the same time the quality is retained, safety is ensured and sales are promoted. The coupled procedure slows down metabolism, but long–residual life results for tissues, that derive energy through the process of respiration. This consists in the transformation of carbohydrates and organic acids involving O_2 depletion, together with the production of waste metabolic heat, CO_2 and moisture. Different fruits and vegetables, and even different varieties of a given fruit or vegetable, will vary in their respiration rates (Fonseca et al. 2002; Lee et al. 1991).
The best way to reduce respiratory metabolism and thus conserve the plants stores of carbohydrate, acids and moisture, is to reduce the temperature. Most produce will maintain its best quality at temperatures near 0 °C, but established industrial practice may differ considerably. When temperature is adequately controlled, MAP can be used to further reduce respiration rate, loss of moisture, production of metabolic heat, yellowing, browning, decay and sensitivity to ethylene: O_2 content is decreased, and in turn CO_2 is raised enough to avoid counter–effects such as aneorobiosis. This can be accomplished through the proper balance of several variables that affect package atmosphere.
Nowadays the optimization of technological process and their operating conditions are often looked upon with the aid of numerical modelling of transfer phenomena. Integration of governing Partial Differential Equations (PDEs) allows for a fundamental and quantitative way to understand complex phenomena which is complementary to the traditional approaches of theory and experiment. This approach is becoming increasingly widespread in basic research and advanced technological applications, cross cutting the fields of physics, chemistry, mechanics, engineering, and biology.
Among the research papers on post–harvest, two recent ones dealt with modelling. (Uchino et al. 2004) improved the ability to predict respiration rate evolution of produce, while (Cefola et al. 2005) presented a complete model of two–dimensional transport, which was validated by the associated experiments.
In the present paper, that model has been extended for the first time to a three–dimensional geometry, describing degrading shelf–life during a passive transport storage in MAP. All governing PDEs and related biochemical notations have been solved by a Finite Element Method (FEM) commercial solver, in order to determine temperature and species concentration distribution in the food matrix and the headspace. Fruits are placed that realistically fill the subject box; by this way, every packaging configurations (available film permeability), food products (shape, consistence, kinetics) and

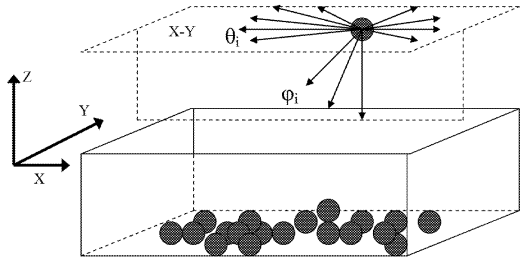

Figure 1: Angle nomenclature for fruit random falling in the box.

operating (environmental) conditions can be configured and analyzed. The adopted modelling can easily be extended to comprise the mass and heat transfer through the specific packaging film, as well as transport and sequestration of water vapor and ethylene.

A REALISTIC GEOMETRY GENERATION

An in–house code in MATLAB^{TM} has been applied to generate a random filling of spherical fruit in a 3-D rectangular box. First, the fruit diameters d are computed based on a gaussian distribution with average and standard deviation (respectively 22.81 and 1.00 mm) experimentally determined from a batch of real fruits, and the box geometry is been defined (in this case, length is 165 mm, width is 95 mm and height is 80 mm).
Then, fruits are let fall down in the box from a given Z height (Fig. 1). Prior to this, each fruit is tested to move along is initial plane and its azimuth. Along the $X-Y$ plane, all possible directions of fruit movement are discretized, by determining an angle θ_i sequence (with $0 \leq \theta_i < 2\pi$). After its computation,

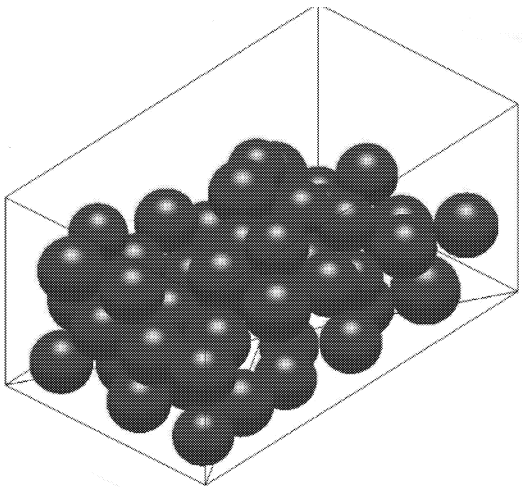

Figure 2: Typical box filling.

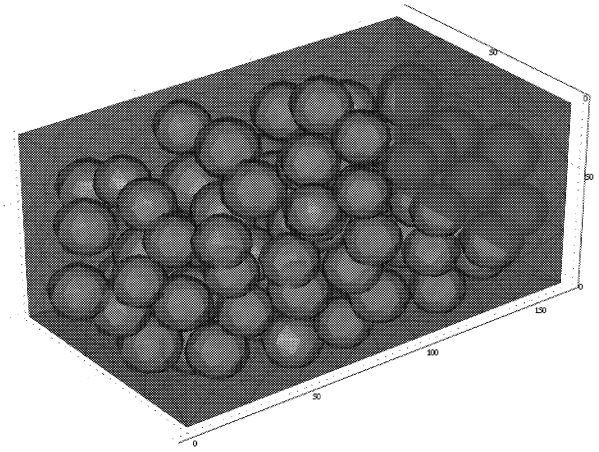

Figure 3: A view of the discretized subject geometry, with the front and top limiting surface removed.

this sequence is randomly permutated by means of a uniform–distribution random number generator. The fruit's second degree of freedom is also tested by discretizing all possible directions of fruit movement in the half–space below the starting $X-Y$ plane and the negative Z semi–axis, as depicted in Fig. 1. So, an angle ϕ_j sequence (with $3\pi/2 \leq \phi_j < 2\pi$) is also determined and randomly permutated. Therefore the fruit is moved from its initial position to occupy the new position defined in terms of spherical coordinates (r, θ_i, ϕ_j), by incrementing r, as first guess, by $\Delta r = d$. In the new fruit position, the distances to the box walls and the neighboring fruits already in place are computed: if the smallest distance is greater than the allowed positioning error (0.01 mm in this case), the fruit displacement can take place, otherwise the radial displacement Δr is halved, and the process is iterated until displacements smaller than the allowed positioning error are obtained. Thus, an algorithm to search for a locally minimum (stable or indifferent) of the potential energy is obtained, which is compatible with the contingent bonds represented by other fruits or the box walls that may impede the positioning. The procedure is iterated until all units are positioned.
After a predetermined fruit batch, the algorithm provides to eliminate all objects that stretch out from the box upper opening along Z, so the box is realistically filled almost completely, and a headspace is created between the enclosing top film and the fruit region (Fig. 2). Having determined the box and fruit geometry, this can be passed seamlessly to the FEM software through a custom–made script. The geometry is discretized in over 44500 cell, as depicted in Fig. 3, and modelling by PDEs integration can be applied.

PROBLEM FORMULATION

In the present paper a passive storage configuration during transportation of fresh tomatoes cv. Shiren are

tested, to correlate the shelf–life to the gas emission by produce respiration. Diffusion of O_2 and CO_2 in the fruits and in the headspace, as well as conduction heat transfer in the fruits, have been analyzed and monitored in time, by describing the relative local concentration distributions, for the box filled with small fruits, earlier described. Each subdomain features (fruits, headspace) its own species permeabilities.
The standard unsteady–state governing mass conservation and energy PDEs are enforced, in three–dimensional Cartesian coordinates x, y and z for constant properties to yield for molar concentrations c for each gas species and temperature T (Bird et al. 2002):

$$D\left(\frac{\partial^2 c}{\partial x^2}+\frac{\partial^2 c}{\partial y^2}+\frac{\partial^2 c}{\partial z^2}\right)+R=\frac{\partial c}{\partial t} \tag{1}$$

$$\left(\frac{\partial^2 T}{\partial x^2}+\frac{\partial^2 T}{\partial y^2}+\frac{\partial^2 T}{\partial z^2}\right)+\frac{\dot{q}}{k}=\frac{1}{a}\frac{\partial T}{\partial t} \tag{2}$$

where D, k and a are the mass diffusivity of each species, in the headspace air, the air conductivity and thermal diffusivity respectively, R is the respiration rate, $\dot{q}$ is the released heat flux due to cellular respiration and t is time.
Adequate values of fruits and gas properties are found in (Singh and Heldman 1993) and (Bertola et al. 1990). In order to take into account the respiration kinetics of the product and its dependance on gas species concentrations, a number of additional notations need to be incorporated into the FEM model. The time variation of R has been modelled by a Michaelis–Menten enzymatic kinetics for the non–competitive inhibition by CO_2 (Lee et al. 1991):

$$R=\frac{R_r\ x_{O_2}}{K_m+\left(1+x_{CO_2}/K_i\right)\ x_{O_2}} \tag{3}$$

where x_{O_2} and x_{CO_2} are the volume fractions of the gases, K_m is Michaelis-Menten constant (3% O_2), K_i is the inhibition constant (10% CO_2) (for each product variety and physiological state), and the thermal boundary condition is given by a uniform T_s value. The dependence on temperature of such kinetics has been defined using a Vant'Hoff–type equation (Fonseca et al. 2002):

$$R_r=R_r^*\cdot Q^{(T_s-293)/10} \tag{4}$$

where the temperature quotient Q and the nominal respiration rate R_r^* are respectively 3 and 4.615×10^{-9}m^3/kg s for tomatoes, determined experimentally. Finally, $\dot{q}$ is related to storage temperature T_s by the following:

$$\dot{q}=c_1\ \exp\left(c_2\ T_s\right) \tag{5}$$

where c_1 and c_2 are constants, 0.087 W/m^3 and 0.173 K^{-1} respectively, again determined experimentally.

It is useful to define an average species concentration, computed in a given volume V, as:

$$\bar{c}=\frac{1}{V}\int_V c\ \mathrm{d}V \tag{6}$$

RESULTS

The problem has been attacked by using COMSOL Multiphysics v.3a, for a total of over 23500 degrees of freedom. No grid–independency analysis was carried out for this preliminary study. The run has taken under 20 min of computing time for an elapsed time of 2 days, on a Xeon server (3GHz CPU, 2GB RAM) running under Windows XPPro.
In this study, the food matrix is initially at 274 K, while the package is kept in a controlled storage cell at 275.5 K. In order to exercise a passive transportation storage the thermal boundary condition is such that T_s increases by 0.2 °C per day, and an impermeable packaging film is employed. The initial O_2 and CO_2 volume fractions were 20.8% and 0.03% respectively.

Heat transfer

First, the temperature distribution in the headspace and in the fruits, after 2 days of passive cold storage, is shown in Fig. 4 by providing several horizontal and vertical slices of the whole package in which the fruit spheres are outlined. The distribution is still very similar to the initial one, the fruits temperature being lower than the headspace. This helps control the aerobic metabolism, as said earlier, that will degrade the fruit features, however a small temperature rise should be admitted in the package to avoid cold damages to the tomatoes, that are usually stored at about 283 K.

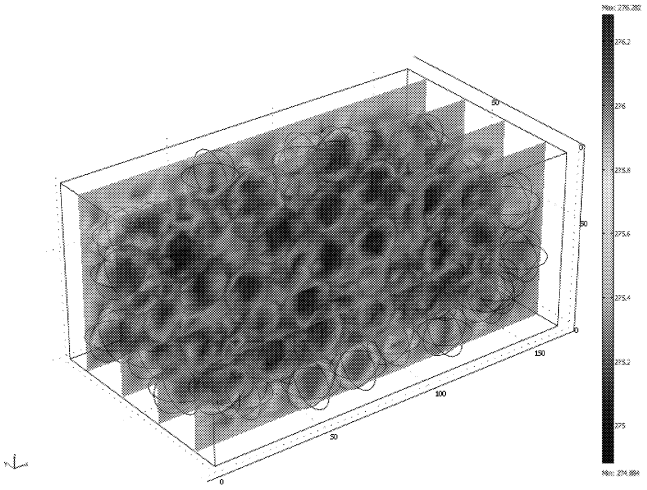

Figure 4: Temperature distribution after 2 days in the packaging.

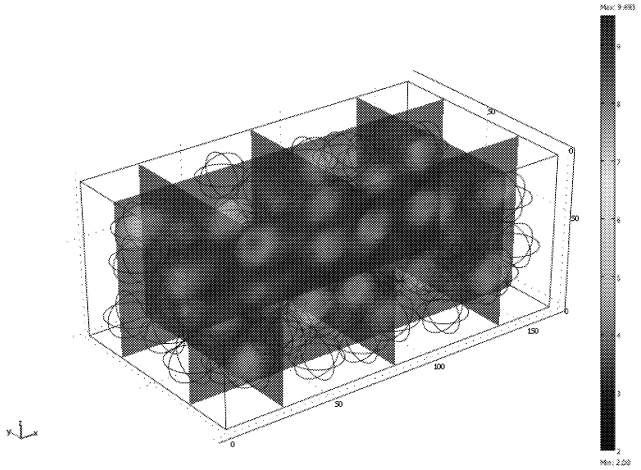

Figure 5: O_2 concentration in the packaging, at the beginning of storage.

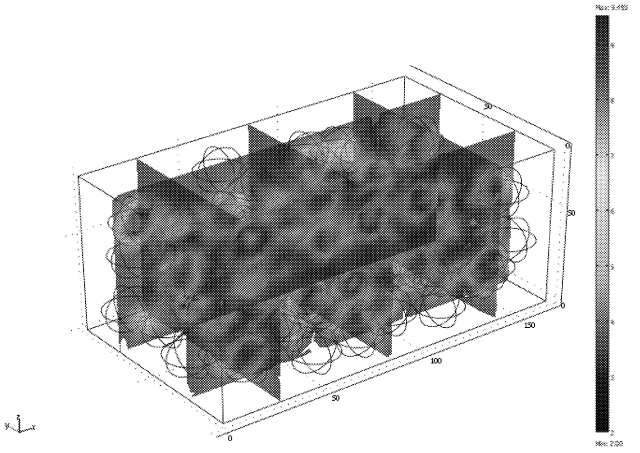

Figure 7: O_2 concentration after 48 h in the packaging.

Mass transfer

Figures 5 and 6 report the initial distributions of c_{O_2} (9.09 mol/m^3) and c_{CO_2} (0.0131 mol/m^3) respectively, evidencing a gaseous composition in equilibrium with the fruits. In the present study, the headspace gas composition is altered solely by respiration as the packaging film is impervious to diffusion.
With the storage time, the evolution of concentrations is such that CO_2 increases at the expenses of O_2. Such effect is naturally evidenced within the fruits themselves, where is much higher the concentration dependence on metabolism. An inverted concentration gradient is therefore created that represents the driving force for the gas diffusion in the headspace: CO_2 diffuses from the fruits to the headspace, as opposed to O_2 that travels towards the produce, being depleted by respiration. This is confirmed by examining the concentration distributions after about 2 storage days in Fig. 7 and 8. c_{O_2} gets up to 8.51 mol/m^3 in the headspace, and to its minimum of 5.55 mol/m^3 in the fruits (Fig. 7), while c_{CO_2} evolves up to about 0.660 mol/m^3 in the headspace and to its maximum of 3.57 mol/m^3 in the food matrix. Accordingly, concentration gradients start to appear around the produce.
Finally, the evolution of the average concentration, as defined by Eq. 6, is summarized in Fig. 9. The computation has been carried over on the headspace and produce total volumes, respectively. At the beginning of passive storage, a very low temperature regime helps limiting the aerobic metabolism, as anticipated earlier. Even for a slight temperature rise, the metabolism is increased accordingly, but then it is limited by higher c_{CO_2} that inhibits the respiration process itself, and the ripening is slowed down, due to the adopted K_m

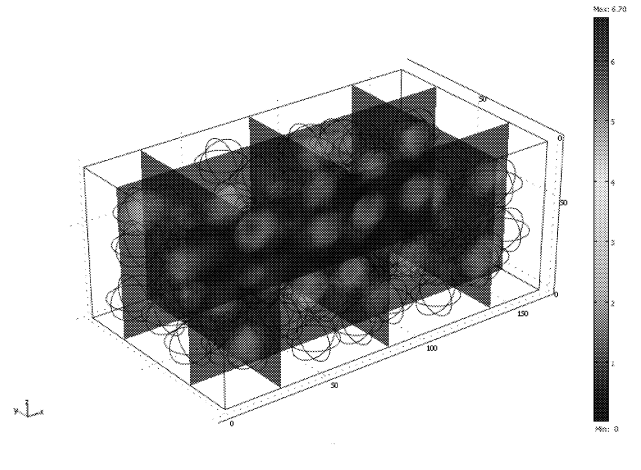

Figure 6: CO_2 concentration in the packaging, at the beginning of storage.

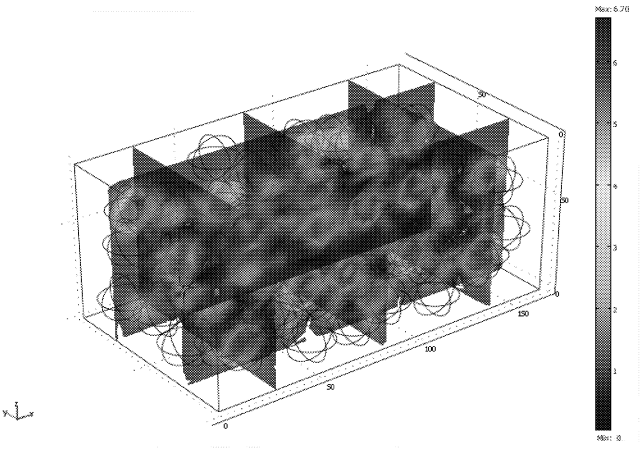

Figure 8: CO_2 concentration after 48 h in the packaging.

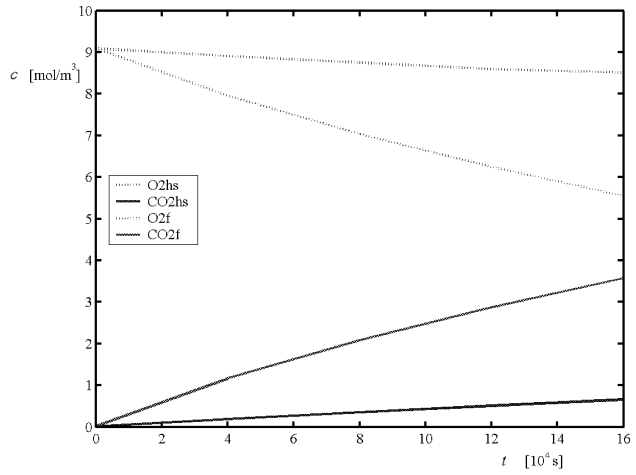

Figure 9: Average concentrations $\bar{c}$ of O_2 (blue) and CO_2 (red), in the headspace (hs) and fruits (f) subdomains.

and K_i values in Eq. (3). However, the composition keeps being spoiled with time in the observed period; O_2 varies symmetrically with CO_2, as expected. The average results compare fairly well with the associated experimental activity carried out at CNR–ISPA of Bari, Italy.

CONCLUSIONS

In this work a distributed–parameters model has been described by integration of standard mass and heat transfer partial differential equations combined with respiration kinetics notations. The adoption of a predictive mathematical model is an economic method to evaluate packaging performance, compared to more expensive experimental methods.
The model has been applied to passive storage in protective atmospheres of fresh–cut produce, and local concentrations of gas species and temperature have been computed. In this preliminary application the combined effect of low temperature regime and gas composition variation for a give packaging configuration has been assessed. A fairly large accumulation of CO_2 has been detected that slows down further respiration and ripening, in the short period observed, improving produce keeping quality.
Flexible designs of new packaging configurations, and the verification of existing ones can be worked out: useful information on shelf–life and the relationships between specific produce respiration rate and gas diffusion have been brought forth, giving more insight with respect to the available literature. Potential new designs can be explored with this tool, including various geometries, frequency of micro–holes in the packaging film, application of oxidative films or inner patches for O_2 scavenging (for those sensible foods), topology of pouches or bacterial active substrates, and the like.

ACKNOWLEDGEMENT

Dr. G.L. Zanotelli of COMSOL s.r.l. (Brescia, Italy) is gratefully acknowledged for his help with the software.

REFERENCES

[1] Bertola, N., A. Chaves and N.E. Zaritzky. 1990. "Diffusion of Carbon Dioxide in Tomato Fruits during Cold Storage in Modified Atmosphere" International Journal of Food Science and Technology 25, 318-327.

[2] Bird, R.B.; W.E. Stewart; and E.N. Lightfoot. 2002. *Transport phenomena.* John Wiley & Sons, New York, N.Y.

[3] Cefola, M, M.V. De Bonis, L. Massignan and G. Ruocco. 2005. "Mass and Heat Transfer Modelling of Food in Modified Atmosphere." In Proceedings of the Eurotherm Seminar 77–Heat and Mass Transfer in Food Processing (Parma, Italy, Jun. 20-22). Edizioni ETS, Pisa, Italy, 147-152.

[4] Fonseca, S.C., F.A.R. Oliveira and J.K. Brecht. 2002. "Modelling Respiration Rate of Fresh Fruits and Vegetables for Modified Atmosphere Packages: a Review." Journal of Food Engineering 52, 99-119.

[5] Lee, D.S., P.E. Haggar, J. Lee and K.L. Yam. 1991. "Model for Fresh Produce Respiration in Modified Atmospheres based on Principles of Enzyme Kinetics." Journal of Food Science 56, 1580-1585.

[6] Singh, R.P. and D.R. Heldman. 1993. Introduction to Food Engineering. Academic Press, San Diego, Ca.

[7] Uchino, T., D. Nei, W. Hu and H. Sorour. 2004. "Development of Mathematical Model for Dependence of Respiration Rate of Fresh Produce on Temperature and Time." Postharvest Biology and Technology 34, 285-293.

[8] Zagory, D. and A.A. Kader. 1988. "Modified Atmosphere Packaging of Fresh Produce." Food Technology 42, No. 4, 70-77.

NUMERICAL SIMULATION OF THE MULTI EXTRUSION PET FOOD WITH RHEOLOGICALLY COMPLEX BEHAVIOUR

Thierry Marchal
Fluent Benelux
Avenue Pasteur 4
1300 Wavre
Belgium
E-mail: tmm@fluent.com

Antoine Dozolme
Fluent Benelux
Avenue Pasteur 4
1300 Wavre
Belgium
E-mail: ado@fluent.com

Benoit Marchal
Université Paul Verlaine,
Lycée Charles Jully,
Plastinnov
Metz
France

KEYWORDS
Multi-extrusion, Pet food, visco-elastic, inverse design, CFD, POLYFLOW.

ABSTRACT

During the last two decades, numerical simulation has been used extensively to improve the performance of manufacturing processes in the metal, glass and polymer industries. More recently, a growing interest, and success, is emerging from the food processing industry, despite the complexity of the food materials properties. This paper describes the numerical modelling of a relatively complex flow distributor together with the deformation of the extrudate. A special technique, known as the inverse technique, allows to automatically design the shape of the die in order to get the requested extrudate shape.

INTRODUCTION

During the extrusion of food materials, modifying the operating conditions, such as screw speed, feed rate, characteristics of the environment (temperature, humidity, etc.), affect the specificities of the extruded product. Furthermore, rheological properties, die swell, friction along the die wall, among others, depend on the equipment design (geometries of the extruder, die, manifold and die lands): the food materials properties depend upon the full flow history during its transit throughout the die. Some of these variables can be adjusted in order to obtain the desired texture of the product.

Furthermore, complex rheological aspects such as thixotropy, visco-elasticity, puffing, etc. are key attributes of the food properties that the designer needs to take into account when numerically modelling certain processes [1], [2]. Although there are, to our knowledge, no accepted viscosity models or measurement methods which are considered to provide a complete description of the physics involved, some models have been developed to allow at least a description of the main effects. Those are generally associated with a "structural" parameter that varies with shear and time to reflect the change in the structure of the material being processed.

Extrusion has been conventionally used for the manufacture of cooked food, pet food, raw meat and even ice cream. In typical extrusion equipment, the material comes from the extruders; it next flows through a single entry section before entering the manifold. This device is feeding numerous die lands where the food is acquiring its final shape before leaving the die and expanding. The geometrical design of the manifold is extremely important in order to ensure similar local flow rates across each die outlet section. Different velocities profiles may lead to longer extrudates between two knife cuts, what significantly affects the quality and the commercial value of the product. Furthermore, for higher flow rates, some unexpected behaviours, such as viscoelastic phenomena, may become important. In this case, a die having different local flow rates across different outlet sections may exhibit different material relaxations after the die lip, hence different die swells. The resulting product exiting the die at different outlet sections can then have radically different shapes.

NUMERICAL MODEL

We use the POLYFLOW software, from Fluent Inc, to model the extrusion process [3]. A 3-D Finite Element Method (FEM) solves the momentum and incompressibility equations. Furthermore, to accurately model the viscoelastic behaviour of the material, the Navier-Stokes equations are coupled with an appropriate constitutive equation. In this specific case, a Phan Thien-Tanner differential viscoelastic model is selected.

Mass conservation: $$\nabla \cdot \mathbf{v} = 0 \quad (1)$$

Momentum conservation: $$-\nabla p + \nabla \cdot \mathbf{T} + \mathbf{f} = \rho \mathbf{a} \quad (2)$$

Where p is the pressure
$\mathbf{T}$ is the extra-stress tensor
$\mathbf{f}$ is the volume force given by $\mathbf{f} = \rho \mathbf{g}$
$\mathbf{a}$ is the acceleration term given by
$$\mathbf{a} = \frac{\partial \mathbf{v}}{\partial t} + \mathbf{v} \cdot \nabla \mathbf{v}$$

The presence of moving "free surfaces" for the deforming extrudate introduces an additional equation,

known as the kinematic condition, which results from the constraints that the normal force must vanish along free surfaces whereas the velocity vectors must be tangent (in steady-state simulations):

- stress free surface: $f = 0$
- tangent to the velocity field: $< \mathbf{v} \cdot \mathbf{n} > = 0$

The set of equations solved defines a "velocity - pressure - position" formulation for the generalised Newtonian case (purely viscous effects) and a "stress-velocity-pressure-position" formulation for the viscoelastic case.

A particularly helpful feature of the POLYFLOW software is the availability of the so-called "inverse extrusion", an *automatic* die lip design functionality. Figure 1 illustrates the extrusion analysis capabilities of the software for the die and free surface flow. In the usual case, referenced as "Extrudate Prediction", the code starts with a given die geometry and calculates the deformations of the free surfaces originating from the die lip. The deformation of the free surfaces might be due (i) to the velocity rearrangement in the sudden absence of friction outside the die and (ii) to the relaxation of stresses developed during the shearing experienced by materials with a considerable viscoelastic component.

The die design technique implies a strategy to adapt the die lip to a section that is modified during the simulation to satisfy those requirements. This means that the result of the calculation is a design close to the die that will take those deformations into account to produce the desired profile [4].

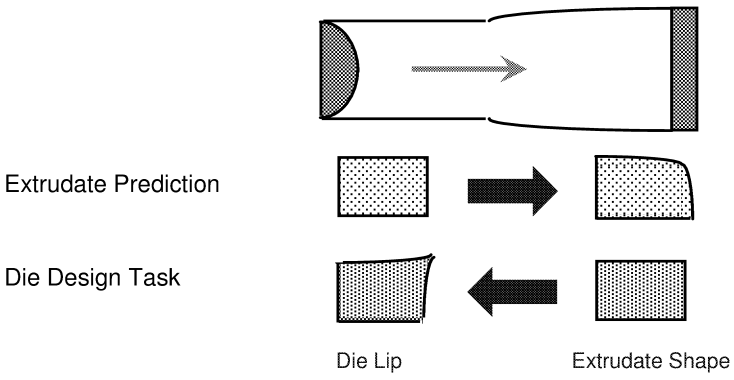

Figure 1: The inverse technique

With this tool, it is therefore possible to reduce considerably the number of trial dies one needs to manufacture and test to obtain the required profiles. Reports attest considerable increase in the product quality, the production rates and reduction of set-up times by allowing skilled designers to apply the die design capability of the software [5, 6].Type in capitals, beginning flush with left-hand margin. Use a bold font. Skip half a line space, then begin.

NUMERICAL RESULTS

A die involving one inlet section and 5 outlets was considered. The geometry of the equipment has been simplified in order to reduce the number of finite elements what allows to run a large number of simulations quickly on a standard PC or even a laptop. For this preliminary analysis, a simple square outlet section has been considered in order to pay a closer attention to the geometry of the manifold. In reality, more complex die land geometries, having a typical 'X' outlet shape, are considered. Performing numerical analyses on these devices are a simple extension of this preliminary study that will be later illustrated.

The initial and modified geometries are shown in figure 2. In both cases, the dimensions of the outlet sections are identical. However, the second geometry is presenting a more compact configuration of the whole device. Furthermore, the trajectories of food particles inside the die have been considerably reduced.

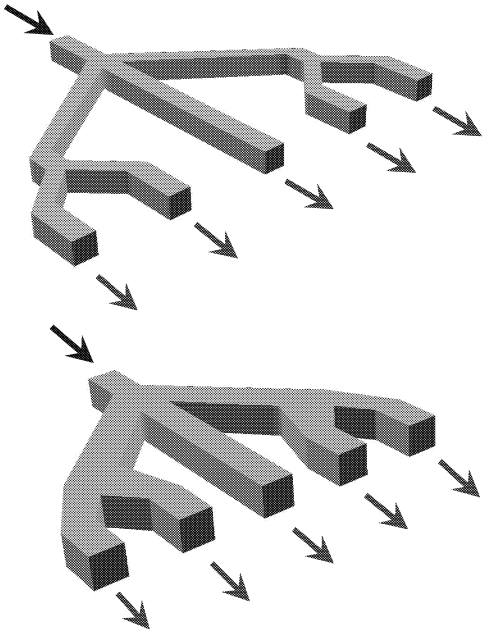

Figure. 2: Initial geometry with unbalanced velocity, modified, more compact geometry

For the initial geometry (Figure 3, a.), the speed of particles flowing through the central channel is four times larger than the food flowing in the side channels. This difference is graphically illustrated by the velocity vectors across the outlet section. As the central narrow flow channel is straight, the pressure drop due to the friction along the wall for a given velocity is smaller than in the side channels: it is easier for the particles to reach the die lip in a straight die. As the global pressure drop between the single inlet section and the different outlet sections is the same, the local flow rate across the central channel is larger. This is the privileged particles path leading to the largest local flow rate.

If the manifold geometry is modified in such a way to facilitate the flow of material in the side channels, (e.g.

by enlarging the local flow sections and reducing the particles journey inside the device (Figure 3, b.)), the local flow rate is reduced in the central section and increased in the side channels. This results in a much better balanced manifold. The simulation calculating the flow pattern in a given geometry is running in less than 1 minute on a high end laptop computer.

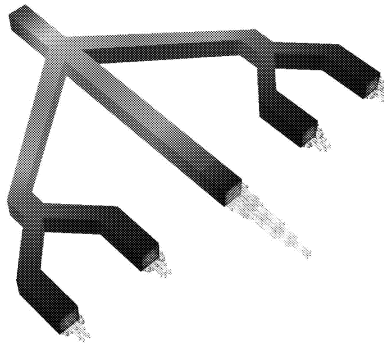

a.

b.

Figure 3: Contour lines of the velocity magnitude and velocity vectors across the outlet sections; normalized pressure on the die wall

Once a device, with a satisfyingly balanced velocity profile, has been designed, it is important to predict the deformations of the extrudate shape, when the food material is free to deform after the die lip. The deformations come from the fact that the particles can flow freely outside the die where no friction is affecting the flow anymore. Furthermore, the relaxation of the stress undergone by the food while flowing throughout the die land, is leading to additional swelling. For the materials properties that are considered in the current analysis, taking into account the visco-elastic behavior of the material, a die swell of 95% has been calculated despite the fact that puffing phenomena have been neglected in this simulation.

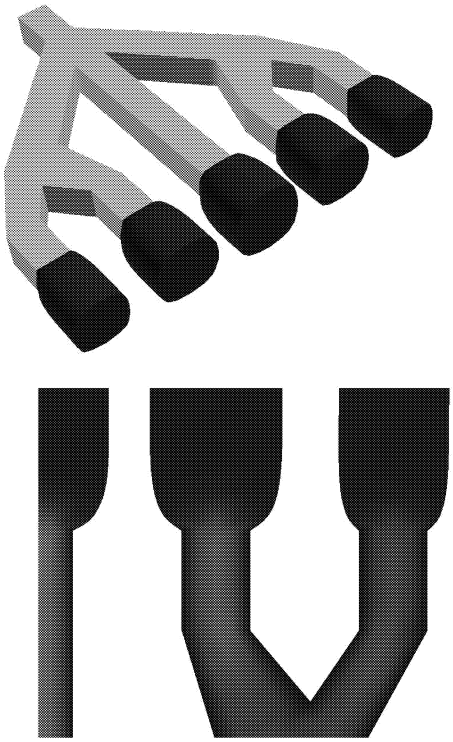

Figure 4: Deformation of the extrudate for a visco-elastic material

In order to complete the design of the die, it is possible to activate the inverse die design capability of the software. Considering the large deformations undergone by the materials after the die lip, the code automatically modifies the shape of the die lip so that the desired extrudate shape, here a simple square, will be obtained after the deformations undergone by the free jet.

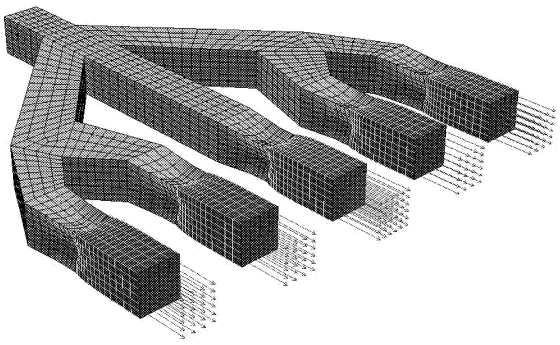

Figure 5: Deformation of the extrudate using the inverse die design technique

The modified die lip, displayed in red in the Figure 6, strongly depends on the expected die swell, due to both the die balancing and the visco-elastic effects under given flow conditions. It is well known that these visco-elastic behaviours affect the flow more significantly, especially if the local flow rate is large. Hence, an increase of the global flow rate will increase the calculated swelling. In addition, a local variation of the flow may lead to different die lip shapes in order to get the same extruded profile.

The calculated die lips, illustrated in the top two rows of outlet sections in Figure 6, do not show major differences despite the fact that some significant variations of the local flow rates have been calculated. A generalized Newtonian model was considered for these first two simulations. The bottom row illustrates the results obtained with the optimized geometry while considering a visco-elastic behaviour. It appears that the die lip calculated for the central channel (c. in Figure 6) is showing larger deformations that the side channels (a. & b.). Rheological behaviours may induce larger deformations than geometrical adjustments.

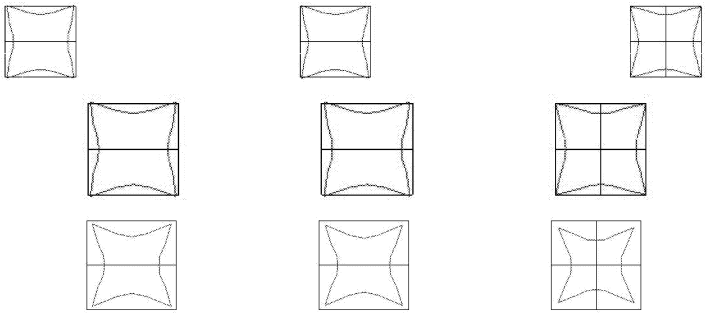

a. b. c.

Figure 6: Comparison between the necessary die lip shape (in red) and the desired extrudate shape (black) for the initial geometry (top), modified geometry (middle) and modified geometry with a visco-elastic behavior of the material (bottom); a. is the extreme channel whereas c. is the central channel

CONCLUSIONS AND FUTURE WORK

Despite the complexity of the rheological behaviour of food materials, the commercial software, POLYFLOW, allows to perform quick design of multi-extrusion die. In order to get an accurate desired shape of the extruded product, a combination of die balancing and inverse die design is necessary.

In the near future we expect to introduce more complex phenomena such as Bingham models, thixothropy and moisture dependence in the physical modelling of the material behaviour while considering more complex geometries.

REFERENCES

[1] R. K. Connelly, J. L. Kokini, 2-D numerical simulation of differential viscoelastic fluids in a single screw continuous mixer: Application of viscoelastic finite element methods, Advances in Polymer Technology, Vol. 22 No.1, 22-41 (2003)

[2] F. Edi-Soetaredjo, G. Nashed, R.P.G. Rutger, P. J. Torley, Numerical analysis of the effect of extrusion conditions on flow in slit die rheometer, Proc. Of the 3rd International Conference on CFD in the Minerals and Process Industries, CSIRO, Melbourne, 2003

[3] POLYFLOW Users Manual, Lebanon, NH, 2003

[4] Legat, V. and Marchal, J-M., Die design: an implicit formulation for the inverse problem, Int. J. Numerical Methods in Fluids, 16, 29-42 (1993).

[5] Reese, C., Marchal, T. and Marchal, J-M., Use of die modeling to improve the manufacturing process for extruded silicone rubber, Proc. of the ANTEC'94 conference, ed. Society of Plastics Engineers, Brookfield CT, (1994), vol. I, 94-99.

[6] Andrejewski, D., Polyflow: a treatise on inverse die/mandrel design for high consistency silicone elastomer, Proc. of the ANTEC'97 conference, ed. Society of Plastics Engineers, Brookfield CT, (1997), vol. I, 308-314

On Data Modeling for Batch Processes with an Application to Wine-making

Luigi Glielmo, Francesco Vasca
Department of Engineering, Università degli Studi del Sannio
glielmo@unisannio.it, vasca@unisannio.it.

Oreste Riccardo Natale
Mosaico Monitoraggio Integrato
Spin-off company of Università degli Studi del Sannio
o.r.natale@mosaico-mi.it

Introduction

Properties and quality of agriculture products and food transformation processes may strongly depend on raw materials characteristics, which however can vary with harvest year by year. Due to these almost unpredictable variations, production processes are subject to controlled modifications in order to induce the desired organoleptic features on the final products. Smart comparisons among final lots and their characteristics may suggest a feedback for the next production process to help the selection of the best stage parameters and sequence, especially for those processes whose relations between causes and effects are not yet well understood. In this scenario it is important to reconstruct product history up to the lots of raw materials from which the production process has started.

To this aim, an object based model of the production process and the involved data can be very useful, and if implemented through modern database methodologies, it can be also integrated in supervisory and traceability tools of the whole process [1].

The data model presented in this paper has been designed with the Unified Modeling Language (in the sequel called UML), which is a formal graphic tool used to describe the structure and the behavior of a software system conceived within the object oriented paradigm [2], [3]. Its semantics has been developed to help designers to communicate almost without ambiguity among each other, and between designers and final users. Despite its lack of ambiguity, UML is not a rigid set of rules but its notations and meanings can be extended according to developer's needs. Some recent works show that UML can be used to describe physical systems behavior under computer control such single controlled machines [4], distributed control systems [5], and entire flexible manufacturing systems [6], [7]; the main advantage of such an approach is that with a single tool a designer can identify system requirements, plan system architecture, and physical component features as well as their dynamic behavior [8], [9].

The UML model proposed in this paper to handle batch processes data is based on the *design pattern* approach [10]. With such a modeling procedure, UML diagrams represent a general system model parametrized with respect to the meaning of the elements of the structure, so that it can be specialized to the particular designer needs. In particular the proposed model is inspired by the *Process pattern* data model for continuous production process (see [11]), which is based upon product flows among the possible paths in the plant; here, however, the accent is placed on relating each production phase and its parameters to the corresponding production sequence, thus ensuring final product traceability, that is the capability of back-tracing the production phases and components of each final product or lot.

This paper is organized as follows: in the first section the application domain is explored; the UML formalization of the proposed model is presented in the second section, and model properties such as flexibility in modifying process structure and some traceability features are also analyzed; in the third section, a

case study regarding the application of the model to the wine-making process, as well as the integration of the software system with a supervisory control system for the alcoholic fermentation reaction are described; some insights on the future evolution of the proposed model, and its possible exploitation as a tool for decision support and product traceability are presented in the last section.

Application domain

The production process considered in this paper complies with the following assumptions:

- The final product is manufactured along a sequence of production phases (see Figure 1); some phases can be optional rather then repeated more than once.
- Activities such as product design, production planning, and production control are excluded from the set of stages considered.
- Each phase transforms one or more input quantities of semi-products into one or more output quantities of semi-products. Raw materials and final products, the latter collected in production lot, are the two extremes of the production-chain.
- A semi-product is at the same time one of the products of its upstream phase and one of the components of its downstream phases, in which it can be partially or entirely involved until it is completely exhausted or discarded.
- A semi-product is (logically) created, and permanently stored, when the corresponding production phase starts.
- Each phase is related to a proper set of parameters, and to some other information like the type of machinery used and the operator(s) involved in the production phase.
- Each semi-product is related to a set of relevant measurements, additives additions, and storage systems (for instance a tank).
- Measurements and additive additions are executed at time instants ranging between the time-stamp at which the semi-product is logically created, and the time-stamp at which it is completely exhausted or discarded.

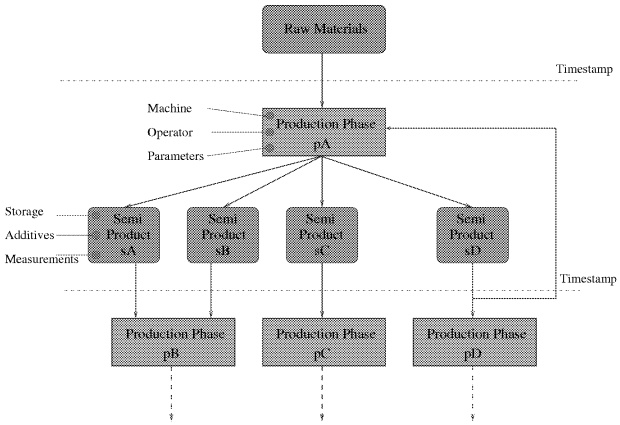

Figure 1: Process flow. A sequence of phases and semiproducts builds up the process flow, and a specified sets or features can be assigned to each phase or semiproduct; note that multiple instances of measurements and additives are allowed for each semi-product.

The block diagram of Figure 1 can be recursively rearranged in that of Figure 2, thus determining the core of the model proposed, yet unformalized. In this model, the temporal sequence of the phases is recorded associating a time-stamp to each phase and each semiproduct.

Object oriented data model

Formalization

Each of the entities *ProductionPhase* and *SemiProduct*, depicted informally in Figure 2, can be considered belonging to a UML *class* (see [2]-[3]) with their proper attributes (see Figure 3); entity instances can be subsequently represented as the corresponding class instances or *objects*.

The two non formal relations between *SemiProduct* and *ProductionPhase* entities in Figure 2 can be considered as two distinct *associations* between the classes *SemiProduct* and *ProductionPhase* with distinct *roles* on the *SemiProduct* side (*+componentOf* and *+productOf* in Figure 3), thus identifying the association meaning of each *SemiProduct* instance with its preceding phase and its subsequent phases.

Note that visibility tags of all the class attributes and the classes roles in associations are not relevant to our discussion, however they are set to *public*, and prefixed

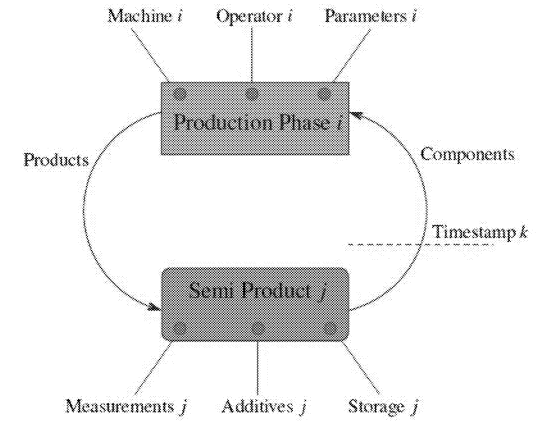

Figure 2: Recursive representation of data involved in a production process. This pictures depicts the same information presented in Figure 1, but in a compact way more suitable for formalization; raw materials are considered as a particular instance of semi-products.

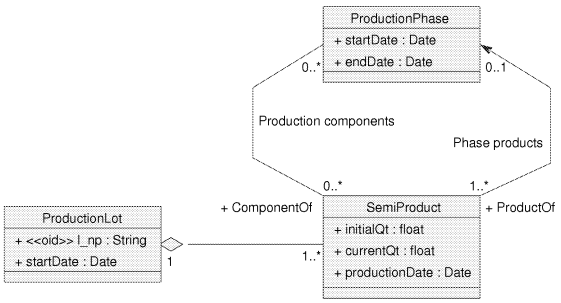

Figure 3: Core UML class diagram for phases sequence data handling. This figure represents the first step for the formalization of the model in Figure 2.

with the "+" symbol, to compy with the UML conventions requiring a visibility tag specification.

To relate the phase sequence to the history of a single production, a class *ProductionLot* can be thought of as composed by a set of *SemiProduct* objects; each object represents the result of a production phase, and the sequence of objects obtained ordering the sets by production date forms the history line.

The UML class diagram in Figure 3 must be further detailed to record data on additives additions, measurements and storage systems (see Figure 1). Formally (see Figure 4), each association between *SemiProduct* and *Store* is linked to a *Contents* association class, which is in turn associated with all the needed *Measure* and *Additive* objects through the association classes *Measurement* and *Addition*; further elements reported in Figure 4 are

- an *Operator* class associated to the *ProductionPhase* class, thus selecting the employee(s) involved in each phase;
- the association class *PrComponent* added to the association *Production components* to record the amount of a *SemiProduct* participating as a component in a *ProductionPhase;*
- a *Machine* class to take into account the specific equipment used in the corresponding production phase.

Thus, Figure 4 synthesizes the proposed model which is quite general and can be simply specialized to a specific production process. No assumptions have been made on the phases sequence or, more specifically, on how many times each phase is executed in the process. In particular, the model can be set up for a specific production process by deriving from the class *SemiProduct* and the class *ProductionPhase* all the needed classes with their proper attributes, so as illustrated in the case study in the next section. Since derived classes inherit relations defined on their parent classes, enlarging the hierarchies at need does not affect the database structure integrity even if the database is already operating. Moreover, the phases sequence is not controlled at the database level, thus ensuring database structure flexibility and scalability at the process changes. Product history can be reconstructed selecting recursively the last created *SemiProduct* instance from a *ProductionLot*, and, walking backwards, retrieving the data regarding the preceding production phases.

Model implementation

The last issue to be considered is the selection of the database engine. Currently full featured object relational database engines are not yet available, so the possible choices are to manage with existing products (see, for instance, [12]), or to translate the object oriented structure proposed in a traditional relational architecture according to the almost one-to-one method discussed in [11].

If the translation method is selected, the following considerations on the diagram of Figure 4 can simplify the procedure:

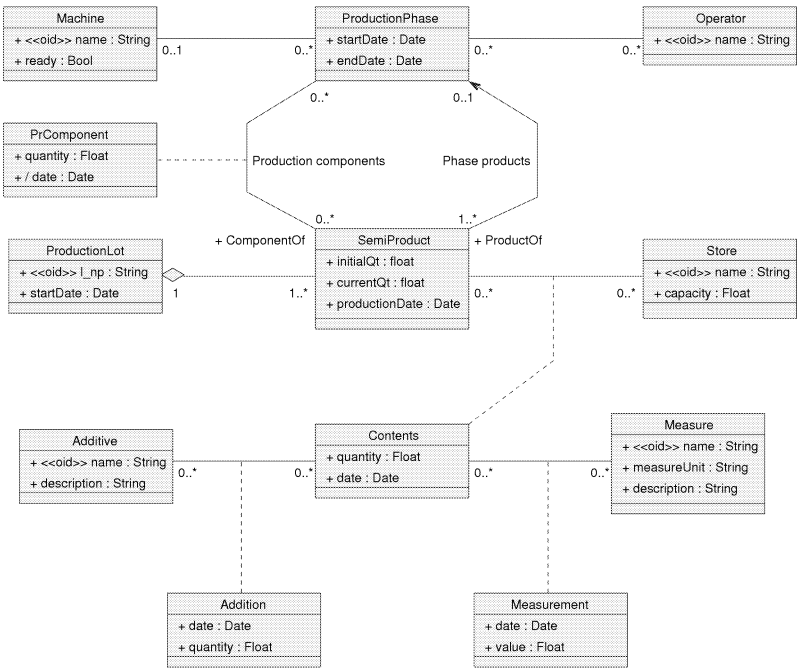

Figure 4: UML class diagram for the proposed model. This diagram represents the complete formalization of the process model in Figure 2.

- Each class can be represented with a table. The tables are provided with an object identifier (*oid*) field, except for association classes which have a double oid field referencing two instances of the objects associated, thus determining the association instance.
- Each table representing a class involved in an association on the, so called, *not navigable side* (on the starting side of the arrow) is equipped with an oid field referencing the associated instance oid, again except for association classes.
- Inheritance associations are represented hierarchically, with the son classes realized with tables whose instances refer to the correlated parent instances, thus binding common fields instances with specialized fields instances.

Case study

Wine-making process

The process of wine-making is quite complex and articulate, and, above all it cannot be considered as a repetitive sequence of phases, meaning that the process can be changed according to the chemical and physical characteristics of the grapes harvested and the productive tradition of the particular cellar [13], [14].

Figure 5 shows a possible block diagram for a typical white wine production process. The construction of this diagram identifying the main production phases and related parameters, is the first fundamental step of our modeling approach, and must be carried out by merging expertises of object oriented systems modeling, emerging skills in control engineering, and those of the process experts (in our case oenologists and cellar operators). Recording the phases and the corresponding parameters will eventually allow to trace the entire productive history for each bottle of wine.

Enostoria: a production information system

The model described in the previous section has been implemented in a production information system, which we called *Enostoria*. Enostoria is a software conceived to describe, catalogue and manage wine-making data; it allows to reconstruct the history of each bottle

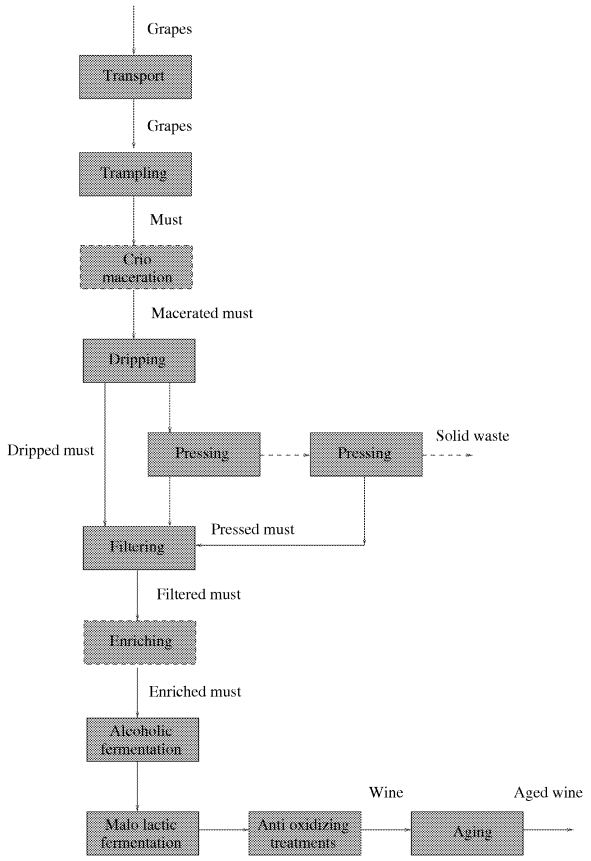

Figure 5: A flow diagram for the white wine-making production process. For readability purposes semiproducts type is only indicated between phases and not represented in a separate block so as in Figure 1; dashed boxes represent phases commonly considered as optional.

of wine up to the lots of grapes from which the process started, thus providing a tool for the traceability of the wine-making production flow.

Figure 6 shows the hierarchy classes diagram for some of the wine-making semi-products, as well as their corresponding parameters of interest. Note that the data model core remains unchanged regardless of cardinality and structure of the *ProductionPhase* and the *SemiProduct* hierarchies; furthermore it is possible to insert relations between derived classes to satisfy particular needs.

To detail more and further motivate the proposed model, the following example shows the objects organization in a common but not easily handled situation.

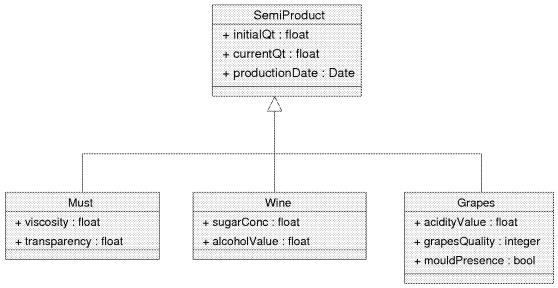

Figure 6: Process specialization class diagram. SemiProducts hierarchy for some wine-making semiproducts.

Let us consider this scenario: two production lots are planned (represented on the two central columns of Figure 7), the one on the left obtained by two distinct lots of wine grapes. At a certain time, after the trumpling and the pressing production phases, the alcoholic fermentation phase is needed for both lots. Suppose that for some reasons the fermentation of the first lot does not start; a typical escamotage is to use part of the fermenting to start the chemical reaction in the first.

In order to model this situation, a separation phase acting as the must in fermentation is introduced; the resulting two *SemiProduct*s of must will belong one to the first lot (exploited to start the fermentation) and the other to the second lot (continuing its ongoing fermentation). The object diagram of Figure 7 shows how the proposed model can be instantiated to handle the situation.

At last note that at any time, a cellar owner can decide to vary the production process, and the database structure must be changed accordingly, e.g. enlarging *SemiProduct* and *ProductionPhase* hierarchies; in this case the preceding recorded objects relations will be not influenced by the subsequent created structures.

Enostoria architecture

The architecture proposed is web based: a database server (*MySQL*) is accessed by dynamic scripts (*Php*) executed by a web server (*Apache*); the users interact with the software system through a standard web browser.

The key benefits of this architecture range from the simplicity of software maintenance, because there is no need to recompile when updating a web page both locally and from a remote software developer, to the

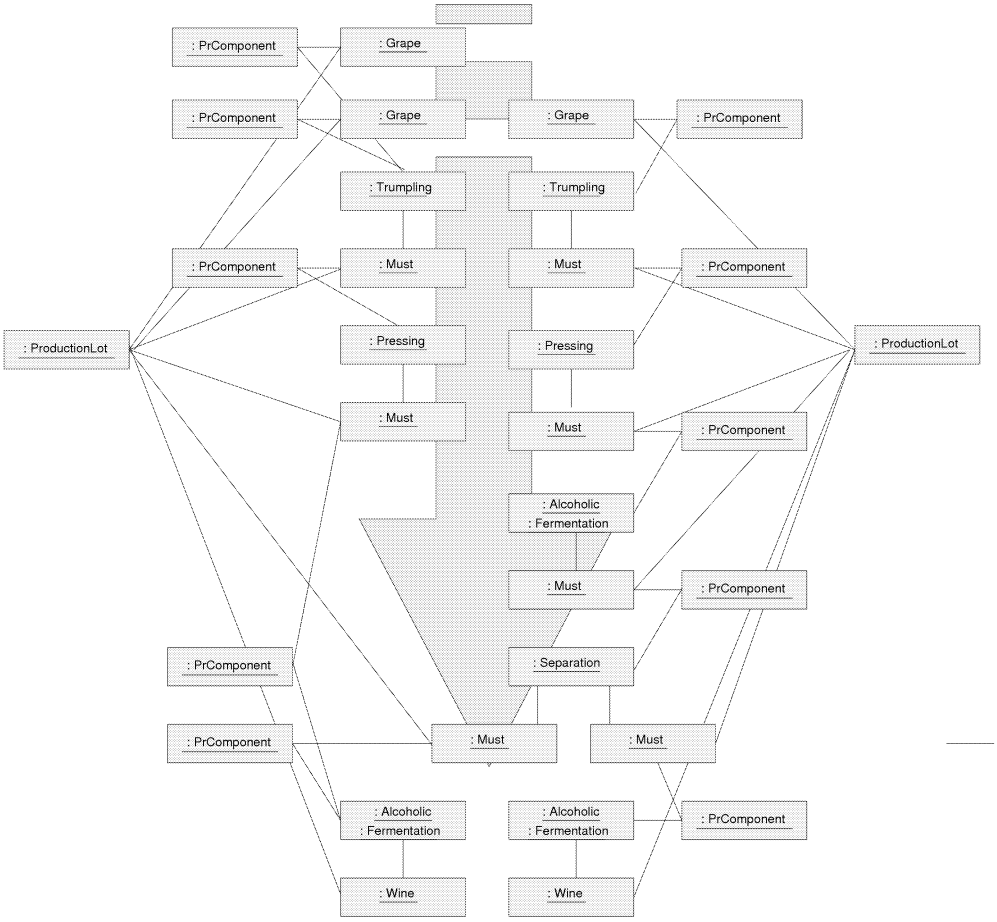

Figure 7: Objects diagram for a generic production flow history. Objects attributes are not shown; time-stamps values increase from the top of the figure.

users familiarity with web applications, and finally to the recent possibility of SCADA systems exchanging data with operators through a web interface. Taking advantage of the distributed architecture, the functionalities released to the Enostoria are of support to the management of machinery, suppliers, supply and production lots, and data tracing.

Enostoria with a SCADA

Beyond all doubts the most delicate phase of wine-making is the alcoholic fermentation of grape must. Supporting the Enostoria system, a supervisory control system for the alcoholic fermentation process has been prototyped. The fermentation process involves a strong exothermic reaction that transforms sugar in ethyl alcohol and carbon dioxide according to

$$C_6H_{12}O_6 \rightarrow 2C_2H_5OH + 2CO_2;$$

the reaction can be considered completed when sugar concentration in the grape must drops below $2\frac{g}{hl}$.

Therefore, the supervisory system must guarantee first of all tank temperature control to the optimal levels indicated by oenologists. On the other hand, during the reaction, it is of interest to trace other quantities like pH, dissolved oxygen, sugar concentration, and alcohol content. To measure these quantities, the cellar has to choose between a real time acquisition using a proper set of sensors, and a manual acquisition through laboratory analysis. To handle both these situations, or a combination of them, coherence and integrity of the process data must be ensured. This is obtained by means of a

suitable communication between Enostoria and the fermentation SCADA.

The architecture prototyped is based on a three level network system. The first level is the device level, where all sensors and actuators, dislocated on each tank in the cellar, are connected to a Programmable Logic Controller which operates temperature control and real time measurements. The second level is the control level; here, the PLC interacts with a SCADA system, where the oenologist can choose the proper temperature set point or insert off line data in the system. Last level is where the SCADA system communicates with Enostoria through a conventional local area network.

Conclusions and future work

In this paper an object oriented model for batch process data has been proposed, and a method to specialize the model to a specific production process has been also described. The software system, prototyped with the illustrated method for the wine-making process, has been tested together with a SCADA system for the alcoholic fermentation process interacting with it.

Enostoria allows smart comparisons of production data across years to select the best process variations to reproduce; this is an important issue in a field, such as wine-making, where the relations between causes and effects are not yet well understood, and where few experimentations are possible (once per year for wine-making). Moreover Enostoria can be used as a tool to support quality certification.

Future work will deal with testing the proposed model for production processes where a semi-product is *assembled* rather than transformed.

References

[1] D. I. Lewin, "Vintage computing," *Computing in Science and Engineering*, vol. 4, pp. 4–10, Nov/Dec 2002.

[2] G. Booch, I. Jacobson, and J. Rumbaugh, *The Unified Modeling Language user guide*. Technology Series, Addison Wesley, 1995.

[3] M. Fowler and K. Scott, *UML Distilled (3^{th} Ed.)*. Addison Wesley Technology Series, 2004.

[4] B. Bordbar, L. Giacomini, and D. Holding, "A UML-based approach to the modelling and supervisory control of manufacturing machinery," *IEE Seminar on Model Validation for Plant Control and Condition Monitoring (Ref. No. 2000/044)*, pp. 3/1–3/3, 2000.

[5] B. Bordbar, L. Giacomini, and D. Holding, "UML and petri nets for design and analysis of distributed systems," in *Proc. 2000 IEEE International Conference on Control Application*, pp. 610–615, 2000.

[6] H. Köhler, U. Nickerl, J. Niere, and A. Zündorf, "Integrating UML diagrams for production control systems," in *Proc. 2000 International Conference on Software Engineering*, 2000.

[7] W. Han and M. Jafari, "Component and agent-based FMS modeling and controller synthesis," *IEEE Tran. Systems, Man, and Cybernetics - Part C: Applications and reviews*, vol. 33, pp. 193–206, May 2003.

[8] J.-S. Lee and P.-L. Hsu, "UML-based modeling and multi-threaded simulation for hybrid dynamic systems," in *Proc. 2002 IEEE International Conference on Control Application*, pp. 1207–1212, 2002.

[9] H. Gomaa, *Designing concurrent, distributed, and real-time applications with UML*. Addison Wesley, 2000.

[10] E. Gamma, R. Helm, R. Johnson, and J. Vlissides, *Design patterns: elements of reusable object-oriented software*. Addison Wesley Longman Inc., 2000.

[11] R. Muller, *Database design for smarties: using UML for data modeling*. Academic Press, 1999.

[12] B. Momjian, *PostgreSQL: introduction and concepts*. Addison Wesley, 2000.

[13] R. Boulton, *Principles and practices of winemaking*. Chapman and Hall, 2000.

[14] R. Jackson, *Wine science: principles and applications*. Academic Press, 1999.

AN INNOVATIVE MATHEMATICAL METHOD FOR THE THERMAL DIFFUSIVITY ESTIMATION AND THERMAL PROCESS MODELLING

Massimiliano Rinaldi
Giampaolo Betta
Roberto Massini
Dipartimento di Ingegneria Industriale
Università degli Studi di Parma
Via Usberti 181/A, Parma,
43100 - Italia
E-mail: massimiliano.rinaldi@nemo.unipr.it

KEYWORDS
Thermal diffusivity, finite difference solution, heat treatments, process modeling.

ABSTRACT

In this work a new method for thermal diffusivity estimation in conductive foodstuffs has been developed. The proposed method couples a measure cell for the reliable heat penetration curves acquisition with a software for the data processing. The software, developed in Matlab® language, solves the Fourier's equation by means the finite difference technique with explicit method. By using this method it was possible to estimate the thermal diffusivity values of several foods, both at temperature near to sterilizing and to freezing/thawing processes. In order to evaluate the proposed method goodness, the obtained values have been compared with those obtained by means four different methods. Largely, the obtained values are analogous to the literature and to those obtained with other methods; for particular tests the proposed method gives apparent values that don't have the thermal diffusivity physical meaning but can be successufully used in the process modelling.

INTRODUCTION

The conductive heat exchange is an almost simple physical phenomenon and the mathematical law, the Fourier's equation (1), is a very simple differential equation. Thus, a lot of modelling software have been developed to solve successfully this problem: a wide application should be expected in the food processing practices, but these tools are not largely used and their capabilities are modestly applied. In order to take advantage of modelling tools it's necessary that the results were highly precise and reliable; this fact strictly depends on the software goodness and on the properties values knowledge. By considering the Fourier's equation:

$$\frac{\partial T}{\partial t} = \frac{\kappa}{\rho \cdot c_p} \cdot \nabla^2 T \qquad (1)$$

it's possible to appreciate that the conductive heat exchange depends on three physical properties that are density, thermal conductivity and specific heat capacity. All these properties can be included in a single parameter called thermal diffusivity:

$$\alpha = \frac{\kappa}{\rho \cdot c_p} \qquad (2)$$

Unluckily, in foodstuffs the value of thermal properties depend on cell structure, intracellular air content, water content, operating pressure and temperature; they vary also along system directions cause of physical anisotropy and composition heterogeneity. It appears clear that in foodstuff the α value presents high variability and so, it's not enough a mean value knowledge but it's necessary to estimate the thermal diffusivity value time after time and then easily.
The most used methods to determine thermal diffusivity values in foods are based on food composition (Singh 1993) or on experimental heat penetration curves (Ball 1957; Carciofi 2002; Rinaldi 2005). As explained above, the second way is the most suitable to our aims. It will be desirable to couple a precise software with an easy-to-use and reliable experimental standardized way of analysis.

MATERIALS AND METHODS

Samples

Tomato-based products
Three different types of tomato products have been used: two different tomato purees and a tomato sauce with basil.
The first tomato puree, packed in aseptic bricks and purchased on the market, has been used as representative of conductive heating liquid foodstuff. Preliminary tests on the tomato puree have been carried out in order to confirm the conductive-way of heat transfer. The tomato puree was alternatively filled in four different container types: 80x60 and 110 x 75 mm glass jars with 20 mm headspace and closed by metal cap; 80 x 50 mm cylindrical aluminium can and 125 x 80 mm cylindrical tinplate can filled without headspace.
The second tomato puree, packed in glass bottle and purchased on the market was filled in two different glass jar sizes (85.5 x 66.8 and 61.5 x 57 mm) with headspace (20 mm) and metal caps; and in 125 x 80 mm tinplate can without headspace.
The third tomato-based sample was a tomato sauce with basil and was filled in two different glass jar sizes (85.5 x 66.8 and 61.5 x 57 mm) with headspace (20 mm) and metal caps.

Starch suspension
Samples of 20% pre-gelatinized starch (Cerestar s.p.a. Ferrara, Italy) water suspension were filled in 80x60 mm glass jar and were heated for 60 minutes at 80°C. Samples were subsequently cooled at room temperature for at least 24 hours to obtain the whole gelatinization, then the samples were ready for the heat treatment tests. The starch concentration has been obtained from preliminary tests that gave 20% as the best level to have a good consistency. In other tests the starch suspension was filled in 125x80 mm tinplate cans.

Potatoes
Freshly harvested potatoes of a single production lot (*Solanum tuberosum, cv. Agata*) were locally purchased. Potatoes were stored in polythene bags in the dark at room temperature (20-22 °C) for a maximum of three days before testing, to avoid texture and colour changes associated to long storage time. Only potato tubers having weights (g) within the confidence interval of $121.7 \leq \mu \leq 165.4$ were used. The periderm was peeled immediately before testing. Cylindrical specimens (diameter 25 mm, height 30 mm) were extracted from the central part of the tubers, cutting off the top and the bottom ends with a knife. Three cylinders were obtained from each potato using a borer, operating perpendicularly to the two cut planes.

Truffle sauce
Samples of a truffle and oil sauce, purchased on the market, were filled in 85.5 x 66.8 and 61.5 x 57 mm glass jars, both with headspace and metal caps.

Spinach samples
Frozen spinach leaves packed in plastic bag (450g) have been purchased on the market and filled in 125x80 mm tinplate can after a slow thawing at 4°C. The water lost within this step has been removed.

Ice cream
Ice cream in 500g plastic box has been purchased on the market and filled in 125x80 mm tinplate can, being aware to avoid the samples thawing.

Heat treatment

Above-zero temperature tests
The high temperature tests have been carried out in three different ways that differs from the heating medium: air, hot water and steam.
For the first one an electrical oven (Whirlpool Europe) set at 180°C, with 5 different humidity levels (5.6, 7.4, 14.3, 20.0, and 31.3%), has been used ; only potatoes has been treated with this equipment, three samples have been used in each test.
For the second set of experiments tomato-based and starch samples have been processed at 80 and 45°C in a thermostatic bath (Julabo Circulators VC, JulaboItalia, Milano, Italy). For every test two samples have been used at each time.
Finally for the last one, samples of tomato purees and sauce and truffle sauce have been processed by means a pressure cooker and a steam retort (De Lama S.p.A., Pavia , Italy) at 5 different temperatures: 100, 113, 119, 123 and 125°C

Below-zero temperature tests
Tomato puree, ice cream and spinach have been frozen at -30°C in the same bath filled with a 50 % (w/w) ethylene glycol/water solution until the thermocouple placed in the geometrical centre of the canned product reached a substantial equilibrium at -29.9°C. Afterwards, the bath temperature was increased from –30 to 0°C in three different conditions: by a single step, by steps of 10°C, and by steps of 5°C. In all the conditions the bath temperature was maintained until the same value was substantially measured in the product centre. The samples have been also heated by an electrical oven (Whirlpool Europe) which was set at 25°C in natural convection air mode, until product was completely thawed.

Heat penetration curves measurement

For the atmospheric pressure tests, heat penetration curves were measured using wire thermocouples K type (Ch/Al – Ni/Al) connected with a multimeter/data acquisition system (Keithley Instruments Inc., Cleveland, Ohio, U.S.). Process recordings were planned measuring temperature variation inside the samples, in the thermal centre and in a point near it ("internal"), on the internal surface ("wall") and in the surroundings during all the heating treatments. Particularly, temperature measurements were carried out using the equipments described by Rinaldi 2005.
For the pressurized tests, a datalogger system has been used: this is represented by three time-temperature acquisition loggers Pt 1000 (Ebro Electronic GmbH & Co KG, Ingolstadt, Germany), programmed with a PC interface and hermetically fixed by means an adapter on the jar caps. In every tests an acquisition rate of 1 minute has been chosen and in each test both the centre and the surroundings temperatures have been recorded.

Thermal diffusivity determination

Thermal diffusivity values have been calculated by means five different methods, that use alternatively the temperature data or the sample composition.
For methods that use the experimental heat penetration curves, thermal diffusivity calculation has been carried out coupling alternatively centre thermocouple with others. Using surrounding and centre thermocouple we obtain an "apparent" thermal diffusivity because the container material is considered. Using one of the thermocouples inside the container and thermocouple at centre we obtain the "only product" thermal diffusivity value.

Theoretical method
For the theoretical prediction of thermal diffusivity equations proposed by Singh 1993 were used. This method considered food centesimal composition for the calculation of thermal properties at a certain temperature. This method can't be used for the below-zero tests.

Direct measurement
For the thermal diffusivity direct measurement a digital analogical instrument based on the hot wire method has been used (KD2 - Decagon Device Inc. Pullman, Washington, USA). This thermal properties-meter uses a single-needle sensor (length 60 mm, diameter 0.9 mm) to measure the thermal conductivity, thermal diffusivity and thermal resistivity of any medium in a temperature range from 5 to 40°C. The needle has to be insert into the product and after 2 minutes (1.5 minutes are needed for the stabilisation and 0.5 minutes for the measurement) the thermal data are displayed on the lcd screen. Unluckily, also this instrument can't be used for the freezing and thawing tests.

Graphical method
This is the typical approach considering heat penetration curves. Thermal diffusivity was graphically calculated by Ball & Olson (Ball 1957) equation (3).

$$\alpha = \frac{0.398}{\left(\frac{1}{R^2} + \frac{0.427}{h^2}\right) \cdot f_h} \tag{3}$$

Temperature differences between centre and related thermocouple were reported into a semi-log plot, the straight-line portion of the curve was used for thermal diffusivity calculation. Time (minutes), needed to have a logarithmic cycle, represented the f_h value in the Ball & Olson equation.

Taylor's series mathematical method
This method coupled a Taylor's series algorithm (Falcone 1999) for the Fourier's equation with the not linear least square estimation method for the thermal diffusivity calculation.
A visual basic platform for the calculation of the thermal diffusivity has been developed to allow the direct use of ASCII Excel® files. The platform is divided into two parts: the first one for data acquisition and NLLSE matrix building; the second one for temperature modelling and the error function build up for thermal diffusivity calculation. The developed routine models the samples thermal history by varying the thermal diffusivity value inserted in the software with 0.02 mm^2s^{-1} increases. The great limitation of this method is represented by the low customizing possibilities: the software, in fact, doesn't allow to change the Taylor's series resolution. Another great limitation is that's not possible to automate the routine, because the software codex is protected. So, every calculations carried out by means this method is handily made.

Finite difference mathematical method (proposed method)
This method coupled a finite differences solution for the Fourier's equation with the not linear least square estimation method for the thermal diffusivity calculation.
With explicit solving way it's possible to obtain temperature expression at coordinate (M,N) at moment (p+1) depending on its temperature value and temperature near it at previous time. By considering cylindrical coordinates the characteristic equation is:

$$T_{(M,1)}^{(p+1)} = \frac{4\cdot\alpha\cdot\Delta t}{(\Delta r)^2}\cdot T_{(M,2)}^{p} + \frac{\alpha\cdot\Delta t}{(\Delta z)^2}\cdot(T_{(M+1,N)}^{p} + T_{(M-1,N)}^{p}) + \\ + T_{(M,N)}^{p}\cdot\left[1 - \frac{2\cdot\alpha\cdot\Delta t}{(\Delta r)^2} - \frac{2\cdot\alpha\cdot\Delta t}{(\Delta z)^2}\right] \tag{4}$$

The software inputs are the treatment and the desired point heat penetration curve that can be directly open from an ASCII file. By varying the thermal diffusivity value, the software finds the error function minimum and gives the α value that gives the best fitting of the experimental heat penetration curve.

Statistical analysis

Means and standard deviations (SD) were calculated with SPSS (Version 11.5.1, SPSS Inc., Chicago, Illinois, USA) statistical software. SPSS was used to perform one-way-analysis of variance (ANOVA) and Least Significant Difference test (LSD) at a 95 % confidence level ($p \leq 0.05$) to identify differences among groups.

RESULTS AND DISCUSSION

Software development

For the software development the MatLab® programming environment has been chosen and an appropriate interface has been developed (Figure 1).

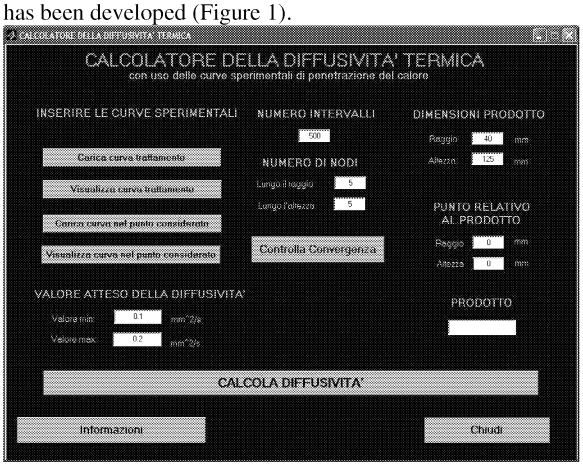

Figure 1: software input interface

The interface allows the user to define all the parameters needed for the thermal diffusivity calculation. Firstly, the user has to define the experimental curves, both the treatment and the sample one. The user has to defined also the number of nodes, both for radius and for height, and the number of intervals in which the treatment time will be divided. All these values will be print onto the final graph. Moreover the user can defined the product type by using a text box that generate a text string that will be print onto the final graph too. In order to reduce the iterations it's also possible to define the upper and the lower thermal diffusivity values that will be used for the calculation. In this way a thermal diffusivity range is obtained. In the developed interface there's also a "push button" that allows to verify that the

function converges; however there's an automatic control that active a dialog window when the function doesn't converge.

Above-zero temperature tests

Tomato-based products
All the considered methods allowed to estimate the "apparent" diffusivity (value that comprehends the container wall thermal diffusivity), but with the graphical method it isn't possible to calculate the "only product" diffusivity. This technique in fact requires a constant treatment temperature and obviously in an internal point we can't have a constant temperature. Moreover, both the proposed method and the Taylor's series one gave not significantly different values but the second one is lowly customizable and it represents a great limitation. In the main, "apparent" values are greater than "only product" ones, because container materials are generally more conductive than a food product.

Starch suspension
For the starch suspension samples results similar to the tomato-based products have been obtained: thus the proposed method allows to estimate both the "apparent" and the "only product" diffusion values even in this case.

Truffle sauce
In Table 1, the truffle sauce values are reported.

glass jar 66.8 x 85.5				
Treatment		**Ball and Olson**	**Proposed method**	**SIMULA + NLLSE**
pressure-cooker	100°C	0.151^{a} (0.002)	0.165^{b} (0.006)	0.167^{b} (0.005)
	113°C	0.147^{a} (0.002)	0.183^{b} (0.002)	0.180^{b} (0.003)
vertical retort	119°C	0.145^{a} (0.001)	0.139^{a} (0.005)	0.141^{a} (0.004)
	125°C	0.137^{a} (0.002)	0.139^{a} (0.001)	0.148^{b} (0.003)
glass jar 56.7 x 61.5				
pressure-cooker	100°C	0.137^{a} (0.001)	0.164^{b} (0.006)	0.174^{c} (0.005)
	113°C	0.150^{a} (0.004)	0.166^{b} (0.005)	0.168^{b} (0.005)

Table 1. Truffle sauce thermal diffusivity

As shown, the "apparent" thermal diffusivity values of the truffle sauce varied with the treatment type and with the container size, this is probably due to the surface heat coefficients that are different for each treatment plant and for each jar size. By using the thermal diffusivity obtained by means the proposed method, it's possible to have good heat penetration simulations (not shown).

Below-zero temperature tests

Tomato-based products
As reported by other authors (Jaramillo-Flores 2000), thermal diffusivity values linearly decrease with the temperature increasing cause of the difference between the ice and water thermal conductivity.

Spinach samples
In Table 2, the spinach thermal diffusivity values obtained by means both the graphical and the proposed method are reported. All these values are to be considered apparent because of the phase transition inside the samples. Only the α values referred to the "external" thermocouple will be reported. Same results have been obtained by considering the "wall" and the "internal" thermocouples

Steps	**Graphical**	**Proposed**
-30°C ÷ -25°C	$0.844^{a} \pm 0.154$	$0.871^{b} \pm 0.067$
-25°C ÷ -20°C	$0.723^{a} \pm 0.138$	$0.751^{b} \pm 0.051$
-20°C ÷ -15°C	$0.602^{a} \pm 0.163$	$0.644^{a} \pm 0.076$
-15°C ÷ -10°C	$0.452^{a} \pm 0.128$	$0.530^{b} \pm 0.041$
-10°C ÷ -5°C	$0.274^{a} \pm 0.143$	$0.381^{b} \pm 0.056$

Table 2. spinach α values

The thermal diffusivities obtained by means the proposed method are quite different compared to the graphical ones, but only the first can be successfully used to model the samples thawing curves. The α values present a linear trend vs. sample temperature, as mentioned above. Unluckily, great variability has been found probably cause of the high fibres content. The samples in fact are not homogeneous and the container filling was very difficult cause of the leaf and fibers presence.

Ice cream
Also for the ice cream samples, the thermal diffusivity presents a linear trend vs. the acquired temperature (Figure 3) with a good correlation coefficient..

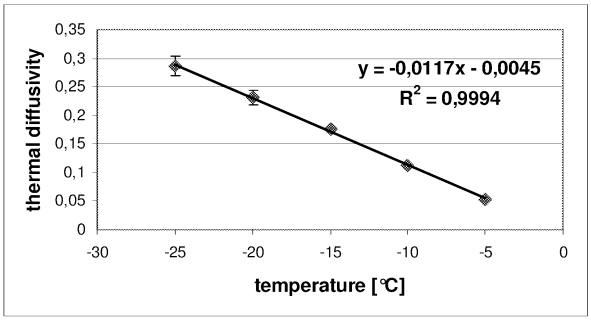

Figure 3: ice cream thermal diffusivity vs temperature

Measure cell development

In order to determine the error on thermal diffusivity calculation due to a wrong positioning evaluation, hypothetical simulations have been carried out. If we consider an ideal thermocouples distance equal to 15 mm, a 1

mm positioning error (6.7%) generates a 13.6% thermal diffusivity error while a 2 mm positioning error (13.4%) generates a 28.2% thermal diffusivity error; that's not acceptable for the thermal process modelling. Same results have been reported by other authors (Benigni 1997).
It's now necessary the development of a sample cell that allows to remove every positioning error; in Figure 4 the proposed measuring cell design is reported. As shown, the experimental apparatus will be made of stainless steel and will allow to reach also relatively high operating pressure thanks to the closing system that presents six bolts and silicon gasket.

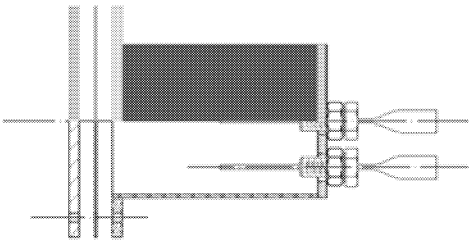

Figure 4. Measuring apparatus design.

In order to avoid any thermocouple positioning error, this measuring cell is designed to be filled in the overturned position. Thus, the temperature probes are connected to a fixed part, and they are not further moved except for maintenance operations. The cell is completely filled from the bottom side, subsequently it is hermetically closed and finally it is turned over and placed in the thermostatic bath. Now the possibly present air can reach a little area near the nipples, eventually after shaking. The cell is in fact designed to ensure a without headspace filling.
The cell should be as symmetrical as possible: the influence of the flange and the cover has been evaluated with simulations by using the software Femlab®. For a metallic container the asymmetry due to the flange and the cover results negligible. Because of thermocouples cables flexibility, rigid supports must be used but in order to avoid any perturbation on heat flux these supports should be made of a thermal insulating material and must be as thin as possible.
Many possible solutions have been compare with the aid of the software Femlab® (Figure 5).

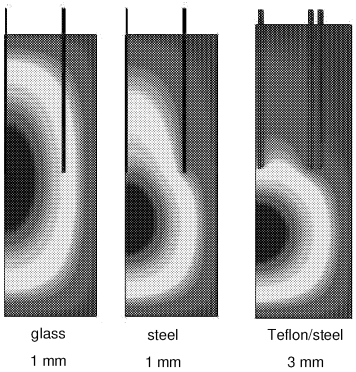

Figure 5. Support materials simulations

Particularly three supports with different thickness, made of steel, glass and steel/Teflon have been considered. As shown, the solution with glass, mainly thanks to the little thickness, is the best. Even if Teflon is an insulating material, it is not enough rigid referred to the thickness required for our aim. So, it's necessary to couple it with a thin steel cover but in this case the heat flux is deeply perturbed. Thus, the material to be choosen is glass with a thickness of 1 mm.

Conclusions

A new fast, easy to use and reliable method for the thermal diffusivity calculation based on the experimental data has been developed. This method allows to overcome the graphical method limits and to estimate the "only product" thermal diffusivity values.
For the method development a software and a mechanical part have been realized and coupled in order to have standard analysis conditions. After preliminary tests the system has been improved: for the computer based part, a user-friendly interface with a complete and clear output page has been developed, while for the mechanical one an appropriate measuring cell has been built in.
The "apparent" and "only product" thermal diffusivity of several commercial products have been successfully calculated. Excellent results have been obtained both for sterilization treatments (generally with constant diffusivity) and freezing-thawing treatments (diffusivity vs. temperature function).

Acknowledgments

Carlo Dall'Asta, Andrea Rossi, Luigi Volgarino and Gabriele Sperandio are acknowledged for technical support and help in prototypes development.

REFERENCES

Ball, C.O.and F.C.W. Olson, 1957. "Sterilization in food technology", McGraw-Hill Book Co., New York.

Benigni, P. and J. Rogez 1997. "High temperature thermal diffusivity measurement by the periodic cylindrical method: The problem of contact thermocouple thermometry". Rev. Sci. Instrument No.68 (7), 2767-2773.

Carciofi, A.M., J. Faistel, M.F. Aragão and J.B. Laurindo, 2002. "Determination of thermal diffusivity of mortadella using actual cooking process data", *Journal of Food Engineering*, No.55(nov), 89-94,.

Falcone, P., M. Anese, C. Severini, R. Massini, 1999. "Extrapolation of lab simulations at the thermic sterilization conditions used in the canned industry". *Industrie Alimentari*, No.38(378), 129-131.

Jaramilo-Flores, M.E. and H. Hernandez-Sanchez, 2000. "Thermal diffusivity of soursop (Annona muricata L.) pulp", *Journal of Food Engineering*,No.46(feb), 139-143,

Rinaldi, M., G. Betta, E. Chiavaro, D. Barbanti, R. Massini, 2005. "Experimental determination of thermal diffusivity using a numerical technique to solve heat transfer equation in heat conductive foods". *Proceedings of EUROTHERM Seminar 77, Heat and Mass Transfer in Food Processing*, Parma, 111-115.

Singh, R.P., 1993. Heat Transfer in Food Processing, in "Introduction of Food Engineering", Academic Press Inc., New York.

AUTHOR LISTING

AUTHOR LISTING

AUTHOR LISTING